UNIVERSITÀ
DEGLI STUDI
DI PADOVA

Head Office: Università degli Studi di Padova

Department of Chemical Sciences

Ph.D. COURSE IN MOLECULAR SCIENCES
CURRICULUM OF CHEMICAL SCIENCES
XXXV SERIES

SPACE MATTERS: CRYSTALLIZATION OF INORGANIC SYSTEMS IN CONFINED SPACES

Coordinator: Prof. Leonard Prins
Supervisor: Prof. Silvia Gross

Ph.D. student: Francesca Tajoli

Abstract

One of the most ambitious aims of a chemist is the development and comprehensive understanding of synthetic approaches to finely control reaction pathways and, ultimately, chemical reactions' outcomes. A promising strategy that has been adopted to pursue this goal is the confinement of reactions within *confined spaces*, *i.e.* enclosed volumes in the nanometer scale range with limited accessibility, employed as nanoreactors. Within this framework, this Ph.D. Thesis investigated differently sized enclosed environments as reactors for the spatially controlled synthesis of inorganic systems, with the aim of evaluating the effects of space confinement on the syntheses outcomes. In particular, different classes of inorganic materials, encompassing metal oxides (MoO_3 and undoped and Eu-doped $CaMoO_4$) and metal nanoparticles (Pd), were synthesized in the increasingly constrained environment of i) a continuous-flow microreactor, ii) nanodroplets produced by inverse (water-in-oil) miniemulsions, and iii) nanopores of mesoporous silica materials. Moreover, the effects of the differently sized confined spaces were evaluated by comparing the constrained synthesis outcomes with those obtained in a macroreactor (batch approach). The systematic and comprehensive experimental approach was supported by a wide array of characterization techniques, from the compositional, structural, dimensional, and functional point of view, exploiting both *ex situ* laboratory techniques and more advanced *in situ* studies, performed at synchrotron facilities in a time-resolved fashion.

Abstract

Uno degli obiettivi più ambiziosi che possa porsi un chimico riguarda lo sviluppo di approcci sintetici che permettano un controllo fine sul meccanismo di una reazione, e quindi sui suoi esiti, e una fondamentale comprensione dei fenomeni ad essa correlati. Una strategia che è risultata promettente per perseguire questo obiettivo risulta essere il confinamento delle reazioni in uno *spazio confinato*, *i.e.* un volume delimitato di dimensione nanometrica con limitata accessibilità, utilizzato quindi come nanoreattore. In questo contesto, in questa Tesi di dottorato sono stati esplorati ambienti confinati di diversa dimensione come reattori per controllare da un punto di vista spaziale la sintesi di sistemi inorganici, con l'obiettivo di valutare gli effetti del confinamento spaziale sugli esiti delle sintesi. In particolare, sono stati sintetizzate diverse classi di materiali inorganici, *i.e.* ossidi metallici (MoO_3 e $CaMoO_4$ puro e drogato con ioni Eu^{3+}) e nanoparticelle metalliche (Pd), in condizioni di confinamento crescente in i) un microreattore in flusso continuo, ii) nanogocce prodotte da miniemulsioni inverse (acqua in olio) e iii) nanopori di silice mesoporosa. Inoltre, gli effetti degli spazi confinati di diversa dimensione sono stati valutati per confronto degli esiti sintetici ottenuti in ambiente confinato con i risultati ottenuti effettuando le sintesi in un macroreattore (approccio di sintesi *batch*), con un approccio sperimentale sistematico ed esaustivo. I materiali ottenuti sono stati caratterizzati in dettaglio attraverso numerose tecniche di caratterizzazione, sia da un punto di vista composizionale, strutturale e dimensionale, che da quello funzionale, utilizzando sia tecniche di caratterizzazione *ex situ* di laboratorio che studi *in situ* più avanzati, effettuati in modo risolto nel tempo impiegando luce di sincrotrone.

List of acronyms

AHM	ammonium heptamolybdate
AR	aspect ratio
ATR	attenuated total reflectance infrared spectroscopy
BET	Brunauer, Emmett, and Teller
BJH	Barrett, Joyner, and Halenda
CM	calcium molybdate
cmc	critical micellar concentration
CNT	classical nucleation theory
CS	confined space
CTAB	cetyltrimethylammonium bromide
DFT	density functional theory
DLS	dynamic light scattering
DLVO	Derjaguin, Landau, Verwey, and Overbeek
DRS	diffuse reflectance spectroscopy
EDL	electrical double layer
EDX	energy dispersive X-ray spectroscopy
EXAFS	extended X-ray absorption fine structure
FT	Fourier transform
FWHM	full width at half maximum
HLB	hydrophilic-lipophilic balance
ICP-MS	inductively coupled plasma mass spectrometry
i.d.	internal diameter
IR	infrared
IS	iron sulfides
IUPAC	international union of pure and applied chemistry
IWI	incipient wetness impregnation
LCA/LCF	linear combination analysis/fitting

MCR-ALS	multivariate curve resolution – alternating least square
µE	microemulsion
ME	miniemulsion
mE	macroemulsion
MFC	mass flow controller
MO	molybdenum oxide
MS	mass spectrometry
NCC	non-classical crystallization
NMR	nuclear magnetic resonance
NP	nanoparticle
OA	oriented attachment
o.d.	outer diameter
OR	Ostwald ripening
PCA	principal component analysis
PDF	powder diffraction file
PDI	polydispersity index
PEO	polyethylene oxide
PGM	platinum group metal
PMO	periodic mesoporous organosilica
PPO	polypropylene oxide
PTFE	polytetrafluoroethylene
rpm	revolutions per minute
SAXS	small angle X-ray scattering
SDA	structure directing agent
SEM	scanning electron microscopy
SERS	surface enhanced Raman spectroscopy
SSA	specific surface area
STEM	scanning transmission electron microscopy
TEM	transmission electron microscopy
TEOS	tetraethylorthosilica
th.	thickness
TMOS	tetramethylorthosilica
TPR	temperature programmed reduction

US	ultrasound
UV	ultraviolet
WAXS	wide angle X-ray scattering
WHSV	weight hourly space velocity
WPPF	whole powder pattern fitting
XAFS	X-ray absorption fine structure
XANES	X-ray absorption near-edge structure
XAS	X-ray absorption spectroscopy
XRD	X-ray diffraction

Table of contents

1

Introduction

The development and comprehensive understanding of synthetic approaches to precisely control reaction pathways, and thus chemical reaction outcomes, is one of the most ambitious aims of a chemist. A promising methodology that has been adopted to pursue this goal is the confinement of the reaction within confined spaces, defined as enclosed nanoscale volumes with limited accessibility.[1] They are represented by nanoscale hosts, employed as nanoreactors. Confined space represents a fascinating playground for the spatially and phase-controlled formation of a variety of chemical systems, ranging from molecules to drugs, extended networks, polymers, and ending to inorganic nanostructures.[1–4] Indeed, both experimental and computational studies evidenced that downsizing the available spatial volume to the nanoscale can affect the physical properties of molecules, *e.g.* the phase behavior, dielectric constant, density and anisotropic orientational dynamics of dipoles of confined water,[5,6] as well as the underlying mechanisms and thermodynamics of the subsequent chemical transformations occurring within these enclosed volumes. However, despite it is well known that constrained environment plays a crucial role on the outcomes of the syntheses that are performed within it, the understanding of its effect is far from being complete.

Among nanoscale hosts, two classes can currently be actually considered as "nanoreactors", in which reactions take place in a parallel fashion: *miniemulsion droplets* and *porous inorganic materials*.[7] Indeed, both miniemulsion droplets and pores of mesoporous inorganic materials can be exploited as independent and separated nano-compartments, due to the special features of the former with respect to microemulsions (*vide infra*) and the solid nature of the latter, not affected by dynamic restructuration problems.

Miniemulsions are a special class of emulsions, prepared by high-shear treatments (*e.g.* by high power ultrasounds) of a mixture of two immiscible phases, a surfactant and an additive that is soluble only into the dispersed phase. The nanodroplets produced by miniemulsion (diameter of 30-500 nm) are critically stabilized towards collisions by the surfactant and stabilized towards Ostwald ripening by the employed additives, and are therefore considered to be independent of each other, as there is no inter-droplet reactant exchange and they maintain their identity on a scale of days to months.[8] This particular feature of miniemulsion droplets is one of the most important differences between micro- and miniemulsions, as microemulsion droplets (d < 100 nm) are highly dynamic and cannot be established to be "nanoreactors" in the strict sense.[7]

Mesoporous inorganic materials, such as zeolites or mesoporous silica, are materials containing an ordered system of pores with diameters between 2 and 50 nm,[9] usually easily tuned by varying their synthetic conditions. They can be exploited as nanostructured confinements restricting the reaction to the inside of the pore systems, thus implying a heterogeneous processing of the synthesis, with the related transport limitations.

Within this framework, the main objective of this Ph.D. Thesis is the experimental investigation of the nucleation and growth of selected model inorganic systems, encompassing metal nanoparticles and metal oxides, in the confined spaces of nanodroplets produced by miniemulsion and nanopores of mesoporous frameworks. In addition, a related aim is the eventual rationalization of how and to what extent constrained environments affect the crystallization of the studied inorganic materials, by thoroughly compare confined space synthetic outcomes with those obtained employing a macroreactor. Moreover, as a link between the total absence of space constrain that characterizes macroreactors (batch approach) and the highly confined volume of nanoreactors (miniemulsion droplets and mesopores), a continuous-flow microreactor (microfluidic approach), whose dimensions are in between the former two, is also addressed. Indeed, even if it could not be termed "confined space" in a strict sense, a microfluidic reactor manipulates and controls fluids that are geometrically constrained within environments having internal dimensions on a scale of micrometres, thus it displays intrinsic advantages associated to the scale-dependent process of heat and mass transfer. Indeed, the microfluidic approach allows a high reaction control, due to the efficient mixing of reactants and the high surface-to-volume ratio, which enables the minimization of concentration and thermal gradients.[10,11] A schematic representation of the reaction

environments employed in this Ph.D Thesis, differing both in size and in the nature of the confining environment (*i.e.* liquid/liquid or solid/liquid interface), is shown in Figure 1.1.

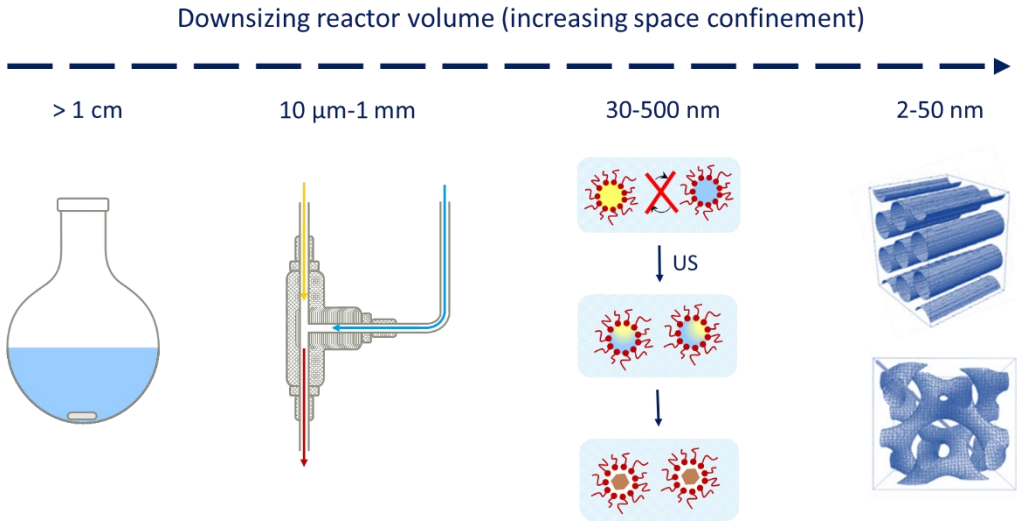

Figure 1.1 Schematic representation of the synthetic approaches investigated in this Ph.D. Thesis, encompassing different space constraint conditions. From left to right, increasing space confinement: batch (macroreactor) approach (size > 1 cm), continuous-flow microreactor (microfluidic approach) (size 10 µm-1 mm), water-in-oil nanodroplets produced by miniemulsion (size 30-500 nm), nanopores of mesoporous materials (size 2-50 nm)

This Ph.D. Thesis is organized in seven chapters. In particular, the current Chapter 1 outlines the theoretical background underlying the experimental work performed, presenting the main aspects in its subsections. In particular, Chapter 1.1 describes classical and non-classical crystallization models, as well as crystallization in space confinement; Chapter 1.2 focuses on the employed synthetic approaches, encompassing different space constraint conditions, *i.e.* nanodroplets produced by miniemulsion, continuous-flow microreactors, and nanopores of mesoporous materials; Chapter 1.3 provides an overview about the potentialities of *in situ* combined and simultaneous synchrotron-based techniques to probe crystallization in a time-resolved fashion. The experimental results of the synthesis and characterization of the inorganic systems investigated in this Ph.D. Thesis are presented in detail in Chapter 2, Chapter 3, and Chapter 4, focused on molybdenum oxide, undoped and Eu-doped calcium molybdate, and palladium nanoparticles supported on mesoporous silica, respectively. In order to evaluate the effects of space confinement, the synthetic outcomes of different confined environments are discussed and compared with reference batch samples, synthesized without any space constraint. Chapter 5 draws conclusions of the Thesis, highlighting the obtained results as well as the perspectives disclosed by this work.

Experimental details of the experimental work are collected in Chapter 6, while the details of the employed characterization methods and the basics aspects of the less common ones are presented in Chapter 7. Finally, in the Appendix, a case study presenting a time-resolved *in situ* XAS investigation of the evolution of iron species over the course the miniemulsion and batch synthesis of iron sulfides, and supplementary graphics and tables of the experimental results are reported.

1.1 Crystallization of inorganic materials

In this Section, a general overview of the theoretical principles of crystallization, according to both classical and non-classical models, is presented, outlining the limitations of the classical theory and the current challenges in understanding the complexity of the crystallization process. The LaMer model for the formation of monodispersed particles is then described, and a discussion on how space confinement affects the main outcomes of crystallization is provided.

1.1.1 Classical crystallization

Crystallization – the formation of solid crystalline[i] particles – is one of the most studied and most fascinating scientific topics. Its understanding is also of great practical significance, since the crystal structure, shape and texture of crystals are known to dictate important physicochemical properties of materials, such as electronic, magnetic and catalytic ones.[12–15]

The thermodynamic driving force for crystallization is supersaturation, S,[16] defined as a dimensionless ratio of the actual concentration of the species in solution, c, divided by its equilibrium molecular solubility product, k_{sp}, under the given set of conditions:[ii]

$$S = \frac{c}{k_{sp}} \tag{1.1}$$

The change in chemical potential during crystallization process, $\Delta\mu$, is related to the supersaturation by the following equation:

$$\Delta\mu = -kTlnS \tag{1.2}$$

where k is the Boltzmann constant and T is the absolute temperature. It follows that supersaturated solutions can be easily obtained by a temperature or pressure variation,

[i] A crystal is a solid constructed by the 3D highly ordered, infinite and periodic repetition of identical building blocks (*e.g.* atoms, ions, molecules). The smallest repeating unit of the crystal is its unit cell.
[ii] It is worth noting that the definition of supersaturation assumes the structure of the final precipitate, *i.e.* when different polymorphs are taken into account, the same concentration of the solute can mean different supersaturations depending on which species is precipitated, as different crystalline polymorphs – and also amorphous matter – may have different solubilities. This differences in supersaturation can be exploited as a tool for polymorph control.

exploiting reactions generating the respective insoluble species or adding non-solvents to the mixture.

Generally, and as described in more detail in the following, the crystallization process from a supersaturated solution encompasses three steps: i) nucleation, *i.e.* the formation of the first crystallization seeds, *i.e.* the nuclei, which can be either homogeneous (spontaneous) or heterogeneous (induced by foreign particles), ii) growth, typically by deposition and attachment of further material on the formed nuclei, and iii) aggregation, coalescence or ripening.

I. Nucleation. Many models have been proposed for explaining the phenomenon of nucleation, starting from the beginning of the past century. The most popular, yet sometimes quite simplistic, nucleation model is the *classical nucleation theory* (CNT), a concept derived in the 1930s by Becker and Döring,[17] and whose mathematical foundation was developed in the late 19th century by Gibbs.[18] The classical nucleation theory is a thermodynamic-based model for nucleation that assumes the spontaneous (*homogeneous*) formation of nuclei in a supersaturated solution, as a consequence of stochastic microscopic fluctuations of density on microscopic length scales, that occur by random collisions of the dissolved constituents.[19] It defines the free energy change of the particle formation as the sum of the free energy changes for the formation of a new surface ΔG_A and of the bulk crystal ΔG_V as follows:

$$\Delta G = \Delta G_A + \Delta G_V = 4\pi r^2\gamma + \frac{4}{3}\pi r^3 \Delta G_v \quad (1.3)$$

where r is the radius of the nucleus, which is assumed to be spherical, γ is the free energy of the surface per unit area, *i.e.* the interfacial tension between the supersaturated solution and the nucleus solid surface, and ΔG_v is the free energy difference for the transition from solution to solid particle per unit volume. ΔG_v is negative in supersaturated solutions and its absolute value is equal to:

$$|\Delta G_v| = kT\frac{lnS}{v} \quad (1.4)$$

where S is the supersaturation defined in Equation 1.1, k is the Boltzmann constant, T is the temperature and v is the volume of the nucleus.

The graphical illustration of the free energy profile of a growing nucleus as a function of its radius r, as well as of its single contributions of the favorable bulk free energy (ΔG_V) and the surface free energy penalty (ΔG_A) is reported in Figure 1.2. Because the bulk and surface free energy contributions scale with the cube and the square of the radius of the nucleus, respectively, ΔG_V begins to balance the energetic costs of the generation of a phase interface (ΔG_A) when the radius of the nuclei is equal to the *critical radius of the nucleus* r_{crit}, which is the value of nuclei radius corresponding to the maximum value of ΔG (*i.e.* the energy barrier that a nucleation process must overcome). The critical nucleus is the smallest crystalline unit capable of continue further growth: smaller nuclei are thermodynamically unstable and would dissolve again, while bigger ones will continue to grow. In both cases the driving force is a decrease of the critical nucleation energy.[19,20]

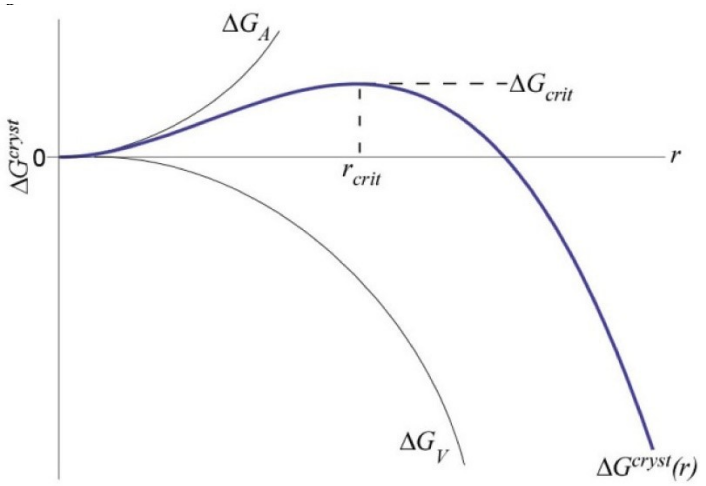

Figure 1.2 Free energy versus radius of nuclei in classical nucleation theory. The bulk (ΔG_V) and the surface (ΔG_A) free energies scale with the cube and square of the radius, respectively. Thus, their sum (ΔG^{cryst}) shows a maximum when the energetically unfavorable surface generation starts to get balanced by the bulk energy at the critical nucleus size (r_{crit}). Reprinted from Hamilton *et al.*[70] with permission of the American Chemical Society

By differentiating and equating to zero Equation 1.3, the critical nucleus size and the critical nucleation energy (*i.e.* the thermodynamic barrier for nucleation) can be calculated as:

$$r_{crit} = -\frac{2\gamma}{\Delta G_v} \tag{1.5}$$

$$\Delta G_{crit} = \frac{16\pi\gamma^3}{3(\Delta G_v)^2} = \frac{4\pi}{3} {r_{crit}}^2 \tag{1.6}$$

The classical homogeneous nucleation (or barrier-crossing) rate J, *i.e.* the number of nuclei formed per unit of time and unit of volume, can be expressed in the form of the Arrhenius

reaction velocity equation; substituting in it ΔG_{crit} (Equation 1.6) and ΔG_v (Equation 1.4) gives the final expression for the nucleation rate J:

$$J = A \cdot exp\left[-{\Delta G_{crit}}/{kT}\right] = A \cdot exp\left[-{16\pi\gamma^3 v^2}/{3k^3T^3(lnS)^2}\right] \qquad (1.7)$$

From Equation 1.7, it follows that the nucleation rate can be tuned by varying three experimentally controllable parameters: the supersaturation level S, the temperature T and the surface free energy γ, that can be adjusted employing different surfactants or additives in the reaction mixture. Theoretical studies demonstrated that the nucleation rate is extremely sensitive to the supersaturation level: it was calculated to increase by about 10^{70} times when the supersaturation level is increased from 2 to 4 for the synthesis of CdSe.[21]

When the nucleation is induced by foreign particles, the process is termed *heterogeneous nucleation*. Heterogeneous nucleation may occur in very clean solutions along surfaces and interfaces, *e.g.* the container wall, or on gas bubbles or on solid impurities, such as dust. It is always energetically more favorable than homogeneous nucleation, as the interface energy if the nucleus being formed with the substrate is lower than the corresponding one in impurity-free solution. When impurities or seeds are chemically similar to the nucleus being formed, this is especially favored.[iii] This concept is exploited in the so-called *seeded-growth approach*,[22] where seeds are specifically introduced in the reaction mixture to trigger nucleation (not detailed in this Thesis).

II. Growth. The classical model of crystallization addresses the growth stage as a diffusion-controlled amplification process in which stable nuclei are simply enlarged by a replication

[iii] Even if favorable seeds are present in the reaction mixture, it is worth pointing out that nucleation events usually occur through different processes at the same time, controlled by crystallization kinetics. Indeed, the area of the container surface and/or of foreign particles is usually smaller than the effective homogeneous seeds: at high supersaturation the homogeneous nucleation will be the prevailing process, while at low supersaturation the heterogeneous nucleation will be dominant. Moreover, from a practical point of view, sometimes even heterogeneous nucleation might be not easy to achieve, and on the other hand it can be effectively suppressed if desired. Indeed, it is worth noting that, in order to be soluble, the cohesion energy or polarity of molecules must be not too different from each other, and consequently the interface tension between crystals and the mother liquor is usually quite low. Thus, nucleation cannot be promoted by impurities or containers with significantly different cohesion energies from the solute, and, remarkably, heterogeneous nucleation might be even harder to obtain than homogeneous nucleation. As a consequence, the choice of an appropriate surface for the reaction vessel can play a role on controlling the relative kinetic of the nucleation processes. For example, when aqueous solutions are taken into account, non-nucleating surfaces are hydrophobic polypropylene or Teflon vessels.[16]

of the unit-cell without being subjected to structural changes at the surface or in the bulk.[23] In particular, as originally suggested by Volmer,[24] the initially formed nuclei are supposed to grow *via* layer-by-layer adsorption of solute atoms, ions or molecular building blocks onto an existing crystal face. The growth unit is not immediately integrated into the crystal lattice, but it loosely adsorbs to the surface and is able to migrate on the crystal surface in two dimensions, until it connects to an "active center" (*i.e.* steps and kinks). The attachment of further atoms/ions to the steps and kinks completes the surface growth, and a new layer is formed by surface nucleation. A schematic representation of the ideal layer-by-layer growth is shown in Figure 1.3.

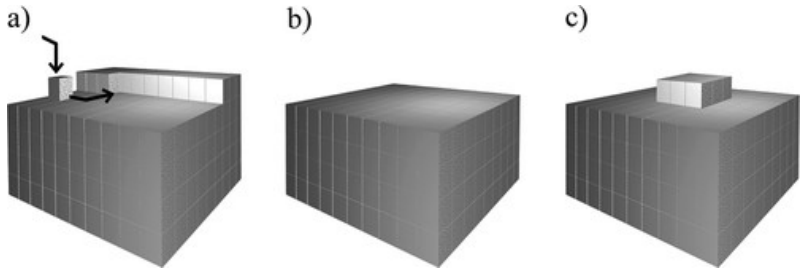

Figure 1.3 Schematic representation of ideal layer-by-layer crystal growth: migration of a unit toward a kink on the surface (**a**), completed layer (**b**), and surface nucleation (**c**). Reprinted from Meldrum *et al.*[23] with permission of the American Chemical Society

III. Aggregation and ripening. After the nucleation and growth stages of particle formation, the dimension of the obtained (nano)particles, if not effectively stabilized, may further evolve by Ostwald ripening (OR) and/or coalescence phenomena.[25,26] Ostwald ripening occurs when smaller solid particles dispersed in their own saturated solution dissolve and subsequently deposit on larger solid particles, as a consequence of the difference in their chemical potentials (see Chapter 1.2.1.1).[27] On the other hand, coalescence involves the collision and fusion of two or more particles and the disappearance of the boundary between them, to form a single larger one.[9] The driving force for both processes is the reduction of the surface free energy of the particles, achieved reducing the extension of the interfacial area, and they can occur through particles collision caused by Brownian motion and consequent interparticle attractive interaction.

The particle-particle interaction, possibly leading to their aggregation and coalescence, is conventionally understood employing the DLVO theory of colloidal stability, named after B. Derjaguin, L. Landau, E. Verwey, and T. Overbeek.[28–30] The DLVO theory quantitatively describes the force between charged surfaces interacting through a liquid medium,

combining the effects of the van der Waals attraction and the electrostatic repulsion due to the double layer of counterions surrounding the suspended particles. In particular, the electrostatic stabilization is governed by the thickness of the electrical double layer (EDL) around the particles, *i.e.* the Debye length κ^{-1}, that defines the extent to which the ionic atmosphere, differing from the bulk ionic medium, extends from the particle surface and that can be calculated as:

$$\kappa^{-1} = \sqrt{\varepsilon kT / 2e^2 I} \tag{1.8}$$

where ε is the relative permittivity (or dielectric constant) of the medium, k is the Boltzmann constant, T is the absolute temperature, e is the elementary charge, and I is the ionic strength of the medium.

From Equation 1.8, it follows that the aggregation of particles is ultimately influenced by the ionic strength and by the dielectric constant of the medium, as their electrostatic stabilization is higher (*i.e.* the EDL thickness is larger) when the medium their suspended into is more polar (*i.e.* higher dielectric constant) and with lower concentration of electrolytes (*i.e.* lower ionic strength).

Another common and effective approach for providing stabilization to particles suspended in a liquid medium against aggregation and coalescence is the employment of surfactants and/or ligand, that typically adsorb on the particles surface and generate steric stabilization. The role of surfactants in steric stabilization of colloidal systems is discussed in Chapter 1.2.1.1, with particular reference to emulsions.

1.1.2 Non-classical crystallization

Although the classical nucleation theory (CNT) is the one of the most commonly used formalism to analyze and rationalize nucleation phenomena, and it still represents the main framework for the understanding of nucleation phenomena, a number of phenomena or experimental findings associated with crystal formation cannot be satisfactory be explained or be predicted by it. For example, the experimental observations of the proceeding of nucleation in solution through intermediate (possibly amorphous) stages before reaching a thermodynamically stable phase, or the occurrence of irregular and branched crystal morphologies. In addition, classical nucleation theory fails in providing a reliable and sound understanding of several features of the experimentally measured kinetic curves of many systems, such as for instance nucleation rates, which are orders of magnitude lower than the classical prediction. Big deviations between classical nucleation theories and experimental findings indicate that the real crystallization scenario is more complicated than the one hypothesized by the CNT, based on several approximations and assumptions,[31] and many models were proposed to capture the complexity at molecular level of the events occurring during nucleation and growth.

For example, the assumption of CNT that an ordered nucleus is formed directly in solution, *i.e.* clustering and reorganization to the new phase occur simultaneously and the solution-to-crystal transformation occurs as a simultaneous modification of both density and crystallinity parameters (pathway outlined by a black arrow in Figure 1.4), was contradicted by experimental evidences of nucleation events, that showed a sequential path of i) formation of cluster with a higher density and ii) its structural reorganization to form a crystal. This scenario, called *two-step mechanism*,[32,33] assumes that the first step of nucleation is the formation of droplets of dense liquid with little or no spatial order (*clusters*) by density fluctuations, and then the local density remains constant while structural ordering of molecules or atoms/ions occurs and form the crystal nucleus. A schematic representation of the two-step mechanism is reported in Figure 1.4, following the pathway outlined by red arrows. A similar, although not totally coinciding, mechanism of nucleation is the *pre-nucleation cluster* model,[19,34,35] that predicts the formation of thermodynamically stable and highly dynamic solutes that coexist with ions in a single-phase system and are

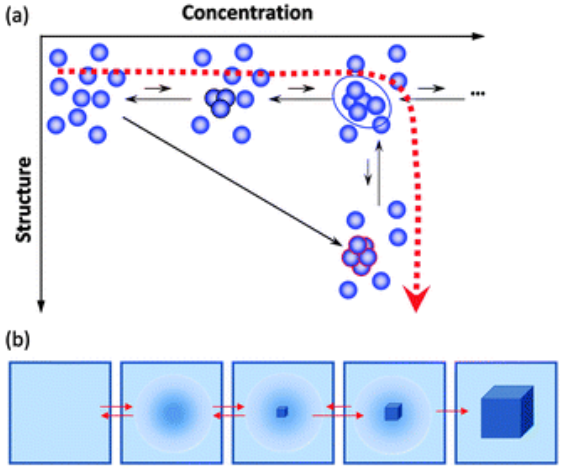

Figure 1.4 Schematic illustration of the single step (black arrow) and two-step (red arrows) mechanism of nucleation of crystals, in the Concentration *vs* Structure plane from a microscopic viewpoint (**a**) and from a macroscopic viewpoint (**b**) for the events along dashed red line in (a). Reprinted from Vekilov[32] with permission of the Royal Society of Chemistry

the molecular precursors to the phase nucleating from solution (*i.e.* pre-nucleation clusters)[iv] and subsequently precipitate in the process of phase separation.

Moreover, the classical crystallization model, that describes a layer-by-layer growth of crystals involving atoms, ions or molecular building blocks, typically fails to describe the formation of complex and/or irregular crystal morphologies. Thus, in recent years, different pathways of non-classical particle-mediated growth, involving larger building blocks, such as droplets, complexes, clusters, oligomers, or nanoparticles, whether crystalline, amorphous or liquid, were proposed to explain experimental observations. These crystallization strategies (*i.e. non-classical crystallization (NCC)* pathways) are schematically represented in Figure 1.5, b-d. They encompass i) oriented aggregation, ii) mesocrystals formation, and iii) crystallization via liquid droplets or amorphous precursors phases.[16,36,37] Indeed, along with the classical diffusion-controlled model of crystal growth by addition of monomeric species (pathway a in Figure 1.5), the nanocrystals (primary particles) can aggregate in crystallographic register into a superstructure of iso-oriented nanoparticles by

[iv] Pre-nucleation clusters differ from the dense liquid predicted by the two-step mechanism from a thermodynamic point of view: prenucleation clusters are thermodynamically stable *solutes*, and the energy barrier separating the state of pre-nucleation clusters and the state of free ions is negligible compared to the thermal energy. On the other hand, dense liquid of the two-step model is a *metastable phase* that has been nucleated, and the formation of the crystal occurs *via* structural transitions within the dense liquid.[19]

oriented aggregation (pathway b in Figure 1.5).[v] These oriented meso-assembled primary particles can fuse together into a single crystal by the process of *oriented attachment* (OA). The self-assembly in crystallographic register by oriented aggregation of nanoparticles weakly stabilized by organic moieties can lead also to the formation of a *mesocrystal*,[vi] with

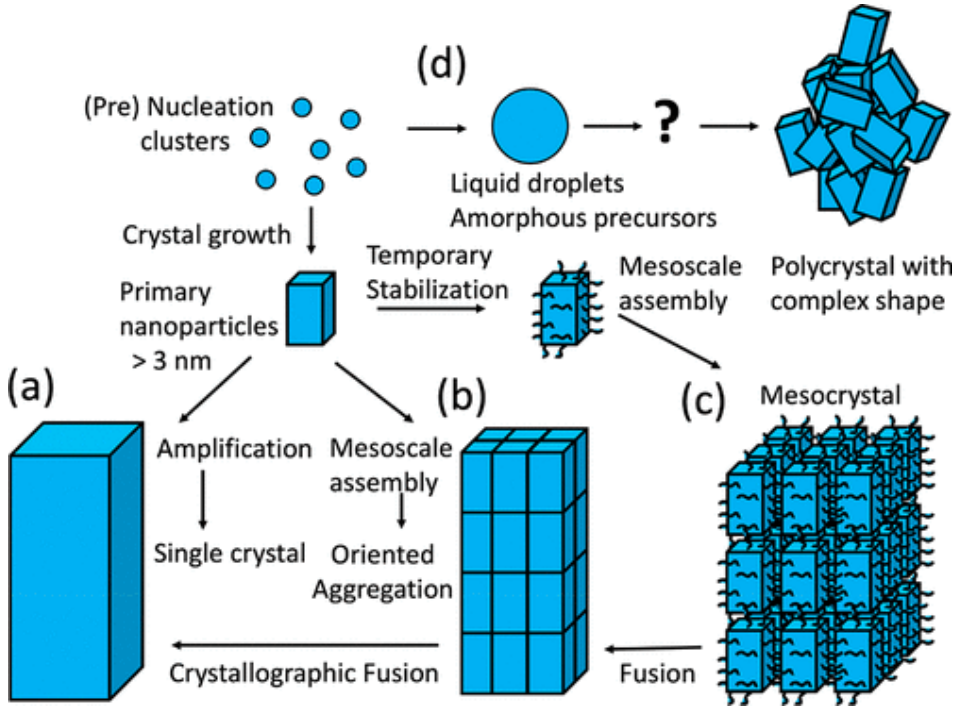

Figure 1.5 Schematic representation of classical and nonclassical crystallization. Classical crystallization pathway involving layer-by-layer growth by atom/ion/molecule addition (**a**); oriented aggregation of primary nanoparticles forming an iso-oriented crystal (**b**); mesocrystal formation via self-assembly of primary nanoparticles covered with organics (**c**); and crystallization via liquid droplets or amorphous precursor phases (**d**). Pathways involving clusters, complexes or oligomers are not shown for simplification. Nanoparticles are drawn to the same size for clarity reasons. Reprinted from Jehannin *et al.*[36], with permission of the American Chemical Society

[v] It is worth noticing that the classical DLVO theory for understanding particle-particle interactions is unable to predict the orientation dependence of nanoparticle growth *via* oriented aggregation or attachment; this can be partly ascribed to forces not accounted by the DLVO theory, such as solvation, and Coulombic interactions between interacting particles. Indeed, Coulombic and Lewis acid/base interactions between inorganic particles predominate over van der Waals interactions and random Brownian forces, thus leading the interacting particles to find a crystallographic orientation that is energetically favorable for attachment.[42,418–420]

[vi] The term *mesocrystal* is an abbreviation for "mesoscopically structured crystal", and it refers to a superstructure of crystalline nanoparticles aligned in a common crystallographic fashion, with external crystal faces on the scale of some hundreds of nanometers to micrometers, and exhibiting scattering properties similar to a single crystal. The term has also been used in the less restricted sense of a mutual three-dimensional translational order of various nanocrystals.[37] The mosaic structure shown in Figure 1.5,b could also be termed as mesocrystal, as long as the individual nanoparticles are distinguishable.

nanoparticles spatially separated and oriented in a common crystallographic register (pathway c in Figure 1.5). By fusion of the primary nanoparticles and oriented attachment, mesocrystals can convert themselves to single crystals. Finally, another nonclassical crystallization pathway consists in the transformation of *liquid droplets* or a*morphous or sacrificial precursor* phases (pathway d in Figure 1.5), that can occur through multiple pathways, involving distinct pre-crystalline entities.[36] In addition to the possibility of following different mechanisms, the crystallization processes can be multicomponent in nature (*e.g.* with the presence and/or incorporation of solute clusters, droplets, gels, or amorphous or crystalline particles)[38] and also multistep: combinations of the above mentioned pathways are also possible and have been reported in literature.[36,39–41] Moreover, the dominance of one or another pathway in the same system under selected conditions was observed as well, and the probability of a direct or indirect pathway is difficult to predict with the present understanding of crystallization, since a major hurdle in the theoretical treatments is also posed by complicated kinetics and various factors governing the formation of metastable clusters.[20]

Finally, it is worth noting that, despite the wide structural diversity of the building blocks involved in non-classical crystallization pathways, the key features of many of them can be understood by considering the interplay of free-energy landscapes and reaction dynamics, as shown in Figure 1.6.[42] In particular, the thermodynamic preference for the structure, shape and size distribution of the particles at different assembly stages is determined by the free-energy landscapes. On the other hand, whether the thermodynamically preferred pathway or an alternate kinetically controlled one are followed is determined by dynamic processes, such as monomer and particle diffusion. Indeed, a simple pathway entailing monomer-by-monomer addition to incipient nuclei displaying a single structure (Figure *1.6*, A) can occur as predicted by the classical crystallization model, as well as by more complex ones, involving intermediate metastable particles that may be structurally distinct from the final thermodynamically stable phase (Figure 1.6, B and C). This is the case of the pathway commonly referred to as the Ostwald's step rule[43] (*vide infra*). When the free energy landscape of the system is not characterized by local minima, from a thermodynamic point of view the system should prefer to grow as one large particle: particle-based pathways (Figure 1.6, D) can only occur for dynamic reasons, affecting for example attachment on specific facets in the case of hierarchical pathways of growth by oriented attachment. On the other hand, if local minima are exhibited by the free energy landscape,

dynamics issues can cause the formation of long-lived thermodynamically metastable or non-equilibrium materials, *e.g.* gels (Figure 1.6, E).

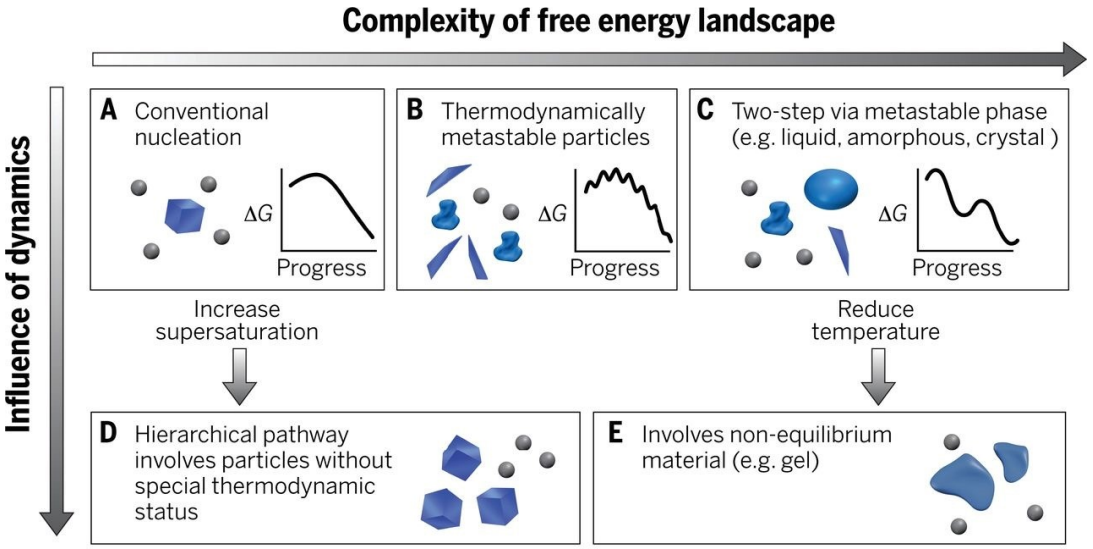

Figure 1.6 Schematic representation of the possible pathways by which monomers form a stable bulk crystal, and the physical mechanisms that give rise to them, with a thermodynamic (A, B and C) or kinetic (D and E) origin. Classical monomer-by-monomer addition (**A**); aggregation of metastable particles (**B**), such as liquid, amorphous, or poorly crystalline particles, or of oriented attachment of metastable nanocrystals; crystallization *via* the formation of a metastable bulk phase (**C**), such as a liquid or solid polymorph; kinetically dominated aggregation of clusters or oligomers (**D**); aggregation of unstable particles whose internal structures are not those of equilibrium phases (**E**). Reproduced from De Yoreo *et al.*[42]

Ostwald's step rule. As mentioned, modern experimental techniques have shown that the nucleation process in solution crystallization commonly proceeds through intermediate stages before reaching a thermodynamically stable phase. Indeed, when the crystallization is kinetically controlled, it cannot be described as a single-step thermodynamically-driven pathway, but rather as a sequential process involving structural and compositional modifications of amorphous precursors and crystalline intermediates, as shown in Figure 1.7.[44] These phase transformations proceed along a series of increasingly more stable intermediates, and the final product is dependent on the solubilities of the species and on the free energies of activation of their interconversions, that can be influenced by the presence of additives. The structural and compositional modifications of the species usually occur through processes of dissolution and re-nucleation, that are closely associated with the surface and/or the interior of pre-formed particles, or through aggregation, solid-phase transformation or other mesoscopic transformations. Thus, the nucleation of a specific

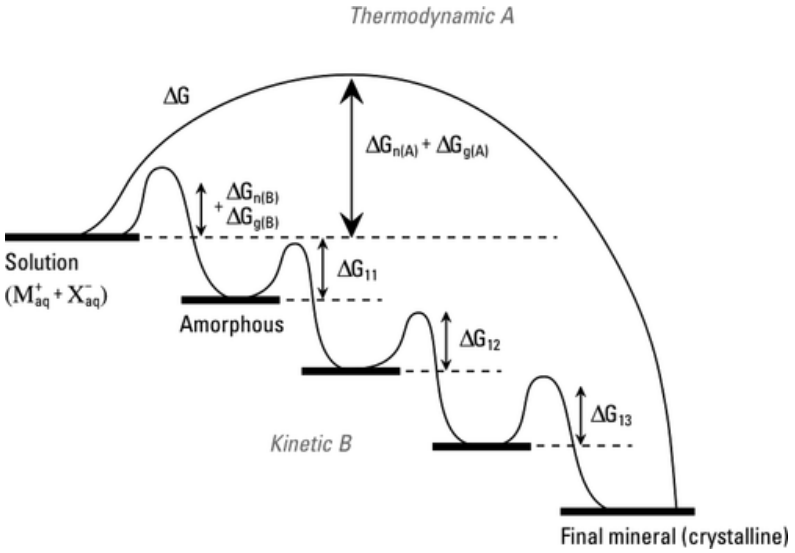

Figure 1.7 Simplified scheme of the crystallization pathways under thermodynamic (**A**) and kinetic (**B**) control. Whether a system follows a one-step route to the final mineral phase (pathway A) or proceeds by sequential precipitation (pathway B) depends on the free energy of activation associated with nucleation (n) and growth (g). Reprinted from Cölfen *et al.*[45] with permission of Wiley

crystalline phase is a highly heterogeneous process, dependent on reaction kinetics, but also on interfacial and hydrodynamic properties.[23,45] For these reasons, the classical model of nucleation, based on a thermodynamic treatment, as described in Chapter 1.1.1, cannot described this process.

This stepwise kinetically controlled process, that defined as "kinetic cascade", is a manifestation of W. *Ostwald's rule of stages*, that allows an empirical prediction of the sequence of phases formed during a crystallization event.[27,43] The initial phases usually involved in kinetically driven crystallization are the least dense ones, and they may be non-stoichiometric, hydrated amorphous phases, that are susceptible to rapid phase transformations to denser phases, until the most dense one (*i.e.* the most stable one) is formed. Indeed, this kinetic sequence follows the order of increasing thermodynamic stability.[23] The most common example of crystallization ruled by kinetics reported in literature is amorphous calcium carbonate, which is highly soluble and, unless kinetically stabilized with ions such as Mg^{2+} and PO_4^{3-}, readily transforms into calcite, vaterite or aragonite.[23,41,44,45]

1.1.3 LaMer model for particle formation

The most acknowledged model for particle formation, albeit underlain by the classical nucleation theory (*i.e.* atom/ion-mediated), was postulated by LaMer and Dinegar in their pioneering work of 1950.[46,47] In particular, the LaMer model for homogeneous nucleation describes the evolution of the solute concentration over the course of time during particle formation, shown in Figure 1.8, and it identifies the above described individual and separated stages of i) formation of supersatured solution, ii) nucleation, and iii) growth.[vii] Indeed, according to the LaMer model for homogeneous nucleation, an initial growth of solute concentration over its solubility limit leads to the formation of a metastable state of supersaturation, which is followed by the nucleation event, that occurs with an effectively infinite rate ("burst nucleation") and consists in the formation of a massive amount of small individual nuclei in a very short time frame, relaxing the supersaturation conditions, lowering the solute concentration below the nucleation threshold and ceasing further nucleation. Subsequently, a diffusion-controlled growth occurs, until the saturation concentration of the solute is reached.

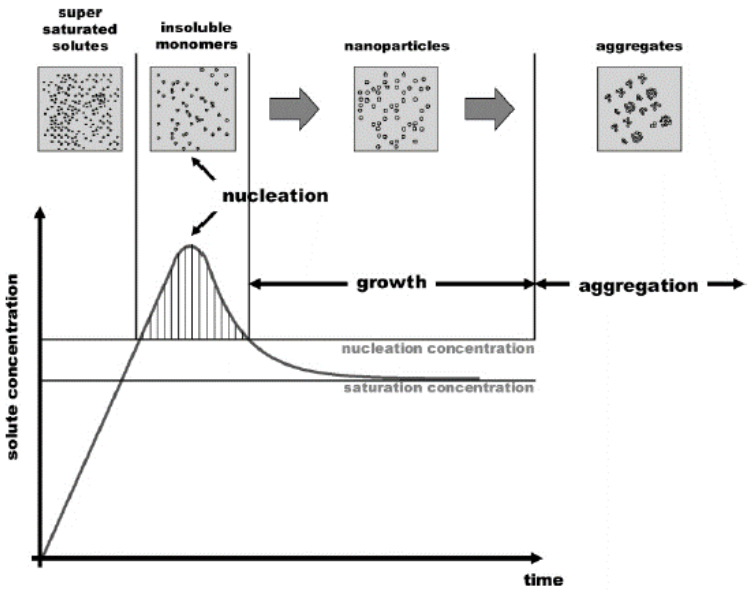

Figure 1.8 Diagram of LaMer for the homogeneous formation of particles, adapted including possible aggregation events. Reprinted from deMello *et al.*[11] with permission of the Royal Society of Chemistry

[vii] The possible further evolution of particles dimension by ripening and aggregation, commonly observed if adequate particles stabilization is not provided and described in Chapter 1.1.1, was not included in the LaMer model.

The qualitative model of LaMer was validated by experimental reports,[35,46,48,49] and some attempts to build a quantitative description of the process were also reported by Sugimoto,[50,51] and more recently implemented by Chu *et al.*[52] In particular, these authors described each stage of the LaMer burst nucleation process employing differential equations, that relate the solute concentration $C(t)$ with its supply rate per unit volume Q, the nucleation rate J, and the growth rate G. In particular, they defined a species balance equation for the solutes as:

$$\frac{dC}{dt} = Q - Jn^* - Gp_T \tag{1.9}$$

where n^* is the critical nucleus size, $p_T(t)$ is the number of nuclei and the nucleation rate is defined as $J = dp_T/dt$. Theoretically, the final average size and size distribution formed in each homogeneous burst nucleation reaction could be modelled by solving Equation 1.9; however, the validity and the predictive power of the obtained results are limited by the several approximations required, such as the growth rate G which is independent from size and concentration, and the variation of the nucleation rate when the solute concentration reaches its maximum value is zero ($dJ/dt = 0$). From these assumptions, Chu *et al.* derived that i) the total number of generated nuclei (*i.e.* consequently their final size) is dependent from $2Q/G$ and independent from the nucleation rate, and ii) the nucleation rate J controls the particle size distribution, as it affects the critical time and concentration at the supersaturation bursts. Thus, according to these implementations of the LaMer model, a higher solute supply rate results into a higher number of nuclei, and consequently into smaller nanoparticles, as the solute available for the growth stage is distributed over a higher number of nuclei.

Despite the assumptions that underlie the classical picture of the LaMer model and its quantitative interpretation and validation outlined above, its description of the particle formation process, and in particular the concept of nucleation-growth separation, are a widely recognized route to the synthesis of monodisperse particles, also supported by experimental evidences. Indeed, a temporal separation of the short nucleation burst producing the initial nuclei and the subsequent growth stage allows the nuclei to evolve simultaneously and, in principle, with the same growth rate, thus leading to a uniform final size. On the other hand, if the two events occur simultaneously, *i.e.* if they are both relevant in the same timeframe, different nuclei will grow for a different period of time until the saturation concentration is reached, and a polydisperse population of particles will be

obtained. Based on these considerations, a careful optimization and adjustment of the relevant experimental parameters might allow to keep temporally separated the nucleation and growth stages, therefore yielding an almost monodisperse colloidal suspension of the targeted nanoparticles.

1.1.4 Crystallization in confined spaces

Crystallization in confined spaces has a particular relevance since it represents both an intriguing playground for synthetic chemists as well as a critical issue for the world architectural heritage, due to the internal mechanical stresses created by the growth of crystals confined within pores of stones or masonries.[1,2,53] In the last decades, the effects of confinement on crystallization processes have been investigated exploiting diverse well-defined enclosed volumes as confined environments, offering length scales varying from the nanoscale to hundreds of micrometers, such as porous systems (*e.g.* zeolites, mesoporous solids, controlled pore glass),[54,55] track-etched membranes,[4] arrays of picolitre droplets,[56] emulsion droplets (micro- or miniemulsion droplets),[57,58] microfluidic devices,[59] and manufactured reaction chambers.[60–62] It was reported that confinement effects operate over different length scales and geometries, affecting both thermodynamic and kinetic parameters ruling the crystallization pathway and the synthetic outcome. Indeed, it is worth noting that the chemistry occurring within confined spaces results from the interplay of different factors and forces, often beyond the molecular scale, and it cannot be easily ascribed to singular factors. Confinement can influence virtually every aspect of crystal nucleation and growth, and the most relevant ones affected by space constraints include i) melting and freezing points, ii) nucleation rates, iii) crystal size, morphology and orientation, and iv) polymorph selection. A short overview of the effects of confinement on the above-mentioned phenomena, and their potential mechanistic origins, is provided in the following:

I. Melting and freezing points. Liquids display dramatically different physical properties from those in the bulk state when the size of the available environment is reduced to the nanometer range. Indeed, the freezing and melting points of compounds are typically depressed in small nanoscale volumes, with a linear ΔT *vs* $1/r$ behavior, and usually the formation of a liquid-like layer adjacent to the confined space wall is reported. The melting and freezing behavior in confinement has been studied in different constrained environments, ranging from rigid cylindrical pores (*e.g.* MCM-41 mesoporous silica) to droplets, and specific reviews may be found, describing the thermodynamic origin of the phenomenon.[63,64] As an example relevant for this Thesis work, the crystallization of aqueous solutions of NaCl in confined nanodroplets produced by inverse miniemulsion and of hexadecane in direct miniemulsions was investigated by Montenegro *et al*.[58] The

authors observed that, for both systems, the crystallization (freezing) temperature decreased compared to the bulk, due to the suppression of the heterogeneous nucleation. The required undercooling was higher reducing the droplets size.

II. Nucleation rates. The nucleation rate in small volumes is usually reduced with respect to bulk solutions, and this observation was ascribed to i) the exclusion of impurities that may promote nucleation in bulk, thus only homogeneous nucleation can occur, ii) a kinetic effect due to the dependence of the probability of nucleation from the available volume, and iii) the continuous depletion of the supersaturation due to the consumption of the finite and limited reservoir of solute during nucleation, thus reducing the driving force for the formation of a critical nucleus (see Equation 1.4).[2,65–67] Notably, these effects were observed to operate even in droplets with a diameter in the order of hundreds of micrometers.[2] Finally, the nucleation rate can be influenced also by the geometry of the site in which nucleation occurs, as demonstrated also by theoretical simulations.[68]

III. Crystal size, morphology and orientation. Constrained rigid volumes can have templating effects on the crystal growth, that can be ultimately limited by the size of the environment, as well as they can define the crystal morphology.[69] This can lead to the formation of complex three-dimensional morphologies, that could not be formed by conventional approaches employing additives. Moreover, strong orientation effects are often observed when crystallization of compounds with anisotropic structures occurs in anisotropic constrained volumes, such as cylindrical pores: unimpeded growth is only possible parallel to the pore axis.[2,70] On the other hand, crystallization can also influence the confining medium, as it was observed that crystallization within porous/confined media is often associated with the formation of a thin fluid layer between the growing crystal and the walls of porous substrates, generating a crystallization pressure.[53,71,72] Consequently, the crystal continues to grow exerting a stress on the pore walls and causing damage to the host material. This phenomenon is common in rocks and building materials.

IV. Polymorph selection. One of the most fascinating effects of space confinement on crystallization regards polymorph selection, that can occur within environments with dimensions comparable to the size of the critical nucleus (*i.e.* few nanometers). Indeed, different crystal polymorphs can have different stabilities at the critical size, and in space constraint conditions normally metastable phases can become the thermodynamically

favored forms. Figure 1.9 shows how the most stable polymorph, and thus the polymorphs stability ranking, can be adjusted by imposing nanometric constraints on the growing nuclei. This phenomenon can be exploited to screen for, and even control, polymorphism.[1,70] In addition to a thermodynamic effect, which is relevant in highly constrained environments, polymorph selectivity can be influenced also by kinetic effects, as demonstrated by the stabilization of metastable polymorphs of inorganic compounds in confined spaces of hundreds of nanometers. For example, experiments reported by Fiona Meldrum and her group demonstrated that the lifetimes of amorphous precursor phases or of the metastable polymorphs of calcium carbonate, calcium sulfate, calcium phosphate, and potassium ferrocyanide can be extended under confinement.[4,55,60,62,73] Various possible factors were proposed to influence the observed stabilization of metastable phases, such as statistical effects associated with small volumes and low probabilities for the nucleation of stable phases, limit of the presence of water and constraint in its mobility, and/or inability to aggregate into larger particles, leading to more stable bulk phases in the case of aggregation-based growth mechanisms (see Chapter 1.1.2).

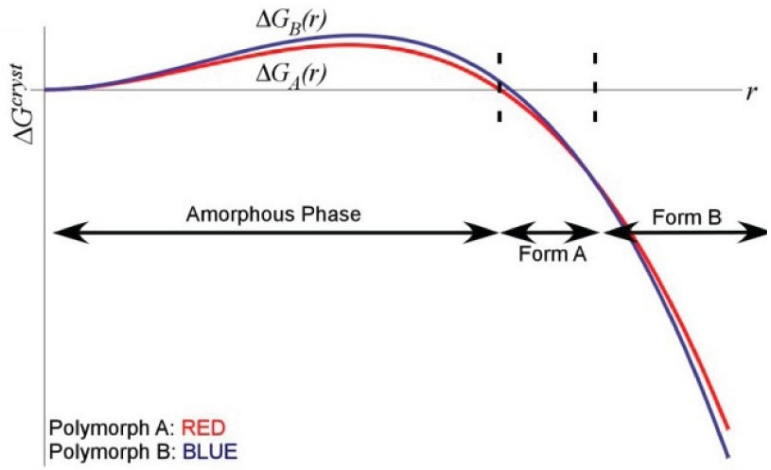

Figure 1.9 Energetic profiles for two competing nuclei, polymorph A and polymorph B, over a range of characteristic lengths. The thermodynamically preferred phase corresponds to the lowest free energy, which can be adjusted by imposing nanometer size constraints upon the growing nuclei. Reprinted from Hamilton *et al.*[70] with permission of the American Chemical Society

1.2 Confined spaces as controlled environments for inorganic synthesis

In this Section, a general overview on the theoretical principles and state of the art of the constrained environments that are exploited in the work described in this Ph.D. Thesis is presented. Nanodroplets produced by miniemulsion, continuous-flow microreactors and mesoporous materials are described as synthetic hosts and their exploitation for inorganic synthesis is discussed.

1.2.1 Inverse miniemulsion droplets

In the last decades, colloidal systems[viii] have gained special relevance among wet-chemistry methods for inorganic materials synthesis, since they allow to achieve a good control on the uniformity, size and shape of the synthesized materials, meanwhile requiring low temperatures and energy consumptions, thus complying some of the Green Chemistry principles.[74,75] Within this framework, the use of emulsions as soft templates for the synthesis of inorganic materials has found its beginning in the pioneering work of the Pileni's group.[76–80]

1.2.1.1 Emulsion classification, formation and stability

Emulsions, defined by IUPAC as a dispersion of liquid droplets (*dispersed phase*) in another, non-miscible liquid (*continuous phase*),[9] can be termed as *direct* or *inverse* depending on the nature of the continuous phase: direct emulsions are characterized by oil droplets dispersed in water (oil-in-water, o/w), while in inverse emulsions water droplets are dispersed in an oil phase (water-in-oil, w/o) (Figure 1.10). A commonly used, yet not rigorous, classification of emulsions is based on the size of the dispersed droplets, and it classifies them in i) *microemulsions* (*μE*, d < 100 nm), ii) *miniemulsions (ME),* sometimes

[viii] According to the *Gold Book* of IUPAC, a colloidal system is defined as "a state of subdivision, implying that the molecules or polymolecular particles dispersed in a medium have at least in one direction a dimension roughly between 1 nm and 1 μm, or that in a system discontinuities are found at distances of that order".[9]

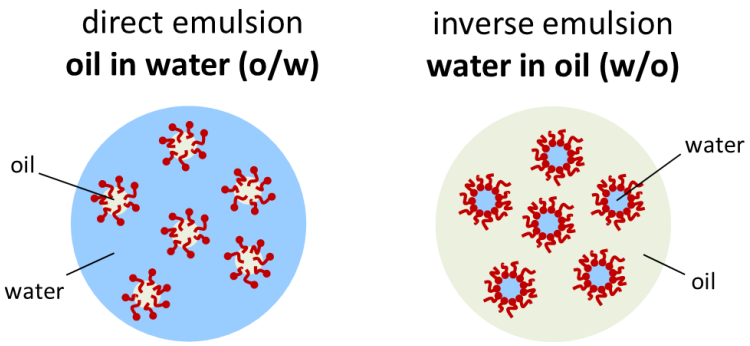

Figure 1.10 Emulsion classification according to the nature of the continuous phase

referred to also as *nanoemulsions,*[ix] (30 < d < 500 nm), and iii) *macroemulsion* (*mE*, d > 1 µm) (Figure 1.11). Besides being characterized by different dimensional ranges, these three types of emulsions are characterized by different relative amounts of the two immiscible liquids and of the amphiphilic molecule (surfactant)[x], ultimately determining their thermodynamic stability. Indeed, while microemulsions are generally considered to be thermodynamically stable systems, mini- and macroemulsions are metastable, with different temporal ranges of stability: miniemulsions are typically stable from days to months; on the other hand macroemulsions are characterized by a shorter stability, up to minutes or hours.

[ix] The term *miniemulsion* was proposed by Chou *et al.* in 1980,[421] and it has been typically linked not merely to the droplets size, but also to mechanistic and thermodynamic aspects of the emulsion (*i.e.* the formation by application of high shear forces and the specific relevance of osmotic pressure agents into the system, as outlined in the following). On the contrary, the more recent term *nanoemulsion* is mostly found in literature as a "quasi-synonym" of miniemulsion, but it seems to be essentially based on the droplets size, going beyond the mechanistic implications required by the definition of *miniemulsion*. In general, any emulsion with nanometric droplets could be termed as *nanoemulsion*.

[x] Surfactants are amphiphilic molecules that are formed by a hydrophilic part (*i.e.* the polar "head", containing ionic or polar groups) and a hydrophobic part (*i.e.* the hydrophobic "tail", such as hydrocarbon chains).[422] Their classification based on the nature of the hydrophilic part divides them in *ionic surfactants* (*e.g.* sodium dodecyl sulfate, SDS, and cetyltrimethylammonium bromide, CTAB), that provide also electrostatic stabilization, and *non-ionic surfactants* (*e.g.* amphiphile molecules whose hydrophilic part is a polyether such as PEO or PPO, a polyethylene glycol, a polyester of triglyceride etc.), that provide mostly steric stabilization. Surfactants are "surface active" molecules, that lower the surface tension of the medium in which they are dissolved and/or the interfacial tension with other phases, adsorbing at the interface.[9]

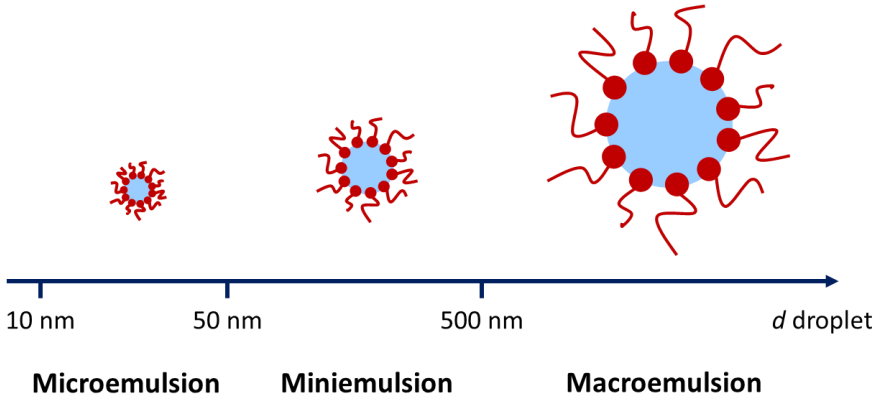

Figure 1.11 Classification of emulsions according to the droplets size. Inverse (water-in-oil) emulsions are represented

The thermodynamic stability of emulsions is achieved when the Gibbs free energy variation ΔG_{form} associated to the process of emulsion formation is negative:

$$\Delta G_{form} = \gamma_{12}\Delta A - T\Delta S_{conf} < 0 \quad (1.10)$$

where γ_{12} is the interfacial tension between the two liquid phases 1 and 2 (water and oil), ΔA is the change in interfacial area upon emulsion formation, T is the temperature and ΔS_{conf} is the corresponding change in configurational entropy, which is positive as the number of droplets is increased during emulsification. Thus, for the emulsion formation process to be spontaneous and thermodynamically favored (*i.e.* ΔG_{form} < 0), the energy required to create a new interface ($\gamma_{12}\Delta A$) must be smaller than the absolute value of the latter term ($T\Delta S_{conf}$). For *macroemulsions*, $\gamma_{12}\Delta A$ is much greater than the entropic term, leading to a positive value of ΔG_{form}: external work has to be provided to generate a macroemulsion. When *miniemulsions* are taken into account, the $\gamma_{12}\Delta A$ term is still greater than $T\Delta S_{conf}$ (*i.e.* ΔG_{form} > 0), but closer in magnitude with respect to the macroemulsion case. Even if external work is required for both macro- and miniemulsion formation (ΔG_{form} > 0), while simple mixing and stirring of bulk phases typically transfer enough energy for generating a macroemulsion, high shear forces (*e.g.* ultrasonication or high-pressure homogenization) are required to comminute large macroemulsion droplets into smaller ones and obtain a miniemulsion (Figure 1.12).[xi][8,81] As discussed in the following

[xi] High intensity ultrasounds (20-100 kHz, 10-1000 W cm^{-2}) are commonly employed as miniemulsion homogenizers for lab-scale applications, while high pressure devices or microfluidizers are most typical of upscaled applications. Several mechanisms for the droplet formation and disruption under

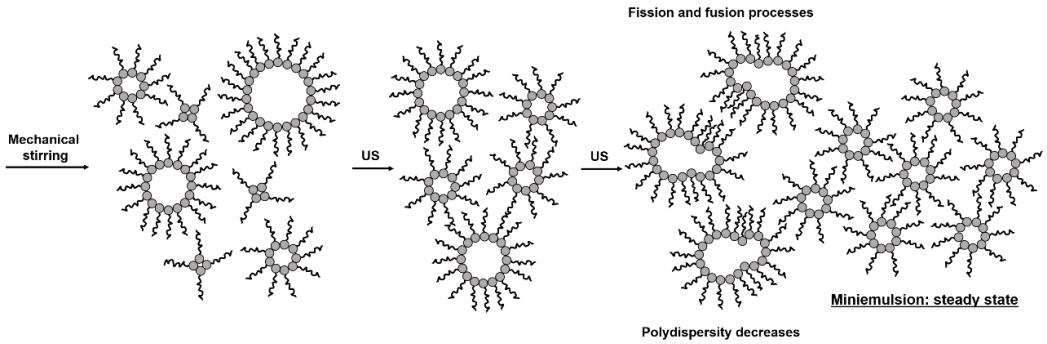

Figure 1.12 Schematic representation of the homogenization process leading to the formation of *miniemulsion* systems. High intensity shear forces applied by ultrasounds (US) induce constant fusion and fission processes between droplets. As a consequence, droplets polydispersity decreases, until a stationary state is achieved, and the droplet size does not change anymore. Adapted from Antonietti *et al.*[85] with permission of Elsevier

in more detail, once energy is supplied for macro- and miniemulsion formation, the systems will return to the initial two immiscible bulk phases state if the dispersed droplets are not kinetically stabilized by adopting specific measures. Finally, for *microemulsion* systems, thermodynamic stability is achieved ($\Delta G_{form} < 0$), as the interfacial tension is low enough that $\gamma_{12}\Delta A < T\Delta S_{conf}$, resulting into a spontaneous formation of a stable emulsion, *i.e.* no external work is required. Notably, the interfacial tension γ_{12} can be significantly lowered by addition of a certain amount of a surfactant (*surface active agent*) and possibly a co-surfactant (either another surfactant or a medium-chain alcohol), that are adsorbed at the liquid-liquid interface, allowing to obtain an overall negative ΔG_{form}.

In addition to the evident major role of surfactants in decreasing the interfacial tension, thus allowing the formation of (kinetically or thermodynamically, depending on its amount) stable emulsions, it is noteworthy that the chemical nature, structure and concentration of the employed surfactants are key elements in determining the type of emulsion that is

---

the influence of ultrasounds were proposed, the most crucial one being *cavitation*.[84] Cavitation is a phenomenon associated with bubbles implosion, causing the formation of intensive shock waves in the surrounding liquid and high-velocity liquid jets with strong elongational fields, that may cause droplets disruption.[423] The exact mechanism of droplet disruption as a result of cavitation is not yet fully understood.

Miniemulsion homogenization by ultrasonication can be followed by turbidity and surface tension measurements: throughout sonication, a decrease in droplet size occurs, associated with an increase of the overall oil/water interface and consequently also of the surface area per surfactant molecule (a constant amount of surfactant is distributed over a larger interface), until a steady state is reached. The surface tension of the system varies accordingly and reaches values close to 50-60 mN m^{-1} (droplets are not fully covered by surfactant molecules). Turbidity measurements are sensitive to the size and size distribution of the droplets.[81,84,85]

formed, both in terms of whether a direct or inverse emulsion is obtained, and in terms of the droplet size range (*i.e.* ruling if a macro-, mini- or microemulsion is formed). In particular, the formation of *oil-in-water or water-in-oil droplets* is driven by hydrophobic and hydrophilic interactions of the hydrophobic tails and polar heads of the amphiphilic molecule, respectively. The nature of the surfactant can be evaluated by means of its *hydrophilic-lipophilic balance* (HLB), an empirical parameter that may guide the selection of the most suitable surfactant according to the application.[82,83] A method for the calculation of the HLB valid for both ionic and nonionic surfactants was proposed by Davies in 1957,[82] and it quantifies the ratio between the polar and apolar parts within the amphiphilic molecules as follows:

$$HLB = 7 + \sum n_H \cdot H - \sum n_L \cdot L \tag{1.11}$$

where H and L are empiric tabulated values relative to the hydrophilic and lipophilic groups, respectively, and n_H and n_L are the number of those groups within the surfactant molecule. The empirical group values increase in order of increasing hydrophilicity (*e.g.* $–CH_2–$ groups have a value of -0.475, $–SO_4^-\ Na^+$ of 38.7),[82] thus the higher the HLB index, the more hydrophilic the surfactant, and, as a consequence, the more appropriate for stabilizing o/w emulsions. Indeed, the HLB value directly correlates to the emulsifying and solubilizing properties of the surfactants, as shown in Table 1.1.

Table 1.1 Classification of surfactant according to HLB values[82,83]

Range of HLB values	Application
3.5-6	w/o emulsifier
7-9	Wetting agent
8-18	o/w emulsifier
13-15	Detergent
15-18	Solubilization

In addition, as mentioned above, the amount of surfactant into the system, together with the relative amount of the two immiscible phases, rules the average *size of the emulsion droplets*: by increasing its concentration the droplets size decreases, as well as the

thermodynamic stability increases (as the interfacial tension decreases and the ΔG_{form} decreases accordingly, following Equation 1.10). The simplified ternary phase diagram for a water/oil/surfactant system (Figure 1.13) shows that the relative amount of the three components (water, oil and surfactant) determines the formation of a macro- or mini- or microemulsion, as well as if the emulsion will be direct or inverse. Indeed, macroemulsions are characterized by low amounts of surfactant, which is not enough to effectively stabilize the droplets, and thus in the ternary diagram are localized in the region between the water and oil apexes, where the amount of surfactant is minimum. On the contrary, microemulsions generally require a surfactant concentration well above the critical micelle concentration (cmc),[xii] and they are thus found along the water-surfactant or oil-surfactant sides of the diagram, depending on whether they are direct or inverse, respectively, meaning that the dispersed/continuous phases ratio is very low. Finally, in miniemulsions the relative percentage of dispersed phase in the system is higher than for microemulsions and the amount of surfactant is higher than in macroemulsions and lower than in

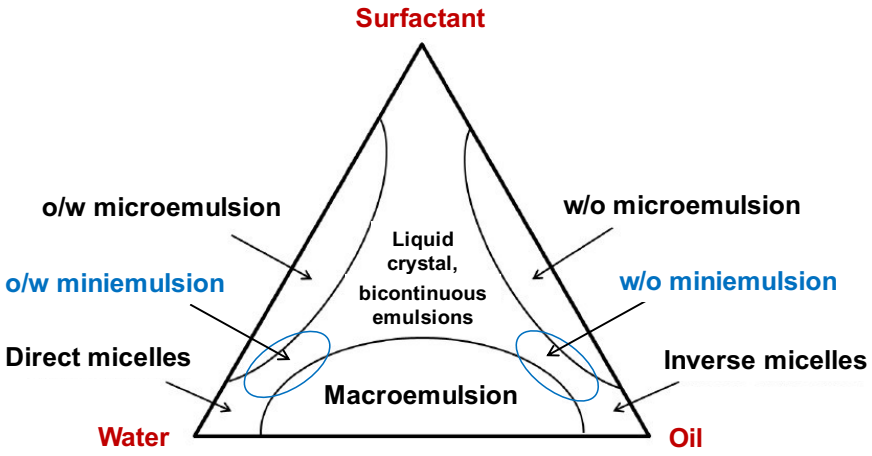

Figure 1.13 Simplified ternary phase diagram for a water/oil/surfactant system

[xii] The critical micelle concentration (cmc) is defined as the concentration of surfactant above which micelles are formed and all additional added surfactant forms micelles: no more surfactant is adsorbed at the liquid-liquid interface, thus it does not contribute to further lowering of the interfacial tension. Cmc is dependent on the chemical nature of the surfactant (the more hydrophobic the surfactant, the lower its cmc), as well as on temperature (the higher the temperature, the lower the cmc; micelles only form above the critical micelle temperature), pressure and possible presence of additives. The cmc value of an amphiphilic molecule in a medium can be evaluated as the transition point in its concentration above which sharp changes in some chemico-physical properties of the system occur, such as the surface tension (no further lowering by increasing surfactant concentration above cmc), the conductivity (sudden drop after cmc), and the turbidity (steep increase after cmc).[424]

microemulsion (always under its cmc), resulting into a non-complete coverage of the droplets with the surfactant molecules (calculated as about 10% of a dense layer of surfactant). Indeed, it may be stated that in miniemulsions the surfactant is exploited in the most efficient way possible.[81,84,85]

Finally, the addition of an appropriate surfactant also increases the *stability* of the obtained emulsions, providing either electrostatic and/or steric stabilization of the droplets against coalescence, a bimolecular degradation process occurring upon collision and merging of droplets (τ_2 mechanism, schematic representation in Figure 1.14a). Besides coalescence, emulsion destabilization may occur also through a second mechanism, arising from the Laplace pressure, that is the pressure difference between the inside and the outside of a curved surface:

$$\Delta p_{Laplace} = p_{inside} - p_{outside} = \frac{2\gamma_{12}}{r} \quad (1.12)$$

where γ_{12} is the interfacial tension between the two immiscible phases 1 and 2 and *r* is the radius of the curved surface of the droplet.[8] From Equation 1.12, it follows that the smaller the droplets, the higher the Laplace pressure: the chemical potential increases with decreasing droplet size. This difference in chemical potential is the driving force for a molecular diffusion from the smaller droplets with higher Δp_L to the bigger droplets with lower Δp_L. In this way, bigger particles grow at the expenses of the smaller ones, which eventually disappear, and the average droplets size is increased. This phenomenon is referred to as *Ostwald ripening* (OR) or molecular diffusion degradation (τ_1 mechanism,

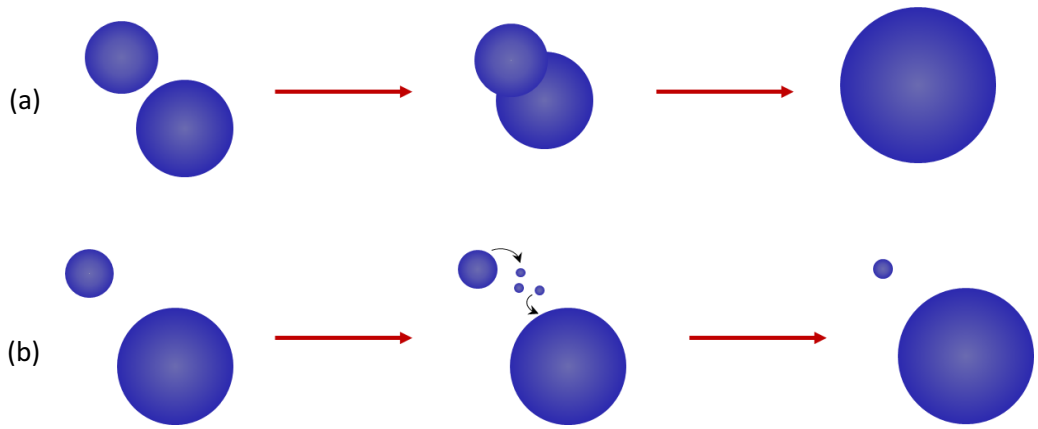

Figure 1.14 Schematic representation of coalescence (**a**) and Ostwald ripening (**b**) mechanisms

schematic representation in Figure 1.14b).[26,86] The OR degradation process is enhanced when i) the droplet size distribution is broad and ii) molecules in the dispersed phase are soluble also in the continuous phase, accelerating the rate of transfer between droplets. The diffusion of molecules between droplets is even faster if the surfactant concentration is above the cmc: micelles are able to solubilize and easily transport molecules within their core and participate to the mechanism of OR.

The Ostwald ripening can be minimized by narrowing the size distribution of the droplets, as strictly monodisperse systems are not subjected to molecular diffusion degradation: when all the droplets have the same radius, Δp_L is equal for each one and thus there is no difference in the chemical potential of the droplets. As a consequence, no net mass flux of solute molecules between droplets occurs. Moreover, the emulsion droplets can be stabilized against molecular diffusion degradation by adding another component, soluble in the dispersed phase but not in the continuous one, termed *osmotic pressure agent* or *co-stabilizer*,[87] whose role is particularly essential for *miniemulsion* systems. Actually, the effectiveness of the osmotic pressure agent in droplets stabilization against OR increases as its solubility in the continuous phase decreases: an (ultra)hydrophobe (*e.g.* alkanes with different chain length, either fluorinated or not, hydrophobic dyes, silanes, siloxanes, isocyanates, polyesters, etc) is typically employed for direct (o/w) miniemulsions, whereas a lipophobe (*e.g.* an ionic compound, a salt or a sugar) for inverse (w/o) miniemulsions. The role of the osmotic pressure agent is to provide an inward osmotic pressure π_{osm} counteracting the Laplace pressure:[88,89]

$$\pi_{osm} = \frac{3nRT}{4\pi r^3} \tag{1.13}$$

where n is the number of moles of the osmotic agent, R is the universal constant of gases, T *is* the temperature and r is the radius of the droplet. From Equation 1.13, it follows that the higher the amount of osmotic agent and the smaller the size of the droplets, the higher the osmotic pressure. As mentioned above, during Ostwald ripening, the solute of the dispersed phase diffuses from smaller droplets to the bigger ones through the continuous phase, decreasing the starting droplet size and consequently increasing the Laplace pressure, driving for further diffusion of the solute into bigger droplets. However, the osmotic agent, insoluble into the continuous phase, does not diffuse out of the dispersed droplets and thus its concentration increases in the smaller droplets with the diffusion of

the solute, arising into a pressure difference experienced by the small and big droplets, opposing to the Laplace pressure. As a consequence, the progressive disappearance of the smaller droplets caused by the Ostwald ripening phenomenon is slowed down and the system reaches a "steady state".[8,81] However, the overall pressure is not zero, because the Laplace pressure is usually larger than the osmotic one: the miniemulsion droplets are metastable (*critical stability*) and experience a pressure, that will lead to an overall growth of the system on the timescale of days to weeks.[90] Interestingly, while this observation holds true for direct (oil-in-water) miniemulsions, in the case of inverse (water-in-oil) miniemulsion systems, it was observed that the size of the droplets is dependent on the amount of osmotic pressure agent: the droplets experience a real zero effective pressure ($\Delta p_L = \pi_{osm}$) and are therefore very stable.[84] Nevertheless, it is worth noting that the pressure balance can be significantly altered by even slight changes in droplet size, because the Laplace pressure Δp_L and the osmotic pressure π_{osm} show a r^{-1} and r^{-3} dependence, respectively.[84]

1.2.1.2 Micro- and miniemulsion droplets as confined environments for inorganic synthesis

As mentioned, starting from the pioneering work of Pileni's group,[76–80] emulsion droplets have been exploited as templating environments in which performing chemical transformations. In particular, micro- and miniemulsion droplets have been employed as confined reactors for the synthesis of inorganic (as well as organic, albeit not covered herein) systems, leading to the controlled formation of crystalline materials.[91] Since inorganic precursors are generally soluble into aqueous solutions (*e.g.* metal salts), the synthesis of inorganic materials is typically carried out within inverse emulsion droplets, *i.e.* water-in-oil droplets, and the inorganic salt dissolved in the water droplets acts also as osmotic pressure agent. Nevertheless, less commonly, oil-soluble metal precursors have also been employed in direct (oil-in-water) emulsion.[92–94]

As discussed in Section 1.2.1.1 and summarized in Table 1.2, the main differences between micro- and miniemulsion systems – i) droplet size (being smaller than 100 nm and in the 30-500 nm range for micro- and miniemulsions, respectively), ii) thermodynamic stability (microemulsions are thermodynamically stable, while miniemulsions are metastable), and iii) thermodynamic of formation (spontaneous for microemulsions and requires high-shear

forces for miniemulsion) – result from the different relative amount of the three components of the heterogeneous system, *i.e.* the two immiscible liquids and the surfactant. In particular, microemulsions are obtained with significantly higher amounts of surfactant with respect to miniemulsions: the concentration of the surfactant is usually above the cmc for microemulsions, while it is well below the cmc for miniemulsions. Notably, this is reflected into a different coverage of the dispersed droplets with the surfactant molecules, and ultimately into different optical properties (*i.e.* scattering) and retaining of the droplet identity over time of the two emulsions. Indeed, *microemulsion* systems, thanks to the high amount of surfactant employed (and also the small relative amount of dispersed phase), are isotropic, optically transparent dispersions characterized by oil-swollen (or water-swollen) micelles dispersed in water (or in oil), covered by the presence of a monolayer of surfactant molecules.[95] For this reason, the interfacial tension of the system is close to zero and the droplets are in equilibrium: upon collision, they coalesce and exchange material. Indeed, microemulsions are dynamic systems, in which interchange of dispersed phase occurs between droplets, with characteristic times slower than the diffusion of reactants in bulk conditions (10 μs – 1 ms).[96] However, even if the rate

Table 1.2 Summary of the main differences between micro- and miniemulsion systems

	Microemulsion	**Miniemulsion**
Droplet size	< 100 nm	30-500 nm
Dispersed/continuous phase ratio	Higher	Lower
Surfactant amount	Above cmc (20-30 wt% of the cont. phase)	Below cmc (1-2 wt% of the cont. phase)
Droplets coverage with surfactant	Complete	Not complete
Interfacial tension	Almost zero	Not null
Stability	Thermodynamically stable	Metastable
Optical property	Isotropic, optically clear	Optically turbid
Formation	Spontaneous	Requires high shear treatment
Identity of droplets	Not retained: changes over time (*dynamic system*)	Retained: constant over time (*nanoreactor*)

of reactant mixing is controlled and slower if compared to "batch" syntheses, the identity of the droplets is not maintained over time and they cannot be strictly termed as "confined nanoreactors". On the contrary, *miniemulsions* are optically turbid dispersions of droplets (*n.b.* not *micelles*) that are not fully covered by the surfactant molecules (surface coverage of about 30%).[84,85] As a consequence, the surface tension of the system is not zero and miniemulsions are metastable: they are *critically stabilized* against coalescence and fully stabilized against Ostwald ripening by the osmotic pressure agent.[8] Therefore, exchange of material between droplets does not occur and the identity of miniemulsion droplets does not change over the timescale involved for chemical reactions: the miniemulsion droplet growth is usually not of relevance for synthetic applications and they can be considered as ideal "confined nanoreactors". Indeed, reactions occurring within a droplet are actually confined to the same droplet and reactions between droplets are only possible by forcing their coalescence, and consequently reactants mixing, by external application of shear forces. Consequently, by miniemulsion approach, syntheses can be performed in a highly parallel fashion in the confined space of nanodroplets, *i.e.* reactions take place in 10^{18}-10^{20} nano-compartments per liter that are separated from each other by a continuous phase.[84] Moreover, as no exchange among the droplets spontaneously occurs, the growth of the crystallized particles is controlled by the starting amount of material present in the confined space.

The different dynamic nature of micro- and miniemulsion systems with respect to reactant exchange between droplets has a great effect on the reaction kinetics and it was exemplarily demonstrated by classical color reactions, such as the formation of Prussian Blue[97] and of nickel murexide complex.[90] Indeed, in the Prussian Blue formation experiment, when two inverse miniemulsions, containing one a $FeCl_3$ aqueous solution and the other one a $K_4[Fe(CN)_6]$ aqueous solution, are mixed together, the obtained miniemulsion does not display any color variation for weeks, demonstrating the extraordinarily high ME droplet stability against exchange processes. The droplets with the two reactant species remain separated as colloidal entities on the time scale of most chemical reactions. Then, when droplets fusion and fission processes (and consequently the exchange of their content) is induced by ultrasonication, the miniemulsion turns blue, as Prussian blue complex is formed. If the same experiments are repeated with two microemulsions or micellar solutions, upon mixing of the starting microemulsions, an immediate color variation is observed, since immediate reaction takes place because of unblocked droplet exchange.

Another advantage of employing inverse miniemulsion systems as opposed to inverse microemulsion ones for inorganic synthesis arises from their different water to oil ratio: being it necessarily lower in the case of microemulsions, the quantitative yield of the reaction is more limited. In addition, in order to synthesize the same amount of product, a greater amount of organic solvent is required, affecting the environmental compatibility of the synthetic approach. The synthesis of crystalline materials in microemulsions is the subject of many reviews;[94,98–100] the use of inverse miniemulsion droplets in inorganic synthesis is discussed in more detail in Section 1.2.1.3.

1.2.1.3 Experimental approaches for inorganic synthesis in inverse miniemulsion droplets

The synthesis of inorganic systems in inverse (water-in-oil) miniemulsion droplets has been explored since the beginning of the 21st century by Landfester's group. Since their pioneering work, inverse ME nanodroplets have been employed as nanoreactors for the synthesis of many inorganic compounds, encompassing metal nanoparticles and alloys (Ga, Na, Fe, Wood's and Rose's metals),[101] metal oxides (*e.g.* TiO_2,[102–104] SiO_2,[105,106] CeO_2,[107,108] ZnO,[109–111] CuO,[112] Fe_2O_3,[108] ferrites[113]), hydroxides ($ZrO(OH)_2$, $HfO(OH)_2$, $Ca(OH)_2$, and $Mg(OH)_2$),[114,115] sulfides (ZnS),[116] and fluorides (CaF_2),[117] mainly through precipitation, co-precipitation and sol-gel methods. The synthesis of inorganic materials has been carried out in inverse miniemulsions starting either from aqueous solutions of metal precursor solution and even from molten salts or metals, and many details may be found in specific reviews.[118–120]

The most typical apolar solvent employed as continuous phase in inverse miniemulsions is cyclohexane, which is characterized by a low boiling point (80.7 °C), allowing an easy evaporation after preparation. Moreover, other higher boiling low-polarity solvents have been used for inverse miniemulsions, such as toluene (boiling point 110.6 °C), hexadecane and isoparaffinic fluid (*e.g.* Isopar M, boiling point higher than 150 °C). The stabilization of inverse miniemulsions against coalescence is always provided by a surfactant with a low HLB value (generally lower than 7), or a mixture of surfactants with appropriate final HLB, given as the weighted sum of the HLB values of the single surfactants. Non-commercial and synthetically complex block copolymers, such as P(S/EO) (poly(styrene-*block*-ethylene oxide)) and P(E/B)-PEO (poly(ethylene-*co*-butylene)-*block*-poly(ethylene oxide), as well as

commercial alternatives, such as Span80 (sorbitane monooleate) and PGPR (polyglycerol polyricinoleate), have been efficiently employed. Finally, as mentioned above, when inverse miniemulsions are exploited for inorganic synthesis purposes, the stabilization of the nanodroplets against molecular diffusion is provided by the metal salts dissolved in the dispersed aqueous phase as precursors.[119,120]

Because of the low operating temperatures of organic solvents, the synthesis of inorganic compounds in inverse miniemulsion typically involves a precipitation reaction or sol-gel processes. When binary compounds are targeted, and the precipitation reaction from aqueous solutions of the metal precursor and the precipitating agent is exploited, two synthetic procedures may be followed, namely i) "co-homogenization" or "two-miniemulsion" method and ii) diffusion approach (schematic representation in Figure 1.15 a and b, respectively). By the *two-miniemulsions method*, two pre-formed MEs containing the metal precursor and the precipitating agent, respectively, are combined together and the mixing of the reactants inside the droplets is triggered by forcing fusion and fission processes between droplets through ultrasonication (step 2 in Figure 1.15a). In this way, the crystallization of the inorganic structures occurs inside the ME droplets in a parallel fashion. The *diffusion approach* consists into an external addition of the precipitating agent to a pre-formed miniemulsion containing the metal precursor. When an aqueous solution of the precipitating agent is employed, it is not miscible to the continuous phase and an additional step of homogenization by US is required to promote the diffusion of the precipitating agent into the ME droplets (step 2 in Figure 1.15b). On the other hand, the addition of an oil-soluble precipitating agent can lead to the mixing of reactants at the interface between the two immiscible phases and to the formation of hollow nanostructures. This latter strategy is usually employed when sol-gel reactions are targeted, and often the obtained materials are amorphous and require a subsequent thermal treatment to crystallize.[112,120]

In conclusion, the inverse miniemulsion approach is an unconventional synthetic method that offers a good versatility for the preparation of inorganic systems, whilst providing an effective control on their final feature by confining their crystallization inside nanometric independent droplets. Indeed, ME droplet confinement affects the size and size distribution

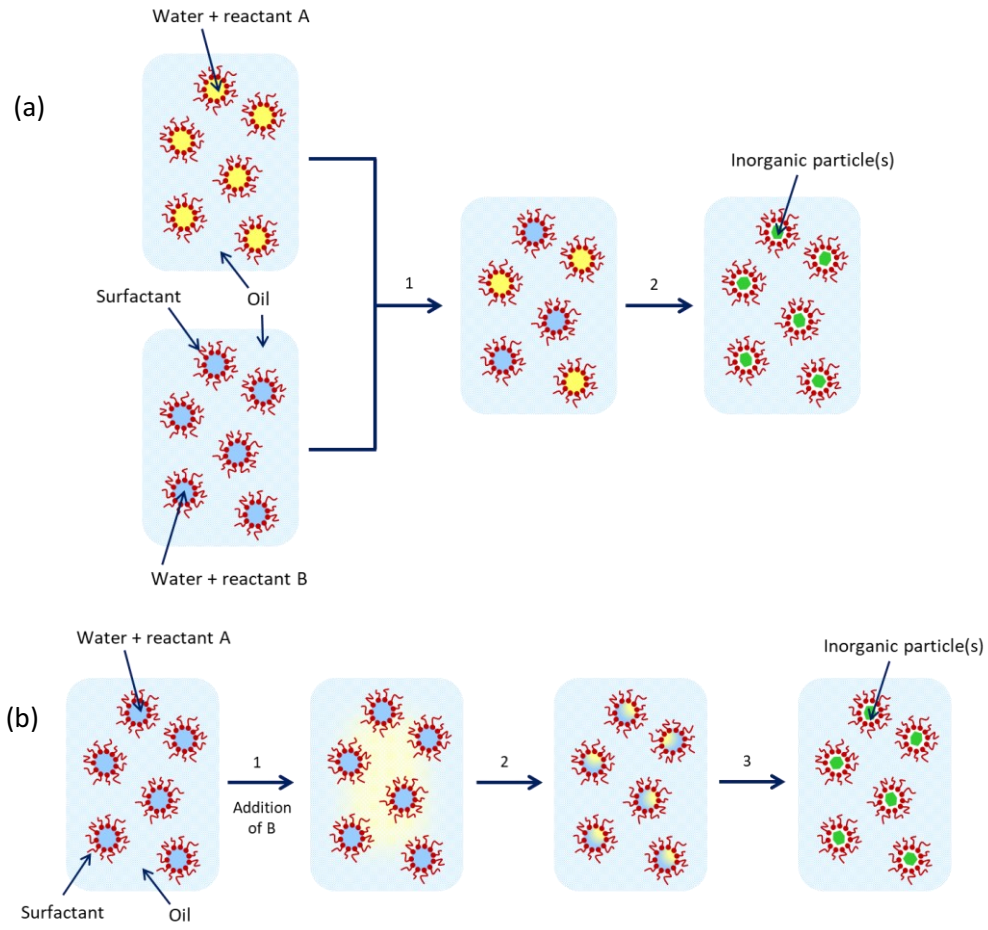

Figure 1.15 Schematic representation of the synthesis of nanoparticles in water-in-oil miniemulsions through *two-miniemulsion* method (**a**) and *diffusion* method (**b**). *Two-miniemulsion method*: step 1) mixing of MEs of the precursors A and B; step 2) application of US to trigger reactant mixing, resulting in the crystallization of the product within the CS of the droplets. *Diffusion method*: step 1) addition of reactant B to the continuous phase of ME of precursor A; step 2) application of US; step 3) crystallization of the product within the CS of ME droplets.

(and in some cases also the shape)[xiii] of the synthesized inorganic materials, and it may also allow the synthesis of certain phases under milder conditions than required by other approaches, such as lower temperature and/or pressure. The major drawbacks of the method are represented by the limited operative temperature range, dictated by the boiling point of the continuous phase, and sustainability, as larger amounts of organic solvents are

[xiii] Since the size of the synthesised material particles is usually smaller than the size of the starting ME droplet, there is not a "one-to-one" templating effect of the nanodroplets. As a consequence, other particles shapes outside the spherical one are possible. It has been reported that under certain conditions, *e.g.* with high concentration of surfactant, cylindrical droplets may be obtained, that could lead to the formation of particles with a rod-like shape.[120]

required with respect to the volume of the aqueous phase in which the reaction is carried out (*i.e.* usually the water to oil weight ratio ranges between 1:3 and 1:4). Moreover, specific work-up procedures are often necessary to remove organic impurities from the NPs surface. Finally, the scale-up of the synthesis might be challenging as different strategies must be pursued for the homogenization of greater volumes (*e.g.* the employment of high pressure homogenizers instead of ultrasonicator tips) and the reaction parameters might not be straightforwardly transferred to a scaled up system.

In this Ph.D. Thesis, an inverse miniemulsion approach was employed for the confined space synthesis of molybdenum oxide (Chapter 2), and undoped and Eu(III)-doped calcium molybdate (Chapter 3), by exploiting both the two-miniemulsion approach and the diffusion approach at room temperature. The effects of miniemulsion nanodroplets confined space on the crystallization of the studied systems was evaluated by comparing the results obtained in miniemulsion with those obtained in batch conditions (without space constrain).

1.2.2 Continuous-flow microreactors

In recent years, continuous-flow microreactors have emerged as an attractive technology for the synthesis of inorganic materials, offering a higher level of control than that can be achieved in conventional macroscale batch reactors. Indeed, continuous-flow chemistry can disclose several advantages with respect to one-pot approaches, mainly derived by its continuous nature, such as facile automation, generally a higher safety, an easy temporal control, an easy process scale-up and a better reproducibility of the reaction conditions. Hence, a superior reliability of the process is ensured at the cost of a more elaborate setup with respect to a simple stirred flask.

1.2.2.1 Continuous-flow approaches

In a continuous-flow reaction, the precursors are continuously pumped into in tubular reactors, come in contact and are eventually mixed in an *ad hoc* engineered mixer, and the products are continuously collected. The continuous nature of these approaches leads to differences in the concepts of reactants stoichiometry and reaction times, if compared to traditional batch approaches, as well as it offers several intrinsic advantages, introducing the possibility of controlling additional experimental parameters, such as flow rate. Indeed, while in batch approaches the molar ratio between reactants is ultimately defined by the volumetric ratio of the solutions employed, given their molar concentration, in continuous-flow conditions the relative amount of reactants at the mixing point is also determined by the flow rate of precursors solutions. The concept of reaction time in batch conditions is conventionally simply considered as the interval of time between reactants mixing and the end of the reaction. Conversely, the reaction time in continuous-flow approaches is straightforwardly reflected by the residence time in the reactor, defined by the ratio of the reactor volume (namely determined by the tubing diameter and length) and the total flow rate (given by the sum of the individual flow rates of each solution introduced into the reactor). Consequently, in a continuous-flow reactor, a direct and accurate time-space correlation is established, enabling different points in space of the reactor after the mixing point to give a direct access to different reaction times. This precise interrelationship between time and space appears particularly advantageous for performing *in situ* time-resolved investigations, with the powerful opportunity to access also to extremely short reaction times.[121] Indeed, by integrating into the continuous-flow setup an on-line

detector, the reaction outcome can be easily probed at different specific lengths of the reactor (*i.e.* at specific reaction times) by exploiting for example spectroscopic techniques, such as IR,[122,123] Raman,[122,124] SERS,[125] UV,[126] photoluminescence,[127–129] XAS[130] and NMR[131] (Figure 1.16). This discloses the opportunity of rapidly screening reaction conditions (*e.g.* reactants concentration and molar ratio, reaction time, flow rate, temperature, and so on) and quasi-simultaneously evaluating their effect on the synthetic outcome, ultimately making possible to easily and fast (in the µs or ms time scale) optimize synthetic parameters. In addition, the time-space correlation existing in continuous-flow setups offers particularly attracting perspectives when dealing with multi-step processes. Indeed, home-made flow setups can be relatively easily assembled and elaborate multi-step syntheses can be transformed into a single input-output process by introducing at a specific length of the reactor (*i.e.* at a specific reaction time) reactants that are usually added in a successive step. This results extremely useful when reactions involving unstable short-lived reactive intermediates are taken into account.[132,133]

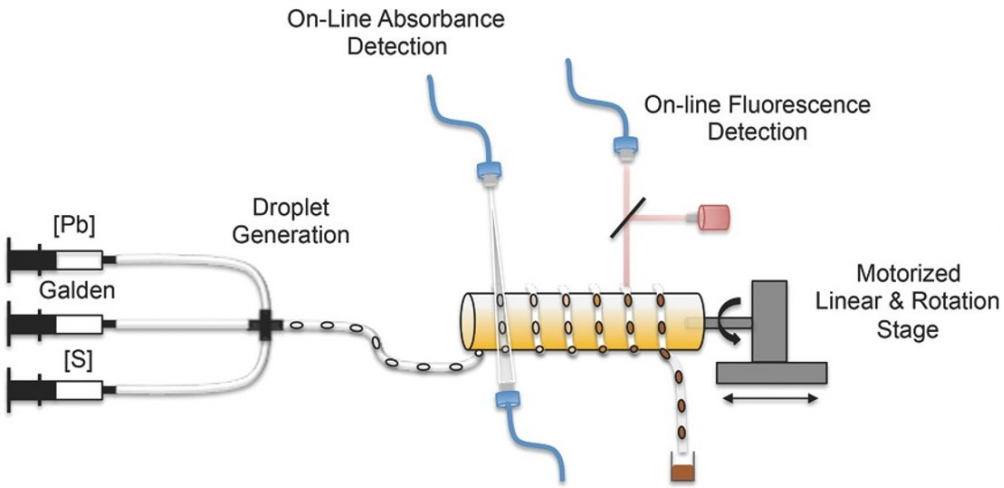

Figure 1.16 Schematic representation of droplet-based microfluidic setup built by Lignos *et al.* for the synthesis of PdS quantum dot. The setup is integrated with online absorbance and fluorescence detection for kinetic analysis. Reprinted from Lignos *et al.*[128] with permission of Wiley

In addition, the continuous nature of flow approaches allows to extend the definition of the total amount of product that can be obtained with respect to batch processes, which are discontinuous by definition. Indeed, the production of batch processes is limited and pre-determined by the volume of the starting precursors solutions, given their concentration and the reaction yield. On the contrary, by operating within continuous-flow regimes, the

product amount is determined by the time frame at which the synthesis is performed at entire flow regime, allowing a theoretically unlimited production,[xiv] as reactants can be indefinitely fed.[134] This leads to substantial advantages in the processes scale-up, since, to produce a higher amount of product, syntheses do not need to be cyclically repeated or vessels dimensions increased, at the expenses of the homogeneity of reaction mixture and consequently of the synthetic control, as for batch approaches. Actually, in continuous-flow processes, products may be simply accumulated by maintaining the setup operative for enough time or by using several reactors in parallel (numbering up or scaling out approach), rather than by conventional scaling up approaches, *i.e.* by increasing the size of the channels, that may lead to the loss of the optimized reaction conditions. These approaches can provide several advantages in large-scale production of nanoparticles, while maintaining the control on the kinetic parameters of the reaction, *i.e.* on the final features of the product, typically achievable in laboratory-scale syntheses.

1.2.2.2 Microfluidic synthesis of inorganic materials

Over the past years, miniaturization of continuous-flow reactors towards *meso*- or *minifluidic* (from 500 µm to few mm) and *microfluidic* (from 10 to 500 µm)[135] setups has emerged as a promising strategy for the controlled synthesis of high-quality inorganic nanocrystals. Indeed, downsizing reactor dimensions has demonstrated to allow a great improvement of the control over reactants mixing and heat transfer, offering fundamentally new capabilities in the synthetic control of concentration of molecules in space and time.

In addition to the reactor size-based one, a general and more flexible categorization of continuous-flow reactors can be made based on the Reynolds number (R_e)[xv] of the fluids

[xiv] From a practical point of view, a common challenge to implementation of inorganic particle synthesis in continuous-flow systems, and in particular in microsystems, concerns the handling of solids, that can lead to *clogging* of flow reactors.[425] As a consequence of clogging, a continuous unlimited production of suspensions is impeded and periodic flushing of the system for dissolving any deposited solids is carried out. Many measures can be taken in order to minimize the risk of clogging, among which a thorough design of the synthetic conditions (*e.g.* temperature, pressure, concentration, possible employment of additives, etc) and of the setup (*e.g.* chemical compatibility, stability in the operating conditions, etc) and combinations thereof. For example, in order to mitigate solid formation along the walls of a flow reactor, smooth perfluorinated surfaces are commonly employed, as they do not promote solid nucleation on the walls of the reactor.[426]

[xv] Reynolds number (R_e) is a dimensionless quantity that predicts the flow regime (*e.g.* laminar *vs* turbulent flow) in different fluid flow situations, and it is a function of both the fluid and the environment in which it is manipulated. It is calculated as: R_e = (inertial forces)/(viscous forces) = $\rho dv/\mu$, where ρ is the fluid density, d is the environment dimension, v is the speed of the flowing fluid

flowing into the channels, quantifying the relative contribution of inertial and viscous forces within the fluid. Microfluidic devices generally operate at Reynolds numbers below 250,[10] characteristics of a laminar flow regime where viscous forces dominate. With this in mind, even reactors with a larger size (500-1000 μm), overlapping the mesofluidics definition, can be defined as microfluidic devices when operating at low flow rates. The low Reynolds number of fluids manipulated in microfluidic devices ensures a regular parallel flow within the channels, without any turbulence or back-mixing within the reactor. In laminar flow regime, reactants are mainly mixed by lateral diffusion, and, thanks to the small size of the channels, this occurs rapidly. Alternatively, mixing of reactants can be forced by introducing dedicated mixing sections into the setup, also tailored for specific purposes,[136,137] and it occurs with fast rates, typically unachievable in macroreactors.

Thus, as a consequence of its continuous-flow nature and the small size of reactors, in microfluidic devices a highly homogeneous reaction mixture is ensured, both in reactants' concentration and in temperature. Indeed, the effective mixing strategies of microfluidic technology allow a remarkably higher control on reaction homogeneities than what can be achieved in batch macroreactors, where non-complete mixing may lead to concentration gradients. Moreover, the high surface area to volume ratio of microfluidic channels, resulting from their small diameter, enables rapid and highly controlled heat transfer processes, ensuring thermal homogeneity to the reaction mixture, more efficiently than macroreactors. This finds particularly notable advantages when dealing with quenching steps of exothermic reactions, allowing a rapid dissipation of heat in excess, and avoiding the formation of hot spots and thus potential non-desired side reactions. As a consequence, reactions can be run more safely.

The avoidance of concentration and thermal gradients in the reaction mixture is a key advantage of the microfluidic approach, ensuring a highly homogeneous environment and stable reaction conditions. Conversely, in batch macroreactors, concentration and/or thermal gradients likely lead to the coexistence of nucleation and growth processes in the reaction mixture, causing a poor control on the final products' features, such as size, size distribution and morphology of the nanoparticles. Indeed, considering the LaMer model of homogeneous nucleation of nanoparticles (see Chapter 1.1.3),[46,47] monodispersed NPs can

and μ is the dynamic viscosity of the fluid. When a tubing with a circular cross section is taken into account: laminar regime $R_e < 2300$; transition regime $2300 < R_e < 4000$; turbulent regime $R_e > 4000$.

be produced when the nucleation occurs on a shorter time-scale than the growth. Thanks to the highly homogeneous and reproducible chemical environment achievable in microfluidic conditions, random (both timely and spatially) nucleation bursts and uncontrolled growth by agglomeration are typically avoided. As a consequence, a temporal (*i.e.* also spatial) separation of the nucleation and growth stages is promoted, resulting in an improved size distribution and uniform morphology of the obtained nanoparticles.[11,138] Moreover, being the reactants feeding dynamic, the rate of precursor supply can be easily tuned, enabling a spatial control of the concentration of the solute. This possibility can be exploited to ultimately tune the final size of the nanoparticles, which is affected by the precursor supply rate according to Sugimoto[50] and Chu[52] implementations of the LaMer model, as discussed in Chapter 1.1.3. A nice example is reported in Figure 1.17.[139] As mentioned *supra*, this effect may be promptly observed by exploiting the time-space correlation established in continuous-flow methods and integrating into the setup on-line analytical techniques. Indeed, different reaction parameters, such as flow rate, can be easily screened and their effect on the reaction outcome (*e.g.* NPs size and size distribution) can be quasi-simultaneously evaluated, thus undemandingly optimizing the syntheses. Ultimately, a quenching step, such as the introduction of an additional reactant and/or dilution and/or cooling down of the reaction mixture, may be introduced after a certain

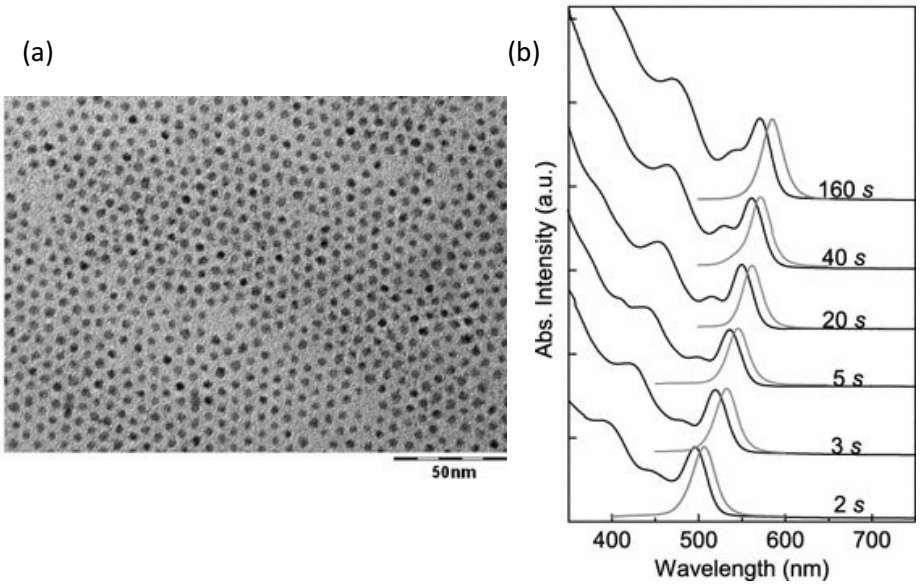

Figure 1.17 TEM micrograph of CdSe nanocrystals synthesised by Yang *et al.* at 280 °C in 160 s and absorption and emission spectra of a series of samples synthesised by varying the residence time from 2 s to 160 s, resulting in a modulation of CdSe size.
Reprinted from Yang *et al.*[139]

residence time (*i.e.* after a certain tubing length), in order to minimize NPs growth by aggregation and/or ripening phenomena and obtain narrow size distributions.

The first microfluidic synthesis of inorganic nanoparticles was reported by deMello *et al.*, who prepared high quality cadmium sulfide quantum dots.[140] Since their pioneering work, the microfluidic approach has been employed for the synthesis of different classes of inorganic compounds, encompassing metal nanoparticles (*e.g.* Au,[141–143] Ag,[143] Pd,[144,145] Pt[145,146]), metal oxides (*e.g.* SiO_2,[147–149] TiO_2,[150,151] ZnO,[152,153] Fe_xO_y[154,155]), chalcogenides (*e.g.* CdS, [127,140,156,157] CdSe,[139,158] ZnS[159,160]), also as core-shell structures (*e.g.* CdS/CdSe,[133] ZnS/CdS[161]), by exploiting the versatility of the method. Indeed, the microfluidic setup can be engineered as desired and both conventional and unconventional synthetic techniques can be implemented in continuous flow. Many details for inorganic synthesis in microfluidics may be found in specific reviews.[138,162–164]

Microfluidic syntheses can be either carried out in home-made setups built by assembling several discrete flow chemistry components together (such as pumping and metering of reactants systems, mixers, tubing, possible reaction temperature controller, chemical and/or thermal quench, pressure control, *in situ* probe detectors, collection of products) or in commercial compact units (*i.e.* "on chip" microsystems). The combination of isolated discrete components (schematic representation in Figure 1.18) might result more flexible for exploring a diverse portfolio of chemical synthesis, while "on chip" microsystems allow a more facile integration of monitoring components.

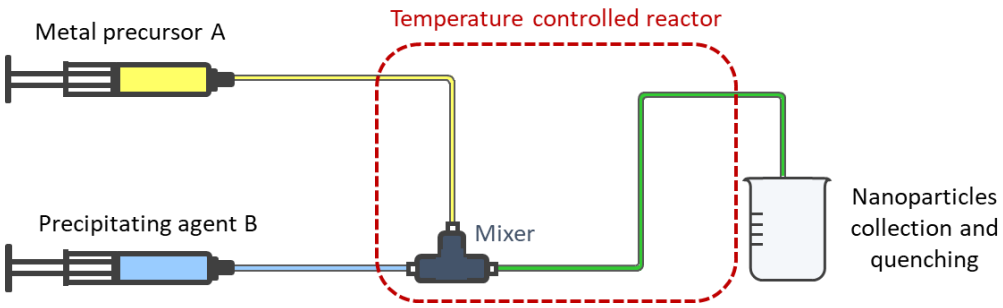

Figure 1.18 Schematic representation of continuous-flow setup for the synthesis of inorganic systems

In this Ph.D. Thesis, a microfluidic approach was employed to synthesize undoped and Eu(III)-doped calcium molybdate micro- and nanostructures (Chapter 3) using a simple ligand-free co-precipitation strategy and exploiting the peculiar features of continuous

flows in micro-channels to tune the final product outcomes. In particular, the role of the quenching step and the efficient control over the reaction mixture temperature offered by microfluidic were explored.

1.2.3 Mesoporous materials

According to the IUPAC definition,[9] porous materials[xvi] are classified into three categories, based on their pore size: microporous materials (< 2 nm), mesoporous materials (2-50 nm) and macroporous materials (> 50 nm). The scientific and technological importance of these materials can be attributed to the presence of voids of controllable dimensions at the atomic, molecular and nanometer size, that rule the field of their application. Indeed, according to their pore dimension, porous materials find different applications, ranging from industry to environmental applications, medicine (*e.g.* controlled release of drugs), sensor design, chromatographic supports, catalysis, etc.[165]

1.2.3.1 Synthesis of mesoporous materials

The most studied and applied members of the microporous class are zeolites, whose first scientific report dates back to Cronstedt in 1765, who discovered the mineral *stilbite*, which he described as "boiling stones" (hence the name zeolites, from the Greek ζέω "to boil" and λίθος "stone").[166] Since the development of their industrial synthesis in the 1950s, zeolites have been exploited for decades as heterogeneous acid catalysts, ion exchangers for water softening, molecular sieves and drying agents. However, despite their paramount importance in many processes, their applications are limited by their relatively small channels and cavities (5-12 Å), and they become inadequate when bulky reactants, that exceed the dimensions of the pores, have to be processed. Due to this drawback, research has been focused on pore enlargement and on the synthesis of *mesoporous* materials, whose major breakthrough is the publication of the synthesis of the M41S family of materials (most representative materials in Figure 1.19) by the Mobil Oil Corporation in 1992.[167,168] Since then, the development of siliceous mesoporous materials,[169–175] as well as non-siliceous[171,176–181] and organo-silica hybrid[182–185] mesoporous materials (*i.e.* periodic mesoporous organosilicas (PMOs), not covered herein), has been an area of extensive research.

[xvi] Porosity, or void fraction, Φ, is a measure of the void spaces of a material and it is defined as the ratio of *cavity* or *pore volume*, V_P, to the total volume: $\Phi = V_P/(V_P + V_S)$, with V_S as the *true volume* of the solid. It can be expressed also as $\Phi = 1 - \rho/\rho_0$, where ρ is the bulk density (*i.e.* geometrical, apparent density of a porous solid, including cavities) and ρ_0 is the true density (*i.e.* absolute density of the skeleton, without cavities). The total porosity of a material composes of the sum of the cavities which are connected with each other (*open* or *usable porosity*) and the isolated non-connected pores (*non-accessible* or *closed porosity*).

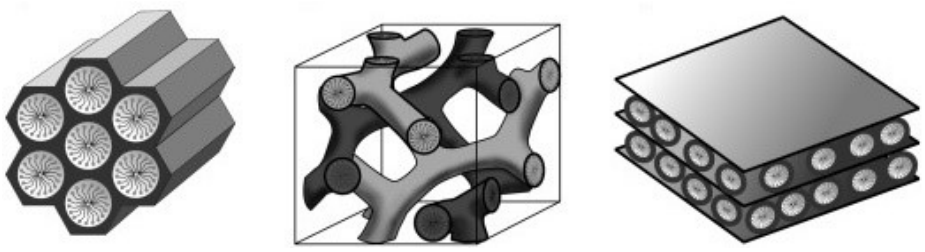

Figure 1.19 Structures of mesoporous M41S materials, characterized by pore diameters in the 2-10 nm range with different arrangements, and exhibiting amorphous pore walls: MCM-41 (2D hexagonal, space group *p6mm,* **left**), MCM-48 (cubic, space group *Ia-3d*, **center**), and MCM-50 (lamellar, space group *p2*, **right**). The MCM acronym stands for *Mobil Composition of Matter.* Reprinted from Hoffman *et al.*[183] with permission of Wiley

Most of the synthetic approaches for inorganic mesoporous materials are typically based on the use of organic template molecules that are exploited in different assembly processes around which the condensation of the inorganic precursor occurs (*endotemplate method* or *soft-matter templating*).[186] In particular, the original approach for the synthesis of MCM-41 materials, represented schematically in Figure 1.20, involves the employment of supramolecular aggregates of ionic surfactants,[xvii] such as long-chain alkyltrimethylammonium halides like CTAB, as structure-directing agents (SDA). Under basic conditions, these SDAs form a lyotropic liquid-crystalline phase and drive the condensation of the silica precursors (*i.e.* usually tetraethyl- (TEOS) or tetramethylorthosilica (TMOS)) into an assembly of an ordered mesostructured composite (pathway a in Figure 1.20). At lower concentrations of surfactant, a mechanism of cooperative self-assembly of the structure directing agent and the inorganic species (pathway b in Figure 1.20) is also possible. Subsequently, the surfactant is removed by extraction or calcination and the mesoporous materials are obtained. Depending on the employed surfactant,[xviii] on its concentration and on the temperature and pH, different liquid-crystal phases of the SDA can be obtained according to its phase diagram, and consequently mesoporous materials with different porous arrangements can be synthesizes, *i.e.* characterized by hexagonal, cubic or laminar pore symmetry (Figure 1.19).

[xvii] Surfactants are discussed in Chapter 1.2.1.1.

[xviii] The packing properties of the surfactant are described by the *packing parameter* g, that links the molecular structure of the amphiphilic molecule to the architecture of its aggregates, thus the mesophase (its symmetry and space group) that is formed. The packing parameter can be calculated as $g = V/(a_0 \cdot l)$, where V is the volume of the hydrophobic core, a_0 is the area of the head group and l is the length of the alkyl chain, and it is inversely related to the curvature of the surfactant self-assembly: surfactants with a small packing parameter (*i.e.* a high area of the head group and short chain) form self-assemblies characterized by a high curvature.[427]

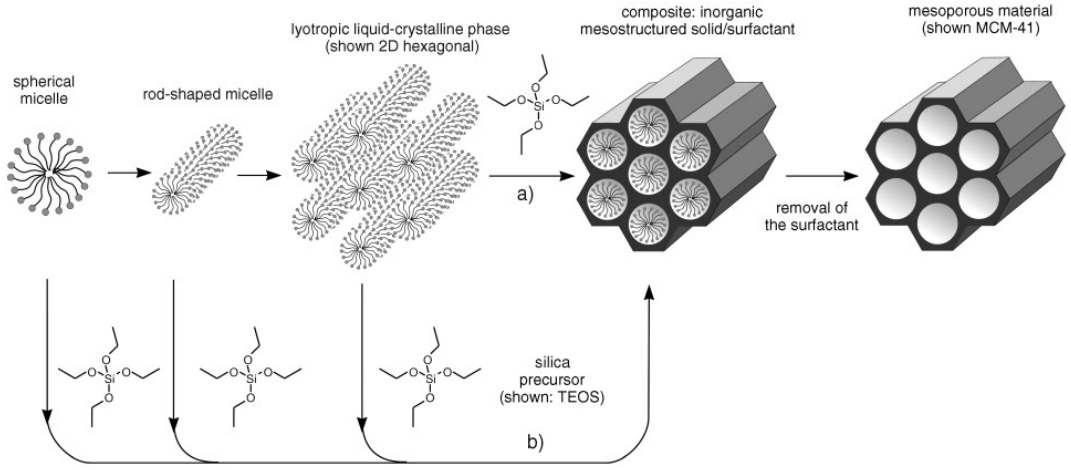

Figure 1.20 Schematic representation of the formation of mesoporous materials by structure-directing agents: true liquid-crystal template mechanism (**a**), cooperative liquid-crystal mechanism (**b**). Reprinted from Hoffman *et al.*[183] with permission of Wiley

Over the past decades, other mesoporous silica materials with ordered and tunable porous structures, such as the FSM (Folded Sheet Materials),[187] SBA (Santa Barbara Amorphous),[188] KIT (Korean Institute of Science and Technology),[189] and FDU (Fudan University)[190] families, have been developed by modification of the original synthetic approach. The fundamental requirement that drives the selection of the synthetic conditions (*e.g.* the choice of the surfactant, acidity of the medium, possible use of additives, etc.) employed for the synthesis of mesoporous materials is the establishment of an attractive interaction between the structure directing agent and the silica precursor, to ensure the inclusion of the SDA and avoid a phase separation. The interaction between the inorganic species and the head groups of the surfactants can be either direct or mediated by ionic soluble inorganic species, and, depending on the nature of the surfactant employed (*i.e.* ionic or nonionic), it can be governed by electrostatic interactions or occur through hydrogen bonds.[191,192] When a ionic surfactant is used, four different pathways can occur: i) S^+I^-: under basic conditions, the silica species are negatively charged and cationic quaternary ammonium surfactants are positively charged; ii) $S^+X^-I^+$: under acidic conditions, and in particular at pH < 2 (isoelectric point of the Si-OH bearing species), the silica species are present as cations and a mediator anion X^- (*e.g.* a halide) is necessary to ensure the interaction with the cationic surfactant; iii) $S^-M^+I^-$: an anionic surfactant (*e.g.* long-chain alkyl phosphates) and basic media are employed, thus a cationic mediator M^+ (*e.g.* Na^+) is added to produce the interaction; iv) S^-I^+: under acidic conditions, no mediator is needed. When a nonionic surfactant (*e.g.* long-chain amine) is employed, the attractive interactions may

occur through hydrogen bonds, and two pathways can be followed: i) S^0I^0: when uncharged silica species are present, and ii) $S^0(X^-I^+)^0$: when the surfactant interacts with a ion pair formed by the silica species and a mediator. The different interactions that can take place between the inorganic component and the surfactant are illustrated in Figure 1.21.

As mentioned, in the original synthetic approach for M41S family of mesoporous silica *long-chain alkyl ammonium salts* are employed as structure director agent in alkaline conditions, and the formation of mesoporous silica occurs through a S^+I^- direct interaction. Notably, this approach enables to tune the diameter of the porous system from 2 to 6 nm by changing the length of the alkyl chain of the surfactant molecule employed (typically C_{14}-C_{22} chains).[168,193] Another synthetic strategy that was reported to adjust the pore sizes consists of the addition of an "expander molecule", *e.g.* 1,3,4-trimethyl benzene, that dissolves in the hydrophobic region of the micelles, thus increasing their size.[168,192,193] New opportunities in the field were opened with the use of *nonionic surfactants* and polymeric-based organized systems as templating agents, such as the *polyalkylenoxide triblock copolymers* $(PEO)_{5\text{-}106}(PPO)_{33\text{-}70}(PEO)_{5\text{-}106}$ (*e.g.* Pluronic 123, $(PEO)_{20}(PPO)_{70}(PEO)_{20}$),[xix] that

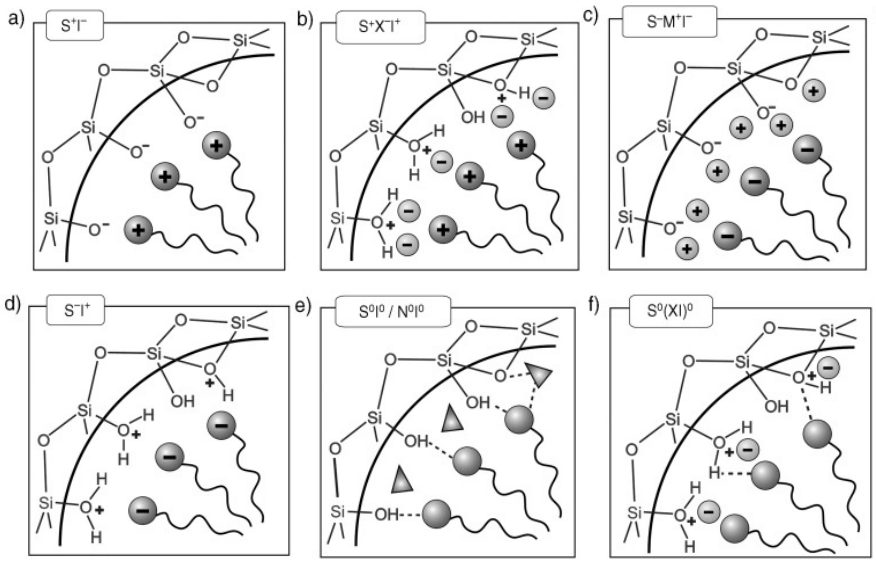

Figure 1.21 Interactions between the inorganic species and the head group of the surfactant with consideration of the possible synthetic pathways in acidic, basic or neutral media. Electrostatic interactions (**a-d**): S^+I^-, $S^+X^-I^+$, $S^-M^+I^-$, S^-I^+; interactions through hydrogen bonds (**e-f**): S^0I^0 or $S^0(X^-I^+)^0$, where S is the surfactant, I the inorganic species and M^+ and X^- are mediator ions. Adapted from Hoffman *et al.*[183] with permission of Wiley

[xix] The ratio of the number of hydrophilic (PEO) to hydrophobic (PPO) units in the triblock co-polymer $(PEO)_{5\text{-}106}(PPO)_{33\text{-}70}(PEO)_{5\text{-}106}$ is responsible for the formed mesophase (lamellar, hexagonal, cubic, etc) of the structure, according to its phase diagram.[197,428]

are employed in acidic conditions and interact with the inorganic species following a $(S)^0(X^-I^+)^0$ pathway. When polyalkylenoxide triblock copolymers, such as P-123, are used as structure directing agents, micelles constituted by a core of hydrophobic PPO blocks and a corona of hydrophilic PEO blocks are obtained, ultimately leading to composites (and eventually mesoporous materials) with a bimodular hierarchical pore structure. Indeed, the hydrophilic PEO chains of the copolymer interact with the polymerizing silica species during mesophase formation and penetrate within the silica framework, resulting into micropores formation, after the removal of the template. As a consequence, by employing different structure directing agents and exploiting different SDA-silica species interactions, mesoporous materials with the same mesoporous structure can be obtained, but they might differ in pore thickness and by the additional presence of intra-wall pores. This is the case of MCM-41 and SBA-15 mesoporous silicas, which are obtained with CTAB in alkaline conditions and P-123 in acidic conditions, respectively, and they are characterized by hexagonally ordered uniform mesopores (space group *p6mm*) not connected with each other in MCM-41, while linked by not ordered micropores in SBA-15 (see Figure 1.22 and Section 1.2.3.2).[173,194] Moreover, the employment of triblock copolymers as SDA as opposed to ionic surfactants allows to obtain thicker mesoporous walls (3-6 nm *vs* 1.0-1.5 nm for SBA-15 *vs* MCM-41, respectively),[193] responsible for a higher hydrothermal stability of the materials,[188,195] and to more freely tune the mesopores size (5-26 nm) and pore connectivity of the final mesoporous material by varying easily tunable synthetic parameters such as temperature[196–200] and reaction time,[188] but also changing pH,[201]

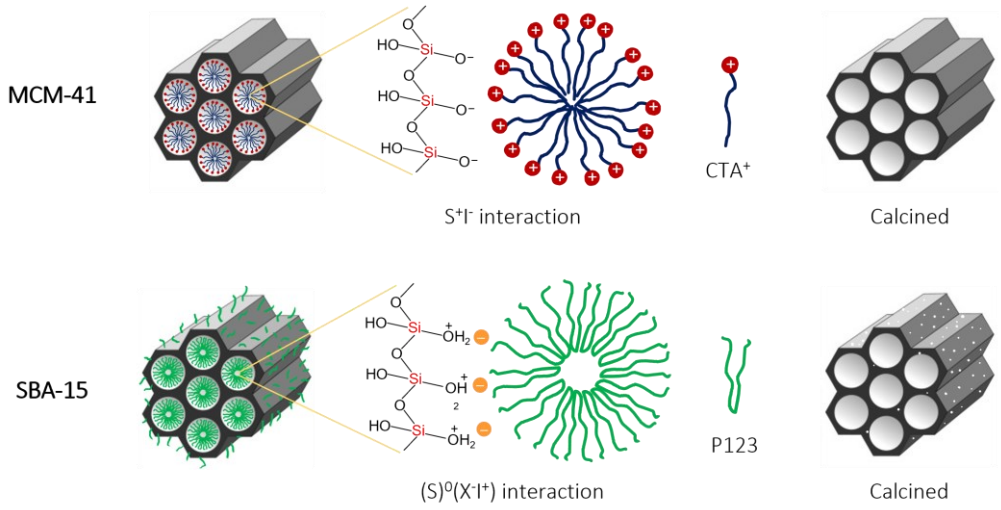

Figure 1.22 Schematic representation and comparison between MCM-41 and SBA-15 materials

adding co-surfactants, swelling agents and salts,[202–204] and modifying the lengths of the PEO blocks that enlarge the hydrophobic micelle core[197,205,206] (approach similar to the M41S family one).

A different class of synthetic methods for obtaining ordered mesoporous solids is represented by the *exotemplate methods* ("hard-matter templating"),[186] which are based on the employment of a rigid porous material as scaffold for the formation of another solid. The exotemplate framework is filled with inorganic species precursor and then removed; its porous system is then copied as a "negative image". By this approach, mesoporous silica phases, such as MCM-48 and SBA-15, as well as mesoporous carbon (CMK-1 and SNU-X materials)[207,208] were synthetized.

In the following, a brief description of the mesoporous structure and synthetic approach of SBA-15 and KIT-6 mesoporous silica materials, that were employed as confined environments in this Thesis work, are provided (Chapter 1.2.3.2 and 1.2.3.3, respectively).

1.2.3.2 SBA-15 mesoporous silica

As mentioned *supra*, SBA-15 mesoporous silica[188] is a combined hierarchical mesoporous and microporous material, characterized by highly ordered, two-dimensional parallel pores hexagonally arranged (space group *p6mm*) connected by micropores. As clearly visible by TEM micrographs (Figure 1.23), the parallel cylindrical pores of SBA-15 materials are typically slightly curved.

It is usually synthesized employing TEOS or TMOS as silica precursor and the triblock copolymer Pluronic 123 (P-123, $(PEO)_{20}(PPO)_{70}(PEO)_{20}$) as structure directing agent under acidic conditions (pH < 1), exploiting a $(S^0)(X^-I^+)^0$ interaction. The reaction mixture can be

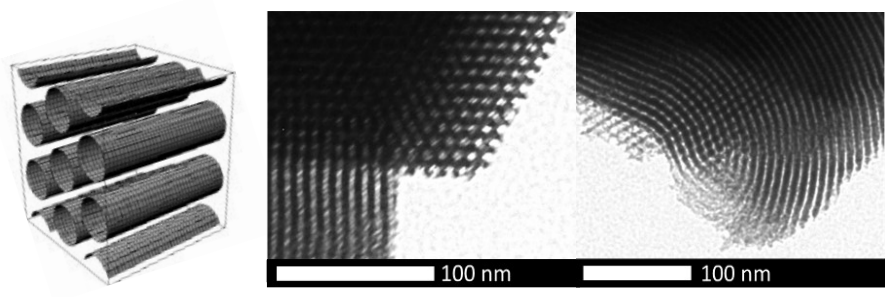

Figure 1.23 Schematic representation and TEM micrographs of SBA-15 mesoporous silica

treated hydrothermally at different temperatures (35 to 140 °C) for different lengths of time (11 to 72 hours), to result in systematically different uniform pore sizes and thickness of silica walls: higher temperatures or longer reaction times result in larger pore sizes and thinner silica walls.[188] Indeed, by variation of the synthetic parameters, SBA-15 with tunable pore diameter between 5 and 15 nm can be obtained. Generally, the SBA-15 pore walls are amorphous and thick (3.1-6.4 nm), and they are responsible for the high hydrothermal stability of SBA-15 compared to other mesoporous materials with thin pore walls, such as MCM-41.[188,195]

1.2.3.3 KIT-6 mesoporous silica

KIT-6 mesoporous silica,[189] the large-pore analogue of MCM-48, is characterized by a bi-continuous mesoporous system with a cubic symmetry (space group *Ia-3m*), constituted by a three-dimensional interpenetrating cylindrical porous network (Figure 1.24). If compared to mesoporous materials with bi-dimensional channels like SBA-15, the interconnected mesostructure of KIT-6 is advantageous when processes limited by diffusion or susceptible to pore blockage are targeted, such as catalysis or separation processes.

It is usually synthesized employing TEOS as silica precursor and a mixture of the triblock copolymer Pluronic 123 (P-123, $(PEO)_{20}(PPO)_{70}(PEO)_{20}$) and butanol (1:1 wt) as structure directing agent under acidic conditions, exploiting a $(S^0)(X^-I^+)^0$ interaction. The addition of butanol is responsible for the preferred swelling of the hydrophobic core of the co-polymer micelles, leading to micellar aggregates with decreased curvature, and ultimately to the formation of the cubic mesophase as silica condensation proceeds. As for SBA-15 materials, the reaction mixture is treated hydrothermally at different temperatures (35-130 °C), to effectively tailor the mesopore diameters, ranging from 4 to 12 nm (the higher the temperature the larger the pore diameter). Moreover, with increasing synthesis

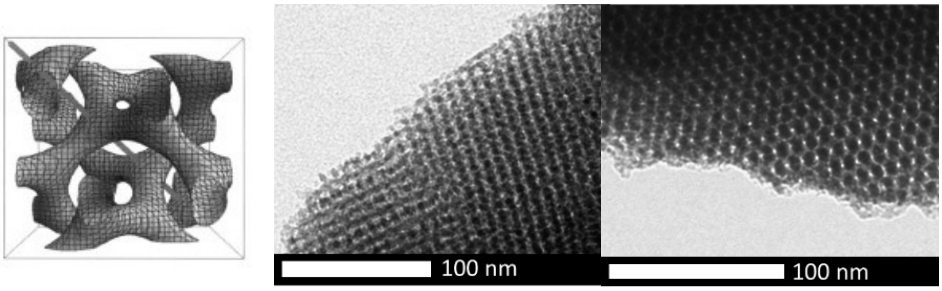

Figure 1.24 Schematic representation and TEM micrographs of KIT-6 mesoporous silica

temperature, the wall thickness and the number of micropores are gradually decreased.[189,209]

1.2.3.4 Mesoporous materials as supports for metal nanoparticles

Among the numerous applications of mesoporous materials, particularly attractive ones are usually pursued by exploiting their nanoporous structure as confined space for guest species. In this framework, the mesoporous materials can be employed as supports for catalytically active materials (*e.g.* precious metal nanoparticles).

Since it is well known that the performance of a supported catalyst is often dependent on the dispersion of the active component on the internal surface of the porous support, which is desired to be homogeneous, a particular care must be taken for loading the mesoporous system with the metal precursor. This procedure is usually carried out starting from a metal salt solution, and the most common preparation methods encompass the electrostatic adsorption, the ion-exchange, the reactive adsorption, and the wet impregnation.[210] The latter approach comprises three main steps: i) *impregnation step*: contacting a dry or wet support with an impregnating solution of the precursor, ii) *drying step*: drying the product under mild conditions, and iii) *activation step*: calcining and/or reducing the product if necessary. It has been reported that the first two steps have a major influence in determining the impregnation profile (*i.e.* the distribution of the impregnated active species over the support) of the final catalyst, while the third one is mainly affecting its activity.[211] In particular, depending on the amount of precursor solution employed, and incidentally on its concentration, the impregnation step can be termed as *wet impregnation* (*i.e.* the support is dispersed as a powder in an excess of volume of a diluted solution of the precursor) or *dry impregnation*, also called *incipient wetness impregnation* (*i.e.* the volume of the precursor solution is restricted to the total pore volume of the matrix to be filled, and thus a concentrated solution is usually employed). Typically, the incipient wetness impregnation (IWI) technique allows to efficiently load the pore system with the precursor, avoiding its deposition in significant amount at the external surface of the support. Indeed, the purpose of the IWI approach is that the precursor solution is entirely drawn into the pores by capillary forces and no precursor species is deposited on the outer surface of the support. The optimal conditions for efficiently infiltrate the pores of the support are mainly dependent on the pore surface polarity, on the polarity of the solvent and on the solubility

of the precursor in the solvent.[212] When a support with a polar surface such as mesoporous silica, and especially when it is rich of free silanol groups,[xx] a polar solvent is ideally employed to obtain adequate wettability and diffusion of the precursor solution through the pores. In the simplest case, water is the preferred solvent, since metal salts are typically employed as precursors, *e.g.* nitrates that are highly soluble in water and characterized by a low decomposition temperature. In addition to these considerations, when designing the impregnation of a porous support with a metal precursor solution, it is worth keeping in mind that when nanopores are concerned, confinements effects occur, and they are dependent on the pore diameter and surface chemistry of the pore wall.

At the end of the impregnation step, the pore volume is filled with solution and the metal precursor species in it are distributed between the adsorbed phase on the pore walls and the liquid phase in the pore volume. The following drying step is carried out to evaporate this liquid and in this process a redistribution of the impregnated species remaining in the pore volume may occur and the extent of its effect depend on the adsorptivity of the impregnated species (strong adsorptions are less affected by drying). For this reason, controlled drying processes are preferrable.[213,214]

In this Ph.D. Thesis, the pores of mesoporous silica materials (SBA-15 and KIT-6) were exploited as confined spaces in which palladium nanoparticles were synthesized, using an incipient wetness impregnation method followed by mild drying and a reduction step (Chapter 4). The effect of silica mesopores confined space on the crystallization of Pd nanoparticles was evaluated by comparing the structural, dimensional and functional (catalytic activity for CO oxidation) properties of Pd NPs synthesized on mesoporous silica with those of Pd NPs synthesized on a non-porous silica batch counterpart (without space constrain).

[xx] The number of silanol groups on the surface of mesoporous silica is influenced by the method employed for template removal. Indeed, a maximized polarity of the pore surface (*i.e.* with more silanol groups) is obtained when the surface directing agent (P-123 in the case of SBA-15 and KIT-6) is removed by solvent extraction with respect to calcination, that facilitates additional condensation of adjacent silanol units. In addition, the pore surface of mesoporous silica can be further modified and functionalized after the synthesis to tune its hydrophilicity and chemical compatibility with the guests. This ensures a higher degree of freedom in the choice of impregnation solvent and metal precursor.

1.3 Probing crystallization: *in situ* time-resolved techniques

In order to understand at an atomic/molecular level the pathway through which the crystallization proceeds and the influence of space confinement on it, it is of paramount importance to be able to characterize the (nano)crystals at each stage of crystallization and at different length scales. The characterization of the system can be carried out either *ex situ*, after the isolation of the product from the reaction medium, in case at different crystallization stages, or ideally *in situ*, exploiting time-resolved characterization techniques. *In situ* time-resolved experimentations represent the most powerful means by which the key stages of inorganic crystallization can be unraveled, also allowing to overcome many limitations typical of *ex situ* characterization techniques (*e.g.* isolation from reaction medium, deadtimes). Many literature studies reported the successful employment of a variety of characterization techniques for following the crystallization process, such as X-ray and neutron scattering, X-ray absorption, microscopy and tomography-based methods, and some specific reviews may be found.[215–220]

As largely discussed in Chapter 1.1, according to either classical or non-classical models, crystallization occurs through different stages, encompassing i) the formation of particles precursor and the increase of its concentration over the supersaturation threshold, ii) nucleation, iii) growth and iv) aggregation. During these stages, the evolution of the species with time occurs over the molecular (*i.e.* local coordination state), nano- (*i.e.* primary units), and longer scale (*i.e.* crystallite formation). Since each characterization method usually provides information on a limited size range, data acquired with a single characterization technique rarely provide all the necessary information to comprehensively unveil multiple key stages of the crystallization pathway. Thus, integrating various techniques represents a promising multimodal strategy for collecting information over different length scales and different time scales. However, since with separate *in situ* studies it is usually difficult to obtain consistent and corroborative information about complex processes at different length scales, intelligent combinations of complementary techniques into one experimental setup disclose the most exciting opportunities. This multi-scale approach can be pursued by carrying out combined or simultaneous experiments: in *combined experiments*, the sample is measured at different times using different techniques and experimental settings in

sequence, while, in *simultaneous experiments*, the sample is excited and different signals produced by the sample are measured at the same time.

Among the available techniques for following the formation of inorganic materials, X-rays-based methods demonstrated to be extremely powerful in bridging the molecular and macro length scales during the crystallization process. Indeed, thanks to the i) short wavelength (*i.e.* comparable to molecular/atomic bond lengths), ii) large penetration depth, and iii) energies comparable with those of the atom core levels and consequent iv) chemical sensitivity of X-rays, X-ray scattering and absorption techniques offer excellent opportunities to monitor the entire course of crystallization of inorganic materials *in situ* under real reaction conditions. With the use of high photon flux X-ray beams generated by synchrotron facilities and/or more sensitive detectors, crystallization can be probed *in situ* in a time-resolved fashion also in diluted suspension, obtaining high quality (*i.e.* high signal-to-noise ratio) spectra and scattering patterns with short exposure times, and thus datasets of high temporal resolution, crucial to probe fast dynamics. Moreover, with respect to microscopy-based methods, X-ray scattering and absorption techniques do not provide information on a single (or few) particle(s), but average data from ensembles of many particles are collected, providing higher statistics to describe the sample with better fidelity and thus offering a more reliable insight on the reaction mixture.[220] As shown in Figure 1.25, the conversion of precursor reactant(s) into nanoparticle precursor can be probed by

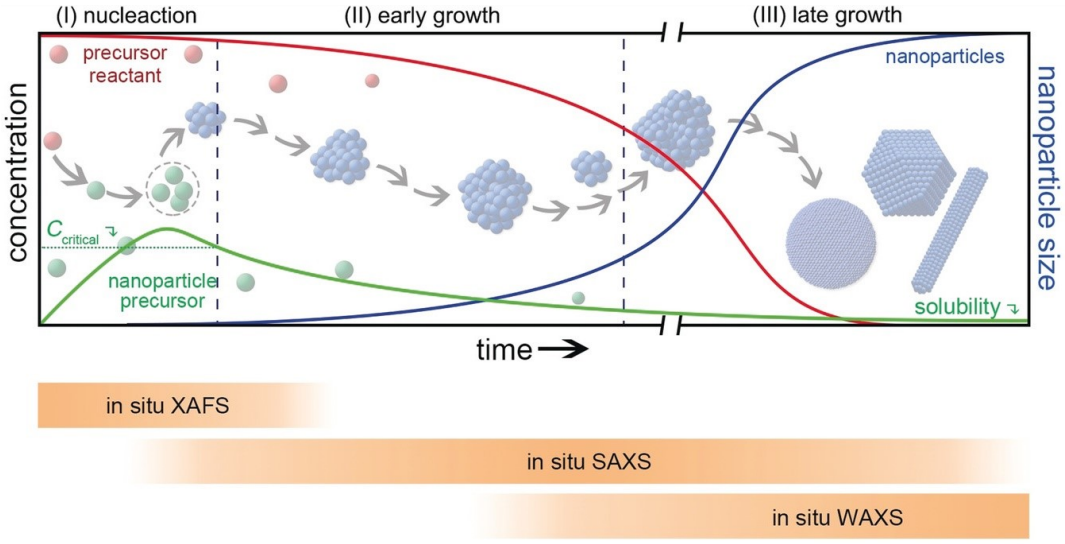

Figure 1.25 Schematic representation of the time-dependent evolution of the concentrations of precursor reactants (red), nanoparticle precursor (green) and size of nanoparticles (blue) involved in colloidal syntheses of nanoparticles, together with the appropriate *in situ* X-ray techniques for the different evolution periods. Reproduced from Wu *et al.*[215] with permission of Wiley

in situ X-ray absorption spectroscopy (XAFS), that determines variations in the local chemical environment of target element, through both electronic investigations and structural determination at the local state. The reaction of NP precursor and formation of nuclei can be followed by *in situ* small angle X-ray scattering (SAXS), which is size-sensitive and is the most appropriate technique to monitor the growth of the primary particles, also into anisotropic structures. Finally, the growth and structural reconstruction of the crystalline structure can be probed by *in situ* wide angle X-ray scattering (WAXS), enabling polymorph identification, and determination of crystallite size and structural features. A more detailed description of these analytic techniques is provided in Chapter 7.

Some interesting literature works employed X-ray absorption spectroscopy and/or scattering to gain some mechanistic insights into nucleation and/or growth stages of various inorganic materials,[218,221–226] also extracting some quantitative information about crystallization, and the most notable ones exploited intelligent combinations of XAFS, SAXS and WAXS techniques, providing complementary chemical, electronic and structural information.[227–229] However, nowadays the characterization of crystallization processes remains a significant open challenge, especially when multiple pathways operate simultaneously. Indeed, the design and building of a suitable experimental setup for reproducing real reaction conditions at the beamline could be demanding, also considering technical, albeit fundamental, issues, such as i) the radiation must be able to penetrate the cell walls, ii) the signal-to-noise ratio must be high enough, thus for example the possible contribution of reaction solvent, such as intensity attenuation or diffuse scatter, must be taken into account, iii) geometrical constraints in positioning detectors for different signals might be present, iv) the experiment must be optimized to enable rapid enough data acquisition, depending on the kinetics of the phenomenon of interest. Moreover, another challenge regards the extraction of time-resolved quantitative kinetic parameters from acquired data, mostly because data fitting usually requires previous assumption of empirical models, often simplified to reduce the complexity of data analysis. On the other hand, the use of too complicated models can lead to inaccurate analysis due to the risk of overfitting. Complementary information about the size, shape and polydispersity of the studied system from additional *ex situ* characterization techniques, such as TEM imaging, results particularly useful for data interpretation.

In this Ph.D. Thesis, synchrotron-based *in situ* time-resolved techniques were exploited to follow i) the crystallization of molybdenum oxide in the confined space of miniemulsion droplets and in batch conditions by simultaneous SAXS/WAXS experiments (Chapter 2.3), ii) the thermal-induced structural evolution of molybdenum oxide by combined XAS/XRD (Chapter 2.4), iii) the electronic changes of palladium NPs supported over mesoporous and non-porous silica materials under *operando* conditions, *i.e.* catalytic oxidation of CO, by XAS (Chapter 4.4), and iv) the evolution over time of the Fe-species during the synthesis of iron sulfides in the confined space of miniemulsion droplets and in batch conditions by quick-XAS (case study presented in Appendix A, due to preliminar data discussion).

2

Molybdenum oxide

In this Chapter, the synthesis of molybdenum(VI) oxide nano- and microrods with hexagonal section in miniemulsion and in batch conditions is addressed, evaluating the effects of spatial confinement offered by miniemulsion droplets on their crystallization. Several synthetic parameters were screened and their effect on the crystal structure of h-MoO_3, as well as on its size, size distribution and morphology, were investigated. Moreover, a direct insight on the crystallization pathway of MoO_3 in both synthetic conditions and as a function of synthetic parameters was provided by an *in situ* time-resolved SAXS/WAXS study performed at Elettra Sincrotrone Trieste. Finally, the phase-transition behavior of the metastable hexagonal MoO_3, obtained with and without space constraint, to the thermodynamically stable orthorhombic polymorph was investigated exploiting *in situ* combined XAS and XRD techniques at Diamond Light Source.

2.1 Introduction

Molybdenum displays one of the most complex chemistries of the transition elements, thanks to its wide variety of oxidation states and possible coordination numbers and geometries. Different molybdenum oxides are known, but the most stable product is molybdenum(VI) oxide MoO_3, which can be obtained by heating the metal or other compounds, *e.g.* sulfides, in the presence of oxygen. MoO_3 is acidic and insoluble in water, it is a n-type semiconductor with a wide band gap (> 2.8 eV) and it has been employed in various fields of application, including photocatalysis,[230–233] photochromic and electrochromic devices,[234,235] and gas sensors.[236–239]

Molybdenum(VI) oxide is known to crystallize in three main polymorphs, depending on the crystallographic arrangement of MoO_6 building blocks: α-MoO_3, β-MoO_3, and h-MoO_3. The thermodynamically stable orthorhombic α-MoO_3 (space group *Pnma*) is constituted by MoO_6 distorted octahedra sharing edges and corners along [001] and [100] directions respectively, resulting in zigzag chains and a distinctive 2D layered structure parallel to the (010) plane (Figure 2.1, top).[240] The metastable monoclinic β-MoO_3 ($P2_1/n$) is characterized by a ReO_3-type structure in which the MoO_6 octahedra share corners to build a distorted cube.[241] On the other hand, metastable hexagonal h-MoO_3 ($P6_3/m$) is constituted by zigzag chains of MoO_6 octahedra interlinked through the *cis*-position, giving rise to a crystalline structure with large one-dimensional tunnels (ca. 3.0 Å in diameter) with hexagonal symmetry along the *c*-axis (Figure 2.1, bottom).[242,243] Due to the stronger bonding of MoO_6 octahedra along the *c*-axis thanks to the zigzag structure formed by sharing edges, h-MoO_3 usually shows high anisotropy, growing as rods with hexagonal cross-sections.[243] Thanks to its peculiar tunnel-structure, the metastable hexagonal polymorph of molybdenum(VI) oxide may show enhanced properties when compared to the other polymorphs. For instance, ion exchanges in h-MoO_3 are facilitated and electron-hole separation under

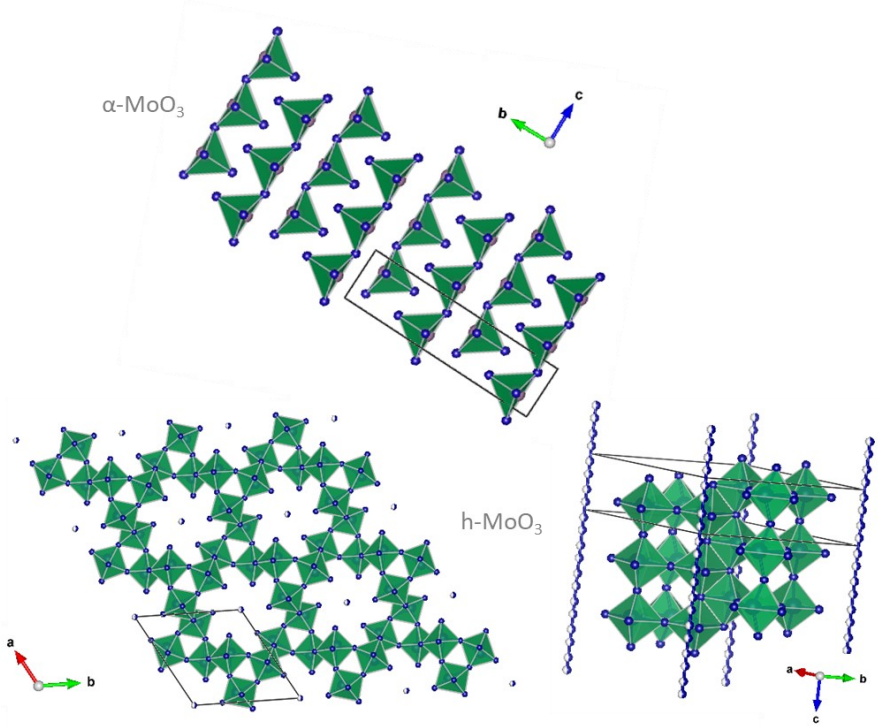

Figure 2.1 Schematic representation of the crystalline structure of α-MoO_3 (**top**) and h-MoO_3 (**bottom**) polymorphs of molybdenum(VI) oxide

irradiation is accelerated, ensuring a better photocatalytic activity towards the degradation of organic pollutants with respect to α-MoO_3.[231,244]

According to Lunk *et al.*,[245] the first report of hexagonal molybdenum oxide dates back to 1906, when A. Rosenheim precipitated a "molybdic acid hydrate" ($MoO_3 \cdot 2H_2O$) by acidification of an aqueous solution of ammonium paramolybdate with nitric acid.[246] Subsequently, several reports of hexagonal MoO_3 nanorods synthesis have been published, both *via* simple chemical precipitation of molybdate precursors[230,243,245,247,248] and *via* decomposition of peroxomolybdate precursors.[233,244,249,250] Crystalline h-MoO_3 is often prepared in hydrothermal conditions,[231,233,244,247,250] or, in general, the reported procedures involve heating the reaction mixture above 70-100 °C.[230,243,245,248] On the contrary, in this Ph.D. Thesis the synthesis of crystalline hexagonal molybdenum oxide was addressed at room temperature, both in *batch conditions* and in the confined space of *inverse miniemulsion (ME) droplets*.

To crystallize molybdenum(VI) oxide by both inverse miniemulsion and batch approaches, the dehydration and polycondensation reactions occurring in acidified solutions of Mo(VI) were exploited. Indeed, it is well known that molybdate ions $[MoO_4]^{2-}$ are a weak base and through the acidification of their aqueous solution they undergo several equilibria that generate polynuclear species, *i.e.* polyoxomolybdates, or mononuclear protonated species, according to the following general equation:

$$p\,[MoO_4]^{2-} + q\,H^+ \;\rightleftarrows\; [(MoO_4{}^{2-})_p(H^+)_q]^{(q-2p)-} \qquad (2.1)$$

The presence of polyoxomolybdates in solution is strongly influenced by the concentration of molybdenum(VI) and by the pH of the solution,[251–254] as reported in the distribution diagram in Figure 2.2. Although the mechanism for the formation of polyanions is not clear, it is generally accepted that the process is governed by the ability of Mo^{6+} to expand its coordination sphere from four to six. Indeed, the polyanions normally consist of MoO_6 octahedra, which are assembled by sharing edges and vertices.[251] By decreasing the pH of the solution, the nuclearity of the polyoxomolybdates increases due to condensation and polymerization of metal oxo-buildings, until molybdenum oxide is obtained.[255]

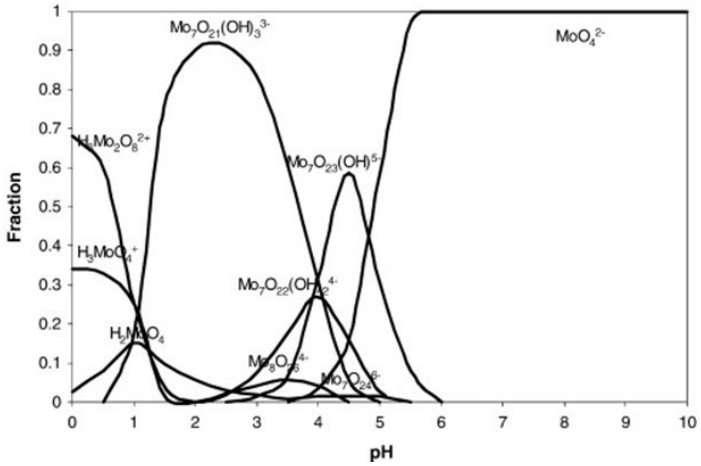

Figure 2.2 Distribution of molybdenum species in the Mo-H_2O system as a function of pH (total concentration of $[MoO_4]^{2-}$ = 21.20 mM).
Reproduced from Zeng *et al.*[252] with permission of Elsevier

In this Ph.D. Thesis, the polymerization of molybdate solutions by pH lowering was exploited in two different reaction environments: in a macroreactor (*batch approach*) and in inverse *miniemulsion* nanodroplets. The effects of the confined space of ME droplets, as compared to the macroreactor, as well as the influence of the main synthetic parameters screened on the synthesis outcomes are discussed in Chapter 2.2. The effect of space confinement offered by ME droplets on the synthesis of MoO_3 was further investigated through *in situ* time-resolved SAXS/WAXS experiments, performed varying the synthesis conditions, and the results are presented in Chapter 2.3. Finally, Chapter 2.4 reports a direct insight on the phase transition between the metastable and the thermodynamically stable polymorphs of molybdenum(VI) oxide that was acquired by a *in situ* combined XAS and XRD study.

2.2 Synthesis of hexagonal molybdenum oxide by inverse miniemulsion and batch approaches

As mentioned in the Introduction section and described in detail in Chapter 6.1, for the synthesis of molybdenum(VI) oxide by both inverse miniemulsion and batch approaches, the dehydration and polycondensation reactions occurring in acidified solutions of Mo(VI) were exploited. Briefly, an excess of concentrated nitric acid (65 wt%, 14.0 M) was added to aqueous solutions of ammonium heptamolybdate (AHM, $(NH_4)_6Mo_7O_{24} \cdot 4H_2O$) at room temperature, and molybdenum(VI) oxide was precipitated according to the reaction:

$$(NH_4)_6Mo_7O_{24} + 6\,HNO_3 \rightarrow 7\,MoO_{3_{(s)}} + 6\,NH_4NO_3 + 3\,H_2O \qquad (2.2)$$

While the *batch approach* involved the simple mixing of the two precursors (dropwise addition of HNO_3 to AHM solution), the *ME approach* was performed by the addition of a concentrated HNO_3 solution to a pre-formed inverse miniemulsion of AHM and subsequent further ultrasonication to promote the acid diffusion into ME droplets (*diffusion method*, described in Chapter 1.2.1.3). The obtained reaction mixtures were left stirring at room temperature and the product was purified and dried in vacuum. A systematic variation of different synthetic parameters was carried out, within both synthetic approaches, partly in cooperation with the Master student Maria Vittoria Massagrande. In particular, the following parameters were screened: i) the AHM molar concentration (0.10, 0.15, 0.20, and 0.25 M), ii) the AHM: HNO_3 molar ratio (1:10, 1:15, 1:20, and 1:25), iii) the application of ultrasounds (*vide infra*), and iv) the reaction time (5 min, 1 h, 3 h, 6 h, 18 h, and 24 h).

As a first step, the formulation of stable inverse (water-in-oil) miniemulsions of AHM was addressed, in cooperation with the Bachelor student Pietro Ostellari. As extensively described in Chapter 1.2.1, inverse miniemulsions are generally exploited for inorganic synthesis, and they are produced by application of high shear forces (*e.g.* ultrasounds) to a mixture of an excess of oily phase and an aqueous phase (water:oil 1:3 or 1:4 wt), in the presence of a surfactant and of an osmotically active agent, which is commonly the precursor's metal salt. Typical experimental conditions comprise cyclohexane as continuous phase and a "small enough" amount of a low HLB surfactant, always below its critical micelle concentration (cmc). In the present work, for the formulation of stable inverse miniemulsions of AHM, cyclohexane was employed as oil phase and ammonium heptamolybdate was exploited as osmotic agent. Two different water-to-oil weight ratios were screened (1:3 and 1:4 wt). Two different nonionic surfactants were tested, namely Span80 and PGPR (chemical structure in Figure B.1), and their amount with respect to the oil phase was varied between 1 and 10 wt% (1, 1.5, 2, 3, 6, and 10 wt%). Span80 (sorbitane monoleate) is characterized by an HLB value of 4.3 and a cmc in cyclohexane of 0.035 mol/L[256] (corresponding to about 2 wt%), while the HLB value of PGPR (polyglycerol polyricinoleate) is of 1.5-2.0 and its cmc in cyclohexane is equal to 1.8 wt%.[257] It was observed that stable inverse miniemulsions were obtained when both Span80 and PGPR surfactants were employed, in concentration ranging from 1 to 3 wt% and from 1 to 2 wt% with respect to the oil phase, respectively, in agreement with the reported cmc values. The average hydrodynamic diameter of the ME droplets produced with the two different surfactants ([Span80 or PGPR] = 1-10 wt%, [AHM] = 0.2 M, water:oil = 1:3 wt) was estimated

by dynamic light scattering (DLS) and it was found that the smallest droplets were obtained by using Span80 at 1.5 wt%. Indeed, ME droplets produced with Span80 were characterized by a size ranging from 250 to 330 nm (with a minimum at 1.5 wt%), while PGPR-stabilized ME droplets were significantly bigger (350-460 nm, with a minimum at 1.5%). Moreover, it was observed that, by increasing the concentration of the osmotically active agent (*i.e.* AHM) and keeping constant all the other parameters, the hydrodynamic diameter of the ME droplets increased accordingly. Analogously, a variation of the water-to-oil ratio from 1:3 wt to 1:4 wt resulted in an increase in ME droplets size. As a consequence of these considerations, in the following AHM miniemulsions were formulated by using Span80 as surfactant, at a concentration of 1.5 wt%, and a water-to-oil ratio of 1:3 wt.

After the formulation of stable miniemulsions was optimized, the synthesis of molybdenum(VI) oxide was addressed in miniemulsion and batch conditions, and the synthetic parameters were screened as mentioned above. As "reference" miniemulsion and batch samples, the following synthetic conditions were employed: [AHM] 0.2 M, AHM:HNO_3 1:10 mol, reaction time 24 hours. The synthesized products were characterized from a structural (XRD) and morphological (TEM and SEM) point of view, as well as their purity was assessed by ATR.

XRD analysis of both batch and miniemulsion samples showed that molybdenum(VI) oxide crystallized as the metastable hexagonal polymorph, h-MoO_3, without the formation of any secondary products (Figure 2.3). Interestingly, the obtained product seemed to accommodate NH_4^+ and H^+ cations in its hexagonal framework, since the experimental data better matched the crystalline structure of $(NH_4)_{0.944}H_{3.304}Mo_{5.292}O_{18}$ (ICSD 01-083-1175) rather than pure MoO_3 (JCPDS 00-021-0569). This result was expected, since it has been thoroughly reported in the literature on how monovalent cations (*e.g.* Na^+, K^+, H^+, and NH_4^+) are present in the cavity of the hexagonal structure of metastable h-MoO_3, stabilizing the tunnel oriented along the *c*-axis, as well as they acting as structure directing agents for the formation of elongated structures.[231,244,245] Moreover, it was found that the relative intensities of the experimental reflections did not match with the ones reported in the databases, as an indication that the samples were characterized by a clear preferred orientation. In particular, the (200) and (300) reflections were more intense than the reference database ones (see inset of Figure 2.3), meaning that the preferred orientation was along the [100] direction, likely along the tunnel structure. The enhancement of (h00)

family of reflections intensity with respect to the reference ones was found more evident for miniemulsion samples than batch ones. From the fitting of XRD patterns (Figure 2.3), average crystallite sizes in the 150-200 nm range and in the micron-range were estimated for the miniemulsion and batch samples, respectively, confirming a certain control on the material growth in ME conditions (effect of space confinement).

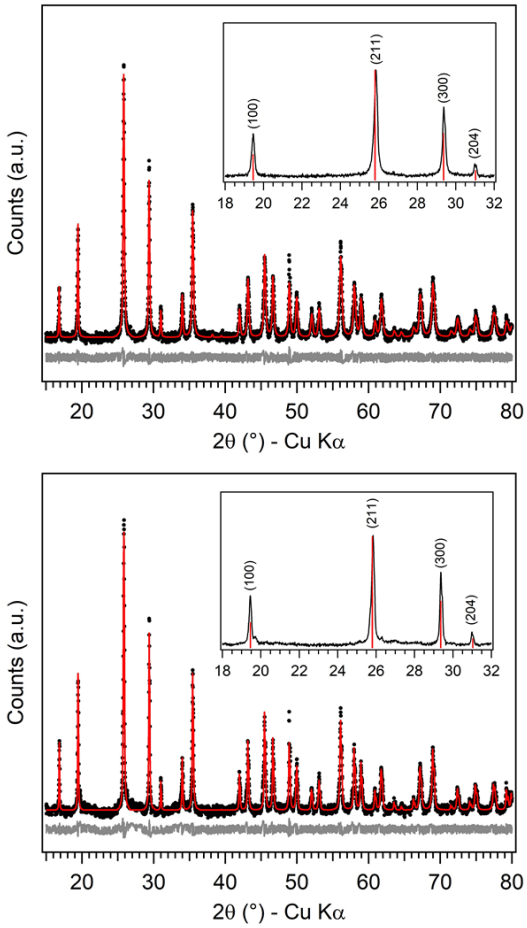

Figure 2.3 XRD fittings of miniemulsion (**top**) and batch (**bottom**) samples ([AHM] = 0.20 M, AHM:HNO_3 1:10 mol, 24 h). **Insets:** XRD pattern (18-32° 2θ), superimposed with reference database pattern (red sticks)

These observations are consistent with TEM and SEM analyses (some representative micrographs are reported in Figure 2.4, together with rod length and aspect ratio distributions), which showed that the obtained products by both synthetic approaches crystallized as rods with hexagonal section, as expected for the hexagonal polymorph of MoO_3. However, it is worth noting that the synthetic strategy played a relevant role in determining the size of the rods and their aspect ratio (*i.e.* the ratio between the width and

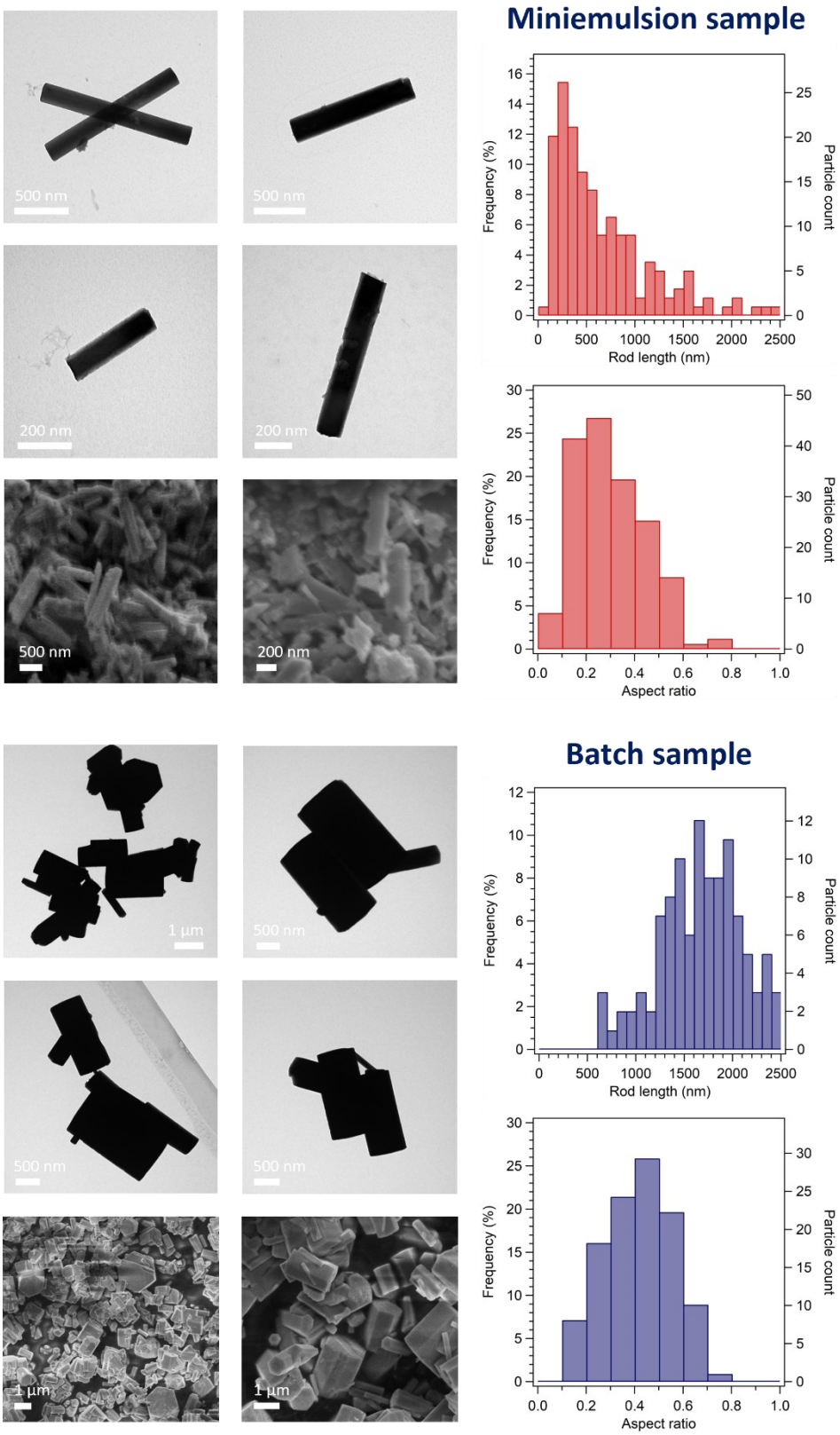

Figure 2.4 Representative TEM and SEM micrographs of miniemulsion (**top**) and batch (**bottom**) 24 h samples [AHM] = 0.20 M, AHM:HNO_3 1:10 mol, together with histograms representing the rod length and aspect ratio distributions of the samples (ME in red, batch in blue), estimated from TEM micrographs

the length of the rods), obtaining on average smaller and more elongated rods by ME approach. Indeed, by confining the synthesis of MoO_3 in miniemulsion nanodroplets, rods characterized by a relatively low aspect ratio (AR = 0.3) and an average rod length of 650 nm (average rod width of 170 nm) were obtained, while the batch ones showed larger average dimensions (average rod length of 1.7 µm and width of 730 nm) and a higher aspect ratio (AR = 0.4). It is noteworthy to outline that, in literature, no smaller MoO_3 rods than the here discussed ME ones were reported, as micron-sized rod lengths were generally obtained.[230,233,243,244,247,258–261] As mentioned, TEM results were in agreement with XRD results, both in terms of average size (larger for batch samples) and aspect ratio (smaller for ME samples). Indeed, the more pronounced preferred orientation of ME samples was confirmed by their more elongated shape observed by TEM. However, for both samples, the average size of the h-MoO_3 particles measured by TEM micrographs was larger than the crystallites sizes estimated from XRD fittings, indicating that the rods were polycrystalline. Since the rod-like particles evidenced by TEM and SEM were found to be well-faceted and their cross section resembled the crystalline symmetry of h-MoO_3, it could be argued that the aggregation of the primary particles occurred in an oriented fashion, and the resulting rods could likely be mesocrystals (*i.e.* obtained by the oriented aggregation of primary particles in a common crystallographic register).

Furthermore, the effectiveness of the purification method in removing surfactant moieties in ME samples was confirmed by ATR measurements: no vibrational bands ascribable to Span80 were found in the IR spectra in the 4500-500 cm^{-1} range. Along with characteristic Mo-O stretching vibrations for h-MoO_3 ($\nu_{O\text{-}Mo\text{-}O}$ 500-600 cm^{-1}, $\nu_{Mo=O}$ at 892 and 975 cm^{-1}),[261] stretching and bending vibrations of N-H and O-H were observed ($\nu_{N\text{-}H}$ at 3204 cm^{-1}, $\delta_{N\text{-}H}$ at 1426 cm^{-1}, $\nu_{O\text{-}H}$ at 3430 cm^{-1}, and $\delta_{O\text{-}H}$ at 1616 cm^{-1}),[262] confirming the presence of ammonium ions and water in the structure. IR spectra of miniemulsion and batch samples are reported in Appendix B.1 in Figure B.2.

I. Effect of AHM concentration. As outlined in detail in Chapter 1.1.3, according to the most accomplished models of particles formation, generally the number of formed primary particles, as well as their final size, can be experimentally tuned by varying the precursor concentration. In addition, as reported in the literature and observed in the initial ME formulation optimization study, the size of the miniemulsion droplets is influenced by the amount of osmotic agent (*i.e.* ammonium heptamolybdate in this specific case), offering the

possibility of tuning the constrained conditions the formed particles are subjected to. For these reasons, a series of both miniemulsion and batch syntheses in which the concentration of the aqueous solution of AHM was systematically varied from 0.10 M to 0.25 M was carried out, by keeping constant the AHM:HNO_3 molar ratio to 1:10 mol and the reaction time to 24 hours.

The crystalline structure of the ME and batch samples was investigated by XRD, and, with all synthetic conditions, the formation of the metastable hexagonal polymorph of MoO_3 was observed. As per the reference samples discussed above, the relative intensities of the experimental reflections were consistent with preferred orientation of the crystallites. A comparison of the diffraction patterns of miniemulsion and batch samples synthesized with increasing AHM concentration is reported in Figure 2.5, left and right, respectively. While in the case of batch samples no significant changes in the diffraction patterns as a function of the starting AHM concentration were observed, for miniemulsion samples a slight increase in crystallinity with increasing AHM concentration was noticed.

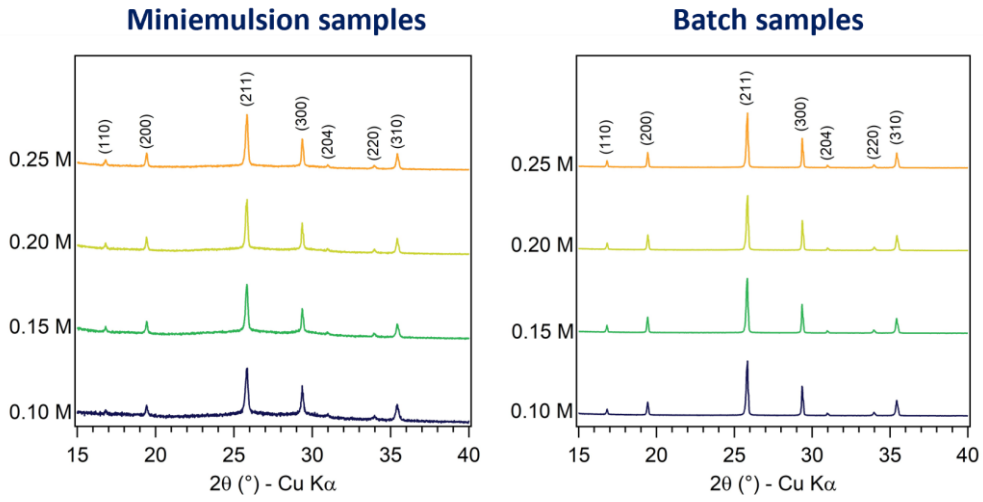

Figure 2.5 Comparison of XRD pattern (15-40° 2θ) of h-MoO_3 samples synthesized in miniemulsion (**left**) and in batch (**right**) starting from AHM solutions with different concentration (0.10, 0.15, 0.20 and 0.25 M) and constant AHM:HNO_3 molar ratio (1:10 mol) and reaction time (24 h)

Slightly more evident effects of the precursor solution concentration were observed on the size and morphology of MoO_3 particles, investigated by TEM (in Figure 2.6). Generally, smaller and more elongated rods by ME with respect to the batch approach were observed in all the screened conditions. No clear trend was found in the average length of MoO_3 rods synthesized by the batch approach as a function of AHM concentration, while a slight

increase in rod length with increasing AHM concentration could be appreciated for miniemulsion samples. This finding, even if not pronounced, is in agreement with the observed increase in ME droplets size by increasing the concentration of the osmotic agent described above. In addition, a clearer trend as a function of AHM concentration was observed in the aspect ratio of MoO_3 rods, synthesized by both approaches. Indeed, by increasing the precursors concentration, and keeping constant the AHM:HNO_3 molar ratio, the aspect ratio of the rods decreased, and this effect was particularly marked for batch samples, obtaining quasi-cubic microparticles at low AHM concentration, and more elongated (aspect ratio of 0.5) prisms at higher AHM concentration. Histograms of rod length and aspect ratio distributions, as well as average lengths and widths, of miniemulsion and batch samples as a function of AHM concentration are reported in Figure B.3, Figure B.4 and Table B.1, respectively, in Appendix B.1.

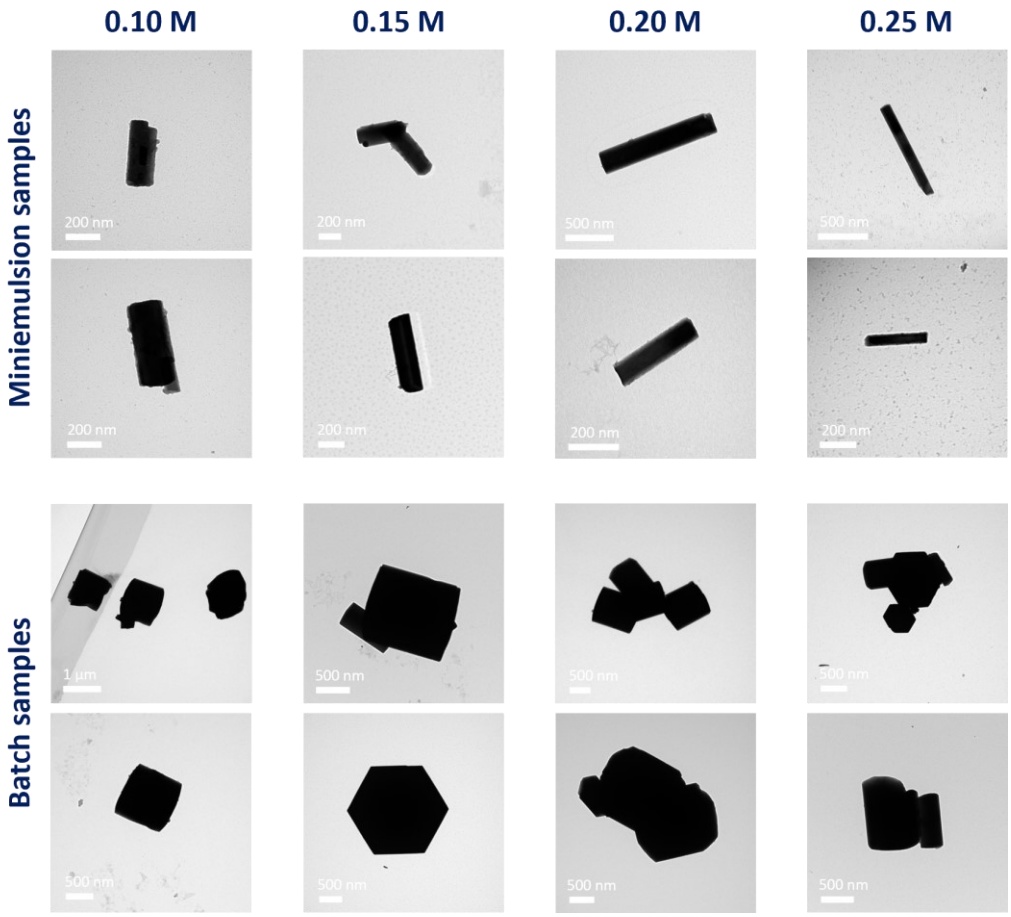

Figure 2.6 TEM micrographs of miniemulsion (**top**) and batch (**bottom**) samples synthesized with different AHM concentrations (0.10, 0.15, 0.20, and 0.25 M) and constant AHM:HNO_3 molar ratio (1:10) and reaction time (24 h)

II. Effect of AHM:HNO_3 molar ratio. Since the diffraction pattern of miniemulsion samples displayed a minor amount of amorphous material in addition to the metastable hexagonal polymorph of MoO_3, a series of syntheses with increasing acid amount were carried out to evaluate if the crystallinity of the product could be improved by a variation of the synthetic conditions. In particular, the AHM:HNO_3 molar ratio was screened between 1:10 to 1:25 within both approaches, keeping the AHM concentration constant to 0.20 M. As can be observed in Figure 2.7, an increase in the amount of acid added to the reaction mixture led to the disappearance of the amorphous halo from 20° to 40° 2θ in the XRD pattern of miniemulsion samples, thus to an increase in crystallinity of h-MoO_3 (up to an 80 % decrease of the amorphous halo).[xxi] On the contrary, for batch samples, that were highly crystalline already with AHM:HNO_3 of 1:10 mol, no appreciable differences were found.

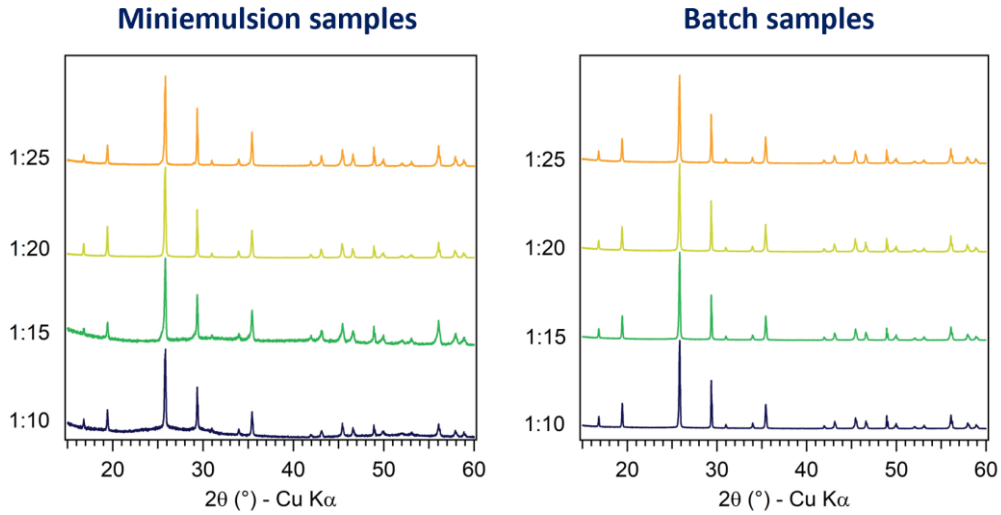

Figure 2.7 Comparison of XRD pattern (15-60° 2θ) of h-MoO_3 samples synthesized in miniemulsion (**left**) and in batch (**right**) as a function of AHM:HNO_3 molar ratio (1:10, 1:15, 1:20, and 1:25 mol), keeping constant the AHM concentration and the reaction time ([AHM] = 0.20 M, reaction time of 24 hours)

Besides affecting the crystallinity of h-MoO_3, the molar ratio between $Mo_7O_{24}^{6-}$ and HNO_3 was found to play a role also in determining the size and morphology of molybdenum oxide nano- and microstructures, for miniemulsion and batch samples, respectively, as shown in Figure 2.8. In particular, it was found that, with higher amounts of nitric acid, MoO_3 rods

[xxi] The crystallinity of the samples was estimated as the ratio between the area of the reflections and the total area of the reflections and amorphous halo in the range 20-40° 2θ. The increase in crystallinity was estimated by comparing the percentage of amorphous material (*i.e.* 100 - %crystallinity) between different samples.

obtained by ME were likely to grow stacked one on top of the other, as fewer independent non-aggregated rods were observed by electronic microscopies as compared to the reference sample. In addition, the obtained rods seemed more well-faceted. A more significant effect on MoO_3 morphology by varying AHM:HNO_3 molar ratio was observed by batch approach: an increase in acid amount led to the formation of evidently smaller and more elongated rods (see average length and AR in Table B.2, and size distributions in Figure B.5 and Figure B.6 for miniemulsion and batch samples, respectively).

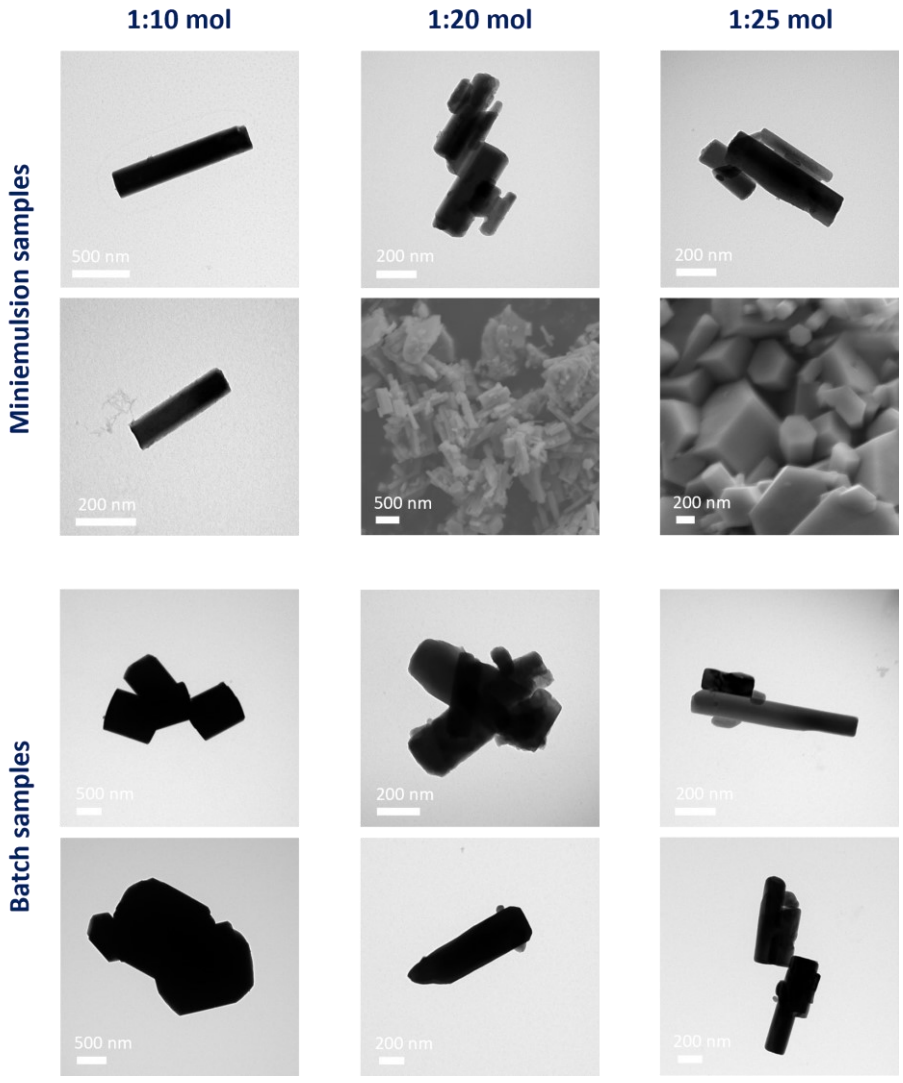

Figure 2.8 TEM and SEM micrographs of miniemulsion (**top**) and batch (**bottom**) samples synthesized with different AHM:HNO_3 molar ratios (1:10, 1:20, and 1:25 mol) and constant AHM concentration ([AHM] = 0.20 M) and reaction time (24 h)

III. Effect of ultrasounds on HNO_3 diffusion into ME droplets. As described in Chapter 1.2.1.3, when inorganic synthesis in miniemulsion is carried out exploiting the *diffusion approach* (*i.e.* external addition of the precipitating agent to a pre-formed miniemulsion containing the metal precursor, exploited for this study), the penetration of the precipitating agent into the ME droplets is usually triggered by an additional step of homogenization of the reaction mixture (*i.e.* pre-formed ME and added aqueous solution of precipitating agent). With the aim of investigating the spontaneous diffusion of nitric acid into the pre-formed ME nanodroplets containing molybdenum precursor, miniemulsion synthesis without applying ultrasounds to the reaction mixture after the acid addition was carried out ([AHM] = 0.20 M, AHM:HNO_3 1:10 and 1:20 mol).

The crystalline structure of the sample was characterized by XRD, and its diffraction pattern showed that the formation of the hexagonal polymorph of MoO_3 occurred even without triggering the mixing of the precipitating agent with AHM solution inside the droplets by ultrasonication, indicating that nitric acid diffused spontaneously into ME droplets. It could be argued that the diffusion of HNO_3 occurs more slowly without the ultrasounds trigger, which is therefore not mandatory for the penetration of the added dispersed phase (nitric acid) into the droplets, which occurs anyway, but the application of the ultrasound trigger likely acts as a prompt for a more effective mixing of the precursor and the precipitating agent in the confined space of ME droplets, facilitating and accelerating it. The hypothesis of a slower diffusion is based on the fact that, from TEM investigations of the samples, it was observed that rods characterized by a smaller length (average of about 450 nm *vs* 650 nm) and similar aspect ratio (average AR of 0.3) were obtained without applying US after acid addition, as compared to rods synthesized with the same synthetic conditions and carrying out the US step (rod length and aspect ratio distributions in Figure 2.9). Moreover, it was observed that the different approach of mixing molybdenum precursor with the precipitating agent played a role also in determining the aggregation of MoO_3 rods, and this effect could likely be ascribed to different kinetics of particles formation. In particular, while rods obtained by applying an US step after the acid addition did not display any regular aggregation, the formation of flower-like structures constituted by the aggregation of long microrods with hexagonal section developing from the center was observed for samples obtained without ultrasonication after acid addition, as shown in SEM images reported in Figure 2.10, top and center, respectively. The formation of hierarchical flower-like architectures of h-MoO_3 rods was reported also in literature, and it is usually observed

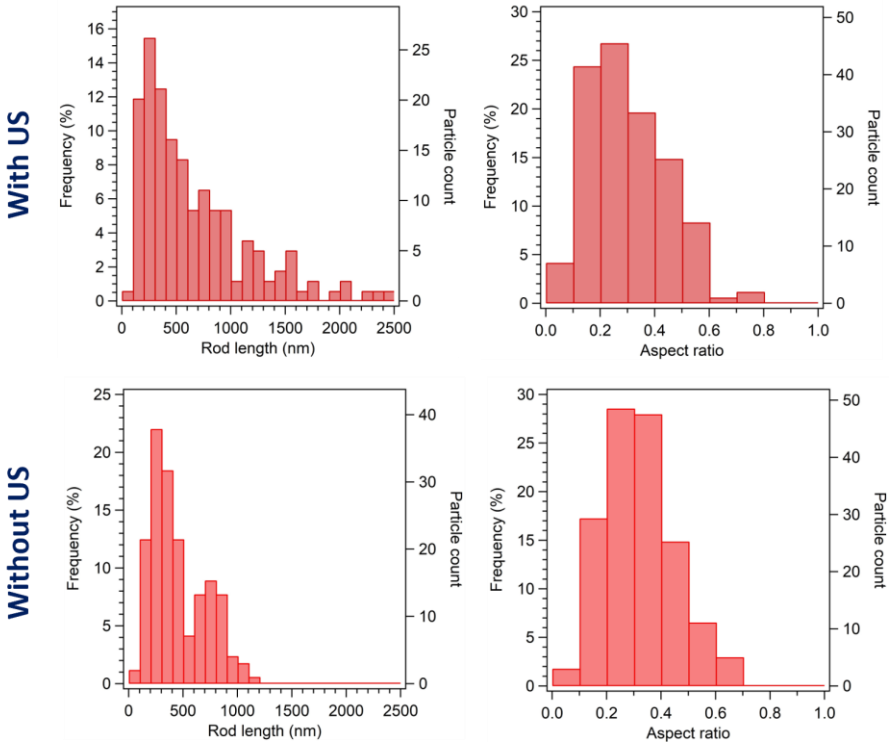

Figure 2.9 Histograms representing rod length and aspect ratio distributions of miniemulsion samples synthesized by applying (**top**) or not applying (**bottom**) US after acid addition. [AHM] = 0.20 M; AHM: HNO_3 1:10 mol, 24 h

under heat treatment (70-120 °C).[230,231,234,248,263] Chithambararaj *et al.* proposed that they are obtained through an oriented attachment mechanism of the 1D hexagonal structures: a spontaneous self-assembly of hexagonal rods occurs by strong interparticle forces, leading to an oriented anisotropic growth of branched flower-like structures.[230] However, by running the reaction in miniemulsion without the US step after acid addition for a longer period of time (48 hours *vs* 24 hours), flower-like aggregates were not observed anymore, and disordered, not aggregated and elongated rod-like structures were obtained (SEM micrographs in Figure 2.10, bottom). This finding is in agreement with the hypothesized slower reaction kinetics in miniemulsion droplets without the external trigger of ultrasounds providing effective and rapid mixing of the reactants.

In order to exclude the role of ultrasounds on the morphology and aggregation of MoO_3 rods obtained in miniemulsion, besides enhancing and accelerating the diffusion of the acid into ME droplets, ultrasounds were applied also to a batch synthesis, after the acid addition, with the same experimental conditions employed for ME synthesis (details in Chapter 6.1.3). By comparing TEM micrographs of the batch samples obtained by applying or not applying US after acid addition, it was evidenced that ultrasound-treated batch h-MoO_3 rods

were smaller than non-treated h-MoO_3 (average rod length of 1250 nm *vs* 1700 nm, same AR of about 0.4), but always significatively larger than miniemulsion rods, indicating that the major parameter controlling the particle size in miniemulsion is the space confinement provided by the ME droplets, while the US effect is negligible. Histograms representing the rod length and aspect ratio distributions of batch samples synthesized with and without US are reported in Figure B.7 in Appendix B.1, as well as average values (Table B.3).

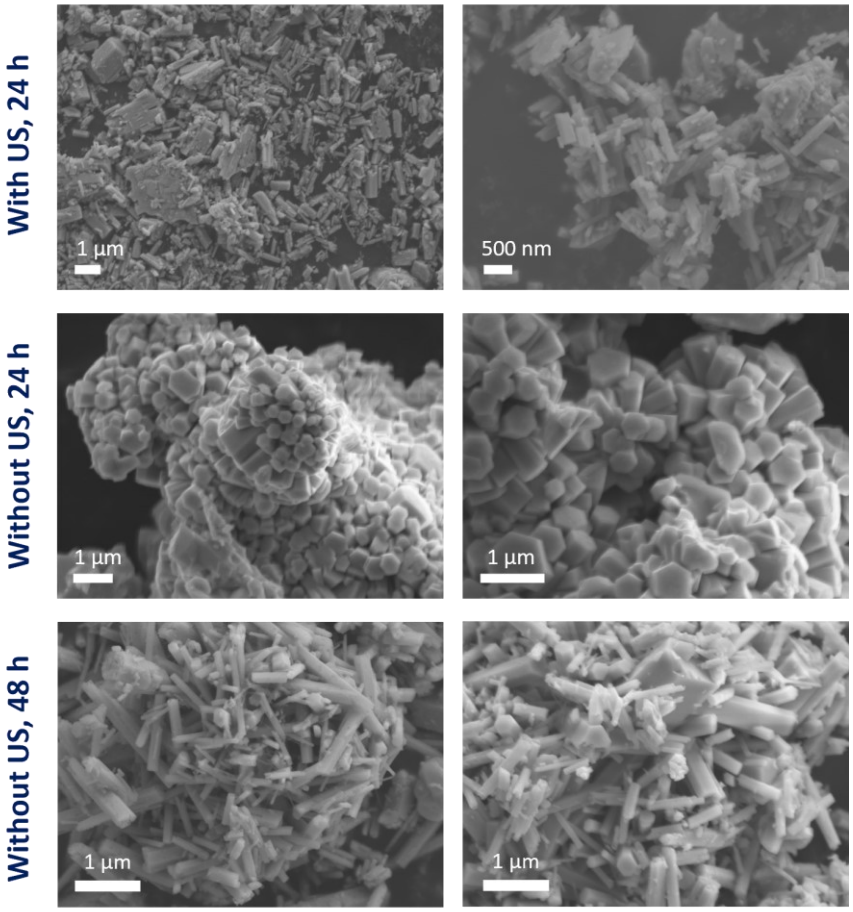

Figure 2.10 SEM images of miniemulsion samples synthesized by applying (**top**) or not applying (**center** and **bottom**) US after acid addition and running the reaction for 24 hours (**top** and **center**) or 48 hours (**bottom**). [AHM] = 0.20 M; AHM: HNO_3 1:20 mol

IV. Effect of reaction time. To elucidate the formation mechanism of h-MoO_3 rods by miniemulsion and batch approaches, with and without applying ultrasounds after the acid addition, the intermediates at different reaction times (*i.e.*, 5 minutes, 1, 3, 6, and 18 hours) were *ex situ* analyzed through XRD. The comparison between the diffraction patterns of the samples obtained after selected reaction times is shown in Figure 2.11. It was observed that reaction times shorter than 18 hours did not lead to the crystallization of any

molybdenum(VI) oxide polymorphs. Otherwise, the formation of several ammonium polyoxomolybdates with different nuclearities, such as $(NH_4)_4(Mo_8O_{26})(H_2O)_4$, $(NH_4)_6(Mo_9O_{30})(H_2O)_5$, $(NH_4)_2(Mo_3O_{10})$ and $(NH_4)_2(Mo_4O_{13})$, with all synthetic approaches, was instead evidenced. These structures, characterized by quite big unit cells, displayed the most intense reflections at low Bragg angles ($2\theta < 15°$), and are constituted by MoO_6 octahedra sharing vertices or edges.[254,264,265] As discussed in the Introduction section of this Chapter (Chapter 2.1), despite the chemistry of polyoxometalates is very complex and their formation mechanism is far away from being completely clear, such finding was expected, as it is known that the acidification of a solution of molybdate ions gives rise to metal-oxide fragments, which increase in nuclearity as the pH of the solution decreases, until the most stable product, *i.e.* the metal oxide itself, is formed.[255] After 18 hours, by batch approach crystalline h-MoO_3 was obtained. On the other hand, in the case of miniemulsion samples, while less intense principal reflections of the hexagonal molybdenum oxide were observed superimposed to the amorphous pattern from 25° to 35° 2θ and coexisting with it when US were applied (Figure 2.11, left), an amorphous pattern was observed for non US-treated miniemulsion sample (Figure 2.11, center). This observation further supported the hypothesis of a slower (*i.e.* lower, after the same reaction time) diffusion of nitric acid into ME droplets containing AHM solution without the application of US. After 24 hours, the

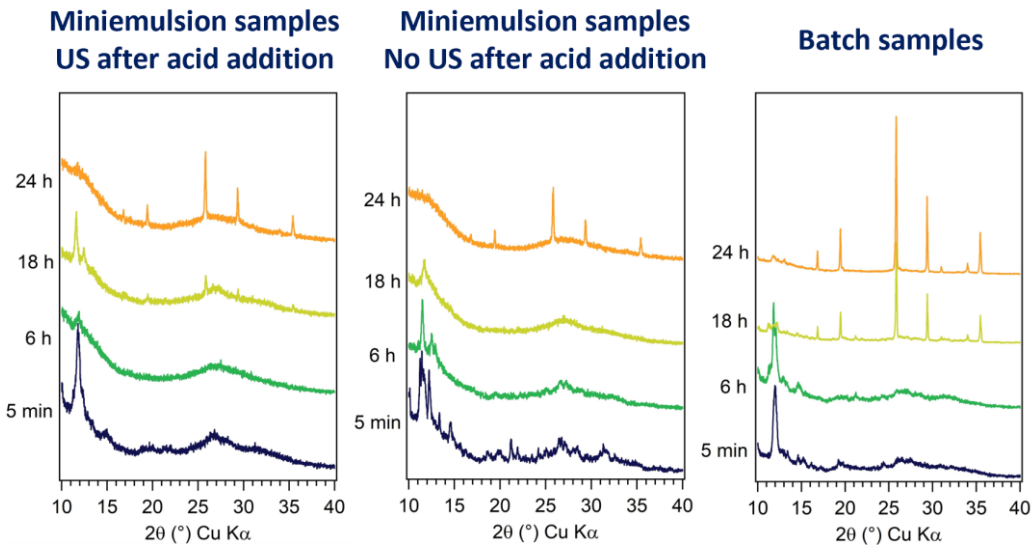

Figure 2.11 Comparison between XRD patterns of samples obtained in ME with (**left**) and without (**center**) applying US after acid addition and in batch (**right**), after different reaction times (5 min, 6 h, 18 h, and 24 h). [AHM] = 0.20 M; AHM: HNO_3 1:10 mol

crystallinity of the samples was further improved, and a decrease in the amorphous percentage was observed for miniemulsion samples.

The observed evolution of the diffraction patterns of the samples as a function of reaction time, and the final formation of a metastable polymorph of MoO_3 instead of the thermodynamically stable one, is consistent with a kinetic polymorph control and with the Ostwald's rule of stages, which predicts the phase that is energetically closest to the initial state to be kinetically most readily accessible.[27] Indeed, in the case of kinetic polymorph control, crystallization does not follow a single-step pathway, but rather a sequential process involving structural and compositional modifications of amorphous and/or crystalline intermediates. According to the Ostwald's "step rule", the least dense phase is formed first, and gradually transforms into the next dense phase until the most dense one (*i.e.* usually also the most stable phase) is formed. This kinetic transformation cascade occurs in order of increasing thermodynamic stability.[23,44] Taking into account the Ostwald step rule, and considering that both polyoxomolybdates and molybdenum oxide are constituted by the same primary unit of MoO_6 octahedra differently arranged, it is likely that the investigated crystallization is a stepwise process that occurs through subsequent transformations of kinetically accessible transient phases into the final polymorph. These transformations involve the condensation and rearrangement of MoO_6 octahedra from the polyoxomolybdates phases into the most stable phase (h-MoO_3).

The evolution of the size and morphology of MoO_3 rods synthesized by miniemulsion and batch approaches as a function of time (18 hours *vs* 24 hours) was investigated by TEM microscopy (Figure 2.12). As expected, and supported from XRD patterns evolution, the average length of the rods increased by extending the reaction time by both synthetic approaches (from about 450 nm to 650 nm for ME rods, and from about 1050 nm to 1700 nm for batch rods). However, in the case of miniemulsion samples, an increase in the average aspect ratio (from 0.2 to 0.3) and in the center values of the size distribution was observed, indicating that the rods mostly grew more in width than in length from 18 to 24 hours. This trend was not observed in batch conditions. Size distributions and average length, width and AR of the samples are reported in Figure B.8 and Table B.3 in Appendix B.1.

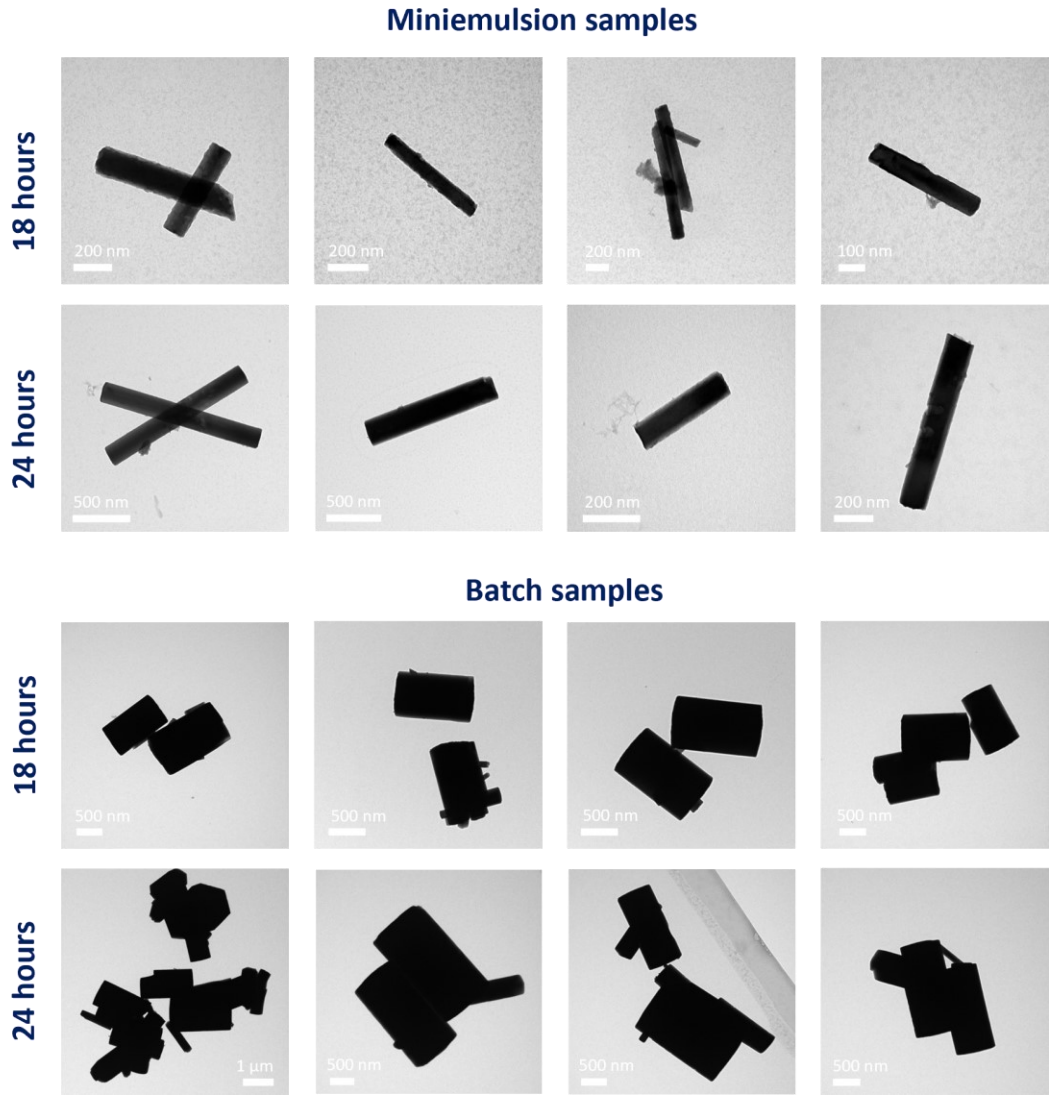

Figure 2.12 TEM micrographs of miniemulsion (**top**) and batch (**bottom**) samples synthesized with reaction times of 18 hours and 24 hours [AHM] = 0.20 M; AHM: HNO_3 1:10 mol

2.3 Time-resolved *in situ* SAXS/WAXS study of MoO_3 crystallization by inverse miniemulsion and batch approaches

With the aim of shedding light on the time evolution of the crystallization of molybdenum(VI) oxide, and further deepen the acquired knowledge on the effect of the synthesis parameters and approaches (*i.e.* batch *vs* confined space miniemulsion) investigated and discussed in Chapter 2.2, a time-resolved *in situ* simultaneous SAXS/WAXS study was performed at the Austrian SAXS beamline at Elettra Sincrotrone (Trieste). The adopted combination of the two complementary scattering-based characterization techniques provided a comprehensive picture of the structural and morphological evolution at different length scales of the studied system. Indeed, at small scattering angles (SAXS, small angle X-ray scattering), material structures at large (> 1 nm) distances could be studied (*e.g.* long-range structural order, nuclei growth, aggregation of primary particles), while at wider scattering angles (WAXS, wide angle X-ray scattering)[xxii] atomic scales (< 1 nm) were detected (*e.g.* arrangement of atoms within a crystalline material, providing insight on different polymorphs). This is a consequence of the different factors giving rise to the measured scattering intensity for SAXS and WAXS techniques, that are the contrast between the objects and the surrounding for the former and local changes in the electron density on the Ångstrom-scale for the latter. Moreover, exploiting high-flux facilities such as synchrotron sources allowed to study the nucleation and growth of MoO_3 in real time and on the time scale of seconds, under the reaction environment, without the need of making any approximation.[219,266]

As extensively described in Chapter 6.1.4, a continuous-flow setup was built at the beamline to follow *in situ* in a time-resolved fashion the evolution of the studied system during the different reaction steps by both miniemulsion and batch approaches. In particular, it consisted in i) a thermostated reaction vessel, ii) a flow system that circulated the reaction mixture through a measuring quartz capillary, iii) a remotely controlled ultrasonicator and iv) a remotely controlled syringe pump, to homogenize the miniemulsion and allow the addition of the precipitating agent while the experiment was running. This continuous-flow setup efficiently simulated the procedures employed during the laboratory syntheses, at the same time providing the flexibility for designing different series of experiments by

[xxii] Wide angle X-ray scattering (WAXS) might also be found in literature as X-ray diffraction (XRD), see Chapter 7.9.

exploiting both synthetic approaches. Finally, thanks to the possibility of remotely controlling each reaction step, it enabled us to get an insight on the entire process without blind periods of time. As discussed in Chapter 2.2 and described in detail in Chapter 6.1.4, in the case of the *ME approach*, the synthesis stages were: i) formation of inverse ME droplets containing aqueous solution of Mo(VI) precursor (AHM) by ultrasonication, ii) addition of concentrated nitric acid, and iii) further step of ultrasonication to enhance the mixing of reactants within ME droplets. The *batch approach* was performed by adding concentrated nitric acid to an aqueous Mo(VI) precursor solution under stirring. From the previous *ex situ* investigation of the effects of different reaction parameters (*i.e.* AHM concentration, AHM:HNO_3 molar ratio, ultrasonication step after acid addition), it was observed that the molar ratio between molybdenum precursor and the precipitating agent played the major role on determining MoO_3 crystallinity, size and morphology. Moreover, it was found that the diffusion of nitric acid inside ME droplets occurred also without applying the external trigger of ultrasounds, likely with a slower kinetics. Based on these considerations (see Chapter 2.2), three series of experiments were performed, aiming at reproducing at the beamline molybdenum(VI) oxide syntheses and exploiting:

i) the miniemulsion approach (*first series* of experiments);
ii) the miniemulsion approach without applying US after acid addition (*second series* of experiments);
iii) the batch approach (*third series* of experiments).

Within each series of experiments, the AHM:HNO_3 molar ratio was varied between 1:10 and 1:25 mol and the AHM concentration in aqueous solution was kept constant to 0.20 M. The small-angle and wide-angle scattering profiles of the reaction mixture were followed simultaneously as a function of time up to 1-3 hours (depending on the observed variation of profile features), setting as t = 0 s the start of acid injection.

Likely due to the relatively high concentration of the reaction mixtures and to the large dimensions of the scatterers (*e.g.* ME droplets and/or aggregates of particles and/or large-scale species) with respect to the beamline resolution (about 30 nm, see Chapter 6.1.4), the Guinier region[xxiii] of the SAXS profiles obtained by both approaches could not be observed,

[xxiii] The Guinier approximation describes asymptotic behavior of the scattering curve in the small q range, and states that any form factor function can be approximated to a Gaussian function in the small angle limit. It provides a method for accurately determine the size of a particle by SAXS. However, it requires scattering data that do not contain any structure factor, a condition usually met

therefore the scatterers size could not be determined from SAXS data. Nevertheless, as discussed in detail for each series of experiments (*vide infra)*, the occurrence of Bragg reflections in the higher q SAXS region (from 2 to 7 nm^{-1}) was evidenced in all investigated conditions, indicating the nucleation and growth of a material characterized by a long-range order. Since the spacing of the Bragg peaks relative to each other in the *q*-scale brings information on the symmetry of the crystal system or on the shape of periodic microdomain structures,[267,268] the relative positions of the Bragg peaks, together with their widths and relative rate of growth, were employed for comparing the observed features evolution. For instance, for the following microdomains ordered arrays, the ratio of the q-values at the scattering maxima should be:

- For lamellae: 1, 2, 3, 4, 5, …
- For spheres in a body-centered cubic array: 1, $\sqrt{2}$, $\sqrt{3}$, 2, $\sqrt{5}$, …
- For cylinders in a hexagonal array: 1, $\sqrt{3}$, 2, $\sqrt{7}$, 3, …

As far as the simultaneously acquired WAXS patterns are concerned, the q-range from 16 to 22 nm^{-1}, corresponding to about 23-31° 2θ with a Cu K_α radiation (*i.e.* λ = 1.54 Å), was taken into account, enabling us to directly compare the *in situ* measurements with the *ex situ* characterizations carried out by XRD at Home Institution. In the following, the three series of experiments performed are discussed and the results compared with each other.

I. First series: miniemulsion synthesis. Starting from the non-homogenized mixture of aqueous solution of AHM and oil solution of 1.5 wt% Span80 in cyclohexane, the ultrasonication step (2 minutes) was followed by the evolution of the SAXS profile (Figure 2.13, top left). As miniemulsion droplets were produced by fission and fusion processes, an increase in the intensity of the scattering signal and a change in its slope at low q was observed. This evolution was expected because of the increase of the number of scattering objects as a consequence of miniemulsion formation (see Chapter 7.9). Subsequently, the remotely controlled injection of concentrated nitric acid was started (set as t = 0 s, as mentioned),[xxiv] and a further increase in scattering intensity was evidenced (Figure 2.13, top

for dilute solutions, the data must be measured to sufficiently small angles, and the sample must be constituted by monodisperse particles.[266]

[xxiv] To directly compare the reaction times and evaluate the kinetics of the experiments carried out with different AHM:HNO_3 molar ratios, the rate of acid addition was kept constant to 1 mL min^{-1}. Since the amount of AHM in the reaction mixture was kept fixed throughout the series, different amounts of acid were added, depending on the desired AHM:HNO_3 molar ratio to be achieved. Thus, the period of time for the acid addition to be complete was dependent on the AHM:HNO_3 molar

right), as the added nitric acid generates likely bigger droplets dispersed in cyclohexane, also increasing the overall number of scattering objects. Concurrently, the growth of a feature between 1 to 2 nm^{-1} was observed. Finally, a further step of ultrasonication (2 min) was performed, and the intensity of the scattering profile decreased, as the penetration of nitric acid into ME droplets reduced the total number of scattering objects (Figure 2.13, bottom left). The occurrence of dehydration and polycondensation reactions of molybdates

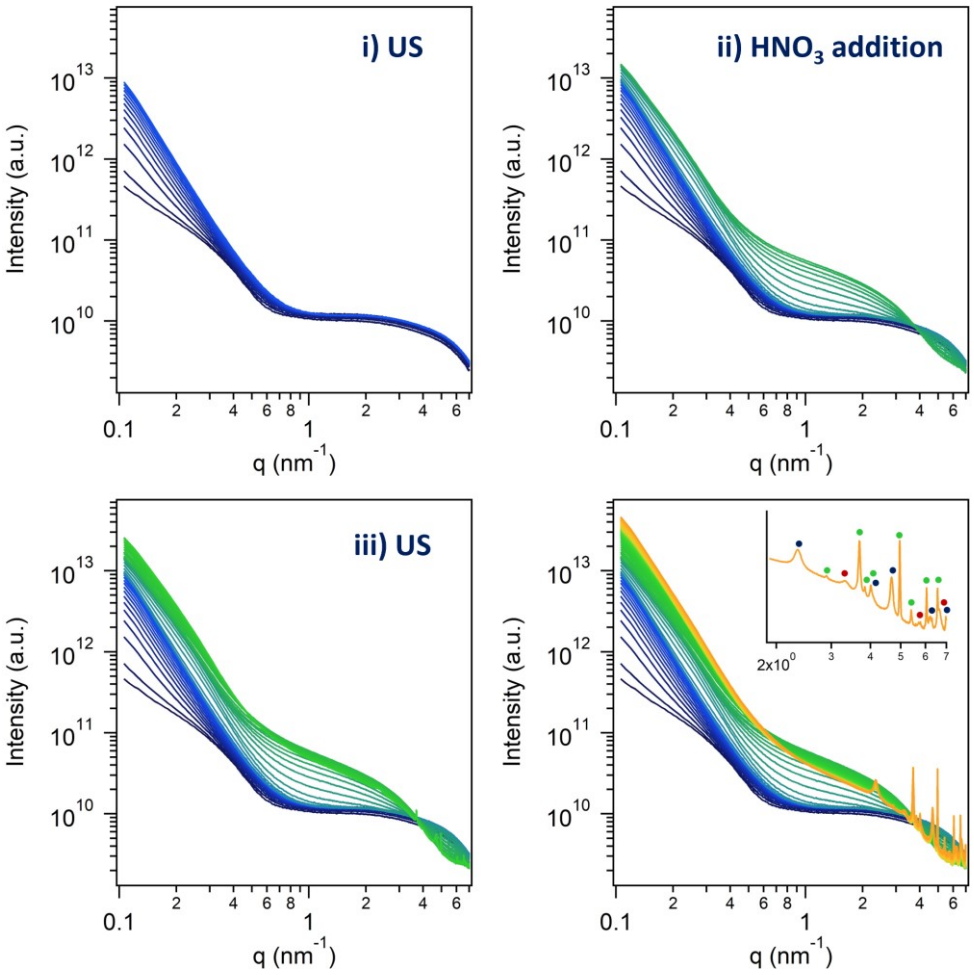

Figure 2.13 Evolution of log-log plot of the SAXS profiles (0.1-7.0 nm^{-1}) of miniemulsion reaction mixture as a function of time (resolution: 10 s) during the synthesis steps: i) ultrasonication to produce the starting ME (**top left**), from -120 s (dark blue) to 0 s (blue), ii) addition of concentrated nitric acid (**top right**), from 0 s (blue) to 40 s (green), iii) further ultrasonication to enhance HNO_3 diffusion into ME droplets (**bottom left**), from 120 s (green) to 240 s (bright green), and iv) evolution of the synthesis (**bottom right**), from 240 s (bright green) to 760 s (orange). Inset: zoom on Bragg reflections (1.9-7.0 nm^{-1}), marking the symmetry relationship between their positions with differently colored dots. [AHM] = 0.20 M, AHM:HNO_3 1:10 mol

ratio. The start of the following reaction step (iii: US, when applied) was set for all the experiments after the time necessary for completing the acid addition in 1:25 mol experiments (*i.e.* 120 s).

in acidic medium (discussed in Chapter 2.1) was observed by a further increase of scattering intensity (formation of molybdenum-based particles characterized by a higher electron density than surfactant-stabilized water droplets dispersed in cyclohexane) and by the formation of Bragg reflections in the higher q SAXS region (2-7 nm^{-1}), as shown in Figure 2.13, bottom right. The different widths of the Bragg reflections and their relative position suggested that the observed diffractograms consisted of the superimposition of different individual patterns ascribable to different species and/or derived from different origins (*e.g.* from a long-range order in a crystalline structure or from the ordered array of primary particles). Indeed, the pattern was observed to be constituted by at least two patterns having hexagonal symmetry (*i.e.* whose relative position followed the relation 1, $\sqrt{3}$, 2, $\sqrt{7}$, 3, …, more evident with higher amounts of HNO_3), characterized by broad peaks, marked by blue and red dots in the inset of Figure 2.13, bottom right, and whose positions are listed in Table 2.1. These patterns could be ascribed to the formation of two hexagonal mesophases (*e.g.* due to rods arranged in a hexagonal array), through a nonclassical crystallization pathway (see Chapter 1.1.2). Additionally, sharper reflections, whose q positions are marked with green dots in the inset of Figure 2.13 and did not display any specific spatial relationship, were observed at 2.89 nm^{-1}, 3.69 nm^{-1}, 3.84 nm^{-1}, 4.01 nm^{-1}, 4.96 nm^{-1}, 6.05 nm^{-1}, 6.29 nm^{-1}, and 6.56 nm^{-1}.

Table 2.1 List of two patterns with hexagonal symmetry observed in miniemulsion SAXS patterns, starting with $q_{0,1}$ = 2.33 nm^{-1} (blue dots in Figure 2.13, bottom right) and $q_{0,2}$ = 3.33 nm^{-1} (red dots in Figure 2.13, bottom right)

	1	$\sqrt{3}$	**2**	$\sqrt{7}$	**3**
$q_{0,1}$ (nm^{-1})	2.33	4.04	4.66	6.16	6.99
$q_{0,2}$ (nm^{-1})	3.33	5.72	6.66	-	-

As mentioned, the molar ratio between the molybdenum(VI) precursor and nitric acid was varied between 1:10 and 1:25, keeping constant all the other synthetic parameters. A comparison of the evolution of the SAXS patterns as a function of time and AHM:HNO_3 molar ratio for the first series of experiments is reported in Figure 2.14. Interestingly, by increasing the relative amount of acid in the synthesis in ME, the sharp peaks disappeared

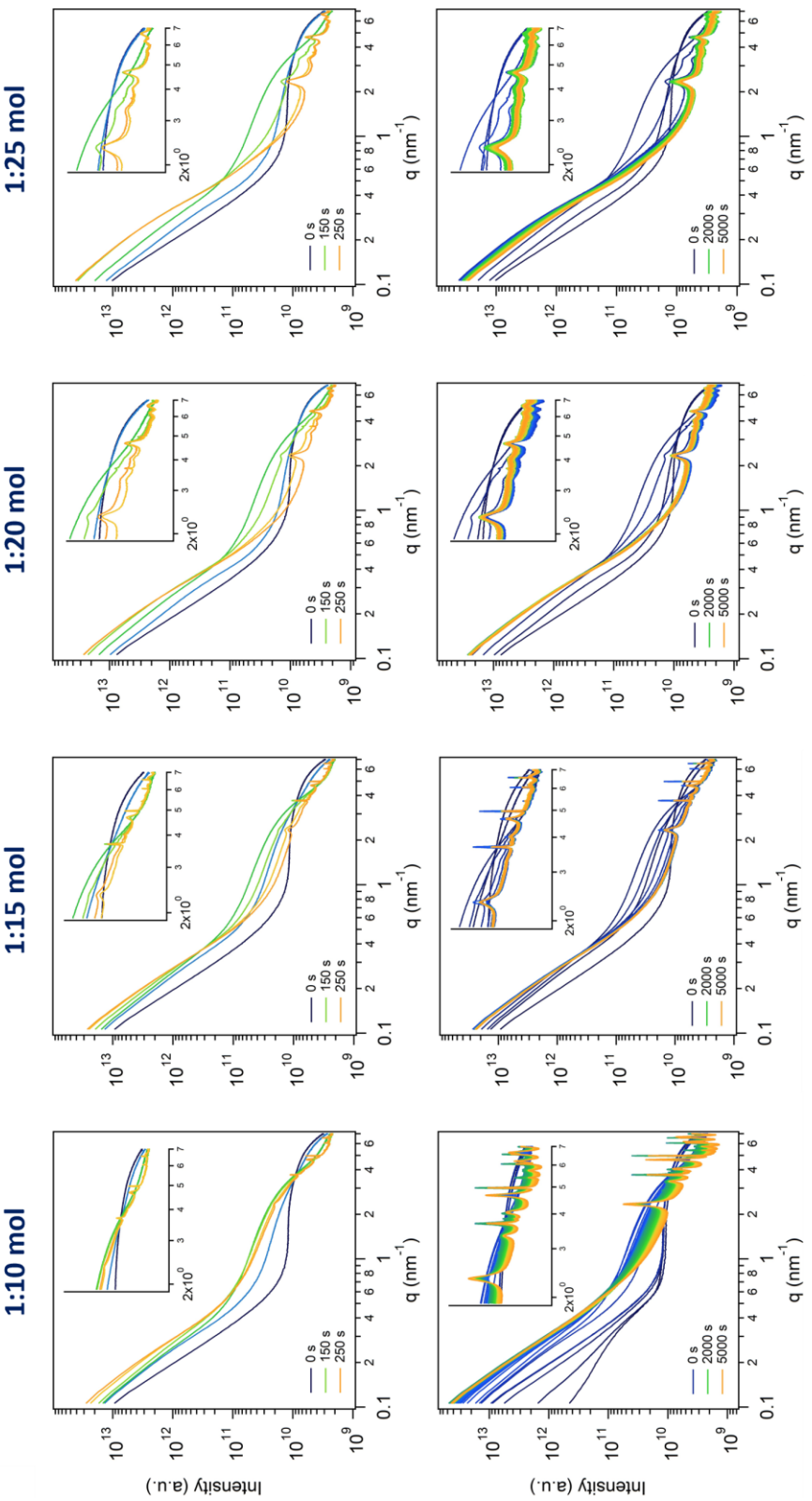

Figure 2.14 *In situ* time-resolved log-log plots of SAXS patterns of the series of experiments performed in ME with different AHM:HNO_3 molar ratios (*first series of experiments*). A pattern every 50 s from the start of acid addition (t = 0 s) to the end of US (step iii) (t = 250 s) (**top**) and to 5000 s (**bottom**). **Insets:** zoom on Bragg peaks (1.9-7 nm^{-1}). [AHM] = 0.20 M

accordingly, showing only two weak peaks at 3.69 nm^{-1} and 4.96 nm^{-1} (the more the acid, the less intense the peaks, almost undetectable at AHM:HNO_3 1:25 mol). Moreover, it was found that the broad peaks (the two hexagonal patterns starting with $q_{0,1}$ = 2.33 nm^{-1} and $q_{0,2}$ = 3.33 nm^{-1}) grew faster by increasing the amount of acid, both in absolute intensity and relatively to the sharper peaks (the more the acid, the more intense the peaks). Indeed, after 250 s (end of the third stage of the synthesis, *i.e.* the ultrasonication), while at AHM:HNO_3 1:10 mol the sharper peaks stood out in the pattern, at AHM:HNO_3 1:25 mol they were barely detectable compared to the broader ones (Figure 2.14, top). Moreover, by following the evolution of the pattern for 5000-10000 s (Figure 2.14, bottom) it was found that, with higher amounts of acid, the observed peaks firstly grew, but subsequently their intensity decreased, suggesting the formation and disappearance of a reaction intermediate(s), more stable (*i.e.* stable for a longer period of time) in the experiments performed with lower amounts of acid (1:10 and 1:15 mol).

Such intermediate species can likely be identified in a (mixture of) polyoxomolydate(s), known intermediates in the polycondensation reactions occurring in acidified Mo(VI) solutions,[264] as discussed in the previous sections. In order to shed light on the nature of the intermediate species, WAXS measurements, displaying the growth of reflections in the wider-angle scattering region (16-22 nm^{-1}, *i.e.* 23-31° 2θ), could be valuable. The evolution of the WAXS profiles of ME experiments as a function of time and AHM:HNO_3 molar ratio is reported in Figure 2.15. First, the *ex situ* time-resolved investigations of the formation of h-MoO_3 (Chapter 2.2) were fully supported: the crystallization of the metastable hexagonal polymorph of molybdenum(VI) oxide is achieved after several hours of reaction at room temperature, and the species present in suspension during the first 1-3 hours of reaction are intermediates. Indeed, the WAXS pattern of a reaction mixture measured after 24 hours of reaction displayed the characteristic reflections of h-MoO_3 (in the acquired q-range: 18.1, 20.5 and 21.6 nm^{-1}, ascribed to the (211), (300) and (204) reflections, respectively, as shown in Figure B.9 in Appendix B.1), that were not observed in the time-resolved *in situ* experiments within the 1-3 h of acquisition. Subsequently, by comparing the displayed WAXS patterns as a function of time and AHM:HNO_3 molar ratio, it appeared clear that increasing the amount of nitric acid in the reaction mixture affected the crystallization pathway of MoO_3, obtaining the transitory formation of crystalline species with higher AHM:HNO_3 molar ratio (1:10 mol, about 5000 s, *i.e.* 1 hour-1 hour and 30 min). The acquired patterns likely resulted from the crystallization of a mixture of compounds, given the

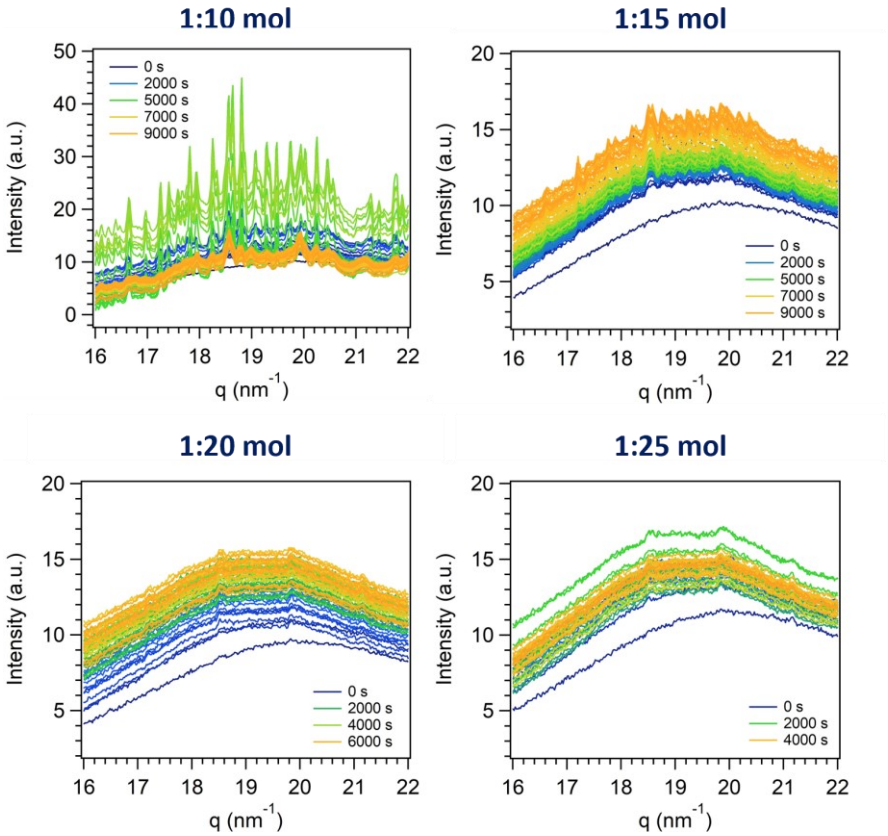

Figure 2.15 *In situ* time-resolved WAXS profiles of the series of experiments performed in ME with different AHM:HNO_3 molar ratios (*first series of experiments*). A pattern every 100 s from the start of acid addition (t = 0 s) to the end of acquisition. [AHM] = 0.20 M

plethora of sharp reflections observed in a small q range; they are consistent with the hypothesized formation of several polyoxomolybdates species. By following the evolution of the profiles for a longer period of time (until about 9000 s, *i.e.* 2 hours and 30 min), the intensity of these reflections decreased until only fewer and larger reflections could be appreciated. From these evidences, it could be supposed that the sharp reflections observed in the WAXS range and the sharp reflections formed at lower angle (SAXS region) are ascribable to the same intermediate species, that crystallizes with a relatively large unit cell. Their absence in the WAXS patterns acquired with higher amounts of nitric acid (AHM:HNO_3 1:20 and 1:25 mol) is consistent with the previously discussed SAXS profile evolutions. Moreover, the absence of MoO_3 polymorphs reflections as well supports the hypothesis that, in these conditions, the formation of MoO_3 occurs likely through an amorphous intermediate, obtaining the final hexagonal polymorph after 18-24 hours of reaction (see Chapter 2.2), through arrangement and densification towards the final structure, according to the Ostwald's rule of stages.[27] Finally, as no broad reflections were

observed in the WAXS region, the large SAXS reflections could likely be ascribed to an ordered hexagonal array of primary cylindrical particles, as mentioned *supra*, thus supporting the hypothesis that a non-classical mechanisms of crystallization, involving the oriented aggregation of primary particles into the formation of a mesoscale assembly, is occurring.[36,37,269]

II. Second series: miniemulsion synthesis without US step after acid addition. Since *ex situ* investigations demonstrated that the ultrasonication step after the addition of nitric acid was not necessary for the precipitating agent to penetrate inside miniemulsion droplets, and the diffusion seemed to occur more slowly in the case of missing US step (see Chapter 2.2), the same series of experiments in ME by varying the amount of nitric acid was performed without this synthetic step. As expected, the evolution of the SAXS profiles as a function of time was comparable to the ones of the series of experiments in ME performed with the US step (*first series of experiments*), *i.e.* overall increase in scattering intensity, variation of profile features and growth of reflections in the high q region, but slower. A comparison of the SAXS profiles of the first and the second series of experiments as a function of the AHM:HNO_3 molar ratio after 240 s (*i.e.* after the end of the third stage of the synthesis of ultrasonication, for the first series) evidencing this outcome is shown in Figure 2.16. This result confirmed what could only be supposed by *ex situ* evidences, and it was

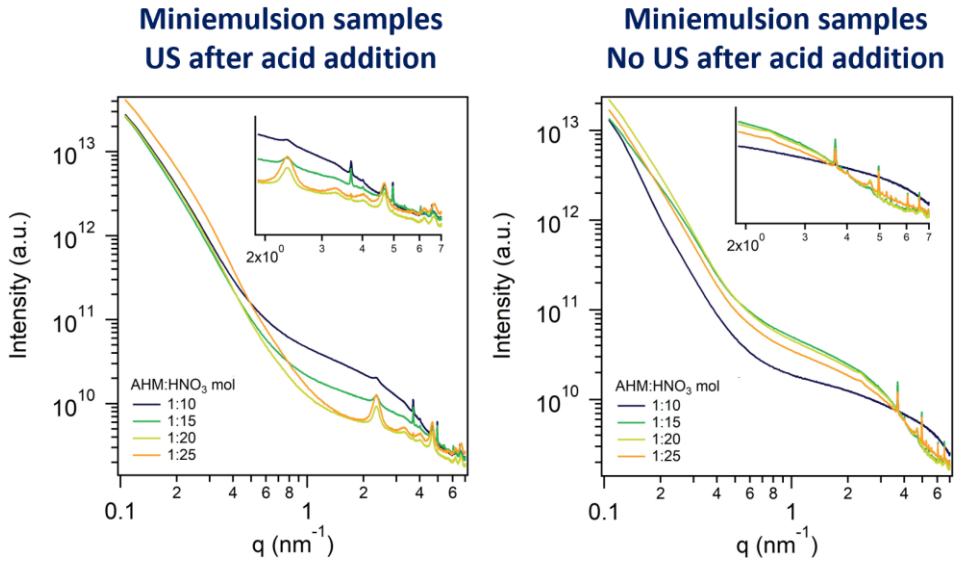

Figure 2.16 Comparison of log-log plots of SAXS profiles (0.1-7.0 nm^{-1}) of experiments performed in ME by applying (**left**) and not applying (**right**) US after the end of HNO_3 addition after 240 s (*i.e.* at the end of the US step when applied) as a function of AHM:HNO_3 molar ratio (1:10, 1:15, 1:20, and 1:25 mol). **Insets:** zoom on Bragg reflections (1.9-7.0 nm^{-1}). [AHM] = 0.20 M

attributed to the fact that the mixing of reactants occurs only *via* diffusion of the acid into the ME droplets, without an external trigger (*i.e.* the US, step iii of the synthesis) that ensures a more rapid and efficient interchange of materials.

A comparison of the evolution of the SAXS patterns as a function of time and AHM:HNO_3 molar ratio for the second series of experiments is reported in Figure 2.17. As observed in the experiment in ME with the US step and the lower amount of acid (1:10 mol, Figure 2.14), the early growth of the sharp peaks was observed in all the experiments of the second series (AHM:HNO_3 from 1:10 to 1:25 mol). This can be explained taking again into account that the mixing of reactants can be ascribed only to the diffusion of acid into the droplets, thus, being it slow, during the first acquisitions (250 s) only a small portion of acid should have diffused into the droplets (the lower actual relative amount of acid with respect to the nominal one). After a longer period of observation, the same conclusions drawn for the first series of experiments could be set: the higher the amount of acid, the higher the relative intensity of the broader peaks with respect to the sharper ones. Interestingly, the disappearance of the initially formed sharp peaks was observed within one hour and a half for the experiments with AHM:HNO_3 of 1:20 and 1:25 mol, meanwhile being their intensity clearly lowered for the 1:15 mol one.

From the comparison of the simultaneously acquired time-resolved evolution of the WAXS profiles of the second series of experiments as a function of AHM:HNO_3 molar ratio (Figure 2.18), these observations were supported. Indeed, the crystallization of transitory crystalline species detected in the first series of experiments (Figure 2.15) was clearly evidenced with higher AHM:HNO_3 molar ratios (1:10 and 1:15 mol), and, although less significatively, also with increasing the amount of nitric acid over 15 times the moles of AHM, in contrast to the first series of experiments, where no reflection growth was appreciated with AHM:HNO_3 molar ratios of 1:20 and 1:25. This evidence further supported that ultrasonication dramatically enhanced the penetration of nitric acid into ME droplets, suddenly increasing the concentration of H^+ in the reaction environment (ME droplets) and shifting the equilibrium of the reactions 2.1 and 2.2 towards the products. On the contrary, when the mixing of the molybdenum(VI) precursor with the precipitating agent was governed only by the diffusion of nitric acid through the continuous phase into ME droplets (second series of experiments), the polycondensation reactions occurred more slowly and

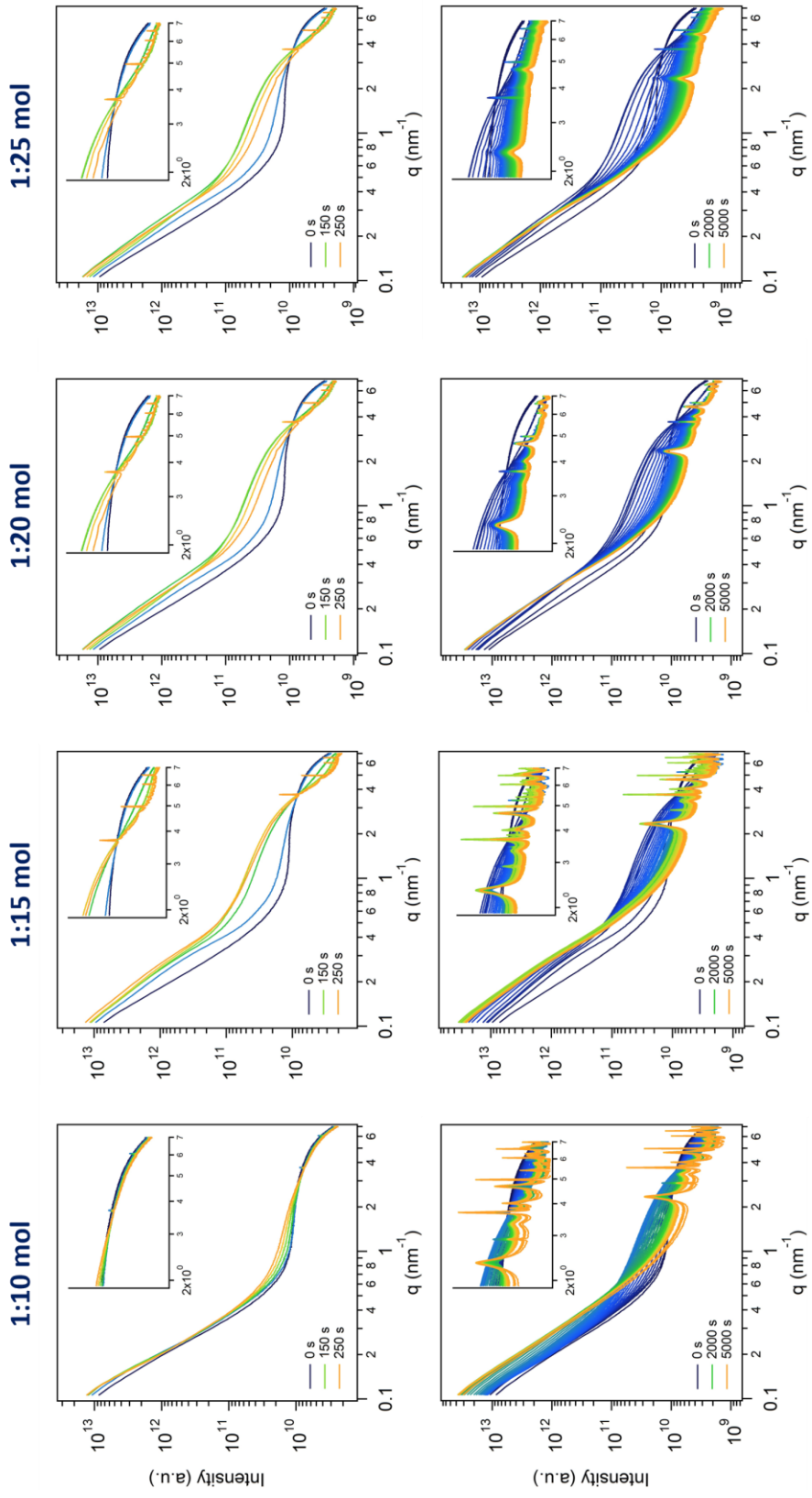

Figure 2.17 *In situ* time-resolved log-log plots of SAXS patterns of the series of experiments performed in ME without the US step with different AHM:HNO_3 molar ratios (*second series of experiments*). A pattern every 50 s from the start of acid addition (t = 0 s) to 250 s (*i.e.* corresponding to the end of US step for the first series of experiments) (**top**) and to 5000 s (**bottom**). **Insets:** zoom on Bragg peaks (1.9-7 nm^{-1}). [AHM] = 0.20 M

an intense diffraction of polyoxomolybdates species could be appreciated also for 1:15 mol experiment, and less markedly for 1:20 and (in the first frames of) 1:25 mol ones. In addition, it was observed that these intermediates were stable for a longer period of time than in the first series of experiments.

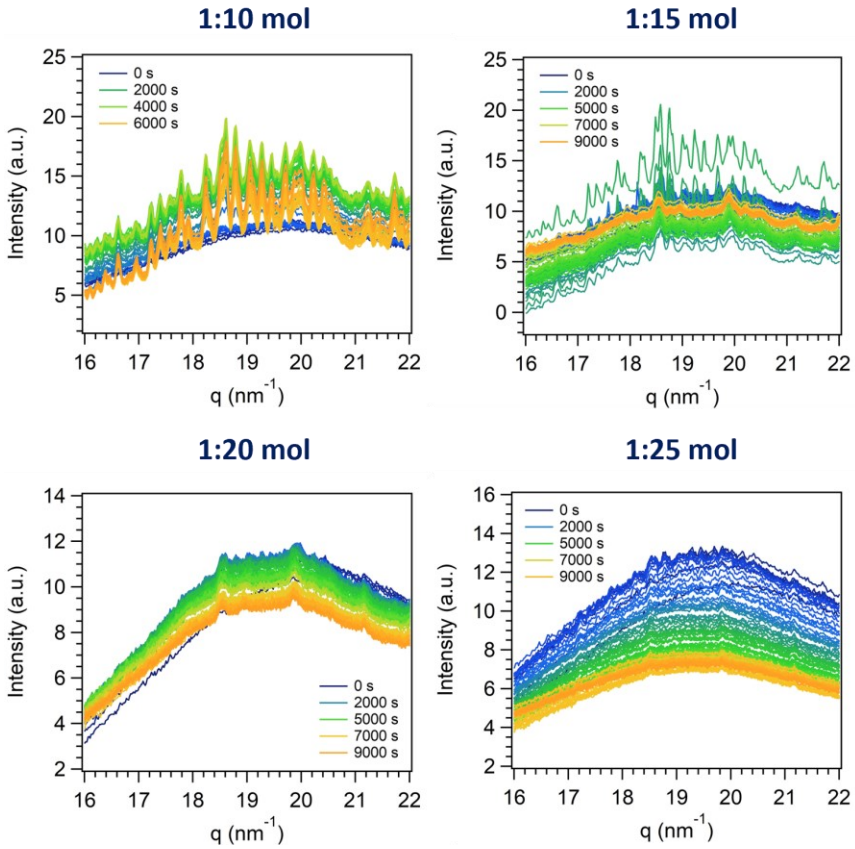

Figure 2.18 *In situ* time-resolved WAXS profiles of the series of experiments performed in ME without applying US after acid addition with different AHM:HNO_3 molar ratios (*second series of experiments*). A pattern every 100 s from the start of acid addition (t = 0 s) to the end of acquisition. [AHM] = 0.20 M

III. Third series: batch synthesis. In order to evaluate the effect of miniemulsion space confinement on the evolution of heptamolybdate ions to molybdenum(VI) oxide by acid addition, and support the *ex situ* investigations discussed in Chapter 2.2, the same series of experiments was performed *via* batch approach, varying the AHM:HNO_3 molar ratio between 1:10 and 1:25 mol. In particular, for these experiments the acquisition of the scattering profiles' evolution started from the aqueous solution of AHM, and the start of nitric acid injection was set as t = 0 s. As can be appreciated in Figure 2.19, left, reporting the first 60 seconds of acid addition, the SAXS profile of the starting aqueous solution of

AHM appeared different from the starting one observed in miniemulsion, and in this case the Guinier region could be observed. However, also in batch conditions an increase in the total scattering intensity, together with a variation of the curve slope in the low q region and disappearance of the Guinier region, was observed as a consequence of acid addition. Moreover, within the end of acid addition (t = 0-200 s, Figure 2.19, right), the appearance of reflections in the high q range of the SAXS region was observed, similar to what was noted in the case of the ME series (first and second one), but the obtained pattern happened to be different in number, position, and widths of the Bragg peaks. In particular, the broad reflections (the two hexagonal patterns starting with $q_{0,1}$ = 2.33 nm^{-1} and $q_{0,2}$ = 3.33 nm^{-1}) were not found, and the lowest q peak was observed at 2.89 nm^{-1}. On the contrary, the sharper reflections obtained by miniemulsion approaches (at 2.89 nm^{-1}, 3.69 nm^{-1}, 3.84 nm^{-1}, 4.01 nm^{-1}, 4.96 nm^{-1}, 6.05 nm^{-1}, 6.29 nm^{-1}, and 6.56 nm^{-1}, marked with green dots in Figure 2.13 and Figure 2.19) were observed, indicating the formation of one or more common species. In addition to these, the batch approach pattern displayed other sharp reflections at q = 4.19 nm^{-1}, 4.40 nm^{-1}, 4.50 nm^{-1}, 4.90 nm^{-1}, 5.08 nm^{-1}, 5.70 nm^{-1}, 5.90 nm^{-1}, 6.76 nm^{-1}, and 6.81 nm^{-1} (see inset in Figure 2.19, right), not showed in the ME ones.

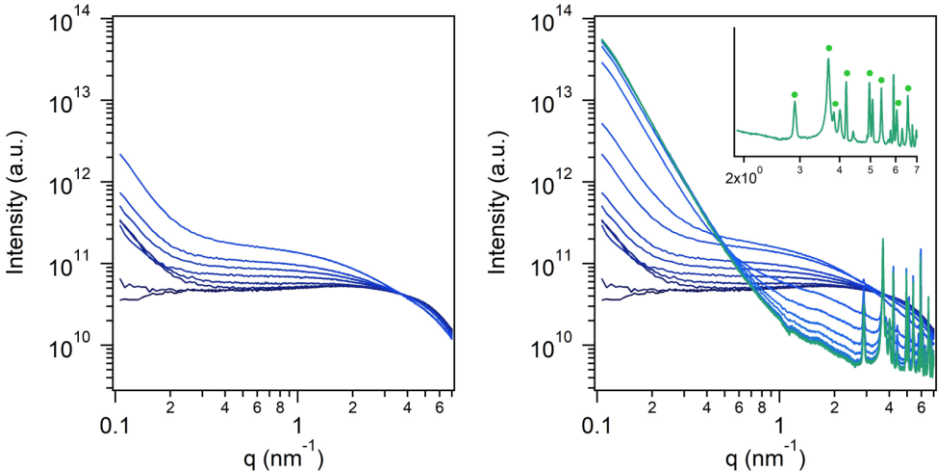

Figure 2.19 Evolution of log-log plots of SAXS profiles (0.1-7.0 nm^{-1}) of batch reaction mixture as a function of time (resolution: 10 s) during the acid addition. The first minute of acid addition (0-60 s, from dark blue to blue) is shown at the **left**, while the whole acid addition (0-200 s, from blue to green) is shown at the **right**. **Inset:** zoom on Bragg reflections (1.9-7.0 nm^{-1}), marking with green dots the reflections observed also in the miniemulsion series. [AHM] = 0.20 M, AHM:HNO_3 1:10 mol

As for miniemulsion series (first and second series of experiments), the evolution of the scattering profiles was followed up to 1-3 hours and different AHM:HNO_3 molar ratios were

tested. A comparison of the evolution of the SAXS patterns as a function of time and AHM:HNO_3 molar ratio for the third series of experiments is reported in Figure 2.20. By comparing the obtained results for a longer period of time, it was observed that the sharp reflection found only in the batch series (q = 4.19 nm^{-1}, 4.40 nm^{-1}, 4.50 nm^{-1}, 4.90 nm^{-1}, 5.08 nm^{-1}, 5.70 nm^{-1}, 5.90 nm^{-1}, 6.76 nm^{-1}, and 6.81 nm^{-1}, listed also above) were likely ascribable to a more reactive reaction intermediate(s), as they first grew and then disappeared, while the other peaks did not (or remained for a longer period of time, in the case of high amounts of acid, *vide infra*). By varying the relative amount of nitric acid, no differences were noted in the relative growth of the peaks during the first acquisitions (Figure 2.20, top, t = 0-600 s), though they were found for the ME series (Figure 2.14, top). However, by comparing the evolution of the pattern for a longer time (until 5500-6000 s, Figure 2.20, bottom), it was evident that, by increasing the amount of acid over 1:20 mol, the intensity of all the Bragg peaks of the pattern decreased until no peaks were found at all (1:25 mol, 7000 s).

Since a similar trend was outlined for the patterns obtained in ME at AHM:HNO_3 1:20 or 1:25 mol (first and second series, Figure 2.14, bottom and Figure 2.17, bottom) – the sharper peaks observed also in batch conditions almost disappeared after 5000-7000 s –, it could be assumed that, in both conditions, the same intermediate was formed and it was more stable in less acidic conditions (AHM:HNO_3 1:10 and 1:15 mol). In addition to this species formed within both conditions, by both approaches at least another product (whose nature is dependent on the synthetic approach) was formed, and it was likely i) ordered microdomains in hexagonal arrays in miniemulsion (characterized by two superimposed patterns of broad reflections with hexagonal symmetry starting with $q_{0,1}$ = 2.33 nm^{-1} and $q_{0,2}$ = 3.33 nm^{-1}) and ii) a more reactive intermediate species leading to sharp reflections in the batch one (the ones at q = 4.19 nm^{-1}, 4.40 nm^{-1}, etc., listed above, that readily formed and disappeared).

As for the two miniemulsion series of experiments, the simultaneously acquired WAXS profiles in the 16-22 nm^{-1} q range, shown in Figure 2.21, confirmed the conclusions derived so far. In particular, the crystallization of MoO_3 is a stepwise process that occurs through the formation of likely a mixture of polyoxomolybdates as reaction intermediates, more stable in less acidic conditions and that gradually go through a phase-transformation from a crystalline polymorph to an amorphous (no reflections in the WAXS region) material and

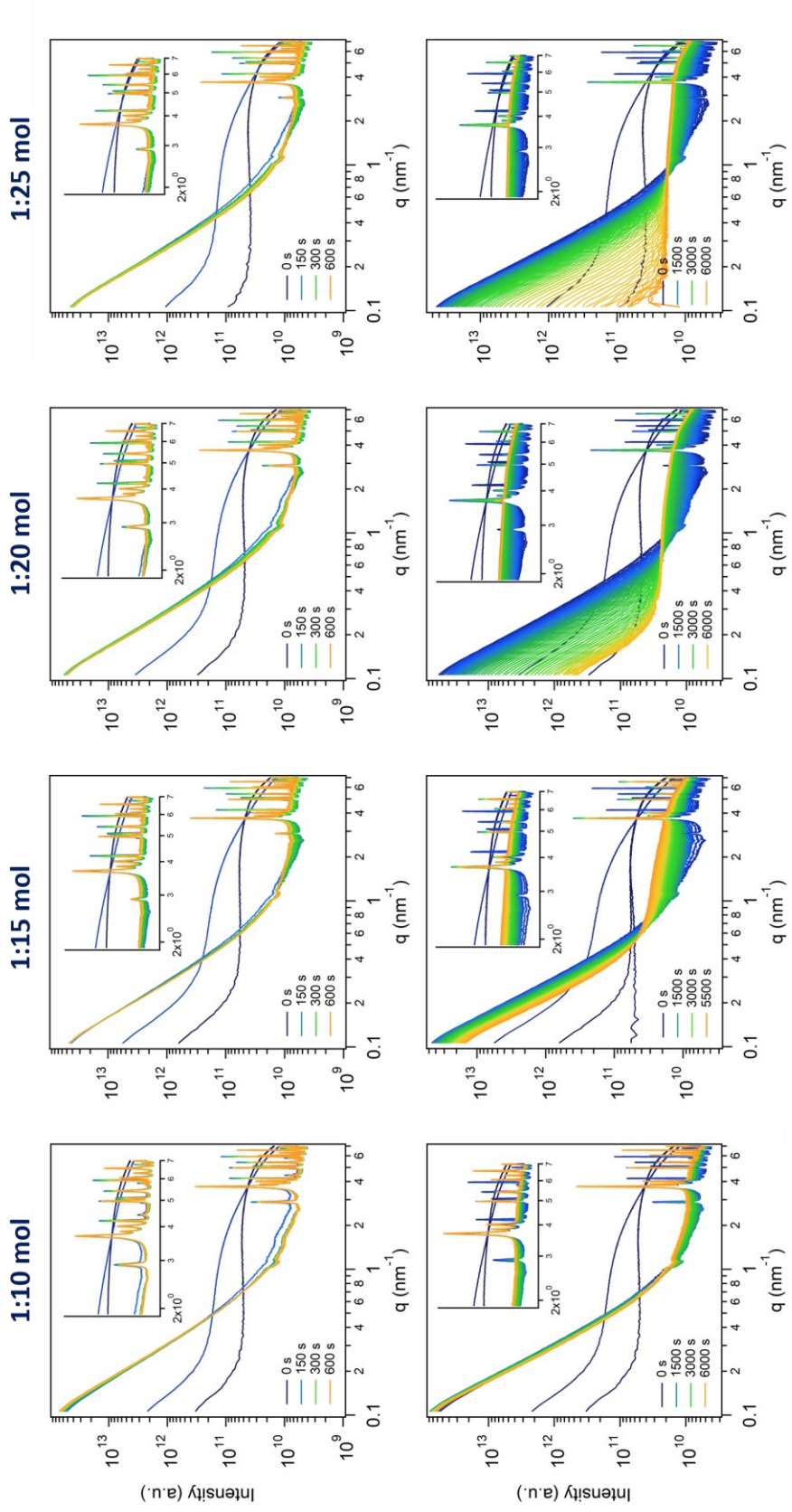

Figure 2.20 *In situ* time-resolved log-log plots of SAXS patterns of the series of experiments performed in batch with different AHM:HNO_3 molar ratios (*third series of experiments*). A pattern every 50 s from the start of acid addition (t = 0 s) to 600 s (**top**) and a pattern every 100 s from the start of acid addition (t = 0 s) to 5500-6000 s (**bottom**). **Insets:** zoom on Bragg peaks (1.9–7 nm^{-1}). [AHM] = 0.20 M

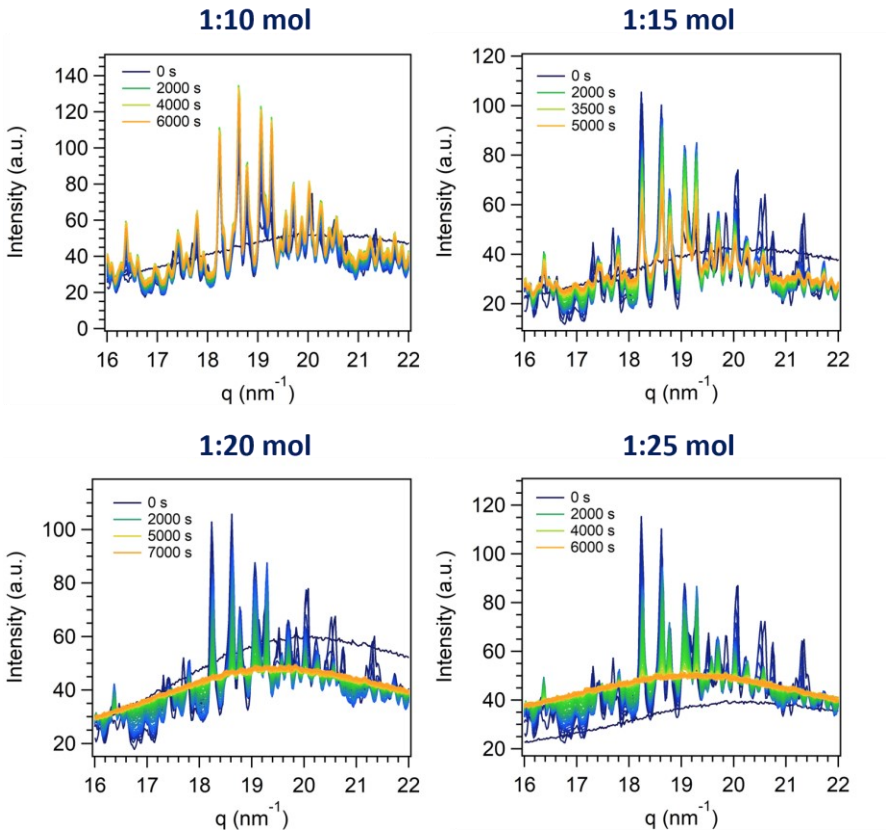

Figure 2.21 *In situ* time-resolved WAXS profiles of the series of experiments performed in batch with different AHM:HNO_3 molar ratios (*third series of experiments*). A pattern every 100 s from the start of acid addition (t = 0 s) to the end of acquisition. [AHM] = 0.20 M

ultimately to the metastable hexagonal polymorph of molybdenum oxide (after 18-24 hours, see Chapter 2.2). As mentioned *supra*, these observed stepwise transformations of the product are consistent with the Ostwald's rule of stages, and likely occur through the gradual condensation and rearrangement of MoO_6 octahedra, primary units of all the observed transient species and the final product h-MoO_3. Interestingly, the synthetic approach was found to affect the crystallization pathway, obtaining a more controlled mixing of the Mo(VI) precursor and the precipitating agent in miniemulsion droplets (first and second series of experiments), and in particular exploiting the spontaneous diffusion of nitric acid into ME droplets (second series of experiments), with respect to the macroreactor approach (batch approach, third series of experiments). Moreover, ME droplets seemed to promote a non-classical crystallization pathway involving the oriented aggregation of primary particles into a hexagonal array (*i.e.* likely a mesocrystal), while preventing the formation of a more reactive reaction intermediate that was observed in batch conditions. From these evidences, it could also be supposed that the space

confinement plays a role in altering the stability of the intermediate products and their transformation to the next stable species according to Ostwald's step rule, which are known to depend on the free energies of activation of nucleation in different environments.[23]

To further confirm the observations related to the origin of the broad peaks interrelated by a hexagonal symmetry found in the miniemulsion series of experiments (first and second series) and not in the batch one (third series), syntheses in miniemulsion droplets stabilized by PGPR instead of Span80 as surfactant, and AHM:HNO_3 molar ratios of 1:10 and 1:25, were also performed. In particular, these experiments aimed to rule out the possibility of ascribing the pattern observed in miniemulsion to the particular surfactant employed (Span80), forming ordered aggregates in solution (*e.g.* micelles or liquid crystals), even if in concentration below the critical micelle concentration, as discussed in Chapter 2.2. The same SAXS pattern was found with PGPR as surfactant and both reactants' molar ratios, as shown in Figure 2.22. Thus, the differences in the patterns observed in ME and in batch conditions were completely ascribed to the different synthetic approaches, affecting the crystallization pathway of MoO_3. Indeed, it is worth reiterating that confining the synthesis of molybdenum oxide within miniemulsion droplets likely enables an earlier oriented aggregation of primary amorphous units into hexagonal arrays, that further condensate into the target hexagonal polymorph of MoO_3. Attempts to increase the reaction temperature by changing the circulating water bath temperature (see details in Chapter 6.1.4) from 15 °C to 30 °C[xxv] did not lead to any variation in the scattering profile of the miniemulsion and batch reaction mixtures.

[xxv] Even if this variation in reaction temperature may seem not significant, it must be taken into account that the application of US strongly affects the temperature of the reaction mixture, creating local hot spots that lead to an overall increase of the reaction mixture temperature. While employing a 15 °C water circulating bath allowed to cool down the reaction temperature to 18-25 °C during the whole synthesis, with a 30 °C water circulating bath, reaction mixture temperatures between 30 and 50 °C (*i.e.* varying throughout the experiment duration) were measured.

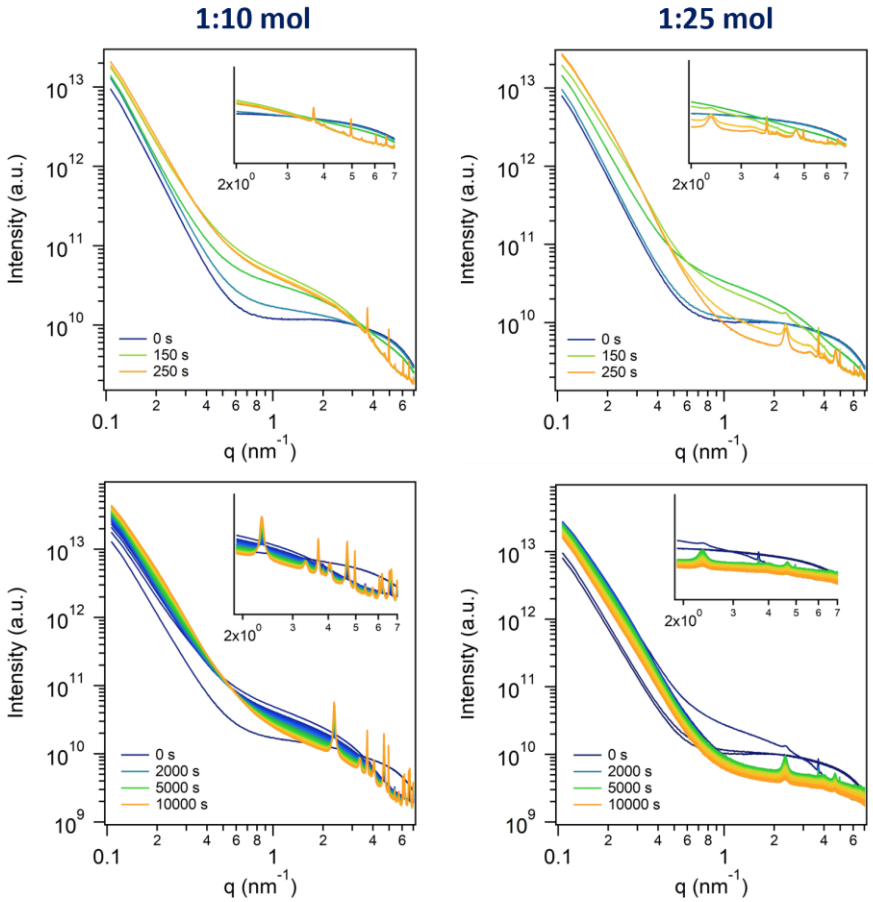

Figure 2.22 *In situ* time-resolved log-log plots of SAXS patterns of the series of experiments performed in miniemulsion with different AHM:HNO_3 molar ratios employing PGPR as surfactant. A pattern every 50 s from the start of acid addition (t = 0 s) to 250 s (**top**) and a pattern every 100 s from the start of acid addition (t = 0 s) to 10000 s (**bottom**). **Insets:** zoom on Bragg peaks (1.9-7 nm^{-1}). [AHM] = 0.20 M

2.4 Thermal evolution of h-MoO_3: *in situ* phase transition investigations

Since it was demonstrated that confining the synthesis of molybdenum oxide in miniemulsion synthesis influences its structural and dimensional features (Chapter 2.2), as well as its crystallization pathway (Chapter 2.3), compared to the batch approach, a further investigation of the role of the synthetic approach on the thermal behavior of molybdenum(VI) oxide was performed. In particular, the thermal evolution of the metastable hexagonal MoO_3 (h-MoO_3) into the thermodynamically stable orthorhombic polymorph (α-MoO_3) upon heating in air was investigated at both long- and short-range orders with a systematic *in situ* study, combining X-ray diffraction and X-ray absorption spectroscopy. The adopted combination of the two complementary characterization techniques provided a comprehensive picture of the structural evolution at different length scales of the studied system, from the local coordination around molybdenum to the crystal structure. Indeed, XAS spectroscopy allowed atomic-scale characterization, probing changes in the local chemical environment of the absorbing atom (Mo), and in particular the rearrangement of the primary unit of MoO_6 octahedra that occurred during phase transition (*vide infra*). On the other hand, the complementary XRD diffraction enabled a more straightforward tracking of the crystalline phase transformation during the heating treatment.

With this purpose in mind, a combined *in situ* XAS/XRD study as a function of temperature was performed at the Mo K-edge (20.0 keV) at the B18 beamline of Diamond Light Source (Didcot, UK), in cooperation with Dr. Paolo Dolcet (Karlsruhe Institute of Technology, Germany), who carried out XAS data analysis. To further support the XRD results obtained at the beamline, whose resolution was quite low because of the high energy at which the diffractograms were acquired (19.8 keV, corresponding to a wavelength of 0.6262 Å), the long-range order evolution upon heating was studied also by *in situ* thermal XRD at the Department of Geosciences, University of Padova, in cooperation with Dr. Federico Zorzi, with whom the Ph.D. candidate carried out the experiments, and Prof. Fabrizio Nestola.

In particular, the thermal behavior from room temperature up to 500 °C in air of samples synthesized both i) in the confined environment of inverse miniemulsion droplets and ii) in batch conditions was investigated stepwise by XRD and XAS techniques. The evolution with temperature of the samples synthesized with the two different synthetic approaches and

with different reaction times (5 minutes and 24 hours were selected as series extremes) was compared to evaluate how the synthetic conditions affect the thermal response of the material. In the case of 5 minutes-samples, the crystallization of the amorphous sample to metastable h-MoO_3 was firstly observed, followed by a further phase transition to the thermodynamically stable α-MoO_3. Only the phase transition was investigated in samples obtained after 24 hours of reaction, which were already crystallized in the hexagonal polymorph at room temperature (see Chapter 2.2).

I. Combined *in situ* XAS and XRD study at Diamond Light Source. As described in detail in Chapter 6.1.5, the *in situ* combined XAS and XRD study of the thermal behavior of molybdenum(VI) oxide was performed at the B18 beamline at Diamond Light Source facility, collecting i) diffractograms at an energy of 19800 eV (λ = 0.63 Å) in the angular range 13-21° 2θ (*i.e.* 38-63° 2θ using the radiation generated by a Co anode with λ = 1.79 Å) and, immediately after, ii) XAS spectra at the Mo K-edge (20000 keV) in the range 19800-20840 eV. Powder samples were pelleted using boron nitride as binder and placed in a furnace where they were heated up to 500 °C, acquiring stepwise and isothermally XRD and XAS data. In the following, the *in situ* XAS spectra and XRD patterns evolution as a function of temperature for the samples synthesized with 24 hours of reaction time is discussed. The results for 5-minute intermediates are presented in Appendix B.1 (see Figure B.10, Figure B.11, and Figure B.12).

The starting X-ray absorption near edge structure (XANES) spectra, acquired at room temperature (RT), allowed to investigate the atomic configuration around the molybdenum atoms of the as-synthesized samples. The experimental spectra are reported in Figure 2.23, top left, together with the spectra of three reference structures (*i.e.* the hexagonal polymorph h-MoO_3, the orthorhombic polymorph α-MoO_3 and the precursor AHM), and they exhibited similar characteristics as polyoxoanions compounds, indicating that the samples contained octahedral polymeric molybdenum.[270] In particular, XANES spectra of both polymorphs of MoO_3, as well as the precursor AHM, exhibited a well-defined pre-edge feature at around 20007 eV, assigned to the 1 s $\rightarrow$ 4d transition within the molybdenum atomic shell and positioned at an energy value typical for compounds containing Mo in octahedral coordination.[271,272] Since this dipole-forbidden transition becomes more pronounced when there is an overlap between O p-orbitals and Mo d-orbitals, the intensity of the pre-edge feature increases when the MoO_6 unit is characterized by a higher

distortion, improving such orbital overlap. Small differences in this feature were observed among miniemulsion and batch samples, founding it to be sharper and less intense for the batch sample, indicating a higher symmetry around Mo compared to the miniemulsion one. Moreover, the region around 75 eV beyond the adsorption edge displayed three successive features at about 20025, 20037, and 20054 eV (denoted A, B and C in Figure 2.23), typical of six-fold coordinated Mo XANES spectra. The origin of these features was thoroughly investigated by Tougerti *et al.*,[270] who employed multiple scattering theory simulations based on DFT-calculated structural models of differently sized clusters of oxomolybdates for interpreting the XANES spectrum features of AHM. In particular, they observed that the post-edge features A, B and C originate from the MoO_6 octahedra sharing edges, and their relative intensity could be associated to the relative XANES contribution of non-equivalent Mo sites (1, 1' or 2, as showed in Figure 2.23, bottom left) occupied in the polyoxoanion structures, typically composed of four long Mo-O bonds and two shorter Mo=O bonds. Mo sites 1 and 1' are characterized by a Mo atom surrounded by three Mo neighbors, displaying a slight difference in Mo-O bond length and O-Mo-O angle. On the other hand, site 2 Mo represents a Mo atom surrounded by six Mo atoms, and originates a much less intense peak B with respect to sites 1 and 1', due to the specific second oxygen shell of site 2 Mo in comparison to sites 1 and 1' (Figure 2.23, bottom left). Indeed, they concluded that the intensity ratio of the post-edge features is determined by the specific surrounding environment (*i.e.* oxygen atoms) of each non-equivalent Mo site forming the polyoxoanion, and that the intensity of the feature B is a spectral fingerprint for the presence or absence of site 2 Mo.[270] In the case of experimental miniemulsion and batch h-MoO_3 samples (red and dark blue lines in Figure 2.23, top left), their XANES spectra exhibited similar features to the reference hexagonal polymorph (blue line), while dissimilarities were noted with respect to the orthorhombic reference (green line) and AHM (pink line) samples spectra. However, the XANES spectrum features of the miniemulsion sample generally appeared more broadened than those of batch sample, as a consequence of the smaller size and the small amount of amorphous material in molybdenum oxide obtained by miniemulsion (*i.e.* more disordered structure; *cfr*. Chapter 2.2).

The Fourier transform of the k^2-weighted extended X-ray absorption fine structure (EXAFS) regions of the XAS spectra of miniemulsion and batch hexagonal MoO_3 samples, compared with the reference compounds (*i.e.* h-MoO_3, α-MoO_3, and AHM), are shown in Figure 2.23, top right. The analysis of the EXAFS curves provided information about bond lengths

between the absorbing atom (Mo) and scattering atoms (neighbor O and Mo). The first coordination shell, ascribed to the Mo-O bond, and the second coordination shell, assigned to the Mo-Mo bond, were detected for all the samples. As represented in Figure 2.23, bottom right,[273] it is worth noticing that, as Mo atoms are found in different sites, different distinct Mo-O and Mo-Mo lengths, named Mo-O_1, Mo-O_2 and so on, are present in the samples, and consequently distinct components are observed by the FT of the EXAFS spectra, the shortest one corresponding to the double bond Mo=O. The metastable hexagonal polymorph synthesized in ME and batch conditions (red and blue lines, respectively) displayed a Mo-O_1 bond length of about 1.6 Å and a Mo-Mo_1 bond length of about 3.4 Å. On the other hand, the pseudo-radial distribution of the distances, obtained from the FT of the EXAFS curve, of the thermodynamically stable orthorhombic α-MoO_3 was characterized by almost equally intense well-separated Mo-O shells (d(Mo-O_1) = 1.6 Å; d(Mo-O_2) = 2.1 Å) and the Mo-Mo one was shifted towards longer radial distances (d(Mo-Mo_1) = 3.6 Å).

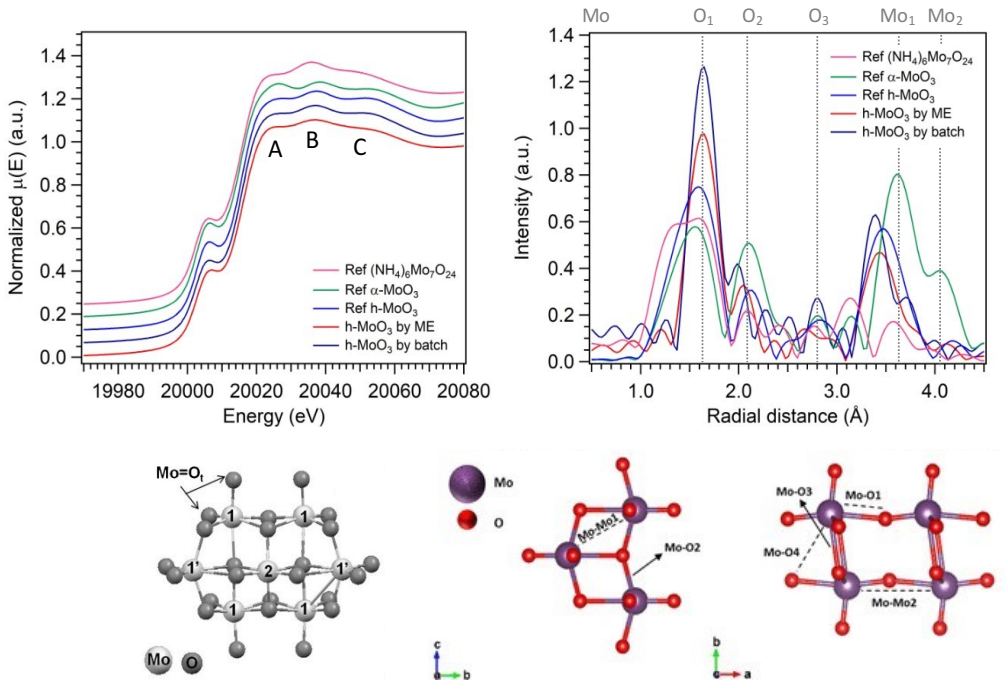

Figure 2.23 Top: comparison of the Mo K-edge XANES spectra of h-MoO_3 synthesized by ME (red line) and batch (dark blue line) approaches, reference h-MoO_3 polymorph (light blue line), reference α-MoO_3 polymorph (green line) and reference precursor AHM (**left**). Spectra are vertically shifted for clarity. Comparison of the Fourier transforms of the k^2-weighted EXAFS functions of the same samples and references (**right**). Data are corrected for phase shift. **Bottom:** details of the AHM structure, highlighting the different Mo sites (left, reproduced from Tougerti *et al.*[270] with permission of Wiley), and of the α-MoO_3 crystal structure marking the atomic distances probed by EXAFS analysis (Adapted from Crisci *et al.*[273] with permission of the American Chemical Society). View along the *a*-axis (**center**) and along the *c*-axis (**right**)

By comparing the evolution of the XANES spectra of ME and batch samples as a function of temperature, reported in Figure 2.24, great differences among the samples obtained with the two different synthetic approaches were noticed. In particular, while for the batch sample the most relevant changes were observed in the room temperature-100 °C range, for the miniemulsion one variations were spread over a wider temperature range (RT-240 °C). In particular, the major variation observed was the decrease of the relative intensity of the feature B, indicative of an increase in the amount of site 2 Mo atoms.[270] At 150 °C, feature A started decreasing in intensity, while feature C shifted towards lower energies and appeared as a shoulder of the main peak B, which gradually shifted towards higher energies, from 20036.8 to 20038.2 eV. At 260 °C, a major change occurred, with a drop in the relative intensity of peak B, while features A and C became once again clearly distinguishable. At 280 °C, the spectra of both samples looked very similar. At 340 °C, feature A started becoming sharper and shifting towards lower energies for the batch sample, indicating the onset of the phase transition to the orthorhombic α-MoO_3 polymorph, as per the peculiar characteristics of the XANES curve discussed above. For the miniemulsion sample, the same changes also started appearing at 340 °C, but were limited to a lesser extent and became more evident at 380 °C.

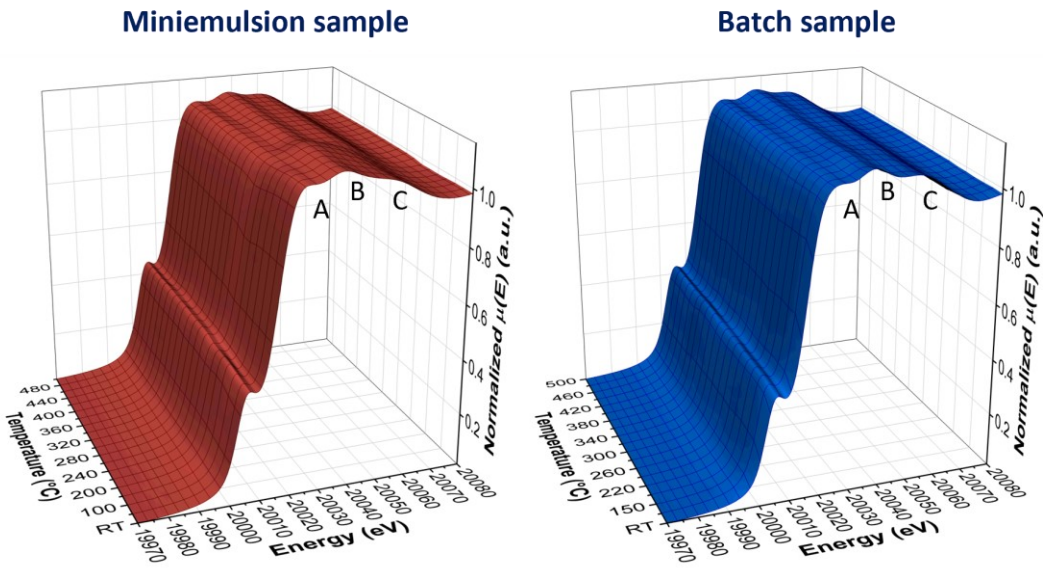

Figure 2.24 Mo K-edge XANES spectra recorded during heating up to 500°C for miniemulsion (**left**) and batch (**right**) samples

From the Fourier transform of the k^2-weighted extended X-ray absorption structure (EXAFS) curves analysis as a function of temperature shown in Figure 2.25, it was observed that the batch sample displayed an earlier distortion of the octahedral coordination around Mo with respect to the ME sample (280 °C *vs* 340 °C). In particular, from similar starting curves, it was found that for the batch sample the intensity of the first shell (Mo-O, at about 1.6 Å) decreased constantly with increasing the temperature, while for the miniemulsion sample the decrease was more gradual, with a sudden drop at 340 °C. After this temperature, for the ME sample the shoulder at about 2.1 Å, indicating a distortion of the octahedral coordination, characteristic of the orthorhombic phase, became more relevant. On the other hand, this shoulder was already evident at 280 °C for the batch sample. Moreover, the observed changes indicated that the different behavior with respect to the polymorphic transition of the two samples particularly affected the Mo-Mo distances (second shell at about 3.5 Å). Indeed, for the miniemulsion sample a sharp peak that remained relatively unchanged until 340 °C was observed, similarly to the first shell. At this temperature, the shell shifted BY about 0.1 Å, and at 400 °C a very weak shoulder appeared at about 4.0 Å, both effects peculiar of the orthorhombic phase.[271] Only after cooling down the presence of this shoulder was evident. Conversely, for the batch sample, this signal was already broader at room temperature, with a shoulder at 3.7 Å, and from 400 °C the signals at 3.5 and 3.6 Å were characterized by the same intensity. Concurrently, the shoulder at 4 Å also appeared and gained intensity. After cooling down, the curve resembled that of the reference orthorhombic phase α-MoO_3.

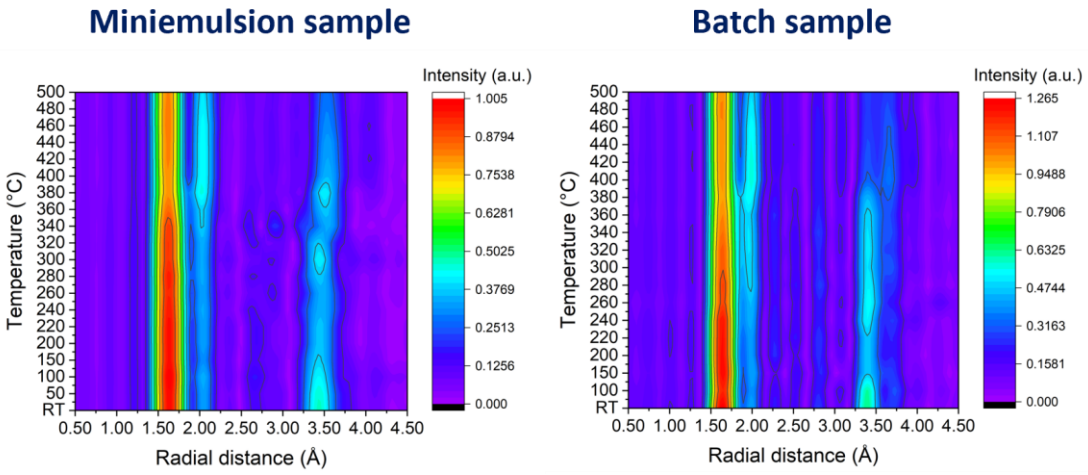

Figure 2.25 Maps of the Fourier transforms of the k^2-weighted EXAFS functions recorded during heating up to 500 °C in air miniemulsion (**left**) and batch (**right**) samples. Data are corrected for phase shift

The starting diffraction patterns of the miniemulsion and batch samples, acquired at room temperature (RT) immediately before each XAS spectrum, were quite similar and, as discussed in Chapter 2.2, they were both corresponding to the hexagonal metastable polymorph h-MoO_3, displaying sharper reflections for the batch sample, *i.e.* larger crystallite size. After the heating treatment up to 500 °C and cooling down (RTpost), the XRD pattern of both samples was ascribable to the thermodynamically stable orthorhombic polymorph α-MoO_3, indicating that the phase transition occurred within the temperature range studied and in accordance with XAS data discussed above. Together with molybdenum(VI) oxide reflections, also the reflections of BN (used as pellet binder), which are positioned at 13.8, 16.3, and 18.2° 2θ at the energy of 19800 eV, were observed. A comparison of the diffraction patterns of the ME and batch samples before and after the heating treatment, together with the pattern of boron nitride is shown in Figure B.13 in Appendix B.1.

The evolution of XRD profiles of miniemulsion and batch samples as a function of temperature is reported in Figure 2.26, left and right, respectively. First of all, as expected, by increasing the temperature, the reflections shifted towards lower angles due to thermal expansion. As observed from the decrease in intensity of the reflections of the hexagonal phase and the growth of the orthorhombic phase ones, the phase transition of both samples occurred in the temperature range of 360-400 °C. In particular, for the miniemulsion sample, the XRD pattern was ascribable only to the hexagonal phase up to 340 °C, and, at 360 °C orthorhombic reflections started to grow, being at 380 °C as intense as the hexagonal ones, which started decreasing. At 400 °C, reflections of the orthorhombic polymorphs were exclusively present, and finally at 420 °C their intensity was increased and further remained

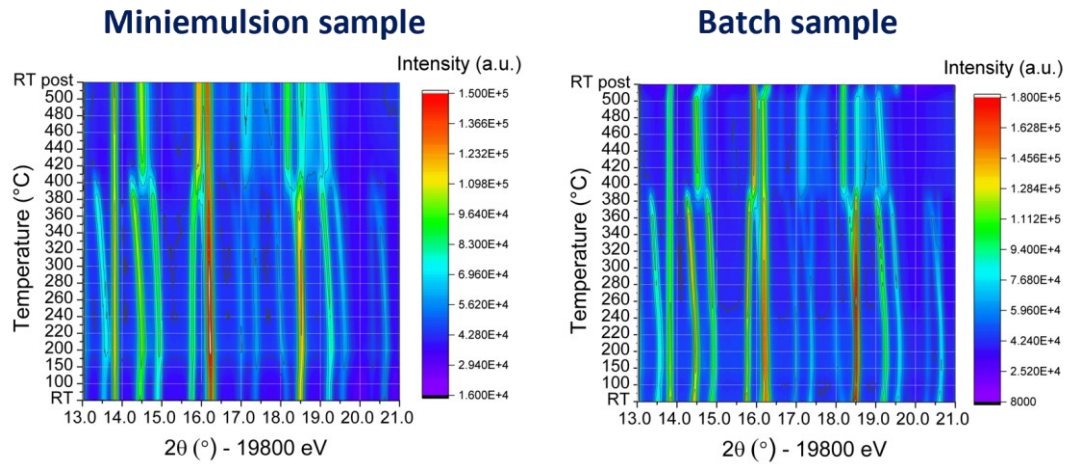

Figure 2.26 Maps of XRD patterns (13-21° 2θ) recorded during heating up to 500 °C in air miniemulsion (**left**) and batch (**right**) samples

unchanged. For the batch sample instead, the XRD pattern was due to the sole hexagonal phase up to 360 °C, and at 380 °C it showed the mutual decrease of the intensity of the hexagonal reflections and growth of the orthorhombic ones. At 400 °C, reflections of the orthorhombic α-MoO_3 were exclusively present.

The experimentally determined temperature range of phase transition between the two polymorphs was found in agreement with the literature.[231,258,259,274] Although the literature studies of the phase-transition did not exploit *in situ* XRD characterizations as herein, but rather XRD analyses after sample annealing at different temperatures, they reported that the sole hexagonal metastable polymorph phase was observed up to 350 °C, and after annealing at 450 °C only the orthorhombic one was detected.[231] After annealing at 400 °C, the presence of both phases was evidenced.[258] A Raman study reported the co-existence of both phases in the temperature range 400-420 °C and the end of phase transformation at 430 °C.[259] In our conditions, the phase transformation of samples synthesized by both conditions was complete at 400 °C. TG, DTG and DSC investigations of thermal stability of h-MoO_3 revealed that, upon annealing in air, first physically adsorbed water was lost around 80-150 °C, then volatile by-products associated with nitrates and ammonium decomposition were liberated between 200 and 250 °C, and finally a sharp exothermic peak between 375 °C and 425 °C, related to the removal of ammonia and coordinated water molecules from the internal structure of MoO_3 and to the phase-transformation from h-MoO_3 to α-MoO_3, was reported.[231,258,275] Indeed, the loss of intercalated species from the internal tunnel of the hexagonal structure led to the stability loss of the h-MoO_3 phase,

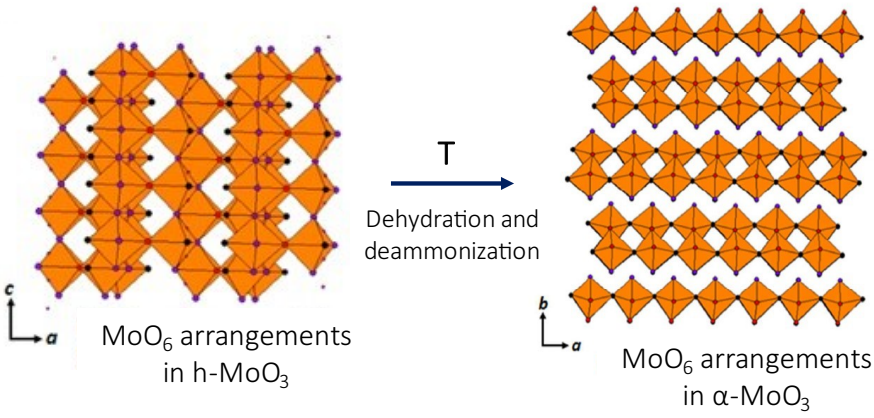

Figure 2.27 Schematic representation of the thermal-induced transition between h-MoO_3 and α-MoO_3 structures and the arrangement of the octahedra in the two polymorphs. Non-equivalent oxygen atoms are represented by different colors

breaking of low energy Mo-O bonds and rearrangement of the MoO_6 octahedra (*reconstructive transition*)[9] to form the orthorhombic phase. In particular, the framework tunnel structure with the tunnels directed along the *c*-axis transformed into a layered structure with the layers parallel to the same axis.[274] A schematic representation of the phase transition and of the arrangement of the octahedra in the two polymorphs is reported in Figure 2.27. The enthalpy of formation of α-MoO_3 by thermal treatment of h-MoO_3 was estimated by Kumar *et al.* to be approximately -501 kJ mol^{-1}.[275]

II. *In situ* XRD study at the University of Padova. As introduced above, the XRD data collected at the B18 beamline at Diamond Light Source at considerably high energy (19.8 keV) displayed a quite low resolution of the reflections, which were narrowed in a small angular range (*i.e.* the range 13-21° 2θ at 19800 eV corresponds to 38-63° 2θ range employing X-rays with an energy of about 7 keV, or λ = 1.79 Å). For this reason, they were further supported by studying the long-range order evolution upon heating also by *in situ* thermal XRD at the Department of Geosciences, University of Padova.

As described in detail in Chapter 6.1.5, the *in situ* XRD study was performed using a diffractometer equipped with a Co anode (λ = 1.79 Å), placing the samples on a platinum heating filament and heating them in air up to 460 °C. XRD patterns as a function of temperature were collected stepwise and isothermally for one hour at each temperature step in the 5-75° 2θ range. Figure 2.29 shows the comparison between the thermal evolution of miniemulsion (left) and batch (right) samples, synthesized with 5 minutes (top) and 24 hours (bottom) of reaction. Only the range 5-46° 2θ is shown, because of the presence of the reflections of the platinum heating filament at 46.3° 2θ and 54.0° 2θ, ascribed to the (111) and (200) planes of Pt, respectively. Nevertheless, such a limited 2θ range is satisfactory for showing the phase transition of molybdenum(VI) oxide. As expected due to the Bragg law, and as mentioned *supra*, along the series of diffractograms collected at increasing temperature, reflections shifted towards lower angles due to the thermal expansion of the unit cell.

As discussed also in Chapter 2.2, the initial room temperature diffractograms of both samples obtained after 5 minutes of reaction (Figure 2.28) evidenced how the samples were mostly present as amorphous materials. Overlapping with the amorphous pattern, some reflections at small diffraction angles (5-15° 2θ), that could likely be ascribable to several polyoxomolybdate species with different nuclearities and hydration grades, were observed.

By increasing the temperature, and dehydrating the samples, such signals gradually disappeared, being the miniemulsion sample (Figure 2.28, left) completely amorphous at 250 °C. At the same temperature, the 5 minutes batch sample (Figure 2.28, right) showed instead some reflections ascribable to the hexagonal polymorph h-MoO_3. At 260 °C, both samples showed the h-MoO_3 diffraction pattern, but the miniemulsion one also displayed reflections ascribable to the orthorhombic thermodynamically stable polymorph, α-MoO_3, at 27° 2θ and 32° 2θ, assigned to the (110) and (021) Miller reflections, respectively. Moreover, together with the two polymorphs signals, at 260 °C the ME sample pattern was still characterized by the presence of the amorphous bump, indicating that the formation of the thermodynamically stable polymorph started even before the crystallization of the whole sample was complete. By further increasing the temperature, the amorphous bump gradually disappeared, being not detectable anymore at 300 °C. On the contrary, in the batch samples, the reflections of the orthorhombic phase started to grow at 270 °C, and, similarly to the ME sample, their intensity increased up to 300 °C at the expense of the amorphous signal, retaining the hexagonal phase signals their intensity. For both samples, in the temperature range 320-360 °C the decrease of the intensity of h-MoO_3 reflections together with the increase of the intensity of α-MoO_3 reflections was observed, indicating that the orthorhombic phase was crystallizing at the expense of the hexagonal one, thus

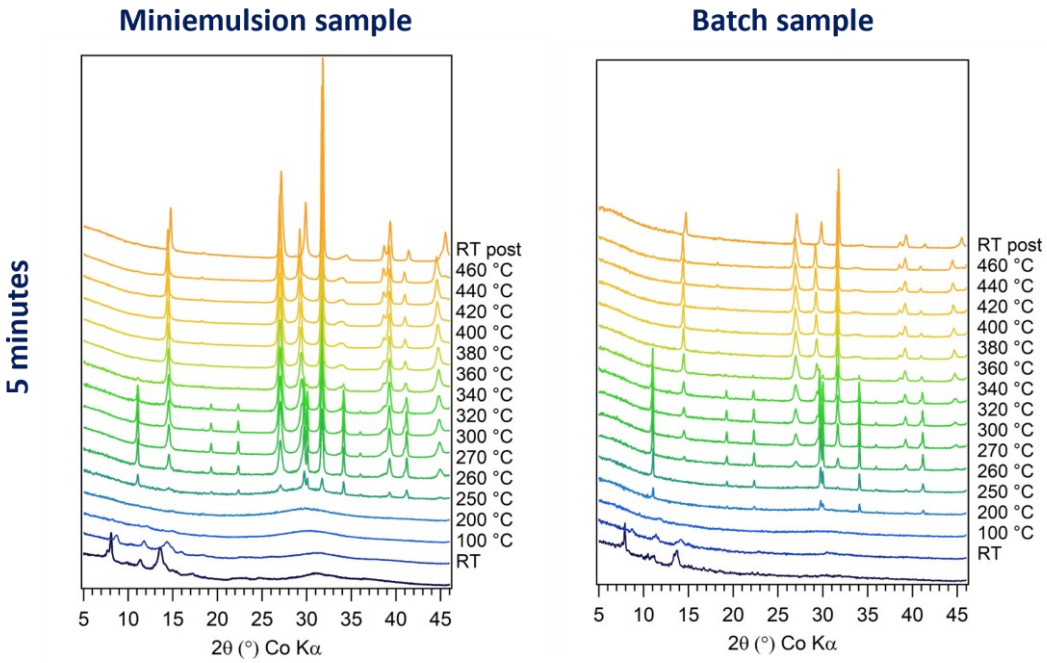

Figure 2.28 Thermal evolution (from room temperature up to 460 °C) of miniemulsion (**left**) and batch (**right**) samples obtained after 5 minutes of reaction, followed *in situ* by XRD. Diffractograms are shifted vertically for clarity

that the phase transition was occurring. At 380 °C, no more reflections ascribable to the metastable polymorph were detectable: the phase transition was complete. Diffractograms registered at room temperature after cooling down (RTpost) showed the typical pattern of α-MoO_3.

Concerning the samples obtained after 24 hours of reaction (Figure 2.29), both the miniemulsion one (left) and the batch one (right) were present as crystalline materials at room temperature, displaying the typical reflections of the hexagonal polymorph of MoO_3. The pure crystalline metastable phase was retained up to 260 °C for batch sample and 270 °C for ME sample, after which reflections of the orthorhombic thermodynamically stable polymorph started to grow. While in the miniemulsion sample (Figure 2.29, left) the growth of α-MoO_3 occurred in parallel with the decrease in intensity of h-MoO_3 reflections already at 320 °C, in the batch sample (Figure 2.29, right) the decrease of h-MoO_3 reflections was not observed until 360 °C. Thus, the phase transition of the ME sample started before the one of the batch sample (320 °C *vs* 360 °C). However, it was observed that the temperature range required for the transition was wider for the ME sample with respect to the batch one, since reflections of the metastable phase were not present anymore at 380 °C for both samples. Above 380 °C, and also after cooling down (RTpost), the diffractograms of both samples displayed the diffraction pattern of pure α-MoO_3. These

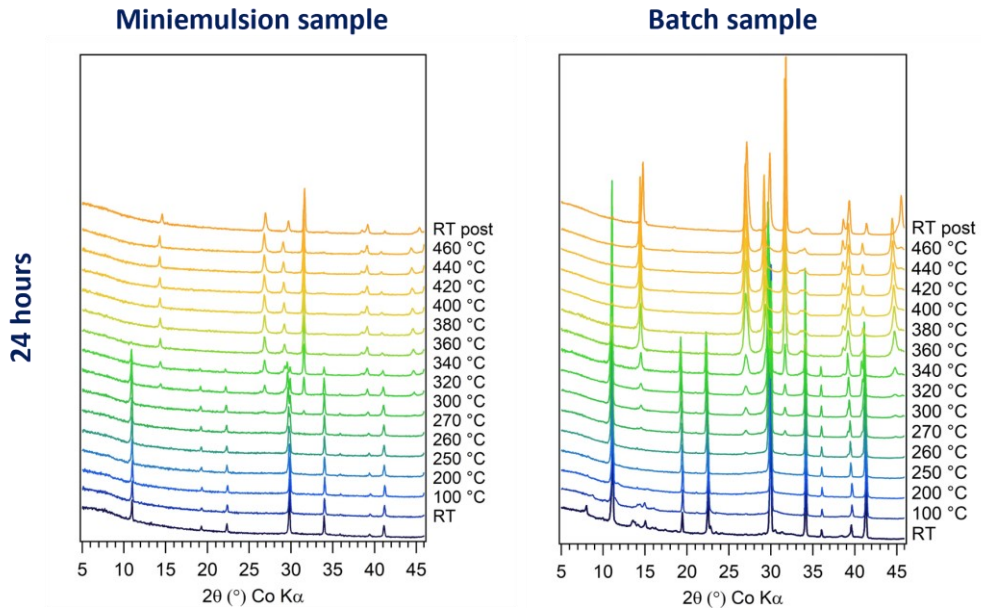

Figure 2.29 Thermal evolution (from room temperature up to 460 °C) of miniemulsion (**left**) and batch (**right**) samples obtained after 24 hours of reaction, followed *in situ* by XRD. Diffractograms are shifted vertically for clarity

results were found in agreement with those collected with the *in situ* combined XAS and XRD study at Diamond Light Source.

By comparing the thermal evolution of the samples obtained after 5 minutes (Figure 2.28) and 24 hours (Figure 2.29), for the batch samples (right) the first α-MoO_3 reflections were observed at 270 °C in both cases, while for the ME ones (left) they started growing at 260 °C for the 5 minutes sample and at 300 °C for the 24 hours one. Such a wide difference in the temperature of crystallization of orthorhombic MoO_3 in ME samples, especially if compared to batch samples, is likely ascribed to the fact that the sample obtained in ME after 5 minutes was characterized by a high amount of amorphous material, which directly crystallizes into the thermodynamic polymorph by increasing the temperature, without a first step of crystallization into the metastable one. As far as the phase transition is concerned instead, the temperature range involved for both ME and batch 5 minutes samples (Figure 2.29, top) was the same (320-380 °C), while it was wider for the ME 24 hours sample (320-380 °C) with respect to batch 24 hours sample (360-380 °C) (Figure 2.29, right and left, respectively).

III. Morphological evolution of h-MoO_3 to α-MoO_3. In order to further characterize the morphology evolution of hexagonal MoO_3 rods into orthorhombic thermodynamically stable polymorph of molybdenum(VI) oxide, a h-MoO_3 sample was calcined at 500 °C for three hours and the resulting powder was characterized by SEM. SEM micrographs of thermally treated MoO_3, shown in Figure 2.30, bottom, compared with SEM micrographs of h-MoO_3, showed that the phase transition affected the morphology of molybdenum(VI) oxide, that evolved from the previously discussed nano- and microrods to microplates. This observation is in agreement with literature,[231,259,276] that reported that, by thermal treatment, the h-MoO_3 nanorods collapse into α-MoO_3 microplates, that ultimately coalesce to form lamellar microplates in the orthorhombic structure. Moura *et al.* observed by Raman spectroscopy that, by increasing the temperature, the vibrational modes in the *a-b* plane are strengthened more than the vibrational modes in the *c*-direction. This event, combined with the loss of intercalated species inside the crystalline structure of the hexagonal polymorph, *e.g.* ammonium ions and water, as observed by other authors and discussed above, further confirmed that the temperature-induced phase transition begins

with the emptying of the structural tunnel of h-MoO_3 that ultimately leads to the collapse of the hexagonal structure.[259]

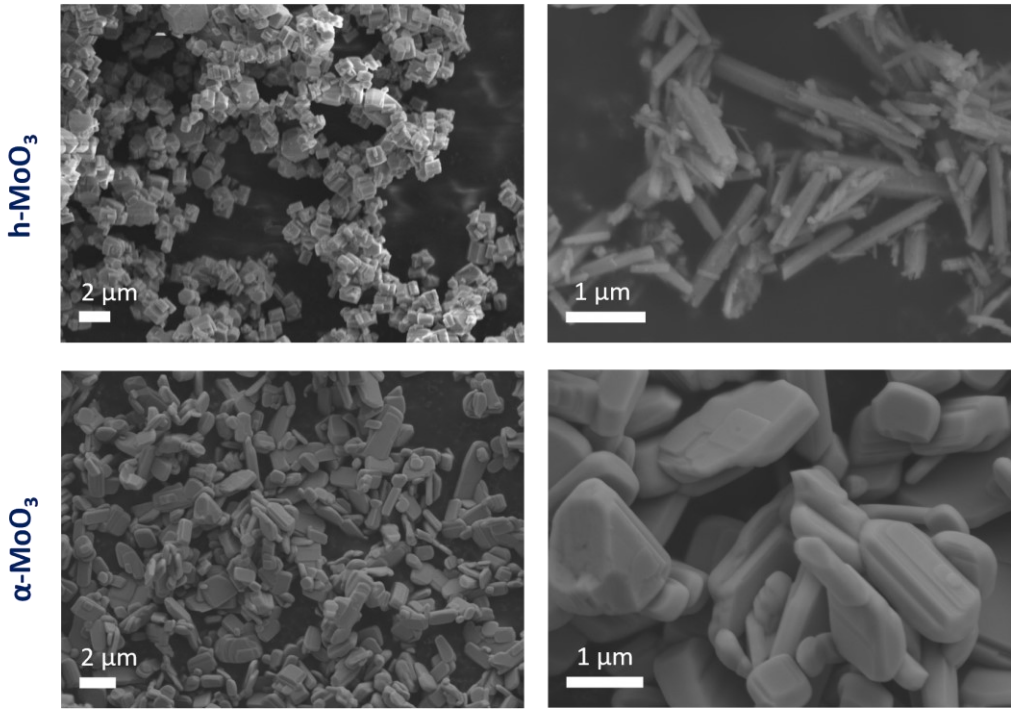

Figure 2.30 Comparison of SEM micrographs of h-MoO_3 synthesized in batch (**top left**) and miniemulsion (**top right**) conditions, and of α-MoO_3 (**bottom**), obtained by thermal treatment of h-MoO_3 at 500 °C

2.5 Conclusions

The synthesis of the hexagonal metastable polymorph of molybdenum(VI) oxide (h-MoO_3) in the confined space of miniemulsion nanodroplets and in a macroreactor (batch approach), by exploiting the dehydration and polycondensation reactions occurring in acidified solutions of Mo(VI), was investigated and optimized by a systematic screening of the reaction parameters. The crystallization of pure hexagonal crystal phase, stabilized by ammonium ions and water molecules in its internal tunnel structure, was evidenced by XRD and confirmed by ATR, in agreement with literature reports. The formation of rods with a hexagonal cross-section with different sizes (nano- to microrods), aspect ratios and aggregation was observed by TEM and SEM as a function of the synthetic approach and synthetic conditions, such as Mo precursor (ammonium heptamolybdate, AHM) concentration, molar ratio between AHM and the precipitating agent (concentrated nitric acid), application of ultrasounds, and reaction time. In particular, smaller and more elongated rods were obtained by miniemulsion approach, as compared to batch-synthesized molybdenum(VI) oxide, confirming the role of space confinement in determining the size and shape of the synthesized inorganic system. Moreover, more crystalline samples characterized by more elongated rods were formed with lower AHM to HNO_3 molar ratios, and flower-like aggregates were observed when the diffusion of the precipitating agent was not forced through the application of ultrasounds, but rather occurred spontaneously. Among the experiments performed, a preliminary *ex situ* evaluation of the formation mechanism of h-MoO_3 rods was performed by analyzing samples obtained at different reaction times through X-ray diffraction. The formation of several ammonium polyoxomolybdates with different nuclearities for reaction times shorter than 18 hours was observed, followed by the final condensation to MoO_3. From these results, it was hypothesized that the crystallization of h-MoO_3 is a stepwise process that occurs following the Ostwald's rule of stages.

A time-resolved *in situ* SAXS/WAXS investigation was performed at Elettra Sincrotrone Trieste in order to further explore the crystallization pathway of molybdenum oxide by miniemulsion and batch approaches, and to evaluate the effect of spatial confinement of ME nanodroplets and of the ratio between the Mo precursor and the precipitating agent. The formation of a mixture of different reaction intermediates (*i.e.* polyoxomolybdates) was evidenced by the growth and disappearance of different superimposed patterns of Bragg

reflections in the high q-region of the SAXS profiles and in the WAXS range as a function of time, further supporting the hypothesis that the crystallization of h-MoO_3 in our conditions follows the Ostwald's step rule. Interestingly, the observed SAXS and WAXS patterns of the reaction mixtures differed depending on the synthetic approach and on the AHM to HNO_3 molar ratio, observing that confining the synthesis in ME droplets promoted a nonclassical crystallization pathway involving the oriented aggregation of primary particles into hexagonal arrays (*i.e.* likely mesocrystals), while preventing the formation of a more reactive reaction intermediate that was observed in batch conditions. It was thus argued that the space confinement plays a role in altering the stability of intermediate products and their interconversion, according to the Ostwald's rule of stages.

Finally, the thermal evolution of miniemulsion and batch samples was studied by a *in situ* combined XRD and XAS investigation at Diamond Light Source synchrotron facility and further supported by an *in situ* XRD study carried out at the Department of Geosciences (University of Padova). The thermal-induced phase transformation between the metastable hexagonal polymorph h-MoO_3 and the thermodynamically stable orthorhombic α-MoO_3 was observed, *via* a first release of ammonia and water molecules from the internal tunnel structure of the hexagonal phase, its subsequent collapse and MoO_6 octahedra rearrangement. It was demonstrated that the synthetic route also affected the thermal response and phase transition behavior of MoO_3, observing that the miniemulsion sample, as compared to the batch one, was characterized by a more evident structure variability at low temperatures (by XANES analysis), and by an onset of phase transition at lower temperatures and a wider temperature range required for the transition to be complete (by combined EXAFS and XRD investigations).

3

Calcium molybdate

In this Chapter, the synthesis of undoped and europium-doped calcium molybdate nano- and microstructures in the confined space of inverse miniemulsion nanodroplets, in a continuous-flow microreactor (microfluidic conditions) and in a macroreactor (batch approach) is addressed, and the synthesis outcomes are compared. Several synthesis parameters were screened in all the different synthetic conditions, and the controlled formation of nano- to mesostructures was pursued, depending on the selected experimental approach. The doping of calcium molybdate with Eu^{3+} ions was investigated by all explored synthetic approaches and the photoluminescence properties of the Eu-doped samples were assessed, to evaluate the effect of space confinement on the functional properties of the synthesized materials.

3.1 Introduction

Calcium molybdate, $CaMoO_4$, is a functional ternary oxide related to molybdenum oxide, with great potential and promising applications. Indeed, thanks to its intrinsic photoluminescence properties in the blue-green region (350-650 nm, upon excitation in the UV range), its chemical and thermal stability (melting point of 1445-1480 °C), and its ability of hosting dopant ions in its structure, calcium molybdate is a versatile photoluminescent material, especially when doped with rare earth ions. Actually, the doping of calcium molybdate with lanthanide ions has been extensively employed for the enhancement of its photoluminescence properties and to confer to the system tunable chromaticity for

application in devices such as phosphors, lasers, scintillators, white light emitting diodes (WLEDs) and up-conversion devices.[277–286]

Calcium molybdate (CM) crystallizes in the tetragonal body-centered *scheelite*-type[xxvi] structure AXO_4 (where A is a large cation, such as Ca^{2+}, Sr^{2+}, Mg^{2+}, or Ba^{2+}, and $[XO_4]^{2-}$ is an anion with X = Mo or W), with Mo atoms surrounded by four equivalent oxygen atoms and Ca atoms coordinated to eight O atoms in a distorted pseudo-cubic configuration, in a S_4 point symmetry with no inversion center (space group $I4_1/a$, schematic representation of the unit cell in Figure 3.1).[287] Each CaO_8 polyhedron shares corners with eight adjacent MoO_4 tetrahedra. As mentioned, it has been extensively reported in literature that $CaMoO_4$ is an interesting host matrix for the development of Ln-based phosphor materials. Dopant lanthanide ions, such as Eu^{3+}, Tb^{3+}, Yb^{3+} and Dy^{3+}, are reported to substitute Ca^{2+} ions in the crystalline lattice of *scheelite*.[288] In Ln-doped calcium molybdate, the $[MoO_4]^{2-}$ unit of the matrix can absorb UV light with a high cross section and excite the doping lanthanide ion through energy transfer process, and the narrow spectral emission lines due to f-f electronic transitions of the lanthanide are observed.[288,289] CM-doping with different dopant Ln ions, as well as co-doping with intelligent combinations of them to pursue desired emission, have been reported in literature.[280,288–293] However, among the reported dopant lanthanide cations, Eu^{3+} ones easily substitute Ca^{2+} ions in the $CaMoO_4$ structure thanks to their similar ionic radius, *i.e.* 1.12 Å and 1.066 Å for Ca^{2+} and Eu^{3+} in VIII coordination, respectively.[294]

In recent years, a variety of methods has been proposed for the synthesis of undoped and Eu-doped CM, such as hydrothermal process,[292,295,296] microwave-assisted synthesis,[297–299]

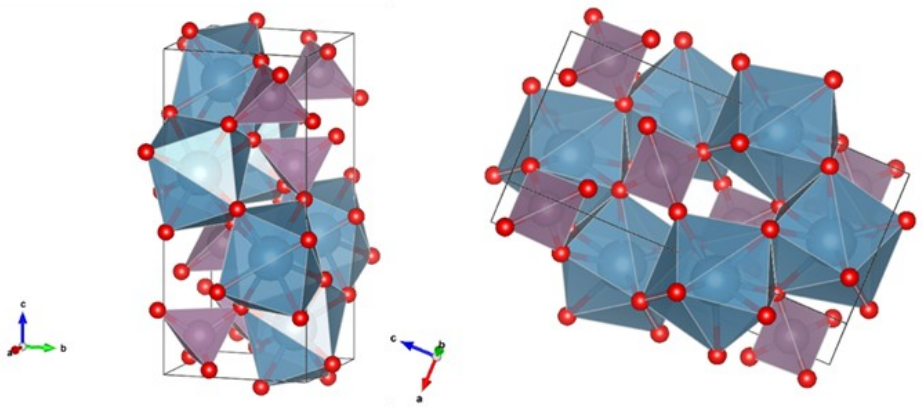

Figure 3.1 Crystalline structure of tetragonal $CaMoO_4$; Ca, Mo and O atoms are represented in blue, purple, and red, respectively

[xxvi] The mineral $CaMoO_4$ is named *powellite*, and it is isostructural with the *scheelite*, $CaWO_4$.[429]

pulsed laser ablation,[300] co-precipitation,[301–304] hot injection route,[305,306] and microemulsion approach.[307,308] Generally, the co-precipitation reaction between Ca^{2+} and $[MoO_4]^{2-}$ was exploited in aqueous solution or in mixed solvents (*e.g.* alcohol and water), and possibly heated in different conditions, and typically good shape control over the final particles aggregation into mesostructures was reported. However, up to date, no studies of the synthesis of calcium molybdate in the confined space of miniemulsion droplets nor in continuous-flow microreactors have been reported. Within this framework, in this Ph.D. Thesis, the synthesis of crystalline tetragonal undoped and Eu-doped calcium molybdate was addressed at room or lower temperature, in *batch conditions*, in the confined space of *inverse miniemulsion nanodroplets* and in a *continuous-flow microreactor*.

To crystallize calcium molybdate by the different proposed approaches, the co-precipitation reaction between calcium nitrate and sodium molybdate in aqueous solution (K_s (at 20 °C) = $1.8 \cdot 10^{-9}$ M^2)[309] or in water/ethanol mixtures was exploited within the different reaction environments. The pH of the reaction mixture was kept higher than 6.5 (*i.e.* autogenous pH of the aqueous solution of the molybdate precursor Na_2MoO_4), since the molybdate ions $[MoO_4]^{2-}$ are a weak base and, at pH above 6, they are the only molybdate species in solution,[251,252] while at lower pH values they undergo several equilibria that generate polynuclear species, as extensively described in Chapter 2 and shown in the distribution diagram in Figure 2.2. The effect of the confined space of ME droplets, as compared to the batch macroreactor, as well as the influence of the screened reaction parameters and the role of reaction environment on the effectiveness of doping, are discussed in Chapter 3.2. The possibility of tuning the assembly of calcium molybdate nanoparticles into differently shaped mesostructures, investigated by microfluidic approach screening different experimental setups and reaction parameters, is presented in Chapter 3.3.

3.2 Synthesis of undoped and Eu(III)-doped calcium molybdate by inverse miniemulsion and batch approaches

As mentioned in the Introduction section and described in detail in Chapter 6.2, for the synthesis of undoped and Eu(III)-doped calcium molybdate at room temperature by both inverse miniemulsion and batch approaches, the co-precipitation between calcium nitrate and sodium molybdate in aqueous solution was exploited. In particular, the syntheses by

miniemulsion approach were performed by mixing two pre-formed miniemulsions of Ca^{2+}_{aq} and $[MoO_4]^{2-}_{aq}$ solutions, and subsequently applying high power ultrasounds in order to promote the mixing of the reactants and precipitate the target product within the confined space of ME nanodroplets (two-miniemulsion method, described in Chapter 1.2.1.3). On the other hand, the synthesis by *batch approach* was performed by simple mixing of two aqueous solutions of calcium and molybdate precursors under stirring, and the product precipitated in the reaction vessel without space constraint. The obtained reaction mixtures were left stirring at room temperature for 24 hours and the product was purified and dried in vacuum. When doped samples were targeted, a stoichiometric amount of europium nitrate was added to the calcium precursor solution and the syntheses were performed as described above. The starting inverse miniemulsions were formulated employing the parameters previously optimized for the synthesis of molybdenum oxide (Chapter 2.2), and an average ME droplet size of 100 nm was estimated by DLS for both precursors. A systematic variation of different synthetic parameters was carried out, within both synthetic approaches, in cooperation with the Master student Chiara Mazzariol. The following parameters were screened: i) the precursors concentration (0.15 M, 0.20 M, 0.25 M, 0.50 M, 1.0 M, 1.5 M, and 2.0 M), while keeping constant the Ca^{2+}:$[MoO_4]^{2-}$ molar ratio to 1:1, ii) the pH of the molybdate solution (pH values of 6.5, 9, 11, and 13), and iii) the percentage of doping with Eu^{3+} (1, 3, 5, and 7 at% Eu/Mo). As "reference" miniemulsion and batch samples, the following samples will be discussed: $[Ca(NO_3)_2]$ = $[Na_2MoO_4]$ = 0.20 M, pH = 6.5, and percentage of doping = 0 at%.

In order to rationalize which are the effects of the confined space of ME droplets on the crystalline structure, size, shape and aggregation of calcium molybdate, X-ray diffraction, transmission and scanning electron microscopies analyses were performed and the miniemulsion and batch samples outcomes were compared (Figure 3.2). XRD analysis showed that by both approaches crystalline tetragonal scheelite-type calcium molybdate (PDF card 85-1267) was obtained. However, the diffraction pattern of $CaMoO_4$ synthesized by ME approach was observed to be characterized by evidently broader reflections as compared to the ones of $CaMoO_4$ obtained by batch approach, thus meaning that crystallites of CM synthesized by miniemulsion were characterized by a considerably smaller size, as an effect of space constraint during the synthesis within miniemulsion droplets. Indeed, the average crystallite size of CM was estimated by whole powder pattern fitting

(WPPF) of diffractograms to be of about 8 nm for ME synthesized one, and of about 30 nm for the batch one (Figure 3.2, top).

A marked effect of the confined space of miniemulsion droplets was observed also on the size, size distribution, shape and aggregation of $CaMoO_4$ nanoparticles, leading to smaller

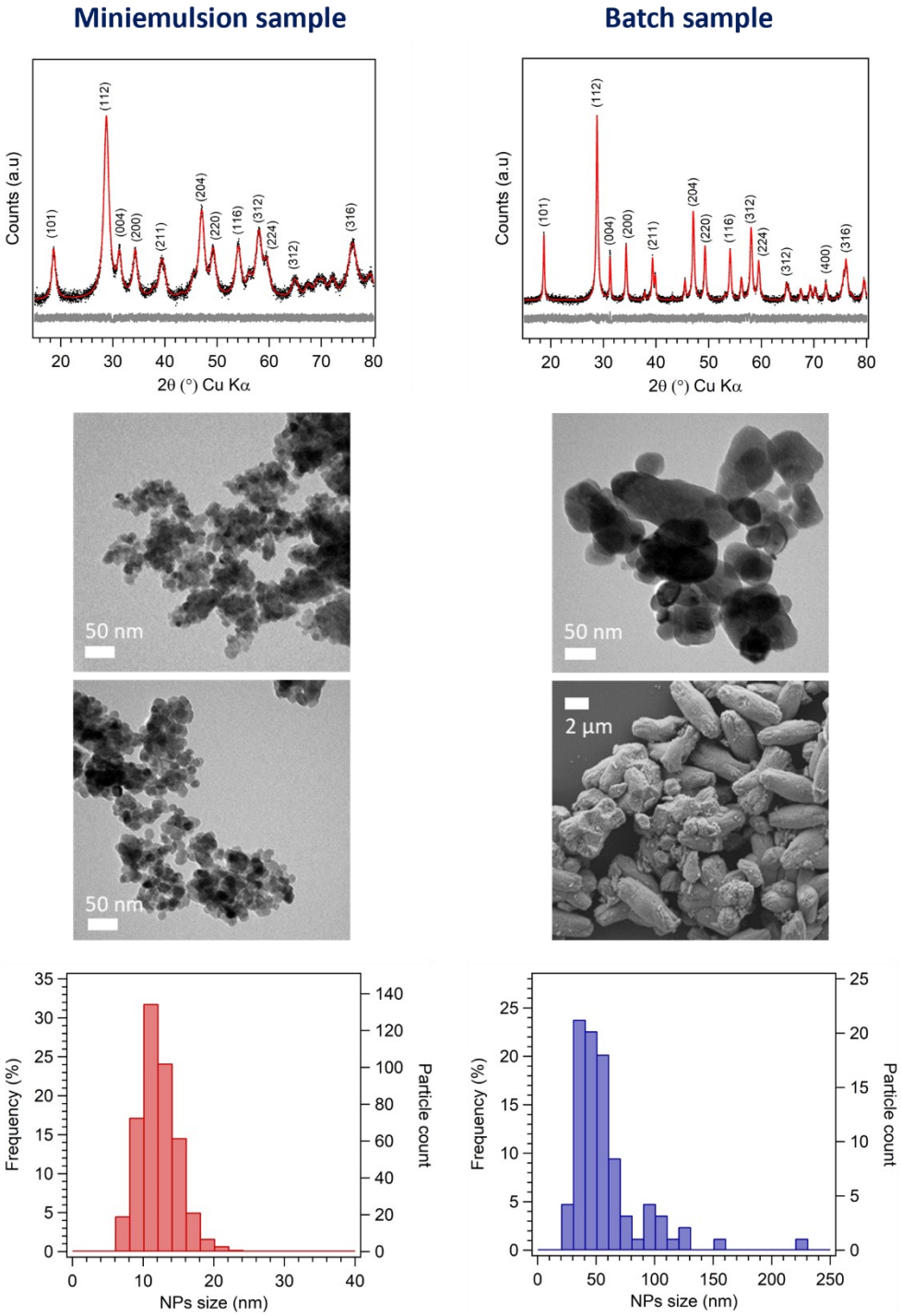

Figure 3.2 XRD fittings (**top**), TEM and SEM micrographs (**center**) and size distribution histograms (**bottom**) of miniemulsion (**left**) and batch (**right**) undoped CM samples

and more regular NPs with respect to batch approach. Indeed, by TEM and SEM analyses, and relative size distribution histograms (Figure 3.2, center and bottom), it was observed that $CaMoO_4$ obtained by miniemulsion was constituted by pretty monodispersed quite spherical and independent nanoparticles with an average size of 12.0 nm ± 2.7 nm (polydispersity index, PDI, of 0.2), non-aggregating into larger structures. On the contrary, by batch approach, more irregular, larger particles with a wider size distribution were obtained (58 nm ± 31 nm; PDI = 0.5), subsequently aggregating into larger microstructures with an ellipsoidal-like shape and with a size of about 5 µm. Similar aggregated microstructures of scheelite-type materials were observed by other authors in similar synthetic conditions and their formation was hypothesized to occur through an oriented aggregation mechanism.[301,306,310] In particular, the initially formed particles were considered to self-assembly in hierarchical microstructures by sharing a common crystallographic orientation due to electrostatic and van der Waals forces. On the other hand, miniemulsion CM NPs did not aggregate into larger structures, indicating that the space confinement and compartmentalization into independent miniemulsion droplets was efficient. Indeed, it is worth highlighting that the formation of aggregated hierarchical microstructures was reported in literature also employing the microemulsion approach,[307,308] that, as opposed to the miniemulsion one, does not guarantee an effective space constraint, as a dynamic exchange between droplets occurs (see more details in Chapter 1.2.1.2). Altogether, the XRD, TEM and SEM results, evidencing marked differences between the synthetic outcome of the two different approaches, are in agreement with the hypothesized controlled and uniform crystallization process taking place within parallel nanoreactors by ME,[118] as opposed to uncontrolled nucleation and growth caused by non-uniform mixing and thereby concentration gradients typical of a macroreactor (batch approach).

Finally, the effectiveness of the purification method in removing surfactant moieties in the miniemulsion samples was assessed by ATR measurements. Along with the characteristic asymmetric stretching vibration of O-Mo-O bonds in the MoO_4 tetrahedra at about 760-770 cm^{-1},[311,312] stretching and bending vibrations of O-H were observed (ν_{O-H} at 3400 cm^{-1}, and δ_{O-H} at 1642 cm^{-1}),[262] suggesting the presence of water, likely physisorbed on the sample surface. In addition, the presence of a small amount of residual surfactant moieties in the ME sample was pointed out by very weak peaks in the 2950-2850 cm^{-1} range and 1450-1350 cm^{-1} ranges, ascribed to the stretching and bending of the sp^3 C-H bond,

respectively. IR spectra of miniemulsion and batch samples are reported in Appendix B.2 in Figure B.14.

I. Effect of precursors concentration. As outlined in detail in Chapter 1.1, and also investigated in Chapter 2.2 for the synthesis of molybdenum(VI) oxide, classical crystallization models state that the precursors concentration affects the number of formed primary particles, and ultimately their size, obtaining the simultaneous nucleation of a higher number of smaller particles when starting with higher precursors concentrations. On the other hand, in miniemulsion conditions, it is known that the amount of osmotic agent, *i.e.* the concentration of the inorganic salt precursor in water-in-oil droplets, affects the size of the miniemulsion droplets, as different amounts of osmotic agent should generate an osmotic pressure that balances out with the Laplace pressure at different droplets dimensions. Thus, a variation of the precursors concentration is supposed to act on tuning the size of the confined environment. For these reasons, the concentration of CM precursors solutions was systematically varied from 0.15 M to 2.0 M (*i.e.* 0.15, 0.20, 0.25, 1.0, and 2.0 M), while keeping constant the calcium to molybdate molar ratio to 1:1, and the effects on the crystalline structure, size, morphology and aggregation were evaluated by XRD, TEM and SEM.

The crystallization of tetragonal scheelite-type calcium molybdate was observed by both approaches and with every tested precursors concentration, and the above discussed differences between diffraction patterns of miniemulsion and batch samples were retained: generally smaller crystallites were obtained in miniemulsion with respect to batch approach. However, different trends in crystallite size as a function of precursors concentration were observed, depending on the synthetic approach. In particular, while for miniemulsion samples an increase in crystallite size with increasing precursors concentration was evidenced,[xxvii] for batch samples the opposite was found, as shown in Figure 3.3 (fittings of ME and batch XRD patterns, as well as estimated fitting parameters, are reported in Figure B.15, Figure B.16, Table B.4, and Table B.5 in Appendix B.2). This observation could be rationalized taking into account the likely different crystallization pathways involved when employing the two synthetic techniques. While in the macroreactor the predictions of the classical models were confirmed (*i.e.* the higher the

[xxvii] A similar trend was also obtained for the miniemulsion synthesis of MoO_3 varying the precursor concentration, as discussed in Chapter 2.2.

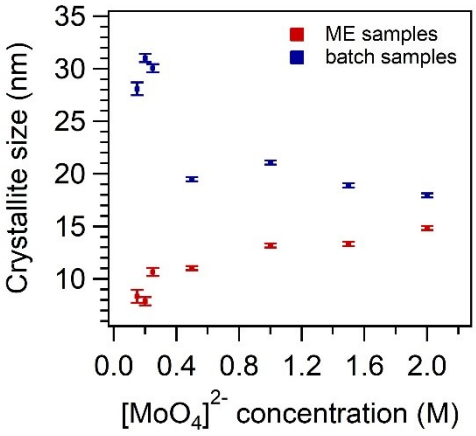

Figure 3.3 Average crystallite size of calcium molybdate synthesized by miniemulsion (red) and batch (blue) approaches as a function of precursors concentration. $[Ca^{2+}] = [MoO_4^{2-}]$

concentration, the faster the reaching of the supersaturation level, the higher the number of nuclei formed and the lower the material available for their growth, and consequently the smaller the average size of the resulting nanoparticles), in the confined environment of miniemulsion nanodroplets the opposite trend suggested that a different mechanism should be hypothesized. As an increased concentration of osmotic pressure agent should produce larger ME droplets, and it has been reported that the crystallization occurs in a parallel fashion inside each nanodroplet, it could be supposed that all the precursor confined in each nanodroplet concurs to the formation of one nanoparticle, thus leading to larger NPs when the amount of starting material is higher.

A similar, even if not marked, trend in ME $CaMoO_4$ nanoparticles size was also observed by TEM investigations, obtaining slightly larger NPs with a broader size distribution when the synthesis was carried out with a higher precursors concentration, as shown in Figure B.17 and Table B.6 in the Appendix. On the other hand, CM batch samples were still observed to form irregularly shaped and aggregated nanostructures, preventing the estimation of the particle size in TEM micrographs. However, SEM micrographs displayed differences in the aggregation of the batch primary particles as a function of the starting precursors concentration, as shown in Figure 3.4. Indeed, while with lower concentrations ellipsoidal-like microstructures were observed, increasing the concentration of the precursors solutions the aggregation of the primary particles into more spherical microstructures was instead evidenced. In particular, the microstructures displayed a quite uniform morphology composed by twinned hemispheres, with a clear joint boundary between them. The average diameter of the hemispheres was approximately 2-4 µm.

Higher magnifications of SEM micrographs clearly revealed that the microstructures are composed by nanosized tetragonal subunits, in agreement with the crystalline structure of CM, the relatively broad reflections observed by XRD (*i.e.* crystallite size between 20 and 30 nm) and with the hypothesis of their formation by oriented aggregation and not by classical growth models. The formation of similar microstructures of calcium molybdate was observed by other authors in similar conditions.[301,304] In particular, Chen *et al.* observed by a time-resolved SEM study that the formation of spherical microstructures of calcium molybdate occurred through progressive stages of self-assembled (hierarchical) growth, starting form ellipsoidal-like structures and passing through the formation of dumbbells, and finally evolving into complete spherules.[304] A very similar morphogenesis was reported by Busch *et al.* for fluoroapatite aggregates,[313,314] and reviewed by Cölfen and Antonietti as a clear example of oriented aggregation controlled by intrinsic electric fields.[269] The authors proposed that the progressive self-assembled growth of the elongated structures occurred at both ends (*fractal branching*), leading to dumbbell-shaped aggregated, which then completed their shapes by successive and self-similar upgrowth to give notched spheres. However, the mechanism of the morphogenesis of these aggregates is still largely unclear. Taking into account these considerations, it could be hypothesized that the formation of twinned hemispheres with higher concentrations of precursors, as opposed to

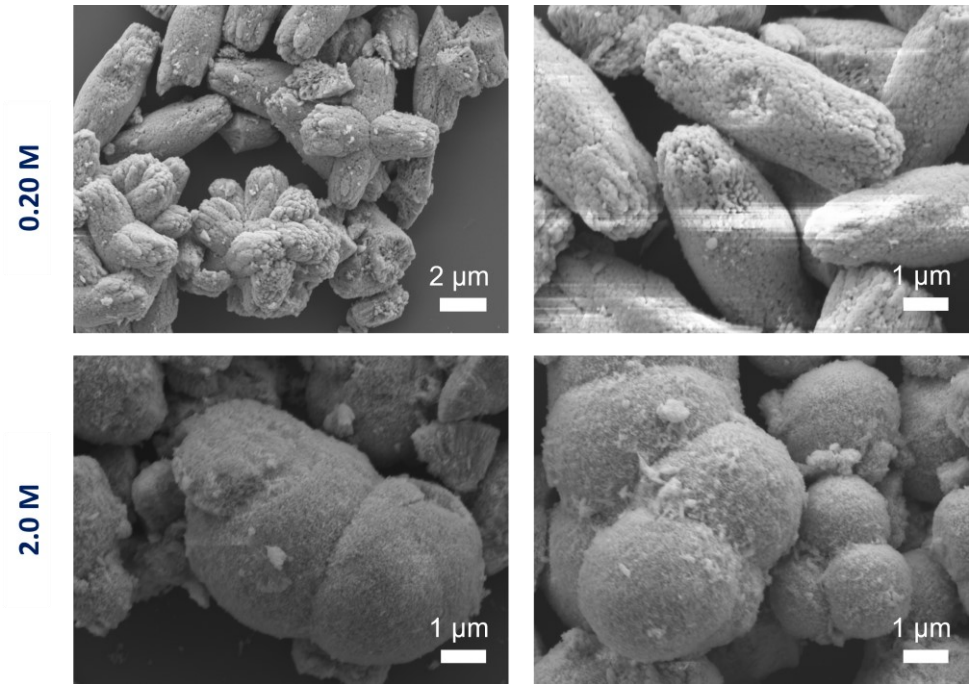

Figure 3.4 SEM micrographs of batch CM samples synthesized starting with different precursors concentrations: comparison of 0.20 M (**top**) and 2.0 M (**bottom**) samples

ellipsoidal-like structures with lower concentrations, was caused by the higher supersaturation achieved, leading to a faster evolution of the self-assembly of these microstructures.

II. Effect of molybdate solution pH. Since literature studies reported that the morphology of the self-organized calcium molybdate microstructures can be influenced by a variation of the pH of the molybdate precursor solution,[301,306] a series of miniemulsion and batch syntheses varying such parameter were carried out. In particular, the pH of the molybdate aqueous solution was risen from 6.5 (autogenous pH) to 9, 11 and 13 by adding $NaOH_{aq}$. First of all, an effect on the kinetics of the precipitation of the white product was experimentally observed in batch conditions: while prompt precipitation occurred at autogenous pH, it took about 10 minutes to observe the macroscopic precipitation when the pH of the molybdate solution was about 13. Such effect was not detectable in miniemulsion, being the suspensions milky white. Since it is well known from the rich chemistry in solution of Mo(VI) that the sole Mo(VI) species present in solution at pH values higher than 6 is the simple mono-molybdate $[MoO_4]^{2-}$, as mentioned in Chapter 3.1 and detailed in Chapter 2.1, this experimental observation was ascribed to an effect involving Ca^{2+} ions. Indeed, by increasing the concentration of hydroxide ions in solution, they likely interacted with calcium ions resulting in calcium hydroxide formation, and thus lowering the Ca^{2+} ions availability for the precipitation of $CaMoO_4$. As a consequence, it was argued that, when increasing the concentration of hydroxide ions, the supersaturation limit was achieved less quickly and the kinetics of precipitation of CM was considerably slowed down.

This experimental observation was further addressed by *in situ* time-resolved WAXS experiments, performed at the SAXS beamline at Elettra Sincrotrone Trieste[xxviii] and following the formation of calcium molybdate in batch conditions starting with molybdate solutions at different pH values. Briefly, by employing a remotely controlled syringe pump, an aqueous solution of the Ca^{2+} precursor was added to the $[MoO_4]^{2-}$ aqueous solution with the desired pH value (*i.e.* 6.5, 9, 11 or 13) and the resulting suspension was funneled through a continuous-flow setup into a measuring capillary mounted in the beamline, where the WAXS profile was acquired every 10 s in a continuous mode. The evolution of the WAXS profiles as a function of time from 60 s (start of calcium precursor injection was set

[xxviii] The same experimental setup and measurement conditions employed for the *in situ* SAXS/WAXS study of the synthesis of MoO_3, detailed in Chapter 2.3 and Chapter 6.1.4, were used.

as t = 0 s) to 360 s (end of Ca^{2+} precursor injection) of the experiments performed at pH = 6.5, 9, 11 and 13 is shown in Figure 3.5. The nucleation and growth of calcium molybdate NPs could be observed from the growth in time and progressive sharpening of the (112) and (004) reflections (about 20.0 nm^{-1} and 21.8 nm^{-1}, respectively), indicating that the initially formed small nuclei were growing into bigger crystallites. By comparing the time-resolved profiles as a function of molybdate precursor solution pH values, a clear effect of the pH on the rate of crystallization of tetragonal $CaMoO_4$ was evident: while the most intense (112) reflection was detected within a minute at autogenous pH (Figure 3.5, top left), it took more than 5 minutes at pH = 13 (Figure 3.5, bottom right). At intermediate pH values, the first detection of the reflection occurred in between 1 and 5 minutes. Moreover, it is worth noting that, by increasing the pH of the molybdate solution, the observed calcium molybdate reflections were broader, indicating an effect of pH also on the crystallite size,

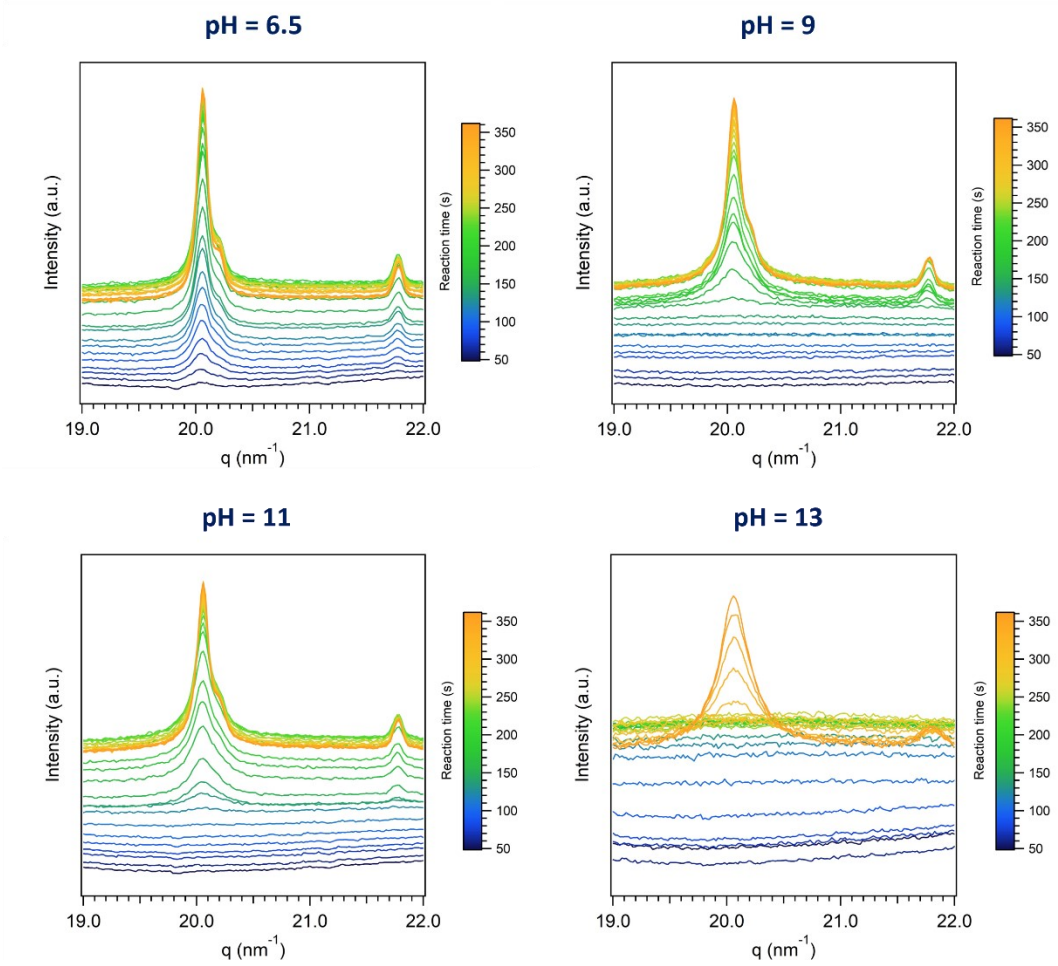

Figure 3.5 *In situ* time-resolved WAXS profiles of batch reaction mixtures with different pH values of $[MoO_4]^{2-}$ solution. A pattern every 10 s from the start of Ca^{2+} addition (t = 0 s) to the end of Ca^{2+} addition (360 s)

i.e. the higher the pH, the smaller the crystallites. Following the evolution of the WAXS profiles further after the end of calcium precursor addition, no relevant changes in reflections growth and shape were observed, besides a slight sharpening indicating further growth. Thus, the nucleation and growth stages of the calcium molybdate NPs formation was complete within the first minutes of the synthesis, after which aggregation phenomena occurred. The evolution of WAXS patterns until the end of acquisitions (up to 2800-6500 s) is shown in Figure B.19 in Appendix B.2.

From WPPF of the *ex situ* XRD patterns of samples synthesized in batch with different pH values of molybdate precursor and purified after 24 hours after the mixing of the two reactants, the crystallite size of the product was estimated (fittings of ME and batch XRD patterns are reported in Figure B.18 in Appendix B.2). A trend of the crystallite size of the 24 hours-synthesized CM as a function of molybdate precursors solution pH was observed, consistent with the observations made *in situ* within the first hour of the reaction. Indeed, the average crystallite size decreased from about 30 nm to about 22 nm with increasing the pH value of the molybdate precursor solution from its autogenous value (about 6.5) to 9 and above, as shown in Figure 3.6, blue dots. On the other hand, the crystallite size of CM samples synthesized within inverse miniemulsion droplets showed a minor influence on the pH value of the molybdate precursor solution (Figure 3.6, red dots). As in the case of the variation of precursors concentration, this observation could be rationalized taking into account the likely different crystallization pathways involved when employing the two synthetic techniques and the confinement effect occurring in the inverse miniemulsion

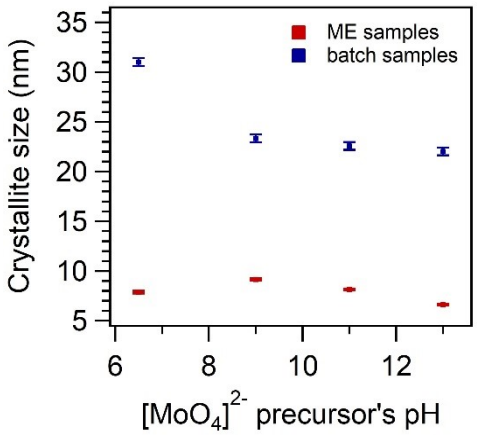

Figure 3.6 Average crystallite size of calcium molybdate synthesized by miniemulsion (red) and batch (blue) approaches as a function of $[MoO_4]^{2-}$ precursor solution pH.
$[Ca^{2+}] = [MoO_4^{2-}] = 0.20$ M

approach. In particular, it could be argued that, in batch conditions, reducing the availability of calcium ions by increasing the pH likely caused that the supersaturation limit was never super-exceeded, and small nuclei were formed during a longer period of time. Moreover, the increase of ionic strength of the reaction mixture caused a higher density of charges on the surface of the nuclei, preventing their growth. This hypothesis is in agreement with the reduced crystallite size of CM obtained at higher pH values. On the contrary, it was likely that the space constraint of miniemulsion droplets mitigated the variation of the reaction kinetics by pH modification, as an effect of space proximity of reactants inside miniemulsion droplets and of limited amount of precursors per droplet that concurred to the formation of NPs, and the crystallite size of the synthesized CM was thus not affected by it.

Analogously, TEM and SEM investigations of miniemulsion and batch samples synthesized starting from molybdate solutions with different pH values showed a stronger influence on the size, shape and aggregation of batch samples with respect to miniemulsion ones. Indeed, the morphology and average NPs size of miniemulsion samples seemed not to be significantly affected by the variation of pH: quite-spherical regular particles of about 13 nm, which do not aggregate, were clearly distinguished. On the contrary, TEM and SEM micrographs of the batch samples clearly showed that a substantial change in morphology occurred as pH of the molybdate solution was increased (Figure 3.7). Indeed, the formation of aggregates with a rod-like or wedge-like shape, in the size range of about 2 μm, in addition to some dumbbell-shaped microstructures, was observed for samples at pH 9 and above, whereas ellipsoidal-like microstructures were identified for CM sample at autogenous pH, as discussed above. Moreover, further observations revealed the presence of pores between the NPs subunits constituting the aggregates, which appeared quite "loose". This observation, in agreement with literature reports of CM microstructures, was ascribed to the polydispersity and stacking defects of nanoparticles in the self-assembly process.[299,308] In addition, the tetrahedral shape of the primary aggregating NPs could be clearly appreciated (Figure 3.7, right). Finally, as discussed in the previous section, the formation of dumbbell microstructures was reported also in literature, as an intermediate between the ellipsoidal aggregates and the spherical ones.[304] The different effect of the pH value of the molybdate solution on the aggregation of primary calcium molybdate nanoparticles according to the synthetic approach could be rationalized taking into account the presence of the surfactant in miniemulsion and the constraint environment in which the

synthesis occurred, as opposed to batch approach and also to some literature reports of microemulsion syntheses,[308] as mentioned above.

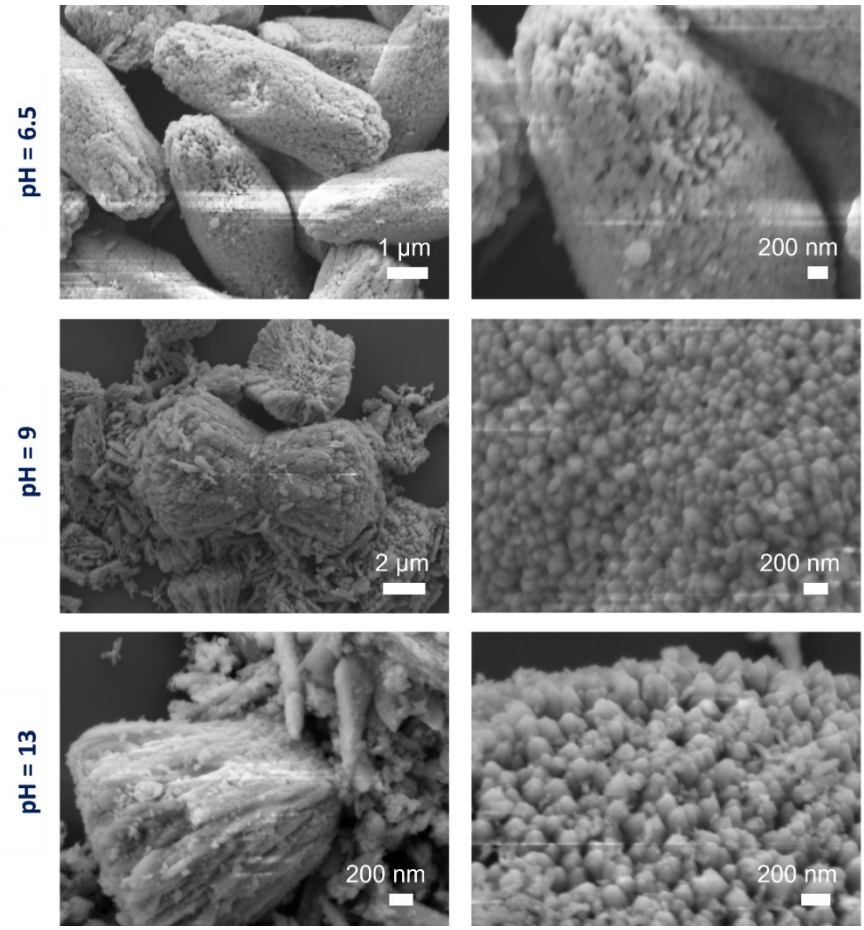

Figure 3.7 SEM micrographs of batch CM samples synthesized starting with different molybdate precursor solution pH: comparison of samples obtained at pH values of 6.5 (**top**), 9 (**center**), and 13 (**bottom**)

III. Doping of $CaMoO_4$ with Eu^{3+}. As introduced in Chapter 3.1, since calcium molybdate was reported to be an interesting matrix for the development of Ln-based phosphors, the synthesis of Eu(III)-doped $CaMoO_4$ was investigated. With the aim of investigating whether the space confinement plays a role on the doping process and dopant insertion in the calcium molybdate matrix or not, a series of experiments by doping of calcium molybdate with different amounts of Eu^{3+} (Eu/Mo: 1, 3, 5, and 7 at%) was performed exploiting both synthetic approaches.

The experimental doping level was assessed by ICP-MS analysis, and it was proven to be in very good agreement with the expected nominal ones, for both miniemulsion and batch samples, meaning that the incorporation of dopant ions in the final products is quantitative

for all samples. Nominal and experimental doping percentages are reported in Table 3.1. Since the doping percentage was calculated as the atomic ratio between europium and molybdenum, an experimental doping percentage higher than the nominal one could be due to the loss of molybdenum during the purification step.

Table 3.1 Nominal and experimental doping percentages, expected based on the concentrations employed in the syntheses and assessed by ICP-MS, respectively, for miniemulsion and batch samples. Doping concentrations were determined as Eu/Mo at.

Nominal at%[a]	Experimental at%	
	ME	Batch
1.0	1.3	1.3
3.0	3.0	3.5
5.0	4.9	5.2
7.0	7.4	7.5

XRD diffractograms of ME and batch Eu-doped CM samples, reported in Figure 3.8, evidenced that no long-range order change in the crystalline structure of calcium molybdate occurred upon doping: the crystallization of pure-phase tetragonal scheelite-type $CaMoO_4$ was observed by both synthetic approaches. No other spurious crystalline phases reflections were found in the diffractograms of all the samples, with exception of the diffraction patterns of 5 and 7 at% doped batch CM, that displayed additional reflections at 23.2° 2θ and 32.5° 2θ (highlighted with the stars in diffractograms in Figure 3.8) and a strong asymmetric shape for the most intense (112) reflection of CM, with "shoulders" at 28.5° 2θ and 29.4° 2θ (evidenced in Figure B.21 in Appendix B.2). The spurious reflections positions were found to be compatible with $Na_{0.93}Mo_6O_{17}$ structure (PDF card 65-3182), while the peculiar shape of the (112) reflection of tetragonal calcium molybdate was well-fitted including cubic Eu_2O_3 (PDF card nr. 65-3182) and monoclinic EuOOH (PDF card nr. 18-0510) structures in WPPF (fittings in Figure B.20). These findings, compatible with the presence of Eu-based crystalline compounds (*i.e.* Eu_2O_3 and EuOOH), indicated that likely not all the Eu^{3+} incorporated in the sample actually substituted Ca^{2+} ions in the CM matrix, but otherwise it formed another crystalline phase. Since, on the contrary, the diffractograms of Eu-doped samples obtained by ME approach at all doping percentages and by batch approach with

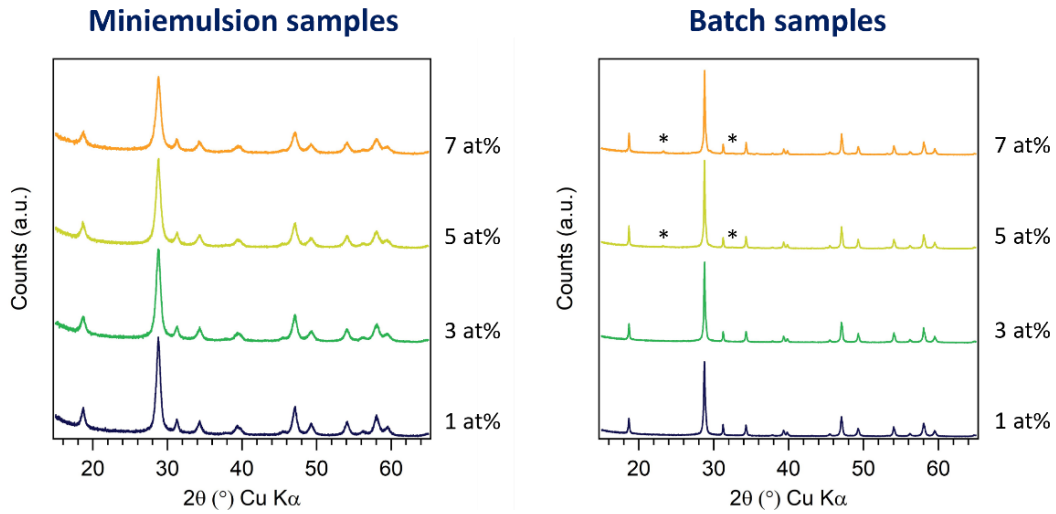

Figure 3.8 XRD patterns of Eu-doped samples, obtained by ME (**left**) and batch (**right**) approaches as a function of experimental doping at%. $[Ca^{2+}] = [MoO_4^{2-}] = 0.20$ M

1 at% and 3 at% Eu content did not show the formation of any Eu-based impurity at any doping level, and were well-fitted by the tetragonal $CaMoO_4$ structure, it could be supposed that for these samples the experimental percentage of dopant assessed by ICP-MS actually corresponded to the doping level. From the whole powder pattern fittings of the diffractograms of the miniemulsion and batch doped samples (in Appendix B.2: fitted patterns are reported in Figure B.20, left and right, for ME and batch samples, respectively; refined parameters are reported in Table B.7 and Table B.8 for ME and batch samples, respectively), the average crystallite size and cell volume were estimated. As for undoped CM samples, confining the synthesis of doped CM in ME droplets led to the formation of smaller crystallites, as compared to batch samples, and no significant variation of the crystallite size with dopant amount was found. On the other hand, an increase in doping percentage in batch samples was complemented with an increase in CM crystallites size, corroborating the hypothesis of poor synthetic control *via* batch approach. The average crystallite size as a function of doping percentage and synthetic approach estimated by WPPF is reported in Figure 3.9, left. Another parameter that was found to be affected by the doping percentage in different extent according to the synthetic approach was the estimated unit cell volume of tetragonal calcium molybdate. In particular, for ME samples a slight increase in the cell volume as a function of the doping percentage was observed (Figure 3.9, right), more appreciable for the samples with a higher amount of dopant, while for batch samples no significant variation was evidenced.

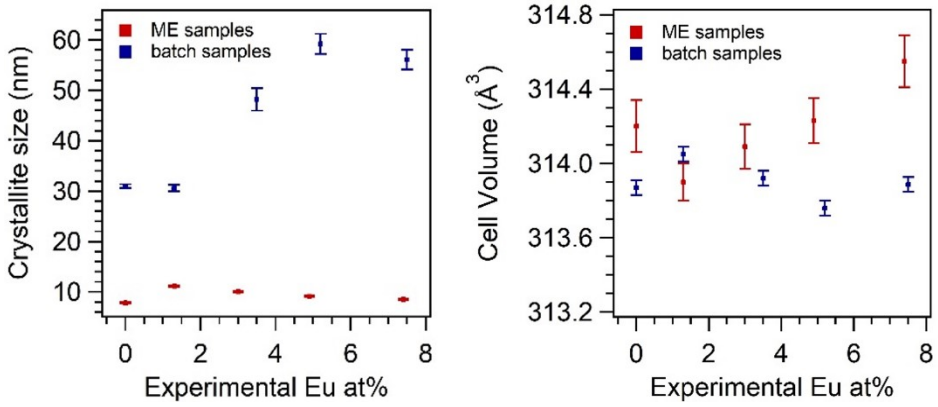

Figure 3.9 Estimated average crystallite size (**left**) and cell volume (**right**) as a function of experimental doping at% for miniemulsion (red) and batch (blue) Eu-doped CM samples, from WPPF. $[Ca^{2+}] = [MoO_4^{2-}] = 0.20$ M

A slight expansion of the unit cell volume of calcium molybdate upon doping with Eu^{3+} ions was expected, as it was previously reported in literature.[286,288,290,315,316] In particular, according to the literature, upon doping of calcium molybdate with europium, Eu^{3+} ions replace Ca^{2+} ions in the crystalline structure of calcium molybdate (*aliovalent ionic substitution*), as their ionic radius in eight-fold coordination is similar (*i.e.* 1.12 Å and 1.066 Å for Ca^{2+} and Eu^{3+}, respectively),[294] as mentioned in Chapter 3.1. Since the ionic radius of Eu^{3+} is slightly smaller than Ca^{2+} one, the observed slight expansion of the unit cell volume could appear counterintuitive. However, it must be taken into account another effect occurring as a consequence of Eu-doping of calcium molybdate: because of the difference in valence state between Ca^{2+} and Eu^{3+} ions, charge neutrality should be re-established involving a charge balance mechanism. Three mechanisms were proposed for charge compensation: i) formation of Ca site vacancies ($3Ca^{2+} = 2Eu^{3+} + \square$, where □ is a Ca site vacancy, forming $Ca_{1-3x}Eu_{2x}\square_xMoO_4$), ii) introduction of interstitial oxygen atoms ($2Ca^{2+} = 2Eu^{3+} + O_i^{2-}$, forming $Ca_{1-x}Eu_xMoO_{4+x/2}$), and iii) co-doping with an alkaline cation A^+, such as Li^+, Na^+, or K^+ ($2Ca^{2+} = Eu^{3+} + A^+$, forming $Ca_{1-2x}Eu_xA_xMoO_4$).[315,317–319] Since Eu-doped CM by miniemulsion and batch approaches was synthesized employing Na_2MoO_4 as molybdate precursor, it could reasonably be argued that Na^+ ions were present in the samples, acting as co-dopants and guaranteeing charge neutrality. However, considering that the scheelite structures can include a large concentration of vacancies in the Ca sublattices, the concurrent presence of some Ca-site vacancies in these samples cannot be excluded,[320] while the interstitial oxygen mechanism is not common for Ca-based scheelite compounds.[319] In any case, the observed slight expansion of the unit

cell is compatible with the presence of Na^+ ions, whose ionic radius (1.18 Å in eight-fold coordination)[294] is larger than Ca^{2+} and Eu^{3+} one. Finally, another factor can be taken into account to explain the slight expansion of the unit cell volume: according to literature,[288,315,319] the higher charge and smaller ionic radius of Eu^{3+}, compared to Ca^{2+}, entail a shorter Eu-O distance, and thus an increase in the volume of the MoO_4 tetrahedron (*i.e.* Eu^{3+} cation attracts oxygen ions apart from Mo^{6+}, resulting in an increase of the Mo-O bond distance).

Therefore, as a consequence of the discussed evidence derived from XRD patterns, *i.e.* no Eu-based impurities and slight expansion of scheelite unit cell, it could be argued that confining the synthesis of Eu-doped calcium molybdate within ME nanodroplets favors a controlled substitution of Eu^{3+} in Ca sites, while the batch approach does not.

TEM and SEM micrographs of miniemulsion Eu-doped samples confirmed the efficiency of miniemulsion droplets in synthesizing quite spherical non aggregated nanoparticles, retaining the previously discussed morphology also upon doping. On the other hand, TEM and SEM micrographs of batch doped samples (see Figure 3.10) displayed the formation of spindle-like microstructures, similar to other aggregated microstructures reported in literature for calcium molybdate.[299,301,304] In addition, the presence of some sheet-like structures was highlighted for 5 at% and 7 at% doped batch samples, possibly ascribable to the spurious phases evidenced by XRD. Indeed, EDX analysis, coupled to SEM, evidenced that the sheet-like structures found in the 7 at% doped batch samples were composed by Eu, Ca, Mo and O, with an Eu/Mo atomic ratio between 15 and 30%, significantly higher than the experimental amount of dopant in the sample assessed by ICP-MS, confirming that these structures were Eu-based impurities.

In order to further elucidate the local structure and chemical environment around Eu and Mo, and confirm the hypotheses obtained by XRD analysis, X-ray absorption spectroscopy measurements at the Eu L_3-edge (6976.9 eV) and at the Mo K-edge (20000 eV) were performed at SAMBA beamline at the Soleil synchrotron (Saint-Aubin, France), in cooperation with Dr. Paolo Dolcet (Karlsruhe Institute of Technology, Germany), who carried out XAS data analysis.

The Eu L_3-edge XANES spectra of Eu-doped samples (Figure 3.11, left) were observed to be quite different from the spectrum of the reference Eu_2O_3 (red line), showing a higher intensity of the white line (6984 eV) and a second band at 7016 eV instead of 7019 eV as in

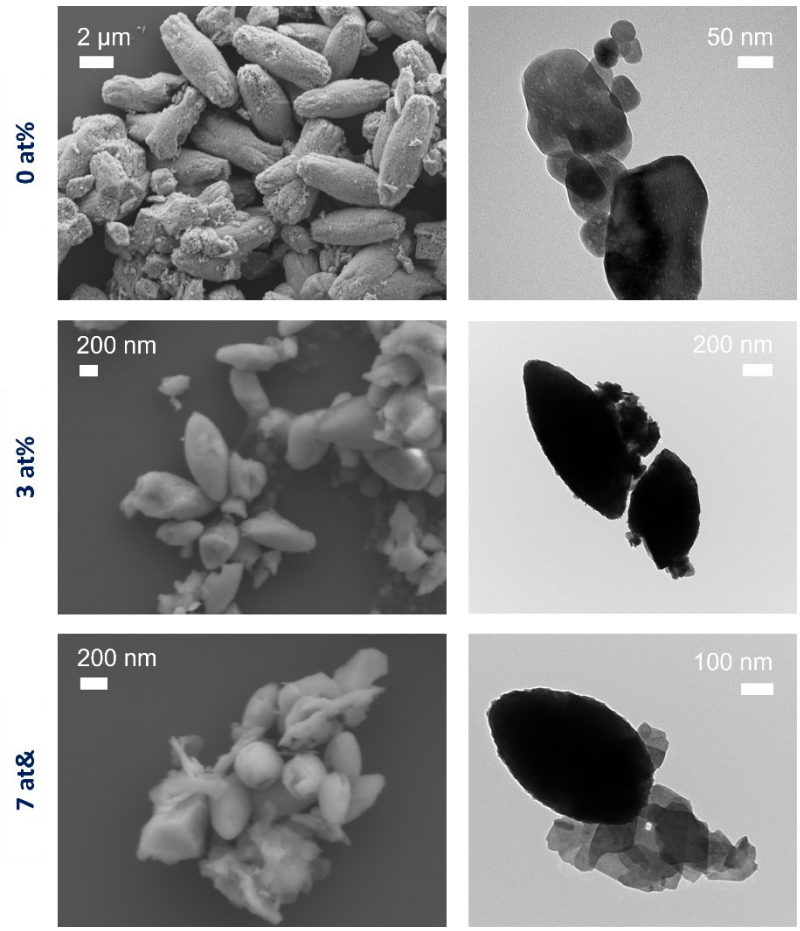

Figure 3.10 SEM (**left**) and TEM (**right**) micrographs of undoped (**top**) and 3 at% (**center**) and 7 at% (**bottom**) Eu-doped batch calcium molybdate samples

the oxide, suggesting that the local coordination around Eu in the doped samples was different from its oxide. Indeed, since the white line is associated with the transition of the $2p_{3/2}$ electrons to the unfilled d orbitals, and thus it is influenced by the splitting of the empty d orbitals, this difference in intensity can be ascribed to a different crystalline habit around the Eu absorbers.[321] As an exception, XANES spectrum of 5 at% doped batch sample (dashed yellow line) showed a less intense white line and the second band at an intermediate position (7017.4 eV), hinting at the presence of Eu_2O_3 moieties, in accordance with the impurity observed by XRD (Figure 3.8). Furthermore, ME samples showed generally a higher intensity of the white line compared to the batch ones, indicating a less disordered environment.

Additionally, also the Fourier Transform of the corresponding EXAFS curves (Figure 3.11, right), together with the EXAFS fitting results (Table 3.2), evidenced the difference between the reference oxide and the doped samples, since for the latter the position of the first peak (Eu-O, at around 2 Å) was shifted towards longer radii and its intensity was increased. In

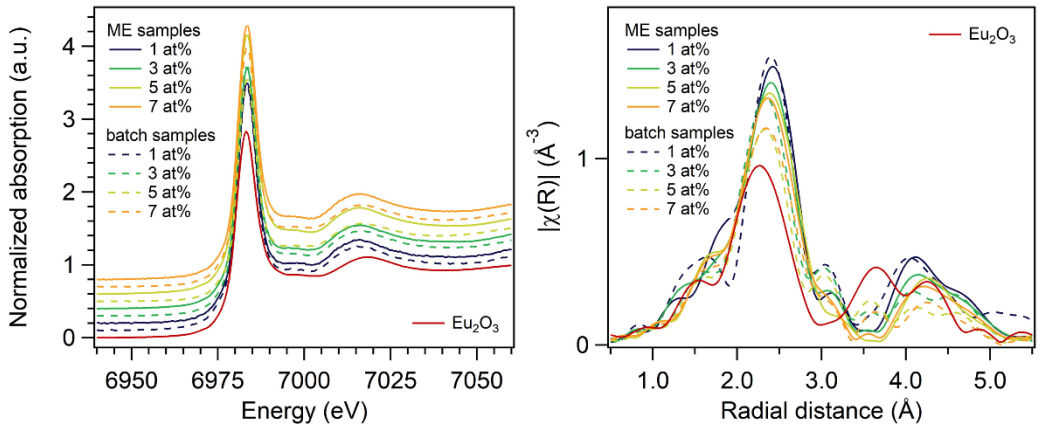

Figure 3.11 Eu L_3-edge XANES spectra (**left**) and Fourier Transform of the k^2-weighted EXAFS functions (k = 3 – 10 $Å^{-1}$), showing the pseudo-radial distribution around Eu absorbers, (**right**) of Eu-doped samples with different doping percentages, synthesized by miniemulsion (solid lines) and batch (dashed lines) approaches, and reference Eu_2O_3 (red curve). XANES spectra are shifted vertically for clarity and FT of EXAFS curves are corrected for phase shift

general, ME samples showed a more intense first shell with respect to the batch counterpart, that could be ascribed to a lower disorder in the structure. Finally, the intensity of the back-scattering contributions decreased, and the estimated Debye Waller factor (DW) increased with increasing Eu concentration for both ME and batch samples, likely because of an increased disorder in the Eu sites as a consequence of the presence of a higher amount of Eu in the samples. A larger variation of DW factor with increasing Eu amount for batch samples could be ascribed to the presence of different Eu-based species, both spurious and as substitutes in Ca sites in the molybdate matrix.

The fitting of the EXAFS curves of ME samples (results in Table 3.2, white rows) evidenced a coordination number of Eu of about 8, compatible with a substitution of Eu^{3+} in Ca^{2+} sites.[288,293] Moreover, the Eu-O distance was found to be close to that reported for Ca-O (2.46 Å),[322] with a small difference ascribable to the higher charge and smaller ionic radius of Eu^{3+} as compared to Ca^{2+}, and significantly larger with respect to that typically found for Eu_2O_3 (ca. 2.33 Å).[323] Overall, the results for ME samples seemed to confirm that Eu^{3+} efficiently substituted Ca^{2+} at all the investigated concentrations, proving what was supposed by combining XRD and ICP-MS analyses results. On the contrary, the results of fitting of the EXAFS curves of batch samples (results in Table 3.2, grey rows) were less straightforward. With the lowest amount of Eu^{3+}, the Eu-O distance was compatible with substitutional doping, but increasing the doping level, the Eu-O bond distance decreased in a significant way (from 2.43 Å to 2.38 Å). In the case of the 5 at% doped sample, already

showing a different XANES, a lower coordination number was determined (about 6), and this might be compatible with the presence of small clusters of Eu_2O_3, well-fitting also XRD patterns, and/or a second Eu-containing species. Since by XRD analysis the 7 at% doped sample also showed a spurious crystalline phase (Figure 3.8), but the coordination number of Eu estimated by fitting of its EXAFS curve was found to be higher than the one of 5 at% doped sample (Table 3.2), it could be possible that the 5 at% doped sample presented both contaminants, while the 7 at% doped one only a second spurious species, likely EuOOH, displaying a coordination number of Eu of about 8 and well-fitting the XRD pattern (*vide supra*). Therefore, confining the crystallization of Eu-doped calcium molybdate within miniemulsion droplets was further proved to lead to a more effective doping with respect to the batch approach.

Table 3.2 Results of the first-shell fitting, in R-space, of the k^2-weighted EXAFS curves (k = 3-10 $Å^{-1}$) at the Eu L_3 edge (6976.9 eV) of ME (white rows) and batch (grey rows) samples

Theor. at%	Synthetic approach	Coord. number	Distance Eu-O (Å)	DW (10^{-3} Å²) [a]	E_0 (eV) [b]	R-factor (%)
1	ME	8.4 ± 1.6	2.42 ± 0.01	7.0 ± 3.4	5.89 ± 1.81	1.9
	Batch	7.0 ± 1.8	2.43 ± 0.02	4.1 ± 2.7	7.13 ± 2.34	3.3
3	ME	8.1 ± 1.1	2.42 ± 0.01	7.5 ± 2.4	5.77 ± 1.28	0.6
	Batch	7.8 ± 1.2	2.39 ± 0.02	8.0 ± 2.8	3.72 ± 1.59	1.8
5	ME	8.5 ± 1.6	2.42 ± 0.01	8.7 ± 3.5	5.16 ± 1.85	2.7
	Batch	6.5 ± 1.0	2.38 ± 0.02	8.4 ± 2.6	3.15 ± 1.52	2.0
7	ME	8.3 ± 1.2	2.41 ± 0.01	9.1 ± 2.5	4.93 ± 1.39	0.5
	Batch	8.3 ± 1.0	2.40 ± 0.01	11.0 ± 2.3	3.94 ± 1.19	1.1

[a] Debye-Waller factor; [b] Threshold energy

The Mo K-edge XANES spectra of Eu-doped samples (Figure 3.12, left) confirmed the tetrahedral coordination of Mo: an intense pre-edge feature was evidenced, assigned to the 1s $\rightarrow$ 4d transition within the molybdenum atomic shell and positioned at an energy value typical for compounds containing Mo in tetrahedral coordination (about 20006 eV).[324] As discussed also in Chapter 2.4 for MoO_3 samples, the intensity of the pre-edge feature is

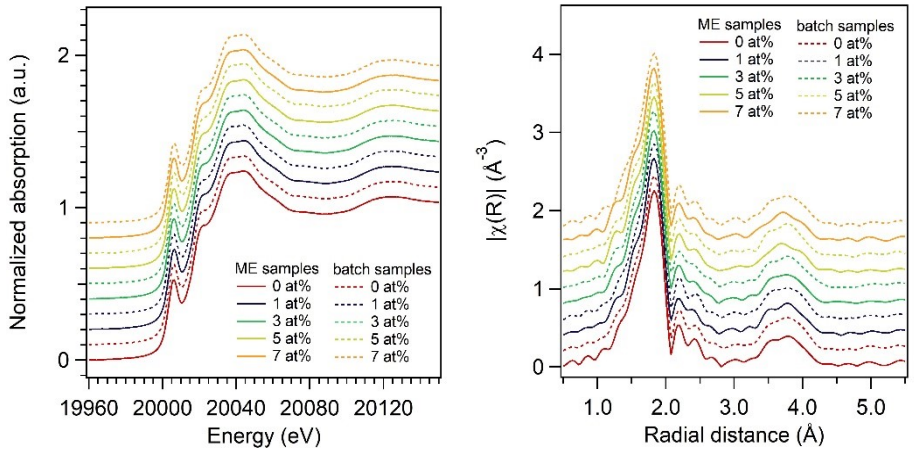

Figure 3.12 Mo K-edge XANES spectra (**left**) and Fourier Transform of the k^2-weighted EXAFS functions (k = 3 – 10 $Å^{-1}$), showing the pseudo-radial distribution around Eu absorbers, (**right**) of undoped and Eu-doped CM samples with different doping percentage, synthesized by miniemulsion (solid lines) and batch (dashed lines) approaches. XANES spectra and FT of EXAFS curves are shifted vertically for clarity; FT of EXAFS curves are corrected for phase shift

considered to be proportional to the number of Mo=O bonds per molybdenum atom and increases with the asymmetry of the species, being the highest for $[MoO_4]^{2-}$ moieties.[272,325] The post-edge features also were found similar to literature spectra of $CaMoO_4$.[272] In addition, a close resemblance between Eu-doped CM spectra and undoped CM was observed, evidencing that the doping process did not significantly alter the local structure around molybdenum. However, from the fitting of the EXAFS curves (Fourier transform shown in Figure 3.12, right; results in Table B.9 in Appendix B.2) it was noticed that the Mo-O bond was longer in the doped samples (1.79 ± 0.01 Å) than in undoped calcium molybdate (1.77 ± 0.01 Å), with exception of the 7 at% doped batch sample. This result confirmed the slight expansion of the unit cell volume upon doping estimated by XRD patterns fitting (*vide supra*) and literature reports.[319] No relevant differences between the miniemulsion and batch samples were detected. Likely due to the low concentration of the dopants even in the samples with the highest doping level (7 at%), attempts to fit the higher shell with the inclusion of Mo-Eu contributions did not yield any meaningful results.

IV. Optical properties of undoped and Eu-doped $CaMoO_4$. In order to assess the effect of ME droplets space confinement on the functional properties of the synthesized material, as well as further studying the doping mechanism, the optical absorption and photoluminescence properties of undoped and Eu-doped CM samples were investigated.

The photoluminescence properties were studied in collaboration with the workgroup of Prof. Klaus Müller-Buschbaum (Justus-Liebig University Giessen, Germany).

As a first step, the optical absorption properties of undoped and Eu-doped CM samples were explored using diffuse reflectance spectroscopy (DRS), and further differences among calcium molybdate samples synthesized in miniemulsion and batch conditions were found. In particular, the optical band gap (E_g) for the direct allowed transition was estimated by deriving the Tauc plot from UV-Vis diffuse reflectance spectra (Figure 3.13),[326,327] and the extrapolated values of band gap of undoped calcium molybdate were found to be about 4.2 eV and 3.9 eV (*i.e.* 295 nm and 318 nm) for miniemulsion and batch sample, respectively. The larger band gap value observed for the miniemulsion sample could likely be ascribed to an effect of quantum confinement as a consequence of the smaller size of ME-synthesized NPs, further confirming the role of space confinement on the synthesis outcome. Values of CM band gap reported in literature were found to vary considerably according to size, shape and degree of structural distortions or defects in the lattice.[277,299,300,328,329] The estimated band gap value for the Eu-doped samples with all doping percentages and synthesized by both synthetic approaches was found in the range 3.8-3.9 eV, as can be seen from the x-axis intersection point of the linear fit (grey dashed lines in Figure 3.13) of the Tauc plots. A slight decrease of the band gap value as a function of increasing doping percentage was found for miniemulsion samples (from 3.9 eV for the 1 at% doped sample to 3.8 eV for the 7 at%

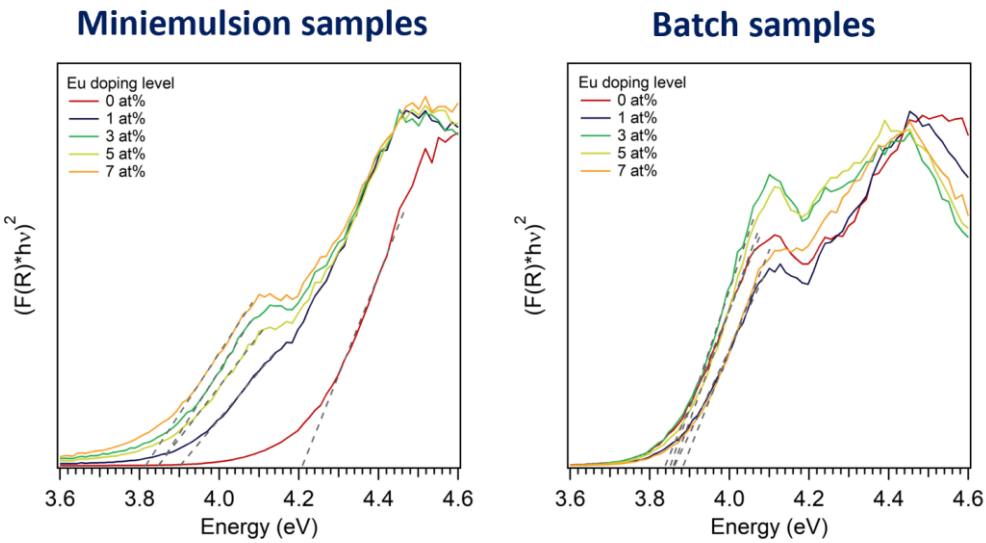

Figure 3.13 Tauc plots derived from diffuse reflectance measurements of undoped (0 at%) and Eu-doped CM samples at different doping percentages synthesized by miniemulsion (**left**) and batch (**right**) approaches. The band gap value was estimated as the x-axis intersection point of the linear fit (grey dashed lines) of the curves

doped one), likely ascribed to a higher degree of distortions in the lattice with increased Eu content. On the other hand, no trend in the band gap values for batch samples was evidenced, suggesting a non-homogeneous distribution of dopant Eu^{3+} ions in the batch host matrix.

Once assessed the absorption properties of the samples, the photoluminescence properties of the doped samples were assessed by the workgroup of Prof. Klaus Müller-Buschbaum (Justus-Liebig University Giessen, Germany). The excitation and emission spectra of 3 at% doped calcium molybdate synthesized by ME measured at room temperature are exemplarily shown in red and in blue in Figure 3.14, respectively. In the excitation spectra of all Eu-doped samples, measured by monitoring the emission of Eu^{3+} (λ_{em} = 615 nm), a broad band in the UV region due to the calcium molybdate matrix and a series of narrow lines due to direct Eu^{3+} f-f excitations ($^5L_6 \leftarrow {}^7F_0$ at 393 nm and $^5D_2 \leftarrow {}^7F_0$ at 468 nm) were observed. In the emission spectra of all Eu-doped samples, measured upon excitation of the host matrix at 270 nm, the typical $^5D_0 \rightarrow {}^7F_J$ (J = 0-4) transitions of Eu^{3+} were evidenced, with the hypersensitive $^5D_0 \rightarrow {}^7F_2$ being the most intense one.[330–332] Moreover, almost no emission intensity from the molybdate matrix was observed. Taken together, these observations indicated that the energy transfer from the excited $CaMoO_4$ matrix to the dopant Eu^{3+} ions was efficient.[330]

Generally, the emission spectra of all the Eu-doped CM samples displayed well resolved f-f transitions $^5D_0 \rightarrow {}^7F_J$ (J = 0-4). As a consequence, it could be argued that Eu^{3+} were located

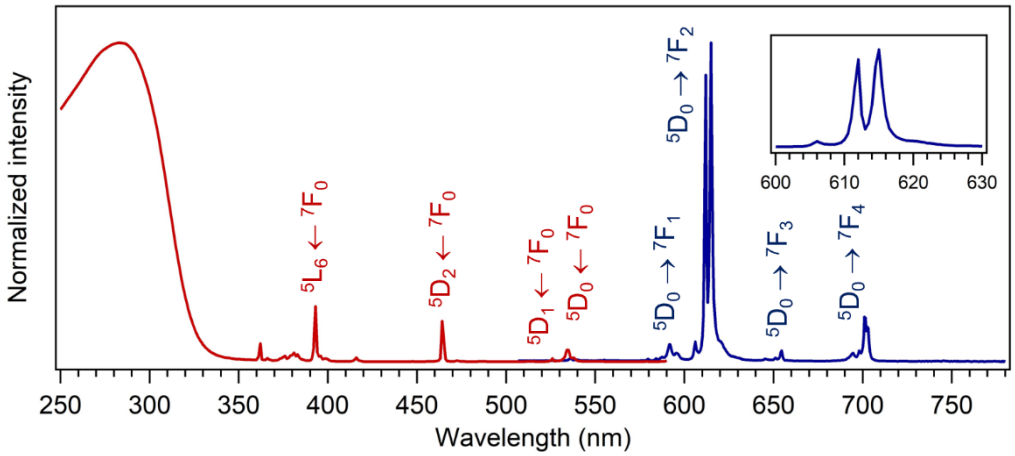

Figure 3.14 Normalized excitation spectrum (red line) measured by monitoring Eu^{3+} emission (λ_{em} = 615 nm) and emission spectrum (blue line) measured by exciting CM host matrix (λ_{exc} = 271 nm) of Eu-doped CM samples, at room temperature. **Inset:** zoom of the splitting of the $^5D_0 \rightarrow {}^7F_2$ transition. 3 at% doped ME sample is displayed as an example

in a defined crystallographic position in the calcium molybdate matrix, in agreement with the hypothesized substitution of Ca^{2+} ions in Ca sites. Since i) a weak $^5D_0 \rightarrow {}^7F_0$ transition,[xxix] ii) a splitting of the emission lines for the $^5D_0 \rightarrow {}^7F_1$ and $^5D_0 \rightarrow {}^7F_2$ transitions into two and four lines, respectively, and iii) a high ratio of a forced electric dipole to a magnetic dipole ($R^{0\text{-}2/0\text{-}1}$ = 14.5-16.4 for all samples)[xxx] were observed, a tetragonal local symmetry of Eu^{3+} with no inversion was determined, though not C_4 or C_{4v}.[330,332] It is worth noting that the tetragonal symmetry fitted with the coordination number of eight calculated from the EXAFS analysis for ME samples, and, as the CaO_8 clusters in calcium molybdate are distorted, they should not be characterized by a C_4 or C_{4v} symmetry. Finally, a conformation of the EuO_8 clusters similar to the distorted CaO_8 was found compatible with the more intense and narrower white line of XANES spectra of ME samples.

Moreover, for the majority of the samples investigated, the emission profiles were observed to be independent on the excitation pathway (*i.e.* excitation of the CM matrix, λ_{exc} = 270 nm, or direct excitation of the f-f transitions of Eu^{3+}, λ_{exc} = 393 nm $^5L_6 \leftarrow {}^7F_0$). Exceptions were found for the 5 at% and 7 at% doped batch samples, already displaying differences in XRD patterns and XAS spectra, whose emission spectra measured upon Eu^{3+}-based excitation (λ_{exc} = 393 nm) showed additional narrow lines, especially noticeable for the $^5D_0 \rightarrow {}^7F_2$ and $^5D_0 \rightarrow {}^7F_4$ transitions (see Figure 3.15). The occurrence of these additional emission lines indicated that Eu^{3+}-based spectroscopically active impurities were present in 5 at% and 7 at% doped batch samples, in agreement with the spurious Eu_2O_3 and EuOOH species hypothesized from XAS analysis and XRD fittings, that are known to be spectroscopically active, and the EDX results of sheet-like structures observed by SEM and TEM of the 7 at% doped sample. It is also worth noting that no spectroscopically active impurities were found in the emission spectra of the other samples, in agreement with other previously discussed characterizations.

A significant difference between excitation spectra of the studied samples was found in the relative intensity of the two excitation processes, *i.e.* through excitation of the matrix and

[xxix] The $^5D_0 \rightarrow {}^7F_0$ transition is allowed only for C_s, C_n, and C_{nv} site symmetries.[430]

[xxx] Since the $^5D_0 \rightarrow {}^7F_2$ transition is hypersensitive, while the $^5D_0 \rightarrow {}^7F_1$ transition is insensitive to the environment, the ratio of the two intensities is a measure for the symmetry of the Eu^{3+} site. In a site with inversion symmetry, the $^5D_0 \rightarrow {}^7F_1$ magnetic dipole transition is the strongest, while in a site without inversion symmetry $^5D_0 \rightarrow {}^7F_2$ electric dipole transition dominates.[431]
The ratio of the forced electric dipole to the magnetic dipole ($R^{0\text{-}2/0\text{-}1}$) was calculated as the ratio of integrated Eu^{3+} transition intensities $I(^5D_0 \rightarrow {}^7F_2)/I(^5D_0 \rightarrow {}^7F_1)$ at room temperature, using λ_{ex} = 271 nm. $I(^5D_0 \rightarrow {}^7F_1)$ was integrated from 588 to 599 nm, while $I(^5D_0 \rightarrow {}^7F_2)$ from 604 to 632 nm.

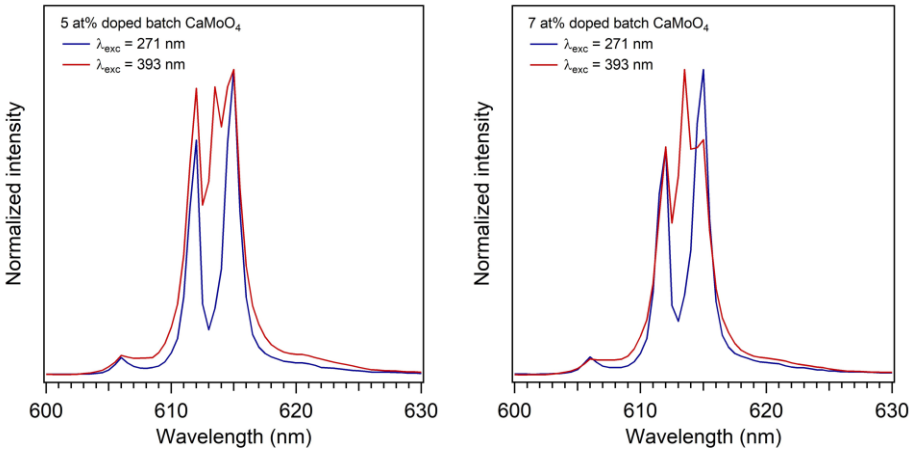

Figure 3.15 Comparison of the $^5D_0 \rightarrow {}^7F_2$ transition lines (600-630 nm) of the solid-state normalized emission spectra of 5 at% (**left**) and 7 at% (**right**) doped batch samples, measured by exciting CM host matrix (λ_{exc} = 271 nm, blue lines) and by directly exciting Eu^{3+} ions (λ_{exc} = 393 nm, $^5L_6 \leftarrow {}^7F_0$, red lines)

direct excitation of the f-f transitions of Eu^{3+}. In particular, a different trend of the relative intensity of the direct f-f excitations as a function of the percentage of doping related to the synthetic method was observed (Figure 3.16, left). This is a significant result, being the participation of the direct f-f excitations in the overall excitation process ($Part_{f\text{-}f}$)[xxxi] directly related to the energy transfer between Eu^{3+} ions, that is stronger when the distance between Eu^{3+} centers is shorter. Since no trend of $Part_{f\text{-}f}$ in the excitation process as a function of dopant amount was observed for batch samples (blue dots in Figure 3.16), it is likely that the average distance between Eu^{3+} ions was quite constant despite the different Eu^{3+} content in the sample, that was assessed by ICP-MS (see Table 3.2). In particular, it is likely that sites with local Eu^{3+} concentration higher than the overall doping level were present. On the contrary, for ME samples (red dots in Figure 3.16), the participation of the direct f-f excitations increased when increasing the doping percentage, suggesting a more homogeneous distribution of Eu^{3+} ions in the doped samples obtained by ME with respect to those obtained by batch approach. Indeed, this result is a consequence of a shortening of the distance between Eu^{3+} centers increasing their concentrations, enabling a higher energy transfer between them. Thus, performing the synthesis within the confined space of

[xxxi] The participation of the f-f excitations in the overall excitation process ($Part_{f\text{-}f}$) was calculated as the ratio of integrated direct Eu^{3+} f-f excitation to the sum of integrated excitation at room temperature. λ_{em} = 615 nm, excitation though $CaMoO_4$ matrix integrated from 250 to 355 nm, direct Eu^{3+} f-f excitation integrated from 355 nm to 545 nm.

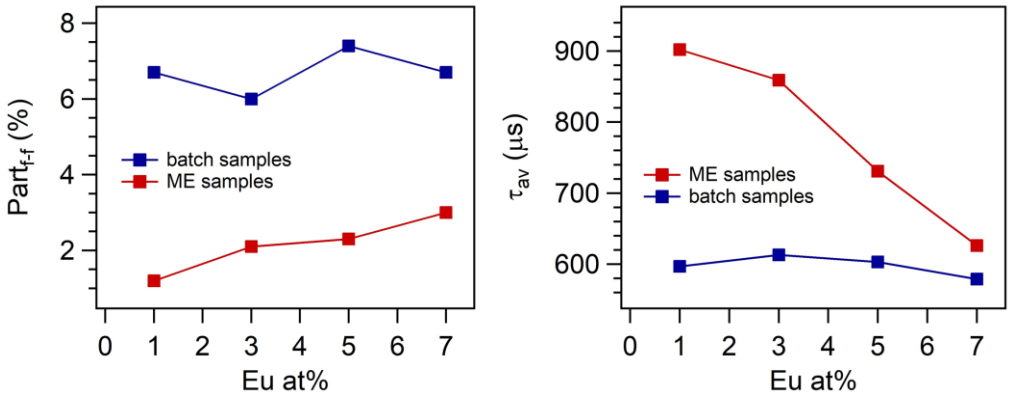

Figure 3.16 Participation of f-f direct excitation in the overall excitation process at room temperature (λ_{em} = 615 nm) (**left**) and average lifetimes of Eu^{3+} emission at room temperature upon excitation through host matrix (λ_{exc} = 271 nm) (**right**) as a function of doping percentage and synthetic method (red dots: samples synthesized by batch approach; black dots: samples synthesized by ME approach)

ME droplets was further demonstrated to have an effect on the dopant distribution in the matrix.

The photoluminescence mechanism of Eu-doped calcium molybdate samples was further investigated by determining the overall emission process decay times at room temperature (experimental data are reported in Table B.10, Table B.11, and Table B.12 in Appendix B.2). For all the samples, the overall emission decay process could be fitted only with a minimum of two exponential functions (see Appendix B.2), indicating a large influence of the samples surface, as expected for nanoparticles with a high surface to volume ratio.[333,334] The measured average lifetimes of emission (τ_{av}) were found to be in the 0.5-0.9 ms range, in agreement with literature reported values for Eu^{3+} containing scheelites.[320,335] In particular, by comparing the average lifetimes of emission of the samples doped with increasing amount of Eu^{3+}, it was again observed a different trend of τ_{av} as a function of doping percentage related to the synthetic method (Figure 3.16, right). In particular, the average lifetimes of emission of ME samples (red dots in Figure 3.16) were higher than those of batch samples (blue dots in Figure 3.16), and they were dependent on the doping level, decreasing as the doping percentage increases, from 0.901(9) ms for the 1 at% doped sample to 0.625(9) ms for the 7 at% doped one. This result was expected as, increasing the doping level, the distance between emissive Eu^{3+} centers should shorten and non-radiative de-excitation has a higher probability through cross relaxation processes.[336–338] On the contrary, for the batch samples (blue dots in Figure 3.16), τ_{av} did hardly depend on the Eu^{3+} content (0.60 ± 0.02 ms for all the samples), implying a non-uniform distribution of Eu^{3+} ions

in the host matrix, as the concentration quenching was found to be quite the same for all the samples. Most likely, in Eu-doped calcium molybdate batch samples, on the atomic level there were spots with a local concentration of Eu^{3+} higher than the macroscopic nominal doping level (assessed by ICP-MS). These results again confirmed that, by confining the crystallization within ME droplets, a more homogeneous distribution of dopant could be achieved, with relevant consequences of the functional properties.

3.3 Synthesis of undoped and Eu(III)-doped calcium molybdate by microfluidic approach

As mentioned in the Introduction section (Chapter 3.1) and described in detail in Chapter 6.2, and analogously to the synthetic approaches proposed in Chapter 3.2, the microfluidic synthesis of undoped and Eu(III)-doped calcium molybdate at room and low temperature was performed by exploiting the co-precipitation between calcium nitrate and sodium molybdate in ethanol and milliQ water mixtures in different weight ratios. This part of the work was carried out in cooperation with the Master student Pietro Ostellari, who performed the syntheses, and in collaboration with Prof. Tommaso Carofiglio and Prof. Michele Maggini, who provided the experimental setup.

The design of the employed microfluidic setups and the selection of the synthetic parameters to be screened were rationally driven by the nowadays most widespread accepted fundamental theories of nanoparticle nucleation and colloid stability, described in detail in Chapter 1.1. Briefly, according to the LaMer model of homogeneous nucleation,[46] the crystallization encompasses four distinct steps: i) formation of a supersatured solution, ii) nucleation, iii) growth and iv) further evolution of NPs dimension and morphology by aggregation. When the supersaturation limit is exceeded by the solute concentration, the formation of a massive amount of small individual nuclei occurs in a short timeframe ("LaMer burst") and the solute concentration is decreased below the critical nucleation concentration, relaxing the supersaturation condition and preventing any further nucleation. Subsequently, all the free solute is consumed by particle growth, decreasing the solute concentration below the saturation concentration and thus lowering also the overall free energy of the system (particles and solute), that may be reduced also by subsequent aggregation of individual particles. As largely discussed in Chapter 1.2.2, the unique conditions of a microfluidic reactor (*i.e.* the efficient and fast mixing and the flowing and dynamic nature of the system) enable the achievement of i) a highly homogeneous chemical environment in terms of solute concentration and temperature and ii) a temporal (and consequently spatial) separation of the NPs nucleation and growth stages. Thanks to these, timely and spatially random nucleation bursts and uncontrolled agglomeration can be avoided in microfluidic conditions. Moreover, the implementation of a quenching step after a certain residence time (*i.e.* after a certain tubing length), either by dilution or thermally, may minimize growth through aggregation, that typically occurs either by Ostwald ripening

or coalescence phenomena. Generally, the aggregation of the NPs may be influenced by varying the ionic strength and dielectric constant of the medium, that are known to regulate the thickness of the electrical double layer (EDL) surrounding the NPs.[29] This relationship is delineated by the DLVO theory of colloid stability (Chapter 1.1.1), that quantitatively describes the force between charged surfaces interacting through a liquid medium, combining the effects of the van der Waals attraction and the electrostatic repulsion due to the double layer of counterions surrounding the suspended particles. In particular, the thickness of the EDL is proportional to the dielectric constant of the medium and inversely proportional to its ionic strength. Furthermore, another factor that may have a role on the NPs aggregation is the viscosity of the flowing reaction mixture, affecting the diffusion coefficient of the solute and the NPs according to the Stokes-Einstein relation,[xxxii] as well as influencing the fluid dynamics and mixing in continuous-flow approaches.

Within this framework, and with the ultimate goal of controlling the final dimension and aggregation of the synthesized calcium molybdate, the viscosity and dielectric constant of the reaction medium were tuned by employing water-ethanol mixtures as solvent and varying the *ethanol content* into it (EtOH/H_2O 20-50 wt%) and the *reaction temperature* (from room temperature to –4 °C). In particular, the viscosity and dielectric constant of water-ethanol mixtures as a function of their relative weight ratio and of the temperature were calculated by using the Jouyban-Acree equation,[339,340] and their trends are shown in Figure 3.17 (see calculated values in Table B.13 in Appendix B.2). It was found that the viscosity of ethanol/water mixtures (η_m) increases by increasing the ethanol content up to 50 wt%, after which it decreases, and it is doubled when lowering the temperature from 20 °C to –4 °C. On the contrary, the dielectric constant of ethanol/water mixtures (ε_m) linearly decreases by increasing the ethanol content and increases by cooling down the solvent. As mentioned above, a modification of the viscosity and dielectric constant of the solvent influences the diffusion of particles in suspension (*i.e.* the higher η_m, the lower the diffusion coefficient), as well as their aggregation (*i.e.* the higher ε_m, the higher the stabilization of superficial charges that minimize aggregation; the lower the diffusion coefficient, the lower the aggregation). Furthermore, an increase in ethanol content in the

[xxxii] The Stokes-Einstein relation is expressed as: $D = k_B T / 6\pi\eta R$, where D is the diffusion coefficient, k_B is the Boltzmann constant, T is the temperature, η is the dynamic viscosity, and R is the hydrodynamic radius of a spherical particle.[432]

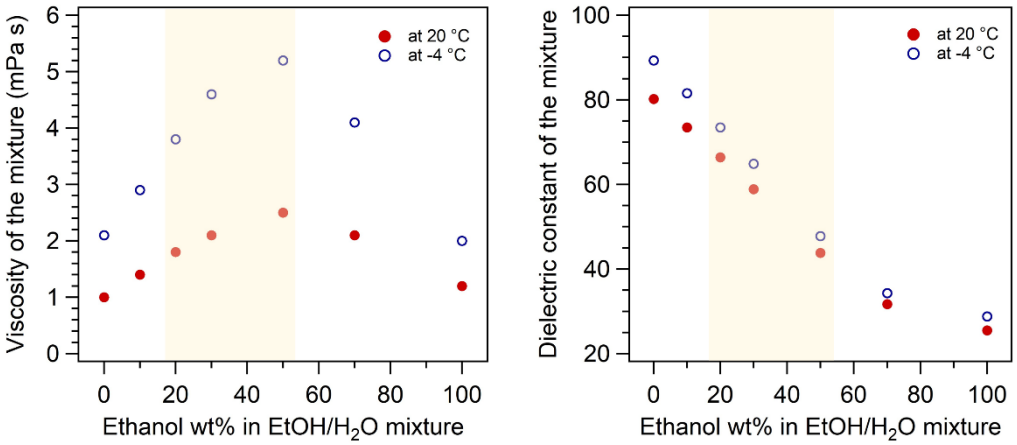

Figure 3.17 Viscosity (**left**) and dielectric constant (**right**) of ethanol and water mixtures with different relative compostions at 20 °C (red dots) and – 4 °C (blue dots). Viscosity and dielectric constant values were calculated using the Jouyban-Acree equation, that relates some chemico-physical parameters of binary mixtures of solvents with their composition and temperature [393,340]

reaction solvent lowers the solubility of calcium molybdate, leading to a faster reach of the supersaturation condition. According to the implementations of the LaMer model by Sugimoto and Chu (see Chapter 1.1.3),[52] this results into a faster solute supply rate, and ultimately into a higher number of nuclei that will lead to smaller nanoparticles.

Taking into account these considerations, the synthesis of undoped and Eu(III)-doped calcium molybdate was addressed in microfluidic conditions employing a home-made continuous-flow setup built by using two syringe pumps, a T-shaped PEEK mixer and Teflon tubes with a diameter of 0.8 mm (Setup A, see Figure 6.4 in Chapter 6.2.4). Calcium and molybdate precursors solutions in ethanol and milliQ water mixtures at different percentages (20, 30, and 50 wt% EtOH/H_2O) were separately pumped into the reactor, and the resulting suspension was collected and quenched in a vessel. A systematic variation of the synthetic parameters, *i.e.* i) the concentration of precursors solutions (0.02 and 0.05 M, with [Ca^{2+}] = [MoO_4^{2-}] and keeping constant the flow rates of the reactant feeds), ii) the relative amount of ethanol into the solvent (20, 30, and 50 wt% EtOH/H_2O), iii) the temperature (room temperature and –4 °C), and iv) the type of quenching (*vide infra*), was carried out. A second setup (Setup B, see Figure 6.4 in Chapter 6.2.4) was also built, by employing three syringe pumps and two T-junction mixers, to introduce the quencher into the continuously flowing suspension of the product and exploit the efficient mixing ensured by microfluidic approach. Finally, the synthesis of Eu(III)-doped calcium molybdate was investigated employing three selected sets of synthetic conditions (*vide infra*).

As a first step, the setup tubing length (*i.e.* the reaction time) was adjusted until opalescent droplets coming out of the continuous-flow reactor were obtained, in order to ensure the reaction to occur within the constrained environment of the microfluidic setup, characterized by controlled fluid dynamics. Once built the optimal setup for our purposes, a systematic screening of the above-mentioned reaction parameters was carried out. In order to rationalize their effect on the crystalline structure, size, shape and aggregation of calcium molybdate, XRD, TEM and SEM analyses were performed. XRD analysis showed that, with every combination of synthetic parameters tested, crystalline tetragonal scheelite-type CM was obtained (space group $I4_1/a$), with no other spurious phases. The average crystallite size was estimated by applying the Scherrer equation to the most intense reflection at 28.7° 2θ (reflection (112)).

I. Effect of the precursors concentration. As discussed in Chapter 1.1, according to classical crystallization models, a variation of the precursors concentration should affect the number and the size of formed primary particles: a higher number of smaller particles should be formed when the starting precursors concentration is higher. This trend was also observed in the results of the batch synthesis of calcium molybdate presented in Chapter 3.2, screening the concentration of the precursors in aqueous solution in the 0.15-2.0 M range. However, the implementation of the synthesis of CM in microfluidic conditions required the employment of a mixture of water and ethanol as solvent, since CM is not fully insoluble in water (K_s (at 20 °C) = $1.8 \cdot 10^{-9}$ M^2)[309] and, to ensure that the reaction was effectively ended into the collecting becker, its solubility had to be lowered by adding a non-solvent (*i.e.* ethanol). Thus, being also the solubility of the precursors lower in the employed reaction solvent, lower concentrations were employed, and a more limited variation of precursors concentration could be carried out. In particular, the precursors concentration was screened between 0.02 M and 0.05 M, while keeping constant and equal the feed rate of their solutions (1.2 mL min^{-1}). Nevertheless, as expected, a slight decreasing trend in average crystallite size as a function of increasing precursors concentration was observed (see Figure 3.18 for samples quenched in an excess of ethanol), in agreement with previous observations. Additional analogous results of variation of precursors concentration employing an excess of solvent mixture as quencher are reported in Figure B.23 in Appendix B.2 and the effect of other screened reaction parameters on crystallite size (*i.e.* ethanol content in the solvent mixture and quenching method) is systematically discussed below. In

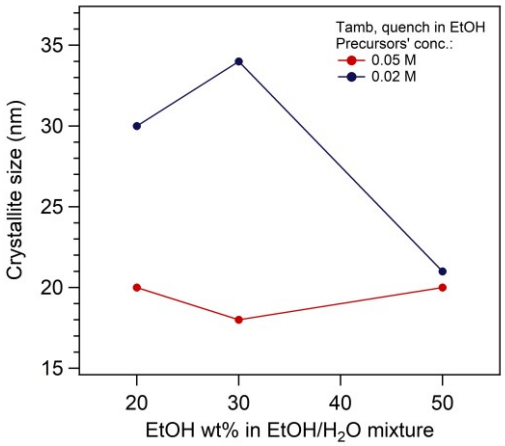

Figure 3.18 Mean crystallite size of calcium molybdate synthesized with Setup A at ambient temperature as a function of ethanol content in the solvent mixture, employing different concentrations of precursors solutions (0.02 M: blue dots; 0.05 M: red dots) and quenching in ethanol

the following, the samples synthesized with a concentration of the starting precursors solution of 0.05 M, that allowed a faster production of CM, are discussed.

II. Effect of the ethanol content in the solvent mixture. As largely discussed above, the ethanol content in the solvent mixture was varied from 20 wt% to 50 wt%, in order to decrease the solubility of CM and modify the viscosity and dielectric constant of the medium. In general, it was observed that, by increasing the ethanol content into the solvent mixture, the XRD pattern of the synthesized calcium molybdate was characterized by broader reflections, *i.e.* smaller crystallite size, as shown in Figure 3.19 for samples quenched in an excess of solvent mixture. This observation could be rationalized

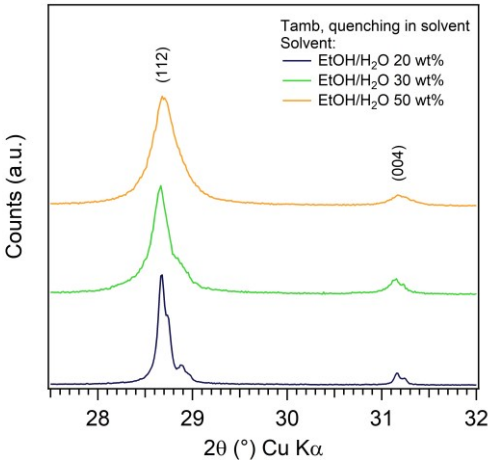

Figure 3.19 Comparison of XRD pattern of calcium molybdate synthesized with Setup A at ambient temperature with different percentages of ethanol in the solvent mixture and quenching in solvent mixture

considering the lower solubility of CM with increasing ethanol percentage in the mixture, leading to a faster solute supply rate and consequently higher number of smaller nuclei as modeled by Sugimoto. Moreover, the increase in viscosity of the solvent with higher contents of ethanol led to a slower growth by diffusion of the initially formed nuclei (Stokes-Einstein relation, *vide supra*).

In addition to having a strong effect on the average crystallite size of calcium molybdate, the ethanol content in the employed reaction solvent was observed to have a clear impact on the aggregation of CM primary particles. As discussed also in Chapter 3.2, several reports of differently shaped microstructures of calcium molybdate were found in literature, and their formation was ascribed to the self-assembly of the initially formed particles in hierarchical microstructures through an oriented aggregation mechanism.[301,304,306,310] It was suggested that the forces involved in the mutual alignment of the particles and subsequent self-assembly are mainly electrostatic and van der Waals interactions. It is reasonable to state that these forces are influenced by the dielectric constant of the reaction medium, that regulates the formation of charges on the surface of the particles, and ultimately their electrostatic stabilization. As a consequence, a role of the ethanol amount in the reaction solvent mixture in the aggregation of the primary particles was expected, and the dielectric constant of the solvent, dependent on the ethanol content, could likely be deemed as the parameter ruling the final morphology of the microstructures. In particular, as shown in Figure 3.20, ellipsoidal-like microstructures were obtained in a 20 wt% ethanol/water solvent, a mixture of dumbbell-shaped and non-uniform spherical assemblies were formed with 30 wt% relative content of ethanol, and more loose and smaller aggregates with a bunch-like shape were found when 50 wt% of ethanol was employed. The formation of less defined and dense aggregates with higher amounts of ethanol in the solvent mixture (50 wt%) was found consistent with the higher viscosity of the reaction medium, slowing the diffusion of primary aggregating particles in solution and their relative orientation along favored directions.

Being significant the effect of the composition of the solvent on the synthetic outcome, this parameter was varied within all series of experiments, discussed below.

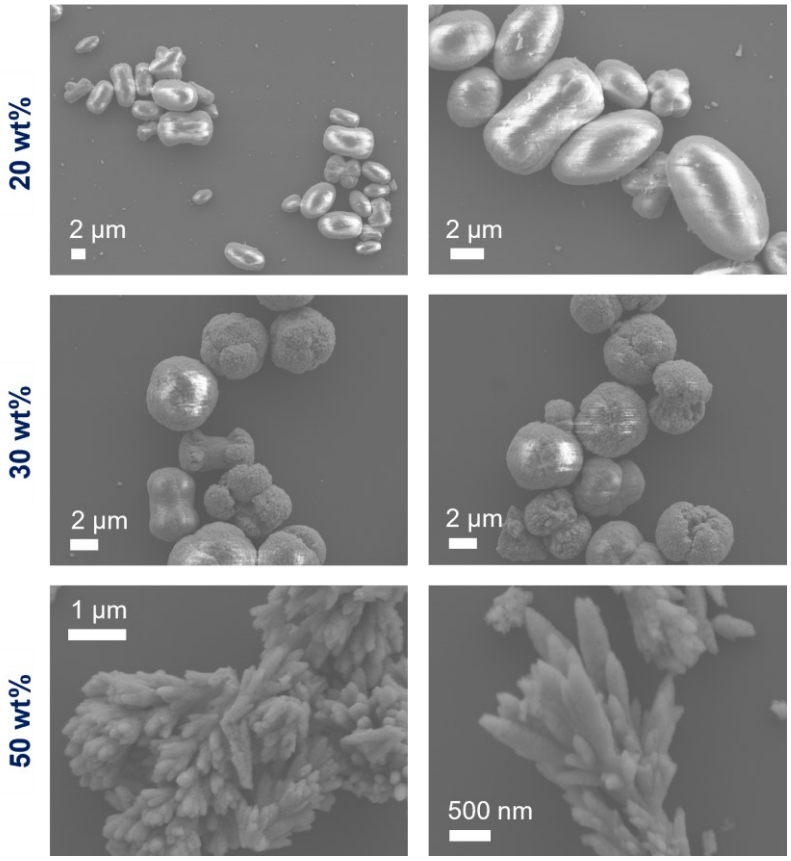

Figure 3.20 SEM micrographs of CM samples synthesized at room temperature by microfluidic with different amounts of ethanol in the solvent mixture and quenched in an excess of solvent mixture: comparison of samples obtained with EtOH/H_2O of 20 wt% (**top**), 30 wt% (**center**), and 50 wt% (**bottom**)

III. Effect of the reaction temperature. As discussed above, also the reaction temperature strongly affects the viscosity of the reaction medium, which is doubled when going from 20 °C to -4 °C, as well as it influences the dielectric constant of the solvent mixture (*i.e.* increased by cooling down) and the solubility of the product (*i.e.* decreased by cooling down).[309] In order to investigate the effect of reaction temperature on the synthetic outcome, as well as exploiting the efficient temperature homogeneity ensured by the high surface-to-volume ratio of microfluidic approach, the experimental setup and the collecting becker were placed in a 3.5 wt% NaCl/ice bath, resulting in a temperature of –4 °C. When samples obtained with the same solvent mixture composition and quenching approach (*vide infra*) but different reaction temperature were compared, it was observed that $CaMoO_4$ with smaller crystallite size was obtained at –4 °C with respect to ambient temperature (yellow and orange trends in Figure 3.21, to be compared with blue and light blue trends, respectively). Moreover, it is worth noting that, when the syntheses were

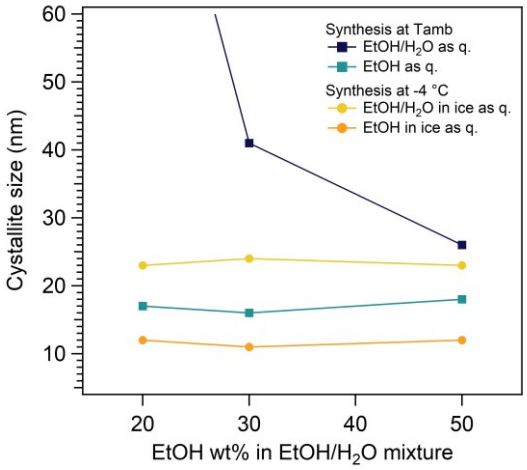

Figure 3.21 Mean crystallite size of calcium molybdate synthesized with Setup A as a function of ethanol content in the solvent mixture and of different reaction temperatures (ambient temperature in squared points, or -4 °C in dots) and quenching approaches (quenching in an excess of reaction solvent or in an excess of ethanol)

carried out at –4 °C, the effect of ethanol content on crystallite size could not be appreciated anymore, obtaining comparable estimated values independently on the solvent mixture composition. Analogously to the effect of ethanol content, the reaction temperature effect was likely ascribed to the lower solubility of calcium molybdate at –4 °C, and to the more dramatic change in viscosity of the reaction mixture, which is doubled (*i.e.* lower diffusion coefficient). The influence of the solvent employed for quenching (blue *vs* light blue and yellow *vs* orange trends) is discussed below.

Scanning electron microscopy characterization of the samples synthesized at –4 °C, employing an excess of solvent mixture as quencher and different ethanol contents in the reaction solvent, are reported in Figure 3.22. It can be clearly observed the formation of microsized aggregates with different morphologies, resembling those obtained at room temperature (Figure 3.20). In particular, going from 20 wt% to 50 wt% of ethanol in the reaction solvent, elongated microstructures, spherical-like ones and loose non-uniform aggregates were obtained, respectively. However, when performing the microfluidic syntheses at low temperature (*i.e.* in a –4 °C cold bath), more defined and slightly different microstructures with respect to room temperature ones were formed. With 20 wt% ethanol to water ratio (Figure 3.22, top), dumbbell-like structures, very similar to those reported in literature,[290,301,304] were observed. Higher magnification micrographs (Figure 3.22, top right) clearly showed that they were composed by the aggregation of primary nanoparticles, with void spaces between them. Increasing the amount of ethanol in the solvent mixture

(Figure 3.22, center), more defined spherical microstructures were formed. Since some dumbbell-shaped microstructures, as well as some twinned hemispheres, were observed in addition to spherules, the morphogenesis mechanism proposed by Busch *et al.*,[313,314] and observed by Chen *et al.*,[304] could be hypothesized, as discussed in Chapter 3.2. In particular, the authors suggested the occurrence of a progressive self-assembled growth of elongated structures at both ends, to form dumbbell-shaped aggregated, which then completed their shapes by successive and self-similar upgrowth to give notched spheres.

Overall, it could be argued that carrying out the synthesis at lower temperature allowed a more controlled formation of calcium molybdate aggregates, as more homogeneously shaped microstructures were observed. This effect could likely be ascribed to the higher viscosity of the reaction mixture, which is the parameter majorly influenced by temperature (see Figure 3.17 and Table B.13), and consequently to the modified diffusion coefficient (Stokes-Einstein relation). Moreover, since different morphologies of aggregates according

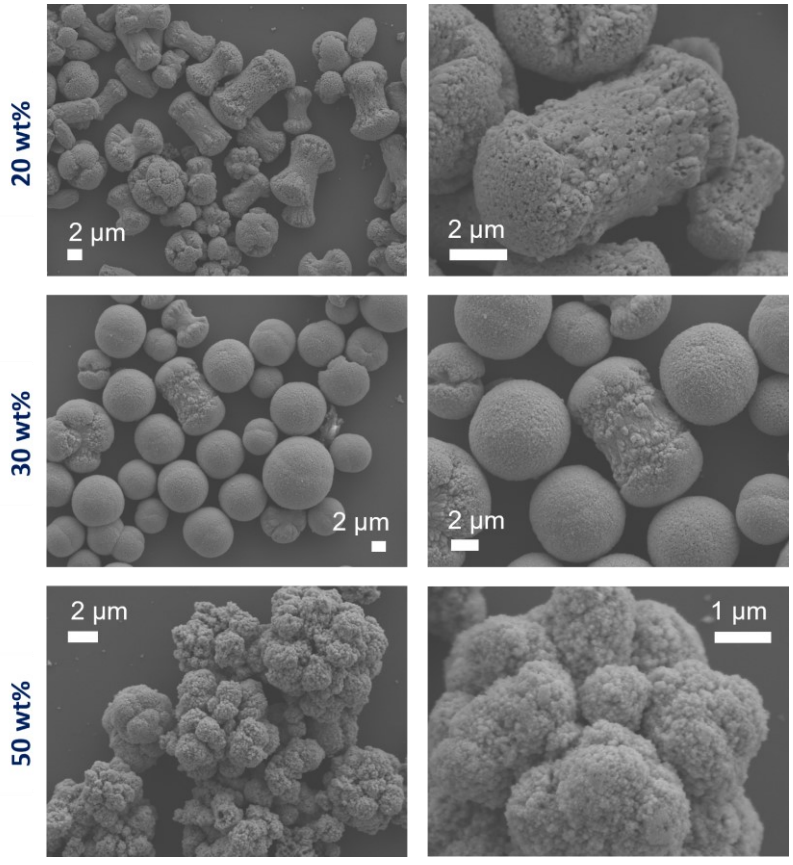

Figure 3.22 SEM micrographs of CM samples synthesized at -4 °C by microfluidic with different amounts of ethanol in the solvent mixture and quenched in an excess of solvent mixture: comparison of samples obtained with EtOH/H_2O of 20 wt% (**top**), 30 wt% (**center**), and 50 wt% (**bottom**)

to the ethanol content in the reaction mixture were observed both at room and low temperature, it could be argued that a primary role in determining the final morphology of the aggregates is played by the dielectric constant, ruling the formation of superficial charges and relative orientation of the primary particles, as also hypothesized above.

IV. Effect of the method of quenching. Finally, the role of quenching step was investigated, firstly dropping the reaction mixtures coming out of the microfluidic reactor in the collecting becker containing an excess of different solvents. In particular, the same ethanol/water mixture employed as reaction solvent (*quenching by dilution*) or pure ethanol (*quenching by dilution in a non-solvent*) were employed. As it can be clearly observed in Figure 3.21 (XRD patterns are shown in Figure B.24 in Appendix B.2), the method of quenching was observed to have a significant role in determining the crystallite size of calcium molybdate, obtaining smaller crystallites when employing an excess of only ethanol as quencher at the same temperature, with respect to employing an excess of solvent mixture. This observation was found consistent with the sudden increase in viscosity of the reaction environment when dropping few microliters of reaction mixture in ethanol/water mixture into an excess of pure ethanol. The sudden decrease in diffusion coefficient and in CM solubility efficiently prevented the reaction to proceed and the growth of the primary particles formed into the microfluidic reactor.

In addition, it was found that the solvent employed in excess for the quenching step played a significant role in determining the final NPs size and aggregation, as showed by SEM and TEM micrographs in Figure 3.23. Indeed, when the quenching was performed by dripping the continuously flowing product into an excess of solvent mixture (EtOH/H_2O 20-50 wt%, discussed *supra*), aggregated microparticles, with different morphologies according to the ethanol content into the solvent and to the reaction temperature, were obtained (see also Figure 3.20 and Figure 3.22). On the contrary, when pure ethanol was employed as quencher, smaller, less aggregated and distinguishable nanoparticles were formed, observable by TEM. As largely discussed above, the formation of microparticles with different morphologies in ethanol/water mixtures was ascribed to the oriented aggregation of primary particles, likely favored by the not complete insolubility of calcium molybdate in water: when diluting the CM-containing droplets into an excess solvent mixture with a non-negligible amount of water (especially for 20 and 30 wt% EtOH/H_2O mixtures), $CaMoO_4$ may dissolve and re-precipitate and/or aggregate to form microstructures. On the other hand, when ethanol was exploited as quencher, even if slight aggregation of NPs and a

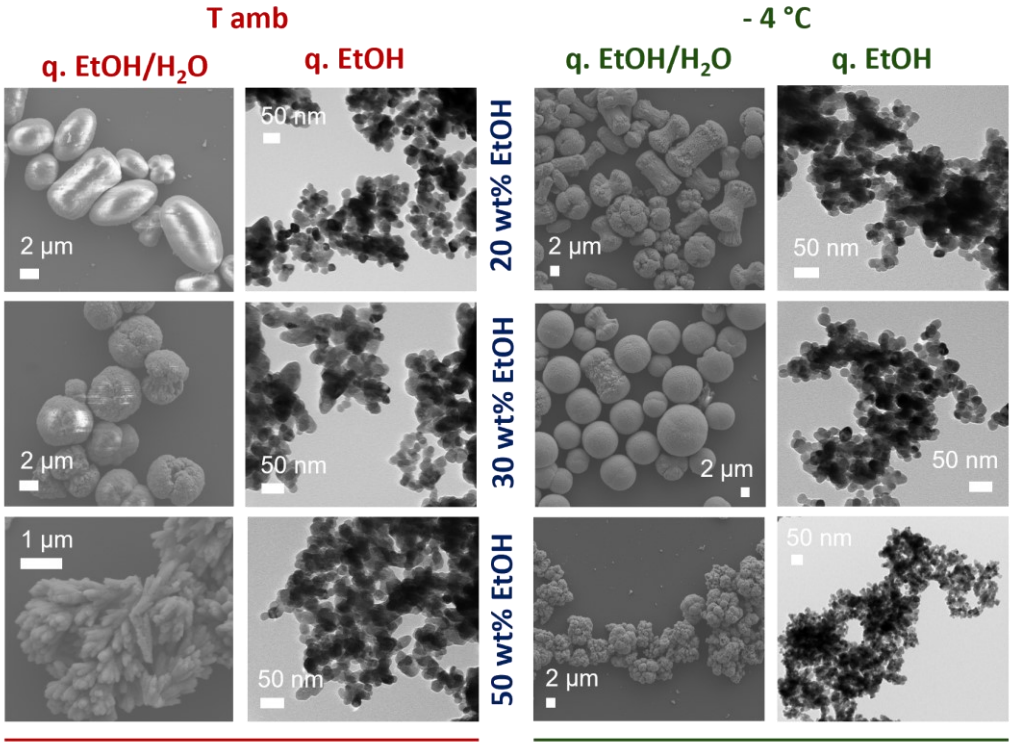

Figure 3.23 TEM and SEM images of calcium molybdate samples obtained with Setup A and varying i) the *content of ethanol* in the solvent mixture (20, 30 and 50 wt% EtOH/H_2O, **top**, **center** and **bottom** respectively), ii) the *reaction temperature* (ambient temperature or –4 °C, **left** red and **right** green respectively) and iii) the *type quenching* (dilution into the solvent mixture or into pure ethanol, **left** and **right** columns in red and green sections, respectively)

non-negligible size polydispersity were still observed, likely due to the variation of the water content into the collecting becker over the course of the synthesis,[xxxiii] the aggregation of the continuously formed CM NPs is evidently quenched more effectively, and distinguishable, although aggregated and/or agglomerated into small irregular clusters, nanoparticles were obtained, likely because of the increase in viscosity that was sufficient for avoiding aggregation into microstructures.

[xxxiii] It is worth noticing that employing an excess of pure ethanol into the collecting becker did not guarantee constant chemico-physical parameters of the solvent from the beginning (first outcoming droplets of reaction mixture dropping into the collecting vessel) to the end of the reaction (last reaction mixture droplets). This variation may cause inhomogeneities in the synthetic outcome, particularly if considering that the viscosity of the solvent mixture as a function of ethanol content is characterized by a maximum value at about 50 wt%, after which it decreases (Figure 3.17, left). However, the volume of the quencher employed was sufficiently high to ensure that throughout the entire synthesis the reaction mixture droplets collected into the quenching solvent experienced an increase in viscosity, even for the syntheses performed with 20 wt% EtOH/H_2O solvent mixture (highest amount of water involved).

In order to investigate if the sole dilution in an excess of solvent mixture actually had a quenching effect, a series of syntheses at low temperature (*i.e.* in a –4 °C cold bath) with different ethanol/water mixtures as reaction solvent and collecting the continuously produced reaction mixture in an empty vessel were performed (*no quenching*). As shown in Figure 3.24, the formation of microstructures by aggregation with different morphologies according to the ethanol content in the solvent occurred also without any dilution of the reaction mixture in the collecting vessel. However, a considerably higher inhomogeneity in aggregates morphologies and dimensions within the same sample was observed, with respect to the analogous samples quenched by dilution in the solvent mixture (Figure 3.22), especially when a 20 wt% content of ethanol was employed (Figure 3.24, top). In particular, a mixture of elongated, dumbbell-like and also spherical microparticles was observed. Taking into account the hypothesis of Chen *et al.* of progressive self-assembled growth of the microstructures from elongated to spherical ones, through dumbbell-shaped

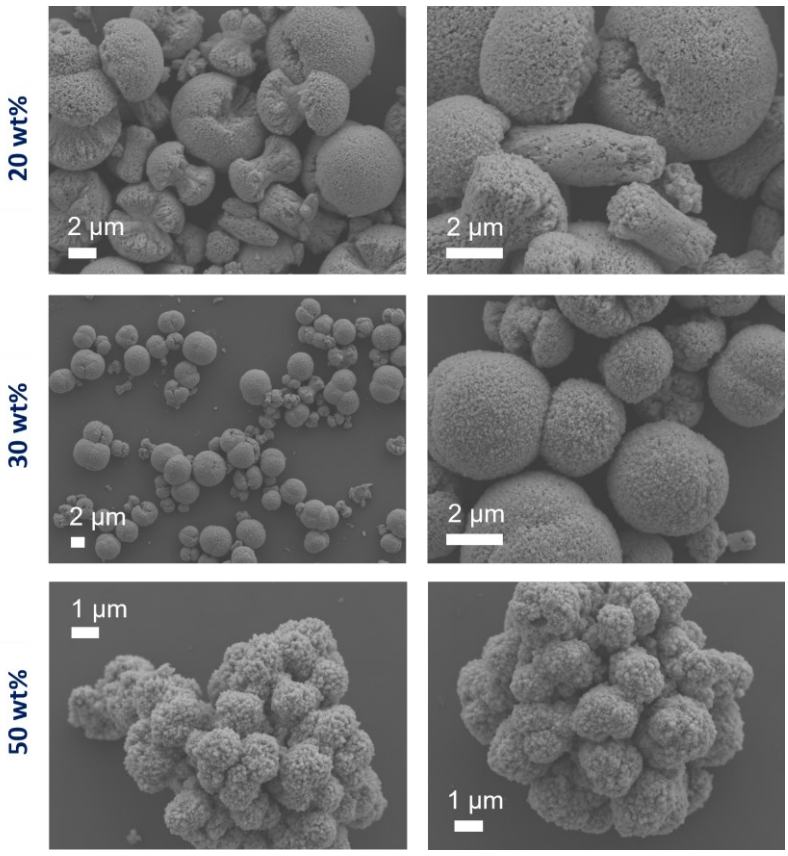

Figure 3.24 SEM micrographs of CM samples synthesized at –4 °C by microfluidic with different amounts of ethanol in the solvent mixture and not quenched (*i.e.* collected in a becker kept at -4 °C): comparison of samples obtained with EtOH/H_2O of 20 wt% (**top**), 30 wt% (**center**), and 50 wt% (**bottom**)

structures,[304] it could be supposed that, when the amount of water in the mixture is high enough (20 wt% EtOH/H_2O mixture) and no quenching step is performed, these stages of growth occurred into the collection vessel simultaneously. Moreover, further nucleation events in the collecting vessel could not be excluded, additionally contributing to reaction environment inhomogeneity. On the other hand, when a dilution was carried out as quenching step, the aggregation of calcium molybdate primary particles occurred in a more controlled and homogeneous way, since the solute concentration was decreased way under the supersaturation level, preventing any further nucleation events and slowing down the rate of aggregation of primary particles.

Finally, in order to i) further improve the effectiveness of quenching of calcium molybdate NPs growth and aggregation, ii) to maintain constant the water/ethanol ratio over the course of the entire synthesis, *i.e.* to maintain constant also the viscosity and dielectric constant of the reaction environment in the collecting becker, and iii) to fully exploit the potential of microfluidic technique described in Chapter 1.2.2, Setup B was built and ethanol as quencher was introduced in line by employing a second T-junction mixer at ambient temperature (see Figure 6.4 in Chapter 6.2.4). As can be appreciated in Figure 3.25, top (green trend), the synthesized CM crystallite size was found to be smaller than that obtained at ambient temperature with Setup A in every synthetic condition, and the TEM micrographs (Figure 3.25, bottom) displayed the formation of nanosized particles with smaller average size with respect to their batch-quenched counterpart (Setup A, ambient T, quenching by dilution in ethanol into the collecting vessel, Figure 3.23). The sudden increase in solvent viscosity and decrease in CM solubility occurring in the second T-junction mixer, that combined the flowing reaction mixture and pure ethanol, allowed an effective quenching of the reaction and avoided the aggregation of primary calcium molybdate nanoparticles into microstructures. At the same time, the possibility of keeping constant the water amount in the mixture for the first and last droplets of reaction mixture provided homogeneity to the reaction mixture.

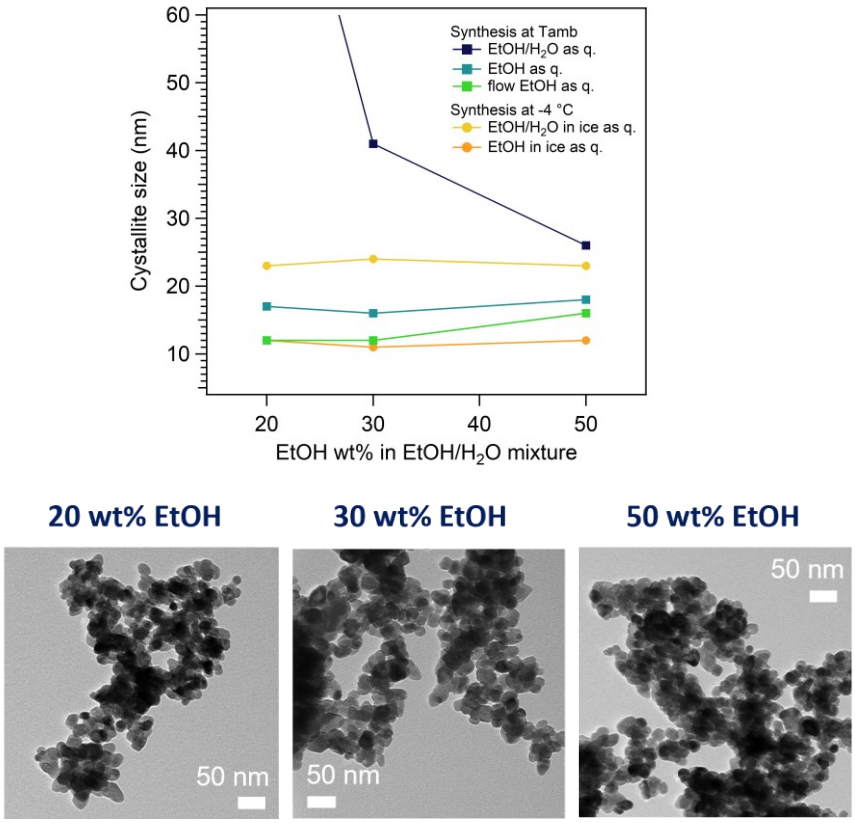

Figure 3.25 Mean crystallite size of calcium molybdate as a function of ethanol content in the solvent mixture and of different reaction temperatures and quenching approaches (**top**), employing with both Setup A (blue, light blue, yellow and orange dots) and Setup B (green dots); TEM micrographs of calcium molybdate samples obtained with Setup B at ambient temperature, employing in flow mixed ethanol as quencher, and varying the content of ethanol in the solvent mixture (**bottom**, 20, 30 and 50 wt% EtOH/H_2O, **left**, **center** and **right** respectively)

V. Doping of $CaMoO_4$ with Eu^{3+}. As investigated employing the miniemulsion and batch approaches discussed in Chapter 3.2, the synthesis of Eu-doped calcium molybdate was studied also in microfluidic conditions with different synthetic parameters, in order to unveil the effectiveness of doping of CM provided by the microfluidic approach. As detailed in Chapter 6.2.4, the syntheses of three samples of 3 at% Eu^{3+}-doped $CaMoO_4$ by microfluidic approach were carried out adding a stoichiometric amount of Eu^{3+} precursor into Ca^{2+} precursor solution and operating with three different sets of synthetic conditions, previously tested for the synthesis of undoped calcium molybdate. In particular, Eu-doped CM was synthesized by employing:

i) Setup A at ambient temperature, with 50 wt% EtOH/H_2O as solvent mixture and quenching the product by dilution with an excess of ethanol in the collecting vessel (sample *EuCM01-mf*);

ii) Setup A at –4 °C, with 50 wt% EtOH/H_2O as solvent mixture and quenching the product by dilution with an excess of ethanol in the collecting vessel kept in the -4 °C cold bath (sample *EuCM02-mf*);

iii) Setup B at ambient temperature, with 50 wt% EtOH/H_2O as solvent mixture and quenching in line the product by dilution in ethanol (sample *EuCM03-mf*).

The experimental doping level of the Eu-doped samples was assessed by ICP-MS analysis, and it was proven to be in very good agreement with the expected nominal one (3 at%), for every sample, meaning that the incorporation of dopant ions in the final products was quantitative for all samples. Nominal and experimental doping percentages are reported in Table 3.3. Since the doping percentage was calculated as the atomic ratio between europium and molybdenum, an experimental doping percentage higher than the nominal

Table 3.3 Nominal and experimental doping percentages, expected based on the concentrations employed in the syntheses and assessed by ICP-MS, respectively, for microfluidic samples synthesized with different sets of conditions. Doping concentrations were determined as Eu/Mo at.

Sample	Nominal at%	Experimental at%
EuCM01-mf	3.0	3.3
EuCM02-mf	3.0	3.3
EuCM03-mf	3.0	3.3

one could be explained taking into account a loss of molybdenum during the purification step.

XRD analysis of the samples evidenced that the crystalline structure of calcium molybdate was retained upon doping with 3 at%, as the crystallization of tetragonal scheelite-type $CaMoO_4$ was observed with every synthetic condition, without the formation any crystalline spurious phase (Figure 3.26). This observation was found consistent with the results discussed in Chapter 3.2, where spurious phases were found in batch samples only with doping percentages higher than 5 at%. The absence of any reflection due to impurities could either be ascribed to effective doping (*i.e.* the Eu^{3+} ions actually substituted Ca^{2+} ions in the scheelite structure) or to their presence in smaller amount than their detection limit by standard laboratory diffraction technique. The presence of Eu^{3+} doping ions in the samples, assessed by ICP-MS, did not affect the average crystallite size estimated by employing the Scherrer equation: comparable crystallite size values were found for undoped and Eu-doped CM synthesized with the same set of experimental conditions. Moreover, TEM and SEM micrographs showed no significant variations in primary particles size, and no aggregation into microstructures was observed as for the undoped counterparts quenched in ethanol. However, as shown in Figure B.25 in Appendix B.2, the formation of spindle-like aggregates in the 100-200 nm range, smaller and less compact with respect to those observed in batch conditions (Figure 3.10, center right) and discussed in Chapter 3.2, was observed for the samples synthesized at ambient temperature with Setup A and B (*EuCM01-mf* and

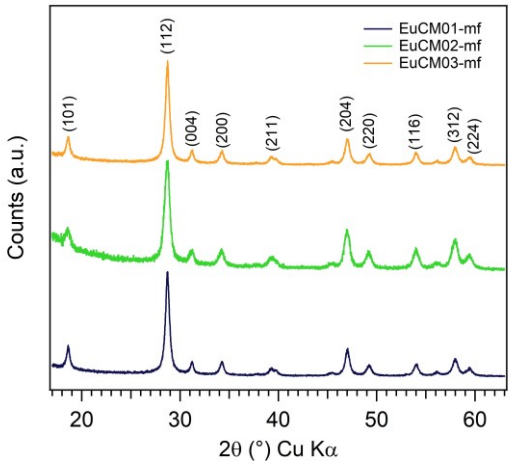

Figure 3.26 XRD patterns of Eu-doped CM synthesized by microfluidic approach with different sets of reaction conditions. *EuCM01-mf*: SetupA, Tamb, 50 wt% EtOH/H_2O as solvent, quenching in EtOH; *EuCM02-mf*: Setup A, –4 °C, 50 wt% EtOH/H_2O as solvent, quenching in EtOH; *EuCM03-mf*: Setup B, Tamb, 50 wt% EtOH/H_2O as solvent, quenching in line with EtOH

EuCM03-mf, respectively). This evidence could likely be accounted for by considering the quenching step in a non-solvent (ethanol) performed in the microfluidic synthesis and not in the batch one, further confirming the effectiveness of quenching in inhibiting the aggregation. Since the formation of any aggregate nano- and microstructure was not observed at –4 °C (sample *EuCM02-mf*), it could be concluded that performing the synthesis at low temperature allowed an even better control on nanoparticles aggregation, likely thanks to the strongly increased viscosity of the reaction mixture and sudden decrease in solubility of the product.

Finally, the functional photoluminescence properties of Eu-doped CM samples synthesized by microfluidics were assessed, in cooperation with Dr. Ilaria Fortunati (Department of Chemical Sciences, University of Padova). The excitation and emission spectra of 3 at% doped calcium molybdate synthesized by microfluidics with the three different sets of reaction conditions are showed in Figure 3.27. Analogously to the Eu-doped CM synthesized by ME and batch approaches presented in Chapter 3.2, the excitation spectra of the microfluidic ones, measured by monitoring the emission of Eu^{3+} (λ_{em} = 613 nm), a broad band in the UV region due to the calcium molybdate matrix and a series of narrow lines due to direct Eu^{3+} f-f excitations ($^5L_6 \leftarrow {}^7F_0$ at 393 nm and $^5D_2 \leftarrow {}^7F_0$ at 468 nm) were observed. In the emission spectra of microfluidic Eu-doped samples, measured upon excitation of the host matrix at 285 nm, the typical $^5D_0 \rightarrow {}^7F_J$ (J = 0-4) transitions of Eu^{3+} were evidenced, with the hypersensitive $^5D_0 \rightarrow {}^7F_2$ being the most intense one (insets of Figure 3.27).[330–332] Moreover, almost no emission intensity from the molybdate matrix was observed. From these observations, an efficient energy transfer from the excited $CaMoO_4$ matrix to the dopant Eu^{3+} ions can be supposed, indicating that the doping process by microfluidics was likely effective.[330]

As observed for ME and batch doped samples in Chapter 3.2, being the f-f transitions $^5D_0 \rightarrow {}^7F_J$ (J = 0-4) in the emission spectra well-resolved, it could be argued that Eu^{3+} were located in a defined crystallographic position in the calcium molybdate matrix, in agreement with the hypothesized substitution of Ca^{2+} ions in Ca sites. Moreover, as largely discussed in Chapter 3.2, Eu^{3+} ions were likely characterized by a tetragonal local symmetry with no inversion, though not C_4 or C_{4v}, since i) a weak $^5D_0 \rightarrow {}^7F_0$ transition, ii) a splitting of the emission lines for the $^5D_0 \rightarrow {}^7F_1$ and $^5D_0 \rightarrow {}^7F_2$ transitions into two and four lines, respectively, and iii) a high ratio of a forced electric dipole to a magnetic dipole

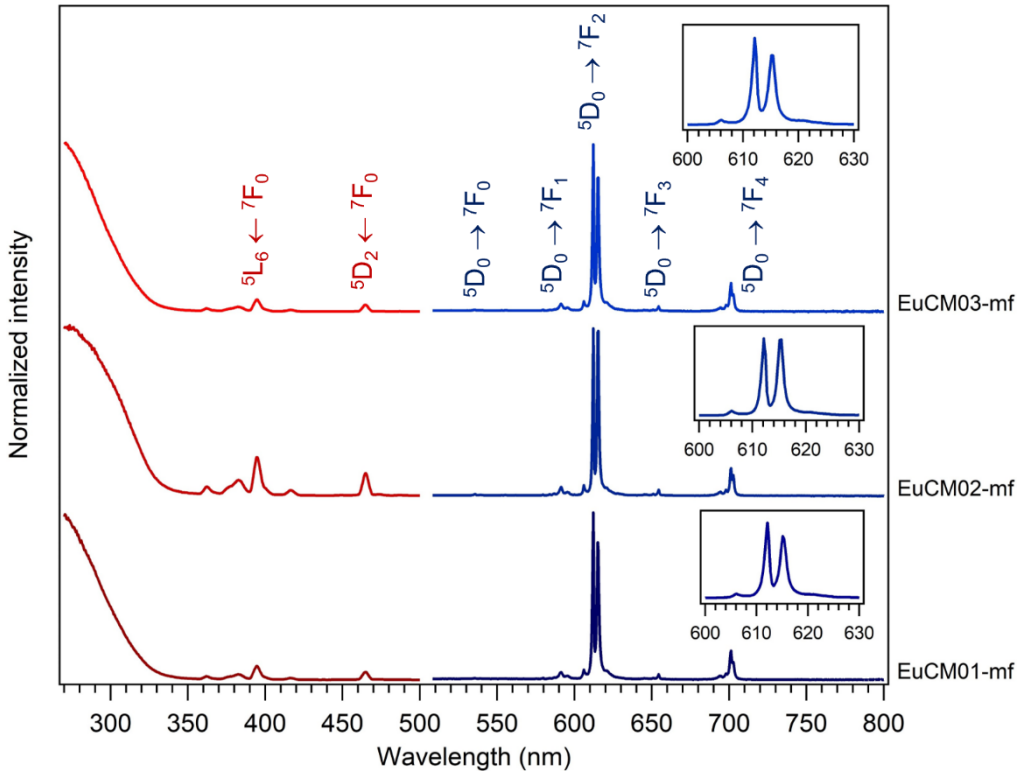

Figure 3.27 Normalized excitation spectra (red lines) measured by monitoring Eu^{3+} emission (λ_{em} = 613 nm) and emission spectra (blue lines) measured by exciting CM host matrix (λ_{exc} = 285 nm) of 3 at% Eu-doped CM samples synthesized by microfluidics with different sets of reaction conditions. *EuCM01-mf*: SetupA, Tamb, 50 wt% EtOH/H_2O as solvent, quenching in EtOH; *EuCM02-mf*: Setup A, –4 °C, 50 wt% EtOH/H_2O as solvent, quenching in EtOH; *EuCM03-mf*: Setup B, Tamb, 50 wt% EtOH/H_2O as solvent, quenching in line with EtOH. **Inset:** zoom of the splitting of the $^5D_0 \rightarrow {}^7F_2$ transition

($R^{0\text{-}2/0\text{-}1}$ = 9.5-11.7) were observed.[330,332] In particular, among microfluidic Eu-doped samples the highest $R^{0\text{-}2/0\text{-}1}$ value was found for the sample synthesized at –4 °C, compared to those obtained at ambient temperature, indicating also better color purity.

Lastly, to shed light on the excited state dynamics, the emission decays of microfluidic Eu-doped calcium molybdate were measured, and the decay curves were well-fitted with a double exponential function (see Appendix B.2). This observation was in agreement with batch and ME doped Eu-doped CM samples (Chapter 3.2) and with a large influence of the samples surface, as expected for nanoparticles with a high surface to volume ratio.[333,334] As shown in Table 3.4, the measured average lifetimes of emission (τ_{av}) were found to be in the 0.7-0.8 ms range, in agreement with literature reported values for Eu^{3+} containing

scheelites,[320,335] and miniemulsion 3 at% doped sample, while slightly longer than batch 3 at% doped sample (Table B.11 in Appendix B.2).

Table 3.4 Emission lifetimes and relative values of the pre-exponential factors of 3 at% Eu-doped microfluidic calcium molybdate samples, synthesized by microfluidics with different sets of reaction conditions. *EuCM01-mf*: SetupA, Tamb, 50 wt% EtOH/H_2O as solvent, quenching in EtOH; *EuCM02-mf*: Setup A, –4 °C, 50 wt% EtOH/H_2O as solvent, quenching in EtOH; *EuCM03-mf*: Setup B, Tamb, 50 wt% EtOH/H_2O as solvent, quenching in line with EtOH. Decay data were calculated employing λ_{exc} = 271 nm (excitation of $CaMoO_4$) and λ_{em} = 615 nm ($^5D_0 \rightarrow {}^7F_2$ emission line of Eu^{3+})

Sample	α_1	τ_1 (µs)	α_2	τ_2 (µs)	τ_{av} (µs)
EuCM01-mf	0.50	483	0.50	953	812
EuCM02-mf	0.32	347	0.68	837	757
EuCM03-mf	0.47	480	0.53	930	789

3.4 Conclusions

The synthesis of undoped and europium-doped calcium molybdate nano- and differently aggregated microstructures was successfully investigated in the confined space of inverse miniemulsion nanodroplets, in a continuous-flow microreactor (microfluidic approach) and in the absence of space constraint (batch synthesis). The co-precipitation reaction between calcium ions and molybdate anions in aqueous or mixed solvent solution was exploited within the three proposed synthetic approaches and various reaction parameters were systematically screened. The crystallization of tetragonal calcium molybdate with every synthetic condition was observed by XRD, and the size, size distribution and aggregation of the primary CM particles were investigated by TEM and SEM. The observed results were compared as a function of the screened synthetic parameters and synthetic approaches.

In particular, a strong effect of space confinement of inverse miniemulsion nanodroplets on the crystallization of pure and doped Eu-doped $CaMoO_4$ was observed. Indeed, confined space effects were observed on the size, size distribution and shape of CM (XRD, TEM, SEM), obtaining NPs with a smaller crystallite size (8 nm *vs* 30 nm), NPs size (12 nm *vs* 60 nm) and size distribution (PDI of 0.2 *vs* 0.5), more regular shape through ME approach as compared to the batch one. In addition, while batch calcium molybdate was found to aggregate in an oriented fashion to form defined microstructures, whose morphology was found to be dependent on the synthetic conditions such as the pH of the molybdate precursor solution and its concentration, no aggregation was observed for ME samples. Remarkably, different trends in CM crystallite size as a function of the concentration of precursors solutions and pH value of molybdate solution according to the synthetic approach were observed, indicating that a different crystallization mechanism was likely involved. In particular, while without any space constraint (batch approach) a classical crystallization pathway could be hypothesized, in miniemulsion a non-classical one was likely to occur.

Moreover, it was found that space confinement played a pivotal role in the doping process of calcium molybdate with Eu^{3+} ions, enabling to obtain an effective doping and a more homogeneous distribution of the dopant ions in the host matrix, without forming any spurious phases. On the contrary, Eu-based impurities (likely Eu_2O_3 and/or EuOOH) were found in the batch samples synthesized with higher dopant concentrations (5 and 7 at%, as evidenced by XAS and photoluminescence analyses).

Subsequently, the synthesis of undoped and Eu(III)-doped calcium molybdate was implemented in microfluidic conditions, designing two experimental setups for systematically controlling the formation of nano- and differently aggregated microstructures. This was achieved by exploiting the peculiarities of the microfluidic approach of efficient mixing of reactants, space-time direct relation and effective control over the reaction temperature, as well as an intelligent variation of the viscosity and dielectric constant of the reaction medium, and of the solubility of calcium molybdate, by i) employing differently composed milliQ water-ethanol mixtures, ii) lowering the reaction temperature to -4 °C, and iii) differently quenching the continuously produced CM. It was observed that, by increasing the viscosity of the reaction medium (*i.e.* increasing the ethanol content and lowering the reaction temperature), less aggregated nano- and microstructures (depending on the quenching method) were obtained, while a variation of the dielectric constant led to differently shaped aggregated microstructures. According to the literature, the formation of these microstructures occurs through a progressive oriented self-assembly, influenced by the superficial charges. Finally, the synthesis of Eu-doped CM was addressed by microfluidic approach, employing different sets of reaction conditions, and it was observed that the proposed continuous-flow synthetic method allowed an easy and efficient doping of calcium molybdate matrix, as demonstrated by XRD and photoluminescence analyses.

4

Pd nanoparticles on mesoporous silica

In this Chapter, the synthesis of palladium nanoparticles in the confined space of pores of mesoporous silica materials is addressed, and the synthesis outcomes are compared with a reference sample of palladium nanoparticles synthesized on non-porous silica. Two different families of mesoporous silica (SBA-15 and KIT-6), characterized by different pore sizes, arrangements and connectivity, were investigated and the effect of mesopores space confinement on the Pd NPs size, size distribution and distribution over the support was explored. Moreover, the synthesized palladium NPs on mesoporous and non-porous silica were tested as catalysts for oxidation of carbon monoxide, both *ex situ* at Karlsruhe Institute of Technology and during *operando* X-ray absorption spectroscopy measurements at the Soleil synchrotron.

4.1 Introduction

As extensively described in Chapter 1.2.3, thanks to their regular pore arrangement and narrow pore size distribution, mesoporous materials (pore diameter 2-50 nm) with ordered structure are of great interest for size- and shape-selective applications, such as molecular sieves,[341] catalysis[170] or as host structures for nanometer-sized guest compounds.[342] Indeed, their uniform mesoporous structure provides a size-selective nano-environment that can be exploited, for example, for supporting metal nanoparticles with a homogeneous distribution.

Among mesoporous materials, silica is one of the most widely studied ones, as highly ordered mesopores architectures, with tunable pore size, arrangement, and accessibility, can be readily synthesized by using soft templating methods. Thanks to their high specific surface area and large porosity, combined with a high-quality structure regularity, they are widely used as supports in the field of catalysis.[343] Indeed, the very ordered, uniform and controllable pore structure of mesoporous silica plays an important role in NPs distribution within the support, which is desired to be homogeneous to limit aggregation phenomena and particle sintering at elevated temperatures, under catalysis operating conditions. Within this framework, in this Ph.D. Thesis the synthesis of palladium nanoparticles within the pores of mesoporous silica materials by incipient wetness impregnation technique was addressed, with the aim of investigating the effect of the spatial confinement offered by differently sized and inter-connected mesopores with different arrangement and accessibility on the size and size distribution of the supported nanoparticles and on their distribution over the support. The evaluation of the effects of spatial confinement of silica mesopores was further investigated by comparing mesoporous silica-supported palladium nanoparticles with a reference "batch" sample, employing non-porous commercial silica as support. Finally, the possible application of the mesoporous and non-porous silica-supported Pd NPs as heterogeneous catalysts for the oxidation of carbon monoxide was explored.

The pristine mesoporous silica materials and of the non-porous reference one employed as confined environment and support for palladium nanoparticles are described in Chapter 4.2. Chapter 4.3 discusses the synthesis and characterization of Pd NPs through incipient wetness impregnation and successive reduction in hydrogen atmosphere. Finally, the assessment of the catalytic activity of Pd@SiO_2 samples for CO oxidation, by both *ex situ* tests carried out at KIT and *operando* XAS experiments performed at the Soleil synchrotron, is described in Chapter 4.4.

4.2 Mesoporous and non-porous silica supports

As mentioned in the Introduction section, in order to unveil the effect of the arrangement and accessibility of pores, as well as their dimension (*i.e.* effect of space confinement) on the Pd nanoparticles, two different families of mesoporous silica (*i.e.* SBA-15 and KIT-6) and two different pore sizes (*i.e.* 7 and 9 nm) within both families of materials were addressed.

This part of the work was performed in collaboration with the Ph.D. student Sarah Claas (workgroup of Prof. Michael Fröba, University of Hamburg, Germany), who prepared the mesoporous silica supports following well-established soft templating synthetic protocols. Moreover, with the aim of comprehensively studying the effect of spatial confinement of mesopores on the final size and crystal structure of Pd NPs, a "batch" silica commercial reference with a lower specific surface area (Aerosil® 200, Degussa GmbH) was also investigated as reference support (no space confinement and equivalent heterogeneous nucleation on the surface of silicon oxide). The employed mesoporous and non-porous silica samples employed as supports for the synthesis of Pd NPs (Chapter 4.3) are schematized in Table 5.1, and their characterization is discussed below.

Table 5.1 Mesoporous and non-porous silica samples employed as supports for the synthesis of Pd nanoparticles

		Pore size		
		-	7 nm [c]	9 nm [d]
Mesoporous silica	SBA-15 [a]		SA	SC
	KIT-6 [b]		KA	KC
Non-porous silica	Aerosil 200	A200		

[a,b] *S* and *K* series samples are SBA-15 and KIT-6 based ones, respectively.
[c,d] *A* and *C* series represent 7 nm and 9 nm sized mesopores, respectively.

As described in more detail in Chapter 1.2.3, the two different families of mesoporous silica that were employed differ in the symmetry of the ordered porous system, as well as in the connectivity and tortuosity between pores. Indeed, SBA-15 silica materials are a combined hierarchical micro- and mesoporous material with a bi-dimensional hexagonal pore architecture (space group *P6mm*). Their porous structure is constituted of long, parallel cylindrical channels independent of each other, typically slightly curved. Micropores, originating from the hydrophilic chains of the surfactant that penetrate into silica framework during the synthesis, act as intra-wall pores. On the other hand, KIT-6 is characterized by a cubic close-packed bi-continuous pore architecture (space group *Ia-3d*), organized in a three-dimensional interpenetrating cylindrical porous network. A schematic representation of the pore architecture of SBA-15 and KIT-6, as well as representative TEM

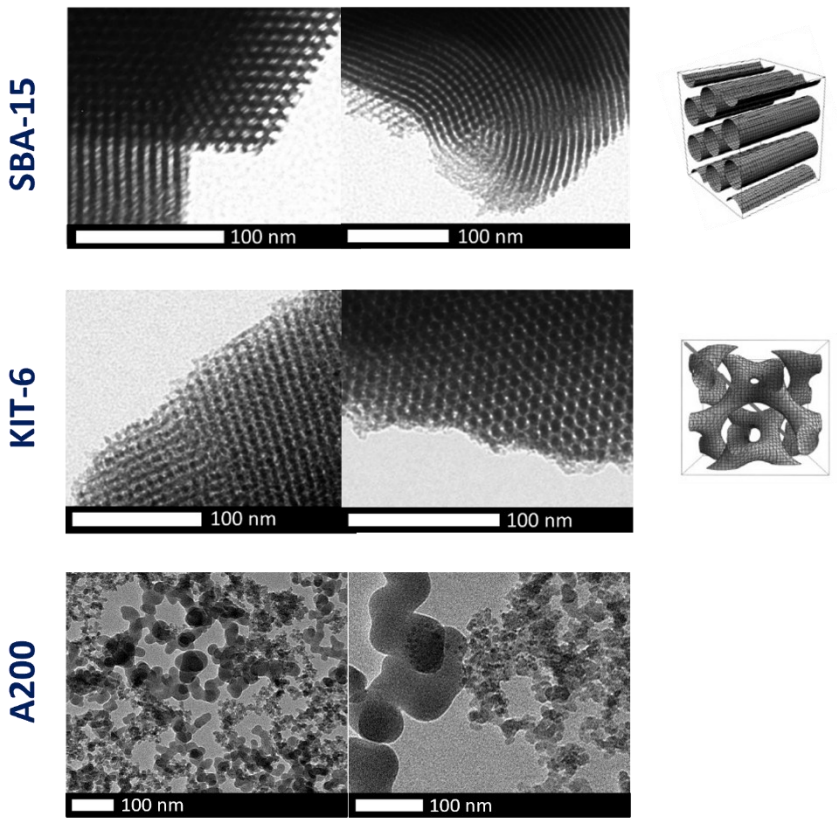

Figure 5.1 TEM micrographs of SBA-15 (**top**) and KIT-6 (**center**) and A200 (**bottom**) pristine samples; schematic representation of the pore systems of SBA-15 and KIT-6 are also reported

micrographs of experimental pristine samples,[xxxiv] are shown in Figure 5.1, top and center, respectively, together with TEM characterization of the "batch" reference sample A200. The reported micrographs clearly showed the above-described regular pore architectures of the two families of mesoporous silica materials, and their dramatical difference with respect to the commercial silica sample *A200* (Figure 5.1, bottom), displaying a mixture of irregularly shaped and sized nanoparticles.

In order to determine the porous structure of the samples, as well as their specific surface area (SSA), total pore volume, and average pore width and pore width distribution, mesoporous and commercial silica samples were characterized by nitrogen physisorption measurements. As shown in Figure 5.2, top, SBA-15 and KIT-6 mesoporous silica samples displayed a Type IV isotherm, typical of mesoporous materials. Indeed, the adsorption isotherms displayed three distinguished regions, corresponding to: i) monolayer-multilayer

[xxxiv] Pristine samples, *i.e.* silica materials prior to impregnation, are referred to as *prist* in samples names.

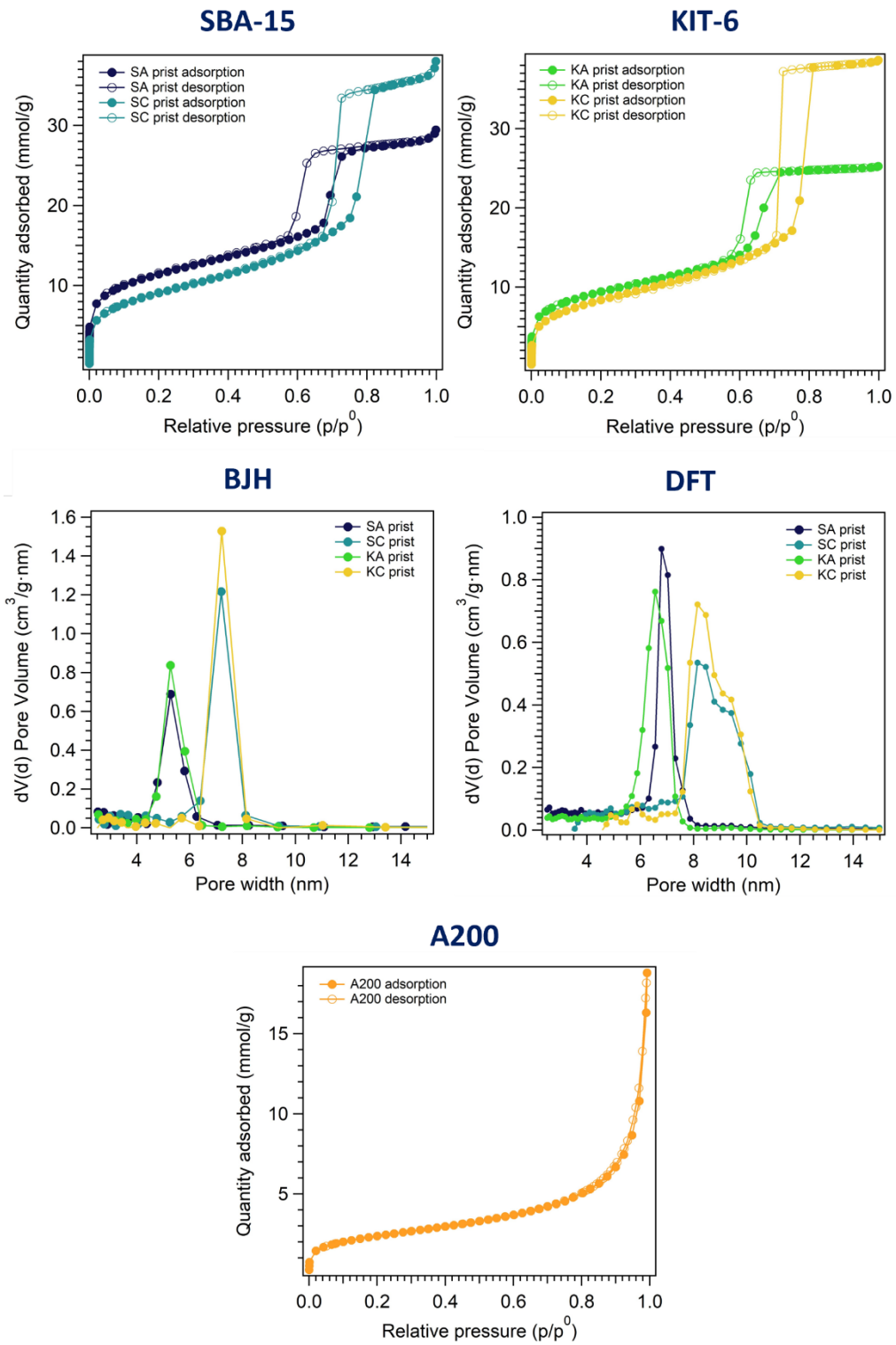

Figure 5.2 N_2-physisorption isotherms (Type IV, H1 hysteresis) of the pristine supports *SAprist* (**top left**, blue lines), *SCprist* (**top left**, light blue lines), *KAprist* (**top right**, green lines) and *KCprist* (**top right**, yellow lines), and corresponding pore width distribution estimated by BJH (**center left**) and DFT (**center right**) methods. N_2-physisorption isotherm (Type II) of *A200prist* sample (**bottom**, orange line). Adsorption and desorption branches points are reported as filled and empty dots, respectively

adsorption, ii) capillary condensation, and iii) multilayer adsorption on the outer particle surfaces. Type H1 hysteresis loops (*i.e.* hysteresis loops relatively narrow and hysteresis branches parallel and almost vertical) were observed, indicating pore channels of constant diameter, as extensively described in Chapter 7.6.[344] Indeed, deriving the pore width distributions by both BJH and DFT methods (Figure 5.2, center), all four mesoporous supports demonstrated quite narrow mesopore size distributions. Since the BJH method typically underestimates the actual pore diameter by 2-3 nm (see Chapter 7.6),[345–347] the average pore size determined by the DFT method was employed for further discussion (*i.e.* pore size of 7 nm for *A* series, and of 9 nm for *C* series of samples). This difference in pore size between the *A* series and the *C* series of samples was also qualitatively observed from the isotherms, as the capillary condensation occurred at higher relative pressures for the *C* series of samples ($p/p^0 \approx 0.75$ *vs* $p/p^0 \approx 0.65$), and it was completed with higher amounts of physisorbed nitrogen. This resulted also in a higher total pore volume for the *C* series with respect to the *A* series of mesoporous silica samples (1.32 $cm^3\ g^{-1}$ *vs* 0.985 $cm^3\ g^{-1}$ for SBA-15 silicas, and 1.50 $cm^3\ g^{-1}$ *vs* 0.91 $cm^3\ g^{-1}$ for KIT-6 silicas; see Table 5.2). On the other hand, the physisorption isotherm of the commercial reference sample *A200* (Figure 5.2, bottom) was identified as a Type II isotherm, typical of macroporous or non-porous samples.[344] Moreover, the specific surface area (SSA) of *A200* sample, determined by the BET method,[348] was found significantly lower than the SSA of mesoporous samples, *i.e.* of about 190 $m^2\ g^{-1}$, compared to SSAs of 750-900 $m^2\ g^{-1}$ of mesoporous silicas (Table 5.2). These results, combined with the above-mentioned TEM characterization, confirmed the commercial sample *A200* as suitable “batch” reference support material, to be compared with high-quality ordered mesoporous silica materials SBA-15 and KIT-6 and to evaluate the effects of their space confinement.

In addition, the pristine mesoporous silica materials were characterized also by small-angle (0.4-6.0° 2θ) and wide-angle (15-90° 2θ) XRD. As expected and shown in Figure 5.3, they displayed crystallinity at the mesoscale level with associated SAXS pattern typical of their structure, *i.e.* hexagonal with space group *p6mm* for SBA-15 and cubic with space group *Ia-3d* for KIT-6 (Miller indexes in Figure 5.3), arising from electron density contrast between the walls and the pores. On the other hand, the corresponding XRD patterns (not shown) were characterized by the amorphous bump of silica (about 15-30° 2θ), indicating glass-like disorder in the walls, in agreement with the literature.[188,195] The SAXS patterns of both *A* and *C* series of SBA-15 and KIT-6 materials displayed in Figure 5.3, left and right,

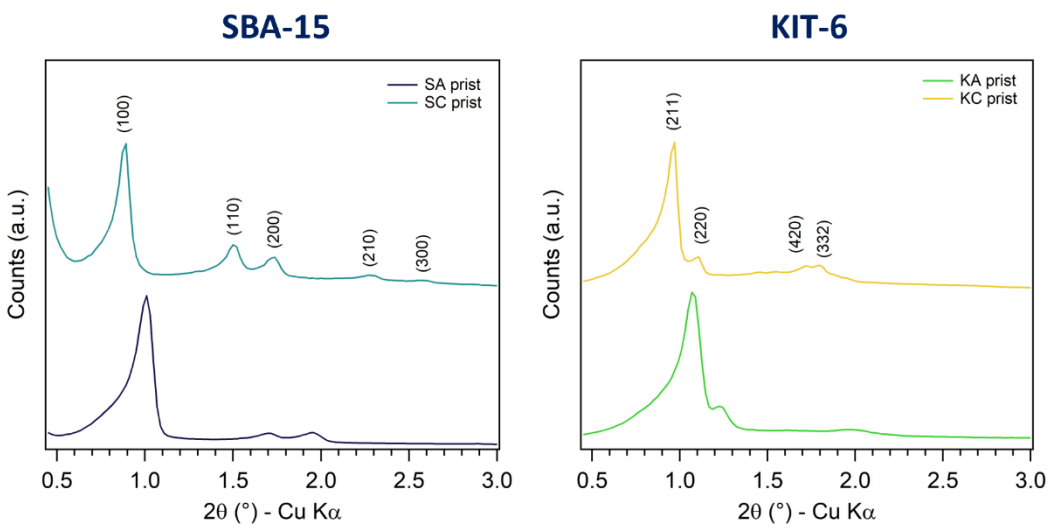

Figure 5.3 SAXS patterns of pristine SBA-15 (**left**) and KIT-6 (**right**) mesoporous samples, with 7 nm (*A* series) and 9 nm (*C* series) sized pores

respectively, further confirmed the different pore sizes of the two series: reflections positions were shifted towards lower scattering angle for the *C* series with respect to the *A* series, indicating larger unit cell parameter. Since the unit cell parameter corresponds to the distance between centers of adjacent mesopores, this result was indicative of a larger pore size. The unit cell parameter a and the pore wall thickness t_{wall} could be calculated from the position in *d*-space of the SAXS reflections and the pore size estimated by DFT from nitrogen physisorption measurements. In particular, for SBA-15 and KIT-6 silica materials, the unit cell parameter a was calculated as: $a = 2d_{(100)}/\sqrt{3}$ and $a = \sqrt{6} \cdot d_{(211)}$, respectively. The silica wall thickness was determined as $t_{wall} = a - d_{DFT}$ and $t_{wall} = (a/2) - d_{DFT}$, for SBA-15 and KIT-6 silicas, respectively.[341] The obtained values are reported in Table 5.2, together with other structural parameters derived by nitrogen physisorption measurements, discussed above.

On the other hand, the SAXS pattern of commercial A200 sample, reported in Figure B.26 in Appendix B.3, did not display any feature, and the corresponding XRD pattern was characterized by the amorphous halo of silica, indicating the absence of any long and medium range structural order, as expected.

Table 5.2 Structural parameters of pristine silica supports derived from nitrogen physisorption and low-angle XRD measurements

	Silica support	Sample name	SSA_{BET}[a] (m^2/g)	d_{DFT}[b] (nm)	d_{BJH}[c] (nm)	V_t[d] (cm^3/g)	a[e] (nm)	t_{wall}[f] (nm)
Mesoporous silica	SBA-15	SAprist	896	7.0	5.4	0.985	10.4	3.4
		SCprist	763	8.8	7.4	1.322	11.4	2.6
	KIT-6	KAprist	746	6.8	5.4	0.905	20.6	3.5
		KCprist	784	8.8	7.3	1.497	23.5	3.0
Non-porous silica	Aerosil 200	A200prist	189	-	-	-	-	-

[a] Specific surface area SSA_{BET} determined by means of the BET equation; [b] Mean mesopore diameter estimated by DFT model d_{DFT}; [c] Mean mesopore diameter estimated by BJH model d_{BJH}; [d] Total pore volume; [e] Unit cell parameter *a* estimated by XRD; [f] Silica wall thickness t_{wall} calculated from *a* and d_{DFT}

4.3 Pd nanoparticles on mesoporous and non-porous silica

As described in more detail in Chapter 6.3.2, the synthesis of palladium nanoparticles was carried out directly into the mesopores of mesoporous silica and on the surface of non-porous reference silica (*pristine* series), through a two-step process, encompassing: i) two subsequent cycles of impregnation of the pristine materials with a solution of Pd(II) followed by slow and controlled drying (*impregnated* series),[xxxv] and subsequently ii) a mild reduction of the impregnated samples (*reduced* series).[xxxvi]

In particular, the first step was carried out employing the *incipient wetness impregnation* (IWI) technique, according to which a volume of impregnating solution equal to the pore volume to be filled is added to the pristine material. By the IWI technique, the impregnating solution is entirely drawn into the pores by capillary forces and theoretically no precursor material is deposited on the outer surface of the support. Thus, the employed impregnation method should guarantee that the role of space confinement on the Pd NPs size, size distribution and distribution over the support could be appreciated by comparing the results with the reference sample, not displaying any micro- or mesoporosity and likely resulting in an external surface decoration by palladium (*i.e.* Pd over non-porous silica). As a palladium precursor, palladium nitrate was employed due to its high solubility in water, low decomposition temperature (150-200 °C) and low contamination of the final catalyst (nitrates are generally preferred catalyst precursors over other inorganic salts such as sulfates and halides), allowing the impregnation with quite concentrated precursor's solution and the facile elimination of nitrate counterion by relatively mild heating treatment.[349] Following the IWI procedure, a precise volume of an aqueous solution of $Pd(NO_3)_2$ (equal to the total pore volume of the mesoporous materials, see Table 5.2) was dropwise added to the pristine silica materials, to achieve a final concentration of 2.0 wt% Pd@SiO_2. The loading of palladium on silica materials was decided taking into account the most typical literature values (0.1-4.0 wt%)[350–352] and balancing the effects of potentially opposing factors, such as i) the catalytic performance of the samples (*i.e.* the higher the loading, likely the more active the catalyst), ii) the Pd NPs size (*i.e.* the lower the

[xxxv] Pd(II)-impregnated samples, *i.e.* pristine samples after IWI and drying, are referred to as *impr* in samples names.

[xxxvi] Reduced samples, *i.e.* impregnated samples exposed to the reducing treatment, are referred to as *red* in samples names.

loading, likely the smaller Pd NPs and the more appreciable the spatial confinement effects), iii) the possible aggregation issues (*i.e.* the higher the loading, the more likely coalescence and sintering phenomena), and iv) the suitability of the Pd@SiO_2 sample for spectroscopic investigation (*i.e.* the lower the loading, the more challenging the probing of Pd in transmission mode by XAS technique).

In order to investigate possible changes in the mesoporous structure upon impregnation with Pd(II) solution, nitrogen physisorption and SAXS measurements of the as-prepared impregnated samples were carried out. All the impregnated mesoporous samples demonstrated that the parent supports were preserved: Type IV isotherms with Type H1 hysteresis loop were observed, as their pristine counterpart, as shown in Figure B.27 and Figure B.28 in Appendix B.3 for SBA-15 and KIT-6 materials, respectively. The mean mesopore diameters remained unchanged, demonstrating negligible pore collapse or restructuring upon palladium incorporation. The only observed exception was the *SA* sample (SBA-15 d_{DFT} 7 nm), whose physisorption isotherm (Figure 5.4, left) was characterized by a Type H5 hysteresis, typical of structures containing both open and partially blocked mesopores.[344] Indeed, the two-step desorption isotherm indicates the occurrence of equilibrium evaporation/desorption and pore blocking/cavitation effects:[353] evaporation of liquid from open pores is associated with the desorption at higher p/p^0, while blocked mesopores remain filled until they are emptied *via* cavitation.[xxxvii] This evidence was further confirmed by the pore size distribution of *SAimpr* sample derived from the adsorption and desorption branches of the isotherm using the BJH method, shown in Figure 5.4, right. In particular, it was found that the pore size distribution estimated from the desorption branch of the isotherm displayed an additional maximum at about 3.9 nm, with respect to that estimated from the adsorption branch. This second desorption step evidenced in the size distribution could be ascribed to the presence of nanoparticles within the mesopores, narrowing part of the mesoporous channels and creating ink bottle-like sections. Similar results were reported in literature for Pd@SBA-15 samples.[351] However, it is worth noting that it was reported that the position of the observed additional maximum exclusively depends on the employed adsorptive (*i.e.* nitrogen) and does not estimate the

[xxxvii] *Cavitation* is an important desorption mechanism in ink-bottle pores, and it refers to the phenomenon of spontaneous nucleation of a gas bubble in a metastable stretched condensed fluid. A non-equilibrium situation is generated after the formation of the bubble, that continuously grows while the pore is emptying. In the case of cavitation-controlled evaporation, no quantitative information about the neck size and size distribution can be obtained.[344]

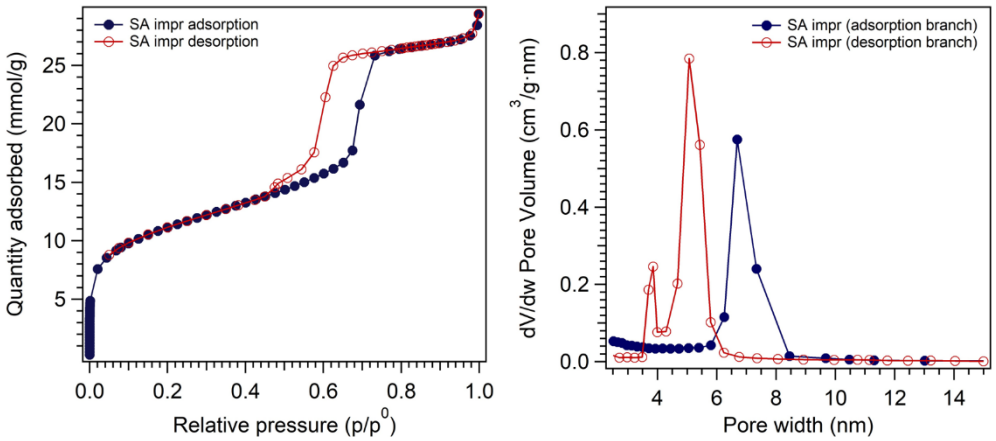

Figure 5.4 N_2-physisorption isotherm of *impregnated SA* sample (SBA-15, d_{DFT} 7 nm), displaying a Type H5 hysteresis (**left**), and corresponding pore size distributions derived using the BJH method on the adsorption and desorption branches (**right**)

size of the partially clogged pores: there is a maximum tension that a liquid can withstand (*i.e.* its tensile strength) and thus there is a minimum value of p/p^0 (*i.e.* consequently of pore size) at which the liquid condensed in the pores can exist. This phenomenon is known as *tensile strength effect*, and it is the reason why, using nitrogen as adsorbent, the hysteresis loop closure takes place always at p/p^0 = 0.42.[345,354–358] The partial clogging of SBA-15 mesopores was found consistent with the hypothesized formation of Pd-based nanoparticles inside the mesopores, and it could be rationalized taking into account the pore structure of SBA-15, that comprises parallel channels poorly interconnected *via* disordered micropores. *SCimpr*, belonging to the same mesoporous silica family, did not display clogging of mesopores, likely due to their bigger size (*i.e.* 9 nm *vs* 7 nm). On the other hand, the highly interconnected mesopore structure of KIT-6 silica supports likely prevented the observation of the pore clogging phenomenon in the isotherm even for the sample with the smaller pore size (*i.e. KAimpr*, KIT-6 d_{DFT} 7 nm).

The comparison of the SAXS patterns of Pd(II)-impregnated mesoporous and non-porous silica samples (solid lines) and of the pristine samples (dashed lines) is reported in Figure 5.5, left: the successful retention of the parent mesopore architecture of the silica support after impregnation was observed, and the absence of long-range order in the non-porous one was further confirmed. No significant variation of the cell parameters of pristine and impregnated mesoporous samples was evidenced, indicating that the palladium-based nanoparticles deposited within mesopores did not significantly affect their long-range order. On the other hand, XRD patterns (Figure 5.5, right) highlighted that the impregnation with palladium nitrate solution and subsequent mild drying in air led to the formation of

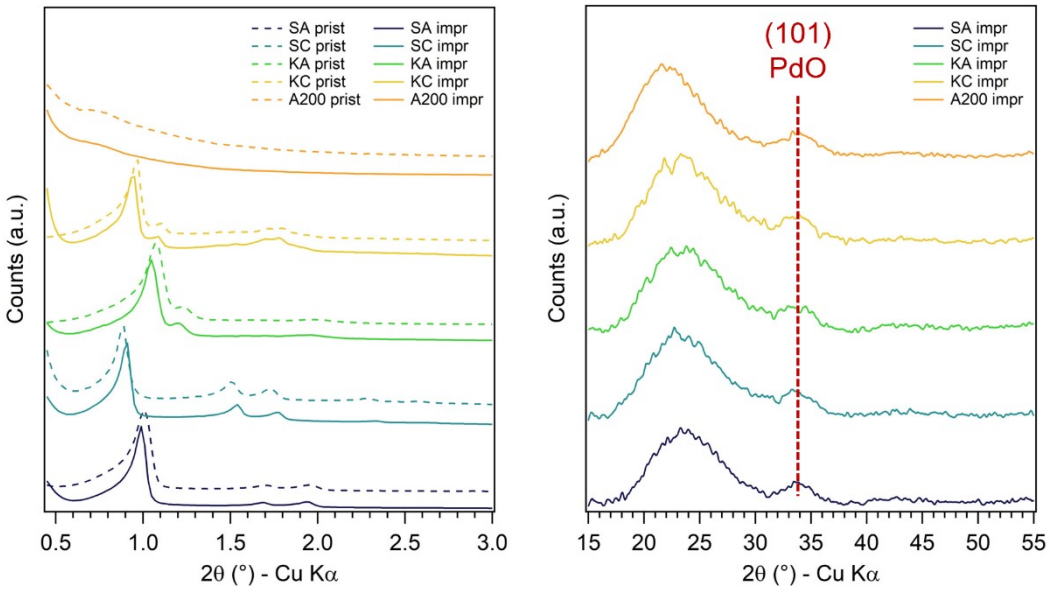

Figure 5.5 SAXS (**left**) and XRD (**right**) patterns of impregnated Pd@SiO_2 (*impr series*, solid lines), compared with SAXS profiles of samples pristine silica materials (*prist series*, dashed lines)

PdO nanoparticles, being the strongest and evidently broad (101) reflection of tetragonal PdO clearly recognizable at 34.4° 2θ (space group *I4/mmm*, PDF nr. 8-2434) along with the amorphous halo of silica supports. This result was expected, as similar results were reported in literature.[349]

The expected oxidized nature of palladium was also confirmed by XAS investigation at the Pd K-edge (24350 eV) at the SAMBA beamline at the Soleil synchrotron. Indeed, a comparison of the white line position of the acquired XANES spectra of the impregnated samples with the spectra of reference Pd(II) species (*i.e.* the precursor $Pd(NO_3)_2$ and PdO) and metallic Pd(0), reported in Figure 5.6, left, demonstrated that palladium in the samples was present in an oxidized state (+2). Moreover, as expected and confirmed by XRD, the predominant species for all samples was found to be palladium oxide, since the XANES features of the impregnated samples closely resembled the XANES profile of the PdO reference material.

The impregnated samples were then mildly treated at 150 °C in a reducing atmosphere (5 vol% H_2/He) at the Karlsruhe Institute of Technology (Germany), in cooperation with Dr. Paolo Dolcet. The reduction of selected samples (*SAimpr*, *SCimpr* and *KCimpr*) was followed by performing a TPR (temperature programmed reduction) analysis while *in situ* monitoring variations in the Pd K-edge XANES spectra at the Soleil synchrotron. As detailed in Chapter 6.3.4, impregnated samples were placed into a capillary, flushed with

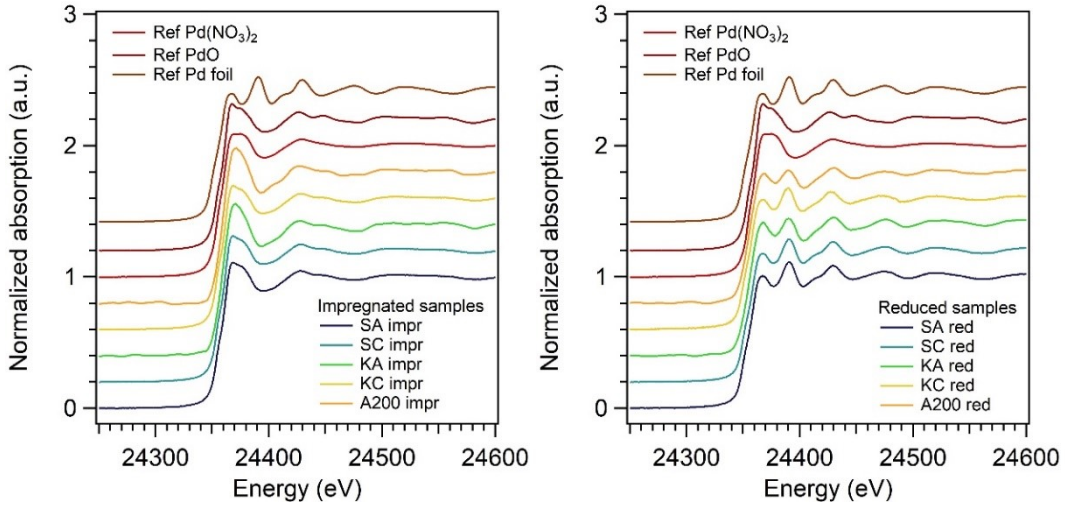

Figure 5.6 Pd K-edge XANES spectra of (**left**) Pd(II) impregnated mesoporous and non-porous silica samples and (**right**) reduced Pd@mesoporous and non-porous silica samples, compared with reference spectra of palladium nitrate, palladium oxide and metallic palladium foil. Spectra are shifted vertically for clarity

2.5 vol% H_2/He atmosphere and heated up to 150 °C, while acquiring XAS data. The XANES spectra of the samples after the reduction step, shown in Figure 5.6, right together with XANES spectra of the *ex situ* reduced samples *KAred* and *A200red* (whose TPR was not followed by *in situ* XAS due to time constraints) and references spectra, were found to strongly differ from those of the impregnated samples (Figure 5.6, left). In particular, the clear change in their near-edge structure was evidenced by the decrease in the white line intensity and shift of the adsorption edge to lower energy by about 2 eV, in agreement with a reduced oxidation state. Indeed, their XANES curves, displaying multiple features, closely resembled those of the palladium foil spectrum, characterized by a second feature with higher intensity than the first one. Altogether, these evidences indicated that the predominant species in the reduced series of samples is metallic palladium. However, it was noticed that the relative intensity of the first two XANES features of *KAred* and *A200red* samples (*i.e.* samples reduced at KIT, stored and measured *ex situ* as pellets at Soleil synchrotron) did not match the metallic Pd reference ones, suggesting the presence of both palladium oxide and metallic palladium species. This observation could be explained considering either that an incomplete reduction took place or a reoxidation of the surface of the small metallic Pd NPs when the Pd materials were stored under air, as reported also by other authors.[350] However, since the reduction step was performed in comparable conditions at KIT laboratories and at the Soleil synchrotron, and XANES spectra of the *in situ* reduced samples (*i.e. SAred*, *SCred* and *KCred*), not exposed to air, closely resembled Pd foil

spectrum, the latter hypothesis was the most likely explanation for the partial oxidation of *ex situ* measured reduced samples.

As mentioned above, the temperature programmed reduction of selected impregnated samples was followed by *in situ* XAS analysis: the fraction of palladium species (*i.e.* PdO and Pd) as a function of the temperature of the heating treatment was determined by linear combination fitting of the measured Pd K-edge XANES spectra (data analysis performed by Dr. Paolo Dolcet). The results of the XANES data analysis for the performed TPR experiments of impregnated SBA-15 mesoporous silica samples with pore diameter of 7 nm and 9 nm (*SAimpr* and *SCimpr*, respectively) are shown in Figure 5.7 (results for *KCimpr* sample are reported in Figure B.30 in Appendix B.3). A very comparable redox behavior of Pd among the two catalysts supported over differently sized porous SBA-15 silica was observed: both impregnated samples displayed completely oxidized PdO at room temperature, in agreement with previous reports, and the reduction of PdO to Pd was complete at about 140-150 °C. Moreover, a relatively sharp reduction edge was observed, as the metallic Pd species increased significantly in a quite narrow temperature interval. This could possibly indicate homogeneously distributed Pd species on the support, both in terms of size and chemical state. However, comparing the temperature at which half of the species were reduced (*i.e.* $T_{50\text{-red}}$), a slightly lower $T_{50\text{-red}}$ was observed for *SC* sample (SBA-15 d_{DFT} 9 nm) with respect to *SA* sample (SBA-15 d_{DFT} 7 nm), *i.e.* 80 °C compared to 82 °C. This result indicated that Pd was more easily reduced when supported over SBA-15 with d_{DFT} 9 nm, compatibly with a larger size of Pd NPs dispersed over *SC* with respect to *SA*, as could be expected accordingly to the less constrained diameter of *SC* mesopores.

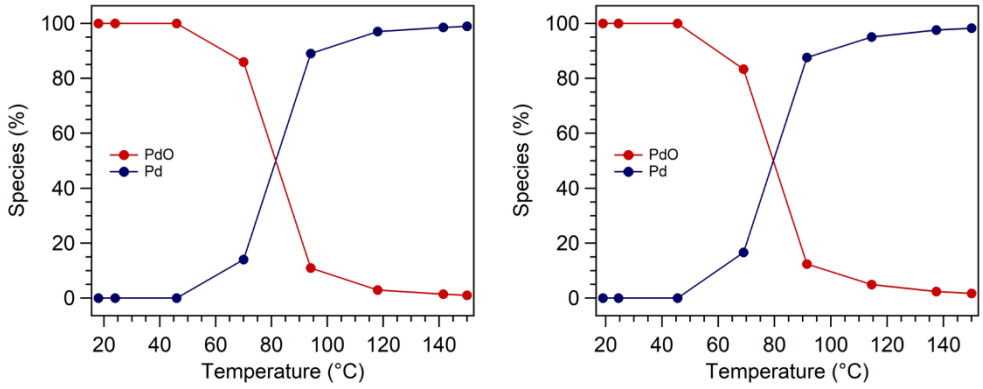

Figure 5.7 Relative fraction of PdO and Pd species as a function of temperature obtained by linear combination fitting of Pd K-edge XANES spectra of impregnated SBA-15 mesoporous silica with d_{DFT} 7 nm (**left**) and d_{DFT} 9 nm (**right**) (*SAimpr* and *SCimpr*, respectively)

Finally, the effectiveness of the performed reducing treatment was further confirmed by XRD characterization. Indeed, the (101) reflection of PdO observed in the *impregnated* series of samples (Figure 5.5, right) was not evidenced in the *reduced* series of samples (Figure 5.8), that, on the other hand, displayed the diffraction pattern of cubic metallic Pd (space group *F3-m3,* PDF nr. 01-1201), along with the previously discussed amorphous halo of silica supports at 2θ < 30°. Metallic palladium reflections were observed to be quite broad, consistent with nanometric crystallite size (*i.e.* 4-6 nm).

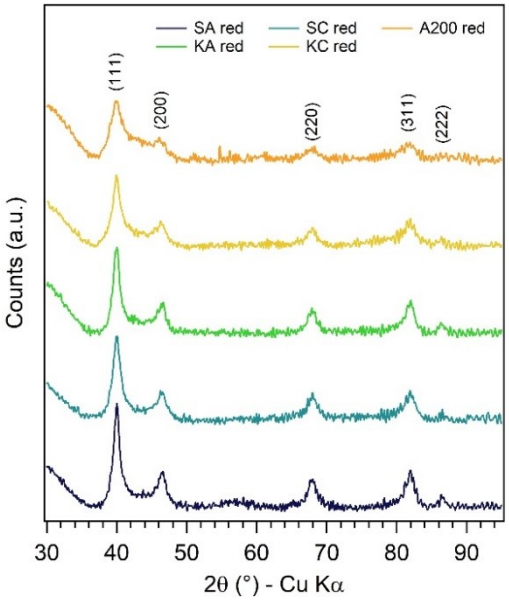

Figure 5.8 XRD pattern of reduced Pd@SiO_2 samples (*red* series), displaying metallic Pd reflections, marked with respective Miller indeces

The size, size distribution, and distribution of palladium nanoparticles over the different screened silica supports (*reduced* series) were investigated by high resolution scanning transmission electron microscopy (STEM) and electron tomography at the Institute of Nanotechnology (INT) of KNMF facility of KIT (Karlsruhe, Germany), in cooperation with Dr. Carina Maliakkal, who acquired STEM micrographs, and Dr. Di Wang. A representative STEM micrograph of *SAimpr* sample is shown in Figure 5.9, together with the EDX map of a selected region of the probed particle, evidencing the nature of the observed features: palladium nanoparticles corresponded to the brighter spots observed in STEM micrographs. A comparison of STEM micrographs of all the prepared reduced samples is reported in Figure 5.10, together with histograms showing the Pd NPs size distributions. The collected micrographs further confirmed the retention of the architecture of both parent mesoporous supports, previously assessed by nitrogen physisorption (Type IV isotherms)

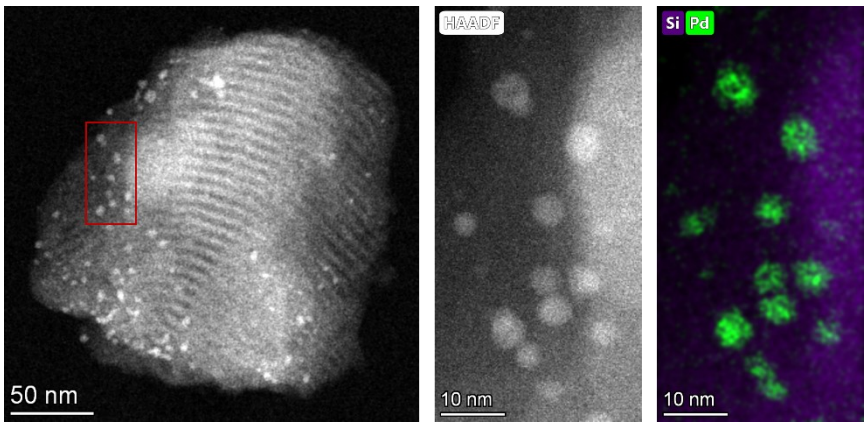

Figure 5.9 High angle annular dark-field (HAAFD) STEM micrographs and EXD map (purple: silicon; green: palladium) of a selected region of *SAimpr* sample

and SAXS (characteristic pattern of SBA-15 and KIT-6), and the nanometric size of palladium, in agreement with the broad XRD reflections. Moreover, they evidenced a quite homogeneous distribution of palladium nanoparticles throughout the silica supports, for all the investigated samples. An average size of Pd NPs in the of 4.0-5.5 nm range, in agreement with the crystallite size estimated by XRD and slightly smaller than literature reports of NPs size of Pd synthesized over SBA-15 (*i.e.* 4-10 nm, depending on the synthetic conditions),[352,359] was estimated for all the samples regardless the nature of the silica support, demonstrating a quite good degree of control and reproducibility of the incipient wetness technique to produce small non-aggregated supported nanoparticles. However, by looking in more detail the average NPs sizes reported in Table 5.3, it can be noted that palladium nanoparticles synthesized over mesoporous supports were smaller than those formed over non-porous silica (*i.e.* 4.0-4.8 nm *vs* 5.4 nm). This observation was found in agreement with the hypothesized space confinement effect of mesopores of SBA-15 and KIT-6, also offering a higher superficial area for deposition, as well as likely leading to a more effective stabilization and/or lower mobilization of the NPs over the support. However, no significant effect of the pore size on the average Pd NPs size was found, as no trend of the nanoparticles' dimensions varying the mesopore diameter was outlined. Actually, among the tested supports, KIT-6 with 9 nm pore size allowed to obtain the smallest Pd NPs with the narrowest size distribution, thus resulting in the best synthetic control over the nanoparticles size and size distribution. Finally, it was noticed that the average size of Pd NPs calculated from STEM micrographs was in agreement with the above-discussed TPR results, suggesting a slightly larger size of Pd NPs deposited over SBA-15 d_{DFT} 9 nm with respect to SBA-15 d_{DFT} 7 nm.

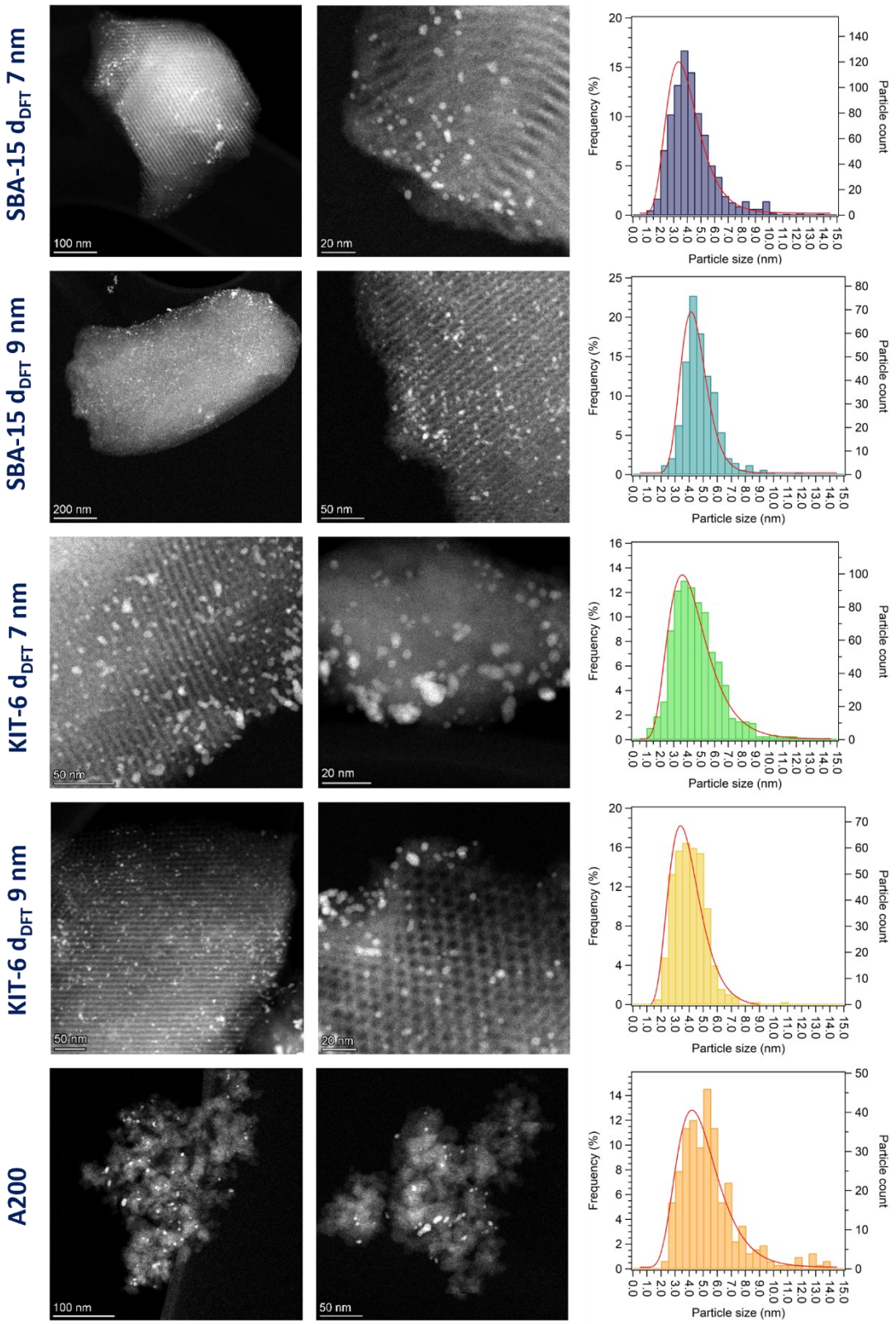

Figure 5.10 STEM micrographs of Pd NPs (brighter spots, as confirmed by EDX) supported over different silica supports, and corresponding histograms reporting the Pd NPs size distribution

Table 5.3 Mean nanoparticles size and polydispersion index (PDI) of Pd NPs supported over mesoporous and non-porous silica (*reduced* series)

	Silica support	Sample name	Mean NPs size (nm)	PDI
Mesoporous silica	SBA-15	SAred	4.4 ± 1.7	0.39
		SCred	4.8 ± 1.2	0.25
	KIT-6	KAred	4.6 ± 1.8	0.39
		KCred	4.0 ± 1.1	0.28
Non-porous silica	Aerosil 200	A200red	5.4 ± 2.1	0.39

From STEM micrographs of mesoporous silica-supported samples (Figure 5.10), a significant number of Pd nanoparticles seemed to be located in/along mesopores and/or pore entrances, as aimed, rather than onto external surfaces. However, although in literature some conclusions about the NPs location were drawn by similar micrographs, even with lower magnification,[350–352,360,361] caution must be paid because STEM micrographs are bi-dimensional projections of tri-dimensional structures, and can be misleading in determining the Pd NPs location over the support. Thus, electron tomographic measurements were performed to map the distribution of palladium nanoparticles on selected mesoporous samples. Some representative "slices" of the tomographic reconstructions of mesoporous silica particles supporting Pd NPs are reported in Figure 5.11, Figure 5.12, and Figure 5.13 for *SAred*, *SCred* and *KCred* samples, respectively. From electron tomography, it was found that palladium NPs supported on SBA-15 silica with d_{DFT} of 7 nm (Figure 5.11) were mostly located on the surface of the silica particle or at the entrance of the pores, in agreement with the nitrogen physisorption results, that reported a partial clogging of the mesopores. It could thus be hypothesized that 7 nm-wide cylindrical non-connected mesopores did not enable a capillary penetration of the precursor solution, that was deposited at their entrance. On the other hand, when SBA-15 silica with higher pore diameter (d_{DFT} 9 nm) was employed as support and confined environment, Pd NPs were easily found in the inner structure of the mesoporous matrix (Figure 5.12), indicating an effective synthesis of palladium nanostructures in the confined space of the mesopores. This result confirmed the findings outlined from physisorption data, not displaying any clogging, and can most likely be rationalized by taking into account the higher pore

dimension of *SCprist* sample with respect to *SAprist* sample. Finally, it is worth noting that the more effective confinement of the synthesis of Pd NPs inside SBA-15 cylindrical parallel mesopores when a larger pore size was exploited resulted into a slightly larger size (4.8 *vs* 4.4 nm), but into a narrower size distribution of Pd NPs (PDI of 0.25 *vs* 0.39, see Table 5.3), thus in a more controlled synthetic outcome. Last, tomographic investigation of the sample supported over KIT-6 d_{DFT} 9 nm (Figure 5.13) demonstrated that the highly interconnected mesoporous architecture of KIT-6 mesoporous material allowed facile and effective incorporation of palladium precursor inside the mesopores, obtaining, after drying and reduction, a quite homogeneous distribution of Pd NPs inside them. *KCred* sample also resulted to be characterized by the smallest average size of Pd NPs with narrow size distribution, indicating optimal synthetic control.

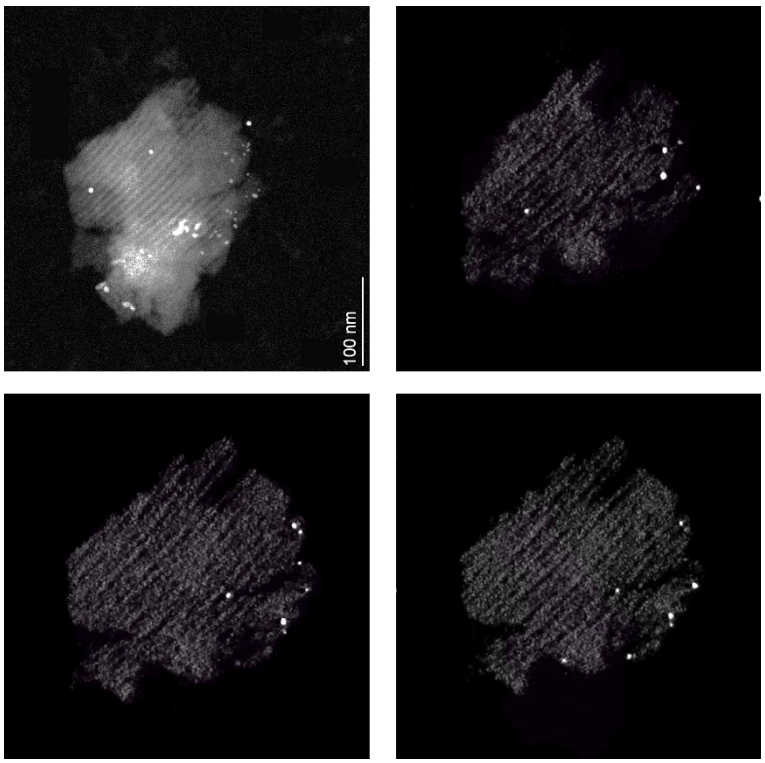

Figure 5.11 STEM image of *SAred* (SBA-15 d_{DFT} 7 nm) acquired at tilt = 0° and employed for tomography (**top left**), together with selected Z slices of reconstructed 3D structure

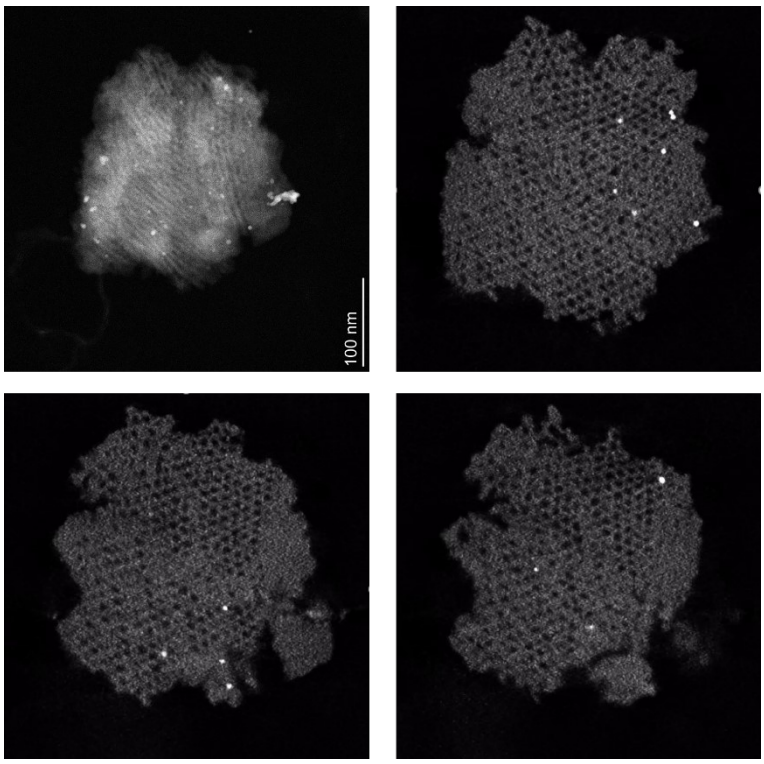

Figure 5.12 STEM image of *SCred* (SBA-15 d_{DFT} 9 nm) acquired at tilt = 0° and employed for tomography (**top left**), together with selected Z slices of reconstructed 3D structure

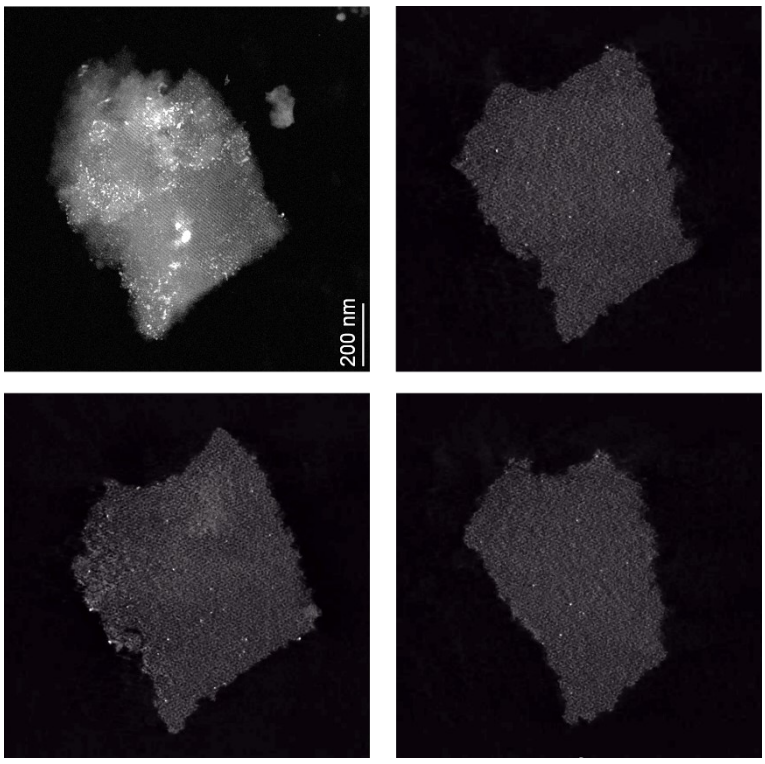

Figure 5.13 STEM image of *KCred* (KIT-6 d_{DFT} 9 nm) acquired at tilt = 0° and employed for tomography (**top left**), together with selected Z slices of reconstructed 3D structure

4.4 Pd NPs on mesoporous and non-porous silica as catalysts for CO oxidation

Catalytic combustion over platinum-group metals (PGM) has been utilized in exhaust gas after-treatment for the last decades[362] and the increasingly strict emission regulations[xxxviii] will enhance the need of finding more efficient exhaust gas catalysts. Noble metals such as palladium, platinum, gold and ruthenium have been extensively studied as supported catalysts, both as single metals or alloyed (bi-metal or tri-metal catalysts). It is well known that the size of noble metal NPs plays a crucial role in ruling their catalytic activity, as well as that a major relevance is also held by the nature, structure and morphology of the support, that can be active (*e.g.* ceria: as reducible oxide, it can act as oxygen storage for oxidation reactions) or inert (*e.g.* alumina or silica).[363,364] Among inert supports, silica has emerged as an attractive environment for supporting metallic nanoparticles, thanks to its low cost, high chemical and thermal stability and tunable porosity. Within this framework, in this Ph.D. Thesis the catalytic activity of Pd supported on mesoporous and non-porous silica materials (samples discussed in Chapter 4.3) was investigated for CO oxidation, chosen as model reaction for catalytic oxidative reactions.

In particular, catalytic activity of the samples towards CO oxidation was tested in collaboration with Dr. Paolo Dolcet and Dr. Maria Casapu (workgroup of Prof. Jan-Dierk Grunwaldt, KIT, Germany) at the Karlsruhe Institute of Technology laboratories and at the Soleil synchrotron with dedicated *operando* XAS experiments at the Pd K-edge.

I. Catalytic activity towards CO oxidation of Pd NPs supported on mesoporous and non-porous silica. The catalytic activity for CO oxidation of the samples discussed in Chapter 4.3 was investigated by the Ph.D. candidate at ITCP-KIT laboratories, employing a home-made setup described in Chapter 6.3.3. In particular, a sieved fraction sized 125-250 μm of the catalysts was loaded into a quartz flow microreactor and tested with three consecutive heating-cooling cycles (*i.e.* 1st, 2nd and 3rd light offs and light outs) up to 300 °C in a gas mixture composed of 1000 ppm CO and 9 vol% O_2 in He, with a total flow of 50 mL min^{-1} and a weight hourly space velocity (WHSV) of 60,000 L h^{-1} g_{Pd}^{-1}. Then, an *in situ* reduction stage was performed, flushing into the reactor 5 % vol H_2 in He up to 150 °C and holding the temperature at 150 °C for 30 minutes. After the reduction step, three additional heating-

[xxxviii] New Euro 7 standards to reduce pollutant emissions from vehicles and improve air quality were proposed by the European Commission in November 2022.[433]

cooling cycles were conducted (4th, 5th and 6th light offs and light outs). The gas mixture after the reaction was analyzed by FT-IR and a mass spectrometer, in order to monitor changes in the reaction mixture composition.

The conversion (%) curves of carbon monoxide as a function of temperature of Pd samples supported over KIT-6 mesoporous silica with pore size of 7 nm and 9 nm are reported as an example in Figure 5.14, while conversion curves for Pd NPs supported over SBA-15 and non-porous silica, displaying analogous behavior, are shown in Figure B.31 and Figure B.32 in Appendix B.3. During the light off (*i.e.* heating phase), three regions of activity were observed: i) low activity region (about 50-150 °C), corresponding to the temperature range in which the reaction is kinetically controlled: at low temperature CO is adsorbed on the catalyst surface and inhibits the adsorption of oxygen (*vide infra*), ii) high activity region at higher temperature, coinciding with the temperature range in which the conversion curve is steeper (about 150-200 °C): the reaction is controlled by the diffusion of the reactive mixture into porous supports, and iii) a stability region (> 200 °C), where the conversion is complete and reaches a plateau: no mass transfer limitations were noticed. When

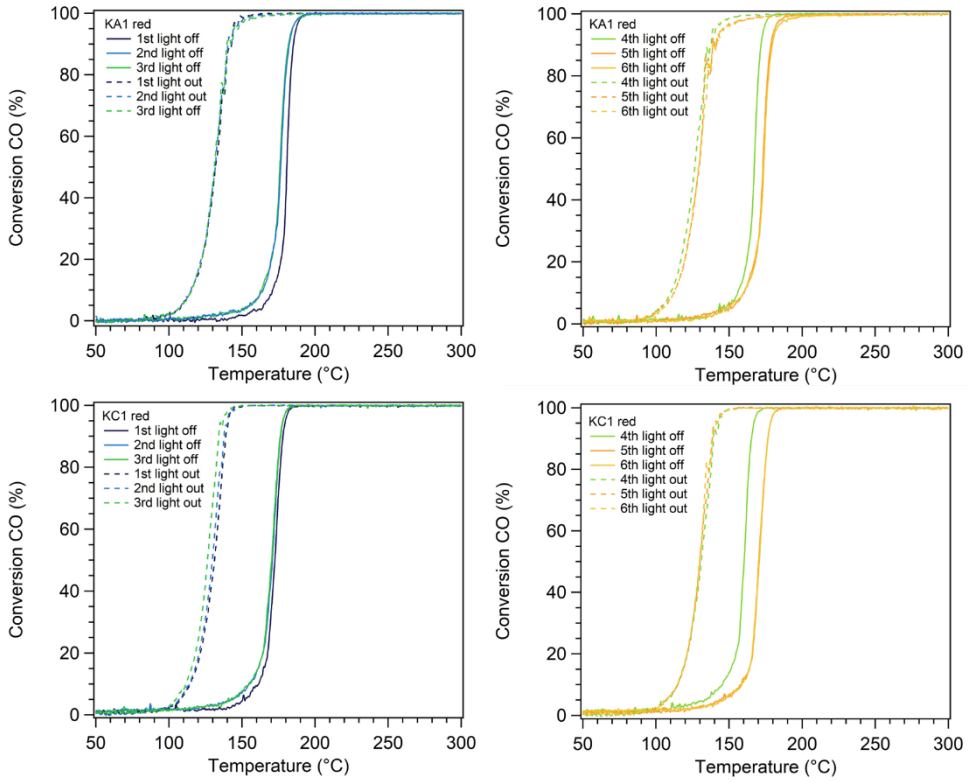

Figure 5.14 Catalytic conversion curves of Pd NPs on KIT-6 mesoporous silica, with pore size of 7 nm (**top**, *KAred* sample) and 9 nm (**bottom**, *KCred* sample), acquired before (1st, 2nd and 3rd cycle, **left**) and after (4th, 5th, and 6th cycle, **right**) the *in situ* reduction step

considering also the light out curve, the formation of a normal hysteresis profile was noted: the ascending (*light off*) and descending (*light out*) branches of the CO conversion percentage *vs* temperature plot did not coincide, and in particular the catalytic activity during the heating process occurred at a higher temperature than during the cooling process. This behavior is quite common for CO oxidation and many other oxidation exothermic reactions using Pd or Pt-based catalysts, such as CO, NO, C_3H_6 and CH_4 oxidations.[365–371] However, its origin is still controversial, and it has been discussed from both a macroscopic (*e.g.* mass and heat diffusion effects) or microscopic (*e.g.* mechanistic and structural aspects) perspective. In particular, it was ascribed to the strong exothermicity and local overheating of the active sites, releasing heat at the surface of the catalyst and determining a surface temperature higher than the reactor temperature: in this way, the catalyst remains active also at lower temperatures during cooling down. In addition, the hysteresis origin has been associated with the multiplicity of steady states, surface coverage, oxidation of the catalyst, and temperature fluctuations.[368,372,373]

The temperature at which 50% of CO conversion was achieved during the light off step (*i.e.* T_{50}), shown in Figure 5.15, was employed as a parameter to compare the catalytic activity of the five catalysts amongst themselves and among different consecutive cycles, given the similarities in the shape of the conversion curves. Generally, T_{50} values in the 145-182 °C range were obtained, comparable or lower than widely distributed literature values of Pd on SiO_2 catalysts (about 140-280 °C).[352,365,374] A clear variation of the T_{50} values according to the microstructural features of silica support was observed, following the trend A200 < SBA-15 d_{DFT} 7 nm < KIT-6 d_{DFT} 9 nm < SBA-15 d_{DFT} 9 nm ≈ KIT-6 d_{DFT} 7 nm for each

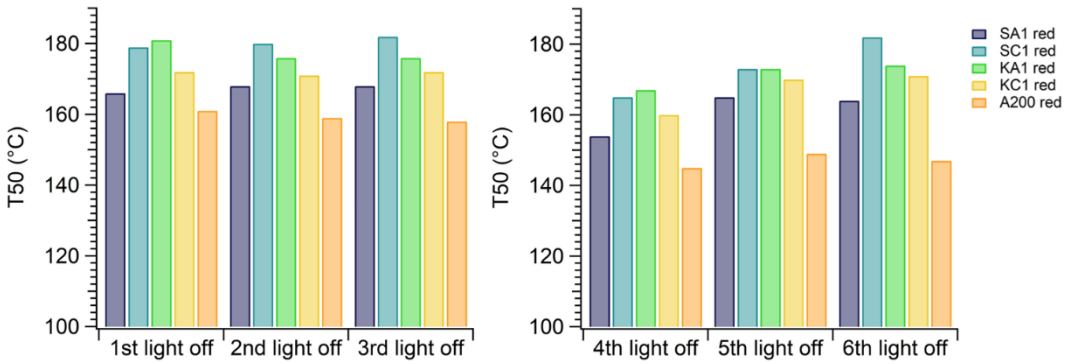

Figure 5.15 Comparison of the T_{50} for CO oxidation light offs on different Pd/SiO_2 catalysts, acquired before (1st, 2nd and 3rd cycle, **left**) and after (4th, 5th, and 6th cycle, **right**) the *in situ* reduction step

catalytic cycle. Indeed, Pd NPs supported on non-porous silica were found to be the more active catalysts for CO oxidation, possibly because 2 wt% Pd NPs on non-porous silica were deposited over a considerably smaller surface area: *A200red* sample was characterized by a higher superficial concentration of Pd than its mesoporous counterparts (*i.e.* about 10 mg_{Pd} m^{-2} *vs* 2-3 mg_{Pd} m^{-2}). This factor, ultimately influencing the distance between Pd NPs, could likely influence their catalytic activity, as reported in literature.[375] Amongst mesoporous samples, the best catalytic performance was shown by Pd NPs on SBA-15 mesoporous silica with a mesopore diameter of 7 nm and this observation, analogously to the non-porous sample, could be in accordance with the presence of Pd NPs mostly on the outer surface of the support and at the entrance of pores, as demonstrated by nitrogen physisorption and electron tomography measurements (Chapter 4.3), thus with a localized higher superficial concentration of Pd NPs. On the other hand, Pd NPs inside mesopores of SBA-15 and KIT-6 silica, whose location was demonstrated by electron tomography, were found less active for the CO oxidation, possibly because the diffusion of the reactive gases was ruled by the geometry porous systems.[376] In particular, Pd NPs synthesized in 9 nm-sized mesopores of KIT-6, already displaying a smaller size and narrower size distribution (see Table 5.3) displayed a lower light off temperature, while a less marked difference was found in the T_{50} values of Pd NPs supported on SBA-15 d_{DFT} 9 nm and KIT-6 d_{DFT} 7 nm, in agreement with their comparable size and size distribution (Table 5.3). However, the observed non-linear trend in catalytic activity of the investigated supported Pd samples could not be fully understood, because of the interplay of multiple factors involved in the studied process, *e.g.* i) Pd NPs size, ii) size distribution, iii) distribution over the support, iv) superficial concentration, and v) their possible variation during catalysis, vi) palladium oxidation state variation, vii) pore size distribution and connectivity, viii) presence of micropores in SBA-15 silica materials.

Since the light off temperature of the samples over the first three different consecutive catalytic cycles was observed to be quite constant (Figure 5.15, left), a good stability of the samples and non-significant de-activation of the catalyst could be argued. However, after the *in situ* reduction step, performed in between the third and fourth catalytic cycle, as mentioned above and detailed in Chapter 6.3.3, a significant increase in catalytic activity of all samples was evidenced, ascribable to the efficient removal of adsorbed moieties from the surface of the catalyst, exposing the active sites (in reduced state) to fresh adsorbates, and therefore to the efficient re-activation of the catalyst.[365]

II. *Operando* XAS analysis. In order to unveil the relation between the catalytic activity of Pd NPs supported on different silica supports and the oxidation state changes of palladium during CO oxidation, *operando* XAS measurements were performed at the Pd K-edge (24350 eV) at the SAMBA beamline of the Soleil synchrotron for selected samples (*SA*, *SC* and *KC*). Indeed, *operando* XAS has been proven to be extraordinarily successful for investigating the atomic structure and oxidation state of heterogeneous catalysts under operative conditions and observing structure-activity correlations.[377–381] In particular, as detailed in Chapter 6.3.4, the impregnated samples into a capillary were placed in a capillary oven and first treated in a reducing atmosphere (TPR, discussed in Chapter 4.3) to obtain *in situ* the reduced samples. Subsequently, the reduced catalysts were flushed with reactive oxidative atmosphere and treated with two consecutive heating ramps, to test their catalytic activity in comparable transient conditions to those employed at the KIT laboratories.[xxxix] During catalytic testing, the Pd K-edge XAS spectrum of the samples was simultaneously acquired (*operando* measurements), and the relative percentage of PdO and Pd species as a function of temperature during CO oxidation was estimated through linear combination fitting of the XANES spectra (data analysis performed by Dr. Paolo Dolcet).

Figure 5.16 and Figure 5.17 show the CO conversion profile during the first and second catalytic cycles, respectively, together with the simultaneous evolution of the relative fraction of palladium species for the investigated samples. First of all, it was observed the comparability of the catalytic tests performed at KIT laboratories and at the beamline, as the light off temperatures estimated with the two setups were found to be in agreement, both in terms of absolute T_{50} values and in terms of relative activity of the samples, following the previously reported T_{50} trend SBA-15 d_{DFT} 7 nm < KIT-6 d_{DFT} 9 nm < SBA-15 d_{DFT} 9 nm. Interestingly, it was observed that the conversion of CO started when the formation of palladium oxide occurred: during the first light off (Figure 5.16, left), the oxidation of metallic palladium (blue lines), obtained from previous *in situ* TPR (discussed in Chapter 4.3), to palladium oxide (red lines) was evidenced, starting concurrently to the ignition of the CO conversion curve. Even though only a partial oxidation of Pd to PdO was observed at the end of the light off cycle (about 80-90 %), it was completed during the dwell step at

[xxxix] Since no significant difference in the catalytic performance of the catalysts between the second and third light offs was observed in laboratory testing (*i.e.* maximum T_{50} difference of 3 °C), two instead of three consecutive catalytic cycles were performed due to time constraints.

300 °C (5 minutes), *i.e.* before starting the cooling ramp (light out), for samples supported over SBA-15 silica, while about 20% of the palladium supported over KIT-6 mesoporous silica remained reduced. On the other hand, during the light out (Figure 5.16, right), in correspondence with the decrease of the conversion curve, a partial reduction of PdO to Pd was observed (about 15-20% of the total Pd species).

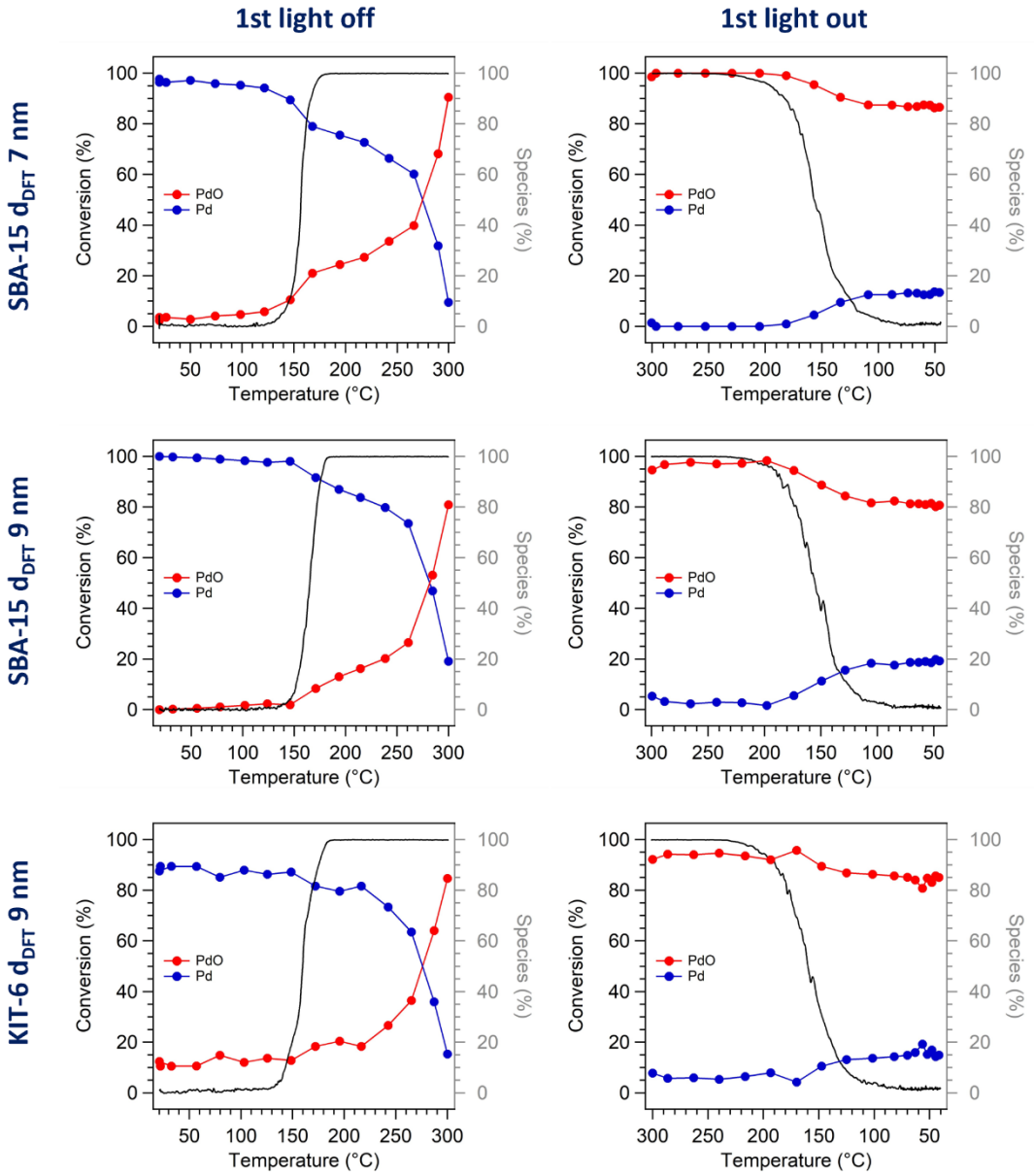

Figure 5.16 CO conversion profile during the first light off (**left**) and light out (**right**) of three different samples (*SAred*, *SCred* and *KCred*, **top**, **center** and **bottom**, respectively), compared with the evolution of the relative fraction of palladium species (Pd and PdO, blue and red curves, respectively) during catalytic activity, obtained by linear combination fitting of Pd K-edge XANES spectra

These findings were observed to be in agreement with the nowadays most accepted mechanism of CO oxidation catalyzed by supported Pd NPs: the Langmuir-Hinshelwood (LH) dual-site mechanism.[382–385] In particular, the LH reaction model foresees a first step of chemisorption of CO onto an adsorption site of the metallic surface of the catalyst, followed by the dissociative chemisorption of the O_2 molecule. Subsequently, the two chemisorbed

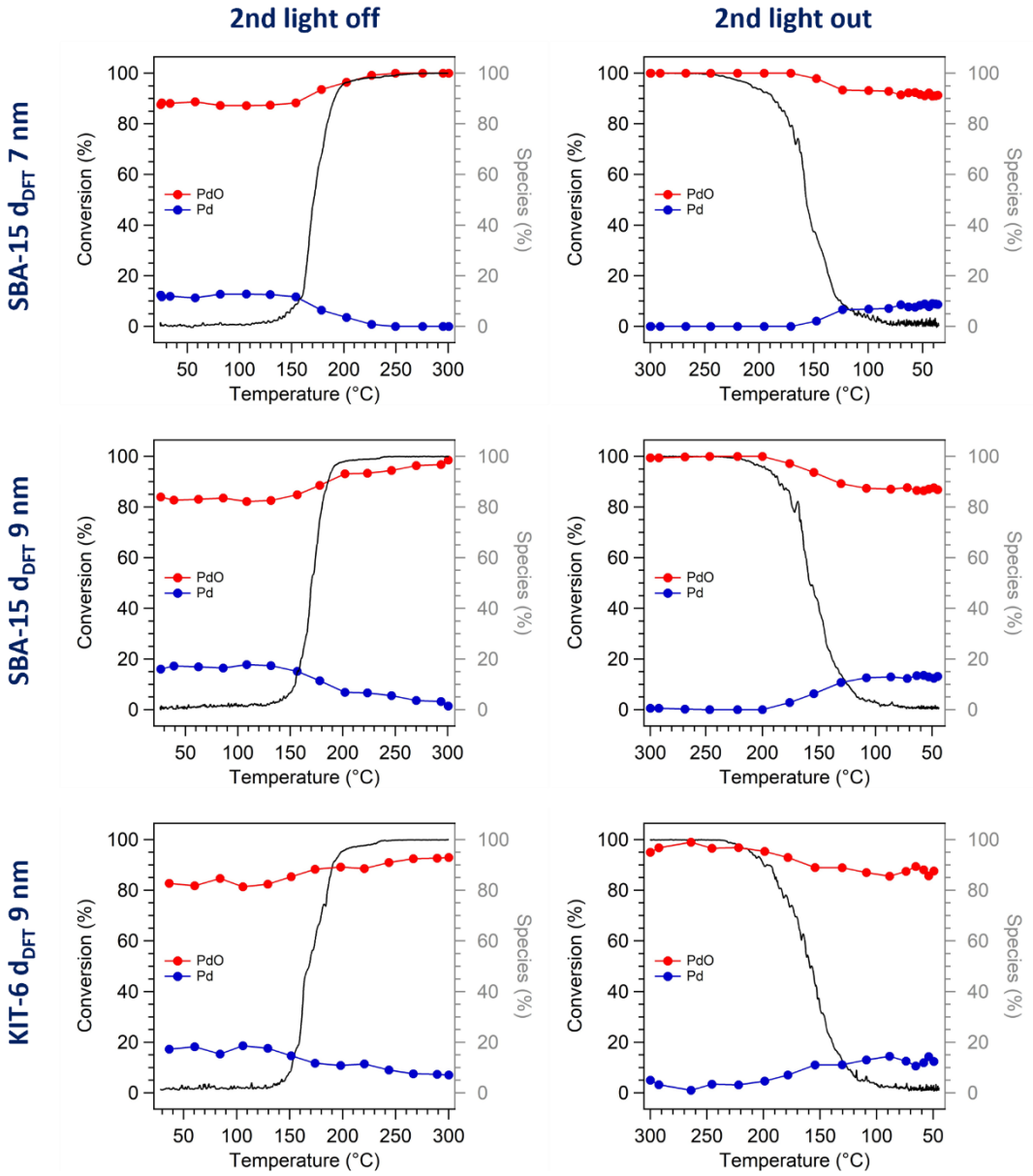

Figure 5.17 CO conversion profile during during the second light off (**left**) and light out (**right**) of three different samples (*SAred*, *SCred* and *KCred*, **top**, **center** and **bottom**, respectively), compared with the evolution of the relative fraction of palladium species (Pd and PdO, blue and red curves, respectively) during catalytic activity, obtained by linear combination fitting of Pd K-edge XANES spectra

species (CO and O) react on the metallic surface and produce CO_2, which eventually desorbs as product.[386] However, the mechanism of CO and O_2 adsorption was reported to be competitive, since the adsorption of CO on Pd sites is very strong and almost exclusive at low temperature, leaving no active sites for O_2 activation: as the temperature rises, O_2 adsorption and activation occur and CO oxidation reaction rate increases.[364] Thus, as demonstrated through spectroscopic studies and theoretical modeling,[387–389] during the ignition of the reaction, a transition from a CO-covered surface (self-poisoned) to a O-covered surface was reported, in agreement with the observed formation of (most likely superficial at the beginning of the conversion, then bulk) PdO concurrently with the starting conversion of CO to CO_2. On the contrary, during the extinction process, the reverse transition, *i.e.* from a O-covered surface to a CO-covered surface, occurs and a partial (likely superficial) reduction was observed.

During both light off and light out of the second catalytic cycle, shown in Figure 5.17, oxidized palladium PdO (red curves) was always the predominant species, and this accounted for the higher light off temperature observed during the second catalytic cycle with respect to the first one, *i.e.* lower catalytic activity, and was in agreement with laboratory setup results (*vide supra*). However, similar variations in the relative percentage of the species with respect to the first catalytic cycle were found: during the light off an increase in the PdO relative fraction was observed in correspondence to the start of CO conversion, while a partial reduction occurred during the light out step. In particular, after the second light out, a lower percentage of reduced Pd was observed with respect to the first light out, *i.e.* about 10% *vs* 15-20%. Relative percentages of palladium species at the beginning and end of each light off and light out are reported in Table B.14 in Appendix B.3.

III. Aging of catalysts. Finally, in order to verify if Pd NPs size, size distribution and distribution over silica supports underwent modifications as a consequence of the catalytic tests, the samples were characterized after complete catalytic cycles treatment by STEM at KNMF facility of KIT (Karlsruhe, Germany), in cooperation with Dr. Carina Maliakkal, who acquired STEM micrographs, and Dr. Di Wang. In particular, as Pd NPs and the inert silica support do not interact strongly, Pd NPs can migrate on the surface and sintering can occur at higher temperatures. A comparison of representative STEM micrographs of the samples after catalytic tests is reported in Figure 5.18, together with histograms showing the Pd NPs size distributions. The collected micrographs further confirmed the retention of the architecture of both parent mesoporous supports upon subsequent heating treatments up

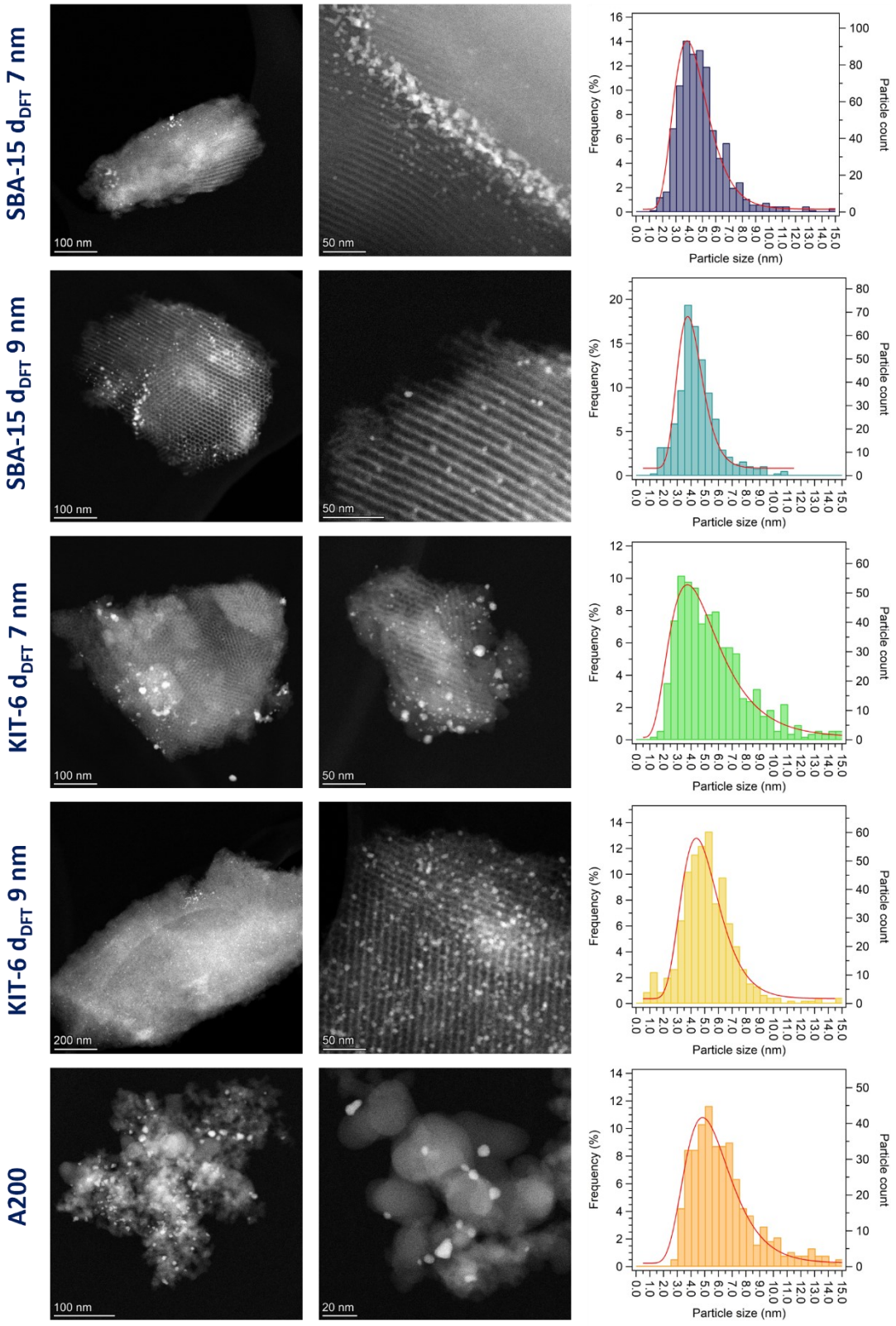

Figure 5.18 STEM micrographs of Pd NPs (brighter spots, as confirmed by EDX) supported on different silica supports after catalytic testing, and corresponding histograms reporting the Pd NPs size distribution

to 300 °C. However, the size and size distribution of Pd NPs, reported in Table 5.4, were found to be affected by the performed catalytic tests, as quite larger nanoparticles, with a broader size distribution with respect to those prior to catalytic tests (see Table 5.3) were observed. In particular, some larger Pd aggregates were found over KIT-6 d_{DFT} 7 nm, which was also the sample that displayed the poorest catalytic activity (*vide supra*), indicating quite bad stability of the catalyst nanoparticles. On the other hand, the catalyst supported over other mesoporous supports demonstrated a slighter increase in average Pd NPs size upon aging and under catalytic conditions.

Table 5.4 Mean nanoparticles size and polydispersion index (PDI) of Pd NPs supported on mesoporous and non-porous silica (*reduced* series) after catalytic testing, and their relative percentage increase with respect to the estimated values prior of catalytic tests

	Silica support	Sample name	Mean NPs size (nm)[a]	Increase in NPs size	PDI	Increase in PDI[b]
Mesoporous silica	SBA-15	SAred	5.0 ± 2.2	14 %	0.44	13 %
		SCred	4.5 ± 1.6	-	0.36	44 %
	KIT-6	KAred	5.7 ± 2.8	24 %	0.49	26 %
		KCred	5.2 ± 2.2	30 %	0.42	50 %
Non-porous silica	Aerosil 200	A200red	6.4 ± 2.4	19 %	0.38	-

[a] Calculated as $(d_{Pd\ post\ catalysis} - d_{Pd\ pre\ catalysis}) \cdot 100/d_{Pd\ pre\text{-}catalysis}$;
[b] Calculated as $(PDI_{Pd\ post\ catalysis} - PDI_{Pd\ pre\ catalysis}) \cdot 100/PDI_{Pd\ pre\text{-}catalysis}$

4.5 Conclusions

The synthesis of palladium nanoparticles in the confined space of 7 nm and 9 nm-sized mesopores of two families of mesoporous silica materials (SBA-15 and KIT-6), characterized by different pore arrangement and connectivity, as well as on the outer surface of a "batch" non-porous silica material, was investigated. In order to synthesize Pd NPs within the constrained environment of the porous systems, an incipient wetness impregnation approach was exploited, followed by a mild reduction step in a hydrogen/helium atmosphere at 150 °C. The impregnated samples were characterized by small-angle and wide-angle X-ray diffraction, and the retention of the mesoporous support architectures and the formation of palladium oxide NPs were observed, confirmed also by X-ray absorption spectroscopy. Moreover, nitrogen physisorption measurements demonstrated the partial clogging of SBA-15 parallel channels when employing the support with a smaller diameter (*i.e.* 7 nm). The reduction of PdO to Pd in hydrogen/helium atmosphere at 150 °C was followed *in situ* by TPR and *operando* XAS at the Soleil synchrotron (France), and the reflections of nanometric metallic Pd NPs were observed by XRD. The size, size distribution and distribution of Pd nanoparticles over mesoporous and non-porous silica samples was characterized by STEM analysis at KNMF of KIT (Germany), observing the formation of smaller Pd NPs (*i.e.* 4.0-4.8 nm) on mesoporous silica with respect to non-porous silica (*i.e.* 5.4 nm). Moreover, electron tomography demonstrated the effectiveness of the employed synthetic approach in confining the synthesis of Pd NPs within SBA-15 silica parallel cylindrical mesopores with a diameter of 9 nm and the more interconnected three-dimensional structure of KIT-6 mesoporous silica.

Finally, the functional properties of the synthesized samples were investigated: the catalytic activity of Pd NPs supported on mesoporous and non-porous silica samples for CO oxidation was tested at KIT laboratories and during *operando* XAS measurements at the synchrotron Soleil. Due to the interplay of multiple factors ruling the catalytic activity of the samples, such as Pd NPs size, size distribution, their location within the supports and possible sintering under catalytic conditions, palladium oxidation state, as well as mesopores diameter and connectivity, also influencing gaseous mixtures diffusion, no clear structure-activity correlation could be outlined, neither an effect of mesopores spatial confinement on functional properties could be identified. However, linear combination fitting of Pd K-edge *operando* XANES spectra during catalytic testing, allowing to correlate the catalytic

activity with palladium oxidation state, demonstrated that the catalytic process occurred through a Langmuir-Hinshelwood dual-site mechanism, involving the competitive adsorption of CO and O_2 on metallic Pd surface. The catalytic conversion of CO to CO_2 was observed to increase concurrently with the formation of (most likely superficial) PdO, subsequently reduced to metallic Pd during the light out step (*i.e.* cooling down), in agreement with literature reports.

5

Conclusions and perspectives

This Ph.D. Thesis aimed at experimentally investigate the crystallization of inorganic systems in confined spaces, and at evaluating the effect of space constraint on the synthetic outcome. In this Ph.D. Thesis, the crystallization of model inorganic systems in constrained environments was addressed with a systematic and comprehensive approach: the synthesis of different classes of inorganic materials, encompassing metal oxides (MoO_3 and undoped and Eu-doped $CaMoO_4$) and metal nanoparticles (Pd), was investigated in differently sized enclosed reactors, *i.e.* nanodroplets produced by water-in-oil miniemulsion, continuous-flow microreactor and nanopores of ordered mesoporous silica. The evaluation of the synthetic outcomes, in terms of crystal structure, particle size, size distribution, as well as functional properties (*i.e.* optical, catalytic), was performed by *ex situ* laboratory techniques and, in some cases, complemented by *in situ* time-resolved studies performed at synchrotron facilities, also combining different characterization techniques. For all the investigated systems, the confined space approaches proved to enable a more controlled synthesis of the addressed systems, with respect to the macroreactor approach, mostly in terms of size, morphology and aggregation of the obtained particles, as well as on functional properties, stoichiometry and doping effectiveness, as far as doped samples are concerned.

In particular, in Chapter 2 the synthesis of the metastable hexagonal polymorph of molybdenum(VI) oxide (h-MoO_3) was investigated within the confined space of inverse miniemulsion and in batch conditions; different reaction parameters were screened and their effect on crystallinity and morphology of h-MoO_3 was assessed. Smaller and more elongated nanorods with hexagonal section were obtained by miniemulsion approach with

respect to unconstrained batch one (XRD, TEM, SEM), proving the role of miniemulsion nanodroplets space confinement in determining size and shape of the synthesized inorganic systems. Moreover, the confined environment and peculiar properties of miniemulsion nanodroplets were demonstrated to strongly affect the crystallization of molybdenum oxide, promoting a non-classical crystallization pathway, as disclosed by an *in situ* time-resolved SAXS/WAXS study performed at the Elettra synchrotron. Finally, an investigation of the thermal evolution of h-MoO_3 synthesized via miniemulsion and batch approaches by combined XRD and XAS was carried out at Diamond Light Source, suggesting a role of the synthetic protocol on the structural transformation of the investigated samples.

The inverse miniemulsion approach employed for the synthesis of molybdenum oxide was then implemented for the synthesis of a related functional ternary oxide, calcium molybdate, both undoped and Eu-doped, discussed in Chapter 3. A strong effect of space confinement of inverse miniemulsion nanodroplets was observed on the size, size distribution and shape of $CaMoO_4$, obtaining nanoparticles with smaller crystallite size, NPs size and size distribution with a more regular shape *via* miniemulsion approach as compared to the batch one (XRD, TEM, SEM). The screening of the synthetic parameters evidenced different outcomes depending on the synthetic approach, indicating a different crystallization mechanism was likely involved when the syntheses were carried out in space constraint conditions. Finally, space confinement played a pivotal role in the doping process of calcium molybdate with Eu^{3+} ions, obtaining an effective doping and more homogeneous distribution of different amounts of dopant ions in the matrix with respect to the batch approach (XRD, Eu L_3-edge XAS, photoluminescence).

The synthesis of undoped and Eu-doped calcium molybdate was then implemented in microfluidic conditions, with the aim of exploring the manipulation of geometrically constrained fluids for the controlled synthesis of functional inorganic materials. A fine tuning of the viscosity and dielectric constant of the reaction medium, as well as of the solubility of $CaMoO_4$, through an intelligent variation of reaction parameters and the exploitation of the peculiarities of the microfluidic approach, enabled to obtained differently sized and shaped nano- to microstructures, obtained through oriented aggregation.

Finally, the highly constrained volume of the nanosized pores of mesoporous silica was explored as reaction environment for the synthesis of supported palladium nanoparticles, and their possible application as heterogeneous catalysts for CO oxidation was investigated (Chapter 4). In particular, Pd NPs were synthesized within differently sized (*i.e.* different constrained conditions) nanopores of two families of mesoporous silica, characterized by different pore arrangement and connectivity, as well as on the outer surface of a "batch" non-porous silica material. The mesoporous matrices allowed to obtain slightly smaller and quite homogeneously distributed Pd NPs with respect to non-porous support (STEM), and their actual location within the constrained environment of mesopores was confirmed by electron tomography. Finally, the functional properties of the samples as heterogeneous catalysts for CO oxidation were tested at Karlsruhe Institute of Technology and during *operando* Pd K-edge XAS measurements at the Soleil synchrotron, that allowed to correlate the catalytic activity of the samples with palladium oxidation state.

In summary, this dissertation work demonstrated the remarkable effects and potentialities of confining inorganic syntheses in differently sized enclosed volumes, from thousands of micrometers to few nanometers, and their applicability in a great variety of materials, encompassing different classes of crystalline inorganic compounds, characterized by different chemistries. Moreover, the synergy of different analytical techniques, also employing *in situ*/*operando* time-resolved methods, was found to be crucial to allow a complete characterization of the systems, as well as to disclose some insights on the effects of space confinement on the crystallization pathways of the investigated systems. The evidences so far collected disclosed interesting perspectives for future developments, in particular a more detailed investigation of the non-classical crystallization pathways observed in confined space.

As exciting inorganic synthesis in confined spaces can be from a fundamental point of view of understanding molecular behavior, reaction pathways and crystallization in constrained environments, it is noteworthy to mention that the industrial potential of the investigated synthetic approaches is not equally interesting, since they display significant differences, and certainly not completely flawless. Indeed, from a scalability point of view, the inverse miniemulsion method shows evident limitations, such as demanding workup of the product, abundant use and waste of organic solvent and homogenization issues as far as processing large amounts of liquids is concerned. On the other hand, the industrial application of the

microfluidic approach appears more promising, thanks to the facile synthesis scale up by the numbering up concept and the absence of any ligand and/or surfactant requiring sample purification, but possible clogging issues must be tackled. Finally, the investigated impregnation of mesoporous silica with Pd(II) could be industrially implemented employing automatized setups, though possible issues in synthesis reproducibility and Pd distribution homogeneity should be carefully addressed.

Although several issues may be encountered in industrial application of the confined space approaches investigated in this Ph.D. Thesis, the promising and extensive results disclosed by confining inorganic syntheses in differently sized enclosed volumes, in terms of thorough investigation and fine control on reaction pathways, could represent a significant step towards a more comprehensive understanding of one of the most complex and fascinating, yet not fully rationalized, topics in chemistry: the crystallization.

6

Experimental details

In this Chapter, the experimental details of all the syntheses that were carried out with different synthetic approaches are explained in detail, including the chemicals employed, the experimental procedures, and the experimental setups employed.

6.1 Synthesis of molybdenum oxide

6.1.1 Chemicals

The reagents employed for the synthesis of molybdenum oxide are listed in Table 7.1. All the chemicals were analytical grade and used as received without any further purification.

Table 7.1 Employed chemicals for the synthesis of MoO_3

Name	Formula	Molecular weight (g/mol)	CAS number	Supplier
Ammonium heptamolybdate tetrahydrate	$(NH_4)_6Mo_7O_{24}{\cdot}4H_2O$	1235.86	12054-85-2	Alfa-Aesar
Cyclohexane	C_6H_{12}	84.16	110-82-7	Sigma-Aldrich
Nitric acid[a]	HNO_3	63.01	7697-37-2	Sigma-Aldrich
Span80	$C_{24}H_{44}O_6$	428.62	1338-43-8	Sigma-Aldrich
PGPR	$(C_3H_5O_2)_n(C_{18}H_{32}O_2)_m$	-	29894-35-7	Palsgaard

[a] 65 wt%

6.1.2 Batch synthesis

The synthesis of molybdenum oxide by batch approach was carried out by dropwise addition of an excess of concentrated nitric acid (65 wt%, 14.0 M) to an aqueous solution of ammonium heptamolybdate (AHM), until the pH became lower than 1, under mechanical stirring and at room temperature. Different concentrations of the precursor solution were screened (0.10, 0.15, 0.20, 0.25 M), as well as different AHM:HNO_3 molar ratios (1:10, 1:15, 1:20, 1:25 mol). A white precipitate was immediately formed, and the suspension was left stirring for 24 hours, otherwise specifically stated (intermediate reaction times of 5 minutes, 6 hours and 18 hours were investigated). The precipitate was then isolated and purified by centrifugation with deionized water (12000 rpm for 5 min), dried under vacuum at room temperature and finely ground for analyses.

All the molybdenum oxide (MO) samples synthesized by batch (b) approach are listed in Table 7.2, together with their experimental synthetic conditions.

Table 7.2 Molybdenum oxide samples synthesized by batch approach

Sample name	Conc. of AHM solution (M)	AHM:HNO_3 mol	US after acid addition	Reaction time
MO01-b	0.10	1:10	-	24 h
MO02-b	0.15	1:10	-	24 h
MO03-b	0.20	1:10	-	24 h
MO04-b	0.25	1:10	-	24 h
MO05-b	0.20	1:15	-	24 h
MO06-b	0.20	1:20	-	24 h
MO07-b	0.20	1:25	-	24 h
MO08-b	0.20	1:10	Yes	24 h
MO09-b	0.20	1:10	-	5 min
MO10-b	0.20	1:10	-	6 h
MO11-b	0.20	1:10	-	18 h

6.1.3 Synthesis in miniemulsion droplets

The synthesis of molybdenum oxide by miniemulsion approach was carried out by employing a Sartorius Stedim LabsonicP homogenizer, mounting a 3 mm titanium tip, and operating at 24 kHz, with a 0.9 s pulse and at amplitude of 70 %, corresponding to an acoustic power of 280 W. A starting mixture containing the molybdenum precursors was prepared by mixing an aqueous solution of ammonium heptamolybdate (AHM) to a solution of 1.5 wt% Span80 in cyclohexane, to achieve the weight ratio between the aqueous to oil phases of 1:3. Different concentrations of the precursor solution were screened (0.10, 0.15, 0.20, 0.25 M). Eventually, the mixture was homogenized by ultrasonication until a white turbid miniemulsion was obtained (2-3 minutes). To the as prepared miniemulsion, an excess of concentrated nitric acid (65 wt%, 14.0 M) was added dropwise, screening different AHM:HNO_3 molar ratios (1:10, 1:15, 1:20, 1:25 mol). After acid addition, a further ultrasonication (280 W, 0.9 s pulse, 2 min) of the reaction mixture was carried out. A series of syntheses in which this last synthetic step was not performed was also carried out (see Table 7.3). The resulting mixture was allowed to stand at room temperature for 24 hours, otherwise specifically stated (intermediate reaction times of 5 minutes, 6 hours and 18 hours were investigated), after which the miniemulsion was coagulated with acetone. The precipitate was then isolated and purified by centrifugation with acetone and deionized water (12000 rpm for 5 min), dried under vacuum at room temperature and finely ground for analyses.

All the molybdenum oxide (MO) samples synthesized by miniemulsion (me) approach are listed in Table 7.3, together with their experimental synthetic conditions.

Table 7.3 Molybdenum oxide samples synthesized by miniemulsion approach

Sample name	Conc. of AHM solution (M)	AHM:HNO_3 mol	US after acid addition	Reaction time
MO01-me	0.10	1:10	Yes	24 h
MO02-me	0.15	1:10	Yes	24 h
MO03-me	0.20	1:10	Yes	24 h
MO04-me	0.25	1:10	Yes	24 h
MO05-me	0.20	1:15	Yes	24 h
MO06-me	0.20	1:20	Yes	24 h
MO07-me	0.20	1:25	Yes	24 h
MO08-me	0.20	1:10	-	24 h
MO09-me	0.20	1:20	-	24 h
MO10-me	0.20	1:20	-	48 h
MO11-me	0.20	1:10	Yes	5 min
MO12-me	0.20	1:10	Yes	6 h
MO13-me	0.20	1:10	Yes	18 h
MO14-me	0.20	1:10	-	5 min
MO15-me	0.20	1:10	.	6 h
MO16-me	0.20	1:10	-	18 h

6.1.4 *In situ* time-resolved simultaneous SAXS/WAXS experiments

The *in situ* time-resolved simultaneous SAXS/WAXS study was performed at the Austrian SAXS beamline at Elettra Sincrotrone (Trieste), in cooperation with the beamline scientists Prof. Heinz Amenitsch and Dr. Barbara Sartori (Graz University of Technology, Austria). The Ph.D. candidate wrote the proposal of the experiment, planned and participated in the beamtime (beamtime 20192141, 22-28/07/2020).

A continuous-flow setup was built at the beamline in order to follow *in situ*, in a time-resolved fashion, the evolution of the species occurring during the synthesis of molybdenum(VI) oxide by both batch and miniemulsion approaches (details of the

syntheses in Chapter 6.1.2 and Chapter 6.1.3, respectively). In particular, a reaction vessel equipped with an external jacket connected to a circulating water bath was employed to keep the reaction mixture cooled (temperature of about 20 °C). The reaction mixture, vigorously stirred, was funneled through a continuous-flow equipment (Viton® tubing, i.d. 3 mm, wall th. 1 mm) with the aid of a peristaltic pump (Ismatec MCP) into a quartz capillary (o.d. 1.5 mm) mounted in the beamline, where SAXS and WAXS profiles were acquired simultaneously every 10 s, as detailed *infra*. The total residence time in the flow system was 7 s. Inverse miniemulsions were produced at the beamline using a remotely controlled Sartorius Stedim LabsonicP homogenizer (US: 2 min, 280 W, 0.9 s pulse). Nitric acid was injected into the reaction mixture by using a remotely controlled syringe pump (Harvard PHD 4400) with a flow rate of 1 mL min^{-1}. A schematic representation of the continuous-flow setup employed is reported in Figure 7.1 and images are shown in Figure 7.2, top. The evolution of the scattering profile of the reaction mixtures was followed starting from 40 s before miniemulsion production (for ME series of experiments) or 40 s before acid injection (for batch series of experiments). For either case, the start of acid injection was set as t = 0 s and the evolution of the scattering profile was followed up to 1-3 hours, depending on the observed variations of patterns features.

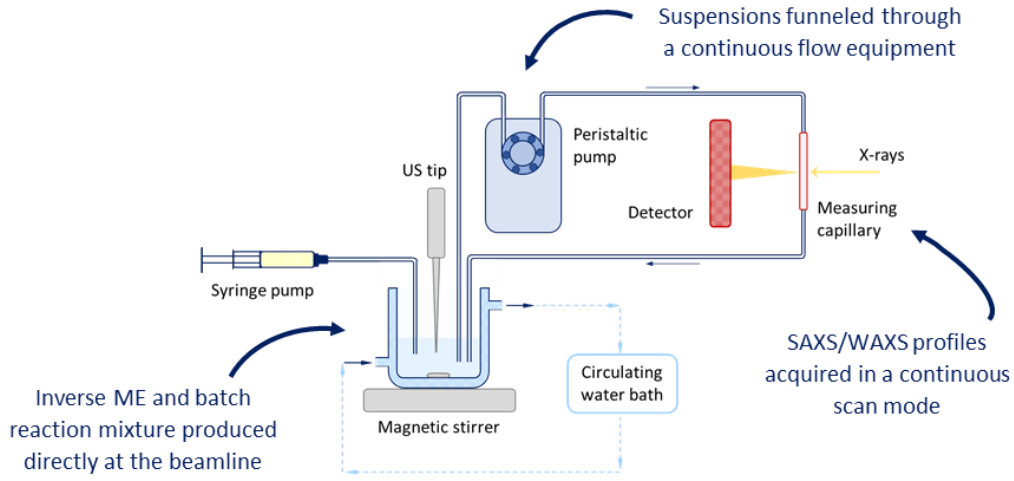

Figure 7.1 Schematic representation of continuous-flow setup built at the SAXS beamline at Elettra Sincrotrone Trieste for the *in situ* time-resolved SAXS/WAXS study of MoO_3 synthesis

Simultaneous SAXS and WAXS measurements were performed by setting the energy of the X-rays to 8 keV, corresponding to a wavelength of 1.54 Å (*i.e.* equivalent to Cu K_α radiation), by employing a Si(111) monochromator, and focusing the beam with a double toroidal

mirror on the measuring quartz capillary. SAXS profiles were collected with a 10 s time step, with an acquisition time of 8 s, by employing a 2D Pilatus3 1M detector, positioned after a vacuum flight tube with a length of 1 m. The collected bi-dimensional patterns were azimuthally and radially integrated into one-dimensional plots of the scattering function, $I(q)$ *vs* q ($q = 4\pi\, sin\theta/\lambda = 2\pi/d$, where λ is the wavelength and 2θ is the scattering angle). The final reciprocal space window available ranged from 0.1 to 7.1 nm^{-1} (*i.e.* 0.1-10.0° 2θ).[xl] Silver behenate (*d*-spacing = 5.84 nm) was used as a standard to calibrate the angular scale of the measured intensity. WAXS profiles were collected simultaneously with a 2D Pilatus 100k detector, positioned with a tilting of approx. 30° with respect to the vertical axis, to result in an accessible q-range of 13.4-23.9 nm^{-1} (*i.e.* 19-34° 2θ). The reference pattern of p-bromobenzoic acid was collected to calibrate the *q*-scale for the WAXS regime. All the data were corrected for fluctuations of the primary intensity and the corresponding background (*i.e.* either water or cyclohexane for batch and miniemulsion syntheses, respectively) was subtracted from each scattering pattern. The geometry of SAXS and WAXS profiles acquisition is shown in Figure 7.2, bottom.

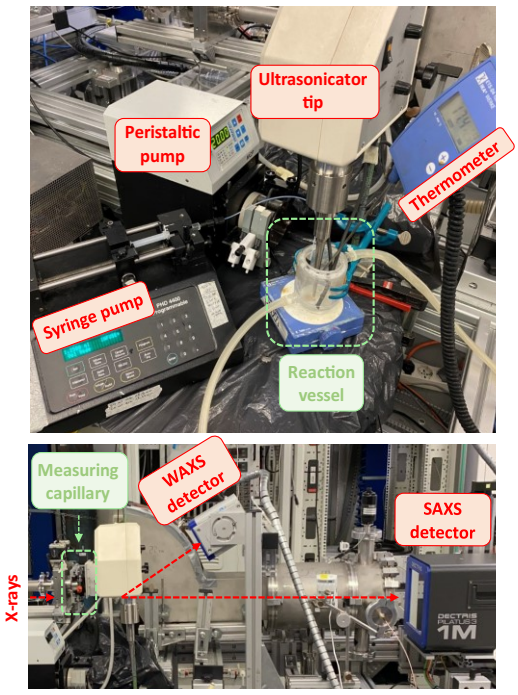

Figure 7.2 Experimental setup for the *in situ* time-resolved SAXS/WAXS study of MoO_3 synthesis performed at the SAXS beamline at Elettra Sincrotrone Trieste

[xl] The resolution of the collected data can be calculated as $d_{min} = \pi/q_{max}$ and $d_{max} = \pi/q_{min}$,[267] so it falls in the range 0.4-30 nm.

6.1.5 *In situ* XRD and combined XAS/XRD experiments

The systematic *in situ* study of the structural evolution of h-MoO_3 to α-MoO_3 upon thermal treatment in air was carried out by both laboratory XRD and synchrotron-based combined XAS/XRD.

In situ thermal XRD was performed at Department of Geosciences (University of Padova), in cooperation with Dr. Federico Zorzi and Prof. Fabrizio Nestola. XRD patterns were collected on powders using a Panalytical θ-θ diffractometer equipped with a Co anode (λ = 1.79026 Å). Samples were placed on a platinum heating filament and heated in air over the range 25-460 °C (60 °C min^{-1}). XRD patterns as a function of temperature were collected stepwise and isothermally (temperature steps: room temperature (RT), 100, 200, 250, 260, 270, 300, 320, 340, 360, 380, 400, 420, 440, 460 °C and, after cooling down, RTpost), acquiring four repeated scans in 1 hour in the 5°-75° 2θ range at each temperature step.

In situ combined XAS/XRD experiments as a function of temperature were performed at the B18 beamline of Diamond Light Source, Didcot (UK), at the Mo K-edge (20000 eV), in cooperation with Dr. Paolo Dolcet (Karlsruhe Institute of Technology, Karlsruhe, Germany). The Ph.D. candidate wrote the proposal of the experiment and participated in the beamtime (beamtime SP23804, 31/01-03/02/2020). XAS and XRD data were collected stepwise and isothermally by placing a pelleted sample (boron nitride was employed as a binder) in a pellet furnace and heating in air from room temperature up to 500 °C (heating rate 10 °C min^{-1}), in a stepwise fashion (*vide infra*). XAS spectra were collected in the range 19800-20840 eV in transmission mode. A Si(111) monochromator was employed for energy selection. Diffractograms were collected immediately before each XAS spectrum at an energy of 19800 eV (below the adsorption edge, corresponding to λ = 0.6262 Å) with a six-element modular Mythen detector in the angular range 13-21° 2θ, corresponding to the angular range 38-63° 2θ using the radiation generated by a Co anode (λ = 1.79026 Å). Three to ten repeated scans (60 seconds each) were acquired, depending on the observed evolution of XAS spectra and XRD patterns. A schematic representation of the acquisition mode employed for the combined XAS/XRD acquisitions is shown in Figure 7.3. The studied temperature steps were RT, 50, 100, 150, 200, 220, 240, 260, 280, 300, 320, 340, 360, 380, 400, 420, 440, 460, 480, 500 °C and, after cooling down, RT post.

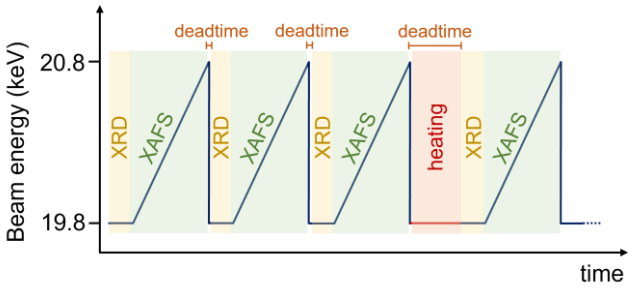

Figure 7.3 Schematic representation of the acquisition mode of combined XAS spectra and XRD patterns for the *in situ* thermal evolution study of MoO_3 at the B18 beamline at Diamond Light Source. For clarification: i) three to ten repetitions of isothermal XRD and XAS acquisition (herein three repetitions are represented), ii) heating step, iii) repeated XRD/XAS acquisitions at higher temperature, and so on

6.2 Synthesis of undoped and Eu(III)-doped calcium molybdate

6.2.1 Chemicals

The reagents employed for the synthesis of undoped and Eu(III)-doped calcium molybdate are listed in Table 7.4. All the chemicals were analytical grade and used as received without any further purification.

Table 7.4 Employed chemicals for the synthesis of undoped and Eu(III)-doped $CaMoO_4$

Name	Formula	Molecular weight (g/mol)	CAS number	Supplier
Calcium nitrate tetrahydrate	$Ca(NO_3)_2{\cdot}4H_2O$	236.15	13477-34-4	Carlo Erba
Cyclohexane	C_6H_{12}	84.16	110-82-7	Sigma-Aldrich
Ethanol	CH_3CH_2OH	46.07	64-17-5	Carlo-Erba
Europium nitrate pentahydrate	$Eu(NO_3)_3{\cdot}5H_2O$	428.06	63026-01-7	Sigma-Aldrich
Sodium hydroxide	NaOH	40.00	1310-73-2	VWR
Sodium molybdate dihydrate	$NaMoO_4{\cdot}2H_2O$	241.95	10102-40-6	Alfa Aesar
Span80	$C_{24}H_{44}O_6$	428.62	1338-43-8	Sigma-Aldrich

6.2.2 Batch synthesis

The synthesis of undoped calcium molybdate in batch conditions was carried out by dropwise addition of an aqueous solution of calcium nitrate to an aqueous solution of sodium molybdate (Ca^{2+}:MoO_4^{2-} 1:1 mol), under mechanical stirring and at room temperature. Different concentrations of precursors solutions (0.15, 0.20, 0.25, 0.50, 1.0, 1.5, and 2.0 M) and different pH values of the molybdate precursor solution (6.5, *i.e.* autogenous, 9, 11, and 13) were screened. A white precipitate was immediately formed, and the suspension was left stirring for 24 hours. The precipitate was then isolated and purified by centrifugation with deionized water (12000 rpm for 5 min), dried under vacuum at room temperature and finely ground for analyses.

The synthesis of Eu(III)-doped calcium molybdate was carried out as described above, adding a stoichiometric amount of europium nitrate to the Ca^{2+} precursor solution. The molar ratio between (Ca^{2+} and Eu^{3+}) and MoO_4^{2-} was kept at 1:1 mol. The doping percentage, calculated as Eu/Mo molar ratio, was varied between 1 and 7 at% (1, 3, 5, and 7 at%).

All the calcium molybdate (CM) samples synthesized by batch (b) approach are listed in Table 7.5, together with their experimental synthetic conditions.

Table 7.5 Undoped and Eu(III)-doped calcium molybdate samples synthesized by batch approach

Sample name	Conc. of precursors solutions (M)	$[MoO_4]^{2-}_{aq}$ solution pH	Doping percentage (at%)
CM02-b	0.15	6.5	0
CM01-b	0.20	6.5	0
CM03-b	0.25	6.5	0
CM04-b	0.50	6.5	0
CM05-b	1.0	6.5	0
CM06-b	1.5	6.5	0
CM07-b	2.0	6.5	0
CM08-b	0.20	9	0
CM09-b	0.20	11	0
CM10-b	0.20	13	0
Eu1CM-b	0.20	6.5	1
Eu3CM-b	0.20	6.5	3
Eu5CM-b	0.20	6.5	5
Eu7CM-b	0.20	6.5	7

6.2.3 Synthesis in miniemulsion droplets

The synthesis of calcium molybdate by miniemulsion approach was carried out by employing a Sartorius Stedim LabsonicP homogenizer, mounting a 3 mm titanium tip, and operating at 24 kHz, with a 0.9 s pulse and at amplitude of 70 %, corresponding to an acoustic power of 280 W. Two starting mixtures of the precursors, A and B, were prepared by mixing an aqueous solution of the precursor (either calcium nitrate or sodium molybdate, respectively) to a solution of 1.5 wt% Span80 in cyclohexane, to achieve the weight ratio between the aqueous to oil phases of 1:3. Different concentrations of precursors solutions (0.15, 0.20, 0.25, 0.50, 1.0, 1.5, and 2.0 M) and different pH values of the molybdate precursor solution (6.5, *i.e.* autogenous, 9, 11, and 13) were screened. Both mixtures A (containing MoO_4^{2-} precursor) and B (containing Ca^{2+} precursor) were homogenized separately by ultrasonication until white turbid miniemulsions A' and B' were obtained. The as prepared miniemulsions A' and B' were mixed together (Ca^{2+}:MoO_4^{2-} 1:1 mol) and ultrasonicated again for 2 minutes, with unchanged amplitude. The resulting mixture was allowed to stand at room temperature for 24 hours, after which the miniemulsion was coagulated with acetone. The precipitate was then isolated and purified by centrifugation with acetone and deionized water (12000 rpm for 5 min), dried under vacuum at room temperature and finely ground for analyses.

The synthesis of Eu(III)-doped calcium molybdate was carried out as described above, adding a stoichiometric amount of europium nitrate to the Ca^{2+} precursor solution. The molar ratio between (Ca^{2+} and Eu^{3+}) and MoO_4^{2-} was kept at 1:1 mol. The doping percentage, calculated as Eu/Mo molar ratio, was varied between 1 and 7 at% (1, 3, 5 and 7 at%).

All the calcium molybdate (CM) samples synthesized by miniemulsion (me) approach are listed in Table 7.6, together with their experimental synthetic conditions.

Table 7.6 Undoped and Eu(III)-doped calcium molybdate samples synthesized by miniemulsion approach

Sample name	Conc. of precursors solutions (M)	$[MoO_4]^{2-}_{aq}$ solution pH	Doping percentage (at%)
CM02-me	0.15	6.5	0
CM01-me	0.20	6.5	0
CM03-me	0.25	6.5	0
CM04-me	0.50	6.5	0
CM05-me	1.0	6.5	0
CM06-me	1.5	6.5	0
CM07-me	2.0	6.5	0
CM08-me	0.20	9	0
CM09-me	0.20	11	0
CM10-me	0.20	13	0
Eu1CM-me	0.20	6.5	1
Eu3CM-me	0.20	6.5	3
Eu5CM-me	0.20	6.5	5
Eu7CM-me	0.20	6.5	7

6.2.4 Microfluidic synthesis

The microfluidic syntheses of undoped and Eu(III)-doped calcium molybdate were carried out with either the continuous-flow Setup A or B (schematic representation in Figure 7.4). Setup A was built by using two syringe pumps (New Era Pump System, Inc.), a home-made T-shaped PEEK micromixer and Teflon tubes[xli] with a diameter of 0.8 mm (Setup A, Figure 7.4 top). Setup B was built by employing three syringe pumps (New Era Pump System, Inc.), two home-made T-junction mixers and Teflon tubes with a diameter of 0.80 mm (Setup B, Figure 7.4 bottom).

[xli] Teflon tubes were chosen as microfluidic reactor since they are considered to be non-nucleating surfaces for syntheses performed in polar solvents, *i.e.* not allowing heterogeneous nucleation on their surface,[16] as discussed in Chapter 1.1.1.

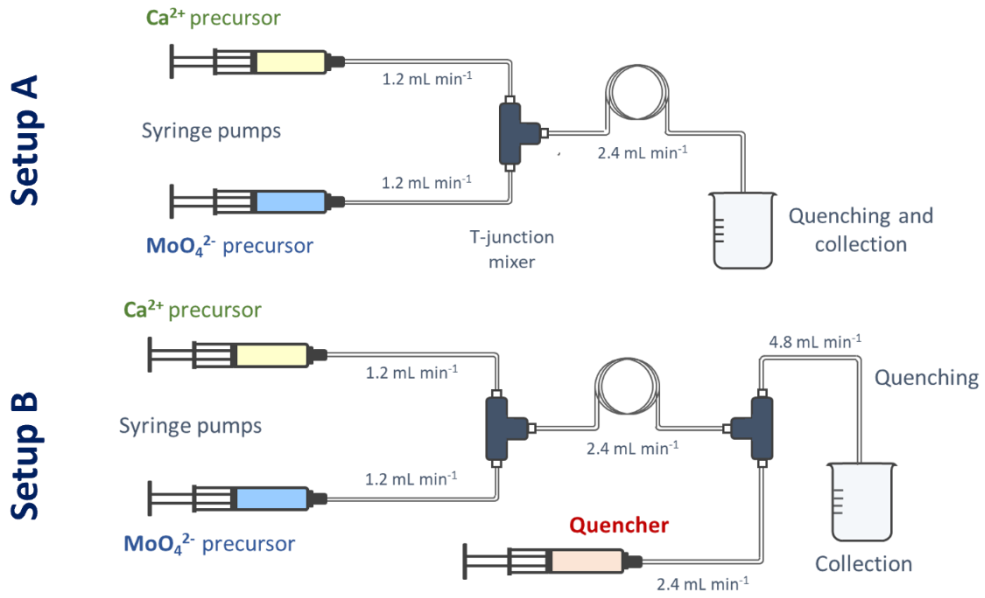

Figure 7.4 Schematic representation of the two microfluidic setups (Setup A, **top** and Setup B, **bottom**) employed for the synthesis of undoped and Eu-doped calcium molybdate

Calcium nitrate and sodium molybdate (pH > 6) were employed as precursors: their solutions in ethanol and milliQ water mixture and equal concentration were separately pumped into the reactor with equal flow rate (1.2 mL min^{-1}), to ensure a constant molar ratio of reactants of 1:1. The resulting suspension was collected and quenched in a vessel containing an excess of volume of solvent. The length of the Teflon tube after the T-junction mixer was set to 165 cm, resulting in a residence time of 20.7 s.

A systematic variation of the synthetic parameters was carried out, screening the effect of i) the concentration of precursors solutions (0.02 and 0.05 M), ii) the relative amount of ethanol into the solvent (20, 30, and 50 wt% EtOH/H_2O), iii) the temperature (ambient temperature and –4 °C), and iv) the method of quenching (quenching by dilution in solvent mixture or dilution in ethanol, acting as non-solvent). The syntheses carried out at –4 °C were performed by placing the entire microfluidic setup and the collecting vessel in a 3.5 wt% NaCl/ice bath, resulting in a temperature of –4 °C.

The synthesis of Eu(III)-doped calcium molybdate (doping percentage of 3 at%, calculated as Eu/Mo molar ratio) was carried out as described above, adding a stoichiometric amount of europium nitrate to the Ca^{2+} precursor solution. The molar ratio between (Ca^{2+} and Eu^{3+})

and MoO_4^{2-} was kept at 1:1 mol. The sets of synthetic conditions employed for the synthesis of Eu(III)-doped calcium molybdate by microfluidics were the following:

iv) Setup A at ambient temperature, with 50 wt% EtOH/H_2O as solvent mixture and quenching the product by dilution with an excess of ethanol in the collecting vessel (sample *EuCM01-mf*);

v) Setup A at –4 °C, with 50 wt% EtOH/H_2O as solvent mixture and quenching the product by dilution with an excess of ethanol in the collecting vessel kept in the –4 °C cold bath (sample *EuCM02-mf*);

vi) Setup B at ambient temperature, with 50 wt% EtOH/H_2O as solvent mixture and quenching in line the product by dilution in ethanol (sample *EuCM03-mf*).

The precipitates obtained with every screened set of reaction conditions in the collecting vessel were then isolated and purified by centrifugation with acetone and deionized water (15000 rpm for 5 min), dried under vacuum at room temperature and finely ground for analyses.

All the calcium molybdate (CM) samples synthesized by microfluidic (mf) approach are listed in Table 7.7, together with their experimental synthetic conditions.

Table 7.7 Undoped and Eu(III)-doped calcium molybdate samples synthesized by microfluidic approach

Sample name	Setup	EtOH wt% in solvent	Conc. of prec. sol. (M)	Temperature (°C)	Quenching method	Doping percentage (at%)
CM01-mf	A	20	0.02	25	EtOH/H_2O	0
CM02-mf	A	30	0.02	25	EtOH/H_2O	0
CM03-mf	A	50	0.02	25	EtOH/H_2O	0
CM04-mf	A	20	0.05	25	EtOH/H_2O	0
CM05-mf	A	30	0.05	25	EtOH/H_2O	0
CM06-mf	A	50	0.05	25	EtOH/H_2O	0
CM07-mf	A	20	0.05	–4	EtOH/H_2O	0
CM08-mf	A	30	0.05	–4	EtOH/H_2O	0
CM09-mf	A	50	0.05	–4	EtOH/H_2O	0
CM10-mf	A	20	0.05	25	EtOH	0
CM11-mf	A	30	0.05	25	EtOH	0
CM12-mf	A	50	0.05	25	EtOH	0
CM13-mf	A	20	0.05	–4	EtOH	0
CM14-mf	A	30	0.05	–4	EtOH	0
CM15-mf	A	50	0.05	–4	EtOH	0
CM16-mf	A	20	0.05	–4	-	0
CM17-mf	A	30	0.05	–4	-	0
CM18-mf	A	50	0.05	–4	-	0
CM19-mf	B	20	0.05	25	EtOH/flux	0
CM20-mf	B	30	0.05	25	EtOH/flux	0
CM21-mf	B	50	0.05	25	EtOH/flux	0
EuCM01-mf	A	50	0.05	25	EtOH	3
EuCM02-mf	A	50	0.05	-4	EtOH	3
EuCM03-mf	B	50	0.05	25	EtOH/flux	3

6.3 Synthesis of palladium nanoparticles on mesoporous and non-porous silica

6.3.1 Chemicals

The reagents employed for the synthesis of palladium nanoparticles on mesoporous and non-porous silica supports are listed in Table 7.8. All the purchased chemicals were analytical grade and used as received without any further purification. Mesoporous silica supports were prepared by the Ph.D. student S. Claas (workgroup of Prof. M. Fröba, University of Hamburg, Germany), following well-established soft templating synthetic protocols.

Table 7.8 Employed chemicals for the synthesis of Pd@SiO_2

Name	Formula	Molecular weight (g/mol)	CAS number	Supplier
Palladium nitrate hydrate	$Pd(NO_3)_2 \cdot xH_2O$	266.46[a]	10102-05-3	Sigma-Aldrich
Mesoporous silica	SiO_2	60.08	-	Synthesis
Aerosil 200	SiO_2	60.08	112945-52-5	Degussa GmbH
Hydrogen	H_2	2.02	1333-74-0	Alphagaz
Helium	He	4.00	7440-59-7	Alphagaz

[a] x = 2 was assumed

6.3.2 Synthesis of palladium nanoparticles

Mesoporous silica supports (two SBA-15 and two KIT-6 mesoporous silica samples, with pore size of 7 and 9 nm) were synthesized and provided by the workgroup of Prof. Michael Fröba (University of Hamburg); Aerosil® 200 (Degussa GmbH) was employed as non-porous silica support (*pristine* series).

Palladium nanoparticles were synthesized directly into the pores of mesoporous and non-porous silica, through two subsequent cycles of *incipient wetness impregnation* (IWI) followed by slow and controlled drying at 50 °C for 18 hours. More specifically, a milliQ water solution of palladium nitrate was added to the pristine silica material, with a

volume equal to the total pore volume of the support to be filled (determined by nitrogen physisorption measurements) and a concentration such as to obtain a final stoichiometry of 2 wt% Pd@SiO_2, after two subsequent cycles of IWI (see Table 7.9). By the IWI technique, the Pd(II) solution is entirely drawn into the pores by capillary forces and theoretically no precursor material is deposited on the outer surface of the support. For the batch non-porous silica sample, the volume of $Pd(NO_3)_2$ impregnation solution could not be determined based on the volume of pores to be filled, as for mesoporous samples. Thus, the synthesis was performed by employing a volume and concentration of $Pd(NO_3)_2$ impregnation solution equal to the ones employed with the mesoporous sample with the lowest pore volume (sample KA, see Table 7.9). The as-prepared samples are referred to as *impregnated* series.

Table 7.9 Experimental conditions employed for the impregnation of mesoporous and non-porous silica with 2 wt% of Pd

	Sample name	Specific V_{pores} (cm^3/g)	m SiO_2 (g)	Total V_{pores} (cm^3)	Pd loading wt% [a]	Conc $Pd(NO_3)_2$ solution (M)	V $Pd(NO_3)_2$ solution (mL) [b]
Mesoporous silica	SA	0.985	0.980	0.965	1	0.097	0.965
	SC	1.322	0.980	1.296	1	0.073	1.296
	KA	0.905	0.980	0.887	1	0.106	0.887
	KC	1.497	0.980	1.467	1	0.064	1.467
Non-porous silica	A200	-	0.980	-	1	0.106	0.887

[a] Pd loading per impregnation step. After two IWI cycles (*i.e.* impregnation and drying), the final Pd loading is 2 wt%; [b] Volume of $Pd(NO_3)_2$ solution added per impregnation step

The impregnated samples were then treated at 150 °C in reducing atmosphere (5 % vol. H_2/He, total flow 100 mL min^{-1}) for 30 minutes in a tubular furnace (Gero), in order to mildly reduce the impregnated Pd(II) precursor to Pd(0) (*reduced* series). The reduction of the as-prepared, impregnated samples was performed at ITCP-KIT (Karlsruhe, Germany), in collaboration with the workgroup of Prof. Jan-Dierk Grunwaldt.

6.3.3 Catalytic tests

The catalytic activity of the synthesized Pd NPs on mesoporous and non-porous silica for CO oxidation was investigated in collaboration with Dr. Paolo Dolcet and Dr. Maria Casapu (workgroup of Prof. Jan-Dierk Grunwaldt) at ITCP-KIT (Karlsruhe, Germany).

The gases employed for the catalytic tests and *in situ* reductive treatment of $Pd@SiO_2$ samples are listed in Table 7.10.

Table 7.10 Employed gases for the catalytic tests for CO oxidation and reductive treatment of $Pd@SiO_2$

Name	Formula	Molecular weight (g/mol)	CAS number	Supplier
Carbon monoxide	CO	28.01	630-08-0	Alphagaz
Oxygen 10 vol% in helium	O_2/He	32.00	7782-44-7	Alphagaz
Hydrogen	H_2	2.02	1333-74-0	Alphagaz
Helium	He	4.00	7440-59-7	Alphagaz

The catalytic activity testing performed at ITCP-KIT were carried out employing a home-made setup, shown in Figure 7.5. A hot air gas blower (Oxford), operated by an in-house LabView software, was employed as heat source. EL-FLOW® Select (Bronkhorst)

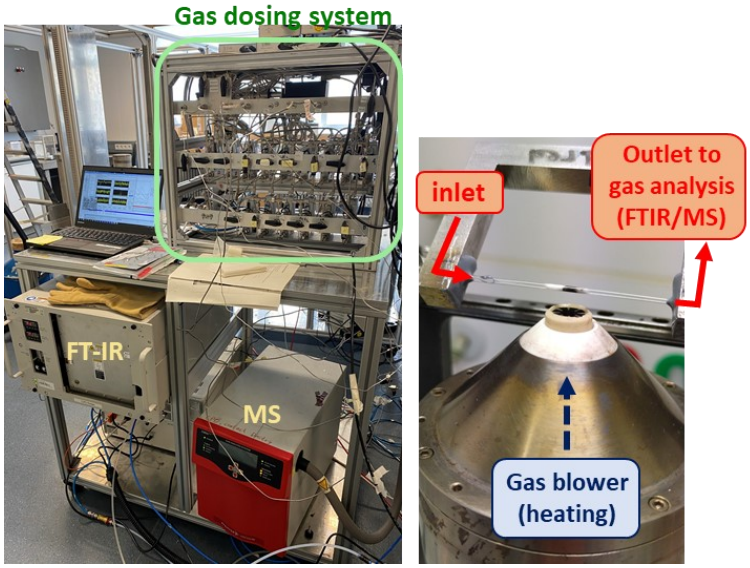

Figure 7.5 Experimental setup at KIT employed for catalytic tests

mass flow controllers (MFCs) and stainless-steel piping lines were employed for gas (He, O_2, CO, H_2) dosing into the reactor. The concentration of CO and CO_2 in the product flow were monitored on-line with a Fourier transformed infrared spectrometer (MultiGas 2030 FTIR Continuous Gas Analyzer, MKS Instruments) and a Omnistar mass spectrometer (MS, Pfeiffer Vacuum).

An exact amount of about 5.0 mg of a sieved fraction of size 125-250 µm of the samples, in a physical mixture with silica (1:1 wt, total amount: 10 mg), was loaded into a quartz flow reactor (i.d. 1.5 mm) and treated with three consecutive catalytic cycles (light offs and light outs) up to 300 °C (heating rate of 10 °C min^{-1}) in a gas mixture composed of 1000 ppm CO and 9 vol% O_2 in He, with a total flow of 50 mL min^{-1} and a weight hourly space velocity (WHSV)[xlii] of 60,000 L h^{-1} g_{Pd}^{-1}. Then, an *in situ* reduction stage was performed, flushing into the reactor 2.5 vol% H_2 in He up to 150 °C (heating rate of 10 °C min^{-1}) and holding the temperature at 150 °C for 30 minutes. After the reduction step, three additional catalytic cycles were conducted. A schematic representation of the treatment performed is reported in Figure 7.6.

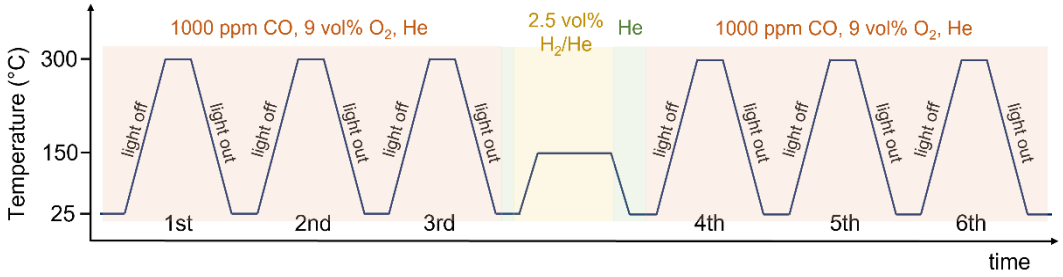

Figure 7.6 Schematic representation of the treatment of the samples for testing the catalytic activity of Pd NPs for CO oxidation at KIT

6.3.4 *Operando* XAS measurements

The temperature programmed reduction and catalytic activity of Pd NPs supported on selected mesoporous silica samples for CO oxidation were further investigated through *operando* XAS measurements were performed at the Pd K-edge (24350 eV) at the SAMBA beamline at the Soleil synchrotron (beamtime 20211613, 08-13/06/2022).

A capillary micro-reactor was used as *in situ* cell at the beamline, analogously as the lab experiments (Chapter 6.4.3), using a capillary oven available at the beamline as heating

[xlii] WHSV is defined as the weight of feed flowing per unit weight of the catalyst per hour.[386]

source. Gas doses were controlled by mass flow controllers using the dosing system already used at KIT, and gas concentration in the product flow was monitored on-line by a Fourier transformed infrared spectrometer (MultiGas 2030 FTIR Continuous Gas Analyzer, MSK Instruments) and a mass spectrometer (Omnistar, Pfeiffer Vacuum), to reproduce the catalytic testing setup employed at KIT.

The capillary reactor was loaded with 5.0 g of the granulated (125-250 µm) sample. A first *in situ* reduction stage (TPR) was performed, treating the impregnated samples with 2.5 vol% H_2 in He up to 150 °C (heating rate of 10 °C min^{-1}) and holding the temperature at 150 °C for 30 minutes. Subsequently, two consecutive catalytic cycles (light offs and light outs) were carried out up to 300 °C (heating rate of 10 °C min^{-1}) in a gas mixture composed of 1000 ppm CO and 10 vol% O_2 in He, with a total flow of 100 mL min^{-1} and a WHSV of 60,000 L h^{-1} g_{Pd}^{-1}. A schematic representation of the treatment performed is shown in Figure 7.7.

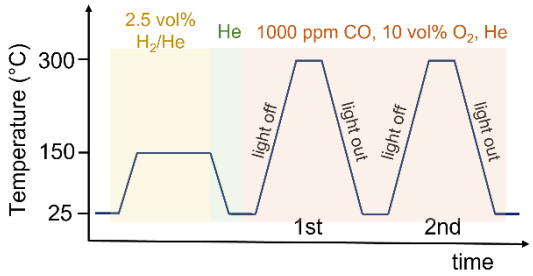

Figure 7.7 Schematic representation of the treatment of the samples for testing the catalytic activity of Pd NPs for CO oxidation at the SAMBA beamline at the Soleil synchrotron

During the above-described sample treatment, XANES spectra at the Pd K-edge (24350 eV) were collected in transmission mode in the 24150-24850 eV range. First and after each cycle, 5 repeated EXAFS spectra in air and/or in reaction mixture were acquired in the 24150-25500 eV range, at room temperature. A Si(311) monochromator was employed for energy selection. Energy calibration was carried out using the spectrum of a Pd foil, measured downstream to the sample. The employed experimental setup is shown in Figure 7.8.

Data reduction and treatment was performed using the Fastosh software, developed at the SAMBA beamline. For linear combination fitting (LCF) of the data acquired during TPR and catalytic testing, the spectra of metallic Pd and PdO were used as references. The data range used for LCF was 24320-24400 eV.

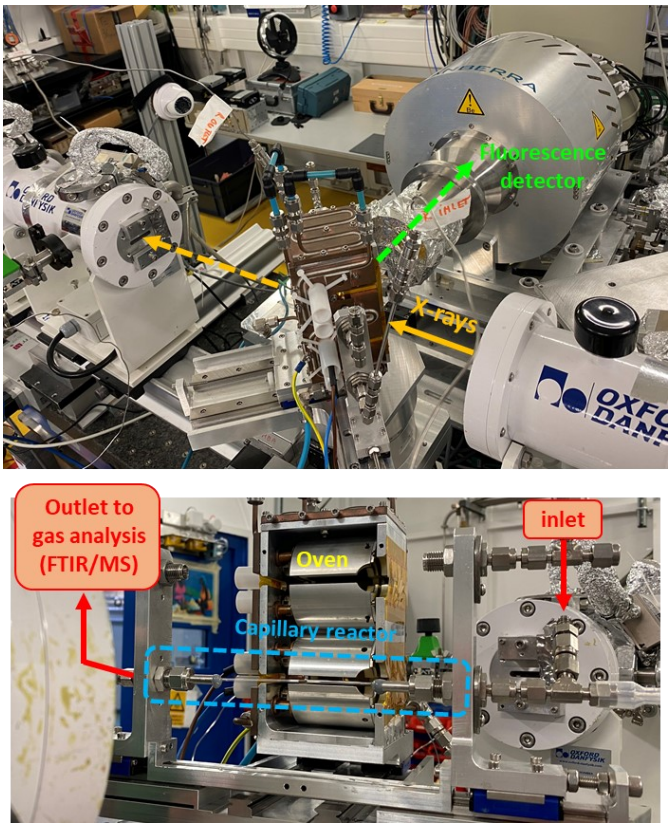

Figure 7.8 Experimental setup employed for *operando* XAS measurements at the SAMBA beamline at the Soleil synchrotron

7

Characterization methods

All the characterizations here reported were performed at the Department of Chemical Sciences, University of Padova, if not differently specified. Data elaboration and graphics were made with Igor Pro software (WaveMetrics Inc., Lake Oswego, OR, USA), if not differently specified.

7.1 Attenuated total reflectance infrared spectroscopy (ATR)

ATR measurements were carried out to investigate the vibrational modes of functional groups present in the samples, in particular to evaluate the possible presence of organic surfactant residues on the surface of miniemulsion synthesized samples (Chapter 2 and 3). ATR experiments were performed with a Nicolet Nexus 870 equipped with an ATR accessory using a diamond crystal. ATR spectra were acquired in the 4000 – 400 cm^{-1} range, collecting 32 scans with spectral resolution of 4 cm^{-1}. The background subtraction was performed interpolating the obtained spectra with a cubic spline function.

7.2 Diffuse reflectance spectroscopy (DRS)

Diffuse reflectance spectra were acquired to investigate the optical absorption properties of calcium molybdate (Chapter 3). An UV-Vis-NIR Cary 5E equipped with an integrating sphere coated with polytetrafluoroethylene (PTFE) was employed. The geometry used allowed to exclude the specular component of the reflected light. The spectra were collected within the 2500-300 nm range, with a scan rate of 600 nm min^{-1} and a spectral

resolution of 1 nm. Baseline was acquired as 100% and 0% of transmittance, while the spectra were recorded as a function of reflectance (%R).

From DRS spectra, the band gap could be calculated employing the Tauc method,[327] based on the assumption that the energy-dependent absorption coefficient α can be expressed by the following equation:

$$(\alpha \cdot h\nu)^{1/\gamma} = B(h\nu - E_g) \quad (7.1)$$

where h is the Planck constant, ν is the photons frequency, E_g is the band gap energy of the material and B is a constant. The γ factor depends on the nature of the electron transition and is equal to ½ or 2, for direct and indirect transition band gaps, respectively.[390] The band gap is determined by transforming the measured diffuse reflectance spectra to the corresponding absorption spectra by applying the Kubelka-Munk function $F(R)$:[391]

$$F(R) = \frac{K}{S} = \frac{(1-R)^2}{2R} \quad (7.2)$$

where K is the molar absorption coefficient, S is the scattering factor, and R is the reflectance of the sample, and putting $F(R)$ instead of α in Equation 7.1, yielding:

$$(F(R) \cdot h\nu)^{1/\gamma} = B(h\nu - E_g) \quad (7.3)$$

The function $[F(R) \cdot h\nu]^{1/\gamma}$ is plotted against $h\nu$ and the band gap is extrapolated from x-axis intersection point of the linear fit of the Tauc plot.
A factor $1/\gamma$ equal to 2 was employed for the determination of the band gap of calcium molybdate in Chapter 3.

7.3 Dynamic light scattering (DLS)

Dynamic light scattering measurements were performed to estimate the hydrodynamic diameter of miniemulsion droplets (Chapter 2 and 3). DLS analyses on the as-prepared miniemulsions of precursors were carried out using a Malvern Zetasizer NanoS, mounting a He-Ne laser (λ = 633 nm) operated in backscattering mode (*i.e.* collection angle of 173°). Suspensions were thermostated at 20 °C for 2 min prior to measurement and acquisitions were repeated three times.

7.4 Electron microscopies and tomography

The size, size distribution and morphology of the synthesized samples was investigated by transmission electron microscopy (TEM), scanning transmission electron microscopy (STEM) and scanning electron microscopy (SEM), also coupled with energy dispersive X-ray spectroscopy (EDX). The three-dimensional structure of $Pd@SiO_2$ samples was also characterized by electron tomography.

I. Transmission electron microscopy. TEM characterization of MoO_3 (Chapter 2) and $CaMoO_4$ (Chapter 3) samples was carried using a Tecnai G^2 (FEI) transmission electron microscope, operating at 100 kV, at the Department of Biology, University of Padova. Images were acquired with a Veleta (Olympus Soft Imaging System) digital camera. Samples were prepared for TEM observations by suspending a small amount of powder either in water or ethanol and depositing one droplet of the suspension on a 400 mesh holey film Cu grid.

II. Scanning transmission electron microscopy. STEM characterization of $Pd@SiO_2$ samples (Chapter 4) was performed at the INT (Institute of Nano-Technology) at Karlsruhe Nano Micro Facility (KNMF) of KIT (Karlsruhe Institute of Technology, Karlsruhe, Germany), in collaboration with Dr. Carina Maliakkal and Dr. Di Wang. The Ph.D. candidate wrote the proposal of the experiment and participated in a part of the measurements (proposal 2022-027-031257, 30/05-03/06/2022). STEM images were acquired using a ThermoFisher Scientific Themis300 transmission electron microscope, operating at 300 kV and equipped with a high brightness Schottky Field Emission Gun (X-FEG), a Ceta 16M bottom-Mount digital camera, BF-/DF-/HAAFD-STEM detector, and a Super-X EDX detector. Samples were prepared for STEM observations by dry transfer or drop casting on a holey Cu gold grid

III. Electron tomography. Electron tomography characterization of $Pd@SiO_2$ samples (Chapter 4) was performed at the INT at KNMF facility of KIT (Germany), in collaboration with Dr. Carina Maliakkal and Dr. Di Wang, in the framework of the 2022-027-031257 KNMF proposal (30/05-03/06/2022). Measurements were performed using a ThermoFisher Scientific ThemisZ transmission electron microscope, operating at 300 kV and equipped with a high brightness Schottky Field Emission Gun (X-FEG) with monochromator, a Gatan Oneview IS camera, BF-/DF-/HAAFD-STEM detector, and a Super-X EDX detector. Samples were prepared for tomographic observation by suspending a small amount of powder in

ethanol and drop casting one droplet of the suspension on a 100x400 holey gold grid. STEM images were collected over a tilt range of ± 74° with angular increments of 2°. Images alignment and 3D tomographic reconstructions were performed by Dr. Carina Maliakkal.

IV. Scanning electron microscopy. SEM-EDX measurements of MoO_3 (Chapter 2) and $CaMoO_4$ (Chapter 3) were performed using a Field Emission (FE-SEM) Zeiss SUPRA 40VP, equipped with an Oxford INCA x-sight X-ray detector. For SEM measurements, a primary beam acceleration voltage of 5.0 kV and a conventional secondary electron detector for the SEM investigations were employed. EDX measurements were carried out using a primary beam acceleration voltage of 20.0 kV. Samples were prepared for SEM-EDX observations by suspending a small amount of powder either in water or ethanol and drop casting 3-5 droplets of the suspension on a silicon wafer, to avoid conduction issues, loaded on a SEM stub.

For all cases, the dimensional analysis on the obtained micrographs was manually performed using Fiji software.[392,393] For isomorphic particles a spherical approximation was employed, and their diameter was measured. In the case of aggregated particles, a manual segmentation method was employed. For anisomorphic particles, the Feret diameter (*i.e.* the maximum traceable diameter) was measured; for molybdenum oxide rods, both length and width were measured and the aspect ratio was calculated as the ratio between their width and length. Histograms obtained from the various measured parameters were fitted using the software Igor Pro.

7.5 Inductively coupled plasma-mass spectrometry (ICP-MS)

ICP-MS analyses were performed to determine the stoichiometry of Eu-doped $CaMoO_4$ samples (Chapter 3), with the aim of verifying the atomic doping percentage of the materials. A precise amount of each sample (50 mg) was placed in a 15 mL digestion vial and digested with a 1:1 wt solution of concentrated nitric acid (65 wt%) and concentrated hydrochloric acid (37 wt%) at 100 °C for 1 hour. Vials were then cooled, and the obtained solutions were diluted to 50 g with a 5 wt% solution of nitric acid in milliQ water. Mo and Eu elements were measured using a Agilent Technologies 7700x ICP-MS system (Agilent Technologies International Japan, Ltd., Tokyo, Japan), equipped with an octupole collision cell and a 1550 W plasm cell. The instruments were optimized daily to achieve the optimum

sensitivity and stability according to manufacturer recommendations. All parameters were checked daily using an in-house optimization program.

7.6 N_2 physisorption measurements

The technical report of IUPAC of 2015 defines a*dsorption* as "the enrichment of molecules, atoms or ions in the vicinity of an interface. In the case of gas/solid systems, adsorption takes place in the vicinity of the solid surface".[344] When an adsorbable gas (*i.e.* the adsorptive) is brought into contact with the surface of a solid (*i.e.* the adsorbent) and only physical interactions (*e.g.* attractive and repulsive forces, van der Waals, polarization, field dipole) are present, and no chemical bonds are formed, the phenomenon of *physisorption* takes place.

Physisorption measurements are carried out using a gas (usually N_2, but Ar and Kr can also be adopted) at cryogenic temperature (*i.e.* 77 K for N_2), to enhance the localization and adsorption of the adsorptive and increase the weak interactions involved. A known amount of pure adsorptive gas is introduced in a confined, calibrated volume containing the adsorbent, kept at constant temperature, the adsorption takes place and an equilibrium pressure in the confined volume is established. By introduction of successive charges of gas to the adsorbent, an adsorption isotherm is constructed point-by-point, displaying the amount of gas adsorbed (in mol g^{-1} or in cm^3 g^{-1}) versus the equilibrium relative pressure p/p^0, where p^0 is the saturation pressure of the pure adsorptive at the operational temperature.

Depending on the pore structure of the adsorbent, different physisorption isotherms may be observed, classified by IUPAC as shown in Figure 8.1. Type I isotherms are typical of microporous solids with relatively small external surface; Type I(a) and I(b) are distinguished depending on the size of the micropores and their size distribution (*i.e.* larger and wider for Type I(b)). Type II isotherms are observed for macro- or non-porous adsorbents; point B represents the monolayer capacity and the formation of multilayers is unlimited. Physisorption measurements of macro- or non-porous samples with weak fluid-wall interactions are characterized by Type III isotherms, not displaying any monolayer formation. Typical isotherms of mesoporous adsorbents are of Type IV: their adsorption behavior is determined by the interactions between the molecules in the condensed state in addition to the adsorbent-adsorptive interaction. In the case of Type VI(a) isotherm, when

the pore width exceeds a certain critical width, capillary condensation leads to the formation of a hysteresis loop. Type V isotherms are a special type of Type IV, characterized by weak adsorbent-adsorbate interactions. Finally, Type VI isotherms are typical of layer-by-layer adsorption on a highly uniform nonporous surface, the step-height representing the capacity for each adsorbed layer.

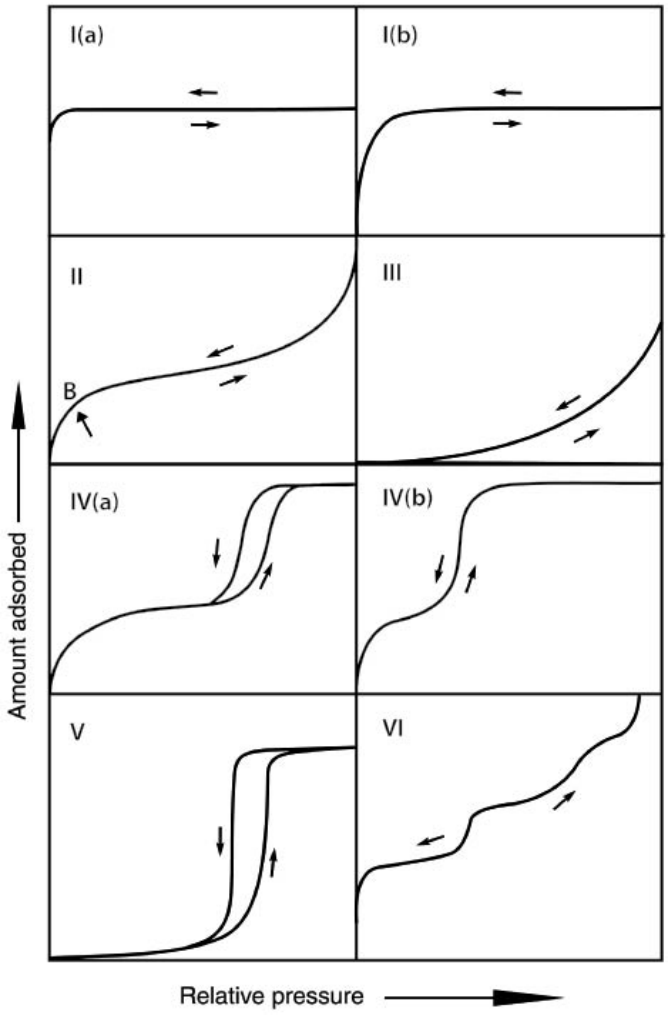

Figure 8.1 Classification of physisorption isotherms by IUPAC.
Reproduced from Thommes *et al.*[344]

As mentioned, hysteresis loops are associated with the capillary condensation phenomenon, and different shapes of hysteresis loops have been reported, as shown in Figure 8.2, depending on the particular features of the pore structure and underlying adsorption mechanism.[344] Type H1 loop is associated with uniform (*e.g.* cylindrical) mesopores in narrow range: capillary condensation is delayed. Type H2 is typical of adsorbent with broader pore size distributions, such as ink-bottle pores (*i.e.* non-uniform and/or two types of pores which form a network): the very steep desorption branch of H2(a)

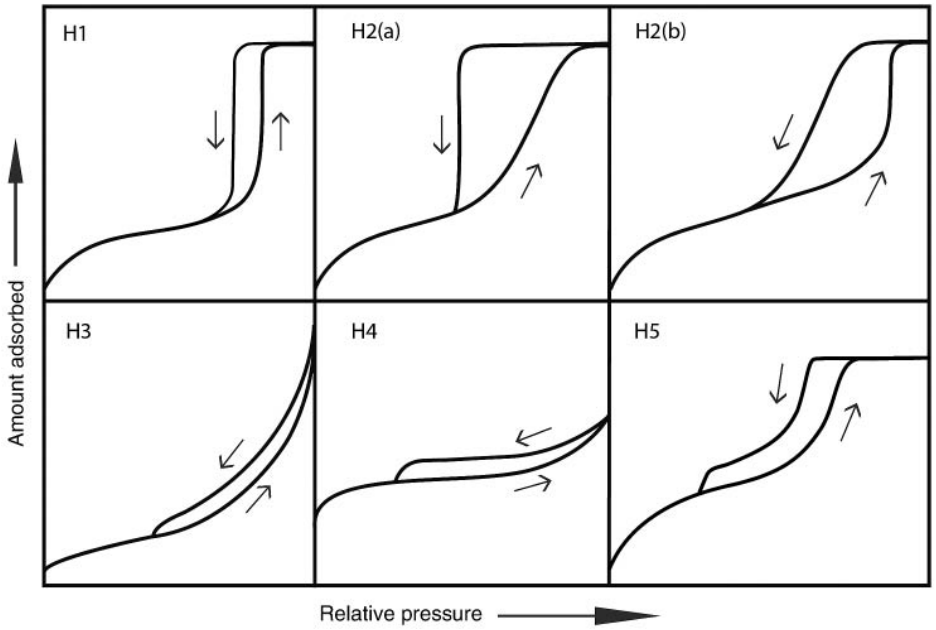

Figure 8.2 Classification of hysteresis loops by IUPAC. Reproduced from Thommes *et al.*[344]

can be attributed to pore blocking, while when the size distribution of neck widths is larger the H2(b) is observed. Type H3 loops, not reaching a plateau, are typical of non-rigid aggregates of plate-like particles or of a network of macropores not completely filled at the condensation. Type H4 hysteresis is typical of slit-shaped pores, and Type H5 loops are pretty unusual and typical of structures containing both open and partially blocked mesopores (*i.e.* "clogged").

Physisorption measurements data are most widely employed for evaluating the specific surface area (SSA, [$m^2\ g^{-1}$]) of porous materials, applying the Brunauer–Emmett–Teller (BET) method[348] to Type II and Type IV isotherms. The SSA is calculated from the volume of gas needed to cover the surface of the material with a monolayer of adsorbate and the area occupied by an adsorbed molecule, employing the following equation:

$$\frac{p/p^0}{n(1-p/p^0)} = \frac{1}{n_m C} + \frac{C-1}{n_m C} \cdot (p/p^0) \qquad (7.4)$$

where C is the BET constant, that must be positive and is related to the affinity of the adsorbent with the adsorbate, *i.e.* to the heat of adsorption.

In particular, the physisorption plot is first transformed in the BET plot ($p/n(1-p/p^0)$ *vs* p/p^0) and the value of the BET monolayer capacity n_m is derived. Secondly, the BET area

A_S is calculated from n_m by adopting an appropriate value of the molecular cross-sectional area σ_a (*i.e.* the area occupied by an adsorbate molecule), as follows:

$$A_S = N_{AV} \cdot n_m \cdot \sigma_a \quad (7.5)$$

The range of linearity of the BET plot is restricted to a limited part of the isotherms at low relative pressures, often within the p/p^0 range of 0.05-0.30 for Type II and Type IV(a) isotherms, corresponding to the relative pressures needed for the formation of a monolayer of adsorbate.[344]

In addition, from physisorption measurements of mesoporous materials (Type IV isotherm), it is possible to determine the total pore volume and the pore size distribution. The total pore volume V_p is derived from the amount of vapor adsorbed at relative pressure close to unit (*e.g.* p/p^0 = 0.95). The mesoporous size distribution can be estimated by the BJH (Barrett, Joyner and Halenda)[394,395] or DFT (density functional theory)[396,397] models. The BJH model is the traditional and most widely used method and it estimates the pore size distribution from the desorption branch of the N_2 physisorption isotherm. It is based on the Kelvin equation (*i.e.* it has a thermodynamic origin), and it has been developed to describe the adsorption-capillary condensation process taking place in mesopores. Basically, it calculates the change in the thickness of the adsorbed film from the decrease of relative pressure in the desorption branch. The BJH method fails to describe micropores and narrow mesopores and it typically underestimates the actual pore diameter by 2-3 nm, since it overestimate the relative pressure at desorption.[346,347] The DFT (density functional theory) model is the most recent and powerful approach; it relies on a theoretical description of the experimental adsorption isotherm and as a consequence it has a wider range of applicability and seems to be the most accurate one (recommended to calculate the pore size distribution, particularly for micropores).[345,397]

Prior to the measurement of the adsorption isotherm, it is recommended to remove all the physisorbed species from the surface of the adsorbent by carrying out an outgassing step, *i.e.* exposure of the surface to a high vacuum at high temperature. When dealing with sensitive samples, attention must be paid to avoid possible irreversible changes of the surface or solid structure of the adsorbent.

Nitrogen physisorption measurements presented in this Ph.D. Thesis were performed to determine the type of porosity and specific surface area of commercial and mesoporous

silica materials (Chapter 4), and for the latter to estimate the pore size distribution and total pore volume. N_2 adsorption/desorption isotherms were recorded at 77 K by using a Micromeritics ASAP 2020 Plus instrument. Before the measurements, the samples were degassed at 100 °C for 20 hours under vacuum, to ensure the complete removal of any previously adsorbate. The specific surface area of the samples was calculated by a multipoint BET analysis in the 0.07-0.28 p/p^0 range. The mesopore size distributions were estimated by both BJH and DFT methods employing the Micromeritics ASAP 2020 Plus software. The total pore volume was determined from the amount of vapor adsorbed at $p/p^0 = 0.95$.

7.7 Photoluminescence

Photoluminescence investigations were carried out to investigate the optical properties of Eu-doped calcium molybdate samples (Chapter 3).

Photoluminescence analyses of Eu-doped CM samples synthesized by miniemulsion and batch approaches (Chapter 3.2) were performed at the Justus-Liebig University (Giessen, Germany), in collaboration with the workgroup of Prof. Klaus Müller-Buschbaum. A Fluorololog 3 (HORIBA) spectrometer equipped with a dual lamp housing, a 450 W short-arc Xe lamp, a UV Xe flashlamp, double-grated excitation and emission monochromators, a photomultiplier tube as a detector, and a TCSPC upgrade, was employed. An edge filter (cut off 455 nm, Newport) was used during the collection of emission spectra (for λ_{ex} = 271 or 285 nm, for emission above 500 nm) and all excitation spectra. Overall emission decay times were acquired using a Xe microsecond flashlamp for excitation. Exponential tail fitting was used for calculation of emission lifetime using a Decay Analysis Software 6. Quality of the fit was evaluated by χ^2 value.

Photoluminescence analyses of Eu-doped CM samples synthesized by microfluidic approaches (Chapter 3.3) were performed in collaboration with Dr. Ilaria Fortunati. A FLS1000 spectrometer (Edinburgh Instruments, UK) equipped with double excitation and emission monochromators, a 450 W Xe lamp and an air-cooled single photon counting photomultiplier (Hamamatsu R13456) was employed. Time-resolved lifetime measurements were performed using a Xe microsecond flashlamp for excitation (λ_{ex} = 285 nm, 100 Hz). Luminescence decays were recorded using the Multi-channel scaling

(MCS) technique in the range 0-10 ms, and analyzed with the Fluoracle software using a two-component equation.

7.8 X-ray absorption spectroscopy (XAS)

X-ray absorption spectroscopy is a powerful tool to investigate the local atomic environment in condensed matter, coupling chemical selectivity, sensitivity (up to a concentration of one atomic percent) and high resolution at the short scale length. In particular, it can provide information on the electronic structure and local coordination geometry of the absorber atom.[398–401]

The XAS technique is based on the acquisition and analysis of the X-ray absorption coefficient $\mu(E)$ as a function of the incident photon energy E in the region around a specific absorption edge of the targeted element present in the sample (element-selectivity). Indeed, when a monochromatic X-ray beam of energy E passes through a homogeneous sample of thickness t, its intensity I_0 is attenuated, and, according to the Lambert-Beer's law, its transmitted intensity is:

$$I(E) = I_0(E) \cdot e^{-\mu(E) \cdot t} \tag{7.6}$$

where $\mu(E)$ is the linear absorption coefficient, that decreases with increasing the energy of the incident beam. When the incident wavelength reaches a threshold (*i.e.* the absorption edge), $\mu(E)$ dramatically increases as a consequence of the ejection of a core electron from the absorber atom. Beyond the adsorption edge, the absorption coefficient of an isolated atom decreases monotonically with increasing energy, until the next absorption edge (corresponding to the subsequent shells from which the electrons are removed). On the contrary, for atoms in molecules or in condensed phase, $\mu(E)$ above the absorption edge shows a fine structure, called EXAFS (extended X-ray absorption fine structure, Figure 8.3). Indeed, when the absorber is surrounded by neighboring atoms, the latter scatter the outgoing photoelectron and, by interference effect, EXAFS fine structure (*i.e.* oscillations) are generated.[402] The analysis of the EXAFS oscillations provides information about the type and the number of neighboring atoms and their distance from the central absorbing atom. On the other hand, the XANES (X-ray adsorption near edge structure, for hard X-rays), or NEXAFS (near edge X-ray absorption fine structure, for soft X-rays), region of XAS spectrum, within 40-50 eV from the edge (orange region in Figure

8.3), gives information about the chemical nature of the absorber, its oxidation state, its coordination symmetry and its orbitals. Moreover, sometimes some features are observed just before the absorption edge ("pre-edge" region, typically about 10 eV before the edge), that carry information about the symmetry (*i.e.* coordination geometry) and electronic structure of the absorber.[403]

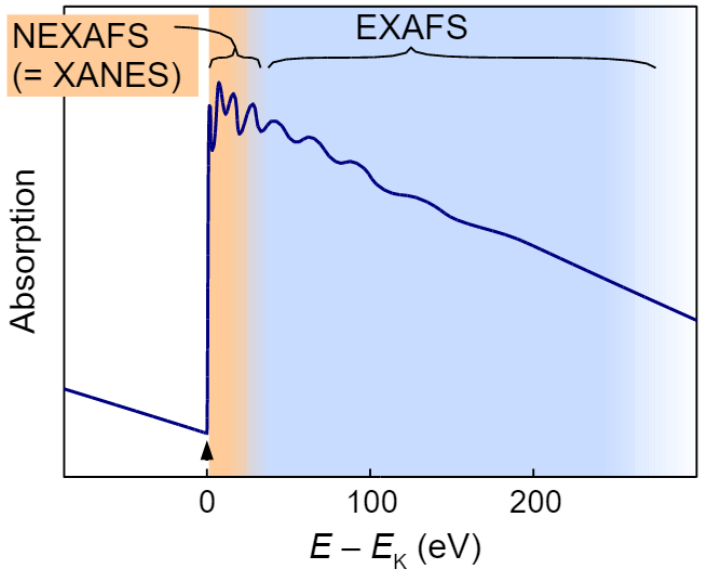

Figure 8.3 Schematic illustration of XANES and EXAFS regimes

XAS measurement are typically performed at synchrotron facilities, requiring high-energy, strong brilliance and collimated radiation, with tunable monochromatic energy. The proper energy is selected with a crystal monochromator before hitting the sample, and two ionization chambers before and after the specimen are employed to measure the incident and the transmitted intensity (*transmission mode*). The modulation of the adsorption coefficient with energy is then calculated as: $\mu(E) = \ln\ (I_0/I)$.Additionally, to calibrate the energy scale and to monitor any beam irregularity, the absorption spectrum of a reference is measured after the second ionization chamber. Another mode of acquisition, typically employed for diluted (concentration < ca. 1 at%) or thick concentrated samples, is the *fluorescence mode,* that involves the detection of X-ray fluorescence (or Auger emission), proportional to the absorption coefficient: $\mu(E) \propto I_0/I_f$. Thanks to the ever-advancing technology and performance of dedicated machineries (*e.g.* monochromators, detectors), XAS technique can be employed in materials research and catalysis to follow the structural and electronic changes occurring during reactions (*in situ*) and under *operando* conditions.[404]

XAS technique was exploited for all the inorganic systems investigated and presented in this Ph.D. Thesis, both as *ex situ* and *in situ/operando* characterization method, in cooperation with Dr. Paolo Dolcet and the group of Prof. Jan Dierk Grunwaldt (Karlsruhe Institute of Technology, Karlsruhe, Germany). In particular, it was employed for investigating i) the thermal evolution of MoO_3, combined with XRD (Chapter 2.4), ii) the local coordination of Eu^{3+} dopant ions in $CaMoO_4$ structure (Chapter 3.2), and iii) the oxidation state and structural features of Pd on silica during TPR and catalytic testing for CO oxidation (Chapter 4).

I. *In situ* combined thermal XAS/XRD of MoO_3. The thermal evolution of the metastable hexagonal polymorph of MoO_3 into the thermodynamically stable orthorhombic one (Chapter 2.4) was followed *in situ* by combined XAS and XRD at the Mo K-edge (20000 eV) at the B18 beamline at Diamond Light Source (UK, proposal SP23804). Experimental details of data acquisition are described in Chapter 6.1.5.

II. XAS of Eu-doped $CaMoO_4$. The effectiveness of doping of $CaMoO_4$ with europium (Chapter 3.2) was investigated *ex situ* both at the Mo K-edge (20000 eV) and Eu L_3-edge (6976.9 eV) at the SAMBA beamline at the Soleil synchrotron (France, proposal 20201498). A Si(220) crystal monochromator was employed for energy selection. XAS spectra were acquired in the 6900-7900 eV range for Eu L_3-edge measurements and in the 19800-21597 eV range for Mo K-edge measurements. Energy calibration at the two edges was carried out using the spectra of commercial crystalline Eu_2O_3 and metallic Mo foil, respectively. The acquisitions were carried out in fluorescence mode, in continuous scanning mode, using a 35-element Ge detector to detect and select the radiation emitted from the samples. Samples were prepared and measured as pellets, using cellulose as binder. To improve the signal-to-noise ratio, at least five spectra were merged per sample. The data were analyzed using the Athena and Artemis software of the Demeter package.[405] Fourier transformation was applied on the k^2-weighted EXAFS curves, in the interval k = 3.0-10 $Å^{-1}$ for Eu L_3-edge or k = 3.0-17 $Å^{-1}$ for Mo K-edge. For the fitting, the backscattering amplitudes and phase shifts for the Eu-O and Mo-O wavefunctions were taken from the Eu_2O_3 (Eu-O; 2.33 Å; coordination number: 6) or MoO_3 (Mo-O; 1.79 Å; coordination number: 4) references.

III. *Operando* XAS of $Pd@SiO_2$ during CO oxidation. *Operando* time-resolved XAS measurements of the catalytic activity of $Pd@SiO_2$ for CO oxidation (Chapter 4.4) were carried out at the Pd K-edge (24350 eV) at the SAMBA beamline at the Soleil synchrotron

(France, proposal 20211613). Experimental details of the employed setup, data acquisition and elaboration are described in Chapter 6.3.4.

7.9 X-ray scattering

X-ray scattering is a structural reciprocal space characterization technique, that enables the study of a variety of systems (*e.g.* powdered materials, suspensions of particles, porous materials, biological systems, etc) making use of the variation of the electron density of a sample to generate contrast. As implied by the term "reciprocal", an X-ray beam will be scattered to low angles when the spatial variation of the electron density is at nanometer length scale, while to high angles when the variation is in the atomic scale. Therefore, *small angle X-ray scattering (SAXS)* techniques provides information on material structures at large distances (*i.e.* small angles), and with *wide angle X-ray scattering (WAXS)* the scattering intensity at large angles (*i.e.* small distances) is measured. When diffraction, *i.e.* constructive interference of waves scattered from different crystal planes, separated by a fixed distance, occurs in addition to scattering, WAXS is also termed as *X-ray diffraction (XRD).*

When X-rays are scattered by atoms (WAXS or XRD) or particles (SAXS), every scattering object emits spherical waves emanating from their position and they produce interference patterns at the detector position. The interference pattern is characteristic of the orientation and distances of the scattering objects relative to each other, and it is usually measured in terms of *scattering angle* 2θ or, to become independent on the wavelength of the incoming X-rays, in terms of the *scattering vector* q [nm^{-1}]:

$$q = \frac{4\pi}{\lambda} \cdot \sin\theta \tag{7.7}$$

Commonly, employing incident X-rays with a wavelength of 0.15406 Å (*i.e.* 8 keV, corresponding to the K_α radiation emitted by a Cu anode), the limit between the SAXS and WAXS ranges is about 10° 2θ, corresponding to a detected size of about 1 nm (Figure 8.4).

The data resolution depends on the maximum scattering vector q_{max} with a significant signal-to-noise ratio, *i.e.* on the maximum angle (θ_{max}) at a given wavelength, and thus it depends on the employed instrumentation: longer specimen-to-detector distances are needed for SAXS with respect to WAXS (XRD).

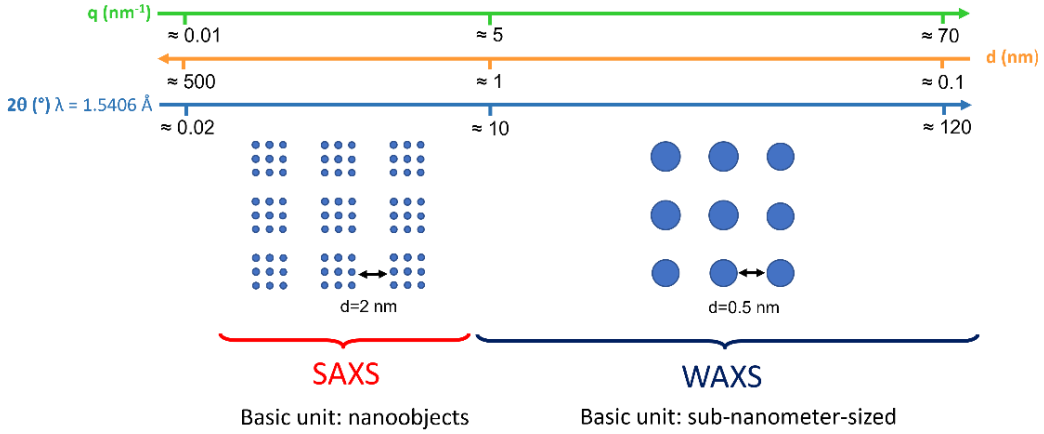

Figure 8.4 Scale ranges investigated by SAXS and WAXS techniques

I. Small angle X-ray scattering. SAXS data (typically 0.1-10° 2θ with Cu K_α) have a nanometric resolution and are therefore employed to access information at the nanoscale. When spatial correlations in the sample are negligible, such as in gas-like dispersions, SAXS data do not contain any structure information but only morphological ones, *i.e.* average particle size and/or shapes.[266,267,406]

For a particle with electron density ρ_1 embedded into a matrix of electron density ρ_2, the SAXS signal intensity $\Delta I_1(q)$ is:

$$\Delta I_1(q) = I_0 \cdot (\Delta\rho)^2 \cdot V_1^2 \cdot F(q) \tag{7.8}$$

where I_0 is the scattered intensity from one electron, $\Delta\rho$ is the contrast (*i.e.* difference in electron density between the particle and the matrix, that can be the solvent: $\rho_1 - \rho_2$), V_1 is the volume of the particle, and $F(q)$ is the *form factor*. The form factor $F(q)$ is the Fourier transform of the electron density of the particles, *i.e.* the interference pattern produced by the waves scattered by every single atom inside one particles, and its oscillations are typical of the particle shape. It is worth noticing that i) the sign of the contrast has no effect as the squared contrast is responsible for SAXS signal: voids in a matrix material give the same scattering intensity as particles in a void matrix (*Babinet's principle*), and ii) the scattering intensity increases with the sixth power of the particle radius.

The scattering intensity of an ensemble of identical particles is:

$$\Delta I(q) = n \cdot \Delta I_1(q) \cdot S(q) \tag{7.9}$$

where n is the number density of particles, and $S(q)$ is the *structure factor* (equal to one in the case of diluted systems). The structure factor $S(q)$ contains contributions from neighboring particles and it is also called *lattice factor* for crystalline materials: in the case of periodic and ordered arrangements Bragg peaks are observed and information on inter-particle distances and degree of order are obtained.

SAXS technique, simultaneously combined with WAXS, was exploited at the SAXS beamline at Elettra Sincrotrone Trieste (proposal 20192141) for an *in situ* time-resolved study of the crystallization of molybdenum(VI) oxide in miniemulsion and batch conditions (Chapter 2.3). Experimental details of the employed setup, data acquisition and elaboration are described in Chapter 6.1.4.

Moreover, SAXS patterns of mesoporous silica samples (Chapter 4) were acquired with a Bruker AXS D8 Advance Plus diffractometer, equipped with a Cu-K$\alpha_{1,2}$ anode (λ = 1.5406 Å) and mounting a LYNEXEYE XE-T detector employed in 1D mode. X-rays were generated suppling a voltage of 40 kV and a current of 40 mA to the Cu anode, and data were collected with a Bragg-Brentano geometry (θ-2θ) over the 0.4-6.0° 2θ range, with a step size of 0.02° 2θ, and a nominal time per step of 1 seconds. Variable primary divergence slit opening, keeping the length of the illuminated specimen area constant to 25 mm, and fixed secondary divergence slit opening (2.34°) were employed, together with Söller slits with an aperture of 2.5°. PSD (position sensitive detector) opening of 0.4° was employed. Automatic motorized air scatter knife was used.

II. Wide angle X-ray scattering (or diffraction). WAXS, or XRD, data (typically 10-100° 2θ with Cu K$_\alpha$) can reach atomic resolution and are therefore used to access information on interatomic distances and on the arrangement of atoms within a crystalline material.

When periodic structures of a given spacing are illuminated with X-rays (*i.e.* with light with comparable wavelength), diffraction arises through constructive interference of scattered waves. In particular, X-rays diffract from planes of atoms in a crystal according to the Bragg equation:

$$2d \cdot \sin\theta = n\lambda \tag{7.10}$$

where d is the separation between atomic planes (*i.e.* the *d-spacing*), θ is half of the diffraction angle, n is an integer number, and λ is the incident X-rays wavelength.

By combining Equation 7.7 and Equation 7.10, the scattering vector q (independent on the wavelength) can be also expressed as:

$$q = \frac{2\pi}{d} \tag{7.11}$$

The position, width, shape and relative intensity of the diffraction peaks (*i.e.* reflections) provide information about the crystalline phases present in the sample, the crystallite size, strain, preferential orientation (texture), shape anisotropy, stacking faults and other crystal defects.[219,407] More or less advanced and accurate diffraction data analyses can be carried out, depending on the entity of approximations made. For example, the average crystallite size (*i.e.* the size of the coherently scattering domains) can be estimated through application of the Scherrer formula:[408–410]

$$L = \frac{K\lambda}{\beta \cdot \cos\theta} \tag{7.12}$$

where K is a shape constant in the 0.89-1.3 range, dependent on the crystal cell shape,[410] λ is the X-rays wavelength, β is the full width at the half maximum (FWHM) of the reflection in the scale of 2θ radians, and θ is the diffraction angle of the reflection considered, which is usually the most intense one. However, the Scherrer equation displays several limitations, such as considering that the broadening and shaping of the reflections is caused only by the finite size of the coherently scattering domains, ignoring strain effects (relevant in the nanoscale) and instrumental contributions (always present). A more reliable evaluation of the crystallite size can be carried out by whole powder pattern fitting (WPPF) or Le Bail fitting or employing the Rietveld refinement method.[xliii] These approaches employ a least square method to refine a theoretical line profile, in order to achieve the best match with the experimental pattern (evaluated through the R factor), and allow to evaluate lattice stresses, strains and preferred orientations as well.[411–416]

XRD patterns of all the samples, if not differently specified, were acquired *ex situ* with a Bruker D8 AXS Advance Plus diffractometer, equipped with a Cu-K$\alpha_{1,2}$ anode (λ = 1.5406 Å) and mounting a LYNEXEYE XE-T detector employed in 1D mode. X-rays were generated

[xliii] The distinction between structure refinement by Rietveld refinement and whole powder pattern fitting (WPPF) approaches relies on the fact that in Rietveld refinement the integrated intensity is related to a structural model (including *e.g.* atomic positions and occupancy, thermal factors, lattice parameters), while in WPPF the structural information is absent or limited to lattice parameters.[415]

suppling a voltage of 40 kV and a current of 40 mA to the Cu anode, and data were collected with a Bragg-Brentano geometry (θ-2θ) over the 10-90° 2θ range, with a step size of 0.014° or 0.026° 2θ, and a nominal time per step of 0.2-0.5 seconds. Fixed divergence slits of 0.50° were employed, together with Soller slits with an aperture of 2.5°. A maximum PSD (position sensitive detector) opening was used (2.83°). Data were analyzed with the Bruker Diffrac.Suite. Crystalline phases were identified using a *Search and Match* method with the software DIFFRAC.EVA. Crystallographic and microstructural information of MoO_3 (Chapter 2.2) and ME and batch $CaMoO_4$ (Chapter 3.2) were estimated by fitting the experimental diffraction patterns using a WPPF method implemented in the DIFFRAC.TOPAS software.[417] The background was fitted with a Chebychev function with 9-15 parameters. The zero-point error or the sample displacement were refined, along with the lattice parameters and the average crystallite size, that was estimated based on the integral breadth of the reflections (*LVol-IB*). The shape of the reflections was modelled through the Fundamental Parameter Approach incorporated in the software, separating the instrumental and sample contributions. The quality of the fittings was evaluated by means of the R_{wp} parameter. Average crystallite size of microfluidic $CaMoO_4$ (Chapter 3.3) was estimated by applying the Scherrer equation to the most intense reflection (reflection (112)) and employing K = 0.89.

Bibliography

[1] Jiang, Q. and Ward, M. D. Crystallization under nanoscale confinement. *Chem. Soc. Rev.* **2014**, *43*, 2066–2079.

[2] Meldrum, F. C. and O'Shaughnessy, C. Crystallization in Confinement. *Adv. Mater.* **2020**, *32*, 2001068.

[3] Miners, S. A., Rance, G. A. and Khlobystov, A. N. Chemical reactions confined within carbon nanotubes. *Chem. Soc. Rev.* **2016**, *45*, 4727–4746.

[4] Cantaert, B., Beniash, E. and Meldrum, F. C. Nanoscale Confinement Controls the Crystallization of Calcium Phosphate: Relevance to Bone Formation. *Chem. Eur. J.* **2013**, *19*, 14918–14924.

[5] Bellissent-Funel, M. C., Chen, S. H. and Zanotti, J. M. Single-particle dynamics of water molecules in confined space. *Phys. Rev. E* **1995**, *51*, 4558–4569.

[6] Mietner, J. B., Brieler, F. J., Lee, Y. J. and Fröba, M. Properties of Water Confined in Periodic Mesoporous Organosilicas: Nanoimprinting the Local Structure. *Angew. Chemie - Int. Ed.* **2017**, *56*, 12348–12351.

[7] Antonietti, M. and Landfester, K. Single Molecule Chemistry with Polymers and Colloids: A Way to Handle Complex Reactions and Physical Processes? *ChemPhysChem* **2001**, *2*, 207–210.

[8] Landfester, K. Recent developments in miniemulsions - Formation and stability mechanisms. *Macromol. Symp.* **2000**, *150*, 171–178.

[9] McNaught, A. D. and Wilkinson, A. *IUPAC. Compendium of Chemical Terminology (the 'Gold Book')*. Blackwell Scientific Publications, Oxford, **1997**.

[10] Elvira, K. S., i Solvas, X., Wootton, R. C. and deMello, A. J. The past, present and potential for microfluidic reactor technology in chemical synthesis. *Nat Chem* **2013**, *5***,** 905–915.

[11] DeMello, J. C. and DeMello, A. J. Microscale reactors: nanoscale products. *Lab Chip* **2004**, *4***,** 11N-15N.

[12] Diodati, S., Dolcet, P., Casarin, M. and Gross, S. Pursuing the Crystallization of Mono- and Polymetallic Nanosized Crystalline Inorganic Compounds by Low-Temperature Wet-Chemistry and Colloidal Routes. *Chem. Rev.* **2015**, *115***,** 11449–11502.

[13] Bretos, I., Diodati, S., Jiménez, R., Tajoli, F., Ricote, J., Bragaggia, G., Franca, M., Calzada, M. L. and Gross, S. Low-Temperature Solution Crystallization of Nanostructured Oxides and Thin Films. *Chem. – A Eur. J.* **2020**, *26***,** 9157–9179.

[14] Thanh, N. T. K., Maclean, N. and Mahiddine, S. Mechanisms of Nucleation and Growth of Nanoparticles in Solution. *Chem. Rev.* **2014**, *114***,** 7610–7630.

[15] Burda, C., Chen, X., Narayanan, R. and El-Sayed, M. A. Chemistry and Properties of Nanocrystals of Different Shapes. *Chem. Rev.* **2005**, *105***,** 1025–1102.

[16] Cölfen, H. and Antonietti, M. *Mesocrystals and Nonclassical Crystallization*. John Wiley & Sons, Ltd, Chichester, UK, **2008**.

[17] Becker, R. and Döring, W. Kinetische Behandlung der Keimbildung in übersättigten Dämpfen. *Ann. Phys.* **1935**, *416***,** 719–752.

[18] Gibbs, J. W. On the Equilibrium of Heterogeneous Substances. *Trans. Connect. Acad. Arts Sci.* **1874**, *3***,** 108–248.

[19] Gebauer, D. and Cölfen, H. Prenucleation clusters and non-classical nucleation. *Nano Today* **2011**, *6***,** 564–584.

[20] Karthika, S., Radhakrishnan, T. K. and Kalaichelvi, P. A Review of Classical and Nonclassical Nucleation Theories. *Cryst. Growth Des.* **2016**, *16***,** 6663–6681.

[21] Kwon, S. G. and Hyeon, T. Formation Mechanisms of Uniform Nanocrystals via Hot-Injection and Heat-Up Methods. *Small* **2011**, *7***,** 2685–2702.

[22] Gao, C., Goebl, J. and Yin, Y. Seeded growth route to noble metal nanostructures. *J. Mater. Chem. C* **2013**, *1*, 3898.

[23] Meldrum, F. C. and Cölfen, H. Controlling mineral morphologies and structures in biological and synthetic systems. *Chem. Rev.* **2008**, *108*, 4332–4432.

[24] Volmer, M. *Kinetik der Phasenbildung*. Theodor Steinkopff, Dresden, **1939**.

[25] Lifshitz, I. M. and Slyozov, V. V. The kinetics of precipitation from supersaturated solid solutions. *J. Phys. Chem. Solids* **1961**, *19*, 35–50.

[26] Voorhees, P. W. The theory of Ostwald ripening. *J. Stat. Phys.* **1985**, *38*, 231–252.

[27] Ostwald, W. Studien über die Bildung und Umwandlung fester Körper. 1. Abhandlung: Übersättigung und Überkaltung. *Z. Phys. Chem.* **1897**, *22*, 289–330.

[28] Derjaguin, B. and Landau, L. Theory of the stability of strongly charged lyophobic sols and of the adhesion of strongly charged particles in solutions of electrolytes. *Prog. Surf. Sci.* **1993**, *43*, 30–59.

[29] *Principles of Colloid and Surface Chemistry, Revised and Expanded*. Ed. Hiemenz, P. C. & Rajagopalan, R., CRC Press, Boca Raton, **2016**.

[30] Verwey, E. J. W. Theory of the Stability of Lyophobic Colloids. *J. Phys. Colloid Chem.* **1947**, *51*, 631–636.

[31] Whitehead, C. B., Özkar, S. and Finke, R. G. LaMer's 1950 model of particle formation: a review and critical analysis of its classical nucleation and fluctuation theory basis, of competing models and mechanisms for phase-changes and particle formation, and then of its application to silver halide. *Mater. Adv.* **2021**, *2*, 186–235.

[32] Vekilov, P. G. The two-step mechanism of nucleation of crystals in solution. *Nanoscale* **2010**, *2*, 2346–2357.

[33] Erdemir, D., Lee, A. Y. and Myerson, A. S. Nucleation of Crystals from Solution: Classical and Two-Step Models. *Acc. Chem. Res.* **2009**, *42*, 621–629.

[34] Gebauer, D., Kellermeier, M., Gale, J. D., Bergström, L. and Cölfen, H. Pre-nucleation

clusters as solute precursors in crystallisation. *Chem. Soc. Rev.* **2014**, *43*, 2348–2371.

[35] Gebauer, D., Völkel, A. and Cölfen, H. Stable Prenucleation Calcium Carbonate Clusters. *Science* **2008**, *322*, 1819–1822.

[36] Jehannin, M., Rao, A. and Cölfen, H. New Horizons of Nonclassical Crystallization. *J. Am. Chem. Soc.* **2019**, *141*, 10120–10136.

[37] Niederberger, M. and Cölfen, H. Oriented attachment and mesocrystals: Non-classical crystallization mechanisms based on nanoparticle assembly. *Phys. Chem. Chem. Phys.* **2006**, *8*, 3271–3287.

[38] Rao, A. and Cölfen, H. From Solute, Fluidic and Particulate Precursors to Complex Organizations of Matter. *Chem. Rec.* **2018**, *18*, 1203–1221.

[39] Schreiber, R. E., Houben, L., Wolf, S. G., Leitus, G., Lang, Z.-L., Carbó, J. J., Poblet, J. M. and Neumann, R. Real-time molecular scale observation of crystal formation. *Nat. Chem.* **2017**, *9*, 369–373.

[40] Peng, Y., Wang, F., Wang, Z., Alsayed, A. M., Zhang, Z., Yodh, A. G. and Han, Y. Two-step nucleation mechanism in solid–solid phase transitions. *Nat. Mater.* **2015**, *14*, 101–108.

[41] Rodriguez-Navarro, C., Burgos Cara, A., Elert, K., Putnis, C. V. and Ruiz-Agudo, E. Direct Nanoscale Imaging Reveals the Growth of Calcite Crystals via Amorphous Nanoparticles. *Cryst. Growth Des.* **2016**, *16*, 1850–1860.

[42] De Yoreo, J. J. *et al.* Crystallization by particle attachment in synthetic, biogenic, and geologic environments. *Science* **2015**, *349*, aaa6760-1–9.

[43] Van Santen, R. A. The Ostwald step rule. *J. Phys. Chem.* **1984**, *88*, 5768–5769.

[44] Söhnel, O. and Mullin, J. W. Precipitation of calcium carbonate. *J. Cryst. Growth* **1982**, *60*, 239–250.

[45] Cölfen, H. and Mann, S. Higher-Order Organization by Mesoscale Self-Assembly and Transformation of Hybrid Nanostructures. *Angew. Chemie Int. Ed.* **2003**, *42*, 2350–2365.

[46] LaMer, V. K. and Dinegar, R. H. Theory, Production and Mechanism of Formation of Monodispersed Hydrosols. *J. Am. Chem. Soc.* **1950**, *72*, 4847–4854.

[47] LaMer, V. K. Nucleation in Phase Transitions. *Ind. Eng. Chem.* **1952**, *44*, 1270–1277.

[48] Sun, Y. Controlled synthesis of colloidal silver nanoparticles in organic solutions: empirical rules for nucleation engineering. *Chem. Soc. Rev.* **2013**, *42*, 2497–2511.

[49] Baronov, A., Bufkin, K., Shaw, D. W., Johnson, B. L. and Patrick, D. L. A simple model of burst nucleation. *Phys. Chem. Chem. Phys.* **2015**, *17*, 20846–20852.

[50] Sugimoto, T. Spontaneous nucleation of monodisperse silver halide particles from homogeneous gelatin solution I: silver chloride. *Colloids Surfaces A Physicochem. Eng. Asp.* **2000**, *164*, 183–203.

[51] Sugimoto, T. *Monodispersed Particles*. Elsevier, Amsterdam, **2001**.

[52] Chu, D. B. K., Owen, J. S. and Peters, B. Nucleation and Growth Kinetics from LaMer Burst Data. *J. Phys. Chem. A* **2017**, *121*, 7511–7517.

[53] Scherer, G. W. Crystallization in pores. *Cem. Concr. Res.* **1999**, *29*, 1347–1358.

[54] Kołodziejczyk, K., Tarnacka, M., Kamińska, E., Dulski, M., Kamiński, K. and Paluch, M. Crystallization Kinetics under Confinement. Manipulation of the Crystalline Form of Salol by Varying Pore Diameter. *Cryst. Growth Des.* **2016**, *16*, 1218–1227.

[55] Anduix-Canto, C., Kim, Y.-Y., Wang, Y.-W., Kulak, A., Meldrum, F. C. and Christenson, H. K. Effect of Nanoscale Confinement on the Crystallization of Potassium Ferrocyanide. *Cryst. Growth Des.* **2016**, *16*, 5403–5411.

[56] Stephens, C. J., Kim, Y.-Y., Evans, S. D., Meldrum, F. C. and Christenson, H. K. Early Stages of Crystallization of Calcium Carbonate Revealed in Picoliter Droplets. *J. Am. Chem. Soc.* **2011**, *133*, 5210–5213.

[57] Nicholson, C. E., Chen, C., Mendis, B. and Cooper, S. J. Stable Polymorphs Crystallized Directly under Thermodynamic Control in Three-Dimensional Nanoconfinement: A Generic Methodology. *Cryst. Growth Des.* **2011**, *11*, 363–366.

[58] Montenegro, R., Antonietti, M., Mastai, Y. and Landfester, K. Crystallization in Miniemulsion Droplets. *J. Phys. Chem. B* **2003**, *107***,** 5088–5094.

[59] Gong, X., Wang, Y., Ihli, J., Kim, Y., Li, S., Walshaw, R., Chen, L. and Meldrum, F. C. The Crystal Hotel: A Microfluidic Approach to Biomimetic Crystallization. *Adv. Mater.* **2015**, *27***,** 7395–7400.

[60] Stephens, C. J., Ladden, S. F., Meldrum, F. C. and Christenson, H. K. Amorphous Calcium Carbonate is Stabilized in Confinement. *Adv. Funct. Mater.* **2010**, *20***,** 2108–2115.

[61] Wang, Y.-W., Christenson, H. K. and Meldrum, F. C. Confinement Leads to Control over Calcium Sulfate Polymorph. *Adv. Funct. Mater.* **2013**, *23***,** 5615–5623.

[62] Wang, Y.-W., Christenson, H. K. and Meldrum, F. C. Confinement Increases the Lifetimes of Hydroxyapatite Precursors. *Chem. Mater.* **2014**, *26***,** 5830–5838.

[63] Christenson, H. K. Confinement effects on freezing and melting. *J. Phys. Condens. Matter* **2001**, *13***,** R95–R133.

[64] Vanfleet, R. R. and Mochel, J. M. Thermodynamics of melting and freezing in small particles. *Surf. Sci.* **1995**, *341***,** 40–50.

[65] Grossier, R., Hammadi, Z., Morin, R. and Veesler, S. Predictive Nucleation of Crystals in Small Volumes and Its Consequences. *Phys. Rev. Lett.* **2011**, *107***,** 025504–025507.

[66] Schweitzer, F. and Schimansky-Geier, L. Critical parameters for nucleation in finite systems. *J. Colloid Interface Sci.* **1987**, *119***,** 67–73.

[67] Shirinyan, A. S. and Wautelet, M. On phase changes in nanosystems. *Mater. Sci. Eng. C* **2006**, *26***,** 735–736.

[68] Page, A. J. and Sear, R. P. Crystallization Controlled by the Geometry of a Surface. *J. Am. Chem. Soc.* **2009**, *131***,** 17550–17551.

[69] Kohler, F., Pierre-Louis, O. and Dysthe, D. K. Crystal growth in confinement. *Nat. Commun.* **2022**, *13***,** 6990.

[70] Hamilton, B. D., Ha, J.-M., Hillmyer, M. A. and Ward, M. D. Manipulating Crystal Growth and Polymorphism by Confinement in Nanoscale Crystallization Chambers. *Acc. Chem. Res.* **2012**, *45*, 414–423.

[71] De Boer, R. B. On the thermodynamics of pressure solution—interaction between chemical and mechanical forces. *Geochim. Cosmochim. Acta* **1977**, *41*, 249–256.

[72] Desarnaud, J., Bonn, D. and Shahidzadeh, N. The Pressure induced by salt crystallization in confinement. *Sci. Rep.* **2016**, *6*, 30856.

[73] Anduix-Canto, C., Levenstein, M. A., Kim, Y. Y., Godinho, J. R. A., Kulak, A. N., Niño, C. G., Withers, P. J., Wright, J. P., Kapur, N., Christenson, H. K. and Meldrum, F. C. Exploiting Confinement to Study the Crystallization Pathway of Calcium Sulfate. *Adv. Funct. Mater.* **2021**, *31*,

[74] Anastas, P. and Eghbali, N. Green Chemistry: Principles and Practice. *Chem. Soc. Rev.* **2010**, *39*, 301–312.

[75] Duan, H., Wang, D. and Li, Y. Green chemistry for nanoparticle synthesis. *Chem. Soc. Rev.* **2015**, *44*, 5778–5792.

[76] Pileni, M. P. Water in oil colloidal droplets used as microreactors. *Adv. Colloid Interface Sci.* **1993**, *46*, 139–163.

[77] Pileni, M. P. Nanosized Particles Made in Colloidal Assemblies. *Langmuir* **1997**, *13*, 3266–3276.

[78] Pileni, M. P. The role of soft colloidal templates in controlling the size and shape of inorganic nanocrystals. *Nat. Mater.* **2003**, *2*, 145–150.

[79] Pileni, M. P. Reverse micelles as microreactors. *J. Phys. Chem.* **1993**, *97*, 6961–6973.

[80] Pileni, M. P. Supra- and nanocrystallinities: a new scientific adventure. *J. Phys. Condens. Matter* **2011**, *23*, 503102–503109.

[81] Landfester, K., Bechthold, N., Tiarks, F. and Antonietti, M. Formulation and Stability Mechanisms of Polymerizable Miniemulsions. *Macromolecules* **1999**, *32*, 5222–5228.

[82] Davies, J. T. A quantitative kinetic theory of emulsion type, I. Physical chemistry of the emulsifying agent. *Gas/Liquid Liq. Interface. Proc. Int. Congr. Surf. Act.* **1957**, *42*, 426–438.

[83] Goodwin, J. W. Emulsions and Microemulsions. in *Colloids and Interfaces with Surfactants and Polymers - An Introduction* John Wiley & Sons, Ltd, New York, **2004**. 177–194.

[84] Landfester, K. Miniemulsions for Nanoparticle Synthesis. in *Top Curr Chem* Springer-Verlag Berlin Heidelberg, Berlin, Heidelberg, **2003**. 75–123.

[85] Antonietti, M. and Landfester, K. Polyreactions in miniemulsions. *Prog. Polym. Sci.* **2002**, *27*, 689–757.

[86] Ostwald, W. Blocking of Ostwald Ripening Allowing Long-Term Stabilization. *Z. Phys. Chem.* **1901**, *37*, 385.

[87] Higuchi, W. I. and Misra, J. Physical Degradation of Emulsions Via the Molecular Diffusion Route and the Possible Prevention Thereof. *J. Pharm. Sci.* **1962**, *51*, 459–466.

[88] Webster, A. J. and Cates, M. E. Stabilization of Emulsions by Trapped Species. *Langmuir* **1998**, *14*, 2068–2079.

[89] Webster, A. J. and Cates, M. E. Osmotic Stabilization of Concentrated Emulsions and Foams. *Langmuir* **2001**, *17*, 595–608.

[90] Landfester, K. The generation of nanoparticles in miniemulsions. *Adv. Mater.* **2001**, *13*, 765–768.

[91] Muñoz-Espí, R., Mastai, Y., Gross, S. and Landfester, K. Colloidal systems for crystallization processes from liquid phase. *CrystEngComm* **2013**, *15*, 2175–2191.

[92] Boutonnet, M. and Sanchez-Dominguez, M. Microemulsion droplets to catalytically active nanoparticles. How the application of colloidal tools in catalysis aims to well designed and efficient catalysts. *Catal. Today* **2017**, *285*, 89–103.

[93] Sanchez-Dominguez, M., Liotta, L. F., Di Carlo, G., Pantaleo, G., Venezia, A. M.,

Solans, C. and Boutonnet, M. Synthesis of CeO_2, ZrO_2, $Ce_{0.5}Zr_{0.5}O_2$, and TiO_2 nanoparticles by a novel oil-in-water microemulsion reaction method and their use as catalyst support for CO oxidation. *Catal. Today* **2010**, *158*, 35–43.

[94] Sanchez-Dominguez, M., Pemartin, K. and Boutonnet, M. Preparation of inorganic nanoparticles in oil-in-water microemulsions: A soft and versatile approach. *Curr. Opin. Colloid Interface Sci.* **2012**, *17*, 297–305.

[95] *Handbook of Microemulsion Science and Technology*. Ed. Kumar, P. & Mittal, K. L., CRC Press, Boca Raton, **1999**.

[96] López-Quintela, M. A., Tojo, C., Blanco, M. C., García Rio, L. and Leis, J. R. Microemulsion dynamics and reactions in microemulsions. *Curr. Opin. Colloid Interface Sci.* **2004**, *9*, 264–278.

[97] Landfester, K. Synthesis of Colloidal Particles in Miniemulsions. *Annu. Rev. Mater. Res.* **2006**, *36*, 231–279.

[98] Boutonnet, M., Lögdberg, S. and Elm Svensson, E. Recent developments in the application of nanoparticles prepared from w/o microemulsions in heterogeneous catalysis. *Curr. Opin. Colloid Interface Sci.* **2008**, *13*, 270–286.

[99] Capek, I. Preparation of metal nanoparticles in water-in-oil (w/o) microemulsions. *Adv. Colloid Interface Sci.* **2004**, *110*, 49–74.

[100] Eastoe, J., Hollamby, M. J. and Hudson, L. Recent advances in nanoparticle synthesis with reversed micelles. *Advances in Colloid and Interface Science* **2006**, *128–130*, 5–15.

[101] Willert, M., Rothe, R., Landfester, K. and Antonietti, M. Synthesis of inorganic and metallic nanoparticles by miniemulsification of molten salts and metals. *Chem. Mater.* **2001**, *13*, 4681–4685.

[102] Rossmanith, R., Weiss, C. K., Geserick, J., Hüsing, N., Hörmann, U., Kaiser, U. and Landfester, K. Porous anatase nanoparticles with high specific surface area prepared by miniemulsion technique. *Chem. Mater.* **2008**, *20*, 5768–5780.

[103] Schiller, R., Weiss, C. K. and Landfester, K. Phase stability and photocatalytic activity of Zr-doped anatase synthesized in miniemulsion. *Nanotechnology* **2010**, *21***,** 405603–405613.

[104] Collins, A. M., Spickermann, C. and Mann, S. Synthesis of titania hollow microspheres using non-aqueous emulsions. *J. Mater. Chem.* **2003**, *13***,** 1112–1114.

[105] Schiller, R., Weiss, C. K., Geserick, J., Hüsing, N. and Landfester, K. Synthesis of mesoporous silica particles and capsules by miniemulsion technique. *Chem. Mater.* **2009**, *21***,** 5088–5098.

[106] Cao, Z., Dong, L., Li, L., Shang, Y., Qi, D., Lv, Q., Shan, G., Ziener, U. and Landfester, K. Preparation of mesoporous submicrometer silica capsules via an interfacial sol-gel process in inverse miniemulsion. *Langmuir* **2012**, *28***,** 7023–7032.

[107] Nabih, N., Schiller, R., Lieberwirth, I., Kockrick, E., Frind, R., Kaskel, S., Weiss, C. K. and Landfester, K. Mesoporous CeO_2 nanoparticles synthesized by an inverse miniemulsion technique and their catalytic properties in methane oxidation. *Nanotechnology* **2011**, *22***,** 135606.

[108] Varol, H. S., Álvarez-Bermúdez, O., Dolcet, P., Kuerbanjiang, B., Gross, S., Landfester, K. and Muñoz-Espí, R. Crystallization at Nanodroplet Interfaces in Emulsion Systems: A Soft-Template Strategy for Preparing Porous and Hollow Nanoparticles. *Langmuir* **2016**, *32***,** 13116–13123.

[109] Dolcet, P., Casarin, M., Maccato, C., Bovo, L., Ischia, G., Gialanella, S., Mancin, F., Tondello, E. and Gross, S. Miniemulsions as chemical nanoreactors for the room temperature synthesis of inorganic crystalline nanostructures: ZnO colloids. *J. Mater. Chem.* **2012**, *22***,** 1620–1626.

[110] Dolcet, P., Latini, F., Casarin, M., Speghini, A., Tondello, E., Foss, C., Diodati, S., Verin, L., Motta, A. and Gross, S. Inorganic Chemistry in a Nanoreactor: Doped ZnO Nanostructures by Miniemulsion. *Eur. J. Inorg. Chem.* **2013**, *2013***,** 2291–2300.

[111] Winkelmann, M., Grimm, E.-M., Comunian, T., Freudig, B., Zhou, Y., Gerlinger, W., Sachweh, B. and Petra Schuchmann, H. Controlled droplet coalescence in

miniemulsions to synthesize zinc oxide nanoparticles by precipitation. *Chem. Eng. Sci.* **2013**, *92*, 126–133.

[112] Singh, I., Landfester, K., Chandra, A. and Muñoz-Espí, R. A new approach for crystallization of copper(II) oxide hollow nanostructures with superior catalytic and magnetic response. *Nanoscale* **2015**, *7*, 19250–19258.

[113] Antonello, A., Jakob, G., Dolcet, P., Momper, R., Kokkinopoulou, M., Landfester, K., Muñoz-Espí, R. and Gross, S. Synergy of Miniemulsion and Solvothermal Conditions for the Low-Temperature Crystallization of Magnetic Nanostructured Transition-Metal Ferrites. *Chem. Mater.* **2017**, *29*, 985–997.

[114] Hajir, M., Dolcet, P., Fischer, V., Holzinger, J., Landfester, K. and Muñoz-Espí, R. Sol-gel processes at the droplet interface: Hydrous zirconia and hafnia nanocapsules by interfacial inorganic polycondensation. *J. Mater. Chem.* **2012**, *22*, 5622–5628.

[115] Butturini, E., Dolcet, P., Casarin, M., Speghini, A., Pedroni, M., Benetti, F., Motta, A., Badocco, D., Pastore, P., Diodati, S., Pandolfo, L. and Gross, S. Simple, common but functional: biocompatible and luminescent rare-earth doped magnesium and calcium hydroxides from miniemulsion. *J. Mater. Chem. B* **2014**, *2*, 6639–6651.

[116] Dolcet, P., Maurizio, C., Casarin, M., Pandolfo, L., Gialanella, S., Badocco, D., Pastore, P., Speghini, A. and Gross, S. An effective two-emulsion approach to the synthesis of doped ZnS crystalline nanostructures. *Eur. J. Inorg. Chem.* **2015**, *2015*, 706–714.

[117] Dolcet, P., Mambrini, A., Pedroni, M., Speghini, A., Gialanella, S., Casarin, M. and Gross, S. Room temperature crystallization of highly luminescent lanthanide-doped CaF_2 in nanosized droplets: first example of the synthesis of metal halogenide in miniemulsion with effective doping and size control. *RSC Adv.* **2015**, *5*, 16302–16310.

[118] Muñoz-Espí, R., Weiss, C. K. and Landfester, K. Inorganic nanoparticles prepared in miniemulsion. *Curr. Opin. Colloid Interface Sci.* **2012**, *17*, 212–224.

[119] Cao, Z. and Ziener, U. Synthesis of nanostructured materials in inverse miniemulsions and their applications. *Nanoscale* **2013**, *5*, 10093–10107.

[120] Muñoz-Espí, R. and Landfester, K. Low-Temperature Miniemulsion-Based Routes for

Synthesis of Metal Oxides. *Chem. – A Eur. J.* **2020**, *26*, 9304–9313.

[121] Maceiczyk, R. M., Lignos, I. G. and deMello, A. J. Online detection and automation methods in microfluidic nanomaterial synthesis. *Curr. Opin. Chem. Eng.* **2015**, *8*, 29–35.

[122] Ferstl, W., Klahn, T., Schweikert, W., Billeb, G., Schwarzer, M. and Loebbecke, S. Inline Analysis in Microreaction Technology: A Suitable Tool for Process Screening and Optimization. *Chem. Eng. Technol.* **2007**, *30*, 370–378.

[123] Carter, C. F., Lange, H., Ley, S. V., Baxendale, I. R., Wittkamp, B., Goode, J. G. and Gaunt, N. L. ReactIR Flow Cell: A New Analytical Tool for Continuous Flow Chemical Processing. *Org. Process Res. Dev.* **2010**, *14*, 393–404.

[124] Mozharov, S., Nordon, A., Littlejohn, D., Wiles, C., Watts, P., Dallin, P. and Girkin, J. M. Improved Method for Kinetic Studies in Microreactors Using Flow Manipulation and Noninvasive Raman Spectrometry. *J. Am. Chem. Soc.* **2011**, *133*, 3601–3608.

[125] Panneerselvam, R., Sadat, H., Höhn, E.-M., Das, A., Noothalapati, H. and Belder, D. Microfluidics and surface-enhanced Raman spectroscopy, a win–win combination? *Lab Chip* **2022**, *22*, 665–682.

[126] Benito-Lopez, F., Verboom, W., Kakuta, M., Gardeniers, J. G. E., Egberink, R. J. M., Oosterbroek, E. R., van den Berg, A. and Reinhoudt, D. N. Optical fiber-based on-line UV/Vis spectroscopic monitoring of chemical reaction kinetics under high pressure in a capillary microreactor. *Chem. Commun.* **2005**, 2857.

[127] Sounart, T. L., Safier, P. A., Voigt, J. A., Hoyt, J., Tallant, D. R., Matzke, C. M. and Michalske, T. A. Spatially-resolved analysis of nanoparticle nucleation and growth in a microfluidic reactor. *Lab Chip* **2007**, *7*, 908–915.

[128] Lignos, I., Stavrakis, S., Kilaj, A. and deMello, A. J. Millisecond-Timescale Monitoring of PbS Nanoparticle Nucleation and Growth Using Droplet-Based Microfluidics. *Small* **2015**, *11*, 4009–4017.

[129] Lignos, I., Stavrakis, S., Nedelcu, G., Protesescu, L., deMello, A. J. and Kovalenko, M. V. Synthesis of Cesium Lead Halide Perovskite Nanocrystals in a Droplet-Based

Microfluidic Platform: Fast Parametric Space Mapping. *Nano Lett* **2016**, *16*, 1869–1877.

[130] Zinoveva, S., De Silva, R., D. Louis, R., Datta, P., S.S.R. Kumar, C., Goettert, J. and Hormes, J. The wet chemical synthesis of Co nanoparticles in a microreactor system: A time-resolved investigation by X-ray absorption spectroscopy. *Nucl. Instruments Methods Phys. Res. Sect. A Accel. Spectrometers, Detect. Assoc. Equip.* **2007**, *582*, 239–241.

[131] Sans, V., Porwol, L., Dragone, V. and Cronin, L. A self optimizing synthetic organic reactor system using real-time in-line NMR spectroscopy. *Chem. Sci.* **2015**, *6*, 1258–1264.

[132] Nightingale, A. M., Phillips, T. W., Bannock, J. H. and de Mello, J. C. Controlled multistep synthesis in a three-phase droplet reactor. *Nat Commun* **2014**, *5*, 3777.

[133] Shestopalov, I., Tice, J. D. and Ismagilov, R. F. Multi-step synthesis of nanoparticles performed on millisecond time scale in a microfluidic droplet-based system. *Lab Chip* **2004**, *4*, 316.

[134] Lummiss, J. A. M., Morse, P. D., Beingessner, R. L. and Jamison, T. F. Towards More Efficient, Greener Syntheses through Flow Chemistry. *Chem. Rec.* **2017**, *17*, 667–680.

[135] Hessel, V., Renken, A. and Schouten, J. C. *Handbook of Micro-Reactor Engineering and Chemistry*. Wiley-VCH, Weinheim, **2006**.

[136] Lee, C. Y., Chang, C. L., Wang, Y. N. and Fu, L. M. Microfluidic mixing: a review. *Int J Mol Sci* **2011**, *12*, 3263–3287.

[137] Ward, K. and Fan, Z. H. Mixing in microfluidic devices and enhancement methods. *J. Micromechanics Microengineering* **2015**, *25*, 094001.

[138] Song, Y., Hormes, J. and Kumar, C. S. S. R. Microfluidic Synthesis of Nanomaterials. *Small* **2008**, *4*, 698–711.

[139] Yang, H., Fan, N., Luan, W. and Tu, S. Synthesis of Monodisperse Nanocrystals via Microreaction: Open-to-Air Synthesis with Oleylamine as a Coligand. *Nanoscale Res.*

Lett. **2009**, *4*, 344.

[140] Edel, J. B., Fortt, R., DeMello, J. C. and DeMello, A. J. Microfluidic routes to the controlled production of nanoparticles. *Chem. Commun.* **2002**, 1136–1137.

[141] Köhler, J. M., Wagner, J. and Albert, J. Formation of isolated and clustered Au nanoparticles in the presence of polyelectrolyte molecules using a flow-through Si chip reactor. *J. Mater. Chem.* **2005**, *15*, 1924–1930.

[142] Wagner, J. and Köhler, J. M. Continuous Synthesis of Gold Nanoparticles in a Microreactor. *Nano Lett.* **2005**, *5*, 685–691.

[143] Boleininger, J., Kurz, A., Reuss, V. and Sönnichsen, C. Microfluidic continuous flow synthesis of rod-shaped gold and silver nanocrystals. *Phys. Chem. Chem. Phys.* **2006**, *8*, 3824–3827.

[144] Song, Y., Kumar, C. S. S. R. and Hormes, J. Synthesis of Palladium Nanoparticles Using a Continuous Flow Polymeric Micro Reactor. *J. Nanosci. Nanotechnol.* **2004**, *4*, 788–793.

[145] Sebastian, V., Smith, C. D. and Jensen, K. F. Shape-controlled continuous synthesis of metal nanostructures. *Nanoscale* **2016**, *8*, 7534–7543.

[146] Uson, L., Arruebo, M. and Sebastian, V. Towards the continuous production of Pt-based heterogeneous catalysts using microfluidic systems. *Dalt. Trans.* **2018**, *47*, 1693–1702.

[147] Khan, S. A., Günther, A., Schmidt, M. A. and Jensen, K. F. Microfluidic Synthesis of Colloidal Silica. *Langmuir* **2004**, *20*, 8604–8611.

[148] Wacker, J. B., Lignos, I., Parashar, V. K. and Gijs, M. A. M. Controlled synthesis of fluorescent silica nanoparticles inside microfluidic droplets. *Lab Chip* **2012**, *12*, 3111.

[149] Carroll, N. J., Rathod, S. B., Derbins, E., Mendez, S., Weitz, D. A. and Petsev, D. N. Droplet-Based Microfluidics for Emulsion and Solvent Evaporation Synthesis of Monodisperse Mesoporous Silica Microspheres. *Langmuir* **2008**, *24*, 658–661.

[150] Takagi, M., Maki, T., Miyahara, M. and Mae, K. Production of titania nanoparticles

by using a new microreactor assembled with same axle dual pipe. *Chem. Eng. J.* **2004**, *101*, 269–276.

[151] Wang, H., Nakamura, H., Uehara, M., Miyazaki, M. and Maeda, H. Preparation of titania particles utilizing the insoluble phase interface in a microchannel reactor. *Chem. Commun.* **2002**, 1462–1463.

[152] Kang, H. W., Leem, J., Yoon, S. Y. and Sung, H. J. Continuous synthesis of zinc oxide nanoparticles in a microfluidic system for photovoltaic application. *Nanoscale* **2014**, *6*, 2840.

[153] Wang, Y., Zhang, X., Wang, A., Li, X., Wang, G. and Zhao, L. Synthesis of ZnO nanoparticles from microemulsions in a flow type microreactor. *Chem. Eng. J.* **2014**, *235*, 191–197.

[154] Abou-Hassan, A., Sandre, O., Cabuil, V. and Tabeling, P. Synthesis of iron oxide nanoparticles in a microfluidic device: preliminary results in a coaxial flow millichannel. *Chem. Commun.* **2008**, 1783–1785.

[155] Frenz, L., El Harrak, A., Pauly, M., Bégin-Colin, S., Griffiths, A. D. and Baret, J.-C. Droplet-Based Microreactors for the Synthesis of Magnetic Iron Oxide Nanoparticles. *Angew. Chemie Int. Ed.* **2008**, *47*, 6817–6820.

[156] Seibt, S., Mulvaney, P. and Förster, S. Millisecond CdS nanocrystal nucleation and growth studied by microfluidics with in situ spectroscopy. *Colloids Surfaces A Physicochem. Eng. Asp.* **2019**, *562*, 263–269.

[157] Hung, L.-H., Choi, K. M., Tseng, W.-Y., Tan, Y.-C., Shea, K. J. and Lee, A. P. Alternating droplet generation and controlled dynamic droplet fusion in microfluidic device for CdS nanoparticle synthesis. *Lab Chip* **2006**, *6*, 174.

[158] Yen, B. K. H., Günther, A., Schmidt, M. A., Jensen, K. F. and Bawendi, M. G. A Microfabricated Gas-Liquid Segmented Flow Reactor for High-Temperature Synthesis: The Case of CdSe Quantum Dots. *Angew. Chemie Int. Ed.* **2005**, *44*, 5447–5451.

[159] Dengo, N., Faresin, A., Carofiglio, T., Maggini, M., Wu, L., Hofmann, J. P., Hensen, E.

J. M., Dolcet, P. and Gross, S. Ligand-free ZnS nanoparticles: as easy and green as it gets. *Chem. Commun.* **2020**, *56*, 8707–8710.

[160] Tajoli, F., Dengo, N., Mognato, M., Dolcet, P., Lucchini, G., Faresin, A., Grunwaldt, J.-D., Huang, X., Badocco, D., Maggini, M., Kübel, C., Speghini, A., Carofiglio, T. and Gross, S. Microfluidic Crystallization of Surfactant-Free Doped Zinc Sulfide Nanoparticles for Optical Bioimaging Applications. *ACS Appl. Mater. Interfaces* **2020**, *12*, 44074–44087.

[161] Wang, H., Li, X., Uehara, M., Yamaguchi, Y., Nakamura, H., Miyazaki, M., Shimizu, H. and Maeda, H. Continuous synthesis of CdSe–ZnS composite nanoparticles in a microfluidic reactor. *Chem. Commun.* **2004**, 48–49.

[162] Abou-Hassan, A., Sandre, O. and Cabuil, V. Microfluidics in inorganic chemistry. *Angew Chem Int Ed Engl* **2010**, *49*, 6268–6286.

[163] Marre, S. and Jensen, K. F. Synthesis of micro and nanostructures in microfluidic systems. *Chem. Soc. Rev.* **2010**, *39*, 1183–1202.

[164] Zardi, P., Carofiglio, T. and Maggini, M. Mild Microfluidic Approaches to Oxide Nanoparticles Synthesis. *Chem. – A Eur. J.* **2022**, *28*, e202103132.

[165] *Handbook of Porous Solids*. Ed. Schüth, F., Sing, K. S. W. & Weitkamp, J., Wiley, **2002**.

[166] Zimmermann, N. E. R. and Haranczyk, M. History and Utility of Zeolite Framework-Type Discovery from a Data-Science Perspective. *Cryst. Growth Des.* **2016**, *16*, 3043–3048.

[167] Beck, J. S., Chu, C. T. W., Johnson, I. E., Kresge, C. T., Leonowicz, M. E., Roth, W. J. and Vartuli, J. W. Synthetic porous crystalline material its synthesis and use. **1991**,

[168] Kresge, C. T., Leonowicz, M. E., Roth, W. J., Vartuli, J. C. and Beck, J. S. Ordered mesoporous molecular sieves synthesized by a liquid-crystal template mechanism. *Nature* **1992**, *359*, 710–712.

[169] Taguchi, A. and Schüth, F. Ordered mesoporous materials in catalysis. *Microporous Mesoporous Mater.* **2005**, *77*, 1–45.

[170] Corma, A. From Microporous to Mesoporous Molecular Sieve Materials and Their Use in Catalysis. *Chem. Rev.* **1997**, *97*, 2373–2420.

[171] Soler-Illia, G. J. de A. A., Sanchez, C., Lebeau, B. and Patarin, J. Chemical Strategies To Design Textured Materials: from Microporous and Mesoporous Oxides to Nanonetworks and Hierarchical Structures. *Chem. Rev.* **2002**, *102*, 4093–4138.

[172] Selvam, P., Bhatia, S. K. and Sonwane, C. G. Recent Advances in Processing and Characterization of Periodic Mesoporous MCM-41 Silicate Molecular Sieves. *Ind. Eng. Chem. Res.* **2001**, *40*, 3237–3261.

[173] Meynen, V., Cool, P. and Vansant, E. F. Synthesis of siliceous materials with micro- and mesoporosity. *Microporous Mesoporous Mater.* **2007**, *104*, 26–38.

[174] Zhao, D., Huo, Q., Feng, J., Chmelka, B. F. and Stucky, G. D. Nonionic triblock and star diblock copolymer and oligomeric sufactant syntheses of highly ordered, hydrothermally stable, mesoporous silica structures. *J. Am. Chem. Soc.* **1998**, *120*, 6024–6036.

[175] Linssen, T., Cassiers, K., Cool, P. and Vansant, E. F. Mesoporous templated silicates: an overview of their synthesis, catalytic activation and evaluation of the stability. *Adv. Colloid Interface Sci.* **2003**, *103*, 121–147.

[176] Antonelli, D. M. and Ying, J. Y. Synthesis of Hexagonally Packed Mesoporous TiO_2 by a Modified Sol–Gel Method. *Angew. Chemie Int. Ed. English* **1995**, *34*, 2014–2017.

[177] Antonelli, D. M. Synthesis of phosphorus-free mesoporous titania via templating with amine surfactants. *Microporous Mesoporous Mater.* **1999**, *30*, 315–319.

[178] Frindell, K. L., Tang, J., Harreld, J. H. and Stucky, G. D. Enhanced Mesostructural Order and Changes to Optical and Electrochemical Properties Induced by the Addition of Cerium(III) to Mesoporous Titania Thin Films. *Chem. Mater.* **2004**, *16*, 3524–3532.

[179] Yang, P., Zhao, D., Margolese, D. I., Chmelka, B. F. and Stucky, G. D. Block Copolymer Templating Syntheses of Mesoporous Metal Oxides with Large Ordering Lengths and Semicrystalline Framework. *Chem. Mater.* **1999**, *11*, 2813–2826.

[180] Antonelli, D. M. and Ying, J. Y. Synthesis of a Stable Hexagonally Packed Mesoporous Niobium Oxide Molecular Sieve Through a Novel Ligand-Assisted Templating Mechanism. *Angew. Chemie Int. Ed. English* **1996**, *35***,** 426–430.

[181] Ciesla, U., Schacht, S., Stucky, G. D., Unger, K. K. and Schüth, F. Formation of a Porous Zirconium Oxo Phosphate with a High Surface Area by a Surfactant-Assisted Synthesis. *Angew. Chemie Int. Ed. English* **1996**, *35***,** 541–543.

[182] Stein, A., Melde, B. J. and Schroden, R. C. Hybrid Inorganic-Organic Mesoporous Silicates—Nanoscopic Reactors Coming of Age. *Adv. Mater.* **2000**, *12***,** 1403–1419.

[183] Hoffmann, F., Cornelius, M., Morell, J. and Fröba, M. Silica-Based Mesoporous Organic–Inorganic Hybrid Materials. *Angew. Chemie Int. Ed.* **2006**, *45***,** 3216–3251.

[184] Vinu, A., Hossain, K. Z. and Ariga, K. Recent Advances in Functionalization of Mesoporous Silica. *J. Nanosci. Nanotechnol.* **2005**, *5***,** 347–371.

[185] Choi, M., Kleitz, F., Liu, D., Lee, H. Y., Ahn, W.-S. and Ryoo, R. Controlled Polymerization in Mesoporous Silica toward the Design of Organic−Inorganic Composite Nanoporous Materials. *J. Am. Chem. Soc.* **2005**, *127***,** 1924–1932.

[186] Schüth, F. Endo- and Exotemplating to Create High-Surface-Area Inorganic Materials. *Angew. Chemie Int. Ed.* **2003**, *42***,** 3604–3622.

[187] Yanagisawa, T., Shimizu, T., Kuroda, K. and Kato, C. The Preparation of Alkyltrimethylammonium–Kanemite Complexes and Their Conversion to Microporous Materials. *Bull. Chem. Soc. Jpn.* **1990**, *63***,** 988–992.

[188] Zhao, D., Feng, J., Huo, Q., Melosh, N., Fredrickson, G. H., Chmelka, B. F. and Stucky, G. D. Triblock copolymer syntheses of mesoporous silica with periodic 50 to 300 angstrom pores. *Science* **1998**, *279***,** 548–552.

[189] Kleitz, F., Hei Choi, S. and Ryoo, R. Cubic Ia3d large mesoporous silica: synthesis and replication to platinum nanowires, carbon nanorods and carbon nanotubes. *Chem. Commun.* **2003**, 2136.

[190] Yu, C., Yu, Y. and Zhao, D. Highly ordered large caged cubic mesoporous silica

structures templated by triblock PEO–PBO–PEO copolymer. *Chem. Commun.* **2000**, 575–576.

[191] Huo, Q., Margolese, D. I., Ciesla, U., Feng, P., Gier, T. E., Sieger, P., Leon, R., Petroff, P. M., Schüth, F. and Stucky, G. D. Generalized synthesis of periodic surfactant/inorganic composite materials. *Nature* **1994**, *368***,** 317–321.

[192] Huo, Q., Margolese, D. I., Ciesla, U., Demuth, D. G., Feng, P., Gier, T. E., Sieger, P., Firouzi, A. and Chmelka, B. F. Organization of Organic Molecules with Inorganic Molecular Species into Nanocomposite Biphase Arrays. *Chem. Mater.* **1994**, *6***,** 1176–1191.

[193] Beck, J. S., Vartuli, J. C., Roth, W. J., Leonowicz, M. E., Kresge, C. T., Schmitt, K. D., Chu, C. T. W., Olson, D. H., Sheppard, E. W., McCullen, S. B., Higgins, J. B. and Schlenker, J. L. A new family of mesoporous molecular sieves prepared with liquid crystal templates. *J. Am. Chem. Soc.* **1992**, *114***,** 10834–10843.

[194] Schwanke, A. J., Balzer, R. and Pergher, S. Microporous and Mesoporous Materials from Natural and Inexpensive Sources. in *Handbook of Ecomaterials* Ed. Martínez, L. M. T., Kharissova, O. V. & Kharisov, B. I., Springer International Publishing, Cham, **2017**. 1–22.

[195] Cassiers, K., Linssen, T., Mathieu, M., Benjelloun, M., Schrijnemakers, K., Van Der Voort, P., Cool, P. and Vansant, E. F. A Detailed Study of Thermal, Hydrothermal, and Mechanical Stabilities of a Wide Range of Surfactant Assembled Mesoporous Silicas. *Chem. Mater.* **2002**, *14***,** 2317–2324.

[196] Kruk, M., Jaroniec, M., Ko, C. H. and Ryoo, R. Characterization of the porous structure of SBA-15. *Chem. Mater.* **2000**, *12***,** 1961–1968.

[197] Kipkemboi, P., Fogden, A., Alfredsson, V. and Flodström, K. Triblock Copolymers as Templates in Mesoporous Silica Formation: Structural Dependence on Polymer Chain Length and Synthesis Temperature. *Langmuir* **2001**, *17***,** 5398–5402.

[198] Yang, P., Zhao, D., Margolese, D. I., Chmelka, B. F. and Stucky, G. D. Generalized syntheses of large-pore mesoporous metal oxides with semicrystalline frameworks.

Nature **1998**, *396*, 152–155.

[199] Fulvio, P. F., Pikus, S. and Jaroniec, M. Tailoring properties of SBA-15 materials by controlling conditions of hydrothermal synthesis. *J. Mater. Chem.* **2005**, *15*, 5049–5053.

[200] Feng, P., Bu, X. and Pine, D. J. Control of Pore Sizes in Mesoporous Silica Templated by Liquid Crystals in Block Copolymer−Cosurfactant−Water Systems. *Langmuir* **2000**, *16*, 5304–5310.

[201] Cui, X., Zin, W.-C., Cho, W.-J. and Ha, C.-S. Nonionic triblock copolymer synthesis of SBA-15 above the isoelectric point of silica (pH=2–5). *Mater. Lett.* **2005**, *59*, 2257–2261.

[202] Zhang, H., Sun, J., Ma, D., Bao, X., Klein-Hoffmann, A., Weinberg, G., Su, D. and Schlögl, R. Unusual Mesoporous SBA-15 with Parallel Channels Running along the Short Axis. *J. Am. Chem. Soc.* **2004**, *126*, 7440–7441.

[203] Zhang, W.-H., Zhang, L., Xiu, J., Shen, Z., Li, Y., Ying, P. and Li, C. Pore size design of ordered mesoporous silicas by controlling micellar properties of triblock copolymer EO20PO70EO20. *Microporous Mesoporous Mater.* **2006**, *89*, 179–185.

[204] Zhao, D., Sun, J., Li, Q. and Stucky, G. D. Morphological Control of Highly Ordered Mesoporous Silica SBA-15. *Chem. Mater.* **2000**, *12*, 275–279.

[205] Bennadja, Y., Beaunier, P., Margolese, D. and Davidson, A. Fine tuning of the interaction between Pluronic surfactants and silica walls in SBA-15 nanostructured materials. *Microporous Mesoporous Mater.* **2001**, *44–45*, 147–152.

[206] Impéror-Clerc, M., Davidson, P. and Davidson, A. Existence of a Microporous Corona around the Mesopores of Silica-Based SBA-15 Materials Templated by Triblock Copolymers. *J. Am. Chem. Soc.* **2000**, *122*, 11925–11933.

[207] Ryoo, R., Joo, S. H. and Jun, S. Synthesis of Highly Ordered Carbon Molecular Sieves via Template-Mediated Structural Transformation. *J. Phys. Chem. B* **1999**, *103*, 7743–7746.

[208] Lee, J., Yoon, S., Hyeon, T., Oh, S. M. and Kim, K. B. Synthesis of a new mesoporous carbon and its application to electrochemical double-layer capacitors. *Chem. Commun.* **1999**, 2177–2178.

[209] Zhou, B., Li, C. Y., Qi, N., Jiang, M., Wang, B. and Chen, Z. Q. Pore structure of mesoporous silica (KIT-6) synthesized at different temperatures using positron as a nondestructive probe. *Appl. Surf. Sci.* **2018**, *450***,** 31–37.

[210] *Catalyst Preparation*. Ed. Regalbuto, J., CRC Press, Boca Raton, **2016**.

[211] Komiyama, M. Design and Preparation of Impregnated Catalysts. *Catal. Rev.* **1985**, *27***,** 341–372.

[212] Roggenbuck, J., Waitz, T. and Tiemann, M. Synthesis of mesoporous metal oxides by structure replication: Strategies of impregnating porous matrices with metal salts. *Microporous Mesoporous Mater.* **2008**, *113***,** 575–582.

[213] Maatman, R. W. and Prater, C. D. Adsorption and exclusion in impregnation of porous catalytic supports. *Ind. Eng. Chem.* **1957**, *49***,** 253–257.

[214] Lekhal, A., Glasser, B. J. and Khinast, J. G. Impact of drying on the catalyst profile in supported impregnation catalysts. *Chem. Eng. Sci.* **2001**, *56***,** 4473–4487.

[215] Wu, S., Li, M. and Sun, Y. In Situ Synchrotron X-ray Characterization Shining Light on the Nucleation and Growth Kinetics of Colloidal Nanoparticles. *Angew. Chemie Int. Ed.* **2019**, *58***,** 8987–8995.

[216] Walton, R. I. and O'Hare, D. Watching solids crystallise using in situ powder diffraction. *Chem. Commun.* **2000**, 2283–2291.

[217] Jensen, K. M. O., Debeer, S. and Koziej, D. Spectroscopy and scattering for chemistry: New possibilities and challenges with large scale facilities. *Nanoscale* **2020**, *12***,** 17968–17970.

[218] Koziej, D. Revealing Complexity of Nanoparticle Synthesis in Solution by in Situ Hard X-ray Spectroscopy - Today and beyond. *Chem. Mater.* **2016**, *28***,** 2478–2490.

[219] Ingham, B. X-ray scattering characterisation of nanoparticles. *Crystallogr. Rev.* **2015**,

*21***,** 229–303.

[220] Wu, S. and Sun, Y. In Situ Techniques for Probing Kinetics and Mechanism of Hollowing Nanostructures through Direct Chemical Transformations. *Small Methods* **2018**, *2***,** 1800165–1800181.

[221] Sai Krishna, K., Navin, C. V., Biswas, S., Singh, V., Ham, K., Bovenkamp, G. L., Theegala, C. S., Miller, J. T., Spivey, J. J. and Kumar, C. S. S. R. Millifluidics for Time-resolved Mapping of the Growth of Gold Nanostructures. *J. Am. Chem. Soc.* **2013**, *135***,** 5450–5456.

[222] Harada, M. and Kamigaito, Y. Nucleation and Aggregative Growth Process of Platinum Nanoparticles Studied by in Situ Quick XAFS Spectroscopy. *Langmuir* **2012**, *28***,** 2415–2428.

[223] Yao, T., Liu, S., Sun, Z., Li, Y., He, S., Cheng, H., Xie, Y., Liu, Q., Jiang, Y., Wu, Z., Pan, Z., Yan, W. and Wei, S. Probing Nucleation Pathways for Morphological Manipulation of Platinum Nanocrystals. *J. Am. Chem. Soc.* **2012**, *134***,** 9410–9416.

[224] Shen, X., Zhang, C., Zhang, S., Dai, S., Zhang, G., Ge, M., Pan, Y., Sharkey, S. M., Graham, G. W., Hunt, A., Waluyo, I., Miller, J. T., Pan, X. and Peng, Z. Deconvolution of octahedral Pt_3Ni nanoparticle growth pathway from in situ characterizations. *Nat. Commun.* **2018**, *9***,** 4485.

[225] Hubert, F., Testard, F., Thill, A., Kong, Q., Tache, O. and Spalla, O. Growth and Overgrowth of Concentrated Gold Nanorods: Time Resolved SAXS and XANES. *Cryst. Growth Des.* **2012**, *12***,** 1548–1555.

[226] Jensen, K. M. Ø., Andersen, H. L., Tyrsted, C., Bøjesen, E. D., Dippel, A.-C., Lock, N., Billinge, S. J. L., Iversen, B. B. and Christensen, M. Mechanisms for Iron Oxide Formation under Hydrothermal Conditions: An in Situ Total Scattering Study. *ACS Nano* **2014**, *8***,** 10704–10714.

[227] Beale, A. M., Van Der Eerden, A. M. J., Jacques, S. D. M., Leynaud, O., O'Brien, M. G., Meneau, F., Nikitenko, S., Bras, W. and Weckhuysen, B. M. A combined SAXS/WAXS/XAFS setup capable of observing concurrent changes across the nano-

to-micrometer size range in inorganic solid crystallization processes. *J. Am. Chem. Soc.* **2006**, *128*, 12386–12387.

[228] Nikitenko, S., Beale, A. M., Van Der Eerden, A. M. J., Jacques, S. D. M., Leynaud, O., O'Brien, M. G., Detollenaere, D., Kaptein, R., Weckhuysen, B. M. and Bras, W. Implementation of a combined SAXS/WAXS/QEXAFS set-up for time-resolved in situ experiments. *J. Synchrotron Radiat.* **2008**, *15*, 632–640.

[229] Grote, L. *et al.* X-ray studies bridge the molecular and macro length scales during the emergence of CoO assemblies. *Nat. Commun.* **2021**, *12*, 4429–4440.

[230] Chithambararaj, A., Sanjini, N. S., Bose, A. C. and Velmathi, S. Flower-like hierarchical h-MoO_3: New findings of efficient visible light driven nano photocatalyst for methylene blue degradation. *Catal. Sci. Technol.* **2013**, *3*, 1405–1414.

[231] Chithambararaj, A., Sanjini, N. S., Velmathi, S. and Chandra Bose, A. Preparation of h-MoO_3 and α-MoO_3 nanocrystals: Comparative study on photocatalytic degradation of methylene blue under visible light irradiation. *Phys. Chem. Chem. Phys.* **2013**, *15*, 14761–14769.

[232] Huang, L., Fang, W., Yang, Y., Wu, J., Yu, H., Dong, X., Wang, T., Liu, Z. and Zhao, B. Three-dimensional MoO_3 nanoflowers assembled with nanosheets for rhodamine B degradation under visible light. *Mater. Res. Bull.* **2018**, *108*, 38–45.

[233] Li, Z., Ma, J., Zhang, B., Song, C. and Wang, D. Crystal phase- and morphology-controlled synthesis of MoO_3 materials. *CrystEngComm* **2017**, *19*, 1479–1485.

[234] Jittiarporn, P., Sikong, L., Kooptarnond, K. and Taweepreda, W. Effects of precipitation temperature on the photochromic properties of h-MoO_3. *Ceram. Int.* **2014**, *40*, 13487–13495.

[235] Jittiarporn, P., Sikong, L., Kooptarnond, K. and Taweepreda, W. Influence of calcination temperature on the structural and photochromic properties of nanocrystalline MoO_3. *Dig. J. Nanomater. Biostructures* **2015**, *10*, 1237–1248.

[236] Barazzouk, S., Tandon, R. P. and Hotchandani, S. MoO_3-based sensor for NO, NO_2 and CH_4 detection. *Sensors Actuators B Chem.* **2006**, *119*, 691–694.

[237] Rahmani, M. B., Keshmiri, S. H., Yu, J., Sadek, A. Z., Al-Mashat, L., Moafi, A., Latham, K., Li, Y. X., Wlodarski, W. and Kalantarzadeh, K. Gas sensing properties of thermally evaporated lamellar MoO_3. *Sensors Actuators B Chem.* **2010**, *145*, 13–19.

[238] Chen, D., Liu, M., Yin, L., Li, T., Yang, Z., Li, X., Fan, B., Wang, H., Zhang, R., Li, Z., Lu, H., Yang, D., Sun, J. and Gao, L. Single-crystalline MoO3 nanoplates: topochemical synthesis and enhanced ethanol-sensing performance. *J. Mater. Chem.* **2011**, *21*, 9332–9342.

[239] Comini, E., Yubao, L., Brando, Y. and Sberveglieri, G. Gas sensing properties of MoO_3 nanorods to CO and CH_3OH. *Chem. Phys. Lett.* **2005**, *407*, 368–371.

[240] Kihlborg, L. Least squares refinement of crystal structure of molybdenum trioxide. *Ark. Kemi* **1963**, *21*, 357–364.

[241] McCarron, E. M. β-MoO_3: a metastable analogue of WO_3. *J. Chem. Soc. Chem. Commun.* **1986**, 336–338.

[242] McCarron, E. M., Thomas, D. M. and Calabrese, J. C. Hexagonal molybdates: Crystal structure of $(Na_{.2}H_2O)Mo_{5.22}[H_{4.5}]_{0.67}O_{18}$. *Inorg. Chem.* **1987**, *26*, 370–373.

[243] Pan, W., Tian, R., Jin, H., Guo, Y., Zhang, L., Wu, X., Zhang, L., Han, Z., Liu, G., Li, J., Rao, G., Wang, H. and Chu, W. Structure, optical, and catalytic properties of novel hexagonal metastable h-MoO_3 nano- and microrods synthesized with modified liquid-phase processes. *Chem. Mater.* **2010**, *22*, 6202–6208.

[244] Zheng, L., Xu, Y., Jin, D. and Xie, Y. Novel Metastable Hexagonal MoO_3 Nanobelts: Synthesis, Photochromic, and Electrochromic Properties. *Chem. Mater.* **2009**, *21*, 5681–5690.

[245] Lunk, H. J., Hartl, H., Hartl, M. A., Fait, M. J. G., Shenderovich, I. G., Feist, M., Frisk, T. A., Daemen, L. L., Mauder, D., Eckelt, R. and Gurinov, A. A. 'Hexagonal molybdenum trioxide' - Known for 100 years and still a fount of new discoveries. *Inorg. Chem.* **2010**, *49*, 9400–9408.

[246] Rosenheim, A. Die Darstellung von Molybdänsäuredihydrat. *Zeitschrift für Anorg. Chemie* **1906**, *50*, 320–320.

[247] Song, J., Ni, X., Gao, L. and Zheng, H. Synthesis of metastable h-MoO_3 by simple chemical precipitation. *Mater. Chem. Phys.* **2007**, *102*, 245–248.

[248] Ramana, C. V., Atuchin, V. V., Troitskaia, I. B., Gromilov, S. A., Kostrovsky, V. G. and Saupe, G. B. Low-temperature synthesis of morphology controlled metastable hexagonal molybdenum trioxide (MoO_3). *Solid State Commun.* **2009**, *149*, 6–9.

[249] Muñoz-Espí, R., Burger, C., Krishnan, C. V. and Chu, B. Polymer-controlled crystallization of molybdenum oxides from peroxomolybdates: Structural diversity and application to catalytic epoxidation. *Chem. Mater.* **2008**, *20*, 7301–7311.

[250] Guo, J., Zavalij, P. and Whittingham, M. S. Metastable Hexagonal Molybdates: Hydrothermal Preparation, Structure, and Reactivity. *J. Solid State Chem.* **1995**, *117*, 323–332.

[251] Cruywagen, J. J. Protonation, Oligomerization, and Condensation Reactions of Vanadate(V), Molybdate(VI), and Tungstate(VI). *Adv. Inorg. Chem.* **1999**, *49*, 127–182.

[252] Zeng, L. and Yong Cheng, C. A literature review of the recovery of molybdenum and vanadium from spent hydrodesulphurisation catalysts. *Hydrometallurgy* **2009**, *98*, 10–20.

[253] Lee, M.-S., Sohn, S.-H. and Lee, M.-H. Ionic Equilibria and Ion Exchange of Molybdenum(VI) from Strong Acid Solution. *Bull. Korean Chem. Soc.* **2011**, *32*, 3687–3691.

[254] *Polyoxometalate chemistry from topology via self-assembly to applications*. Ed. Pope, M. T. & Müller, A., Springer Dordrecht, **2001**.

[255] Long, D. L., Burkholder, E. and Cronin, L. Polyoxometalate clusters, nanostructures and materials: From self assembly to designer materials and devices. *Chem. Soc. Rev.* **2007**, *36*, 105–121.

[256] Zhao, H. Aggregation Behavior of Span-80 in Cyclohexane by Steady-state Fluorescent Probe. in *2011 AASRI Conference on Artificial Intelligence and Industry Application, vol 4* Ed. Deng, W., **2011**, 344–347.

[257] Bahtz, J., Gunes, D. Z., Syrbe, A., Mosca, N., Fischer, P. and Windhab, E. J. Quantification of Spontaneous W/O Emulsification and its Impact on the Swelling Kinetics of Multiple W/O/W Emulsions. *Langmuir* **2016**, *32***,** 5787–5795.

[258] Dhage, S. R., Hassan, M. S. and Yang, O. B. Low temperature fabrication of hexagon shaped h-MoO_3 nanorods and its phase transformation. *Mater. Chem. Phys.* **2009**, *114***,** 511–514.

[259] Moura, J. V. B., Silveira, J. V., da Silva Filho, J. G., Souza Filho, A. G., Luz-Lima, C. and Freire, P. T. C. Temperature-induced phase transition in h-MoO_3: Stability loss mechanism uncovered by Raman spectroscopy and DFT calculations. *Vib. Spectrosc.* **2018**, *98***,** 98–104.

[260] Silveira, J. V., Moura, J. V. B., Luz-Lima, C., Freire, P. T. C. and Souza Filho, A. G. Laser-induced thermal effects in hexagonal MoO_3 nanorods. *Vib. Spectrosc.* **2018**, *98***,** 145–151.

[261] Atuchin, V. V., Gavrilova, T. A., Kostrovsky, V. G., Pokrovsky, L. D. and Troitskaia, I. B. Morphology and structure of hexagonal MoO_3 nanorods. *Inorg. Mater.* **2008**, *44***,** 622–627.

[262] Nakamoto, K. *Infrared spectra of inorganic and coordination compounds*. John Wiley & Sons, Inc., New York, **1963**.

[263] Dhage, S. R., Hassan, M. S. and Yang, O. B. Low temperature fabrication of hexagon shaped h-MoO_3 nanorods and its phase transformation. *Mater. Chem. Phys.* **2009**, *114***,** 511–514.

[264] Jehn, H., Kurtz, W., Schneider, D., Trobisch, U. and Wagner, J. *Gmelin Handbook of Inorganic Chemistry: Mo Molybdenum. Supplement Volume B5*. Ed. Katscher, H., Kurtz, W. & Schröder, F., Springer Berlin Heidelberg, Berlin, Heidelberg, **1989**.

[265] Greenwood, N. N. and Earnshaw, A. *Chemistry of the Elements*. Butterworth-Heinemann, Oxford, **1998**.

[266] Li, T., Senesi, A. J. and Lee, B. Small Angle X-ray Scattering for Nanoparticle Research. *Chem. Rev.* **2016**, *116***,** 11128–11180.

[267] Schnablegger, H. and Singh, Y. *The SAXS Guide*. Anton-Paar GmbH, Graz, **2017**.

[268] Feigin, L. A. and Svergun, D. I. *Structure Analysis by Small-Angle X-ray and Neutron Scattering*. Springer, **2013**.

[269] Cölfen, H. and Antonietti, M. Mesocrystals: Inorganic Superstructures Made by Highly Parallel Crystallization and Controlled Alignment. *Angew. Chemie Int. Ed.* **2005**, *44*, 5576–5591.

[270] Tougerti, A., Berrier, E., Mamede, A.-S., La Fontaine, C., Briois, V., Joly, Y., Payen, E., Paul, J.-F. and Cristol, S. Synergy between XANES Spectroscopy and DFT to Elucidate the Amorphous Structure of Heterogeneous Catalysts: TiO_2-Supported Molybdenum Oxide Catalysts. *Angew. Chemie Int. Ed.* **2013**, *52*, 6440–6444.

[271] Macis, S., Rezvani, J., Davoli, I., Cibin, G., Spataro, B., Scifo, J., Faillace, L. and Marcelli, A. Structural Evolution of MoO3 Thin Films Deposited on Copper Substrates upon Annealing: An X-ray Absorption Spectroscopy Study. *Condens. Matter* **2019**, *4*, 41–47.

[272] Borg, S., Liu, W., Etschmann, B., Tian, Y. and Brugger, J. An XAS study of molybdenum speciation in hydrothermal chloride solutions from 25–385 °C and 600 bar. *Geochim. Cosmochim. Acta* **2012**, *92*, 292–307.

[273] Crisci, M., Dolcet, P., Yang, J., Salerno, M., Bélteky, P., Kukovecz, Á., Lamberti, F., Agnoli, S., Osella, S., Gross, S. and Gatti, T. Design Principles and Insights into the Liquid-Phase Exfoliation of Alpha-MoO_3 for the Production of Colloidal 2D Nano-inks in Green Solvents. *J. Phys. Chem. C* **2022**, *126*, 404–415.

[274] Troitskaia, I. B., Gavrilova, T. A., Zubareva, A. P., Troitskii, D. Y. and Gromilov, S. A. Thermal transformations of the composition and structure of hexagonal molybdenum oxide. *J. Struct. Chem.* **2015**, *56*, 289–296.

[275] Kumar, V., Sumboja, A., Wang, J., Bhavanasi, V., Nguyen, V. C. and Lee, P. S. Topotactic Phase Transformation of Hexagonal MoO_3 to Layered MoO_3-II and Its Two-Dimensional (2D) Nanosheets. *Chem. Mater.* **2014**, *26*, 5533–5539.

[276] Dieterle, M., Weinberg, G. and Mestl, G. Raman spectroscopy of molybdenum oxides

- Part I. Structural characterization of oxygen defects in MoO_{3-x} by DR UV/VIS, Raman spectroscopy and X-ray diffraction. *Phys. Chem. Chem. Phys.* **2002**, *4*, 812–821.

[277] Longo, V. M., De Figueiredo, A. T., Campos, A. B., Espinosa, J. W. M., Hernandes, A. C., Taft, C. A., Sambrano, J. R., Varela, J. A. and Longo, E. Different origins of green-light photoluminescence emission in structurally ordered and disordered powders of calcium molybdate. *J. Phys. Chem. A* **2008**, *112*, 8920–8928.

[278] Groenink, J. A., Hakfoort, C. and Blasse, G. The Luminescence of Calcium Molybdate. *Phys. Status Solidi* **1979**, *54*, 329–336.

[279] Phuruangrat, A., Thongtem, T. and Thongtem, S. Preparation, characterization and photoluminescence of nanocrystalline calcium molybdate. *J. Alloys Compd.* **2009**, *481*, 568–572.

[280] Parchur, A. K., Ningthoujam, R. S., Rai, S. B., Okram, G. S., Singh, R. A., Tyagi, M., Gadkari, S. C., Tewari, R. and Vatsa, R. K. Luminescence properties of Eu^{3+} doped $CaMoO_4$ nanoparticles. *Dalt. Trans.* **2011**, *40*, 7595–7601.

[281] Thongtem, T., Kungwankunakorn, S., Kuntalue, B., Phuruangrat, A. and Thongtem, S. Luminescence and absorbance of highly crystalline $CaMoO_4$, $SrMoO_4$, $CaWO_4$ and $SrWO_4$ nanoparticles synthesized by co-precipitation method at room temperature. *J. Alloys Compd.* **2010**, *506*, 475–481.

[282] Andrade, L. H. C., Li, M. S., Guyot, Y., Brenier, A. and Boulon, G. Optical multi-sites of Nd^{3+}-doped $CaMoO_4$ induced by Nb^{5+} charge compensator. *J. Phys. Condens. Matter* **2006**, *18*, 7883–7892.

[283] Kiss, Z. J. and Pressley, R. J. Crystalline Solid Lasers. *Appl. Opt.* **1966**, *5*, 1474.

[284] Bavykina, I., Angloher, G., Hauff, D., Kiefer, M., Petricca, F. and Pröbst, F. Development of cryogenic phonon detectors based on $CaMoO_4$ and $ZnWO_4$ scintillating crystals for direct dark matter search experiments. *Opt. Mater. (Amst).* **2009**, *31*, 1382–1387.

[285] Annenkov, A. N. *et al.* Development of $CaMoO_4$ crystal scintillators for a double beta decay experiment with ^{100}Mo. *Nucl. Instruments Methods Phys. Res. Sect. A Accel.*

Spectrometers, Detect. Assoc. Equip. **2008**, *584*, 334–345.

[286] Saraf, R., Shivakumara, C., Dhananjaya, N., Behera, S. and Nagabhushana, H. Photoluminescence properties of Eu^{3+}-activated $CaMoO_4$ phosphors for WLEDs applications and its Judd–Ofelt analysis. *J. Mater. Sci.* **2015**, *50*, 287–298.

[287] Sleight, A. W. Accurate cell dimensions for ABO_4 molybdates and tungstates. *Acta Crystallogr. Sect. B Struct. Crystallogr. Cryst. Chem.* **1972**, *28*, 2899–2902.

[288] Becerro, A. I., Allix, M., Laguna, M., González-Mancebo, D., Genevois, C., Caballero, A., Lozano, G., Núñez, N. O. and Ocaña, M. Revealing the substitution mechanism in Eu^{3+}:$CaMoO_4$ and Eu^{3+},Na^{+}:$CaMoO_4$ phosphors. *J. Mater. Chem. C* **2018**, *6*, 12830–12840.

[289] Singh, B. P., Parchur, A. K., Ningthoujam, R. S., Ansari, A. A., Singh, P. and Rai, S. B. Enhanced photoluminescence in $CaMoO_4$:Eu^{3+} by Gd^{3+} co-doping. *Dalt. Trans.* **2014**, *43*, 4779–4789.

[290] Laguna, M., Nuñez, N. O., Becerro, A. I. and Ocaña, M. Morphology control of uniform $CaMoO_4$ microarchitectures and development of white light emitting phosphors by Ln doping (Ln = Dy^{3+}, Eu^{3+}). *CrystEngComm* **2017**, *19*, 1590–1600.

[291] Yan, S., Zhang, J., Zhang, X., Lu, S., Ren, X., Nie, Z. and Wang, X. Enhanced Red Emission in $CaMoO_4$:Bi^{3+},Eu^{3+}. *J. Phys. Chem. C* **2007**, *111*, 13256–13260.

[292] Lei, F. and Yan, B. Hydrothermal synthesis and luminescence of $CaMO_4$:RE^{3+} (M=W, Mo; RE=Eu, Tb) submicro-phosphors. *J. Solid State Chem.* **2008**, *181*, 855–862.

[293] Tranquilin, R. L., Lovisa, L. X., Almeida, C. R. R., Paskocimas, C. A., Li, M. S., Oliveira, M. C., Gracia, L., Andres, J., Longo, E., Motta, F. V. and Bomio, M. R. D. Understanding the White-Emitting $CaMoO_4$ Co-Doped Eu^{3+}, Tb^{3+}, and Tm^{3+} Phosphor through Experiment and Computation. *J. Phys. Chem. C* **2019**, *123*, 18536–18550.

[294] Shannon, R. D. Revised effective ionic radii and systematic studies of interatomic distances in halides and chalcogenides. *Acta Crystallogr. Sect. A Found. Crystallogr.* **1976**, *32*, 751–767.

[295] Liu, X., Li, L., Noh, H. M., Jeong, J. H., Jang, K. and Shin, D. S. Controllable synthesis of uniform $CaMoO_4:Eu^{3+}$,M^+ (M = Li, Na, K) microspheres and optimum luminescence properties. *RSC Adv.* **2015**, *5*, 9441–9454.

[296] Bayat, A., Mahjoub, A. R. and Amini, M. M. Synthesis of high crystalline hierarchical self-assembled $MMoO_4$ (M=Ca, Sr and Ba) super structures: Having hydrophilic surfaces and obvious red-shifted photoluminescence behavior. *Mater. Chem. Phys.* **2019**, *223*, 583–590.

[297] Sung Lim, C. Microwave-assisted synthesis and photoluminescence of $MMoO_4$ (M=Ca, Ba) particles via a metathetic reaction. *J. Lumin.* **2012**, *132*, 1774–1780.

[298] Ryu, J. H., Yoon, J. W., Lim, C. S., Oh, W. C. and Shim, K. B. Microwave-assisted synthesis of $CaMoO_4$ nano-powders by a citrate complex method and its photoluminescence property. *J. Alloys Compd.* **2005**, *390*, 245–249.

[299] Marques, V. S., Cavalcante, L. S., Sczancoski, J. C., Alcântara, A. F. P., Orlandi, M. O., Moraes, E., Longo, E., Varela, J. A., Siu Li, M. and Santos, M. R. M. C. Effect of different solvent ratios (water/ethylene glycol) on the growth process of $CaMoO_4$ crystals and their optical properties. *Cryst. Growth Des.* **2010**, *10*, 4752–4768.

[300] Ho Ryu, J., Geun Choi, B., Yoon, J.-W., Bo Shim, K., Machi, K. and Hamada, K. Synthesis of $CaMoO_4$ nanoparticles by pulsed laser ablation in deionized water and optical properties. *J. Lumin.* **2007**, *124*, 67–70.

[301] Song, J., Xu, L., Li, H., Wang, Y., He, D. and Jiao, H. Morphology-controlled synthesis of Eu^{3+}-doped calcium molybdate red phosphors via a facile room temperature precipitation route. *Powder Technol.* **2014**, *254*, 527–537.

[302] Yang, Y., Li, X., Feng, W., Yang, W., Li, W. and Tao, C. Effect of surfactants on morphology and luminescent properties of $CaMoO_4$: Eu^{3+} red phosphors. *J. Alloys Compd.* **2011**, *509*, 845–848.

[303] Wang, Y., Song, J., Zhao, Y., Xu, L., He, D. and Jiao, H. Effects of organic additives on morphology and luminescent properties of Eu^{3+}-doped calcium molybdate red phosphors. *Powder Technol.* **2015**, *275*, 1–11.

[304] Chen, D., Tang, K., Li, F. and Zheng, H. A Simple Aqueous Mineralization Process to Synthesize Tetragonal Molybdate Microcrystallites. *Cryst. Growth Des.* **2006**, *6*, 247–252.

[305] Wang, W., Zhen, L., Shao, W. and Chen, Z. Colloidal synthesis and formation mechanism of calcium molybdate notched microspheres. *CrystEngComm* **2014**, *16*, 2598–2604.

[306] Wang, W., Hu, Y., Goebl, J., Lu, Z., Zhen, L. and Yin, Y. Shape-and size-controlled synthesis of calcium molybdate doughnut-shaped microstructures. *J. Phys. Chem. C* **2009**, *113*, 16414–16423.

[307] Yin, Y., Gao, Y., Sun, Y., Zhou, B., Ma, L., Wu, X. and Zhang, X. Synthesis and photoluminescent properties of $CaMoO_4$ nanostructures at room temperature. *Mater. Lett.* **2010**, *64*, 602–604.

[308] Gong, Q., Qian, X., Ma, X. and Zhu, Z. Large-Scale Fabrication of Novel Hierarchical 3D $CaMoO_4$ and $SrMoO_4$ Mesocrystals via a Microemulsion-Mediated Route. *Cryst. Growth Des.* **2006**, *6*, 1821–1825.

[309] Mumallah, N. A. A. and Popiel, W. J. Calcium-selective electrode measurements of calcium molybdate solubilities in water. *Anal. Chem.* **1974**, *46*, 2055–2056.

[310] Qian, L., Zhu, J., Chen, Z., Gui, Y., Gong, Q., Yuan, Y., Zai, J. and Qian, X. Self-Assembled Heavy Lanthanide Orthovanadate Architecture with Controlled Dimensionality and Morphology. *Chem. Eur. J.* **2009**, *15*, 1233–1240.

[311] Tarte, P. and Liegeois-Duyckaerts, M. Vibrational studies of molybdates, tungstates and related compounds—I. *Spectrochim. Acta Part A Mol. Spectrosc.* **1972**, *28*, 2029–2036.

[312] Clark, G. M. and Doyle, W. P. Infra-red spectra of anhydrous molybdates and tungstates. *Spectrochim. Acta* **1966**, *22*, 1441–1447.

[313] Kniep, R. and Busch, S. Biomimetic Growth and Self-Assembly of Fluorapatite Aggregates by Diffusion into Denatured Collagen Matrices. *Angew. Chemie Int. Ed. English* **1996**, *35*, 2624–2626.

[314] Busch, S., Dolhaine, H., DuChesne, A., Heinz, S., Hochrein, O., Laeri, F., Podebrad, O., Vietze, U., Weiland, T. and Kniep, R. Biomimetic Morphogenesis of Fluorapatite-Gelatin Composites: Fractal Growth, the Question of Intrinsic Electric Fields, Core/Shell Assemblies, Hollow Spheres and Reorganization of Denatured Collagen. *Eur. J. Inorg. Chem.* **1999**, *1999***,** 1643–1653.

[315] Su, Y., Li, L. and Li, G. Synthesis and Optimum Luminescence of $CaWO_4$-Based Red Phosphors with Codoping of Eu^{3+} and Na^{+}. *Chem. Mater.* **2008**, *20***,** 6060–6067.

[316] Wu, H., Hu, Y., Zhang, W., Kang, F., Li, N. and Ju, G. Sol–gel synthesis of Eu^{3+} incorporated $CaMoO_4$: the enhanced luminescence performance. *J. Sol-Gel Sci. Technol.* **2012**, *62***,** 227–233.

[317] Liu, J., Lian, H. and Shi, C. Improved optical photoluminescence by charge compensation in the phosphor system $CaMoO_4$:Eu^{3+}. *Opt. Mater. (Amst).* **2007**, *29***,** 1591–1594.

[318] Abakumov, A. M., Morozov, V. A., Tsirlin, A. A., Verbeeck, J. and Hadermann, J. Cation Ordering and Flexibility of the BO_4^{2-} Tetrahedra in Incommensurately Modulated $CaEu_2(BO_4)_4$ (B = Mo, W) Scheelites. *Inorg. Chem.* **2014**, *53***,** 9407–9415.

[319] Jiang, P., Gao, W., Cong, R. and Yang, T. Structural investigation of the A-site vacancy in scheelites and the luminescence behavior of two continuous solid solutions. *Dalt. Trans.* **2015**, *44***,** 6175–6183.

[320] Morozov, V. A., Bertha, A., Meert, K. W., Van Rompaey, S., Batuk, D., Martinez, G. T., Van Aert, S., Smet, P. F., Raskina, M. V., Poelman, D., Abakumov, A. M. and Hadermann, J. Incommensurate Modulation and Luminescence in the $CaGd_{2(1-x)}Eu_{2x}(MoO_4)_{4(1-y)}(WO_4)_{4y}$ ($0 \le x \le 1$, $0 \le y \le 1$) Red Phosphors. *Chem. Mater.* **2013**, *25***,** 4387–4395.

[321] Asakura, H., Hosokawa, S., Teramura, K. and Tanaka, T. Local Structure and L_1- and L_3-Edge X-ray Absorption Near Edge Structures of Middle Lanthanoid Elements (Eu, Gd, Tb, and Dy) in Their Complex Oxides. *Inorg. Chem.* **2021**, *60***,** 9359–9367.

[322] Rabuffetti, F. A., Culver, S. P., Suescun, L. and Brutchey, R. L. Structural Disorder in

$AMoO_4$ (A = Ca, Sr, Ba) Scheelite Nanocrystals. *Inorg. Chem.* **2014**, *53*, 1056–1061.

[323] Kohlmann, H., Hein, C., Kautenburger, R., Hansen, T. C., Ritter, C. and Doyle, S. Crystal structure of monoclinic samarium and cubic europium sesquioxides and bound coherent neutron scattering lengths of the isotopes ^{154}Sm and ^{153}Eu. *Zeitschrift für Krist. - Cryst. Mater.* **2016**, *231*, 517–523.

[324] Yokoi, K., Matsubayashi, N., Miyanaga, T., Watanabe, I., Murata, K. and Ikeda, S. Studies on the Structure of Cationic Dimer of Molybdenum(VI) in Acidic Solution by XANES and EXAFS. *Chem. Lett.* **1987**, *16*, 1453–1456.

[325] Takenaka, S., Tanaka, T., Funabiki, T. and Yoshida, S. Structures of Molybdenum Species in Silica-Supported Molybdenum Oxide and Alkali-Ion-Modified Silica-Supported Molybdenum Oxide. *J. Phys. Chem. B* **1998**, *102*, 2960–2969.

[326] Tauc, J., Grigorovici, R. and Vancu, A. Optical Properties and Electronic Structure of Amorphous Germanium. *Phys. Status Solidi* **1966**, *15*, 627–637.

[327] Makuła, P., Pacia, M. and Macyk, W. How To Correctly Determine the Band Gap Energy of Modified Semiconductor Photocatalysts Based on UV–Vis Spectra. *J. Phys. Chem. Lett.* **2018**, *9*, 6814–6817.

[328] Sarantopoulou, E., Raptis, C., Ves, S., Christofilos, D. and Kourouklis, G. A. Temperature and pressure dependence of Raman-active phonons of $CaMoO_4$: an anharmonicity study. *J. Phys. Condens. Matter* **2002**, *14*, 8925–8938.

[329] Zakharko, Y., Luchechko, A., Syvorotka, I., Stryganyuk, G. and Solskii, I. Anisotropy of optical absorption and luminescent properties of $CaMoO_4$. *Radiat. Meas.* **2010**, *45*, 429–431.

[330] Eliseeva, S. V. and Bünzli, J.-C. G. Lanthanide luminescence for functional materials and bio-sciences. *Chem. Soc. Rev.* **2010**, *39*, 189–227.

[331] Bünzli, J.-C. G. and Eliseeva, S. V. Basic of Lanthanide Photophysics. in *Lanthanide Luminescence: Photophysical, Analytical and Biological Aspects* Ed. Hänninen, P. & Härmä, H., Springer-Verlag Berlin Heidelberg, **2010**. 1–45.

[332] Binnemans, K. Interpretation of europium(III) spectra. *Coord. Chem. Rev.* **2015**, *295*, 1–45.

[333] Lai, J., Wang, T., Zhang, H., Ye, L., Yan, C. and Gu, W. Modulating the photoluminescence of europium oxide nanoparticles by controlling thermal decomposition conditions. *J. Lumin.* **2019**, *214*, 116534.

[334] Gomez, G. E., López, C. A., Ayscue, R. L., Knope, K. E., Torres Deluigi, M. del R. and Narda, G. E. Strong photoluminescence and sensing performance of nanosized $Ca_{0.8}Ln_{0.1}Na_{0.1}WO_4$ (Ln = Sm,Eu) compounds obtained by the dry "top-down" grinding method. *Dalt. Trans.* **2019**, *48*, 12080–12087.

[335] Shi, P., Xia, Z., Molokeev, M. S. and Atuchin, V. V. Crystal chemistry and luminescence properties of red-emitting $CsGd_{1-x}Eu_x(MoO_4)_2$ solid-solution phosphors. *Dalt. Trans.* **2014**, *43*, 9669–9676.

[336] Sato, M., Kim, S. W., Shimomura, Y., Hasegawa, T., Toda, K. and Adachi, G. *Handbook on the Physics and Chemistry of Rare Earths*. Ed. Bünzli, J.-C. G. & Pecharsky, V. K., Elsevier, **2016**.

[337] Razumkova, I. A., Sedykh, A. E., Denisenko, Y. G. and Müller-Buschbaum, K. Synthesis and luminescence properties of β-$NaRE_{0.95}Eu_{0.05}F_4$ (RE Y, Lu). *J. Ind. Eng. Chem.* **2020**, *92*, 218–225.

[338] Herrmann, A., Fibikar, S. and Ehrt, D. Time-resolved fluorescence measurements on Eu^{3+}- and Eu^{2+}-doped glasses. *J. Non. Cryst. Solids* **2009**, *355*, 2093–2101.

[339] Khattab, I. S., Bandarkar, F., Fakhree, M. A. A. and Jouyban, A. Density, viscosity, and surface tension of water+ethanol mixtures from 293 to 323 K. *Korean J. Chem. Eng.* **2012**, *29*, 812–817.

[340] Jouyban, A. and Soltanpour, S. Prediction of dielectric constants of binary solvents at various temperatures. *J. Chem. Eng. Data* **2010**, *55*, 2951–2963.

[341] Ciesla, U. and Schüth, F. Ordered mesoporous materials. *Microporous Mesoporous Mater.* **1999**, *27*, 131–149.

[342] Moller, K. and Bein, T. Inclusion Chemistry in Periodic Mesoporous Hosts. *Chem. Mater.* **1998**, *10***,** 2950–2963.

[343] Wu, S.-H., Mou, C.-Y. and Lin, H.-P. Synthesis of mesoporous silica nanoparticles. *Chem. Soc. Rev.* **2013**, *42***,** 3862.

[344] Thommes, M., Kaneko, K., Neimark, A. V., Olivier, J. P., Rodriguez-Reinoso, F., Rouquerol, J. and Sing, K. S. W. Physisorption of gases, with special reference to the evaluation of surface area and pore size distribution (IUPAC Technical Report). *Pure Appl. Chem.* **2015**, *87***,** 1051–1069.

[345] Leofanti, G., Padovan, M., Tozzola, G. and Venturelli, B. Surface area and pore texture of catalysts. *Catal. Today* **1998**, *41***,** 207–219.

[346] Thommes, M. and Cychosz, K. A. Physical adsorption characterization of nanoporous materials: progress and challenges. *Adsorption* **2014**, *20***,** 233–250.

[347] Landers, J., Gor, G. Y. and Neimark, A. V. Density functional theory methods for characterization of porous materials. *Colloids Surfaces A Physicochem. Eng. Asp.* **2013**, *437***,** 3–32.

[348] Brunauer, S., Emmett, P. H. and Teller, E. Adsorption of Gases in Multimolecular Layers. *J. Am. Chem. Soc.* **1938**, *60***,** 309–319.

[349] Yuvaraj, S., Fan-Yuan, L., Tsong-Huei, C. and Chuin-Tih, Y. Thermal Decomposition of Metal Nitrates in Air and Hydrogen Environments. *J. Phys. Chem. B* **2003**, *107***,** 1044–1047.

[350] Parlett, C. M. A., Bruce, D. W., Hondow, N. S., Newton, M. A., Lee, A. F. and Wilson, K. Mesoporous Silicas as Versatile Supports to Tune the Palladium-Catalyzed Selective Aerobic Oxidation of Allylic Alcohols. *ChemCatChem* **2013**, *5***,** 939–950.

[351] Morère, J., Tenorio, M. J., Torralvo, M. J., Pando, C., Renuncio, J. A. R. and Cabañas, A. Deposition of Pd into mesoporous silica SBA-15 using supercritical carbon dioxide. *J. Supercrit. Fluids* **2011**, *56***,** 213–222.

[352] Wang, H. and Liu, C. Preparation and characterization of SBA-15 supported Pd

catalyst for CO oxidation. *Appl. Catal. B Environ.* **2011**, *106*, 672–680.

[353] Thommes, M. Physical Adsorption Characterization of Nanoporous Materials. *Chemie Ing. Tech.* **2010**, *82*, 1059–1073.

[354] Thommes, M., Smarsly, B., Groenewolt, M., Ravikovitch, P. I. and Neimark, A. V. Adsorption Hysteresis of Nitrogen and Argon in Pore Networks and Characterization of Novel Micro- and Mesoporous Silicas. *Langmuir* **2006**, *22*, 756–764.

[355] Kadlec, O. and Dubinin, M. Comments on the limits of applicability of the mechanism of capillary condensation. *J. Colloid Interface Sci.* **1969**, *31*, 479–489.

[356] Burgess, C. G. V. and Everett, D. H. The lower closure point in adsorption hysteresis of the capillary condensation type. *J. Colloid Interface Sci.* **1970**, *33*, 611–614.

[357] Schreiber, A., Reinhardt, S. and Findenegg, G. H. The lower closure point of the adsorption hysteresis loop of fluids in mesoporous silica materials. in *Characterization of Porous Solids VI* Elsevier, **2002**. 177–184.

[358] Sonwane, C. G. and Bhatia, S. K. Analysis of Criticality and Isotherm Reversibility in Regular Mesoporous Materials. *Langmuir* **1999**, *15*, 5347–5354.

[359] Liu, C.-H., Lin, C.-Y., Chen, J.-L., Lu, K.-T., Lee, J.-F. and Chen, J.-M. SBA-15-supported Pd catalysts: The effect of pretreatment conditions on particle size and its application to benzyl alcohol oxidation. *J. Catal.* **2017**, *350*, 21–29.

[360] Soni, Y., Pradhan, S., Bamnia, M. K., Yadav, A. K., Jha, S. N., Bhattacharyya, D., Khan, T. S., Haider, M. A. and Vinod, C. P. Spectroscopic Evidences for the Size Dependent Generation of Pd Species Responsible for the Low Temperature CO Oxidation Activity on Pd-SBA-15 Nanocatalyst. *Appl. Catal. B Environ.* **2020**, *272*, 118934.

[361] Jiao, L. and Regalbuto, J. R. The synthesis of highly dispersed noble and base metals on silica via strong electrostatic adsorption: II. Mesoporous silica SBA-15. *J. Catal.* **2008**, *260*, 342–350.

[362] Votsmeier, M., Kreuzer, T., Gieshoff, J. and Lepperhoff, G. Automobile Exhaust Control. in *Ullmann's Encyclopedia of Industrial Chemistry* Wiley-VCH Verlag GmbH

& Co. KGaA, Weinheim, **2009**.

[363] Al Soubaihi, R., Saoud, K. and Dutta, J. Critical Review of Low-Temperature CO Oxidation and Hysteresis Phenomenon on Heterogeneous Catalysts. *Catalysts* **2018**, *8*, 660–678.

[364] Zhou, Y., Wang, Z. and Liu, C. Perspective on CO oxidation over Pd-based catalysts. *Catal. Sci. Technol.* **2015**, *5*, 69–81.

[365] Al Soubaihi, R. M., Saoud, K. M., Myint, M. T. Z., Göthelid, M. A. and Dutta, J. CO Oxidation Efficiency and Hysteresis Behavior over Mesoporous Pd/SiO_2 Catalyst. *Catalysts* **2021**, *11*, 131–148.

[366] Dadi, R. K., Luss, D. and Balakotaiah, V. Dynamic hysteresis in monolith reactors and hysteresis effects during co-oxidation of CO and C_2H_6. *Chem. Eng. J.* **2016**, *297*, 325–340.

[367] Hauptmann, W., Votsmeier, M., Gieshoff, J., Drochner, A. and Vogel, H. Inverse hysteresis during the NO oxidation on Pt under lean conditions. *Appl. Catal. B Environ.* **2009**, *93*, 22–29.

[368] Etheridge, J. E. and Watling, T. C. Is reactor light-off data sufficiently discriminating between kinetic parameters to be used for developing kinetic models of automotive exhaust aftertreatment catalysts? The effect of hysteresis induced by strong self inhibition. *Chem. Eng. J.* **2015**, *264*, 376–388.

[369] Amin, A., Abedi, A., Hayes, R., Votsmeier, M. and Epling, W. Methane oxidation hysteresis over Pt/Al_2O_3. *Appl. Catal. A Gen.* **2014**, *478*, 91–97.

[370] Abedi, A., Hayes, R., Votsmeier, M. and Epling, W. S. Inverse Hysteresis Phenomena During CO and C_3H_6 Oxidation over a Pt/Al_2O_3 Catalyst. *Catal. Letters* **2012**, *142*, 930–935.

[371] Dadi, R. K., Luss, D. and Balakotaiah, V. Bifurcation features of mixtures containing CO and hydrocarbons in diesel oxidation catalyst. *Chem. Eng. J.* **2016**, *304*, 941–952.

[372] Casapu, M., Fischer, A., Gänzler, A. M., Popescu, R., Crone, M., Gerthsen, D., Türk,

M. and Grunwaldt, J.-D. Origin of the Normal and Inverse Hysteresis Behavior during CO Oxidation over Pt/Al_2O_3. *ACS Catal.* **2017**, *7*, 343–355.

[373] Orlik, S. N., Koval', G. L., Fesenko, A. V., Korneichuk, G. P. and Yablonskii, G. S. Kinetics of CO oxidation on a palladium-containing catalyst. *Theor. Exp. Chem.* **1979**, *15*, 59–61.

[374] Al Soubaihi, R. M., Saoud, K. M., Ye, F., Zar Myint, M. T., Saeed, S. and Dutta, J. Synthesis of hierarchically porous silica aerogel supported Palladium catalyst for low-temperature CO oxidation under ignition/extinction conditions. *Microporous Mesoporous Mater.* **2020**, *292*, 109758–109765.

[375] Maurer, F., Beck, A., Jelic, J., Wang, W., Mangold, S., Stehle, M., Wang, D., Dolcet, P., Gänzler, A. M., Kübel, C., Studt, F., Casapu, M. and Grunwaldt, J.-D. Surface Noble Metal Concentration on Ceria as a Key Descriptor for Efficient Catalytic CO Oxidation. *ACS Catal.* **2022**, *12*, 2473–2486.

[376] Reich, S.-J., Svidrytski, A., Höltzel, A., Florek, J., Kleitz, F., Wang, W., Kübel, C., Hlushkou, D. and Tallarek, U. Hindered Diffusion in Ordered Mesoporous Silicas: Insights from Pore-Scale Simulations in Physical Reconstructions of SBA-15 and KIT-6 Silica. *J. Phys. Chem. C* **2018**, *122*, 12350–12361.

[377] Grunwaldt, J.-D., Wagner, J. B. and Dunin-Borkowski, R. E. Imaging Catalysts at Work: A Hierarchical Approach from the Macro- to the Meso- and Nano-scale. *ChemCatChem* **2013**, *5*, 62–80.

[378] Sarma, B. B., Maurer, F., Doronkin, D. E. and Grunwaldt, J.-D. Design of Single-Atom Catalysts and Tracking Their Fate Using Operando and Advanced X-ray Spectroscopic Tools. *Chem. Rev.* **2022**, doi:10.1021/acs.chemrev.2c00495

[379] Bañares, M. A. Operando methodology: combination of in situ spectroscopy and simultaneous activity measurements under catalytic reaction conditions. *Catal. Today* **2005**, *100*, 71–77.

[380] Weckhuysen, B. M. Determining the active site in a catalytic process: Operando spectroscopy is more than a buzzword. *Phys. Chem. Chem. Phys.* **2003**, *5*, 4351.

[381] Topsøe, H. Developments in operando studies and in situ characterization of heterogeneous catalysts. *J. Catal.* **2003**, *216*, 155–164.

[382] Hendriksen, B. L. M., Bobaru, S. C. and Frenken, J. W. M. Oscillatory CO oxidation on Pd(100) studied with in situ scanning tunneling microscopy. *Surf. Sci.* **2004**, *552*, 229–242.

[383] Russell, A. and Epling, W. S. Diesel Oxidation Catalysts. *Catal. Rev. Sci. Eng.* **2011**, *53*, 337–423.

[384] McClure, S. M. and Goodman, D. W. New insights into catalytic CO oxidation on Pt-group metals at elevated pressures. *Chem. Phys. Lett.* **2009**, *469*, 1–13.

[385] Toyoshima, R., Yoshida, M., Monya, Y., Suzuki, K., Amemiya, K., Mase, K., Mun, B. S. and Kondoh, H. In Situ Photoemission Observation of Catalytic CO Oxidation Reaction on Pd(110) under Near-Ambient Pressure Conditions: Evidence for the Langmuir–Hinshelwood Mechanism. *J. Phys. Chem. C* **2013**, *117*, 20617–20624.

[386] Chorkendorff, I. and Niemantsverdriet, J. W. *Concepts of Modern Catalysis and Kinetics*. Wiley-VCH, Weinheim, **2017**.

[387] Carlsson, P., Österlund, L., Thormählen, P., Palmqvist, A., Fridell, E., Jansson, J. and Skoglundh, M. A transient in situ FTIR and XANES study of CO oxidation over Pt/Al_2O_3 catalysts. *J. Catal.* **2004**, *226*, 422–434.

[388] Lashina, E. A., Slavinskaya, E. M., Chumakova, N. A., Stadnichenko, A. I., Salanov, A. N., Chumakov, G. A. and Boronin, A. I. Inverse temperature hysteresis and self-sustained oscillations in CO oxidation over Pd at elevated pressures of reaction mixture: Experiment and mathematical modeling. *Chem. Eng. Sci.* **2020**, *212*, 115312.

[389] Weng, X., Yang, S., Ding, D., Chen, M. and Wan, H. Applications of in-situ wide spectral range infrared absorption spectroscopy for CO oxidation over Pd/SiO_2 and Cu/SiO_2 catalysts. *Chinese J. Catal.* **2022**, *43*, 2001–2009.

[390] Pankove, J. I. *Optical processes in semiconductors*. Courier Corporation, **1975**.

[391] Kubelka, P. and Munk, F. Ein Beitrag Zur Optik Der Farbanstriche. *Z. Technol. Phys.* **1931**, *12*, 593–601.

[392] Schindelin, J. *et al.* Fiji: an open-source platform for biological-image analysis. *Nat. Methods* **2012**, *9*, 676–682.

[393] Schneider, C. A., Rasband, W. S. and Eliceiri, K. W. NIH Image to ImageJ: 25 years of image analysis. *Nat. Methods* **2012**, *9*, 671–675.

[394] Barrett, E. P., Joyner, L. G. and Halenda, P. P. The Determination of Pore Volume and Area Distributions in Porous Substances. I. Computations from Nitrogen Isotherms. *J. Am. Chem. Soc.* **1951**, *73*, 373–380.

[395] Kruk, M., Jaroniec, M. and Sayari, A. Application of Large Pore MCM-41 Molecular Sieves To Improve Pore Size Analysis Using Nitrogen Adsorption Measurements. *Langmuir* **1997**, *13*, 6267–6273.

[396] Ravikovitch, P. I., Wei, D., Chueh, W. T., Haller, G. L. and Neimark, A. V. Evaluation of Pore Structure Parameters of MCM-41 Catalyst Supports and Catalysts by Means of Nitrogen and Argon Adsorption. *J. Phys. Chem. B* **1997**, *101*, 3671–3679.

[397] Ravikovitch, P. I., Domhnaill, S. C. O., Neimark, A. V., Schueth, F. and Unger, K. K. Capillary Hysteresis in Nanopores: Theoretical and Experimental Studies of Nitrogen Adsorption on MCM-41. *Langmuir* **1995**, *11*, 4765–4772.

[398] Rehr, J. J. and Albers, R. C. Theoretical approaches to X-ray absorption fine structure. *Rev. Mod. Phys.* **2000**, *72*, 621–654.

[399] Bunker, G. *Introduction to XAFS: A Practical Guide to X-ray Absorption Fine Structure Spectroscopy*. Cambridge University Press, Cambridge, **2010**.

[400] Calvin, S. and Furst, K. E. *XAFS for everyone*. CRC Press, Boca Raton, **2013**.

[401] Bordiga, S., Groppo, E., Agostini, G., van Bokhoven, J. A. and Lamberti, C. Reactivity of Surface Species in Heterogeneous Catalysts Probed by In Situ X-ray Absorption Techniques. *Chem. Rev.* **2013**, *113*, 1736–1850.

[402] Sayers, D. E., Stern, E. A. and Lytle, F. W. New technique for investigating

noncrystalline structures: Fourier analysis of the extended X-ray—absorption fine structure. *Phys. Rev. Lett.* **1971**, *27*, 1204–1207.

[403] Rehr, J. J. and Ankudinov, A. L. Progress in the theory and interpretation of XANES. *Coord. Chem. Rev.* **2005**, *249*, 131–140.

[404] Dolcet, P. and Gross, S. Electronic and Chemical Properties: X-Ray Absorption and Photoemission. in *Metal Oxide Nanoparticles: Formation, Functional Properties, and Interfaces* Ed. Diwald, O. & Berger, T., John Wiley & Sons, Ltd, **2021**. 383–434.

[405] Ravel, B. and Newville, M. ATHENA, ARTEMIS, HEPHAESTUS: data analysis for X-ray absorption spectroscopy using IFEFFIT. *J. Synchrotron Radiat.* **2005**, *12*, 537–541.

[406] Pauw, B. R. Everything SAXS: small-angle scattering pattern collection and correction. *J. Phys. Condens. Matter* **2013**, *25*, 383201–383203.

[407] Giannini, C., Ladisa, M., Altamura, D., Siliqi, D., Sibillano, T. and De Caro, L. X-ray Diffraction: A Powerful Technique for the Multiple-Length-Scale Structural Analysis of Nanomaterials. *Crystals* **2016**, *6*, 87–108.

[408] Scherrer, P. Bestimmung der Größe und der inneren Struktur von Kolloidteilchen mittels Röntgenstrahlen. *Nachrichten von der Gesellschaft der Wissenschaften zu Göttingen, Math. Klasse* **1918**, *1918*, 98–100.

[409] Muniz, F. T. L., Miranda, M. A. R., Morilla Dos Santos, C. and Sasaki, J. M. The Scherrer equation and the dynamical theory of X-ray diffraction. *Acta Crystallogr. A Found. Adv.* **2016**, *72*, 385–390.

[410] Langford, J. I. and Wilson, A. J. C. Scherrer after sixty years: a survey and some new results in the determination of crystallite size. *J. Appl. Cryst.* **1978**, *11*, 102–113.

[411] Rietveld, H. M. Line profiles of neutron powder-diffraction peaks for structure refinement. *Acta Crystallogr.* **1967**, *22*, 151–152.

[412] Rietveld, H. M. A profile refinement method for nuclear and magnetic structures. *J. Appl. Crystallogr.* **1969**, *2*, 65–71.

[413] Toby, B. H. R factors in Rietveld analysis: How good is good enough? . *Powder Diffr.*

2006, *21***,** 67–70.

[414] Leoni, M., Di Maggio, R., Polizzi, S. and Scardi, P. X-ray diffraction methodology for the microstructural analysis of nanocrystalline powders: Application to cerium oxide. *J. Am. Ceram. Soc.* **2004**, *87***,** 1133–1140.

[415] Scardi, P. and Leoni, M. Whole powder pattern modelling. *Acta Crystallogr. Sect. A Found. Crystallogr.* **2002**, *58***,** 190–200.

[416] Le Bail, A. *et al. Powder Diffraction*. The Royal Society of Chemistry, Cambridge, **2008**.

[417] Coelho, A. A. TOPAS and TOPAS-Academic: an optimization program integrating computer algebra and crystallographic objects written in C++. *J. Appl. Crystallogr.* **2018**, *51***,** 210–218.

[418] Zhang, H., De Yoreo, J. J. and Banfield, J. F. A Unified Description of Attachment-Based Crystal Growth. *ACS Nano* **2014**, *8***,** 6526–6530.

[419] Zhang, H. and Banfield, J. F. Energy Calculations Predict Nanoparticle Attachment Orientations and Asymmetric Crystal Formation. *J. Phys. Chem. Lett.* **2012**, *3***,** 2882–2886.

[420] Gibbs, G. V., Crawford, T. D., Wallace, A. F., Cox, D. F., Parrish, R. M., Hohenstein, E. G. and Sherrill, C. D. Role of Long-Range Intermolecular Forces in the Formation of Inorganic Nanoparticle Clusters. *J. Phys. Chem. A* **2011**, *115***,** 12933–12940.

[421] Chou, Y. J., El-Aasser, M. S. and Vanderhoff, J. W. Mechanism of emulsification of styrene using hexadecyltrimethylammonium bromide-cetyl alcohol mixtures. *J. Dispers. Sci. Technol.* **1980**, *1***,** 129–150.

[422] Pashley, R. M. and Karaman, M. E. *Applied Colloid and Surface Chemistry*. John Wiley & Sons, Ltd, Chichester, UK, **2004**.

[423] Lauterborn, W. and Ohl, C.-D. Cavitation bubble dynamics. *Ultrason. Sonochem.* **1997**, *4***,** 65–75.

[424] Nagarajan, R. and Ruckenstein, E. Critical micelle concentration: A transition point

for micellar size distribution. *J. Colloid Interface Sci.* **1977**, *60***,** 221–231.

[425] Dressaire, E. and Sauret, A. Clogging of microfluidic systems. *Soft Matter* **2017**, *13***,** 37–48.

[426] Jensen, K. F., Reizman, B. J. and Newman, S. G. Tools for chemical synthesis in microsystems. *Lab Chip* **2014**, *14***,** 3206–3212.

[427] Israelachvili, J. N., Mitchell, D. J. and Ninham, B. W. Theory of self-assembly of hydrocarbon amphiphiles into micelles and bilayers. *J. Chem. Soc. Faraday Trans. 2* **1976**, *72***,** 1525–1568.

[428] Kim, J. M., Sakamoto, Y., Hwang, Y. K., Kwon, Y.-U., Terasaki, O., Park, S.-E. and Stucky, G. D. Structural Design of Mesoporous Silica by Micelle-Packing Control Using Blends of Amphiphilic Block Copolymers. *J. Phys. Chem. B* **2002**, *106***,** 2552–2558.

[429] Crichton, W. A. and Grzechnik, A. Crystal structure of calcium molybdate, $CaMoO_4$, a scheelite-type to fergusonite-type transition in powellite at P > 15 GPa. *Zeitschrift für Krist. - New Cryst. Struct.* **2004**, *219***,** 369–370.

[430] Blasse, G. and Bril, A. Luminescence of europium-activated strontium yttrium oxide (SrY_2O_4-Eu). *J. Inorg. Nucl. Chem.* **1969**, *31***,** 1521–1523.

[431] Kirby, A. F. and Richardson, F. S. Detailed analysis of the optical absorption and emission spectra of Eu^{3+} in the trigonal (C_3) $Eu(DBM)_3$ H_2O system. *J. Phys. Chem.* **1983**, *87***,** 2544–2556.

[432] Einstein, A. Über die von der molekularkinetischen Theorie der Wärme geforderte Bewegung von in ruhenden Flüssigkeiten suspendierten Teilchen. *Ann. Phys.* **1905**, *4***,** 549–560.

[433] New Euro 7 standards. Available at: https://ec.europa.eu/commission/presscorner/detail/en/ip_22_6495. (Accessed: 4th January 2023)

A

Iron sulfides

In this Appendix Section, a case study carried out to follow and compare by time-resolved *in situ* XAS the evolution of iron species over the course of the synthesis of iron sulfides in the confined space of miniemulsion droplets and in batch conditions is briefly presented. The aim of the experiment was to investigate the effects of the spatial confinement offered by miniemulsion droplets on the synthesis of an additional class of inorganic materials (*e.g.* metal sulfides) displaying multiple compounds with different structure, stoichiometry and oxidation state of the species. Notwithstanding the employed experimental approach was quite interesting and comprehensive and an advanced data analysis was carried out, given the preliminary stage of data analysis and discussion, these results are presented in the Appendix.

A.1 Introduction

Iron sulfides (FeS, FeS_2, Fe_2S_3 and non-stoichiometric Fe_xS_y) are model systems displaying different oxidation states of the two involved species (Fe, S), different stoichiometries and structures with a well-established phase diagram. In particular, it has been reported that the most common phase resulting from the reaction between Fe^{2+} and S^{2-} is the tetragonal mackinawite, but under non-equilibrium conditions troilite (hexagonal) or cubic FeS is often formed.[A1-A3]

With the aim of elucidating the possible effects of miniemulsion droplets space constraint on iron sulfides polymorph selection, the syntheses of iron sulfides in miniemulsion and in non-constrained batch conditions were carried out. Numerous color changes were visually

observed to occur during the synthesis of Fe_xS_y in miniemulsion, likely ascribed to the rich structural variability of the Fe_xS_y systems, with different oxidation states and coordination environments. On the other hand, the same changes were not observed in batch conditions, suggesting an impact of the confinement effect on the formation and/or crystallization of Fe_xS_y systems. Within this framework, and due to the high sensitivity towards oxidation of iron sulfides, which makes them very difficult to handle and analyze *ex situ*, an *in situ* experiment was designed to follow the synthesis of iron sulfides within *inverse ME droplets* and in *batch conditions*. In particular, the X-ray absorption spectroscopy technique was employed because of its element selectivity and its sensitivity to the local environment of the target element, thus providing information about oxidation state variation and modifications of the local coordination configuration typical occurring in the first stages of reaction (*i.e.* conversion of reactants into NPs precursor and nucleation), as extensively described in Chapter 1.3 and Chapter 7.8.

A.2 Experimental section

Chemicals. The reagents employed for the synthesis of iron sulfides are listed in Table A.1. All the chemicals were analytical grade and used as received without any further purification.

Table A.1 Employed chemicals for the synthesis of iron sulfides

Name	Formula	Molecular weight (g/mol)	CAS number	Supplier
Ammonium iron sulfate hexahydrate	$Fe(NH_4)_2(SO_4)_2{\cdot}6H_2O$	392.14	7783-85-9	Sigma-Aldrich
Ammonium sulfide[a]	$(NH_4)_2S$	68.14	12135-76-1	Sigma-Aldrich
Cyclohexane	C_6H_{12}	84.16	110-82-7	Sigma-Aldrich
Iron nitrate nonahydrate	$Fe(NO_3)_3{\cdot}9H_2O$	404.00	7782-61-8	Sigma-Aldrich
Sodium hydrosulfide hydrate	$NaHS{\cdot}xH_2O$	56.06[b]	207683-19-0	Sigma-Aldrich
Sodium sulfide nonahydrate	$Na_2S{\cdot}9H_2O$	240.18	1313-84-4	Sigma-Aldrich
Span80	$C_{24}H_{44}O_6$	428.62	1338-43-8	Sigma-Aldrich

[a] 44 wt% in aqueous solution; [b] anhydrous basis

Batch synthesis. The synthesis of iron sulfides in batch conditions was carried out by dropwise addition of an aqueous solution of sulfide precursor to an aqueous solution of iron precursor, under mechanical stirring and at room temperature. Different precursors of iron (iron nitrate and iron ammonium sulfate) and sulfur (sodium sulfide, sodium hydrosulfide and ammonium sulfide) and combinations thereof were screened.

Synthesis in miniemulsion droplets. The synthesis of iron sulfides by miniemulsion approach was carried out by employing a Sartorius Stedim LabsonicP homogenizer, mounting a 3 mm titanium tip, and operating at 24 kHz, with a 0.9 s pulse and at amplitude of 70 %, corresponding to an acoustic power of 280 W. Two starting mixtures of the precursors, A and B, were prepared by mixing an aqueous solution of the precursor (either iron or sulfur precursor, respectively) to a solution of 1.5 wt% Span80 in cyclohexane, to achieve the weight ratio between the aqueous to oil phases of 1:3. Different precursors of iron (iron nitrate and iron ammonium sulfate) and sulfur (sodium sulfide, sodium hydrosulfide and ammonium sulfide) and combinations thereof were screened. Both mixtures A (containing Fe precursor) and B (containing S precursor) were homogenized separately by ultrasonication until white turbid miniemulsions A' and B' were obtained. The as prepared miniemulsions A' and B' were mixed together (Fe : S 1:1 or 1:2 mol) and ultrasonicated again for 3 minutes, with unchanged amplitude.

***In situ* XAS experiments.** The formation of Fe_xS_y inside ME droplets and in batch conditions was followed *in situ* and in a time-resolved fashion by means of X-ray absorption spectroscopy (XAS) at Fe K-edge (7112 eV) at the Super-XAS beamline of Swiss Light Source, Villigen (Switzerland), in cooperation with Dr. Paolo Dolcet (Karlsruhe Institute of Technology, Karlsruhe, Germany). The Ph.D. candidate wrote the proposal of the experiment and participated in the beamtime (beamtime 20191033, 08-12/11/2019).

In particular, inverse ME of two different iron precursors ($Fe^{II}(NH_4)_2(SO_4)_2$ and $Fe^{III}(NO_3)_3$) were produced at the beamline using the remotely controlled Sartorius Stedim LabsonicP ultrasonicator (US: 3 min, 280 W, 0.9 s pulse) into a reaction vessel equipped with an external jacket connected to a circulating water bath (T = 7 °C), to keep the reaction mixture cooled. The resulting suspension was funneled through a continuous-flow equipment[xliv]

[xliv] The continuous-flow setup was built with the same configuration of the one employed for the *in situ* time-resolved SAXS/WAXS study of the crystallization of MoO_3, see Chapter 6.1.4. A representative scheme is reported in Figure 6.1.

(Viton® tubing, i.d. 3 mm, wall th. 1 mm) with the aid of a peristaltic pump (P-1 HE) into a quartz capillary (i.d. 2.0 mm, wall th. 0.01 mm) mounted in the beamline, where XAS spectra were acquired in a continuous scan mode in the energy range 7000-8250 eV, as detailed *infra*. The total residence time in the flow system was 50 s. Inverse miniemulsions of two different iron precursors ($Fe^{II}(NH_4)_2(SO_4)_2$ and $Fe^{III}(NO_3)_3$) were produced at the beamline using the remotely controlled Sartorius Stedim LabsonicP ultrasonicator (US: 3 min, 280 W, 0.9 s pulse). After acquiring XAS data of the precursor, a pre-formed inverse ME of three different sulfur precursors (Na_2S, NaHS and $(NH_4)_2S$, produced by US 3 min, 280 W, 0.9 pulse), or their aqueous solutions, depending on the employed synthetic approach (miniemulsion or batch approach, respectively), was injected into the reaction mixture (t = 0 s) by using a home-made LabView remotely controlled syringe pump with a flow rate of 10 mL min^{-1}. The sulfur precursor addition was completed in 2 min (t = 0-120 s). Subsequently, after a minute of acquisition of the obtained reaction mixture (t = 120-180 s), ultrasounds were applied (3 min, 280 W, 0.9 pulse) in order to induce constant fusion and fission processes between ME droplets containing the reactants and thus promote reactants mixing (t = 180-360 s). Finally, the evolution of the products was followed for

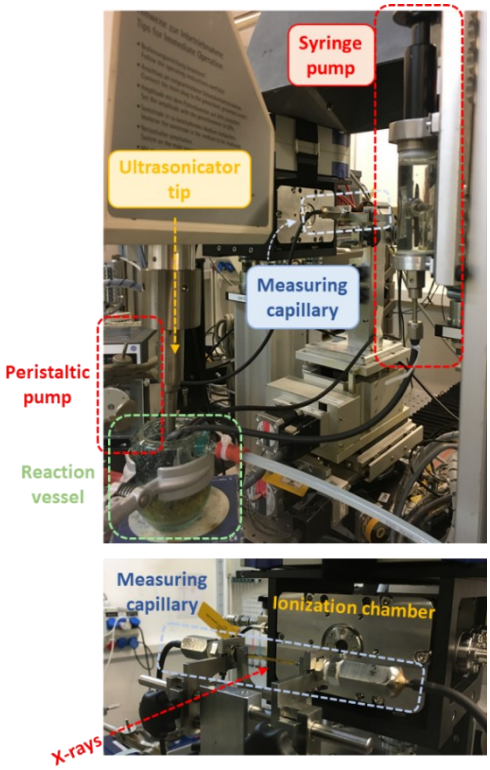

Figure A.1 Experimental setup employed for the *in situ* time-resolved XAS study of Fe_xS_y synthesis performed at the Super-XAS beamline at Swiss Light Source

about 1 hour. On the other hand, batch samples were produced *in situ* by addition of the S precursor with the remotely controlled syringe pump (10 mL min^{-1}) in 2 min (t = 0-120 s) into a solution of the Fe precursor. The evolution of the reaction mixture was followed for 1 hour. All different combinations of Fe and S precursors with relative molar ratios of 1:2 and 1:1 were analyzed with both ME and batch approaches. The experimental setup employed is shown in Figure A.1.

In situ time-resolved XAS data (7000-8250 eV) were acquired in transmission mode using the quick scanning XAS acquisition mode, by exploiting the Si(111) QEXAFS monochromator with an acquisition frequency of 1 Hz (*i.e.* one spectrum every 0.5 s). Energy calibration was carried out by comparison with the collected spectrum of reference metallic Fe foil.
Data were elaborated by using the ProXAS Python-based GUI developed at SLS[A4] by Dr. Paolo Dolcet. In particular, datasets were calibrated, normalized and screened individually for the identification of outliers (*e.g.* due to bubbles passing in the measuring capillary), that were removed.[xlv] The so-cleaned version of the dataset was merged averaging 10 spectra, resulting in a time resolution of 5 seconds, since both up and down oscillations of the monochromator were considered. The number of species contributing to each dataset was determined by single value decomposition, and it never exceeded a total of 4 species. The datasets were further analyzed using an MCR-ALS (Multivariate Curve Resolution – Alternating Least Square) method,[A5] decomposing the datasets separately to identify the different pure species contributing to the measured spectra and possibly

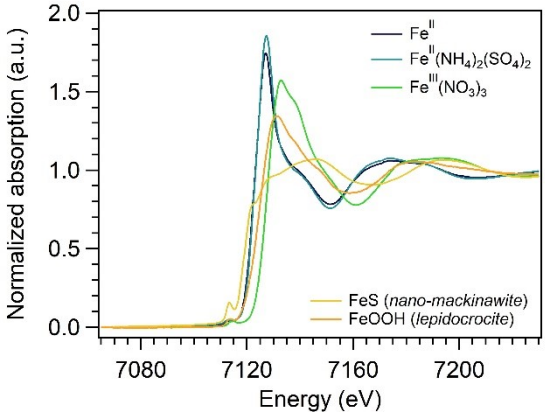

Figure A.2 Fe K-edge XANES spectra of reference compounds and Fe precursors

[xlv] These outliers affected at most four successive spectra, corresponding to 2 s, and therefore did not severely influence the overall analysis. With careful optimization of flow conditions, almost no distorted spectrum was identified in latter experiments.

identifying also short-lived intermediates. The species generating the spectra obtained *via* the MCR-ALS algorithm were identified by comparison with measured references (Figure A.2) and/or spectra from literature. [A3] Then, a matrix of reference species was constructed and used to perform linear combination fitting (LCF) of the different datasets and determine the temporal evolution of the species.

A.3 Time-resolved *in situ* XAS analysis

As extensively described in the experimental section (Section A.2), for the synthesis of iron sulfides by both inverse miniemulsion and batch approaches, the co-precipitation reaction between an iron(II) or iron(III) precursor (*i.e.* $Fe^{II}(NH_4)_2(SO_4)_2$ and $Fe^{III}(NO_3)_3$) and a sulfide precursor (*i.e.* Na_2S, NaHS and $(NH_4)_2S$) in aqueous solution was exploited. A systematic variation of the reaction parameters was carried out: all different combinations of Fe and S precursors with relative molar ratios of 1:2 and 1:1 were analyzed with both ME and batch approaches. A clear variation of the Fe K-edge XANES spectra over the course of the reaction was observed, and three or four distinct species were identified by single value decomposition when $Fe^{II}(NH_4)_2(SO_4)_2$ or $Fe^{III}(NO_3)_3$ were employed as Fe precursor, respectively. Figure A.3 shows representative spectra of these species observed in

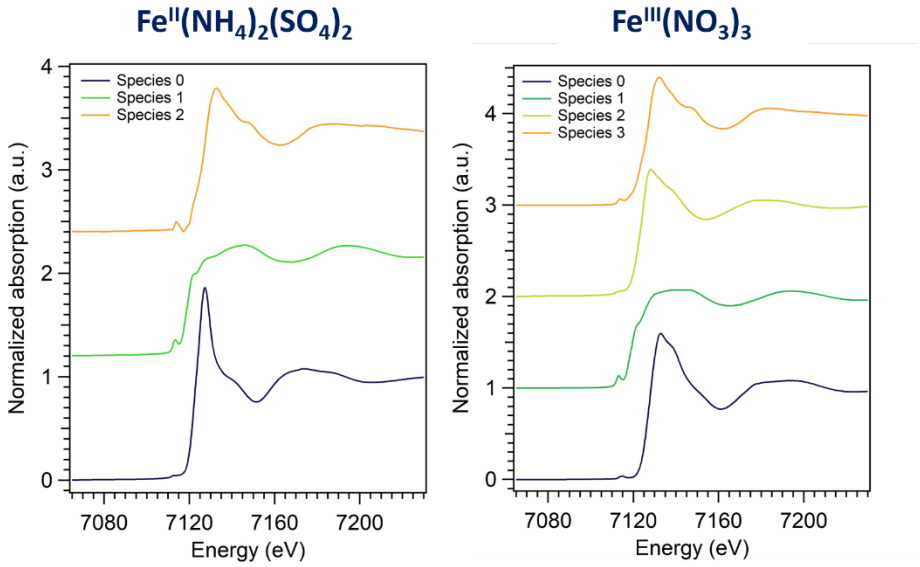

Figure A.3 Fe K-edge XANES spectra of miniemulsion reaction mixture at different reaction times employing $Fe(NH_4)_2(SO_4)_2$ (**left**) or $Fe(NO_3)_3$ (**right**) as Fe precursor and $(NH_4)_2S$ as S precursor in relative molar ratio 1:2 Fe:S

miniemulsion reaction mixtures obtained with $Fe^{II}(NH_4)_2(SO_4)_2$ (left) and $Fe^{III}(NO_3)_3$ (right) as Fe precursors, $(NH_4)_2S$ as S precursor and a Fe:S molar ratio of 1:2.

By comparing the features of the collected XANES spectra with those of reference compounds (Figure A.2), it was observed that FeS as nanosized mackinawite was the iron sulfide formed with all different sets of precursors with Fe:S of 1:2 mol, independently from the oxidation state of the iron precursor. Indeed, when a Fe(III) precursor (*i.e.* $Fe(NO_3)_3$) was employed, a first step of reduction of Fe(III) to Fe(II) was clearly observed by a shift towards lower energies of the white line position, in agreement with the lower oxidation state and reference spectra. On the other hand, when experiments using an iron-to-sulfur molar ratio of 1:1 mol were carried out, no formation of any iron sulfide species was observed with the majority of Fe and S precursors combinations, but the evolution of iron precursors to iron sulfate or oxyhydroxide species was instead evidenced. Moreover, among the sulfur precursors, ammonium sulfide resulted to be the most promising one, allowing to obtain the complete conversion of iron precursors to FeS with all screened synthetic conditions (*i.e.* two different iron precursors and two different Fe:S molar ratios with both synthetic methods). Subsequent to the formation of FeS, its evolution to an oxidized species was observed in the majority of the cases. The nature of the oxidized species could not be unambiguously identified, as the oxidation was not complete at the end of acquisitions, *i.e.* the last acquired spectra were linear combinations of spectra of different species and did not show the features of the single oxidized species. However, it could likely be identified in a sulfide or FeOOH.

The evolution of the relative concentrations of the identified species as a function of reaction time determined by MCR-ALS and LCF analyses for the sets of miniemulsion and batch samples obtained with $(NH_4)_2S$ and $Fe^{II}(NH_4)_2(SO_4)_2$ and $Fe^{III}(NO_3)_3$ is shown in Figure A.4 and Figure A.5, respectively. A comparison between results relative to the miniemulsion and batch reaction mixtures (Figure A.4 and Figure A.5, left *vs* right) clearly showed how the oxidation of iron sulfide occurred more rapidly in miniemulsion conditions with respect to batch ones. This evidence was likely ascribed to the formation, in the constrained environment of miniemulsion droplets, of smaller FeS particles, which, being characterized by a higher surface-to-volume ratio, are more sensible to the oxidation. In addition, high intensity ultrasounds applied in miniemulsion conditions could also play a role in the oxidation of iron sulfide, due to the formation of oxidizing radicals in aqueous solution as a consequence of sonolysis of water.[A6]

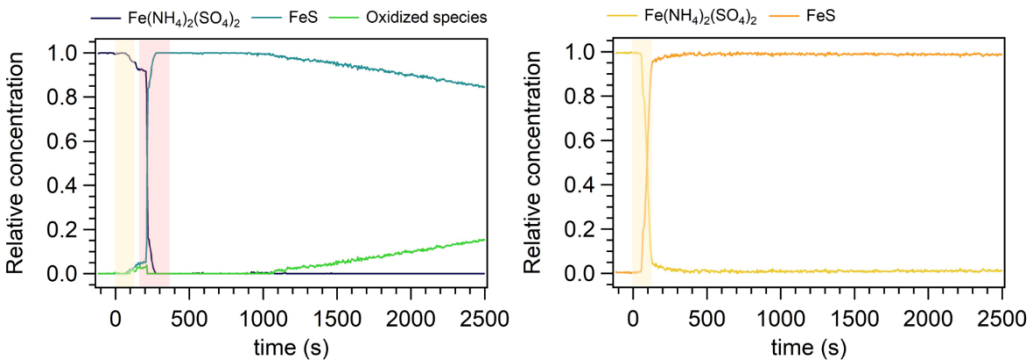

Figure A.4 Evolution of the relative concentrations of the identified species as a function of time of reaction (-120 – 2500 s), employing $Fe(NH_4)_2(SO_4)_2$ as Fe precursor and $(NH_4)_2S$ as S precursor in relative molar ratio 1:2 Fe:S, and exploiting ME (**left**, blue and green lines) and batch (**right**, yellow and orange lines) approaches. The start of S precursor injection (lasting 120 s) was set as t = 0 s. The temporal range of S precursor addition (0-120 s) and US application (180-360 s) are highlighted in yellow and red, respectively

Another difference between the evolution of the species in miniemulsion and batch conditions was observed in the kinetics of reduction of Fe(III) to Fe(II) in the set of experiments performed employing $Fe^{III}(NO_3)_3$ as Fe precursor. Indeed, as shown in Figure A.5, the formation and subsequent consumption of Fe(II) species occurred more slowly in miniemulsion droplet (left) than in batch conditions (right), and this could likely be ascribed to a slow diffusion of sulfide precursor into miniemulsion droplets before the ultrasound trigger was applied (red region in Figure A.5, left), as extensively described in Chapter 1.2.1 and demonstrated and discussed in Chapter 2.3.

Finally, among the two Fe precursors (Figure A.4 *vs* Figure A.5), it was observed that $Fe^{II}(NH_4)_2(SO_4)_2$ allowed to obtain FeS stable for a longer period of time. Indeed, a slow

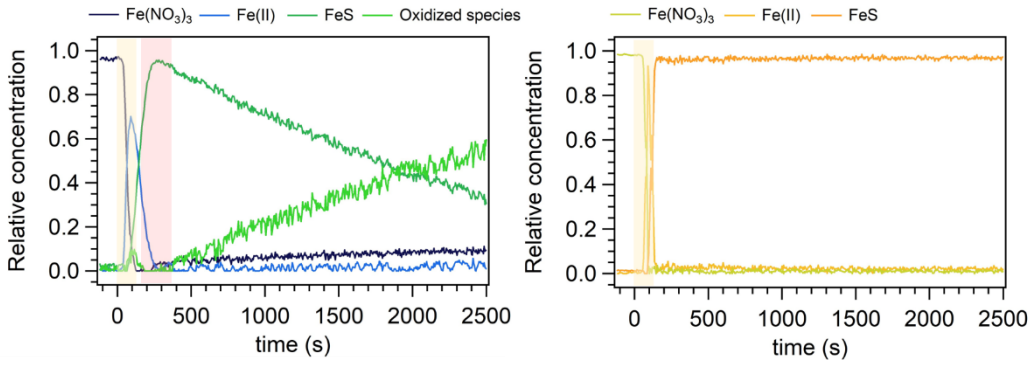

Figure A.5 Evolution of the relative concentrations of the identified species as a function of time of reaction (-120 – 2500 s), employing $Fe(NO_3)_3$ as Fe precursor and $(NH_4)_2S$ as S precursor in relative molar ratio 1:2 Fe:S, and exploiting ME (**left**, blue and green lines) and batch (**right**, yellow and orange lines) approaches. The start of S precursor injection (lasting 120 s) was set as t = 0 s. The temporal range of S precursor addition (0-120 s) and US application (180-360 s) are highlighted in yellow and red, respectively

oxidation was evidenced after 910 s with Fe^{II} precursor, while more rapid oxidation occurred after 270 s with Fe^{III} precursor.

A.4 Conclusions

The time-resolved *in situ* XAS study of the synthesis of Fe_xS_y systems both in ME and batch conditions enabled to identify ammonium sulfide as the best sulfide source among the tested precursors for obtaining stable FeS for the longer period of time. Moreover, it showed that, with the screened reaction conditions, both miniemulsion and batch approaches led to the formation of FeS, as nanosized mackinawite. However, FeS synthesized by miniemulsion approach turned out to be less stable towards oxidation with respect to the one synthesized in batch conditions.

A.5 Bibliography

[A1] Rickard, D. and Luther, G. W. Chemistry of Iron Sulfides. *Chem. Rev.* **2007**, *107*, 514-562.

[A2] Waldner, P. and Pelton, A. Themodynamic modeling of the Fe-S system. *J. of Phase Equilibria and Diffusion.* **2005**, *26*, 23-38.

[A3] Lennie, A. and Vaughan, D. Spectroscopic studies of iron sulfide formation and phase relations and low temperatures. *Mineral Spectroscopy* **1996**, *5*, 117-131

[A4] Clark, A. H., Imbao, J., Frahm, R. and Nachtegaal, M. ProQEXAFS: a highly optimized parallelized rapid processing software for QEXAFS data. *J. Synchrotron Radiat.* **2020**, *27*, 551-557.

[A5] de Juan, A., Jaumot, J. and Tauler, R. Multivariate Curve Resolution (MCR). Solving the mixture analysis problem. *Anal. Methods* **2014**, *6*, 4964-4976.

[A6] Suslick, K. S. and Nyborg, W. K. Ultrasound: Its Chemical, Physical and Biological Effects. *J. Acoust. Soc. Am.* **1990**, *87*, 919.

B

Additional Figures and Tables

In this Appendix Section, additional Figures and Tables of Chapter 2, Chapter 3, and Chapter 4 are reported.

Surfactants employed for miniemulsion formulation

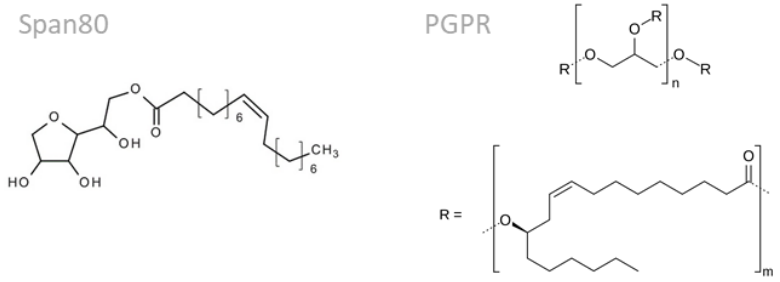

Figure B.1 Chemical structure of Span80 (sorbitane monoleate) and PGPR (polyglycerol polyricinoleate) surfactants, employed for the miniemulsion synthesis of MoO_3 (Chapter 2), $CaMoO_4$ (Chapter 3) and FeS (Appendix A)

B.1 Additional Figures and Tables of Chapter 2. Molybdenum oxide

Comparison of miniemulsion and batch samples

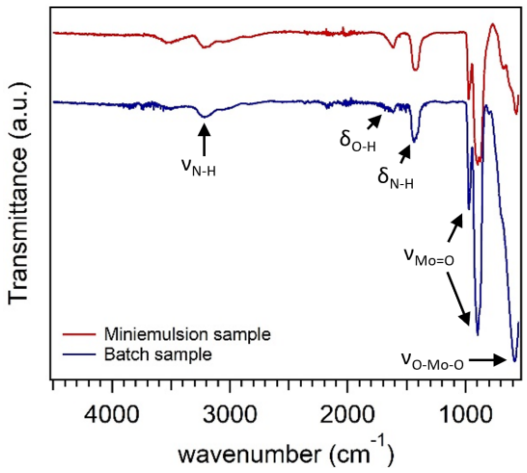

Figure B.2 Comparison of ATR spectra of miniemulsion (red line) and batch (blue line) samples. [AHM] = 0.20 M; AHM:HNO_3 1:10 mol, 24 h

Effect of AHM concentration

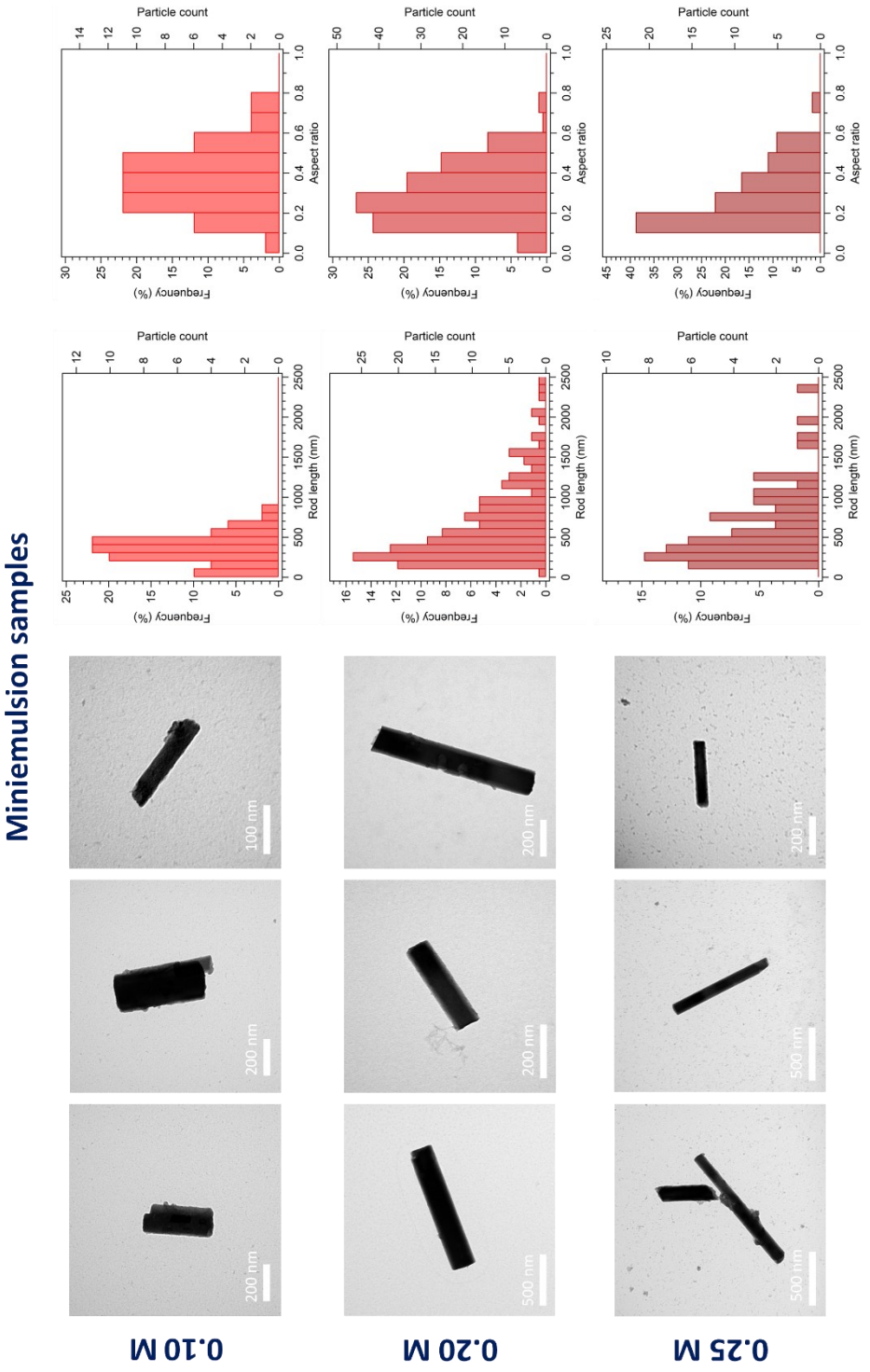

Figure B.3 TEM micrographs and relative histograms of rod length and aspect ratio distribution of miniemulsion samples synthesized at different AHM concentrations (0.10, 0.20 and 0.25 M) and constant AHM:HNO_3 molar ratio (1:10 mol) and reaction time (24 h)
*ME sample 0.15 M not reported because of bad quality of TEM micrographs

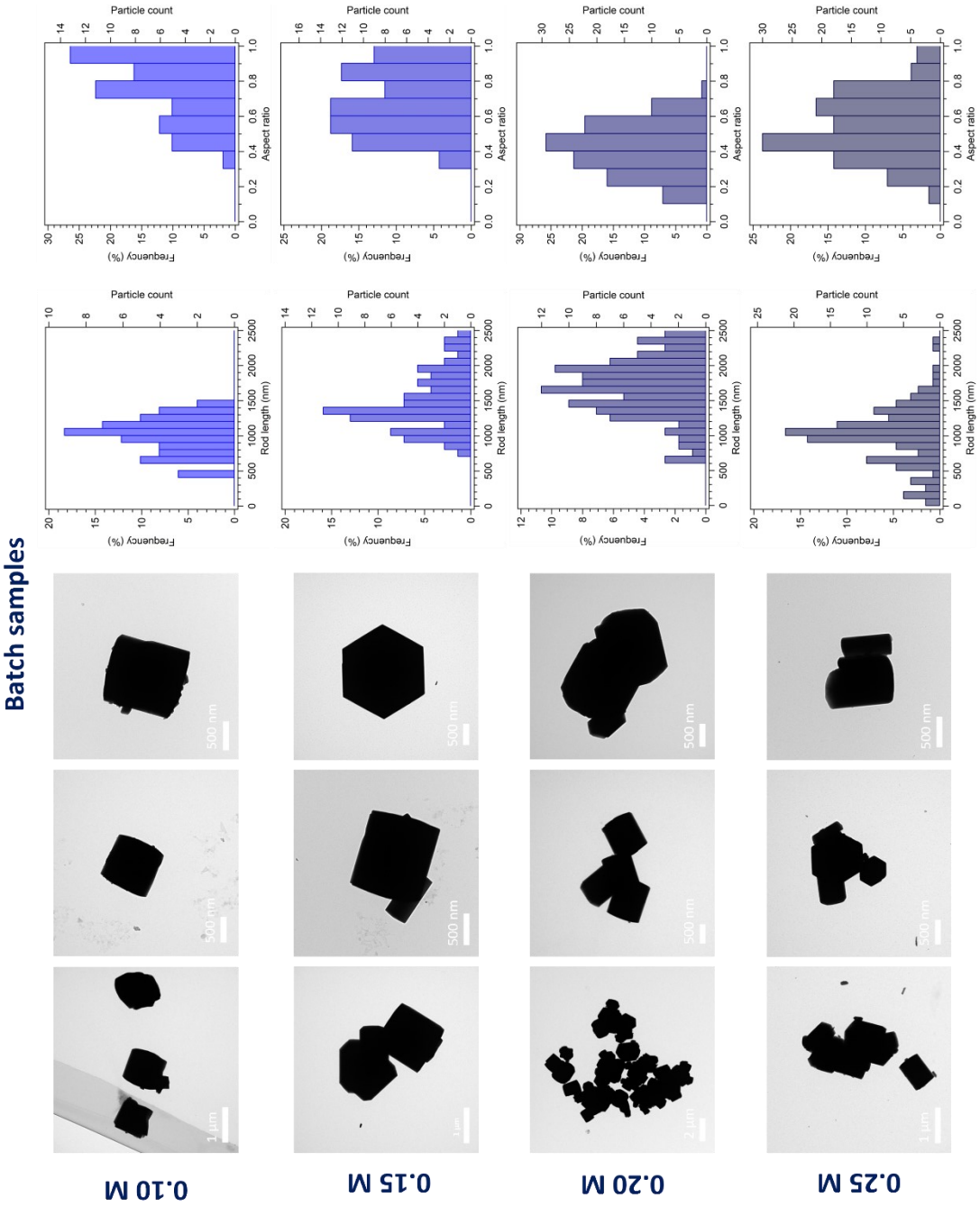

Figure B.4 TEM micrographs and relative histograms of rod length and aspect ratio distribution of batch samples synthesized at different AHM concentrations (0.10, 0.15, 0.20 and 0.25 M) and constant AHM:HNO_3 molar ratio (1:10 mol) and reaction time (24 h)

Table B.1 Average rod length, width and aspect ratio (AR = width / length) and standard deviations of miniemulsion and batch samples synthesized at different AHM concentrations (0.10, 0.15, 0.20 and 0.25 M) and constant AHM:HNO_3 molar ratio (1:10 mol) and reaction time (24 h)

Approach	Sample	[AHM] (M)	Length (nm)	Width (nm)	Aspect ratio
Miniemulsion	MO01-me	0.10	355 ± 180	125 ± 70	0.4 ± 0.1
	MO02-me[a]	0.15	565 ± 271[a]	237 ± 88[a]	0.4 ± 0.2[a]
	MO03-me	0.20	656 ± 499	176 ± 152	0.3 ± 0.1
	MO04-me	0.25	659 ± 486	159 ± 134	0.3 ± 0.1
Batch	MO01-b	0.10	998 ± 259	759 ± 292	0.7 ± 0.2
	MO02-b	0.15	1488 ± 429	1005 ± 418	0.7 ± 0.2
	MO03-b	0.20	1697 ± 445	730 ± 345	0.4 ± 0.1
	MO04-b	0.25	1108 ± 419	576 ± 340	0.5 ± 0.2

[a] Insufficient statistics due to bad quality of TEM micrographs

Effect of AHM:HNO_3 molar ratio

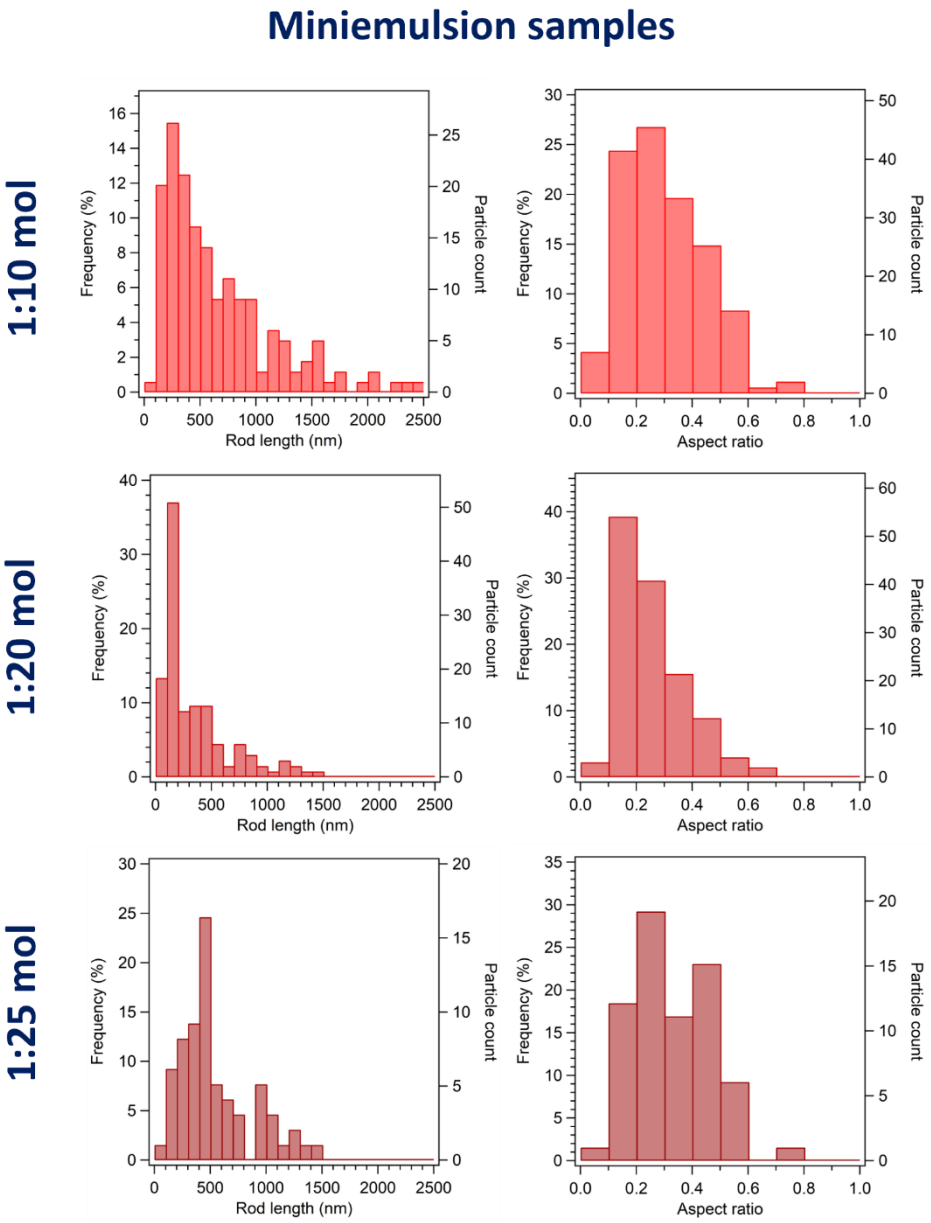

Figure B.5 Histograms of rod length and aspect ratio distribution of miniemulsion samples synthesized with different AHM:HNO_3 molar ratios (1:10, 1:20, and 1:25 mol) and constant AHM concentration ([AHM] = 0.20 M) and reaction time (24 h).
ME sample 1:15 mol not reported because of bad quality of TEM micrographs

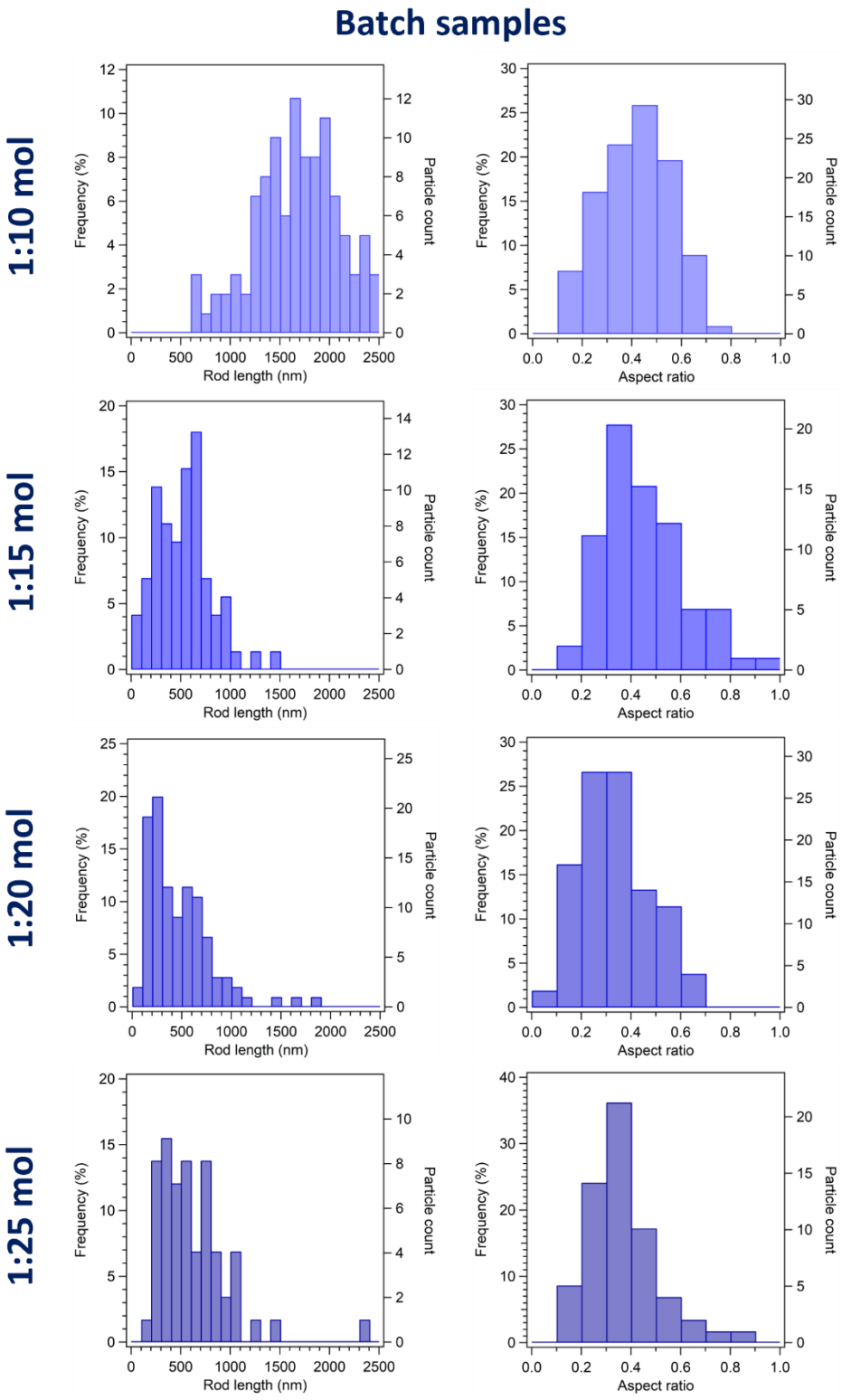

Figure B.6 Histograms of rod length and aspect ratio distribution of batch samples synthesized with different AHM:HNO_3 molar ratios (1:10, 1:15, 1:20, and 1:25 mol) and constant AHM concentration ([AHM] = 0.20 M) and reaction time (24 h)

Table B.2 Average rod length, width and aspect ratio (AR = width / length) and standard deviations of miniemulsion and batch samples synthesized with different AHM:HNO_3 molar ratios (1:10, 1:15, 1:20, and 1:25 mol) and constant AHM concentrations (0.20 M) and reaction time (24 h)

Approach	Sample	AHM:HNO_3 (mol)	Length (nm)	Width (nm)	Aspect ratio
Miniemulsion	MO03-me	1:10	656 ± 499	176 ± 152	0.3 ± 0.1
	MO05-me[a]	1:15	-	-	-
	MO06-me	1:20	358 ± 371	94 ± 107	0.3 ± 0.1
	MO07-me	1:25	544 ± 327	177 ± 134	0.3 ± 0.1
Batch	MO03-b	1:10	1697 ± 445	730 ± 345	0.4 ± 0.1
	MO05-b	1:15	524 ± 280	248 ± 213	0.5 ± 0.2
	MO06-b	1:20	466 ± 322	143 ± 108	0.3 ± 0.1
	MO07-me	1:25	618 ± 365	216 ± 128	0.4 ± 0.1

[a] Insufficient statistics due to bad quality of TEM micrographs

Effect of US step after acid addition and reaction time

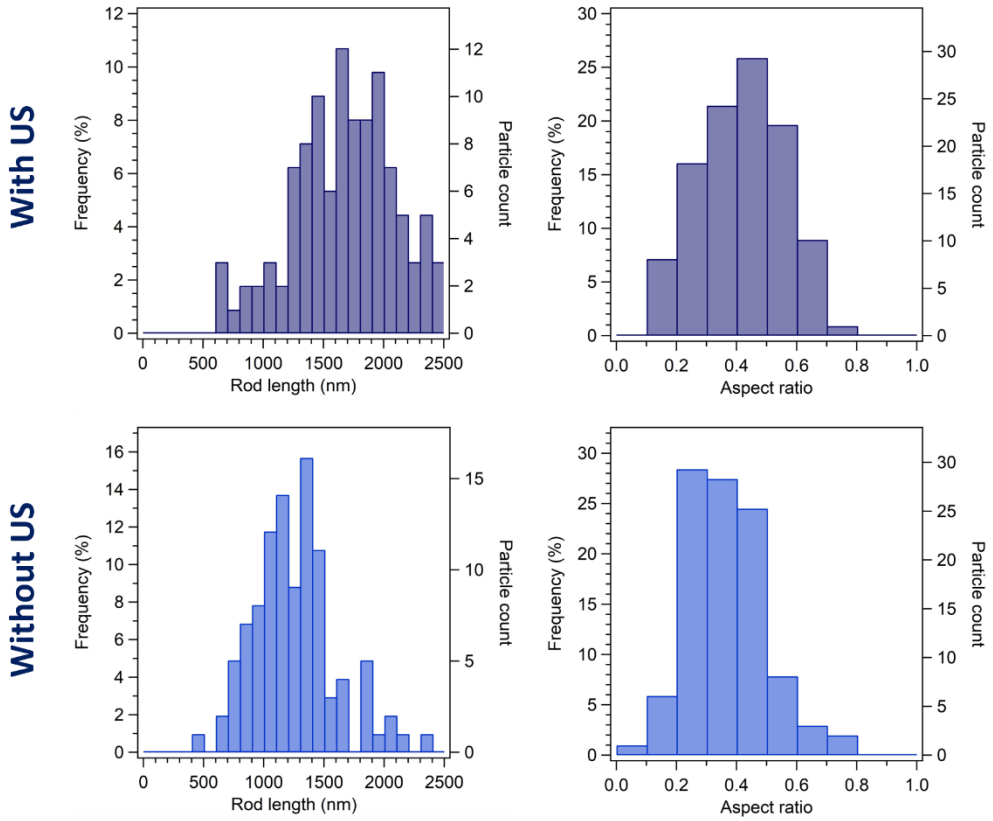

Figure B.7 Histograms representing rod length and aspect ratio distributions of batch samples synthesized by applying (**top**) or not applying (**bottom**) US after acid addition (MO08-b and MO03-b, respectively). [AHM] = 0.20 M; AHM:HNO_3 1:10 mol, reaction time 24 h

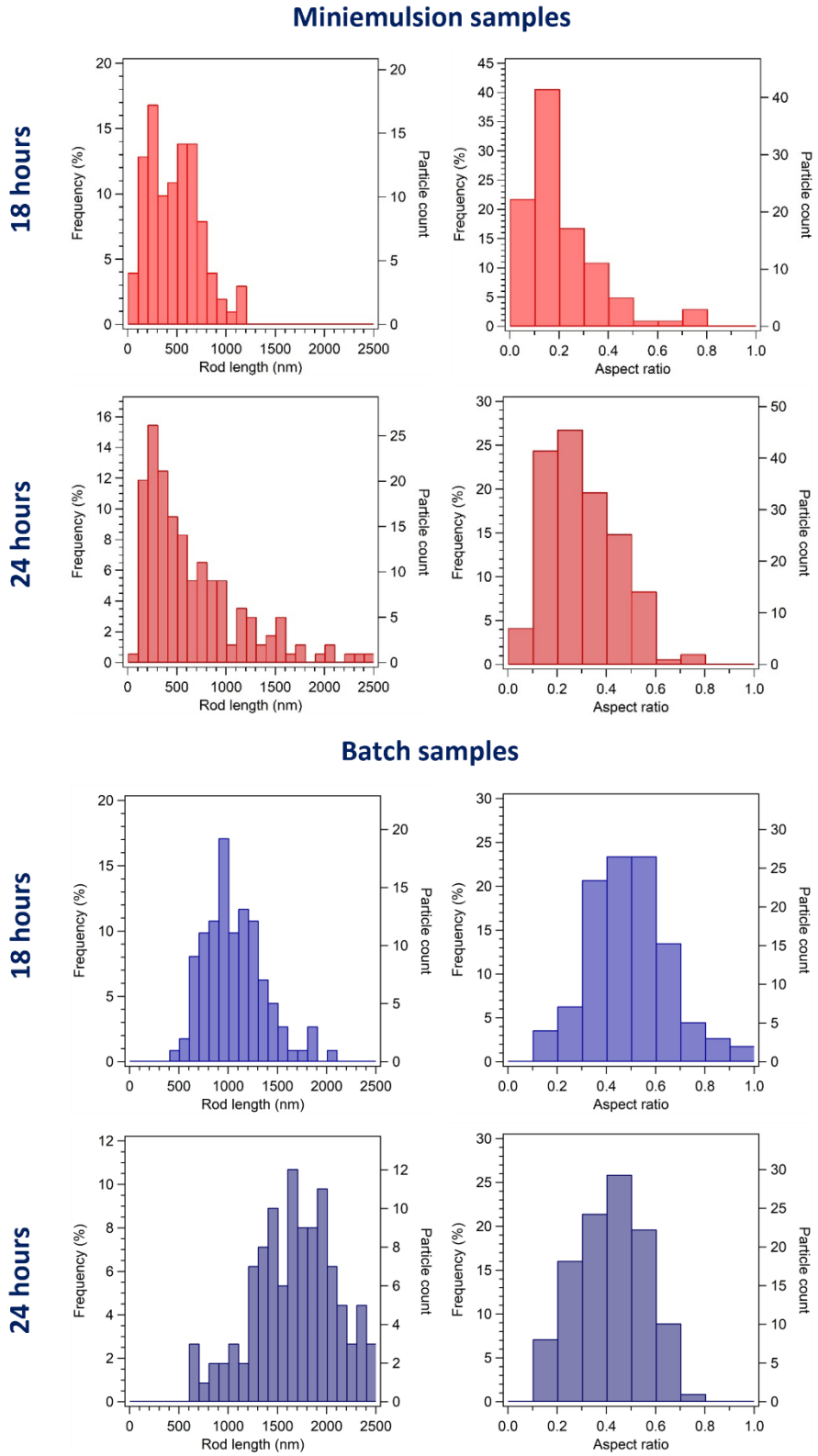

Figure B.8 Histograms representing rod length and aspect ratio distributions of miniemulsion (**top**) and batch (**bottom**) samples synthesized with different reaction times, 18 hours and 24 hours (MO13-me, MO03-me, MO11-b, MO03-b). [AHM] = 0.20 M; AHM:HNO_3 1:10 mol

Table B.3 Average rod length, width and aspect ratio (AR = width / length) and standard deviations of miniemulsion and batch samples synthesized with 18 and 24 hours of reaction time, by applying or not US after acid addition. [AHM] = 0.20 M; AHM: HNO_3 1:10 mol

Approach	Sample	Reaction time (h)	US after acid add.	Length (nm)	Width (nm)	Aspect ratio
Miniemulsion	MO13-me	18	Yes	463 ± 265	79 ± 56	0.2 ± 0.1
	MO03-me	24	Yes	656 ± 499	177 ± 152	0.3 ± 0.1
	MO09-me	24	-	450 ± 248	140 ± 99	0.3 ± 0.1
Batch	MO11-b	18	-	1058 ± 308	547 ± 294	0.5 ± 0.2
	MO03-b	24	-	1697 ± 445	730 ± 345	0.4 ± 0.1
	MO08-b	24	Yes	1248 ± 345	470 ± 234	0.4 ± 0.1

Time-resolved *in situ* SAXS/WAXS study

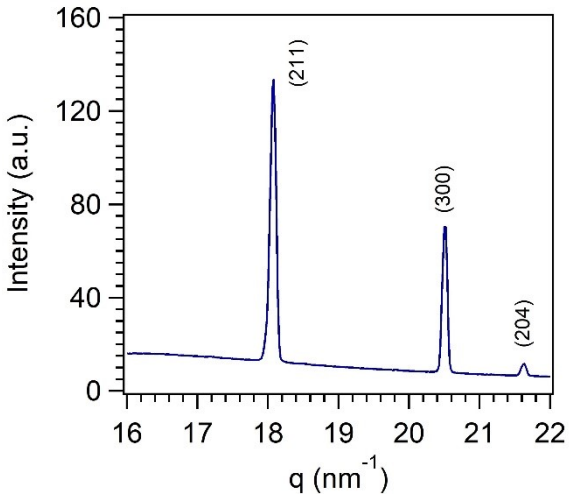

Figure B.9 WAXS profile of a batch sample synthesized with AHM:HNO_3 1:10 mol at the SAXS beamline at Elettra Sincreotrone Trieste and measured after 24 hours

Thermal evolution of h-MoO_3 investigated by *in situ* XAS/XRD

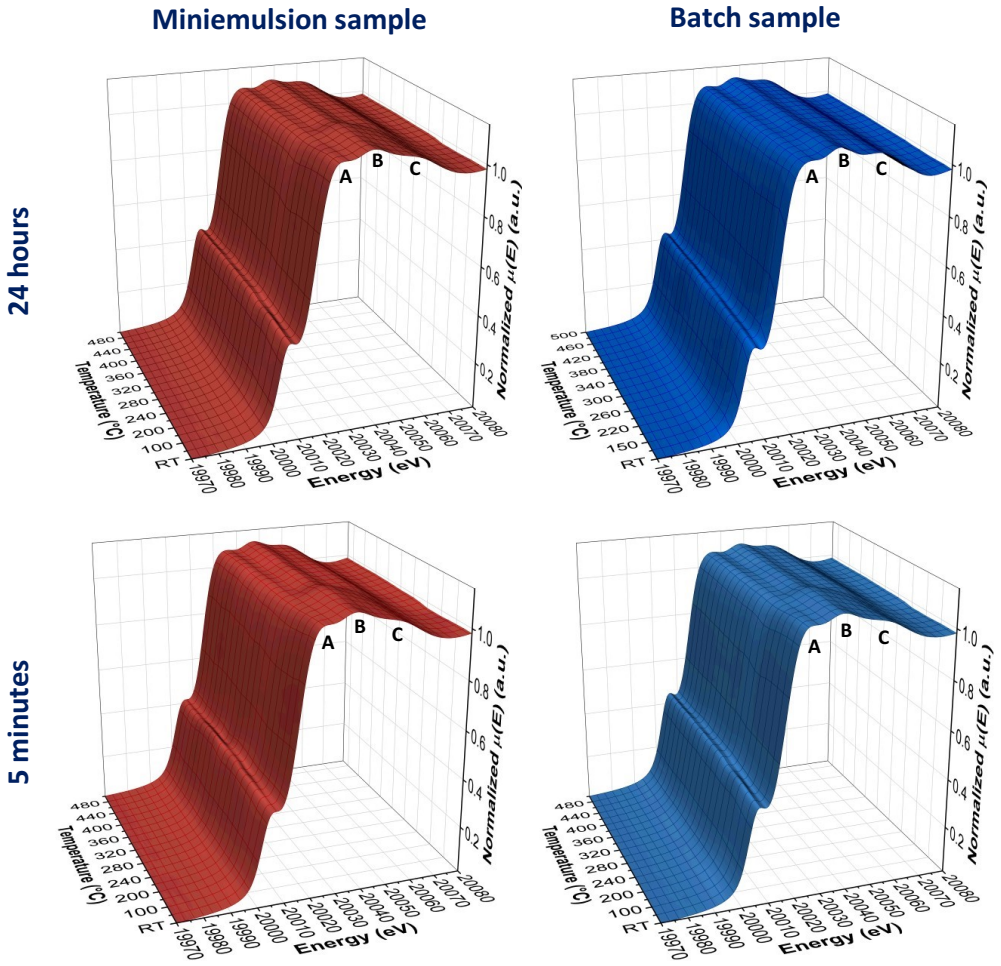

Figure B.10 Comparison of the Mo K-edge XANES spectra recorded during heating up to 500 °C for miniemulsion (**left**) and batch (**right**) samples, synthesized after 24 hours (**top**) and 5 minutes (**bottom**) of reaction time.

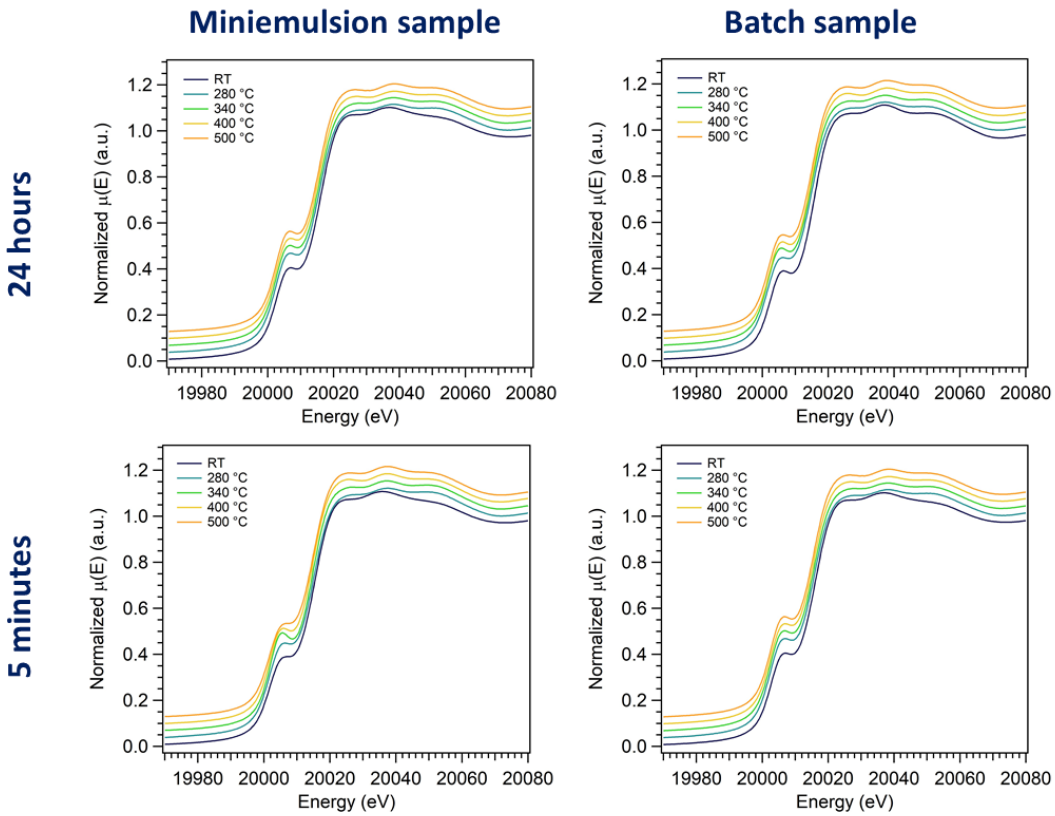

Figure B.11 Comparison of the Mo K-edge XANES spectra recorded during heating up to 500 °C at selected temperatures for miniemulsion (**left**) and batch (**right**) samples, synthesized after 24 hours (**top**) and 5 minutes (**bottom**) of reaction time. Spectra are shifted vertically for clarity.

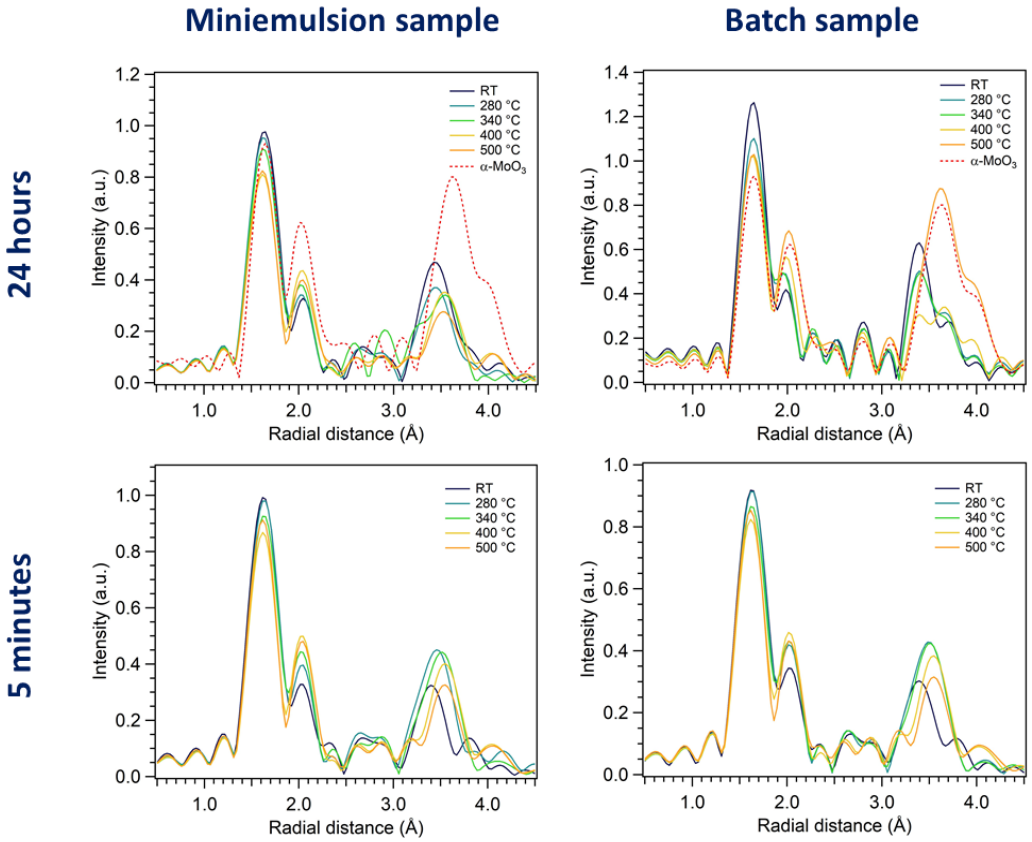

Figure B.12 Comparison of the Fourier transforms of the k^2-weighted EXAFS functions recorded during heating up to 500 °C at selected temperatures for miniemulsion (**left**) and batch (**right**) samples, synthesized after 24 hours (**top**) and 5 minutes (**bottom**) of reaction time. Data are corrected for phase shift

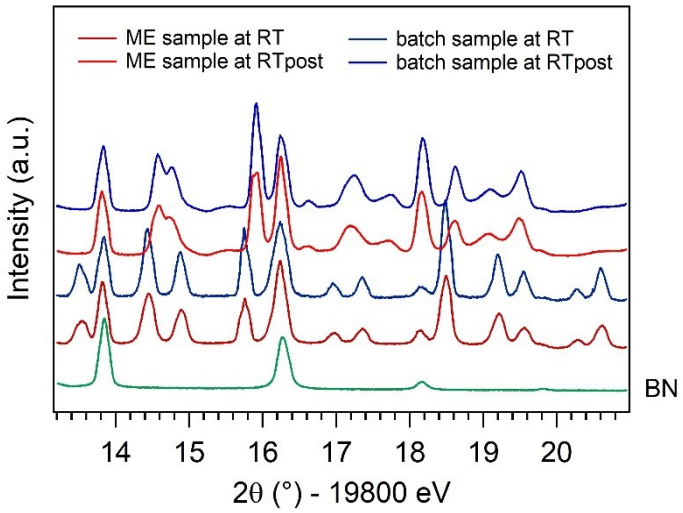

Figure B.13 Comparison of XRD patterns of miniemulsion (red lines) and batch (blue lines) samples pelleted with BN at room temperature (RT) and at room temperature after heating treatment up to 500 °C (RTpost) and XRD pattern of BN (green line) acquired at 19800 eV at the B18 beamline at Diamond Light Source

B.2 Additional Figures and Tables of Chapter 3. Calcium molybdate

Comparison of miniemulsion and batch samples

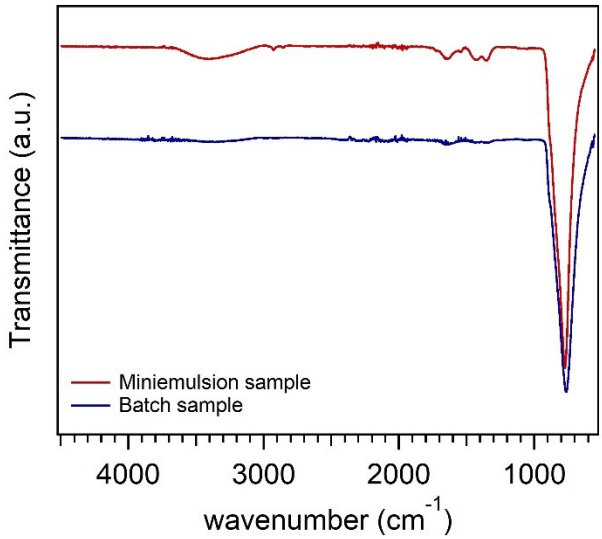

Figure B.14 Comparison of ATR spectra of miniemulsion (red line) and batch (blue line) samples. $[Ca^{2+}] = [MoO_4^{2-}]$; $pH(MoO_4^{2-}) = 6.5$

Effect of precursors concentration

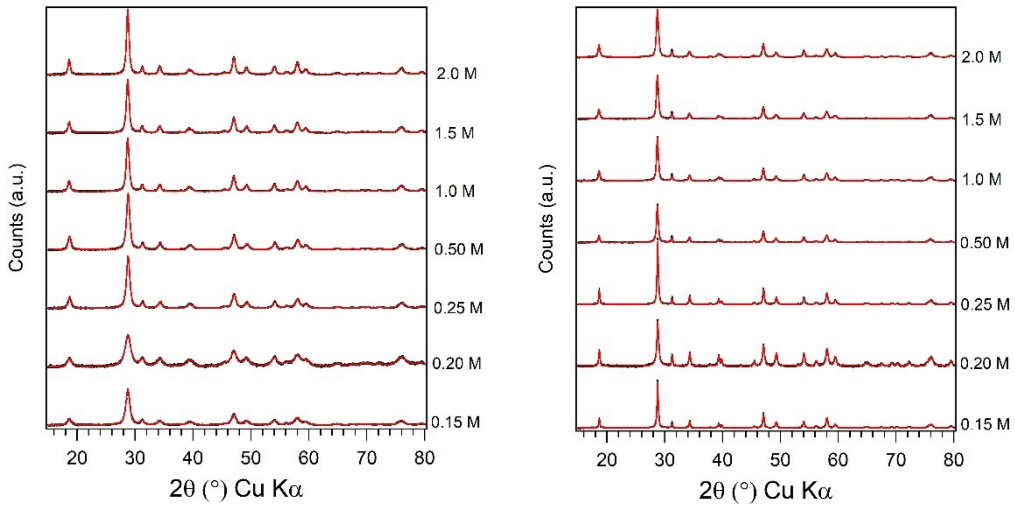

Figure B.15 Fitting of XRD patterns of miniemulsion (**left**) and batch (**right**) samples as a function of precursors concentration. $[Ca^{2+}] = [MoO_4^{2-}]$. $pH(MoO_4^{2-}) = 6.5$

Table B.4 Refined parameters obtained from fitting of XRD patterns of ME samples as a function of precursors concentration. $[Ca^{2+}] = [MoO_4^{2-}]$; $pH(MoO_4^{2-}) = 6.5$

Sample name	$[MoO_4]^{2-}$ (M)	*a* (Å)	*c* (Å)	Cell volume (Å³)	LVol-IB (nm)	R_{wp}
CM02-me	0.15	5.2368 ± 0.0005	11.458 ± 0.001	314.22 ± 0.07	8.36 ± 0.07	7.677
CM01-me	0.20	5.2373 ± 0.0005	11.455 ± 0.001	314.20 ± 0.07	7.87 ± 0.06	7.676
CM03-me	0.25	5.2353 ± 0.0004	11.455 ± 0.001	313.97 ± 0.05	10.68 ± 0.08	7.839
CM04-me	0.50	5.2328 ± 0.0004	11.450 ± 0.001	313.52 ± 0.05	11.04 ± 0.08	8.128
CM05-me	1.0	5.2323 ± 0.0003	11.450 ± 0.001	313.43 ± 0.04	13.18 ± 0.10	8.096
CM06-me	1.5	5.2330 ± 0.0003	11.451 ± 0.001	313.57 ± 0.04	13.33 ± 0.11	8.110
CM07-me	2.0	5.2323 ± 0.0003	11.448 ± 0.001	313.41 ± 0.04	14.84 ± 0.11	7.992

Table B.5 Refined parameters obtained from fitting of XRD patterns of batch samples as a function of precursors concentration. $[Ca^{2+}] = [MoO_4^{2-}]$; $pH(MoO_4^{2-}) = 6.5$

Sample name	$[MoO_4]^{2-}$ (M)	*a* (Å)	*c* (Å)	Cell volume (Å³)	LVol-IB (nm)	R_{wp}
CM02-b	0.15	5.2346 ± 0.0002	11.4631 ± 0.0005	314.10 ± 0.02	28.1 ± 0.3	8.541
CM01-b	0.20	5.2332 ± 0.0001	11.4608 ± 0.0004	313.87 ± 0.02	31.0 ± 0.2	8.109
CM03-b	0.25	5.2338 ± 0.0001	11.4600 ± 0.0004	313.92 ± 0.02	30.0 ± 0.2	8.392
CM04-b	0.50	5.2340 ± 0.0002	11.4557 ± 0.0006	313.83 ± 0.03	19.5 ± 0.1	8.643
CM05-b	1.0	5.2325 ± 0.0002	11.4515 ± 0.0005	313.53 ± 0.03	21.1 ± 0.1	8.451
CM06-b	1.5	5.2322 ± 0.0002	11.4486 ± 0.0005	313.41 ± 0.03	18.9 ± 0.1	8.521
CM07-b	2.0	5.2326 ± 0.0002	11.4509 ± 0.0005	313.52 ± 0.03	17.9 ± 0.1	8.537

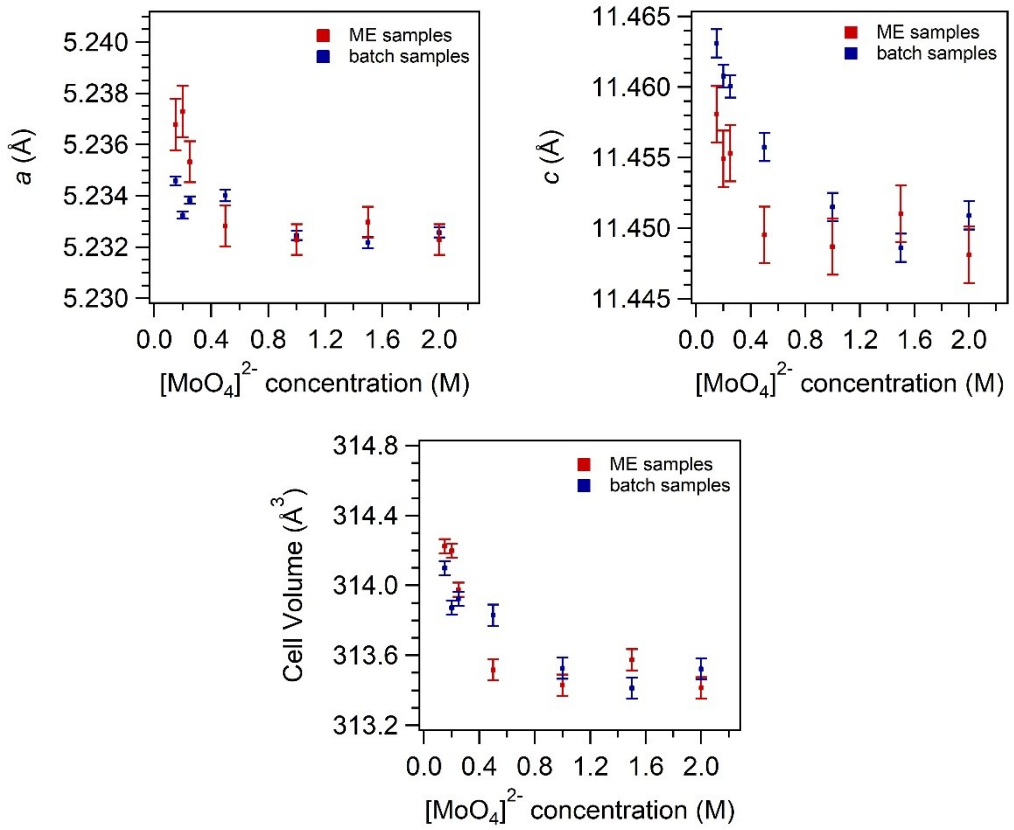

Figure B.16 Estimated cell parameter *a* (**top left**), cell parameter *c* (**top right**), and cell volume (**bottom**), with relative error bars, as a function of precursors concentration, from fitting of XRD patterns of ME (red dots) and batch (blue dots) samples. $[Ca^{2+}] = [MoO_4^{2-}]$; $pH(MoO_4^{2-}) = 6.5$

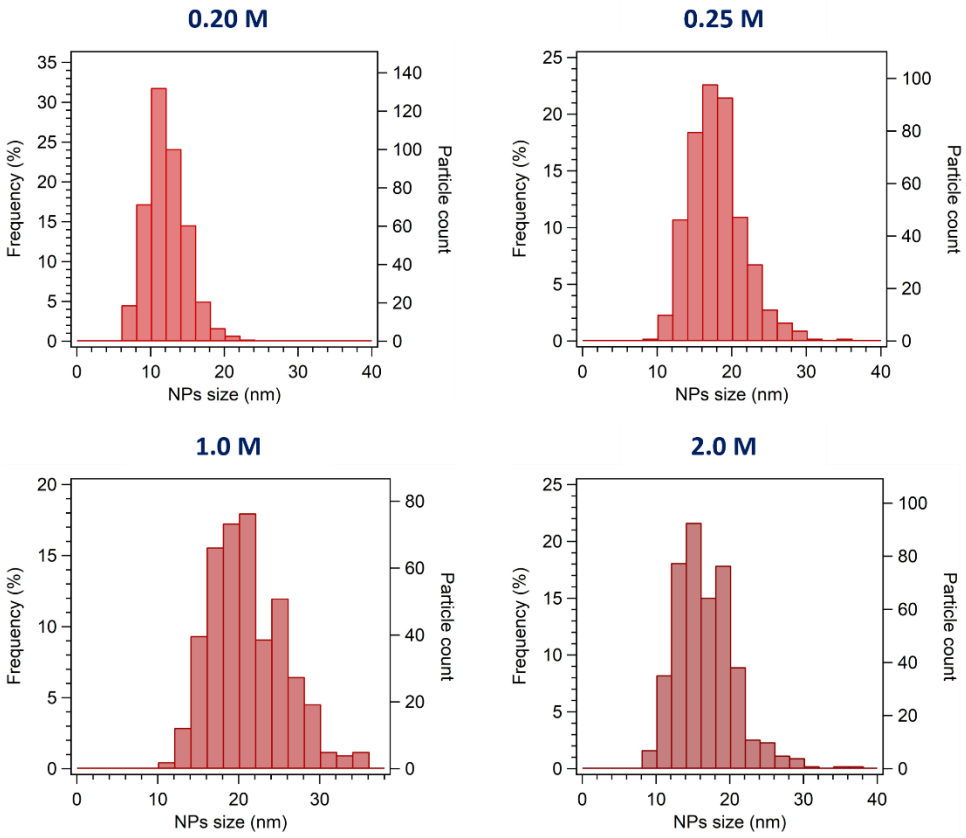

Figure B.17 Histograms displaying NPs size distributions of miniemulsion samples synthesized with different precursors concentrations, determined from TEM micrographs. $[Ca^{2+}] = [MoO_4^{2-}]$; $pH(MoO_4^{2-}) = 6.5$

Table B.6 Average NPs size with relative standard deviations and polydispersity index (PDI) of miniemulsion samples synthesized with different precursors concentrations, determined from TEM micrographs. $[Ca^{2+}] = [MoO_4^{2-}]$; $pH(MoO_4^{2-}) = 6.5$

Sample	$[MoO_4^{2-}]$ (M)	NPs size (nm)	PDI
CM01-me	0.20	12.0 ± 2.7	0.2
CM03-me	0.25	17.9 ± 3.7	0.2
CM05-me	1.0	21.1 ± 4.9	0.2
CM07-me	2.0	16.6 ± 4.1	0.3

Effect of $[MoO_4]^{2-}$ precursor solution pH

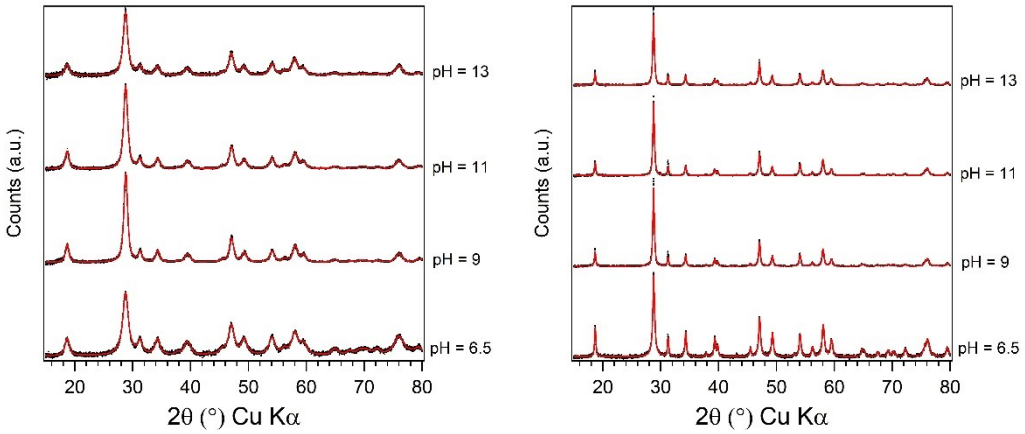

Figure B.18 Fitting of XRD patterns of miniemulsion (**left**) and batch (**right**) samples as a function of $[MoO_4]^{2-}$ precursor solution pH. $[Ca^{2+}] = [MoO_4^{2-}] = 0.20$ M

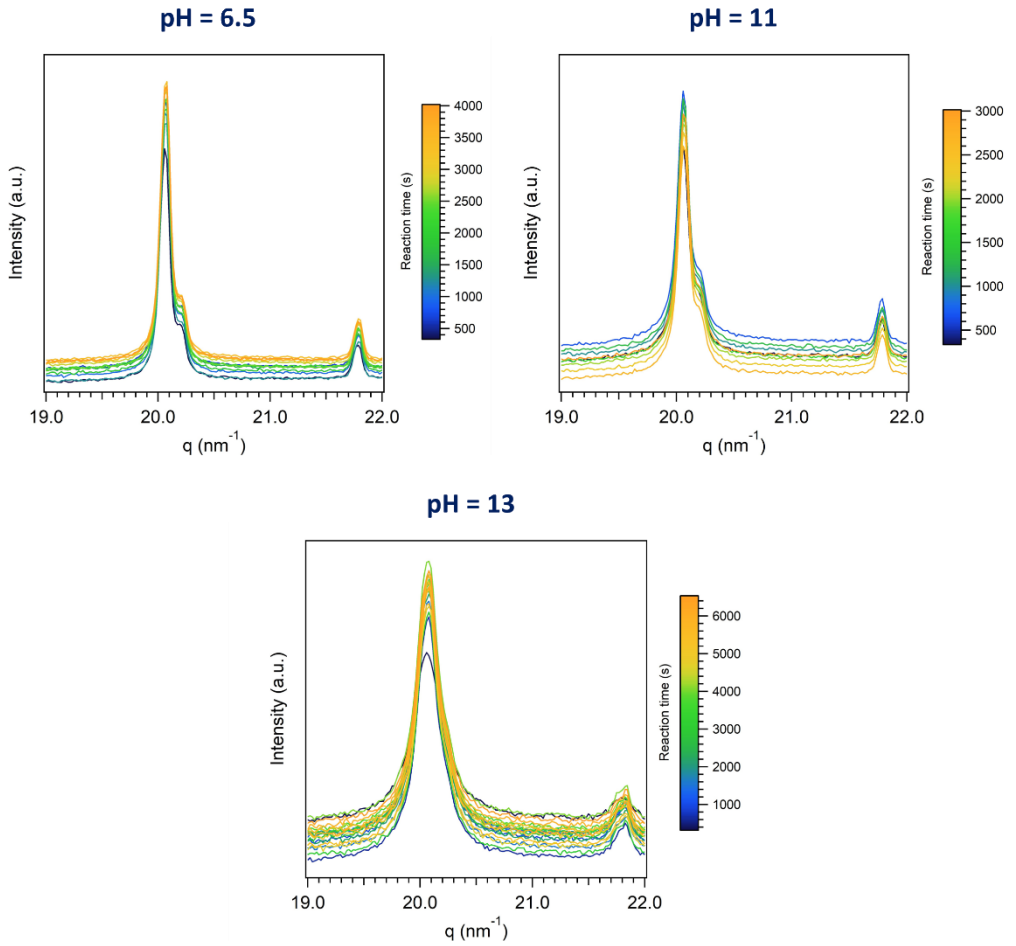

Figure B.19 *In situ* time-resolved WAXS profiles of batch reaction mixtures with different pH values of $[MoO_4]^{2-}$ solution. A pattern every 300 s from the end of Ca^{2+} addition (360 s) to the end of acquisitions (2800-6500 s)

Doping of $CaMoO_4$ with Eu^{3+}

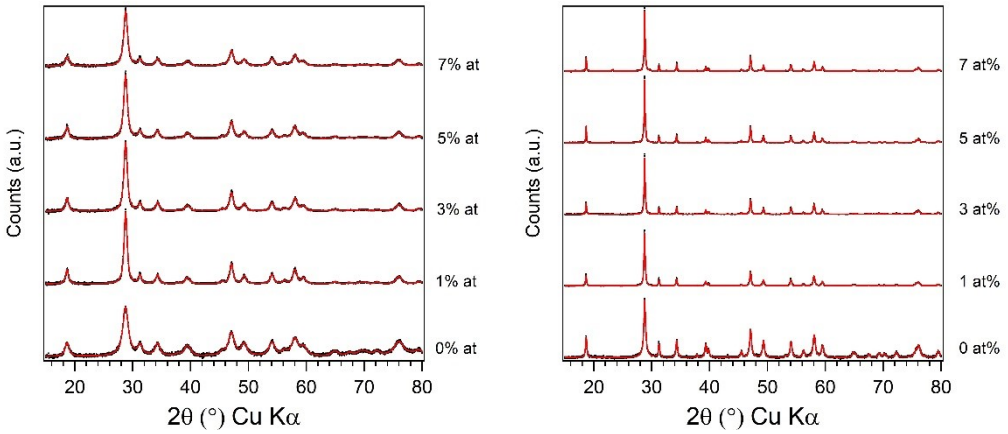

Figure B.20 Fitting of XRD patterns of miniemulsion (**left**) and batch (**right**) samples as a function of doping percentage. $[Ca^{2+}] = [MoO_4^{2-}] = 0.20$ M; $pH(MoO_4^{2-}) = 6.5$; doping percentage calculated as Eu/Mo at.

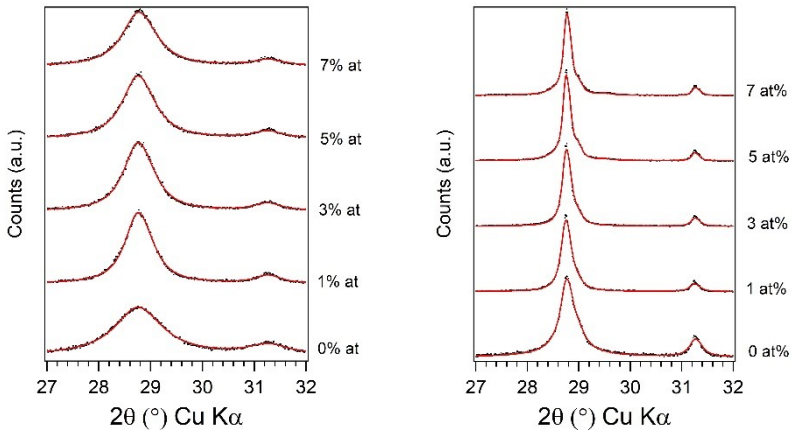

Figure B.21 Zoom of 27-32° 2θ range of the fitted diffractograms of ME (**left**) and batch (**right**) samples as a function of doping percentage, highlighting (112) and (004) reflections, to better visualize the effect of the spurious Eu-based phase on their shape

Table B.7 Refined parameters obtained from fitting of XRD patterns of ME samples as a function of experimental doping percentage. $[Ca^{2+}] = [MoO_4^{2-}] = 0.20$ M; $pH(MoO_4^{2-}) = 6.5$

Sample name	Exp. Eu/Mo at%	*a* (Å)	*c* (Å)	Cell volume (Å^3)	LVol-IB (nm)	R_{wp}
CM01-me	0.0	5.2373 ± 0.0005	11.455 ± 0.001	314.20 ± 0.07	7.87 ± 0.06	7.676
Eu1CM-me	1.3	5.2346 ± 0.0004	11.4559 ± 0.0009	313.90 ± 0.05	10.81 ± 0.06	7.720
Eu3CM-me	3.0	5.2354 ± 0.0004	11.459 ± 0.001	314.09 ± 0.06	9.73 ± 0.06	7.674
Eu5CM-me	4.9	5.2369 ± 0.0004	11.448 ± 0.001	314.23 ± 0.06	8.84 ± 0.05	7.479
Eu7CM-me	7.4	5.2385 ± 0.0005	11.462 ± 0.001	314.55 ± 0.07	8.26 ± 0.05	7.825

Table B.8 Refined parameters obtained from fitting of XRD patterns of batch samples as a function of experimental doping percentage. $[Ca^{2+}] = [MoO_4^{2-}] = 0.20$ M; $pH(MoO_4^{2-}) = 6.5$

Sample name	Exp. Eu/Mo at%	*a* (Å)	*c* (Å)	Cell volume (Å^3)	LVol-IB (nm)	R_{wp}
CM01-b	0.0	5.2332 ± 0.0001	11.4608 ± 0.0004	313.87 ± 0.02	31.0 ± 0.2	8.109
Eu1CM-b	1.3	5.2342 ± 0.0001	11.4631 ± 0.0004	314.05 ± 0.02	30.6 ± 0.3	8.380
Eu3CM-b	3.5	5.2336 ± 0.0001	11.4610 ± 0.0004	313.92 ± 0.02	48.2 ± 1.1	8.911
Eu5CM-b	5.2	5.2326 ± 0.0001	11.4593 ± 0.0004	313.76 ± 0.02	59.2 ± 1.0	8.600
Eu7CM-b	7.5	5.2316 ± 0.0002	11.4613 ± 0.0004	313.88 ± 0.02	56.09 ± 1.0	9.06

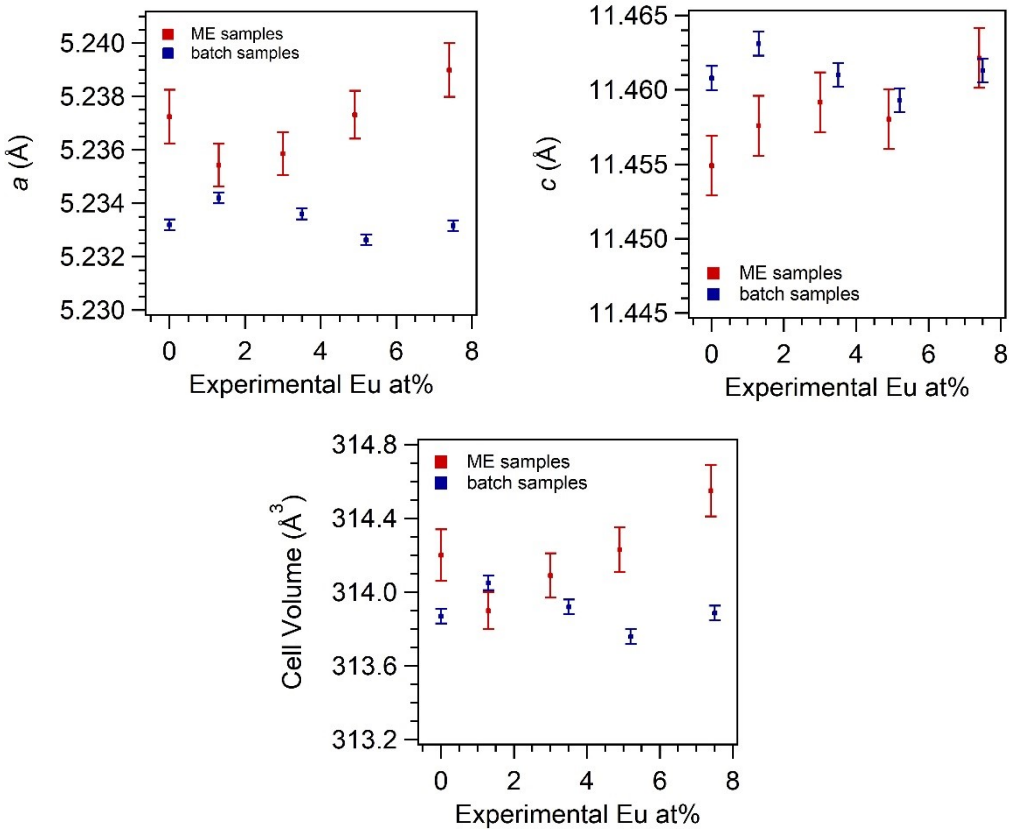

Figure B.22 Estimated cell parameter a (**top left**), cell parameter c (**top right**), and cell volume (**bottom**), with relative error bars, as a function of experimental doping percentage, from fitting of XRD patterns of ME (red dots) and batch (blue dots) samples. $[Ca^{2+}] = [MoO_4^{2-}]$; $pH(MoO_4^{2-}) = 6.5$

Table B.9 Results of the first-shell fitting, in R-space, of the k^2-weighted EXAFS curves (k = 3-17 $Å^{-1}$) at the Mo K-edge (20000 eV) of ME (grey rows) and batch (white rows) samples, as well as reference undoped $CaMoO_4$

Theor. at%	Synthetic approach	Coord. number	Distance Mo-O (Å)	DW (10^{-3} $Å^2$) [a]	E_0 (eV) [b]	R-factor (%)
0	Reference	4	1.77 ± 0.01	2.1 ± 0.5	1.23 ± 0.95	2.0
1	ME	3.8 ± 0.4	1.79 ± 0.01	0.9 ± 0.8	1.67 ± 1.76	1.9
	Batch	3.9 ± 0.4	1.79 ± 0.01	0.8 ± 0.7	2.01 ± 1.66	1.8
3	ME	3.9 ± 0.4	1.79 ± 0.01	1.0 ± 0.8	1.33 ± 1.63	1.7
	Batch	3.9 ± 0.4	1.79 ± 0.01	0.9 ± 0.8	1.67 ± 1.76	2.0
5	ME	3.9 ± 0.3	1.79 ± 0.01	0.9 ± 0.7	1.46 ± 1.52	1.5
	Batch	3.8 ± 0.3	1.79 ± 0.01	1.0 ± 0.7	1.68 ± 1.53	1.7
7	ME	3.9 ± 0.3	1.79 ± 0.01	1.0 ± 0.7	1.34 ± 1.53	1.7
	Batch	3.9 ± 0.4	1.77 ± 0.01	0.8 ± 0.6	1.89 ± 1.47	1.8

[a] Debye-Waller factor; [b] Threshold energy

Photoluminescence properties of Eu-doped CM

Luminescence lifetimes were estimated by fitting the experimental decay data with the following equation:

$$I(t) = A + \sum_i B_\mathrm{i} \cdot e^{\left(\frac{-t}{\tau_\mathrm{i}}\right)}$$

where $I(t)$ is the intensity of emission dependent on time, A is a baseline parameter, B_i are pre-exponential values (partial initial intensity), τ_i is the luminescence lifetime, and t is time.

Relative values of the pre-exponential factors (α_i) were calculated according to:

$$\alpha_i = \frac{B_i}{\sum_n B_n}$$

Average lifetimes (τ_{av}) of emission were calculated according to:

$$\tau_{av} = \frac{\sum_i B_i {\tau_i}^2}{\sum_i B_i \, \tau_i}$$

The quality of the fit was evaluated through χ^2 factor.

Table B.10 Emission lifetimes and relative values of the pre-exponential factors of undoped and Eu-doped ME and batch calcium molybdate samples, calculated at room temperature, employing λ_{exc} = 285 nm (excitation of $CaMoO_4$) and λ_{em} = 500 nm (emission of $CaMoO_4$)

Theor. at%	Synthetic approach	α_1	τ_1 (µs)	α_2	τ_2 (µs)	τ_{av} (µs)	χ^2
0	ME	0.58	2.95(5)	0.42	8.23(4)	8.23(4)	1.097
	Batch	0.36	5.5(2)	0.64	15.14(4)	23.52(7)	1.054
1	ME	0.67	7.0(2)	0.33	12.07(7)	9.4(2)	1.093
	Batch	0.56	4.33(5)	0.44	13.48(3)	10.81(6)	1.122
3	ME	0.71	5.42(6)	0.29	11.63(6)	8.34(9)	1.069
	Batch	0.62	4.02(4)	0.38	11.96(3)	9.13(6)	1.148
5	ME	0.71	3.46(3)	0.29	9.10(4)	6.41(6)	1.048
	Batch	0.65	3.78(5)	0.35	12.00(4)	8.92(7)	1.198
7	ME	0.74	2.90(3)	0.26	7.91(4)	5.36(6)	1.081
	Batch	0.65	7.7(2)	0.35	13.91(8)	10.8(2)	1.078

Table B.11 Emission lifetimes and relative values of the pre-exponential factors of undoped and Eu-doped ME and batch calcium molybdate samples, calculated at room temperature, employing λ_{exc} = 271 nm (excitation of $CaMoO_4$) and λ_{em} = 703 nm or 615 nm ($^5D_0 \rightarrow {}^7F_4$ or $^5D_0 \rightarrow {}^7F_2$ emission lines of Eu^{3+}, respectively)

Theor. at%	Synthetic approach	α_1	τ_1 (µs)	α_2	τ_2 (µs)	τ_{av} (µs)	χ^2
1	ME	0.60	574(8)	0.40	1143(4)	901(9)	1.196
	Batch	0.89	524(5)	0.11	926(10)	596(8)	1.116
3	ME	0.57	570(10)	0.43	1065(4)	858(10)	1.177
	Batch	0.67	470(8)	0.33	784(4)	612(9)	1.112
5	ME	0.62	484(8)	0.38	936(4)	730(9)	1.229
	Batch	0.61	459(8)	0.39	738(4)	602(8)	1.141
7	ME	0.62	432(9)	0.38	792(4)	625(9)	1.150
	Batch	0.44	378(10)	0.56	669(3)	578(7)	1.041

Table B.12 Emission lifetimes and relative values of the pre-exponential factors of undoped and Eu-doped ME and batch calcium molybdate samples, calculated at room temperature, employing λ_{exc} = 393 nm (direct excitation of Eu^{3+}, through $^5L_6 \leftarrow {}^5D_0$) and λ_{em} = 703 nm or 615 nm ($^5D_0 \rightarrow {}^7F_4$ or $^5D_0 \rightarrow {}^7F_2$ emission lines of Eu^{3+}, respectively)

Theor. at%	Synthetic approach	α_1	τ_1 (µs)	α_2	τ_2 (µs)	τ_{av} (µs)	χ^2
1	ME	0.49	477(10)	0.51	908(4)	762(8)	1.141
	Batch	0.92	499(4)	0.08	885(16)	549(7)	1.102
3	ME	0.55	494(12)	0.45	876(4)	719(11)	1.206
	Batch	0.62	419(8)	0.38	664(4)	539(9)	1.057
5	ME	0.51	408(10)	0.49	744(4)	622(9)	1.228
	Batch	0.69	416(8)	0.31	662(4)	519(9)	1.086
7	ME	0.50	317(11)	0.50	629(3)	533(9)	1.142
	Batch	0.70	402(9)	0.30	623(5)	490(10)	1.074

Viscosity and dielectric constant of ethanol/water mixtures

Table B.13 Viscosity and dielectric constant of ethanol/water mixtures with different composition at 20 °C and –4 °C

EtOH wt%	x EtOH	$\eta_{m,20\,°C}$ (mPa s) [a]	$\eta_{m,-4\,°C}$ (mPa s) [a]	$\eta_{m,20\,°C}$ / $\eta_{m,-4\,°C}$	$\varepsilon_{m,20\,°C}$ [b]	$\varepsilon_{m,-4\,°C}$ [b]	$\varepsilon_{m,20\,°C}$ / $\varepsilon_{m,-4\,°C}$
0	0	1.0	2.1	0.48	80.2	89.3	0.90
10	0.042	1.8	3.8	0.47	73.5	81.6	0.90
20	0.089	1.8	3.8	0.47	66.4	73.5	0.90
30	0.143	2.1	4.6	0.46	58.9	64.9	0.91
50	0.281	2.5	5.2	0.48	43.8	47.8	0.92
70	0.477	2.1	4.1	0.51	31.7	34.3	0.92
100	1	1.2	2.0	0.60	25.5	28.8	0.89

[a,b] Viscosity η_m and dielectric constant ε_m of EtOH/H_2O mixtures at 20 °C and –4 °C, calculated by employing the Jouyban-Acree equation, that relates some chemico-physical parameters of binary mixtures of solvents with their composition and temperature.[340] Exp. values of η_m measured by employing a rheometer were found in accordance with theoretical values.

Effect of precursors concentration

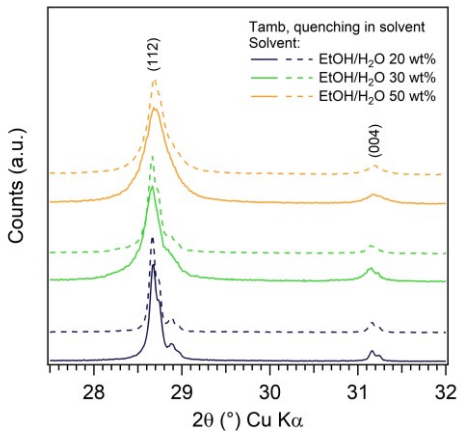

Figure B.23 Comparison of XRD patterns of CM synthesized by microfluidic approach with Setup A at ambient temperature with different percentages of ethanol in the solvent mixture and quenching in solvent mixture, employing different concentrations of precursors solutions (0.02 M: dashed lines; 0.05 M: solid lines)

Effect of method of quenching

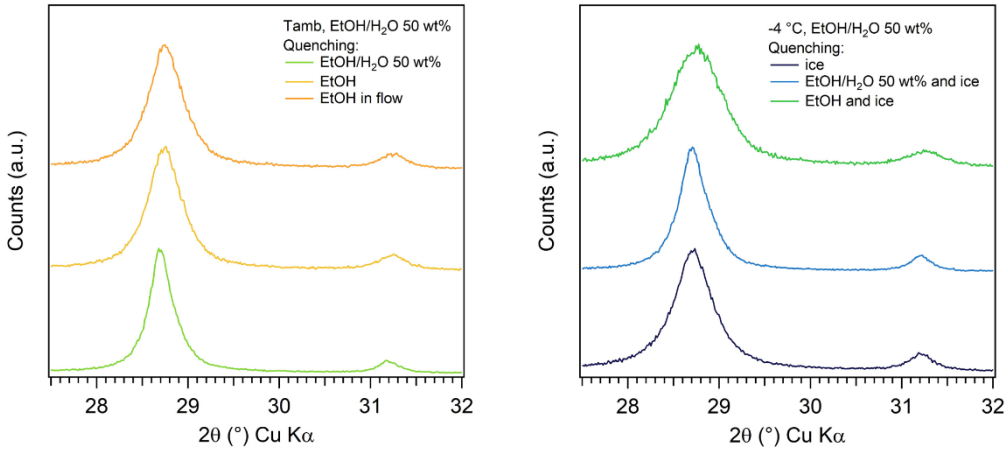

Figure B.24 Comparison of XRD patterns of CM synthesized by microfluidic approach with 50 wt% EtOH/water reaction solvent at room temperature (**left**) and at –4°C (**right**) and quenched with different methods

Doping of $CaMoO_4$ with Eu^{3+}

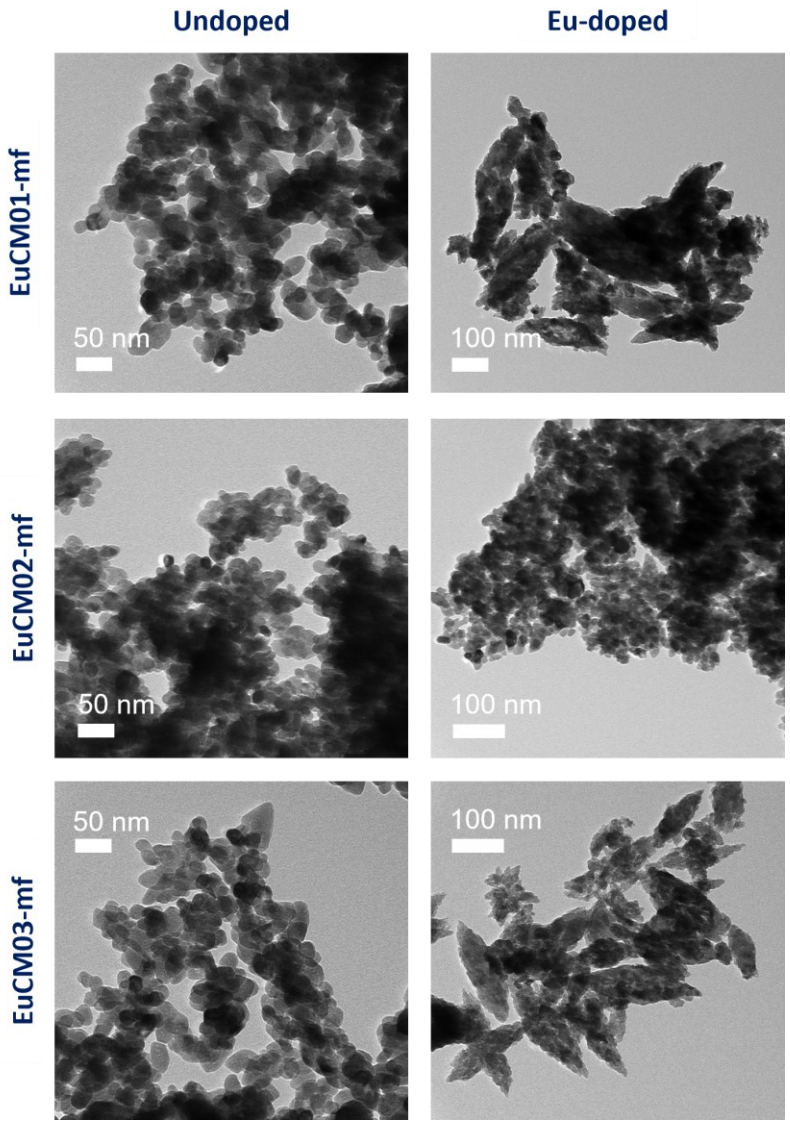

Figure B.25 Comparison of TEM micrographs of undoped (**left**) and Eu-doped (**right**) CM samples synthesized by microfluidics employing different sets of reaction conditions. *EuCM01-mf*: SetupA, Tamb, 50 wt% EtOH/H_2O as solvent, quenching in EtOH; *EuCM02-mf*: Setup A, –4 °C, 50 wt% EtOH/H_2O as solvent, quenching in EtOH; *EuCM03-mf*: Setup B, Tamb, 50 wt% EtOH/H_2O as solvent, quenching in line with EtOH

B.3 Additional Figures and Tables of Chapter 4. Pd nanoparticles on mesoporous silica

Non-porous pristine silica support

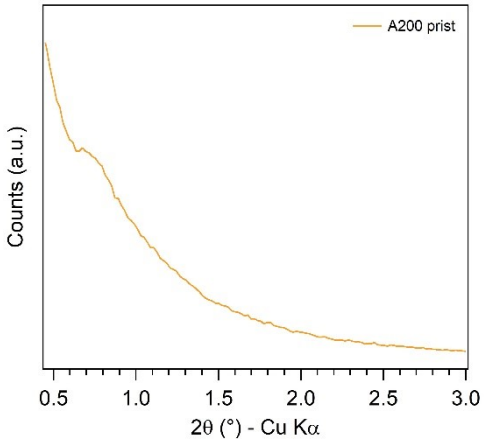

Figure B.26 SAXS pattern of pristine non-porous A200 sample

Pd(II)-impregnated mesoporous and non-porous silica samples

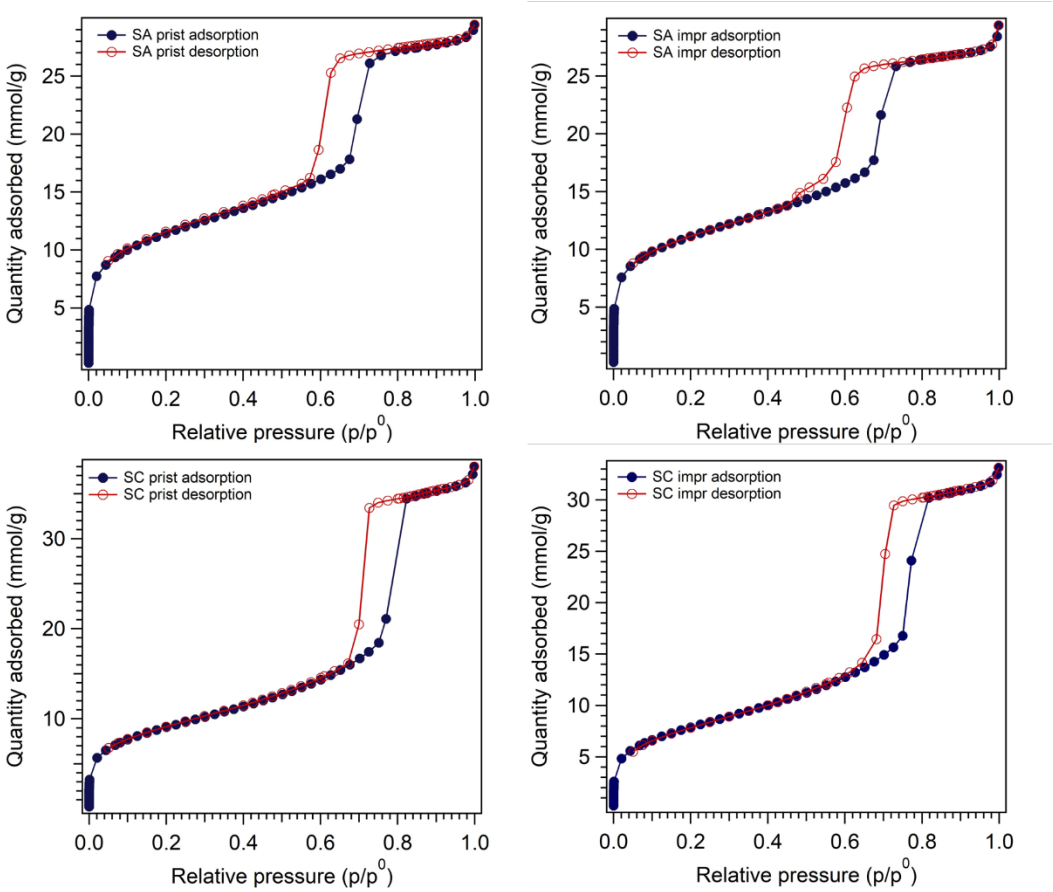

Figure B.27 Nitrogen physisorption isotherms of SBA-15 mesoporous silica samples with pore size of 7 nm (**top**) and 9 nm (**bottom**), before (**left**) and after (**right**) incipient wetness impregnation with Pd(II) solution

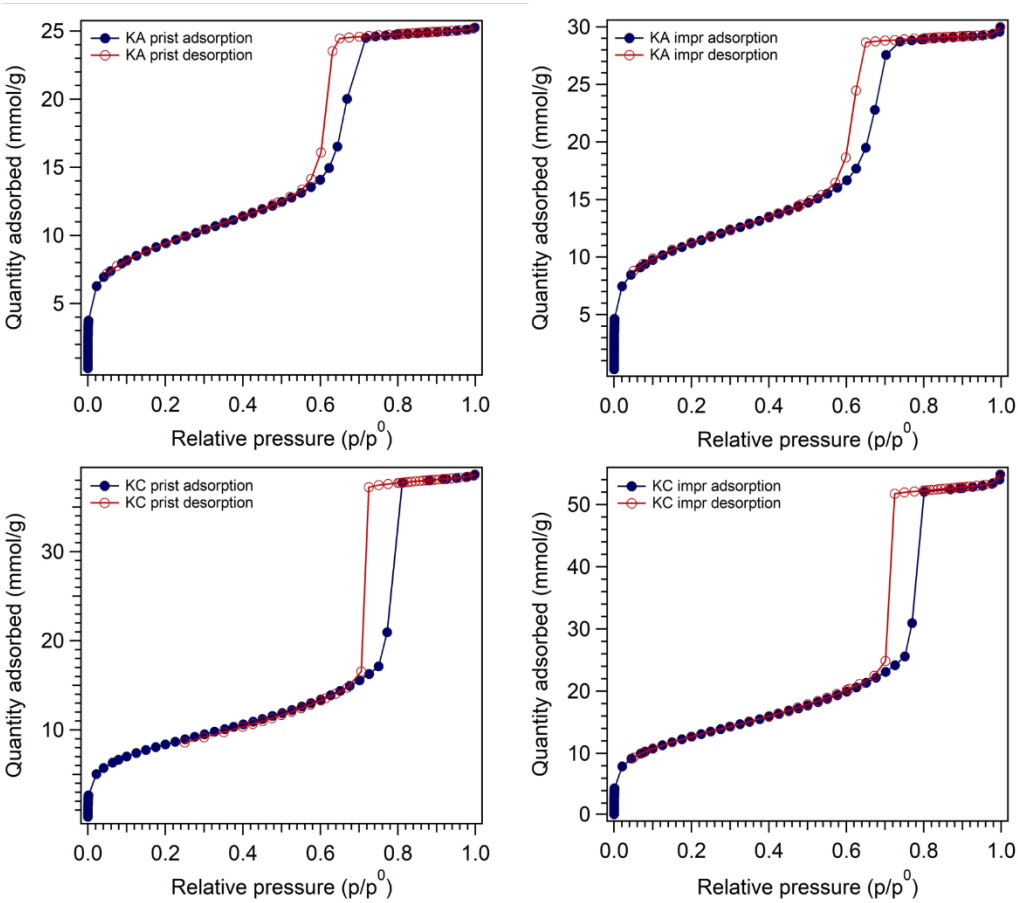

Figure B.28 Nitrogen physisorption isotherms of KIT-6 mesoporous silica samples with pore size of 7 nm (**top**) and 9 nm (**bottom**), before (**left**) and after (**right**) incipient wetness impregnation with Pd(II) solution

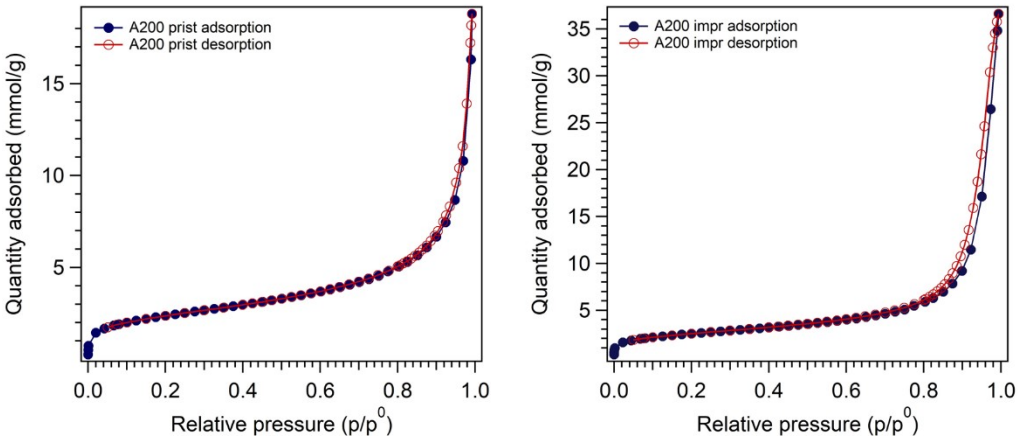

Figure B.29 Nitrogen physisorption isotherms of A200 silica samples, before (**left**) and after (**right**) incipient wetness impregnation with Pd(II) solution

TPR followed by *in situ* Pd K-edge XAS

Sample *KCimpr* was flushed with reducing atmosphere for about 30 minutes before starting the heating ramp: at room temperature the sample was already partially reduced, confirming the high reducibility of PdO nanoparticles.

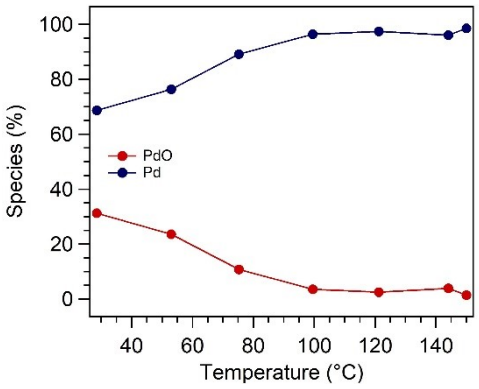

Figure B.30 Relative fraction of PdO and Pd species as a function of temperature obtained by linear combination fitting of Pd K-edge XANES spectra of impregnated KIT-6 mesoporous silica with d_{DFT} 9 nm (*KCimpr*)

Catalytic activity towards CO oxidation

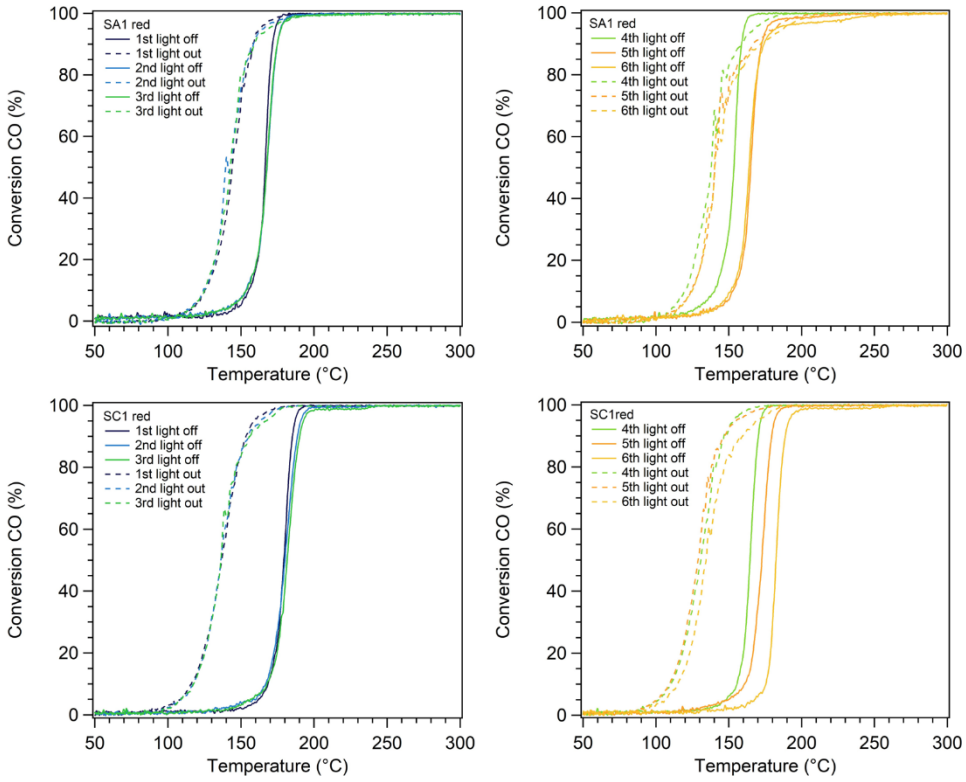

Figure B.31 Catalytic conversion curves of Pd on SBA-15 mesoporous silica, with pore size of 7 nm (**top**, *SAred* sample) and 9 nm (**bottom**, *SCred* sample), acquired before (1st, 2nd and 3rd cycle, **left**) and after (4th, 5th, and 6th cycle, **right**) the *in situ* reduction step

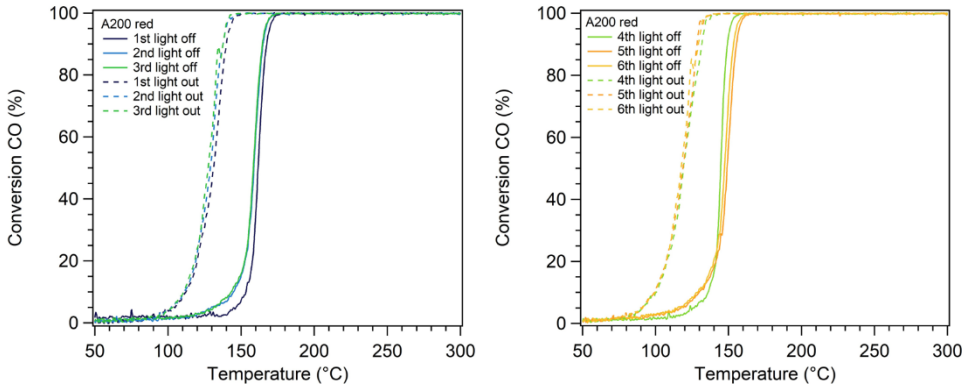

Figure B.32 Catalytic conversion curves of Pd on non-porous silica (*A200red* sample), acquired before (1st, 2nd and 3rd cycle, **left**) and after (4th, 5th, and 6th cycle, **right**) the *in situ* reduction step

Operando Pd K-edge XAS analysis

Table B.14 Relative percentage of PdO species during two consecutive catalytic cycles performed at SAMBA beamline at the Soleil synchrotron, while measuring *operando* XAS, as estimated through linear combination fitting of Pd K-edge XANES spectra. Pd species relative fraction was calculated as Pd(%) = 100 - PdO(%)

Sample	Percentage of PdO species (%)							
	1st light off		1st light out		2nd light off		2nd light out	
	start	end	start	end	start	end	start	end
SA	4	91	100	86	88	100	100	92
SC	0	81	97	81	84	100	100	87
KC	11	84	92	83	83	93	95	88

C

List of Figures and Tables

In this Appendix Section, a list of Figures and Tables of this Ph.D. Thesis is reported.

C.1 List of Figures

C.2 List of Tables

D

Scientific contributions

D.1 Publications

ISI-papers

Exploring the phase-selective, green hydrothermal synthesis of upconverting doped sodium yttrium fluoride: effects of temperature, time and precursors

Nora Jannsen, Stefano Diodati, Nicola Dengo, Francesca Tajoli, Nicola Vicentini, Giacomo Lucchini, Adolfo Speghini, Denis Badocco, Paolo Pastore, Silvia Gross

Chem. Eur. J. **2019**, *25*, 13624-13634; doi:10.1002/chem.201903261

Low-temperature solution crystallization of nanostructured oxides and thin films

Iñigo Bretos, Stefano Diodati, Ricardo Jiménez, Francesca Tajoli, Jesús Ricote, Giulia Bragaggia, Marina Franca, Maria Lourdes Calzada, Silvia Gross

Chem. Eur. J. **2020**, *26*, 1-24; doi: 10.1002/chem.202000448

Microfluidic crystallization of surfactant-free doped zinc nanoparticles for optical bioimaging applications

Francesca Tajoli, Nicola Dengo, Maddalena Mognato, Paolo Dolcet, Andrea Faresin, Giacomo Lucchini, Jan-Dierk Grunwaldt, Xiaohui Huang, Denis Badocco, Michele Maggini, Christian Kübel, Adolfo Speghini, Tommaso Carofiglio, Silvia Gross

ACS Appl. Mater. Interfaces, **2020**, *12*, 44074-44087; doi: 10.1021/acsami.0c13150

Work function tuning in hydrothermally synthesized vanadium-doped MoO_3 and Co_3O_4 mesostructures for energy conversion devices

Pietro Dalle Feste, Matteo Crisci, Federico Barbon, Francesca Tajoli, Marco Salerno, Filippo Drago, Mirko Prato, Silvia Gross, Teresa Gatti, Francesco Lamberti

Appl. Sci. **2021**, *11*, 2016; doi: 10.3390/app11052016

Pursuing unprecedented morphologies of halide-free Pd nanoparticles by tuning nucleation and growth

Federico Spolaore, Francesca Tajoli, Maria Chiara Dalconi, Christoph Hengst, Franz Dornhaus, Silvia Gross

Dalton Trans. **2022**, *52*, 11476-11484; doi: 10.1039/D2DT01498J

Exploring the role of miniemulsion nanodroplet confinement on the crystallization of MoO_3: morphology control and insight on crystal formation by in situ *time-resolved SAXS/WAXS*

Francesca Tajoli, Maria Vittoria Massagrande, Rafael Muñoz-Espí, Silvia Gross

Nanomaterials, in press

Non-ISI not reviewed paper

Sintesi sostenibili di materiali inorganici a bassa temperatura

Federico Barbon, Giulia Bragaggia, Marina Franca, Francesco Lamberti, Chiara Mazzariol, Pietro Ostellari, Francesca Tajoli, Susanna Tinello, Silvia Gross

La Chimica e l'Industria, Anno VI, *1,* gennaio/febbraio 2022, 22-28 doi: 10.17374/CI.2022.104.1.22

Book chapter

Further sustainable and/or unconventional low temperature wet-chemistry synthetic methods

Federico Barbon, Francesca Tajoli, Federico Spolaore, Silvia Gross

In *Green, unconventional wet-chemistry based synthesis of inorganic nanomaterials: combining sustainability with functionality*

Royal Chemical Society, in press (Summer 2023)

D.2 Conferences

Oral presentations

Effect of space confinement on crystallization of MoO_3 synthetized by inverse miniemulsion – an in situ *SAXS/WAXS study*

Francesca Tajoli, Nicola Dengo, Barbara Sartori, Heinz Amenitsch, and Silvia Gross

"SILS Meeting 2019", Camerino (Italy), 09-11/09/2019

Space matters: effect of miniemulsion droplets confinement on the crystallization of undoped and Eu-doped $CaMoO_4$ nanophosphors

Francesca Tajoli, Chiara Mazzariol, Paolo Dolcet, Alexander Sedykh, Klaus Müller-Buschbaum, and Silvia Gross

"7th Crystallization in Porous Media" (CRYSPOM) workshop, online (Pau, France), 07-09/06/2021

Following crystallization of inorganic systems in confined space

Francesca Tajoli, Paolo Dolcet, and Silvia Gross

"Società Italiana Luce di Sincrotrone" meeting (SILS2021), online (Bologna, Italy), 21-23/06/2021

Microfluidic crystallization of surfactant-free doped zinc sulfide nanoparticles for optical bioimaging applications

Francesca Tajoli, Nicola Dengo, Paolo Dolcet, Maddalena Mognato, Michele Maggini, Tommaso Carofiglio, and Silvia Gross

"6th Green and Sustainable Chemistry Conference" (GREEN2021, Elsevier), online, 16-18/11/2021

Following crystallization of inorganic systems in the confined space of miniemulsion droplets

Francesca Tajoli, Paolo Dolcet, and Silvia Gross

Flash presentation at "InoMat2021" Ph.D. international school, Bardonecchia, Italy, 17/12/2021

Does space confinement affect the crystallization of inorganic systems?

Francesca Tajoli, Chiara Mazzariol, Pietro Ostellari, Paolo Dolcet, Klaus Müller-Buschbaum, Jan-Dierk Grunwaldt, and Silvia Gross

"Inorg2022", XLVIII Congresso Nazionale di Chimica Inorganica, Pisa, Italy, 06-09/09/2022

Poster presentations

Continuous-flow synthesis of pure and doped ZnS nanoparticles via a green microfluidic approach

Francesca Tajoli, Andrea Faresin, Nicola Dengo, Tommaso Carofiglio, Michele Maggini, Adolfo Speghini, and Silvia Gross

International Conference "Advanced Inorganic Materials: Green and Unconventional Synthesis Approaches and Functional Assessment" 2018, Padova (Italy) 05-07/09/2018

Continuous-flow synthesis of pure and doped ZnS nanoparticles via a green microfluidic approach

Francesca Tajoli, Andrea Faresin, Nicola Dengo, Tommaso Carofiglio, Michele Maggini, Adolfo Speghini, and Silvia Gross

"VII Workshop Nazionale del Gruppo Interdivisionale di Green Chemistry – Chimica Sostenibile della SCI", Padova (Italy), 05/07/2019

Following crystallization of ZnS nanostructures in confined space by in situ *continuous-flow miniemulsion process*

Nicola Dengo, Francesca Tajoli, Barbara Sartori, Christoph Seitz, Bernd Smarsly, Heinz Amenitsch, and Silvia Gross

"SILS Meeting 2019", Camerino (Italy), 09-11/09/2019

Surfactant-free and green microfluidic synthesis of very small zinc sulfide nanoparticles for optical bioimaging applications

Francesca Tajoli, Andrea Faresin, Nicola Dengo, Tommaso Carofiglio, Michele Maggini, Adolfo Speghini, and Silvia Gross

"29th ATC2020: Industrial Inorganic Chemistry – Materials and Processes" conference, Frankfurt am Main (Germany), 20-21/02/2020

Following crystallization of inorganic structures in confined spaces

Francesca Tajoli

"31st HERCULES2021 European School - Neutrons and Synchrotron Radiation for Science", online, 26/02/2021 – Best poster presentation

Following crystallisation of inorganic systems in the confined spaces of miniemulsion droplets

Francesca Tajoli, Paolo Dolcet, and Silvia Gross

"Understanding crystallisation: Faraday discussion", York (UK), 28-30/03/2022

Acknowledgements

At the end of this journey, there are many people that I would like to sincerely acknowledge for their support in various capacities.

First of all, I would like to deeply thank my supervisor, Prof. Silvia Gross, who has been my mentor during these years. I am deeply grateful to her for giving me the opportunity to undertake this Ph.D., always blindly trusting my capabilities, supporting, encouraging and challenging me, showing passion and enthusiasm. She has provided me manifold scientific opportunities and fostered my personal and scientific growth as an early career academic with many insightful scientific discussions.

Ministero dell'Istruzione, dell'Università e della Ricerca and Scuola di Dottorato in Scienze Molecolari (Dipartimento di Scienze Chimiche, Università degli Studi di Padova) are kindly acknowledged for the financial support.

I am very thankful to Dr. Federico Zorzi and Prof. Fabrizio Nestola (Department of Geosciences, Università degli Studi di Padova), for hosting me in their laboratory and for teaching me a lot about diffraction and giving me insightful advice. I gratefully thank also Prof. Michele Maggini and Prof. Tommaso Carofiglio (Università degli Studi di Padova) for the help in the microfluidic syntheses and for allowing me to use their equipment.

Most sincere thanks to Dr. Paolo Dolcet, who concretely contributed to the beamtime planning and XAS data acquisition and analysis, but also mentored me during these years, providing sound guidance, constantly supporting and trusting me. Thanks for the invaluable help, patience and friendship.

I am very thankful to Prof. Jan-Dierk Grunwald (Karlsruhe Institute of Technology, Germany) for allowing me in his group to perform catalytic tests and to participate in a beamtime with his group, and for the warm hospitality as well. I am also grateful to Dr. Maria Casapu, for the insightful discussions and advice for the interpretation of the catalytic results.

I am very thankful to Prof. Michael Fröba and Sarah Class (University of Hamburg, Germany) for providing me mesoporous silica materials and for the valuable inputs to my research and inspiring advice.

I also thank Prof. Klaus Müller-Buschbaum and Alexander Sedykh (University of Giessen, Germany) and Dr. Ilaria Fortunati (Università degli Studi di Padova) for their work on the characterization of the photoluminescence properties of doped calcium molybdate and for precious discussion on their interpretation.

Kind acknowledgments also to Elettra Sincrotrone Trieste (proposal 20192141), Diamond Light Source (proposal SP23804), Soleil synchrotron (proposal 20201498 and 20211613) and Swiss Light Source (proposal 20191033) for providing beamtimes and to the CALIPSO program of the European Union (Grant agreement ID: 312284) for granting me financial support for many of them. Moreover, I am thankful to the beamline scientists for the help in planning challenging beamtimes and the support during experiments, in particular Dr. Barbara Sartori and Prof. Heinz Amenitsch (SAXS beamline at Elettra Sincrotrone Trieste and Graz University of Technology, Austria), Dr. Veronica Celorrio and Dr. Giannantonio Cibin (B18 beamline at Diamond Light Source, UK), Dr. Emiliano Fonda (SAMBA beamline at Soleil synchrotron, France), and Dr. Adam Clark (Super-XAS beamline at Swiss Light Source, Switzerland).

I am also thankful to KNMF facility for providing machine time (proposal 2022-027-031257) and to Dr. Carina Maliakkal and Dr. Di Wang (INT-KNMF, Karlsruhe Institute of Technology, Germany) for STEM and electron tomography measurement, and also for allowing me to witness them and employ their advanced instrumentation.

I would also like to acknowledge all the people in the University of Padova which helped me by carrying out some analyses on my samples. In particular, Prof. Paolo Pastore and Prof. Denis Badocco, who performed ICP-MS measurements, Dr. Federico Caicci and Dr. Francesco Boldrin, who performed TEM analyses. Prof. Fabrizio Mancin is also acknowledged for allowing me to use the DLS instrument.

I am also grateful to Prof. Antonino Polimeno, Prof. Mirko Zerbetto and Dr. Andrea Piserchia for their work on the theoretical modeling of the effects of space confinement of micelles and for the enriching collaboration.

My sincere thanks to Pietro, Chiara, and Maria Vittoria, who actively helped in this work and whom I had the pleasure to mentor.

There are others not associated with this Thesis in an official capacity, but who have nonetheless significantly contributed. Thanks to my lab-mates who joined beamtimes, and tireless carried out experiments with me during days and nights, thanks for the fun and for being always helpful. I wish to thank Marina, for her precious friendship and for being such a great (also emotional) support during this journey together, I would not have been the same without you. Thanks to Giulia, for being always present, caring and supporting, and to Federico, Nicola D., and Nicola V. for their daily collaboration, mentoring and helpful advice at the beginning of this journey.

Finally, I would like to thank my family and friends for their love, support and motivation. The most hearted thanks go to my husband, who boundless believes in me and encouraged me since the beginning.